NASA TECHNICAL TRANSLATION

NASA TT F-515

c. 1

TECH LIBRARY KAFB, NM
0069018

NASA TT F-515

LOAN COPY: RETURN TO
AFWL (WLIL-2)
KIRTLAND AFB, N MEX

PHYSICS OF PLANETS

by V. I. Moroz

"Nauka" Press,
Moscow, 1967

NATIONAL AERONAUTICS AND SPACE ADMINISTRATION • WASHINGTON, D. C. • APRIL 1968

TECH LIBRARY KAFB, NM
0069018

PHYSICS OF PLANETS

By V. I. Moroz

Translation of "Fizika Planet."
"Nauka" Press, Moscow, 1967.

NATIONAL AERONAUTICS AND SPACE ADMINISTRATION

For sale by the Clearinghouse for Federal Scientific and Technical Information
Springfield, Virginia 22151 – CFSTI price $3.00

TABLE OF CONTENTS

		Page
Introduction		1
Chapter I	Methods of Planetary Astrophysics	4
Section 1.1	Molecular Spectra	4
Section 1.2	Energy Distribution in Planetary Spectra	25
Section 1.3	Telescopes, Spectral Instruments, Radiation Sensors	30
Section 1.4	Quantitative Spectroscopy of Planetary Atmospheres	38
Section 1.5	Radiation Scattering in Planetary Atmospheres	51
Section 1.6	Photometry	64
Section 1.7	Certain Problems of the Structure of Planetary Atmospheres	68
Section 1.8	Radar	76
Section 1.9	Review of Methodological Possibilities	79
Chapter II	Mars	81
Section 2.1	Introduction	81
Section 2.2	CO_2 Content and Total Pressure in the Martian Atmosphere	85
Section 2.3	Chemical Composition of the Atmosphere	100
Section 2.4	Temperature of the Martian Surface	107
Section 2.5	Clouds and Winds, General Circulation	115
Section 2.6	Transparency of the Martian Atmosphere; Blue Haze	122
Section 2.7	Vertical Structure of the Atmosphere	131
Section 2.8	Polar Caps	146
Section 2.9	Continents	150
Section 2.10	Dark Areas	154
Section 2.11	Phobos and Deimos	163
Chapter III	Venus	165
Section 3.1	Introduction	165
Section 3.2	Determination of the Rotation Period and Other Results of Radar Sounding of Venus	168
Section 3.3	Albedo, Phase Curve, Polarization	174
Section 3.4	Carbon Dioxide Absorption Bands	180
Section 3.5	CO and Dissociation of CO_2	193
Section 3.6	Chemical Composition of the Atmosphere and Cloud Layer	200
Section 3.7	Temperatures of Venus Determined from Emission in the Optical Range	208
Section 3.8	Radio Emission of Venus	222
Section 3.9	Vertical Structure of the Atmosphere	239

Page

Chapter IV Mercury 250

Section 4.1 Surface 250
Section 4.2 Hypothetical Atmosphere of Mercury 257
Section 4.3 General Problems of Interiors of the Terrestrial Planets 265

Chapter V The Giant Planets 284

Section 5.1 Introduction 284
Section 5.2 Markings and Phenomena Observable on the Disk of Jupiter 286
Section 5.3 Qualitative Chemical Analysis of the Jovian Atmosphere 302
Section 5.4 Quantitative Interpretation of the Spectra of Jupiter (Chemical Composition and Pressure) 313
Section 5.5 Temperature of Jupiter and Chemical Composition of the Cloud Layer 326
Section 5.6 Vertical Structure of the Supracloud Atmosphere 336
Section 5.7 Short-Wave Radio Emission of Jupiter and Magnetic Field 345
Section 5.8 Decameter Radio Emission. Tentative Radar Observations of Jupiter 357
Section 5.9 Saturn 366
Section 5.10 Uranus and Neptune 377
Section 5.11 Internal Structure of the Giant Planets 380
Section 5.12 Pluto 384
Section 5.13 Satellites of the Giant Planets 385

References 392

Subject Index 409

INTRODUCTION

/5*

Planetary physics deals with the physical characteristics of the planets and their satellites: the temperature of the planet surface and atmosphere; the composition, density and vertical structure (i.e., the altitude dependence of temperature, composition and density) of the atmosphere, the nature of the cloud layer, circulation of the atmosphere, the nature of the observable surface features and surface layer, and lastly, the internal structure. Until recently, planetary physics lagged greatly behind stellar astrophysics, but now this gap is rapidly shrinking.

The use of modern research techniques has led to a number of new observational findings. One of the most striking discoveries is the high brightness temperature of Venus, as indicated by measurements of centimeter-wavelength radiation. This temperature was found to be approximately 600°K. The question of the nature of the centimeter-wavelength radiation of Venus has become the subject of lively discussion. The simplest explanation for the observed radio brightness of Venus is that the source of this radiation must be a surface heated to a high temperature (650 - 700°K; the true temperature should be somewhat above the brightness temperature, since the emission coefficient of real bodies always is less than unity). However, this explanation conflicts with all previous theories on Venus, postulated by astronomers. Owing to the high reflectivity of its cloud layer, Venus receives less energy from the sun, even though it is closer to it. The dimensions and mass of Venus are nearly the same as those of the earth. Apparently, it can be assumed that the climate on the surface of this planet, concealed behind its cloud cover, does not markedly differ from the earth's climate. Hence, to interpret the radio observations, it has been tentatively theorized that the source of the high radio emission is located in more or less high layers of the atmosphere rather than at the surface itself, so that the surface temperature might be at a conventional level. As will be shown in Chapter III, an analysis of the totality of known observational facts leads to a rejection of these hypotheses: The surface of Venus must of necessity be hot.

Another interesting new finding pertains to Mars. As far back as 1948, /6
CO_2 absorption bands were discovered in the Martian spectrum. During the favorable opposition in 1963, new observations carried out with methods of infrared spectroscopy resulted in a marked increase in the number of known CO_2 bands in the spectrum of Mars. Since the relative intensity of strong and weak molecular absorption bands depends on total pressure, it was found possible to estimate the Martian atmospheric pressure according to the intensity of CO_2 bands in the spectrum of Mars. The obtained value was one order of magnitude lower than that given by earlier estimates based on other methods. It can now be stated that atmospheric pressure at the surface of Mars is only 5 - 20 mm Hg.

Radio radiation from Jupiter was investigated over a broad range of wave-

---

* Numbers in the margin indicate pagination in the foreign text.

lengths - from several millimeters to tens of meters; it was found that radio waves in the decimeter range are generated by a region whose dimensions greatly exceed the diameter of the planet. A study of the polarization spectrum and spatial brightness distribution in this region leads to the conclusion that decimeter waves are emitted in the neighborhood of Jupiter by high-energy electrons located in intense radiation belts.

Observations of planets from shorter distances, with the aid of spacecraft onboard instruments, have now become a reality. The first step in this direction was the photographing of the dark side of the moon by the Soviet interplanetary space probe Luna-3. This was followed by flights of American and Soviet space probes to Venus, Mars and, again, to the moon.

The space-probe experiments must be laid out with special care since they require a great deal of effort and funds. It is of prime importance to make a clear decision as to which space-probe experiments must be given priority, what new ground observations could provide additional information, and what new conclusions can be drawn by integrating the already accumulated data. It may be hoped that, as a result of their close flyby of planets and subsequent eventual penetration into planetary atmospheres and soft landings, space probes will rapidly enlarge the available information on the physical characteristics of planets. It must be borne in mind, however, that the accomplishment of such a complex operation as the landing of a space probe on another planet requires certain information on the properties of its atmosphere and surface.

In this book, we are making an attempt to integrate the data on the physical conditions of planets, available as of the beginning of 1966. There exist /7 several good books in Russian on the problems of planetary physics but all are now more or less obsolete. The most up-to-date in this respect is the book by Kellogg and Sagan "The Atmospheres of Mars and Venus" (Ref.1) and the series of volumes "Planets and Satellites", edited by Kuiper and Middlehurst (Ref.2), but even these now stand in need of considerable revision. Among the older guides of value are "The Nature of Planets" by V.V.Sharonov (Ref.3), the series of volumes "The Atmospheres of the Earth and Planets" edited by Kuiper (Ref.4), "Physics of the Planet Mars" by de Vaucouleurs (Ref.5), and "Survey of Physical Conditions on the Moon and Planets" by N.P.Barabashev (Ref.6). Problems of planetary radio emission are discussed at the modern level in the book by V.V. Zheleznyakov (Ref.7) but without adequately relating them to optical observations. We will discuss these questions in some detail whenever such relationship is essential or new important data are available. The book by the late V.V.Sharonov, with whose death planetary astronomy has lost a most skilled expert, elegantly expounded the problems of research on the geometric characteristics of planets, cartography of surface features, and photometry of planetary disks. As these questions arise, the reader will be referred to Sharonov's book. The determination of planetary masses was discussed by Dirk Brouwer and G.M.Clemence (Ref.2) who also gave a good survey over the internal structure of planets (Wildt, Chapt.V). As important references of a general nature, mention should be made of the material of the Liege Symposia on Astrophysics [1962 and 1963 (Ref.8)]. In this book, we will restrict our discussion to the problems for which recent advances have been greatest, namely the physical characteristics of the atmospheres and surfaces of the planets. In many cases the findings cannot be considered conclusive; within the space of a few years the picture may change con-

siderably, but this is inevitable in any new successfully developing domain of research.

Chapter I contains a description of astrophysical methods of planetary study. The competent reader can jump this Chapter without detriment to the understanding. Although the number of investigators in the field of planetary astrophysics is much smaller than in the field of stellar astrophysics, technical arsenal of the former is much greater and not even an astronomer - if he specializes in another discipline - will find it easy to assess the relative roles and real possibilities of the currently existing methods. Of special significance to planetary astronomy is geophysics. The earth is a planet investigated in much greater detail than any other planet and, in planetary astrophysics, plays the same role as the sun does in stellar astrophysics. The basic aspects of the structure of the planetary atmospheres and interiors have now been understood fully thanks to geophysical research. The recent advances in knowledge of the upper atmosphere and magnetosphere of the earth make it possible, for example, to construct theoretical models of the upper atmosphere of /8 the other planets. A comparison of these models with future observations by means of spacecraft will, in turn, permit refinement of the starting premises. For lack of space, we decided against including the earth-moon system in this book, but in our examination of the physical characteristics of the other planets we will occasionally refer to geophysical data. As for the moon, a detailed exposition of all the problems involved would require doubling the volume of this book. Methodologically, exclusion of the moon can be justified in view of the fact that 95% of the material discussed here pertains to the planetary atmospheres, and analogies to the moon would in no way further the understanding of these questions.

CHAPTER I

/9

METHODS OF PLANETARY ASTROPHYSICS

Section 1.1 Molecular Spectra

The observational basis of both planetary and stellar astrophysics is spectroscopy, but in the case of planets a special role is assigned to spectroscopy in the infrared radio range as well as in the ultraviolet region of the spectrum. The point is that planetary atmospheres consist of molecules as far up as the upper layers of the atmosphere, whereas molecular spectra are the poorest precisely in the visible region. The energy of a molecule consists of three components:

$$E = E_e + E_v + E_r,$$

where E_e is the energy associated with the motion of electrons in the force field of nuclei; E_v is the vibrational energy of nuclei with respect to the equilibrium position; E_r is the rotational energy of the molecule. Normally, $E_e \gg E_v \gg E_r$.

These three variables are quantized and vary in the form of discrete transitions from one energy level to another. Rotational transitions produce a sequence of rotational lines located within the range of*

$$1 \leqslant \tilde{\nu}_r \leqslant 500\ cm^{-1}\ (1\ cm \geqslant \lambda \geqslant 20\ \mu),$$

while vibrational transitions produce a sequence of bands located within the range of

$$500 \leqslant \tilde{\nu}_v \leqslant 10\,000\ cm^{-1}\ (20 \geqslant \lambda \geqslant 1\ \mu),$$

with each band consisting of separate rotational lines of frequencies $\nu_v + \nu_r$. For this reason, these bands are known as vibrational-rotational bands. Electronic transitions are chiefly located in the region

$$\tilde{\nu}_e \geqslant 30\,000\ cm^{-1}\ (\lambda \leqslant 3000\ \text{Å}).$$

In the visible region of the spectrum (λ 0.4 - 0.65 μ or 25,000 - 15,000 cm^{-1}) electronic transitions are rarely encountered and usually produce lines of comparatively low intensity; vibrational-rotational transitions are even more rarely encountered there. /10

A detailed analysis of molecular spectra has been the subject of special

---

* We will denote wave numbers by the sumbol $\tilde{\nu}$ to distinguish them from the frequency ν.

monographs [cf. for example Herzberg (Ref.9, 10)]. We will consider only the principal features of these spectra, which must be known in order to comprehend our further exposition. We shall begin with the simplest molecules, the diatomic molecules. A molecule of this kind consists of two nuclei surrounded by a cloud of electrons. Its rotation may best be described by the model of a "rigid rotor" ("dumbbell model"): the masses of the nuclei are assumed to be point masses and the distance between the nuclei is assumed to be invariant (Fig.1). The rotational motion of the rigid rotor has one degree of freedom: It can rotate about an axis perpendicular to the line interconnecting the nuclei. The energy of this rotation is

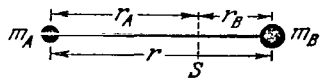

Fig.1 Rigid Rotor.

$$E_r = \frac{I\omega^2}{2}, \tag{1.1}$$

where $\omega = 2\pi\nu$ is the gyrofrequency, I is the moment of inertia,

$$I = \frac{m_A m_B}{m_A + m_B} r^2 = m_0 r^2. \tag{1.2}$$

The quantity m_0 in eq.(1.2) is termed the reduced mass of the molecule. The rotational energy is quantized and may assume only discrete values

$$E_r = K(K+1)B, \tag{1.3}$$

where K is the rotational quantum number, K = 0, 1, 2, ...; B is the rotational constant which is inversely proportional to the moment of inertia

$$B = \frac{h^2}{8\pi^2 I}, \tag{1.4}$$

where h is Planck's constant. Equations (1.1), (1.3), and (1.4) imply that, for a given K, the rotational speed is greater the smaller the moment of inertia.

The rotational energy levels of the rigid rotor are given schematically in Fig.2. As K increases, the distance between the levels also increases. The transitions between the various energy levels are limited by the exclusion principle

$$\Delta K = \pm 1. \tag{1.5}$$

The energy of a quantum emitted or absorbed during these transitions will be /11

$$h\nu = K(K+1)B - (K-1)KB = 2KB. \tag{1.6}$$

Hence the purely rotational (i.e., not accompanied by vibrational transitions)

spectrum of the rigid rotor represents a series of equidistant lines.

Under the action of centrifugal force, however, the internuclear distance varies with a variation in K, and as a result the rotational spectrum of real molecules does not obey this principle. The energy levels of a real molecule deviate from the rigid rotor energy levels to an extent that increases with an increase in K and hence also in centrifugal force. A molecular model in which allowance is made for the change in internuclear distance owing to centrifugal force is termed a nonrigid rotor. For the nonrigid rotor, we have

$$E_r = K(K+1)B + K^2(K+1)D, \qquad (1.7)$$

where $D \ll B$ is the second rotational constant. The rotational spectrum of a diatomic molecule (CO) is exemplified in Fig.3. Table 1 presents the rotational constants of certain diatomic molecules.

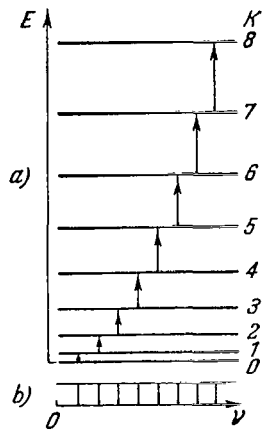

Fig.2 Energy Levels and Infrared Transitions of Rigid Rotor. a - Diagram of levels; b - Spectrum of rigid rotor.

Polyatomic molecules, whose nuclei lie along a straight line, are termed linear (e.g., CO_2, N_2O). They form a rotational spectrum of the same type as diatomic molecules. Nonlinear molecules have two rotational degrees of freedom and their rotational spectrum is much more complex. For example, the rotational spectrum of water vapor has such an intricate structure that, at first glance, it does not seem possible to describe it by laws other than statistical (Fig.4); in addition, it renders the earth's atmosphere nontransparent in the region from 15 μ to 2 mm. As a result, it is not possible to make earth-based astronomical observations over a large portion of the infrared spectrum and within the submillimeter range. /12

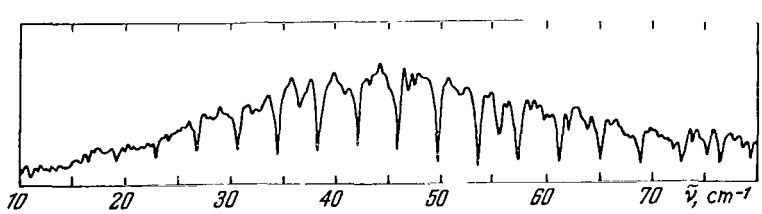

Fig.3 Rotational Spectrum of CO (Ref.11).

If the nuclei A and B (see Fig.1) are displaced from the equilibrium position, the force tending to return them to their original position will be proportional to the displacement $x = r - r_0$:

$$F = -bx. \qquad (1.8)$$

TABLE 1

ROTATIONAL CONSTANTS OF CERTAIN DIATOMIC MOLECULES (REF.9)

Molecule	B_e, cm^{-1}	α_e, cm^{-1} *	Molecule	B_e, cm^{-1}	α_e, cm^{-1} *
H_2	60.872	3.0071	CO	1.9310	0.01744
HD	45.668	1.9931	OH	18.862	0.693
D_2	30.429	1.0492	C_2	1.6320	0.01650
N_2	2.007	0.018	CH	14.453	0.528
O_2	1.4456	0.0158			

* The rotational constant in the vibrational state v is

$$B_v = B_e - \alpha_e\left(v + \frac{1}{2}\right),$$

where v is the vibrational quantum number. In the ground state, we have

$$B = B_e - \frac{1}{2}\alpha_e,$$

so long as $x \ll r_0$ (with b being the force constant). The potential energy of the system

$$E = -\int F\,dx + \text{const} = \frac{x^2 b}{2} + \text{const} \tag{1.9}$$

reaches its minimum when x = 0. Generally, the function E(r) is more complex (Fig.5). For high values of r the bonds between the constituent atoms of the molecule are ruptured and the potential energy E asymptotically tends to zero. For very low r, the potential energy shifts to the region of positive values and tends to infinity as $r \to 0$. When $r = r_0$, the potential energy is at its minimum and when $x \ll r_0$ the value E(r) will be parabolic [eq.(1.9)]. The model of /14 the vibrating molecule satisfying Hook's law [eq.(1.8)] is termed a harmonic oscillator. In the presence of marked deviations from the equilibrium position an allowance must be made for deviations from Hook's law, in which case the model of an anharmonic oscillator, corresponding to the real potential curve, is employed.

The vibrational energy levels are quantized and, for the harmonic oscillator, are equal to

$$E_v = h\nu_0\left(v + \frac{1}{2}\right), \tag{1.10}$$

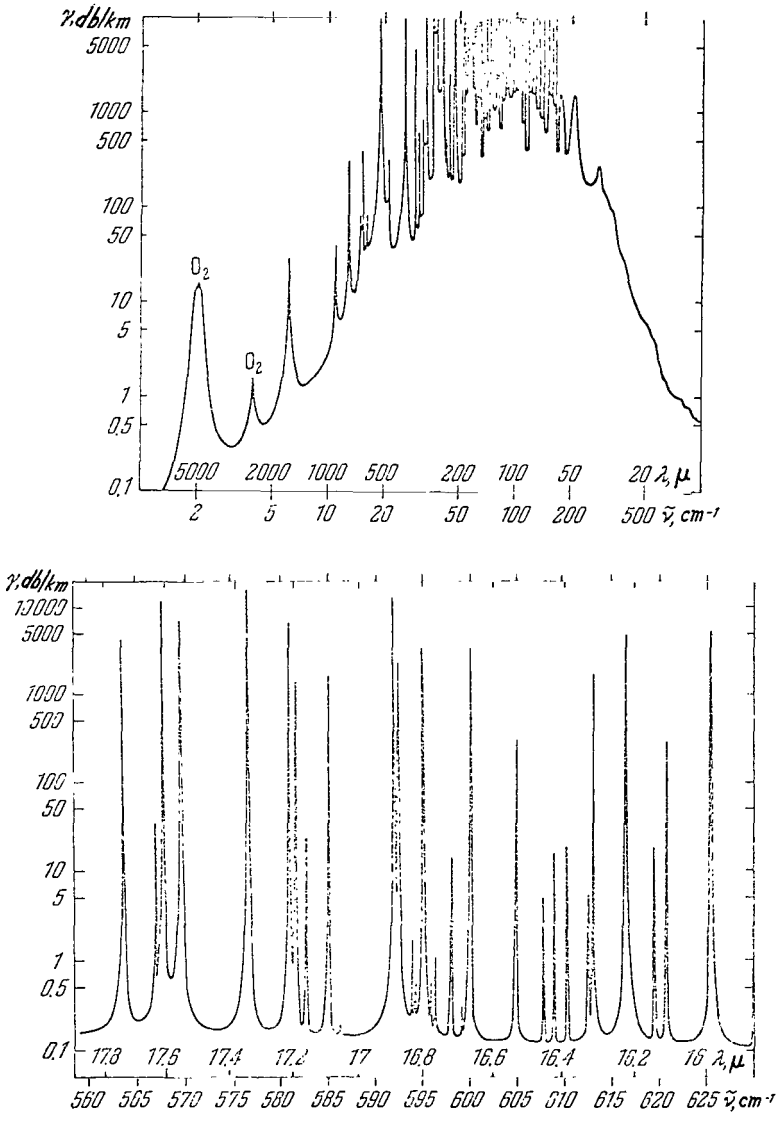

Fig.4

Top: absorption coefficient γ of the rotational band of atmospheric water vapors, at low resolution (T = 253°K, P = 760 mm Hg, absolute moisture content u = 7.5 gm • cm^{-3}). The peaks in the region of ~ 2000 μ are due to the absorption of O_2. Bottom: the same, at high resolution (T = = 214°K, P = 42 mm Hg, u = 7.5 gm • cm^{-3}) (Ref.12).

where ν_0 is the fundamental frequency while v = 0, 1, 2, ... is the spin quantum number.

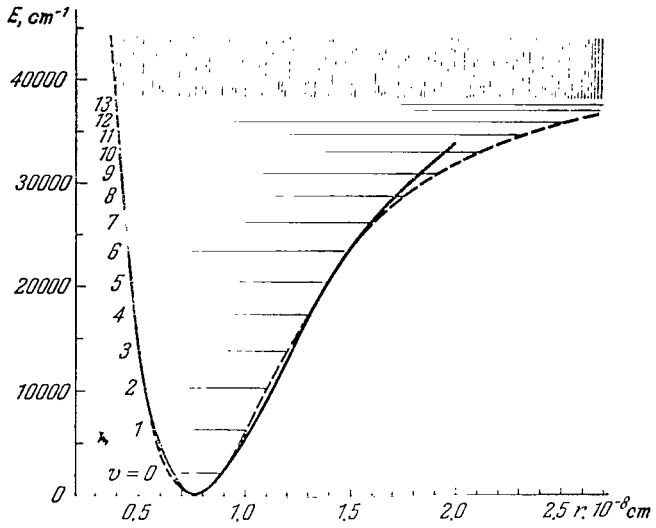

Fig.5 Potential Curve of Ground State of an H_2 Molecule with Vibrational Levels and Continuous Term Spectrum (Ref.9).
The solid curve was plotted according to Rydberg and the broken theoretical potential curve, according to Morse. Upward of v = 14 lies the (described) continuous term spectrum (continuum) corresponding to the dissociation region.

The fundamental oscillation frequency of a harmonic oscillator is /15

$$\nu_0 = \frac{1}{2\pi}\sqrt{\frac{b}{m_0}}.$$

The energy levels of the harmonic oscillator are equidistant, and only the transitions $\Delta v = \pm 1$ are allowed. As a result, the spectrum of the harmonic oscillator consists of a single line with the frequency ν_0. The anharmonic oscillator shows emission and absorption not only at the fundamental frequency but also at the overtones; in other words, for the anharmonic oscillator the additional transitions $\Delta v = \pm 2, \pm 3$, etc. are allowed. This is indeed observed in real molecular spectra. Since the vibrating molecule rotates at the same time, "vibrational lines" are not observed in pure form; instead, in the neighborhood of the oscillation frequencies, vibrational-rotational bands are formed which consist of discrete lines corresponding to various rotational transitions in the presence of a single vibrational transition.

The measured overtone frequencies markedly differ from harmonic frequencies.

Anharmonicity is taken into account in the formula of vibrational energy by the auxiliary terms

$$-h\nu_0 x\left(v+\frac{1}{2}\right)^2+h\nu_0 y\left(v+\frac{1}{2}\right)^3, \tag{1.11}$$

where x, y are small coefficients. The energy levels of the anharmonic oscillator (in contrast to the harmonic oscillator) approach closely as v increases. The potential curve is asymptotic and the energy values lying above the asymptote are no longer quantized. At such energies, the molecules dissociate.

Allowed vibrational transitions with emission and absorption occur only when the dipole moment changes owing to a variation in r. If the molecule consists of two identical nuclei, the dipole moment will be zero since the center of the electron cloud will coincide with the center of the positive charge. In this case, on a change in r the dipole moment will remain zero. Hence the molecules consisting of two identical atoms (H_2, O_2, N_2) will have no vibrational spectrum. Rotational spectra also are excluded in molecules of this kind. Here two qualifications must be made. First, molecules consisting of identical atoms may have a nonzero quadrupole moment and thus may display vibrational and rotational transitions in the form of relatively faint forbidden lines. In the spectrum of Jupiter and Saturn, lines of quadrupole vibrational bands of H_2 absorption have been observed, pointing to an extremely high content of molecular hydrogen in the atmospheres of these planets. Second, a dipole moment may be induced in /16
such molecules by an external electric field or through collisions. In this case, the absorption is termed induced. The dipole moment arising in collisions is due to the deformation of the electric charge distribution in the molecule. Induced infrared absorption by H_2, N_2 and O_2 molecules in the region of their forbidden vibrational transitions becomes distinct in the presence of pressures of several tens of atmospheres [cf. for example (Ref.13)]. The intensity of the induced absorption bands increases roughly in proportion to the square of pressure. Induced absorption bands of H_2 have been discovered in the spectrum of Uranus and Neptune*.

Polyatomic molecules have several fundamental oscillation frequencies ν_1, ν_2, etc. In this case, in addition to overtones also combined (compound) frequencies

$$\nu=n\nu_1+m\nu_2+\cdots, \tag{1.12}$$

where n, m, ... are integers, are observed as a consequence of the anharmonicity. Bands of this kind occur as a result of absorption by molecules existing in the

* It should be noted here that vibration and rotation of symmetric molecules entail a change in their polarizability. Hence their vibration and rotation frequencies may be observed in combination scattering. During illumination with a continuous spectrum the multiple scattering effect is insignificant. In the case of planetary atmospheres this effect may be a factor only in the far ultraviolet where the continuous spectrum of the sun is weak compared with its monochromatic radiation.

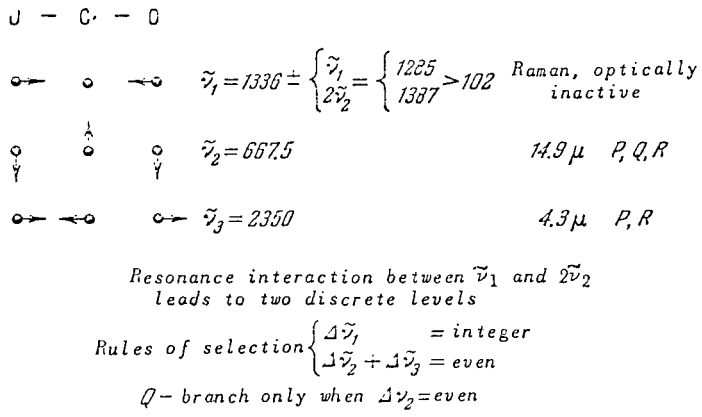

Fig.6 Vibration Modes of a CO_2 Molecule.

ground state. If a molecule existing in an excited state is absorbed, there occurs a difference band (or "hot" band) for example, $\nu_3 - \nu_2$. As a typical example, let us consider the CO_2 molecule. CO_2 bands are distinct in the spectrum of Mars and particularly of Venus (cf. Chapts.II and III). Figure 6 schematically depicts three types of vibrations of this molecule: symmetric ν(s), deformation δ(a) and antisymmetric ν(a). These correspond to the wave numbers

/17

$\tilde{\nu}_1$ 1336 cm^{-1} (7.46 μ),
$\tilde{\nu}_2$ 667.5 cm^{-1} (15.0 μ),
$\tilde{\nu}_3$ 2350 cm^{-1} (4.32 μ).

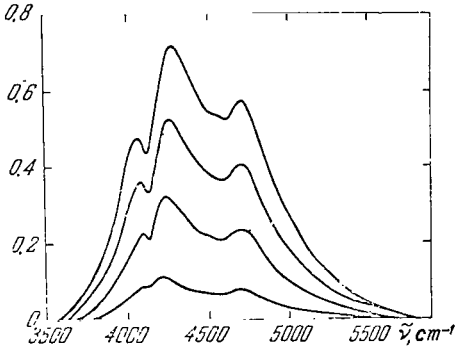

Fig.7 Fundamental Band of Pressure-Induced H_2 Absorption at Gas Densities of 340, 406, 556 and 663 amagats (1 amagat – density of gas at T = 293°K and P = 1 atm). Thickness of absorbing layer 1.3 cm, T = 298°K (Ref.13). Ordinate: Absorbance.

All these frequencies pertain to a spectral region inaccessible to observations from the earth's surface. On the other hand, combination frequencies, e.g.,

$\tilde{\nu}_1 + 2\tilde{\nu}_2 + \tilde{\nu}_3$ 4977 cm^{-1} (2.01 μ),
$4\tilde{\nu}_2 + \tilde{\nu}_3$ 4853 cm^{-1} (2.05 μ),

are clearly observable.

The same bands can be denoted by the numbers of terminal and initial levels: 121–000 and 041–000. The vibrational state of the triatomic molecule from the standpoint of energy is determined by three sequences of terms (levels) each of which corresponds to one of the vibration frequencies. In the ground state, the molecule occupies the lowest levels in all three sequences: 000. The first fundamental frequency corresponds to the transition

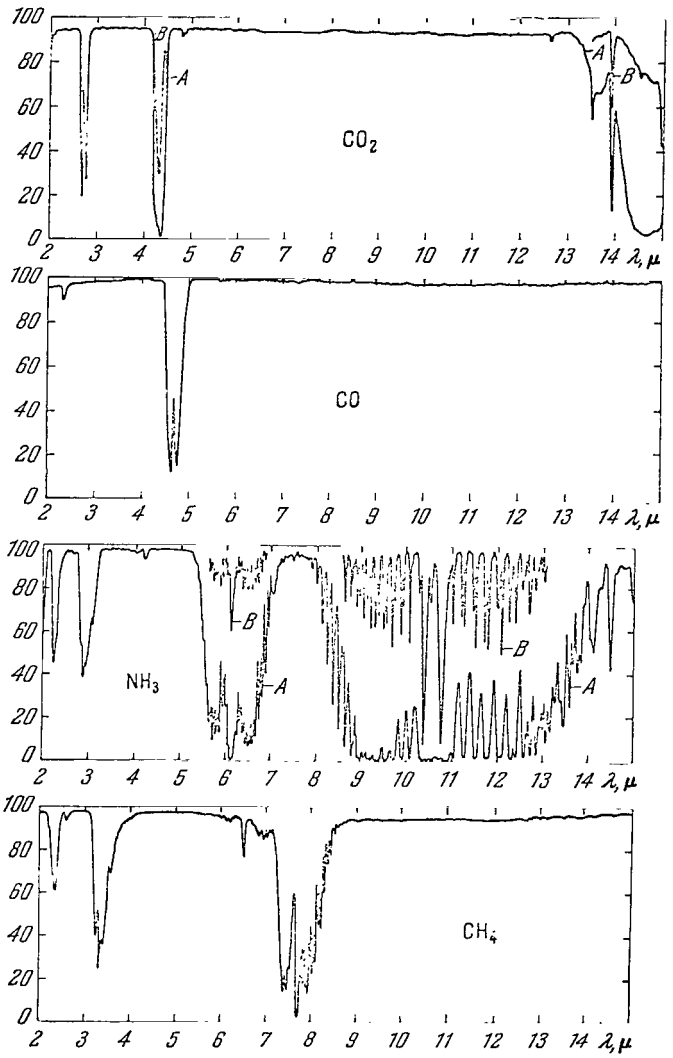

Fig.8 Laboratory Absorption Spectra of CO, CO_2, NH_3, CH_4 in the Range of λλ 2 - 15 μ.
Cuvette length, 10 cm. Pressures: CO, 714 mm; CO_2, 702 (A) and 70 (B) mm; NH_3, 700 (A) and 45 (B) mm; CH_4, 702 mm.
Ordinate: transmission in percent.

100 - 000; the second, to 010 - 000, and so on; the combination frequency $\nu_1 + 2\nu_2 + \nu_3$ corresponds to the transition 121 - 000. For transitions from the ground state, its notation is often dropped and the bands mentioned above are simply denoted as 121 and 041. Tables 2 - 6 present the vibrational transition frequencies of molecules of CO_2, CO, NH_3, CH_4, H_2, while Figs.7 - 10 show specimens of infrared spectra.

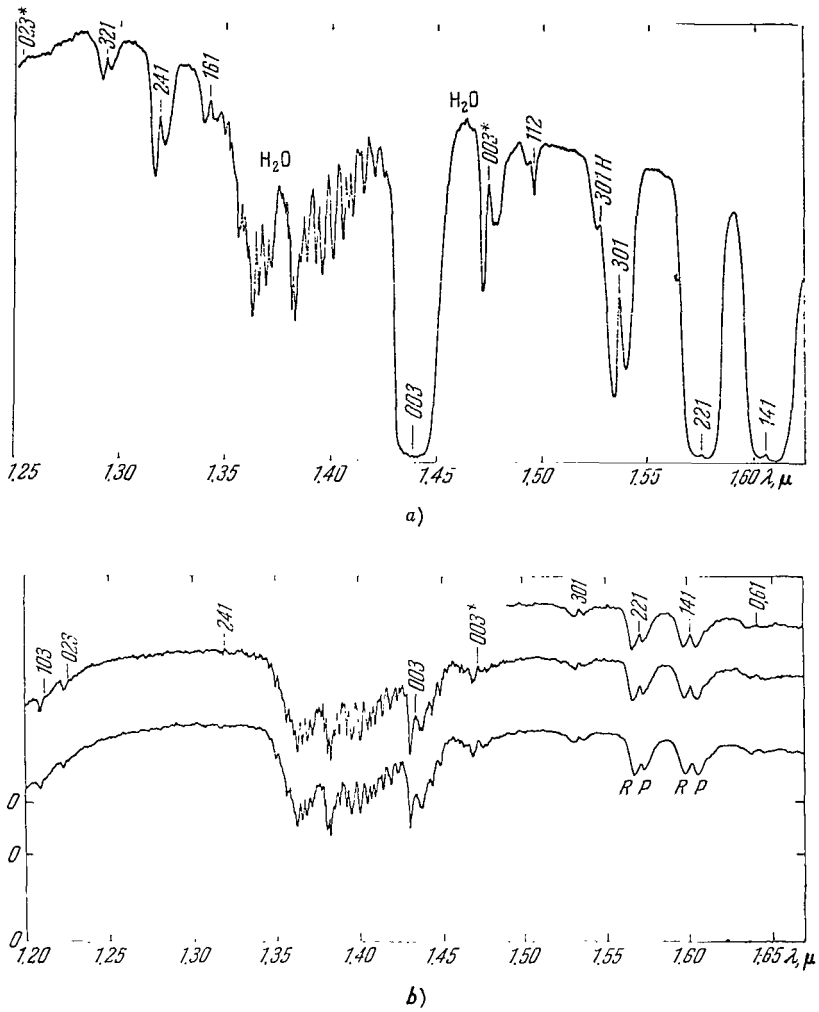

Fig.9 Laboratory Spectrum of CO_2 Absorption in the Range of λ 1.2 - 1.6 μ.
a - Path length 80 m, pressure 5 atm (Ref.15);
b - Path length 360 m, pressure 30 mm Hg (Ref.16).

The total number of oscillatory degrees of freedom is 3N - 5 in a linear /23
molecule and 3N - 6 in a nonlinear molecule, where N is the number of nuclei; owing to molecular symmetry, however, certain oscillation frequencies may coincide.

This may be exemplified by the deformation vibrations of CO_2 or any triatomic molecule: Deformation vibrations in two mutually perpendicular planes have one and the same frequency. However, their phases may not coincide; in this

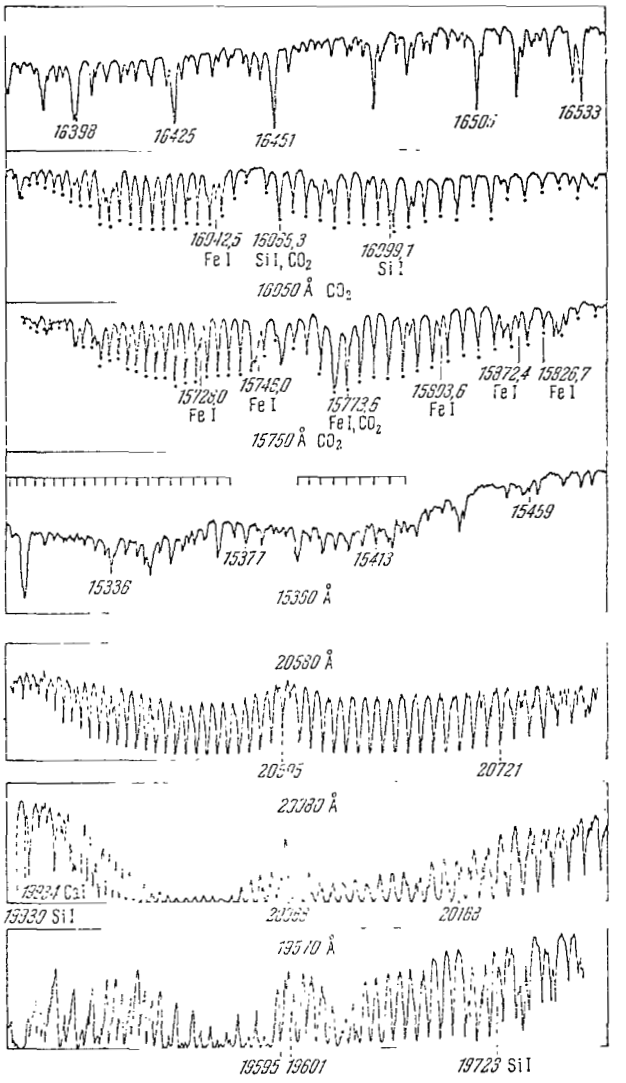

Fig.10 Atmospheric CO_2 Bands in Solar Spectrum with High Resolution (Ref.17).

case motion proceeds along an ellipse, giving rise to the vibrational angular momentum. This is a quantized variable. The quantum number l of the vibrational angular momentum influences the total energy of the vibrational level which thus, in the case of a triatomic linear molecule, is determined by four quantum numbers: v_1, v_2, v_3, l. In the notation of levels, the quantum number l is denoted by the superscript for ν_2 : $2\nu_2^0$ or $02^0\,0$ (cf. Table 2). At some frequencies, vibrational motions occur without a change in the dipole moment and without leading to allowed vibrational transitions. Vibrations of this kind are

TABLE 2

INFRARED VIBRATIONAL–ROTATIONAL BANDS OF CO_2 (REF.10)

$\tilde{\nu}, cm^{-1}$	Upper State	Lower State	Intensity
667,5	$01^{1}0$	$00^{0}0$	Very strong
1932,5	$03^{1}0$	$00^{0}0$	Medium
2076,5	$11^{1}0$	$00^{0}0$	»
2350	$00^{0}1$	$00^{0}0$	Very strong
3609	$02^{0}1$	$00^{0}0$	Strong
3716	$10^{0}1$	$00^{0}0$	»
4853	$04^{0}1$	$00^{0}0$	Medium
4977	$12^{0}1$	$00^{0}0$	»
5169	$20^{0}1$	$00^{0}0$	»
6077	$06^{0}1$	$00^{0}0$	Weak
6321	$14^{0}1$	$00^{0}0$	»
6351	$22^{0}1$	$00^{0}0$	»
6510	$30^{0}1$	$00^{0}0$	»
6976	$08^{0}3$	$00^{0}0$	»
8193	$02^{0}3$	$00^{0}0$	Very weak
8293	$10^{0}3$	$00^{0}0$	» »
11336.5	$05^{0}5$	$00^{0}0$	» »
12672.4	$02^{0}5$	$00^{0}0$	» »
12771.7	$10^{0}5$	$00^{0}0$	» »
618.1	$02^{0}0$	$01^{1}0$	Medium
668.3	$02^{2}0$	$01^{1}0$	»
720.5	$10^{0}0$	$01^{1}0$	»
1886	$04^{0}0$	$01^{1}0$	Weak
2004	$12^{2}0$	$01^{1}0$	Medium
2137	$20^{0}0$	$01^{1}0$	»
596.8	$03^{1}0$	$02^{2}0$	Strong
647.6	$03^{1}0$	$02^{0}0$	»
740.8	$11^{1}0$	$02^{2}0$	»
790.8	$11^{1}0$	$02^{0}0$	Very weak
960.8	$00^{0}1$	$10^{0}0$	Weak
1063.6	$00^{0}1$	$02^{0}0$	»

TABLE 3

INFRARED VIBRATIONAL–ROTATIONAL BANDS OF CO

$\tilde{\nu}, cm^{-1}$	λ, μ	Upper State	Lower State	Intensity
2133.4	4.66	1	0	Very strong
4260.3	2.35	2	0	Weak
6347.7	1.58	3	0	Very weak

TABLE 4

INFRARED VIBRATIONAL–ROTATIONAL BANDS OF CH_4 (REF.10)

$\tilde{\nu}$, cm^{-1}	Notation	Intensity	$\tilde{\nu}$, cm^{-1}	Notation	Intensity
1306,2	ν_4	Very strong	8807	$2\nu_1 + \nu_3$	Strong
			8960	$\nu_1 + 2\nu_3$	
1720	$\nu_4 - \nu_3$		9047	$3\nu_3$	
2660	$2\nu_4$		10114	$2\nu_1 + \nu_2 + \nu_3$	Weak
2823	$\nu_2 + \nu_4$		10300	$\nu_1 + \nu_2 + 2\nu_3$	
3020.3	ν_3	Very strong		$\nu_2 + 3\nu_3$	
			11270	$3\nu_1 + \nu_3$	
4123	$\nu_2 + 2\nu_4$		11620	$2\nu_1 + 2\nu_3$	
4216.3	$\nu_1 + \nu_4$		11885	$\nu_1 + 3\nu_3$	Weak
4313.2	$\nu_3 + \nu_4$			$4\nu_3$	
4546	$\nu_2 + \nu_3$		12755	$3\nu_1 + \nu_3 + \nu_4$	»
5775	$\nu_1 + \nu_2 + \nu_4$			$2\nu_1 + \nu_2 + 2\nu_3$	
5861	$\nu_2 + \nu_3 + \nu_4$		13790	$4\nu_3 + 2\nu_3$	
6006	$2\nu_3$			$3\nu_1 + 2\nu_3$	Weak
7514	$\nu_1 + 2\nu_3$				
8421	$2\nu_1 + 2\nu_4$				
8604	$2\nu_3 + 2\nu_4$				

TABLE 5

INFRARED ROTATION–VIBRATION BANDS OF NH_3 (REF.10)

$\tilde{\nu}$	Notation	Intensity	$\tilde{\nu}$	Notation	Intensity
629.3	$2\nu_2 - \nu_2$	Weak	5053	$\nu_3 + \nu_4$	Strong
931.58	ν_2	Very	6016	$\nu_2 + \nu_3 + \nu_4$	Medium
968.08		strong	6555	$2\nu_1 (2\nu_3, \nu_1 + \nu_3)$	»
1627.5	ν_4	Very strong	6624		
1922	$2\nu_2$	Very weak	7665	$2\nu_1 + \nu_2$	Weak
			7899		
2440.1	$\nu_3 - \nu_2$, $\nu_2 + \nu_4$	Weak	8177	$2\nu_1 + \nu_4$	»
2472.6			8202		
2861	$3\nu_2$	Very weak	8460	$2\nu_3 + \nu_4$	»
			9760.4	$3\nu_1$	»
3219.1	$2\nu_4$	Medium	10099.7	$\nu_1 + 2\nu_3$	»
3335.9	ν_1	Very strong	10104.9		
3337.5			11364	$3\nu_1 + \nu_4$	»
3413	ν_3	Strong	12600.2	$4\nu_1$, $2\nu_1 + 2\nu_3$	»
4176	$\nu_2 + 2\nu_4$	Medium	12619.8		
4216			15440	$5\nu_1$, $4\nu_1 + \nu_3$	»
4269	$\nu_1 + \nu_2$	Strong	18150	$6\nu_1$, $5\nu_1 + \nu_3$	»
4302					
4433	$\nu_2 + \nu_3$	Strong			
4595					

termed optically inactive. This may be exemplified by the frequency ν_1 of the CO_2 molecule: At symmetric vibration, the center of positive charges is not displaced and the dipole moment remains unchanged. Absorption at optically inactive frequencies may be observed at high pressures owing to the occurrence of an induced dipole moment.

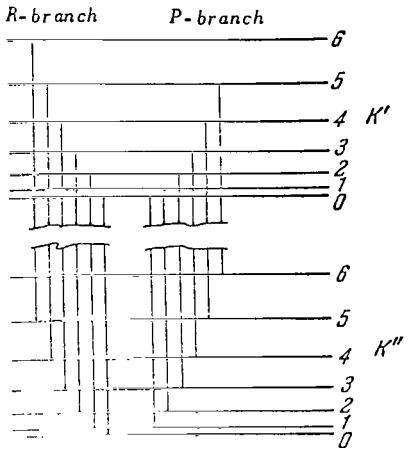

Fig.11 R- and P-Branches of Vibrational-Rotational Transitions.

Until now, vibrational and rotational motions of the molecule have been discussed separately. As pointed out above, however, a vibrating molecule simultaneously rotates. The energy of vibrational motion combines with the total of rotational energies

$$E = E_v + E_r.$$

As a result, the vibrational level splits into a large number of rotational sublevels (Fig.11). The transitions between the individual sublevels ν_1 and ν_2 form rotational lines which, in their entirety, become grouped into the vibrational-rotational band. Because of the asymmetric slope of the potential curve (see Fig.5) the moment of inertia in the state ν_1 is greater than in the state ν_2, and /25

$$B' < B''.$$

Of the possible transitions between the different rotational sublevels ν_1 and ν_2 of the diatomic molecule only those resulting in the change

$$\Delta K = \pm 1,$$

are allowed. The wave number of each line is

$$\tilde{\nu} = \tilde{\nu}_v + \tilde{\nu}_r = \tilde{\nu}_v + B'K'(K'+1) - B''K''(K''+1). \tag{1.13}$$

The transitions $\Delta K = K' = K'' = +1$ are located in the region $\tilde{\nu} > \tilde{\nu}_v$. The sequence of lines formed by these transitions is termed the R-branch:

$$\tilde{\nu} = \tilde{\nu}_v + (B' + B'')(K+1) + (B' - B'')(K+1)^2; \tag{1.14}$$

where $K = K''$. The transitions $\Delta K = K' - K'' = -1$ form the P-branch:

$$\tilde{\nu} = \tilde{\nu}_v - (B' + B'')(K+1) + (B' - B'')(K+1)^2. \tag{1.15}$$

Since the difference $B' - B''$ is negative, the distance between the lines of the R-branch decreases with increasing K while the distance between the lines of the P-branch increases. The lines of the R-branch crowd together and come to a sharply defined edge, known as the band head (Fig.12). A similar structure is displayed by the bands of not only diatomic but also of complex linear symmetric molecules.

TABLE 6

QUADRUPLE ROTATION-VIBRATION SPECTRUM OF H_2 [THEORETICAL WAVE NUMBERS (REF.46)]*

K	1—0						2—0					
	S-Branch		Q-Branch		O-Branch		S-Branch		Q-Branch		O-Branch	
	$\tilde{\nu}, cm^{-1}$	λ, Å	$\tilde{\nu}, cm^{-1}$	λ, Å	$\tilde{\nu}, cm^{-1}$	λ, Å	$\tilde{\nu}, cm^{-1}$	λ, Å	$\tilde{\nu}, cm^{-1}$	λ, Å	$\tilde{\nu}, cm^{-1}$	λ, Å
0	4498	22228	. . .	. . .	. . .	. . .	8403	11898	. . . .	. . .	. . . .	. . . .
1	4713	21213	4155	24060	. . .	. . .	8101	11624	8072	12336	. . .	. . .
2	4917	20333	4143	24129	3807	26263	8782	11384	8048	12422	7729	12935
3	5108	19571	4126	24229	3568	28019	8945	11176	8014	12475	7485	13357
4	5286	18914	4103	24369	3339	29941	9090	10999	7968	12547	7234	13820
5	5448	18351	4074	24541	3091	32342	9213	10851	7911	12637	6979	14325

K	3—0						4—0					
	S-Branch		Q-Branch		O-Branch		S-Branch		Q-Branch		O-Branch	
	$\tilde{\nu}, cm^{-1}$	λ, Å	$\tilde{\nu}, cm^{-1}$	λ, Å	$\tilde{\nu}, cm^{-1}$	λ, Å	$\tilde{\nu}, cm^{-1}$	λ, Å	$\tilde{\nu}, cm^{-1}$	λ, Å	$\tilde{\nu}, cm^{-1}$	λ, Å
0	12080	8276.2	. . .	. . .	. . .	. . .	15530	64332	. . .	. . .	. . .	. . .
1	12261	8153.9	11760	8501.3	. . .	. . .	15695	6369.8	15222	6567.7	. . .	. . .
2	12420	8049.4	11725	8526.3	11423	8752.2	15832	6314.8	15176	6587.5	14890	6713.9
3	12556	7962.4	11674	8563.9	11173	8947.9	15940	6272.0	15108	6617.3	14635	6831.1
4	16667	7892.5	11605	8614.2	10911	9162.7	16018	6241.3	15017	6657.2	14362	6961.1
5	12753	7839.2	11521	8677.5	10639	9396.8	16066	6222 5	14905	6707.3	14073	7103.9

* For laboratory observations of quadrupole lines of H_2 see elsewhere (Ref.47).

If the nuclei in a linear symmetric molecule are transposed, the total eigenfunction either remains unchanged (symmetric state) or changes in polarity (antisymmetric). For even K, the eigenfunction is symmetric and for odd K, it is antisymmetric. Transitions between symmetric and antisymmetric states are forbidden. Hence, in molecules such as CO_2 rotational transitions take place across levels, and every second line is absent.

Not all rotational levels are identically populated. Rotation is excited by collisions during thermal agitation. For the case in which the transition frequency on collision (without emission) exceeds the frequency of spontaneous transitions, the population of the rotational levels is determined by the Boltzmann formula

$$N_K \backsim g e^{-\frac{E_r}{kT}}, \tag{1.16}$$

where g is the statistical weight; k is the Boltzmann constant; T is the temperature. In most practical cases, the rigid rotor model can be used so that, /26

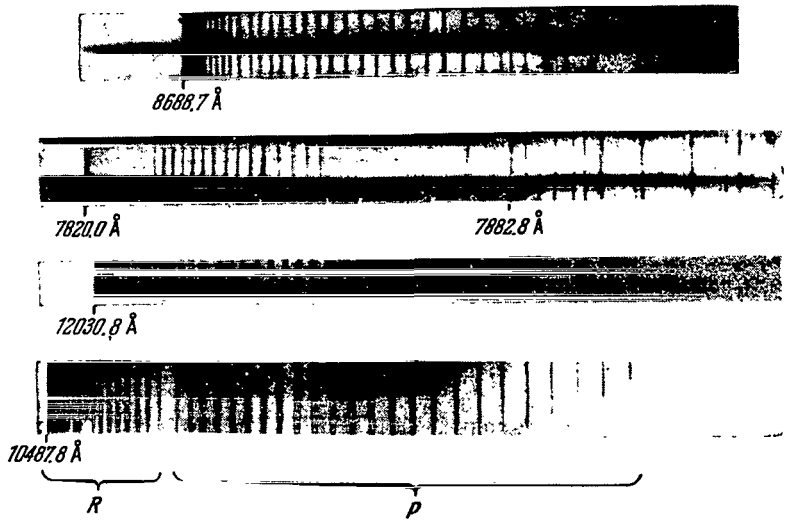

Fig.12 CO_2 Bands in the Photographic Infrared Region.

for diatomic and linear polyatomic molecules, we have

$$N_K \backsim (2K+1) e^{-\frac{BK(K+1)hc}{kT}}, \tag{1.17}$$

where B is given in cm^{-1} and c is the velocity of light. An example of equilibrium distribution of the populations of rotational states is given in Fig.13. The position of the maximum depends on the temperature. The intensity of unab-

sorbed lines is written as

$$I_K \backsim A_K N_K h\nu,$$

where A_K is the Einstein coefficient (transition probability); N_K is the population of the level. Within the confines of a given vibrational transition A_K varies little, like $h\nu$. Hence, the relative intensity of the vibrational lines within the confines of the rotational or vibrational-rotational band will be

$$I_K \backsim N_K. \qquad (1.18)$$

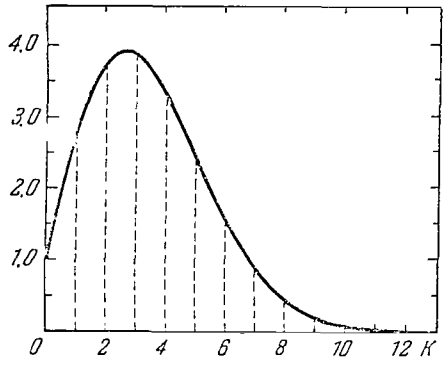

Fig.13 Equilibrium Distribution of HCl Molecule over the Rotational Levels ($T = 300^\circ$ K, $B = 10.44$ cm^{-1}). The curve illustrates the dependence of the function

$$(2K+1)e^{-BK(K+1)hc/kT}$$

on K. The broken-line ordinates give the relative frequency of occurrence of the corresponding rotational states (Ref.9).

Knowing the distribution of I_K from observations, it is possible to calculate the temperature from eq.(1.17). The temperature determined in this manner is known as rotational temperature. For a rough estimate of the rotational temperature it is sufficient to make an eyeball guess at the number of the rotational lines of greatest intensity. If the corresponding quantum number is denoted by K_m, then /27

$$T = \frac{Bch}{2k}(2K_m+1)^2. \qquad (1.19)$$

Figure 12 presents laboratory spectrograms of CO_2 bands in the photographic infrared region. As typical example, let us consider the band λ 10488 Å. The intensity maximum corresponds to the eighth line (reckoning from the minimum between the R- and P-branches), for which K = 16 (odd K are forbidden in the case of the CO_2 molecule; see above). For CO_2, in accordance with Herzberg (Ref.10),

$$B = 0.394 \ cm^{-1},$$

whence, in accordance with eq.(1.19)

$$T = \frac{0.394\times3\times10^{10}\times6.67\times10^{-27}}{2\times1.38\times10^{-16}}\cdot33^2 = 310^\circ \text{ K}.$$

If the rotational structure is not resolved, while the branches R and P are resolved (as in Fig.9), then the rotational temperature can be estimated from the distance $\Delta\tilde{\nu}$ between the maxima of R and P: /28

$$T = \frac{ch}{2Bk}(\Delta\tilde{\nu})^2. \qquad (1.20)$$

For molecules without linear symmetry, the rotational structure is more complex, as pointed out above, and a determination of the rotational temperature according to the bands of these molecules generally is a much more difficult problem.

The relative intensity of the unsaturated vibrational-rotational bands is virtually independent of the temperature if the starting level is the ground level. On the other hand, the intensity of the "hot" bands displays a marked temperature dependence. Based on the Boltzmann distribution, the vibrational temperature can be determined from the intensity ratio of "hot" to normal bands.

The oscillation frequency depends on the reduced mass m_0 and on the force constant b. In molecules differing in their isotope composition, the force constant is virtually the same since the structure of the electron shell is determined by the charges alone and is nearly independent of the mass.

As a result, the oscillation frequencies of diatomic molecules of differing isotope composition are at a mutual ratio of square roots of their reduced masses [cf. eq.(1.10)]:

$$\frac{\nu_v^i}{\nu_{0_r}} = \sqrt{\frac{m_0}{m_i}} = \zeta, \tag{1.21}$$

where the subscripts i and 0 denote molecules of differing isotope composition. For $C^{13}O^{16}$ and $C^{12}O^{16}$,

$$\zeta = 0.99$$

and the frequency ν_v^i is by 1% lower than the frequency ν_v. For polyatomic molecules, the isotopic shifts are determined by more complex relations, but their physical meaning and order of magnitude are the same. The band $C^{12}O_2^{16}$ with $4\nu_2 + \nu_3$ (λ 2.05 μ) corresponds to its isotopic satellite line $C^{13}O_2^{16}$ (λ 2.10 μ) whose wavelength differs by approximately 500 Å. In atomic spectra, isotopic shifts are much smaller and amount to minute fractions of an angstrom. Hence the sole source of information on the features of the isotopic composition of heavenly bodies, including the planets, is the molecular spectra (the only exception being the analysis of deuterium content). /29 The rotational terms also undergo isotopic shifts, but the rotational isotopic effect is small compared with the vibrational, since rotational energies are much lower than vibrational energies.

Let us now consider the energy transitions associated with changes in the electronic state of the molecule. The spectral line frequencies accompanying these transitions are

$$\nu = \nu_e + \nu_v + \nu_r = \frac{1}{h}(E_{e'} - E_{e''} + E_{v'} - E_{v''} + E_{r'} - E_{r''}).$$

Here, the quantity ν_e determines the position of the system of vibrational bands; ν_v is the position of the band within the confines of the system; ν_r is the position of an individual rotational line within the band (Fig.14). In electronic transitions all values of $\Delta\nu$ are allowed. Bands with a common upper

or lower level form a series (or a progression), while bands with $\Delta\nu$ = const form a sequence. The curves of potential energy differ in different electronic states. Thus, the difference

$$B' - B''$$

may be either positive or negative or zero. As a result the band head may be present on both the red and the violet ends. In addition to the transitions $\Delta K = \pm 1$, the transitions $\Delta K = 0$, forming the Q-branch, are sometimes allowed. Since the difference $B' - B''$ may be of a high absolute value, the lines in the branches P and R must converge and diverge more rapidly than in purely vibrational-rotational (infrared) spectra.

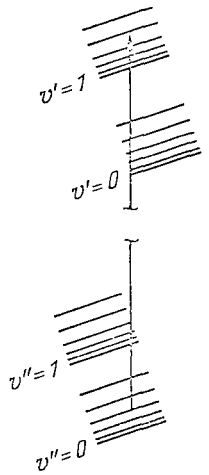

Fig.14 Electronic Transitions.

Molecules with identical nuclei do not give a purely vibrational-rotational spectrum, but a rotational-vibrational structure is present in their electronic transitions; this is such that the rotational lines alternate since transitions between symmetric and antisymmetric states are forbidden.

This may be demonstrated on the system of electron energy levels of the O_2 molecule shown in Fig.15. The Greek letters Σ, Π, Δ, etc. denote the magnitude of the projections of the vector Λ of the total orbital moment onto the internuclear axis (Λ = 0, 1, 2, respectively). The quantum number Λ in molecular spectroscopy is equivalent /30 to the quantum number L in atomic spectroscopy. To the left top of the diagram, the term multiplicity $2\Sigma + 1$ is noted, where Σ is the projection of the total spin moment onto the internuclear axis. To the right bottom, the parity of the molecular configuration is shown, which is determined by whether the sum of the quantum numbers l of the individual electrons is even (g) or odd (u).

The molecules present in the atmospheres of the planets usually are dissociated by radiation of wavelength $\lambda \lesssim 2000$ Å and ionized at $\lambda \lesssim 1000$ Å. Outside these dissociation and ionization ranges, the absorption coefficient is extremely high so that the far ultraviolet radiation of the sun is absorbed in the relatively high layers of the atmospheres of the planets. As typical example, Fig.16 shows the wavelength dependence of absorption with respect to the dissociation of O_2, H_2O and CO_2, while Fig.17 gives this dependence for the ionization of O_2 and O.

The dissociation of ozone O_3 is even greater by visible light, but the principal role in its dissociation is played by absorption in the Hartley bands located within the $2000 < \lambda < 3000$ Å region. Table 7 presents the dissociation energies and ionization potentials for certain molecules. Note that in a number of cases direct dissociation of the type of

$$XY + h\nu \rightarrow X + Y$$

is a much slower process than ionization with subsequent dissociative recombination:

$$XY + h\nu \rightarrow XY^+ + e,$$
$$XY^+ + e \rightarrow X + Y,$$

although the dissociation energy is markedly lower than the ionization potential. In planetary atmospheres such a situation applies to molecules of H_2 and N_2.

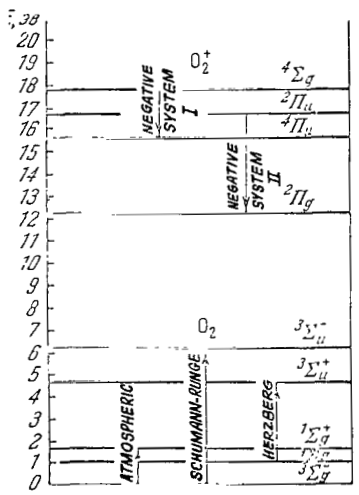

Fig.15 Energy Levels of Neutral and Ionized Molecules of Oxygen.

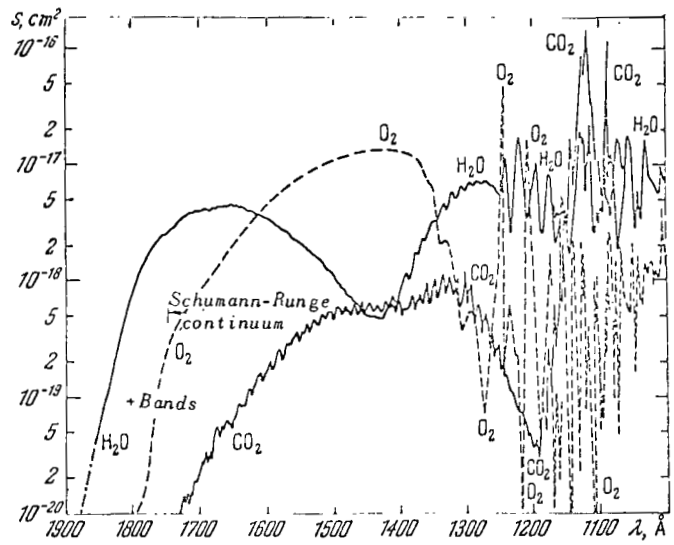

Fig.16 Cross Sections for Photodissociation of O_2, H_2O and CO_2 (Ref.18).

The radiation attenuation is /31

$$\frac{I_2}{I_1} = e^{-Ns}, \tag{1.22}$$

where I_1 is the intensity of incident radiation; I_2 is the intensity of penetrating radiation; N is the number of molecules in a column of a cross sectional area 1 cm^{-2}; s is the absorption coefficient per molecule. The quantity s often is termed the effective cross section having the dimensions [cm^2]. In Figs.16 and 17 the effective dissociation and ionization cross sections are plotted along the ordinate. The quantity

$$Ns = \tau, \tag{1.23}$$

which determines the total attenuation of radiation in a layer of matter is designated as optical thickness in absorption. The quantity

$$k = ns, \qquad (1.24)$$

where n is the density of matter [cm^{-3}], is called the volume coefficient of absorption. A comparison of eq.(1.22) with eq.(1.24) clearly shows the dimensions of the quantity k as being [cm^{-1}].

The optical thickness of the atmosphere with respect to incident radiation is also logically reckoned from $\tau = 0$ at a height $z = \infty$. Figure 18 shows the altitude for which $\tau = 1$ in the earth's atmosphere. The vertically incident radiation is attenuated e times at this altitude. To investigate the radiation of celestial bodies in the region $2000 < \lambda < 3000$ Å it is necessary to ascend to an altitude of at least 50 km, and in the region of $\lambda < 2000$ Å, to an altitude of at least 120 km. Such altitudes are accessible only to rockets. Hence astronomical studies in the ultraviolet spectrum region $\lambda < 3000$ Å are carried out exclusively with the aid of instruments carried aloft by rockets and artificial earth satellites. A very large number of such investigations has so far been made on the sun and stars. The reason for the lack of similar studies of the planets lies in the fact that the radiation intensity of the planets in the ultraviolet spectrum region is low and the flight time of the rockets is insufficient for a detailed investigation of this spectral region of the planets. Ultraviolet spectra of the planets are one of the future tasks of orbiting observatories and interplanetary stations.

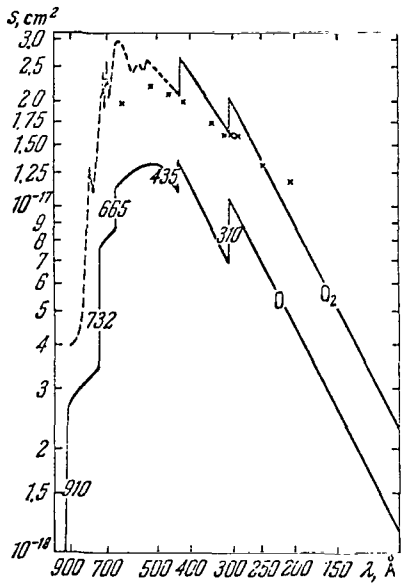

Fig.17 Cross Sections for Ionization of Atomic and Molecular Oxygen (Ref.18).

Much broader vistas for planetary spec-

TABLE 7

IONIZATION POTENTIALS AND DISSOCIATION ENERGIES OF CERTAIN DIATOMIC MOLECULES (REF.20)

Molecule	Dissociation Energy, ev	Ionization Potential, v	Molecule	Dissociation Energy, ev	Ionization Potential, v
N_2	9.76	15.58	CH	3.47	10.64
O_2	5.115	12.08	N_2^+	8.70	?
H_2	4.47	15.46	O_2^+	6.65	38.0
HD	4.51	?	H_2^+	2.646	?
CO	11.09	14.013	CO^+	8.33	?

troscopy exist in the infrared region. The vibrational-rotational bands of H_2O as well as of CO_2, O_3 and CH_4 in the 1 - 20 μ interval do not completely cover this region: There remain transparency windows (1.5 - 1.8, 2.0 - 2.5, 3.0 - 4.0, 4.5 - 5.0, 8 - 13 μ) in which absorption is absent or so small that, within these intervals, it is possible to conduct observations from the earth's surface (Fig.19). As shown above, the region from 20 μ to 1 mm (cf. Fig.4) is fully covered by the band of the rotational spectrum of H_2O. However, the partial pressure of H_2O decreases very rapidly with increasing altitude owing to the decrease in temperature. At altitudes of 25 - 30 km, which are accessible to

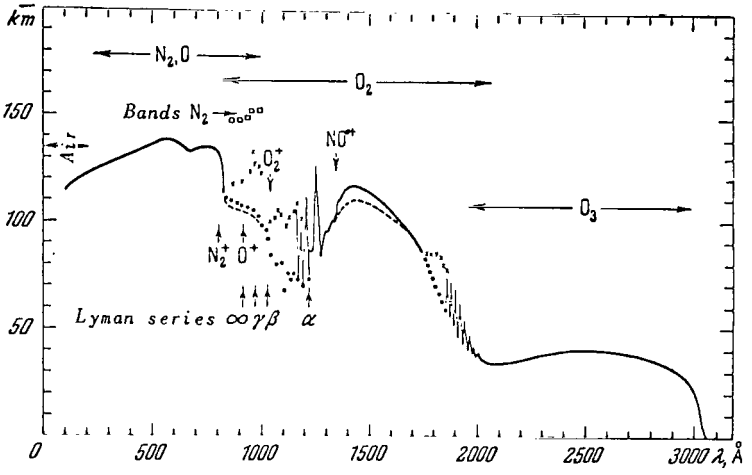

Fig.18 Penetration of Solar Ultraviolet Radiation into the Earth's Atmosphere (Altitude at which the Intensity Decreases e Times) (Ref.19).

balloons, the absorption of infrared radiation already may be disregarded. Consequently, the use of balloon-borne apparatus ("balloon astronomy") is of particular importance to research in the infrared region of the spectrum. The methods of balloon astronomy have already produced substantial results, which we will discuss in later Chapters. Balloon astronomy yields one other advantage which, at first, had been considered more important, namely, the possibility /34 of enhancing the angular resolving power in observations of planetary detail; at such altitudes atmospheric jitter no longer restricts the resolving power. In reality, however, it has not yet been feasible to exploit this advantage.

Section 1.2 Energy Distribution in Planetary Spectra

Spectral lines are observed against the background of a continuous spectrum in the form of absorption or emission lines, depending on the conditions of their formation. The continuous spectrum of the planets essentially differs from that of the stars, being determined by the superposition of two near-Planckian curves. The total energy distribution curve has a dual peak (Fig.20).

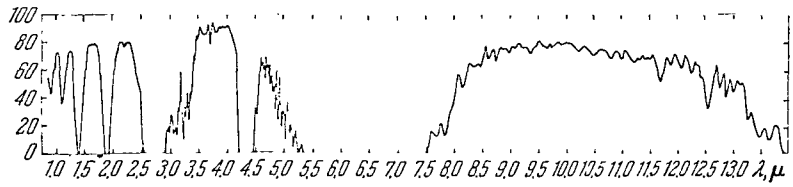

Fig.19 Transparency of the Atmosphere in the 1 - 15 μ Wavelength Region at 17 mm Precipitated Water. Ordinate: transmissivity in percent per nautical mile. The measurements were performed along a horizontal path. Since the altitude scale for H_2O in the earth's atmosphere is ~ 2 km, the horizontal transmission coefficient per nautical mile roughly equals the total vertical transmission of the atmosphere.

The short-wave segment represents the spectrum of solar radiation reflected from the planet, while the long-wave segment gives the characteristic thermal radiation of the planet. There exists a critical wavelength λ_c such that, in the wavelength range above λ_c (region I), the intensity of the thermal radiation is higher than that of the reflected radiation; conversely, in the wavelength range below λ_c (region II), reflected radiation predominates. For the planet nearest to the sun and hottest, namely Mercury ($T = 600^\circ K$ on the illuminated side), we have $\lambda_c \approx 2\mu$. The colder a planet the higher will be its λ_c. For Mars, we have $\lambda_c \approx 4\mu$ and for Jupiter, $\lambda_c \approx 9\mu$.

Knowing the intensity of thermal radiation of a planet it is possible to determine its temperature. If the total intensity Q, integrated from 0 to ∞ with respect to λ, is known, then the Stefan-Boltzmann law

$$\sigma T^4 = Q \tag{1.25}$$

can be used for determining the effective temperature $T = T_e$ ($\sigma = 1.817 \times 10^{-12}$ w · cm^{-2} · deg^{-4} · sterad^{-1}). If the monochromatic intensity I_λ or the intensity within some range $\lambda_1 - \lambda_2$ is measured, the brightness temperature T_B can be found from the relations /35

$$I_\lambda = B_\lambda(T_B) \tag{1.26}$$

and

$$\int_{\lambda_1}^{\lambda_2} I_\lambda \, d\lambda = \int_{\lambda_1}^{\lambda_2} B_\lambda(T_B) \, d\lambda, \tag{1.27}$$

where /36

$$B_\lambda = \frac{c_1 \lambda^{-5}}{e^{\frac{c_2}{\lambda T_B}} - 1} \quad w \cdot sterad^{-1} \cdot cm^{-2} \cdot \mu^{-1} \tag{1.28}$$

is the radiation intensity of an absolutely black body, determined by Planck's law ($c_1 = 1.19 \times 10^4$ w • sterad^{-1} • cm^{-2} • μ^4, $c_2 = 14{,}350$ μ • deg). The temperatures T_e and T_B represent the temperature of an absolutely black body whose brightness equals the measured brightness of the planet. Knowing the wavelength dependence of the intensity it becomes possible to determine the color temperature T_c which is the temperature of a perfectly black body of the same relative intensity distribution.

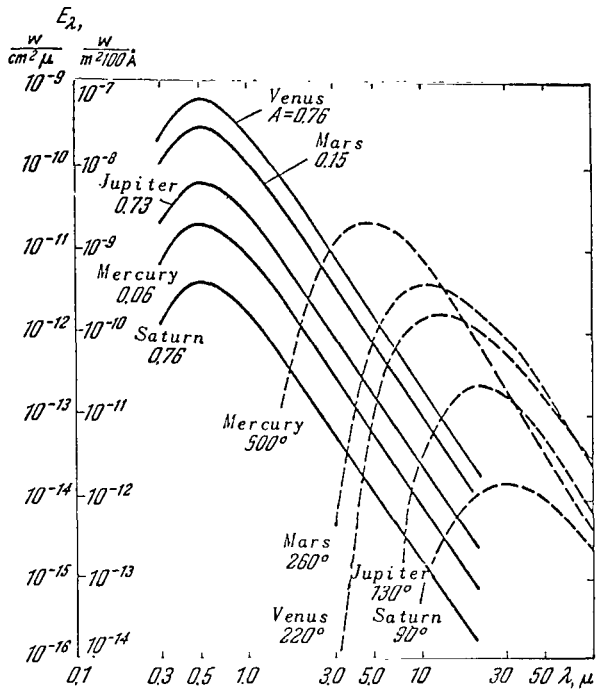

Fig. 20 Absolute Energy Distribution in the Planetary Spectra. Plotted along the ordinate is the monochromatic illumination on earth. The solid lines give the reflected radiation and the broken lines, the natural radiation. The energy distribution in the spectrum of characteristic radiation is calculated from Planck's formula. In calculating the reflected radiation it was assumed that the albedo (A) is independent of the wavelength.

The thermal radiation escaping into space is emitted by the surface and by the atmosphere. In the spectral regions where the atmosphere is transparent the emission source is the ground surface, such that

$$I_\lambda = \varepsilon_\lambda B_\lambda (T_s), \qquad (1.29)$$

where ε_λ is the emission coefficient and T_s is the true temperature of the surface. In the region of low frequencies and, particularly, of radio frequencies, it is possible to apply the Rayleigh-Jeans formula

$$B_\lambda = \frac{c_3 T_B}{\lambda^4} \quad w \cdot sterad^{-1} \cdot cm^{-2} \cdot \mu^{-1}, \qquad (1.30)$$

where $c_3 = 0.828$ w • sterad^{-1} • • cm^{-2} • μ^3 and

$$T_s = \frac{T_B}{\varepsilon}. \qquad (1.31)$$

In radio astronomy, brightness is usually given in a frequency scale. The Rayleigh-Jeans formula then is written as

$$B_\nu (T) = \frac{2kT}{\lambda^2} \quad w \cdot sterad^{-1} \cdot cm^{-2} \cdot cps^{-1}, \qquad (1.32)$$

where $k = 1.38 \times 10^{-23}$ erg • deg^{-1} is the Boltzmann constant and λ is given in cm.

Strictly speaking, the brightness temperature of the thermal emission of a solid body does not pertain to the solid surface itself but to some depth of the body equal to several wavelengths. For infrared radiation this reservation does not apply, but for the radio-frequency range the effective level responsible for the radiation may be at the depth of several tens of centimeters or several meters, at which the temperature markedly differs from the surface temperature.

In the spectral regions where the atmosphere is nontransparent the outgoing radiation is emitted by the atmosphere itself. It can be shown that, to a first approximation, the brightness temperature T_B equals the temperature of the atmosphere at the level where the optical thickness is $\tau = 1$. By measuring the brightness of thermal radiation of the atmosphere in different portions of the spectrum with different absorption it becomes basically possible to calculate the altitude distribution of temperature /37

$$T_a = T(z). \tag{1.33}$$

For this, one can utilize the wavelength dependence of brightness within the confines of some strong molecular band located in the region I. If the temperature of the atmosphere decreases with increasing altitude, as is most often the case, such a band will be externally observed as an absorption band. This method has not yet been employed in actual research since its application involves certain technical difficulties, but the respective prospects are highly interesting.

A direct determination of T_e from measurements of the total characteristic radiation flux also has not yet become reality; this would require placing a telescope, with a nonselective radiation sensor, outside the confines of the terrestrial atmosphere. The continuous spectrum of the planets in the region I generally is utilized only for determining the brightness and color temperatures T_B and T_c. The effective temperature T_e can be calculated by another method, namely by the heat balance of the planet. Since the total flux of absorbed solar radiation - disregarding the internal energy sources of the planet - equals the outgoing infrared flux, we have

$$F = \int_S \sigma T_e^4 \, dS = \frac{E_0 \pi r^2}{R^2} (1 - A_i), \tag{1.34}$$

where E_0 is the solar constant; r is the radius of the planet; R is the distance to the sun in astronomical units; A_i is the integral albedo averaged over the entire spectrum; dS is an element of area of the planet. The spherical albedo of a planet is the ratio of the solar radiation flux reflected in every direction to the incident flux. If T_e is identical at every point on the planet, then

$$\sigma T_e^4 = \frac{E_0}{4R^2} (1 - A_i). \tag{1.35}$$

It follows from eq.(1.35) that

$$T_e = \frac{280 \sqrt[4]{1 - A_i}}{\sqrt{R}}, \tag{1.36}$$

i.e., the temperature is inversely proportional to the square root of distance./38

In the region I, molecular transitions may, in principle, produce both absorption and emission bands (if the temperature of the atmosphere increases with altitude). In the region II, the spectrum of reflected solar radiation will contain molecular bands only in absorption. The solar quanta are absorbed in rotational-line frequencies $\nu_v + \nu_r$ and raise the molecule to a higher energy level. Transition back to the ground level occurs without radiation, owing to collision with another molecule. In the end, the energy of the quantum is converted into heat.

Radiation in the region II is reflected by the surface and the atmosphere. Even in the absence of absorption, the intensity of the light reaching the surface decreases due to scattering in the atmosphere. The scattered light partly escapes into space and partly is absorbed by the surface. Later we will consider in greater detail the problems of light scattering. Here we merely would like to point out the following: In the region $\lambda < 3000$ Å, owing to absorption by molecules (O_3, O_2, N_2, etc.; see Fig.18), the earth's albedo, conditioned by scattered radiation, is very small since the number of scattering molecules is small above the level at which the optical absorption density is $\tau = 1$. A similar picture is bound to prevail also for the other planets: In the ultraviolet spectrum region, at wavelengths shorter than some limiting wavelength λ', the brightness of scattered radiation decreases sharply. In this connection, in the upper layers of the atmosphere recombination processes, collision excitation, and chemical reactions cause the molecules and atoms to glow, and it is not unlikely that in the ultraviolet region ($\lambda < \lambda'$) the spectrum of a planet might be determined by the emissions of the upper atmosphere even on the day side.

The radiation spectrum of the earth's upper atmosphere is observed at night only up to 2.5 μ (Ref.21). This glow accounts for the brightness of the night sky on moonless nights and the brightness of the night side of the earth when viewed by an observer outside the earth. In the high latitudes, the brightness may be markedly enhanced by polar auroras. The spectrum of the unilluminated part (the night side) of the other planets apparently also is determined by the glow of the upper atmosphere - night airglow and polar auroras. The emission spectra of the glow of the upper atmosphere may be in principle a major tool in planetary research. Observations from the earth, however, involve major difficulties owing to the light scattered from the day side of the planetary disk.

As pointed out above, in the far infrared and submillimeter wave range the terrestrial atmosphere is nontransparent. Radio waves in the 1 - 10 mm range /39 still undergo appreciable absorption; however, already beginning with 1.5 - 2 mm it becomes possible to observe cosmic sources of radio radiation. Beginning with roughly from 1 cm to 15 m, absorption in the terrestrial atmosphere can be disregarded. Longer wavelengths are trapped due to refraction and reflection in the ionosphere. The critical frequency (the lowest frequency of radio waves passing through the ionosphere) is

$$f_c \approx 0.01 \sqrt{n_e} \quad mc, \tag{1.37}$$

where n_e is the electron density (cm^{-3}) at the ionization maximum. The thermal

radiation of the planets can also be observed in the centimeter and decimeter wave range. According to eq.(1.32), the brightness of thermal radiation in the radio range diminishes rapidly with increasing wavelength. The brightness temperature T_B, measured in the radio range, characterizes either the surface temperature (if the atmosphere is transparent to radio radiation) or the temperature of some level of the atmosphere. In both cases, this holds only if the radiation is of thermal nature. However, radio radiation may also be generated by nonthermal processes. An elementary example of such nonthermal processes is the emission of electromagnetic waves by radio stations. Natural nonthermal processes of radio-wave generation, operative in sources of cosmic radio emission, also are known. At present two processes (or "mechanisms") of this kind can be named: 1) emission of high-energy electrons in magnetic fields; 2) plasma oscillations excited by fluxes of charged particles. The nonthermal sources of cosmic radio emission may have an extremely high brightness temperature, considerably above the kinetic temperature.

Section 1.3 Telescopes, Spectral Instruments, Radiation Sensors

By contrast with the stars, the planets when observed through a telescope show as disks of considerable diameter. The planetary disks have dark and light parts of detail differing in size, shape, contrast, spectral characteristics, etc. This detail either is stable and specifically localized on the ground surface or else represents clouds rapidly changing in shape, disappearing and reappearing in other places. The stability of the portions of surface detail is not absolute, since these may undergo changes: either seasonal, slow "secular", or sudden (Mars). On the other hand, cloud formations may persist for protracted periods of time (Jupiter). Observations of the detail of planetary disks, compilation of maps of this detail, etc. at one time constituted the substance of /40 planetary studies. Currently, all possibilities in this direction as regards ground-based observations have been exhausted and further advance is being made along the line of physical methods. It is interesting to note that the large optical telescopes built in this century have contributed little if anything to the knowledge of planetary detail. What might be the reason for this, at first glance, strange phenomenon?

The angular resolving power of a telescope is known to be determined by three factors: 1) diffraction at the edges of the lens; 2) aberrations; 3) atmospheric jitter or trembling of image. Diffraction is due to the fact that the image of a point source at the focus of a lens of ideal quality is not a point but a round disk surrounded by a sequence of rings gradually decreasing in intensity. The distance from the center of the system of rings to the first maximum is

$$\Delta\varphi = 1.22 \frac{\lambda}{D} \text{ radian}, \tag{1.38}$$

where λ is the wavelength and D the lens diameter. Two point sources can be observed separately only if the angular distance between them exceeds $\Delta\varphi$. Here, Fig.21 shows the angle $\Delta\varphi$ (in seconds of arc) as a function of the telescope diameter, calculated for two wavelengths: $\lambda = 0.55\ \mu$ which is the effective wave-

length of the radiation perceived by the human eye and 10 μ which is the effective wavelength corresponding to the infrared transparency window at λ 8-13 μ. /41

The second source limiting the angular resolving power is constituted by aberrations. The parabolic mirror which is the principal element of present-day reflectors will cause no aberrations on its optical axis if its entire surface is polished with normal precision (deviations from a paraboloid, ± λ/8). Such a precision usually is attained in any manufacturing plant. Often, additional difficulties arise due to deformations caused by changes in spatial position and by temperature inhomogeneities. However, these effects can always be minimized to such an extent that definition is limited not by aberration but by atmospheric jitter.

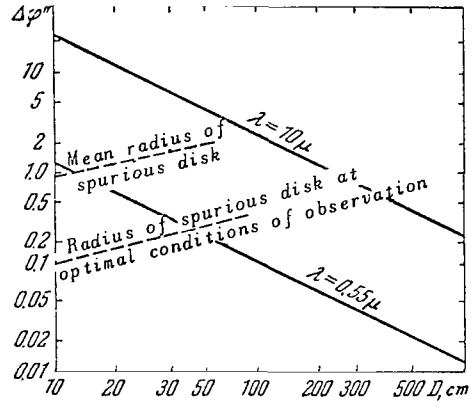

Fig. 21 Theoretical and Practical Angular Resolving Power of Optical Telescopes. The dimensions of the spurious disk are specified for the visible spectrum region.

The effect of atmospheric jitter is due to the fact that the diffraction image of a star undergoes deformation and splits into fragments that vibrate irregularly with respect to each other and become blurred so that, instead of a regular diffraction structure, a pulsating circle - known as the spurious disk - is produced. It is the size of this disk that determines the real definition and quality of the image. The diameter of the spurious disk generally increases with the diameter of the telescope. For a 5-m reflector (Fig. 22) it averages 3 - 4″ or, on good nights, 1 - 2″; for the 3-m reflector of the Lick Observatory this diameter is 0.3″, which is considered a record. Atmospheric jitter is due to fluctuations in the refractive index associated with currents and eddies in the atmosphere outside the telescope tower, within the tower and, lastly, in the tube of the telescope.

To attain an angular resolution of the order of 0.2″, which is considered record-breaking, it is necessary to select with extreme care the site of the telescope and the construction of the tower and tube. Very few ever have succeeded in attaining such a resolution, and that only in visual observations (Ref. 22). In photography, a resolution greater than 0.4″ is impossible to attain at present. The point is that the eye of the trained observer automatically selects the rare instants at which the image suddenly becomes particularly good for a few seconds, whereas a photographic plate registers an illumination that is integral in time.

In the last half-century, photographic and visual ground observations of the detail of planetary disks have contributed nothing new in principle. Appreciable progress was made only after outer-space rockets and interplanetary probes came into use. The Soviet interplanetary probes "Mechta" and "Zond III" revealed the aspect of the dark side of the moon, inaccessible to earth-based observations. With the aid of onboard television cameras of the US spacecraft Ranger /42

VII, Ranger VIII and Ranger IX the lunar surface was photographed from a short distance (as little as a few hundred meters). The spatial resolution of the last frames they transmitted before impacting on the lunar surface was fractions of a meter. An outstanding achievement of modern science was the photographing of the surface of Mars by the American spacecraft Mariner IV, carried out at a

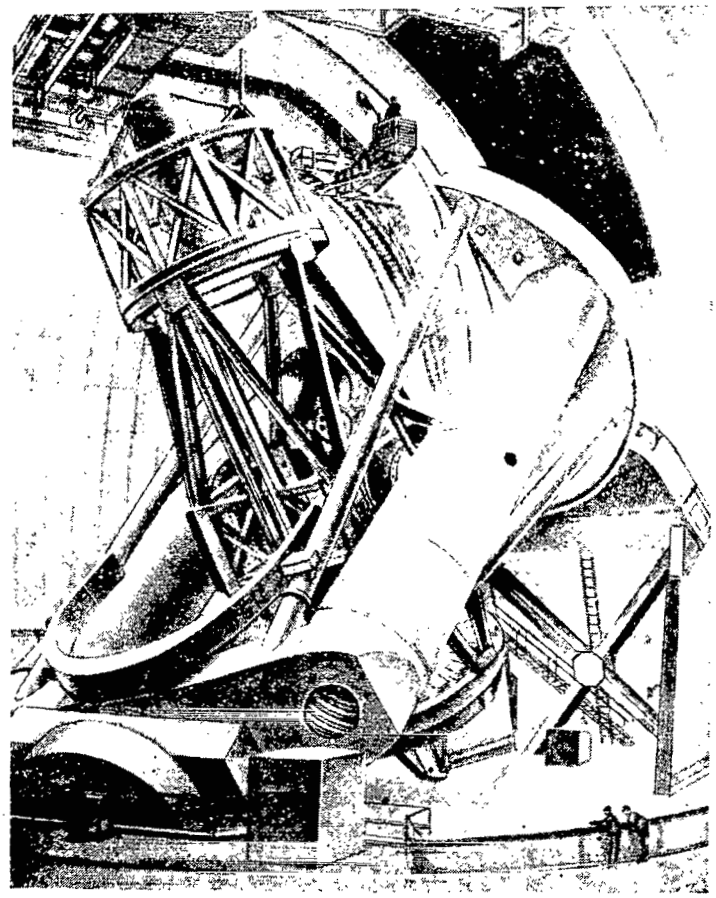

Fig.22 The 5-Meter Reflector of Mount Palomar Observatory.

distance of approximately 200 million km from Earth on July 14, 1965. Mariner IV made a flyby of Mars at a distance of 12,000 km from the surface of the planet. It transmitted 21 photographs, each corresponding to a sector measuring approximately 300 × 300 km (Ref.23). When observed from earth during favorable opposition, a sector of this kind measures 1 × 1″, i.e., verges on the limit of photographic resolution. /43

There exists still another means of increasing the resolving power, less expensive but not as fundamental, namely photographing the planets from the stratosphere by means of balloon-borne telescopes. To accomplish appreciable

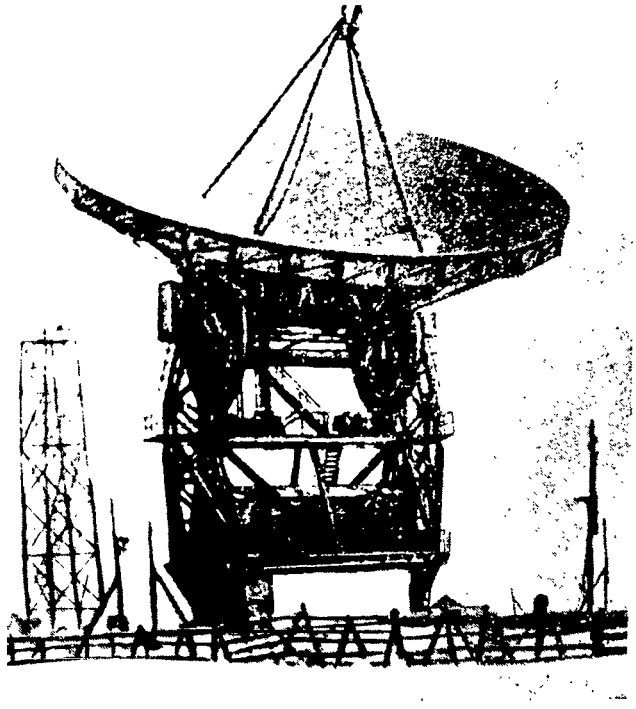

Fig.23 The 22-Meter Precision Radiotelescope of the Physics Institute im. P.N.Lebedev, Academy of Sciences USSR.

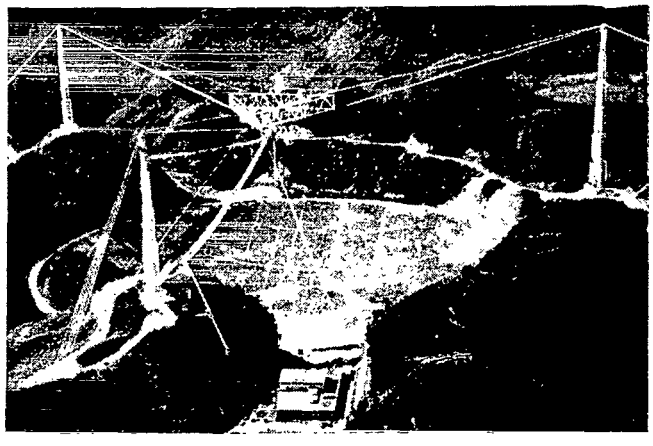

Fig.24 The 300-Meter Fixed Radiotelescope of the Arecibo Ionospheric Observatory (Puerto Rico).

progress a resolution of at least 0.1″ is required. This is the theoretical resolution of a telescope of a diameter of 1 m. A /44 reflector of appreciable dimensions would have to be lifted into the stratosphere and, once there, caused to operate in an ideal manner, which is not always attainable in a normal ground observatory. Attempts of this kind are being undertaken, so far without success.

The resolving power of a radiotelescope is chiefly restricted by diffraction, which also is determined by eq.(1.38); since the wavelengths in the radio range are long (centimeters, decimeters, and meters), the angular resolving power of the largest radiotelescopes is inferior to that of the smallest optical telescopes. Resolution of planetary disks is not feasible with an isolated radiotelescope, but the brightness distribution over the disk can be roughly investigated with the aid of interferometers - systems with interspaced aerials linked to a common receiver. For a two-aerial interferometer the distance between the antennas (base of the interferometer) is entered in eq.(1.38) as the quantity D. Figures 23 - 25 illustrate some of the radiotelescopes used in interplanetary research. The detailed distribution of radio brightness over a planetary disk can be determined with the aid of a small radiotelescope mounted on an interplanetary space platform during overflight at close distance. Observations of this kind were carried out in 1962 during the flight of the American spacecraft Mariner II close to Venus (cf. Chapt.III).

Planetary brightness in the

optical range is measured with methods of photographic and photoelectric photometry. In the region I (natural radiation), photometric measurements reveal /45
the brightness temperature of the surface, while in the region II (reflected radiation) they provide information on the optical properties of the atmosphere and the surface (cf. Sect.1.5).

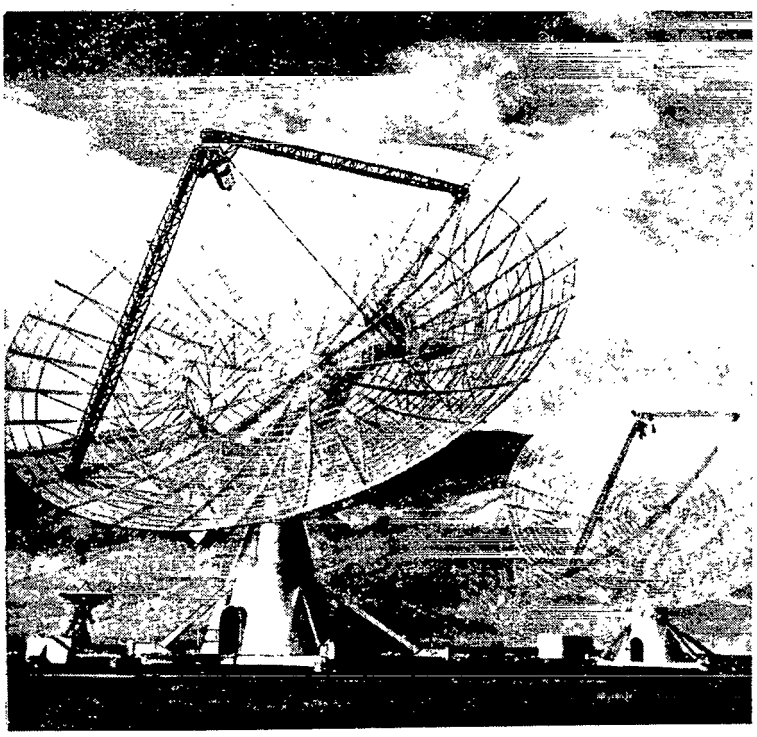

Fig.25 Two-Aerial Interferometer of the California Institute of Technology at Owens Valley.

In the radio range, the flux of natural radiation E_ν is measured at some specified frequency ν (the transmission bandwidth of the receiver usually being $\ll \nu$). The brightness B_ν is found from the relation

$$E_\nu = \int_\omega B_{\nu,\omega}\, d\omega, \tag{1.39}$$

where ω is the solid angle, and the brightness temperature is found from /46
eq.(1.32). Assuming that the brightness is the same at all points on the disk, we have

$$B_\nu = \frac{E_\nu}{\omega}, \tag{1.40}$$

where ω is the solid angle under which the planet is visible.

Note that in radio astronomy the term "flux" (having the dimensions [w • m^{-2} • cps^{-1}] or [erg • sec^{-1} • cm^{-2} • cps^{-1}]) corresponds to the term "illumination" in optics.

A photometer with a set of filters represents an elementary spectral apparatus. The spectral energy distribution can be investigated in greater detail by means of spectrographs and spectrometers. The chief characteristic of a spectral instrument is its spectral resolving power

$$f = \frac{\lambda}{\Delta\lambda}, \tag{1.41}$$

where $\Delta\lambda$ is the minimum distance between two spectral lines at which they still can be separately discerned. In theory, modern spectral instruments allow a resolving power of as much as 10^6 and more, but the actually attainable value of the focal length f depends on the intensity of the source, sensitivity of the sensor, and time of observation.

In the spectral range $\lambda < 11{,}000$ Å, radiation can be recorded with the aid of photographic emulsions and photoelectric sensors with photoemissive effect (photomultipliers and image converters). In planet observations in this region, it is readily possible to achieve a resolving power of

$$\frac{\lambda}{\Delta\lambda} \approx 10^4,$$

corresponding to a resolution of

$$\Delta\lambda \approx 1 \text{ Å}.$$

The resolving power may be increased roughly to 10^5 and in certain special cases to even greater values.

In the region $\lambda > 11{,}000$ Å, the most sensitive sensors are semiconductor photovaristors and photocells or phototubes with photoconductive effect. Although they are the best in this spectral region, their sensitivity threshold in absolute units is two or three orders of magnitude lower than that of sensors used in the region $\lambda < 11{,}000$ Å. At present the photoconductivity of a large number of semiconductor materials has been investigated and numerous photoelectric sensors and photodetectors with different sensitivities and different spectral characteristics have been developed (Ref.24). These instruments normally /47 operate at low temperatures. The greater the wavelength corresponding to the red boundary of the photoelectric effect, the lower will be the operating temperature. Table 8 presents certain types of photovaristors for the infrared region of the spectrum, in comparison with other types having optimal photosensitivity within their operating range.

In the 1 - 4 μ region the optimal detector of this kind is the lead-sulfide photovaristor (PbS). For the bright planets (Mars and Venus) photoelectric spectrometers with PbS photovaristors make possible a resolution of

$$\frac{\lambda}{\Delta\lambda} \approx 10^3$$

TABLE 8

INFRARED RADIATION DETECTORS

Material	Photovaristor (PhV) or Barrier-Layer Cell (BLC)	Cooled With	Red Boundary of Photo-electric Effect	Typical Sensitivity Threshold at the Maximum of Spectral Characteristic for an Area of 1 mm^2, w/cps
Ge, germanium	BLC	Solid CO_2	1.6	10^{-13}—10^{-12}
PbS, lead sulfide	PhV	Uncooled	3.0	10^{-11}
»	PhV	Solid CO_2	3.4	10^{-12}—10^{-11}
»	PhV	Liquid N_2	4.0	10^{-12}—10^{-11}
InSb, indium antimonide	BLC	» »	6	2×10^{-11}
Ge-Au, gold-doped germanium	PhV	» »	9	3×10^{-11}—10^{-10}
Ge-Zn, zinc-doped germanium	PhV	Solid N_2	15	3×10^{-11}—10^{-10}
Ge-Hg, mercury-doped germanium	PhV	Liquid H_2	15	2×10^{-12}
Ge-Ga, gallium-doped germanium	Bolometer	Liquid He, with evacuation (2° K)		2×10^{-12}
Radiation bolometers and thermocouples at room temperature	—			10^{-8}—10^{-10}

within the 1 - 2.5 μ range*. In the 3 - 4 μ transparency window, where the intensity is appreciably lower, we have

$$\frac{\lambda}{\Delta\lambda} \approx 10^2.$$

Similarly, in the 8 - 13 μ range, no spectra of Mars and Venus with a resolving power of more than 10^2 have as yet been obtained, but these observations were /48 chiefly based on heat sensors of relatively low sensitivity (Refs.25, 26). In principle it is feasible to improve the resolution in this range by using doped germanium photovaristors. Recently, a new type of heat sensor, competing in sensitivity with photovaristors, has appeared on the market, the low-temperature (2°K) bolometer of gallium-doped germanium (Ref.27) which has already led to a number of important astronomic discoveries.

At a resolving power of 10^4 - 10^5, it becomes possible to distinguish be- /49 tween separate rotational lines of the vibrational-rotational bands. This cannot be done at a resolving power of 10^2 - 10^3; in the latter case, only the envelope of the rotational structure, which is more or less distorted by the instrument contour of the device, is recorded. An increase in resolving power would

* Recently G. and P.Koppe, using the Fourier method, obtained the spectrum of Venus in the 1 - 2.5 μ range with a resolving power of $\lambda/\Delta\lambda = 10^5$ (galley-proof note).

make it possible to detect still unknown weak bands and to extract more information from the already known bands, but the solution of this problem requires a marked improvement in the technique of observation.

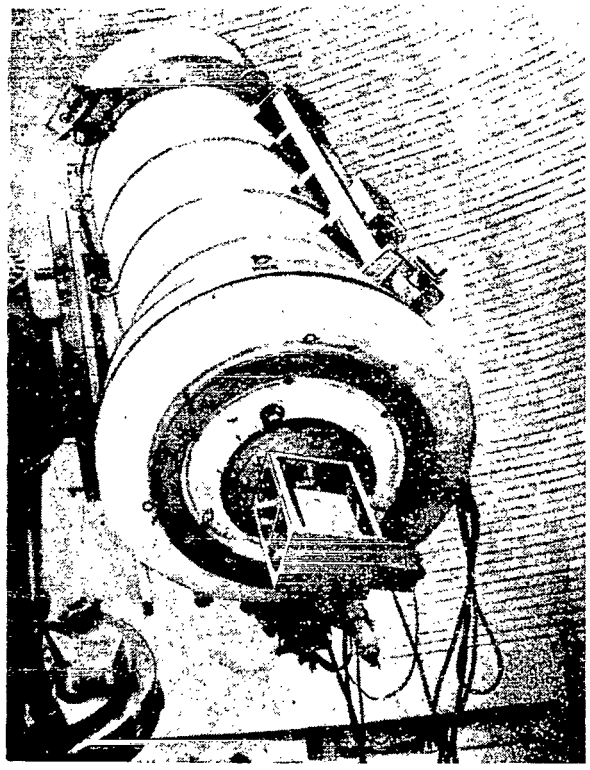

Fig.26 The 125-cm Reflector of the Southern Station of the State Astronomic Institute im P.K.Shternberg, with an Infrared Prism Spectrometer (Crimean Astrophysical Observatory).

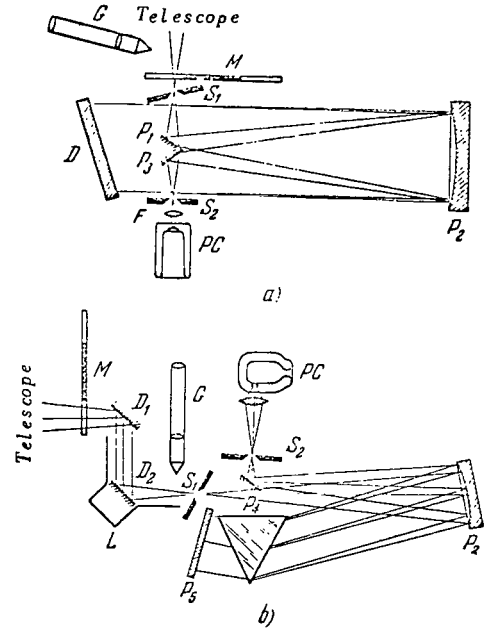

Fig.27 Optical Diagrams of Diffraction (a) and Prism (b) Spectrometers Used by the Author in Planet Observations.

Figure 26 gives a photograph made with the 125-cm reflector of the Southern Station of the State Astronomical Institute im. P.K.Shternberg (GAISh) while Fig.27 shows the optical diagrams of two infrared spectrometers used by the author for measuring planetary spectra on this telescope. Here, S_1 and S_2 are the entrance and exit slits of the spectrometers; P_2 is the parabolic mirror which simultaneously acts as collimator and camera (autocollimation arrangement); P_1, P_3, P_4; D_1, D_2 are plane mirrors. The edges of the first slit are mirror- /50 polished and tilted through an angle such that the planet image on the slit can be seen in the viewing tube G. PC denotes the photovaristor in a Dewar vessel. Mostly lead-sulfide photovaristors cooled with solid carbon dioxide or liquid nitrogen were employed. The spectrum is scanned by turning the diffraction grating D in the diffraction spectrometer and the autocollimation mirror in the prism spectrometer. The beam of light emerging from the telescope is interrupted by a

perforated rotating disk and the signal from the photovaristor is amplified by a narrow-band amplifier tuned to the modulation frequency. After rectification and smoothing in a synchronous detector, the signal is recorded on the strip chart of the electronic potentiometer. The diffraction spectrometer is used in studying relatively bright bodies (Mercury, Mars, Venus, Jupiter, Saturn) with a maximum spectral resolution in the 1 - 2.5 μ range. All observations in the 3 - 4 μ range as well as observations of faint objects (e.g., the Galilean satellites of Jupiter) or small sectors of bright planets in the 1 - 2.5 μ range were performed with the aid of the prism spectroscope.

The use of optical spectrographs and spectrometers permits recording a large spectral interval in its entirety (about an octave and more). In the radio range this cannot be done, since the entrance elements of the radiotelescope (beginning with the exciter) are fine-adjusted. Observations of the planets require a highly sensitive apparatus (note that radio astronomy sensors are generally the most sensitive of all radiation detectors). As a rule, individual astronomical observatories operate with a limited set of radiometers and can conduct simultaneous observations at only one or two frequencies. The spectrum must be plotted along points, on the basis of the data collected by various investigators. This is acceptable only when investigating the continuous spectrum, since new spectral lines cannot be discovered by this procedure except fortuitously. Several spectral lines known in radio astronomy (λ 21 cm H, OH lines) were discovered only because of precise theoretical prediction of their position. No spectral line has been observed in the radio spectra of planets, although these lines may exist in the millimeter and centimeter ranges (Ref.28). Radiospectroscopy offers interesting possibilities for research in planetary physics, but the technical obstacles are as yet too great.

Reflected and scattered radiation is polarized. The degree of this polarization depends on the nature of the ambient medium and the conditions of scat- /51
tering. Hence an analysis of polarization may provide interesting information on the physical characteristics of the scattering medium, whether this be an atmosphere or a solid surface or both. Visual, photographic and photoelectric polarimeters are used for this purpose. The devices most sensitive to small degrees of polarization are the photoelectric types.

The polarization of natural radiation (Ref. 29, 30) also is of considerable interest. While radiation is thermal and belongs to a solid and smooth surface, at the planetary limbs it must be linearly polarized, with the degree of polarization depending on the refractive index in accordance with Fresnel's laws. The radiation of the gaseous atmosphere is not polarized. If the radiating medium is a dense ionosphere (which, in principle, may occur within the radio range; cf. Chapt.III), circular polarization in a magnetic field may occur. The nonthermal emission of high-energy electrons in magnetic fields is characterized by linear polarization, with the orientation of the dominant plane depending on the geometry of the magnetic field.

Section 1.4 Quantitative Spectroscopy of Planetary Atmospheres

a) Width of spectral line. The width of a spectral line (atomic or molecular) is determined by three factors: 1) natural attenuation; 2) attenuation due

to collisions (pressure broadening); 3) Doppler broadening.

Doppler broadening constitutes the statistical effect of the simultaneous observation of a large number of emitting and absorbing atoms moving at various velocities. Were we to isolate a single atom from all other atoms, only the factor (1) would be operative.

The width ruled by the factor (1) is designated as $\Delta\nu_N$; by the factor (2), as $\Delta\nu_C$; by the factor (3), as $\Delta\nu_D$. In quantum mechanics it is shown that

$$\Delta\nu_N = \frac{1}{4\pi}\left(\frac{1}{\tau_i} + \frac{1}{\tau_k}\right), \tag{1.42}$$

where τ_i and τ_k are the lifetimes of the upper and lower states, respectively (the characteristic time of natural attenuation). The quantity $\Delta\nu_N$ is at most 10^8 sec^{-1}, even for the strongest lines.

Collision broadening can be interpreted as the effect of collisions disrupting the process of emission and reducing τ. The lifetime reduced by collisions (the characteristic emission decay time due to collisions) is /52

$$\tau_C = \frac{l}{V} = \frac{1}{4\sigma V n\sqrt{2}}, \tag{1.43}$$

where l is the mean free path; V is the mean velocity of the molecules; σ is the cross-sectional area of the molecule; n is the concentration.

Under normal conditions ($n = 2.7 \times 10^{19}$ cm^{-3}, $T = +20^\circ C$) for an oxygen molecule we have $V = 4 \times 10^4$ $cm \cdot sec^{-1}$. Assuming that $\sigma = 10^{-15}$ cm^2, we have $\tau_C \approx 2 \times 10^{-10}$. In the planetary atmospheres, practically always $\tau_C \ll \tau_N$, $\Delta\nu_C \gg \Delta\nu_N$. It can be shown that

$$\Delta\nu_C = \frac{1}{2\pi\tau_C}. \tag{1.44}$$

Consequently, using eq.(1.43) and considering that $V = \sqrt{\frac{2kT}{m}}$ while $P = nkT$, we obtain the following, in the case of collisions:

$$\Delta\nu_C = \frac{1}{2\pi\tau_C} = \frac{2\sqrt{2}}{\pi}\frac{P\sigma}{kT}\sqrt{\frac{2kT}{m}} = \frac{4}{\pi}\frac{P\sigma}{\sqrt{kTm}}, \tag{1.45}$$

where P is the pressure; T is the temperature; m is the mass of the molecule. Thus, the line width due to collisions is directly proportional to the pressure and inversely proportional to the square root of the temperature. In eq.(1.45) the quantity σ, known as the optical collision cross section, differs somewhat from the kinetic cross section.

The width $\Delta\nu_C$ can be expressed as the width α under normal conditions:

$$\Delta\nu_C = \alpha\left(\frac{P}{P_0}\right)\left(\frac{T_0}{T}\right)^{1/2}, \tag{1.46}$$

where P_0, T_0 are the pressure and temperature under normal conditions. Table 9 presents the value of α in cm^{-1} for various gases. This value depends on the nature of the emitting molecule and of the molecules with which collision occurs. Hence, both molecules to which a given value of α pertains must be specified. For example, the width of the NH_3 line in a mixture with H_2 will be denoted as $\alpha_{NH_3-H_2}$. It can be seen from Table 9 that the values of α are close to 0.1 cm^{-1} or, expressed in wavelength units, $\Delta\lambda = \frac{\Delta\tilde{\nu}}{\tilde{\nu}}\lambda$ i.e., approximately 0.1 Å in the neighborhood of $\lambda = 1\ \mu$.

TABLE 9 /53

LINE BROADENING DUE TO COLLISIONS

Molecule (X)	α_{X-N_2}, cm^{-1}	$\frac{\alpha_{X-X}}{\alpha_{X-N_2}}$	$\frac{\alpha_{X-H_2}}{\alpha_{X-N_2}}$	$\frac{\alpha_{X-He}}{\alpha_{X-N_2}}$
CO_2	0.07 [31]	1.4 [31,32]	1.17 [32]	0.59 [32]
CO	0.13 [33]	1.02—1.08 [32]	0.85 [32]	0.64 [32]
CH_4	0.15 [34]	1.4 [32]	1 [34]	0.56 [32]
NH_3	0.6 [35]	6	1.4	3
H_2O	0.1 [33]	5 [32]	—	—
O_2	0.043 [36]	—	—	—

b) Coefficient of absorption in a line. If the broadening is not exclusively produced by attenuation, the frequency dependence of the line absorption coefficient forms the so-called Lorentz profile

$$s_\nu = \frac{s(\Delta\nu_C + \Delta\nu_N)}{\pi[(\nu-\nu_0)^2 + (\Delta\nu_C + \Delta\nu_N)^2]}. \tag{1.47}$$

The magnitude of s_ν which is maximal when $\nu - \nu_0 = 0$. Here, s_ν decreases to half when $\nu - \nu_0 = \Delta\nu_C + \Delta\nu_N$. Integrating over the frequency from 0 to ∞, we have

$$\int_0^\infty s_\nu\, d\nu = s. \tag{1.48}$$

Therefore, the coefficient s [cm^2] is called the integral coefficient of absorption for a line. The integral absorption coefficient is a function of only the quantity of the absorbing substance, correct to within the multiplier $(1 - e^{-\frac{h\nu}{kT}})$ describing forced emission. When $h\nu \gg kT$, this multiplier is negligibly small. If $T = 300^\circ K$, the equality $h\nu = kT$ is reached for $\lambda \approx 50\ \mu$. The integral absorption coefficient can be found not only for individual lines but

also for an entire band. It is calculated per gram of matter or per cm • atm (see below). The line widths $\Delta\nu_C + \Delta\nu_N$ often are termed Lorentz widths.

If attenuation is absent, the line contour is determined only by the Doppler effect. It can be shown that, in this case,

$$s_\nu = \frac{s}{\Delta\nu_D \sqrt{\pi}} e^{-\left(\frac{\nu-\nu_0}{\Delta\nu_D}\right)^2}. \tag{1.49}$$

The dependence $s = s(\nu)$, expressed by eq.(1.49), is known as the Doppler profile, while the width $\Delta\nu_D$ is termed the Doppler width. Here, s_ν decreases e^2 times when $\nu = \nu_0 = \Delta\nu_D$.

TABLE 10

RELATIVE ROLES OF DOPPLER AND LORENTZ BROADENING IN PLANETARY ATMOSPHERES
(CO_2, ν = 600 cm^{-1})

	Mars $P = 10$ mb $T = 200°$ K	Earth $P = 1000$ mb $T = 270°$ K	Venus $P = 10000$ mb $T = 600°$ K
$\Delta\nu_C$	7×10^{-4} cm^{-1}	0.07 cm^{-1}	1.4 cm^{-1}
a	0.16	11.3	150

The combined effect of Lorentz and Doppler broadenings produces the so-called Voigt contour /54

$$s_\nu = \frac{s\Delta\nu_C}{\sqrt{\pi^3}} \int_{-\infty}^{+\infty} \frac{e^{-y^2}\,dy}{a^2 - (p-y)^2}, \tag{1.50}$$

where

$$p = \frac{\nu - \nu_0}{\Delta\nu_D}, \qquad a = \frac{\Delta\nu_C}{\Delta\nu_D}.$$

The absorption coefficient at the center of the Lorentz profile is

$$s_{\nu_0} = \frac{s}{\pi(\Delta\nu_C + \Delta\nu_N)},$$

while at the center of the Doppler profile it is

$$s_{\nu_0} = \frac{s}{\sqrt{\pi}\,\Delta\nu_D}.$$

For the Voigt contour the relationship between s_{ν_0} and s is more complex, but in this case we always have

$$s_{\nu_0} < \min\left\{\frac{s}{\pi(\Delta\nu_C + \Delta\nu_N)}, \frac{s}{\sqrt{\pi}\Delta\nu_D}\right\}.$$

The magnitude of the integral (1.48) is independent of the nature of the profile. As pointed out previously, $\Delta\nu_C \gg \Delta\nu_N$. In the lower atmospheres of the planets we usually have

$$\Delta\nu_C \gtrsim \Delta\nu_D, \qquad a \gtrsim 1. \tag{1.51}$$

In this, the planetary atmospheres markedly differ from the stellar atmospheres, for which normally $\alpha \ll 1$. The reason for this difference lies in the fact that, in the stellar atmospheres, the temperatures are much higher and the densities lower than in the planetary atmospheres. Table 10 presents the Doppler widths /55 $\Delta\nu_D$ for several typical temperature values in the case of carbon dioxide. It also gives $\Delta\nu_C$ and the a ratios for various pressures. Note that $\Delta\nu_D$ decreases with decrease in ν while a then increases.

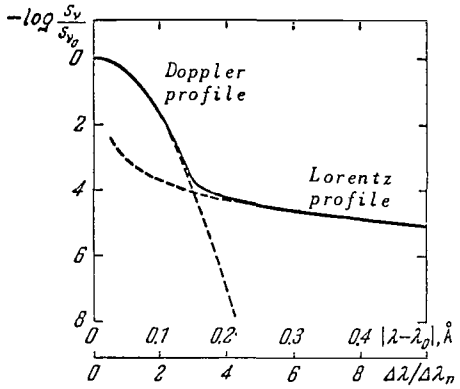

Fig. 28 Doppler and Lorentz Line Profiles.

A comparison of eqs. (1.47) and (1.49) clearly shows that, in the region

$$\nu - \nu_0 \gg \Delta\nu_D$$

the Doppler coefficient decreases at a much faster rate than the Lorentz coefficient (Fig. 28). If $a < 1$, the profile in the central portion of the line is close to a Doppler profile, but as soon as the difference $\nu - \nu_0$ exceeds $\Delta\nu_D$ several times, the profile becomes a Lorentz profile. If $a > 1$, the profile always is close to a Lorentz profile.

c) Growth curves. Consider the absorption spectrum of a plane-parallel uniform layer of gas containing N molecules per column of 1 cm^2 cross section. Suppose the intensity of the radiation penetrating through this layer is I_0 in the continuous spectrum and I_ν in the line with a frequency ν. Let us designate the quantity

$$R_\nu = \frac{I_0 - I_\nu}{I_0} = 1 - \frac{I_\nu}{I_0} \tag{1.52}$$

as monochromatic absorption (Fig. 29). The total absorption in the line

$$W = \int_0^\infty R_\nu \, d\nu = \int_0^\infty R_\lambda \, d\lambda \tag{1.53}$$

is termed the equivalent width (dimensions [cm^{-1}] or [Å]). According to eq. (1.22), we have

$$W = \int_0^\infty (1 - e^{-Ns_\nu}) \, d\nu, \tag{1.54}$$

where s_ν is given by eqs. (1.47), (1.49), or (1.50). If we have

$$Ns_\nu \ll 1$$

everywhere so that also R_ν is small everywhere, then /56

$$W = N\int_0^\infty s_\nu d\nu = Ns. \tag{1.55}$$

Thus, the equivalent width of weak lines is directly proportional to the number of molecules along the line of sight and to the integral absorption coefficient. Such lines are termed unsaturated. A line may be considered unsaturated if its Doppler or Lorentz width (whichever is greater) is several times greater than the measured equivalent width.

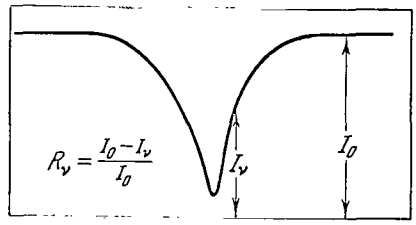

Fig.29 For Determining R_ν.

Another extreme case occurs if, in the central portion of the line,

$$Ns_\nu \gg 1.$$

Such lines are known as saturated. It can be shown that, for sufficiently high Ns,

$$W = 2\sqrt{Ns\Delta\nu_C}. \tag{1.56}$$

The dependence of W on the product of Ns is designated as the growth curve. Knowing s and measuring the W of the unsaturated lines, it becomes possible - with the aid of the growth curve - to determine the number of molecules N along the line of sight. In the case of unsurated lines, only the product of $N\Delta\nu_C$ can be determined. To find N it is necessary to know not only s but also the Doppler width $\Delta\nu_C$, i.e., the parameter α, the pressure, and the temperature [cf. eq.(1.46)]. If W had been measured for both unsaturated and saturated lines of some given absorbing gas, we can find separately N and $\Delta\nu_C$. Since $\Delta\nu_C$ is determined by the total pressure in the atmosphere, then, assuming that α and T are known, it is possible to find not only N but also the total pressure P as well as the relative concentration

$$C = \frac{P_x}{P}, \tag{1.57}$$

where

$$P_x = nkT = \frac{N}{H}kT$$

is the partial pressure of the absorbing gas (H is the altitude scale; cf. Sect.1.6).

In the region of values of Ns close to unity, the slope of the growth curves depends on a. When $a \ll 1$, the linear and quadratic segments of the growth curve are separated by a logarithmic segment over which W increases very little with increasing Ns. If $a \gg 1$, the linear segment almost immediately becomes quadratic (Fig.30). It is essential that, at sufficiently high Ns, the equivalent width is independent of $\Delta\nu_D$ even for low values of a. This is due to the /57

fact that the Lorentz absorption coefficient decreases with distance from the line center more slowly than the Doppler coefficient.

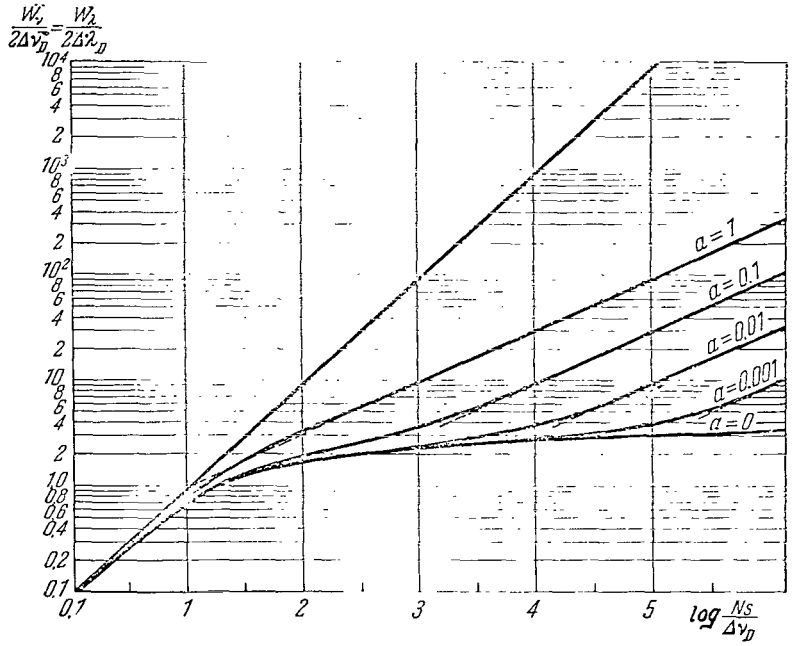

Fig.30 Growth Curve of an Isolated Line as a Function of Different Values of a = $\Delta\nu_C/\Delta\nu_D$.

The conditions of formation of absorption lines in planetary and stellar atmospheres differ not only because of the different relative roles played by the Lorentz and Doppler broadenings. Another and more fundamental difference lies in the very mechanism of line formation. In planetary atmospheres (at any rate, in their lower layers) the lines form as a consequence of true absorption: Each absorbed quantum transmits its energy to the thermal motion of the molecules. The probability of the collisional deactivation of an excited level is /58 greater than the probability of a radiative deactivation. In this case, the absorption will be

$$R_\nu = 1 - e^{-\tau_\nu}.$$

In the stellar atmospheres, the inverse process takes place with respect to strong lines. Radiative deactivation is more likely than collisional deactivation, and absorption lines occur owing to resonance scattering, i.e., multiple successive transradiation or forward scattering. In the continuous spectrum the radiation of the photosphere freely passes through the rotating layer. In line frequencies, part of the quanta is scattered back into the photosphere. Then,

$$R_\nu \approx \frac{\tau_\nu}{1+\tau_\nu}.$$

In sufficiently high layers of the planetary atmospheres resonance scattering also becomes a major factor. The level above which true absorption in some atmospheric molecular band ceases to be essential and is supplanted with scattering is termed the level of vibrational relaxation. For example, the vibrational relaxation level of the band CO_2 λ 15 μ in the earth's atmosphere lies at the altitude of about 75 km, where the density is 10^5 times as low as at the surface.

d) Absorption in bands. In the region $\lambda > 1.1$ μ, individual rotational lines cannot be resolved in the planetary spectra. Hence in this case vibrational-rotational bands are recorded such as to determine mean absorption which (if the rotational lines do not overlap) will be

$$\bar{R}_\nu = \frac{W_\nu}{d_\nu}, \tag{1.58}$$

where W_ν is the equivalent width of the individual rotational lines and d_ν is the distance between the lines. When $W_\nu \ll d_\nu$, the mean absorption may be small even if the rotational lines are saturated.

When W_ν comes close in magnitude to d_ν, the overlap becomes considerable. To find the dependence

$$\bar{R}_\nu = f\left(\frac{W_\nu}{d_\nu}\right); \tag{1.59}$$

in this case, the effects produced by all lines contributing at the frequency concerned must be summed up. This summation can be performed numerically, yielding

$$W = \varphi(N, s, \Delta\nu_C) \tag{1.60}$$

as the growth curve for the entire band. Elsasser (Ref.36a) showed that, in an idealized band consisting of equidistant lines of identical intensity, the mean absorption is /59

$$\bar{R} = 1 - \frac{1}{2\pi}\int_{-\pi}^{+\pi} e^{-\frac{\beta x \sinh\beta}{\cosh\beta - \cos z}}\, dz, \tag{1.61}$$

where $\beta = \frac{2\pi\Delta\nu_C}{d}$, $x = \frac{Ns}{2\pi\Delta\nu_C}$. If $x = 1.25$ and $\beta < 0.3$, then eq.(1.61) can be rewritten in a simpler form

$$\bar{R} = \Phi\left(\sqrt{\frac{2\pi N s \Delta\nu_C}{d^2}}\right), \tag{1.62}$$

where $\Phi(x)$ is the probability integral, $\Phi(x) = \frac{2}{\sqrt{2\pi}}\int_0^x e^{-\frac{t^2}{2}}\, dt$. If $\beta > 3$,

then we have, for any x,

$$\bar{R} = 1 - e^{-\beta x}. \tag{1.63}$$

For sufficiently high values of x, eq.(1.62) satisfactorily describes the $\bar{R}$ function with respect to any ratio of $\Delta\nu_C$ to d. Since in a real absorption band s and d depend on ν, it may be assumed that at every point absorption is described by Elsasser's model with its value of s and d, so that

$$W = \int R_\nu d\nu.$$

Here, it is convenient to introduce the concept of the generalized absorption coefficient,

$$l_\nu = \frac{2\pi s\alpha}{d_\nu^2}. \tag{1.64}$$

Then, taking eq.(1.46) into account, we have

$$\bar{R}_\nu = \Phi\left(\sqrt{l_\nu N\left(\frac{P}{P_0}\right)\left(\frac{T_0}{T}\right)^{1/2}}\right). \tag{1.65}$$

When calculating $\bar{R}_\nu$ from this formula, l_ν must be calculated per molecule since N is the number of absorbing molecules.

Figure 31 shows the frequency dependence of the generalized CO_2 absorption coefficient l_ν calculated for 1 cm • atm, in the neighborhood of 15 μ; several strong overlapping absorption bands can be seen. The mean absorption $\bar{R}$, required for the utilization of Elsasser's model, can be also estimated in a more primitive manner by assuming that $\bar{R}$ = const within the confines of the band. /60 Then,

$$\bar{R} = \frac{W}{\Delta\nu},$$

where $\Delta\nu$ is the band width specified by one method or the other. For example, for CO_2 bands (with the aid of the specified rotational temperature) we calculated, within the confines of each branch, the values of $\Delta\nu_R$ and $\Delta\nu_P$, i.e., the distances between the lines K_1 and K_2 which display the same intensity and are such that

$$\Sigma W(K_1 < K < K_2) = \frac{\Sigma W(K)}{2},$$

where W(K) is the equivalent width of the line with the rotational quantum number K. Subsequently, it was assumed that $\Delta\nu = 2(\Delta\nu_R + \Delta\nu_P)$.

Elsasser's model satisfactorily illustrates absorption in bands with a regular rotational structure, which are characteristic of diatomic and linear polyatomic molecules. The absorption bands with a complex structure (H_2O, CH_4, NH_3)

are better represented by the Goody statistical model. A detailed analysis of the respective advantages of the use of different models can be found elsewhere (Ref.32, 37). The most reliable are the growth curves obtained experimentally by recording spectra in the laboratory for a sufficiently broad range of values of N and P (Ref.16, 32). However, the plotting of laboratory growth curves is very laborious and time-consuming and, besides, by no means always technically possible. In fact, a correct representation of the formative conditions of lines in the planetary atmospheres requires long optical paths commensurate with the altitude scale.

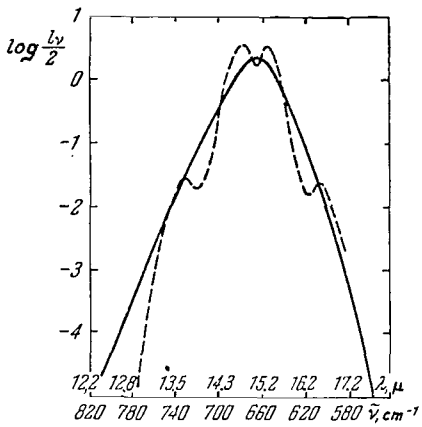

Fig.31 Generalized Absorption Coefficient (for 1 cm • • atm) of CO_2 Bands in the Neighborhood of λ 15 μ. Solid curve - according to (Ref.36a); broken curve - according to (Ref.36b).

Thus, the quantity of the absorbing gas along the line of sight can be determined from weak absorption lines and bands, while the mathematical product of this quantity and the Lorentz width can be determined from strong lines. If a sufficiently high resolution is possible, the line width can be measured directly. Of course, this is feasible only in the "photographic" region of the spectrum (λ < 11,000 Å). As shown in Table 9, the measurement of line width requires a resolving power of at least 10^5. The /61 pressure can be determined from the width of weak absorption lines with the aid of eqs.(1.22), (1.47) and (1.46) [cf. for example (Ref.38)].

In the upper layers of the atmosphere, we have $\Delta\nu_D \gg \Delta\nu_C$; hence, the width of atomic and molecular lines in the luminescence spectrum of the upper atmosphere is determined by the rate of thermal agitation rather than by pressure. By means of the relation

$$\Delta\nu_D = \nu\frac{V}{c} = \frac{\nu}{c}\sqrt{\frac{2kT}{m}}, \qquad (1.66)$$

the temperature T can be determined according to the width of these lines. So far, this method has been applied only to the terrestrial atmosphere (Ref.39, 40) but, in principle, may be useful also in research on the atmospheres of the other planets. In stellar atmospheres, a major portion of the Doppler width may be due to turbulence, mass fluxes, and rotation. In the case of planets, the velocity of motion characteristic of these processes is markedly below the velocity of thermal motion and can be disregarded.

e) Mean air mass. The above formulas of quantitative spectral analysis are suitable only for a description of absorption by a plane-parallel homogeneous layer of a gas. A layer of this kind can be produced in a laboratory spectral cell. In the atmosphere, the gas concentration and pressure change with altitude. Moreover, in observing another planet from earth, light will pass twice through its atmosphere, and at different points on the disk its angles of inci-

dence and reflection will differ. If the atmosphere contains scattering particles or if it is sufficiently dense, a large part of the observed emission (and sometimes virtually the entire emission) will be reflected by the atmosphere rather than by the surface. Lastly, we disregarded the characteristic radiation of the gas, which means that the above formulas are suitable only for the short-wave region of planetary spectra.

Consider an elementary case where the last two factors - scattering and characteristic radiation of the planetary atmosphere - can be disregarded. Solar radiation passes through the atmosphere, is reflected from the surface, and rebounds into outer space. Owing to the presence of absorbing molecules, absorption bands appear at certain frequencies. We measured their equivalent widths and, with the aid of the formulas given above, were able to estimate the quantities N and $N\Delta\nu_c$. Let us suppose that we wish to calculate the number N_0 of molecules over 1 cm^2 of surface at the zenith as well as the total pressure at the surface (for definiteness, we assume that α and T are known). The ratio

$$\bar{M} = \frac{N}{N_0} \tag{1.67}$$

is termed the mean air mass and depends on the conditions of illumination of /62
the disk at the time of observation. If the observations pertain to the spectrum of a small area whose angular dimensions are much smaller than the dimensions of the planetary disk, the air mass will be

$$M = \sec i + \sec z, \tag{1.68}$$

where z is the angle of incidence and i is the angle of reflection (between the beam and the normal to the surface). It is assumed that the sphericity of atmospheric layers can be neglected here (this assumption is justified if the area considered is not too close to the limb or to the terminator). Table 11 presents mean air mass values in the full phase (entire disk illuminated) and in the 90° phase (one quarter of the disk) for two cases: 1) the entire disk is accommodated within the slit; 2) the slit intersects the disk along the equator (Ref.41). Concerning the reflecting properties of the surface, two extreme assumptions can be made: 1) the brightness of the disk is proportional to cos z; 2) the brightness of the disk is identical at any point on the disk.

The figures in Table 11 pertain to unsaturated absorption bands. In the general case, if

$$W \backsim (SN\Delta\nu_C)^n \tag{1.69}$$

and if the brightness of the disk is proportional to cos z, the mean air mass for the narrow equatorial belt of a homogeneous disk in the full phase is determined from the relation

$$\left(\frac{\bar{M}}{2}\right)^n = \frac{\int_0^{\pi/2} \sec^n z \cos z\, dz}{\int_0^{\pi/2} \cos z\, dz} = \int_0^{\pi/2} \cos^{1-n} z\, dz.$$

TABLE 11

MEAN AIR MASS VALUES FOR WEAK ABSORPTION BANDS (REF.41)

	Full Phase				Quarter			
	Entire Disk		Equator		Entire Disk	Equator	Entire Disk	Equator
	const	cos z	const	cos z	const	cos z	const	cos z
$\overline{M}$	4.00	3.00	3.14	2.87	4.00	4.71	3.86	4.00
$\sqrt{\overline{M^2}}$	3.56	2.88						

This integral is expressed by the Γ-functions /63

$$\left(\frac{\overline{M}}{2}\right)^n = \frac{\sqrt{\pi}}{2}\frac{\Gamma\left(1-\frac{n}{2}\right)}{\Gamma\left(\frac{3-n}{2}\right)} = \frac{\sqrt{\pi}}{2}\frac{1}{\left(1-\frac{n}{2}\right)}\frac{\Gamma\left(1-\frac{n}{2}\right)}{\Gamma\left(\frac{3-n}{2}\right)}. \qquad (1.70)$$

The values of M for several values of n are given in Table 12. The case of $n = \frac{1}{2}$ corresponds to the quadratic segment of the growth curve; $n < \frac{1}{2}$, to strong overlapping bands; $1 > n > \frac{1}{2}$, to the transition segment of the growth curve.

TABLE 12

AIR MASSES AVERAGED OVER THE DIAMETER (REF.16)

n	M	n	M	n	M
1.00	3.14	0.50	2.87	0.20	2.78
0.80	3.00	0.40	2.84	0.10	2.74
0.75	2.99	0.33	2.82	0.02	2.21
0.67	2.96	0.25	2.81		

When $n = \frac{1}{2}$ for the integral light of the entire planet in the full phase, we have M = 3.56 (homogeneous disk). Grandjean and Goody (Ref.42) erroneously applied M = 2.67 to this case. The incorrectness of this value was pointed out elsewhere (Ref.31, 43), but Goody (Ref.44) still insisted on it. It is obvious that the first authors (Ref.31, 43) were right:

$$\left(\frac{M}{2}\right)^{1/2} = \frac{\int_0^{\pi/2} \cos z \sin z \,(\sec z)^{1/2} dz}{\int_0^{\pi/2} \cos z \sin z \, dz} = \frac{4}{3}.$$

Limb darkening reduces the value of M. In first approximation, M = 3 can be applied in the full phase for each case.

The effective pressure P, found from a comparison of the quantities N and $N\Delta\nu_c$, is lower than the pressure at the surface

$$N\Delta\nu_C = \text{const} \int_0^\infty P(z)\,\rho_a(z)\,dz,$$

where P(z) is the pressure at the given level, and $\rho_a(z)$ is the density of the absorbing substance at the same level.

The condition of hydrostatic equilibrium of the atmosphere /64

$$dP = -\rho(z)\,g dz, \tag{1.71}$$

where $\rho(z)$ is the total density of the atmosphere at the level z, indicates that

$$N\Delta\nu_C = \text{const} \cdot \frac{1}{g} \int_{P_0}^{0} P(z) \frac{\rho_a(z)}{\rho(z)} dP.$$

If the relative concentration $\frac{\rho_a(z)}{\rho(z)} = c$ does not change with altitude, we have

$$N\Delta\nu_C = \text{const} \frac{cP^2(0)}{2g} = N\frac{\Delta\nu_{C0}}{2}, \tag{1.72}$$

where $\Delta\nu_{C0}$ is the Lorentz width at the surface. Thus the effective value of $\Delta\nu_C$ and P (in an isothermal atmosphere) is half the value at the surface (Ref.45).

The "atmosphere-centimeter" (cm • atm) is often used as the unit of measurement in analyzing the chemical composition of planetary atmospheres. Not all investigators interpret this quantity identically, when expressing the amount of some gas in cm • atm. In most cases, this refers to the reduced thickness - the thickness of a homogeneous layer of gas which, under normal conditions (P = = 1 atm, T = 293°K), contains as many molecules as the investigated planetary atmosphere. Occasionally, however, instead of in reduced thickness the amount of gas which, under normal conditions, gives the same absorption as the observed absorption is expressed in cm • atm. The term "equivalent path" is used in this context and also to denote reduced thickness. Below, we will use the term "reduced thickness" for the actual number of molecules and the term "equivalent path" for the number of molecules giving equivalent absorption (with formal correction for air mass).

In the region I (in which intrinsic radiation predominates over reflected radiation), the profile of the strong absorption band makes it possible to determine the altitude dependence of temperature, as already pointed out in Section 1.2. Obviously, for this the atmosphere must be optically thick at the line frequencies concerned. The theory of this method was developed in detail in studies by Kaplan (Ref.50) and Houghton (Ref.51).

Section 1.5 Radiation Scattering in Planetary Atmospheres

The conditions of formation of planetary spectra are markedly complicated by Rayleigh and aerosol scattering. The apparent surfaces of Venus and of the giant planets are represented by a cloud layer of such density and constancy as to make observation of the true surface generally impossible. In some cases, /65 the top of the cloud layer can be considered a solid surface; here, the formation of absorption lines and bands in the atmosphere above this top obeys the simple laws described in Section 1.4. However, such a simplified concept often proves inconvenient in practice.

The problem of the scattering of light by a many-particle system is divided into two basic parts: 1) scattering by a single particle; 2) transport of radiation in the scattering medium. If the medium consists of particles differing in their physical properties and size, then before proceeding from one problem to the other we must first consider the problem of the scattering of light by a system of particles enclosed within a microvolume. Single-particle scattering is examined in detail in the monographs by van de Hulst (Ref.52) and K.S.Shifrin (Ref.53), while the transport of radiation in the scattering medium is considered in books by V.V.Sobolev (Ref.54) and Chandrasekhar (Ref.55) as well as in studies by V.A.Ambartsumyan (Ref.56)*.

a) Single Scattering. Let us first consider single-particle scattering. The scattering process consists in that a quantum incident on a particle is either backscattered by the particle or forward-scattered in some direction other than the original direction without a change in frequency. The quantum incident on the particle may be not only reflected but also absorbed, either by the particle itself of by the gas surrounding the particle. In the former case the absorption occurs at the instant of interaction between the quantum and the particle and in the latter case, in the ambient medium following reflection.

The probability of the reflection of the quantum in a unitary process (albedo of the unitary scattering event) will be denoted by a. Then the probability of absorption is 1 - a. When a = 1 (no absorption) the scattering is termed conservative. The energy of the absorbed quantum is converted into heat and reradiated in the frequencies of thermal emission of the medium. In the case of planetary atmospheres, the thermal radiation is localized within the range of $\lambda \gtrsim 3\ \mu$ so that the radiation field in the region $\lambda \lesssim 3\ \mu$ is conditioned only by scattering and absorption.

---

* These monographs are available only in Russian. For more details consult (Ref.65).

The probability of scattering in a given direction depends on the angle γ between the direction of incidence and the direction of scattering

$$dP = \varkappa(\cos\gamma)\frac{d\omega}{4\pi}, \tag{1.73}$$

where $d\omega$ is the element of solid angle. The function $\varkappa$ $(\cos\gamma)$ is termed the scattering indicatrix. The sum of scattering probabilities in all the directions is /66

$$\int_{4\pi} \varkappa(\cos\gamma)\frac{d\omega}{4\pi} = \frac{1}{2}\int_0^{\pi} \varkappa(\cos\gamma)\sin\gamma\, d\gamma = a.$$

If the probability is independent of direction, then

$$\varkappa(\cos\gamma) = a, \tag{1.74}$$

and the indicatrix is termed spherical, while the scattering is termed isotropic. In real scattering media the spherical indicatrix is absent; it is employed only as a convenient mathematical simplification.

Suppose the flux of quanta N $cm^{-2}sec^{-1}$ is incident on a gas layer having the thickness dl. Clearly, the number of quanta scattered by this layer is

$$dN = -N\sigma\, dl \ \ cm^{-2}\ sec^{-1}.$$

The quantity σ is called the volume coefficient of scattering; its dimension is cm^{-1}. The scattering coefficient (or the effective scattering cross section) per particle is

$$C_s = \frac{\sigma}{n}\ cm^2, \tag{1.75}$$

where n is the particle concentration [cm^{-3}]. Similarly, we introduce the absorption coefficient C_{abs} per particle and the attenuation (extinction) coefficient C_{ex}

$$C_{ex} = C_s + C_{abs}. \tag{1.76}$$

Let us assume that the geometric cross section of the particle is

$$G = \pi r^2.$$

Then, the scattering effectiveness can be graphically described by the factor

$$Q_s = \frac{C_s}{G} \tag{1.77}$$

i.e., by the ratio of scattering cross section to geometric cross section. Similarly, the efficiency factors of absorption and extinction are

$$Q_{abs} = \frac{C_{abs}}{G}, \quad Q_{ex} = \frac{C_{abs} + C_s}{G}.$$

The scattering theory shows that the quantities Q_s, Q_{abs} and Q_{ex} are functions of the ratio $\frac{r}{\lambda}$, the refractive index, and the absorption coefficient /67 of the particle material. Figure 32 gives an example of the function $Q_{ex}\left(\frac{r}{\lambda}\right)$ calculated for the complex refractive index m = 1.29 (1 - ik) for various values of k. The curve k = 0 corresponds to the case of conservative scattering. The parameter $\frac{2\pi r}{\lambda}$ is plotted along the abscissa. The overall character of the curves $Q_0\left(\frac{2\pi r}{\lambda}\right)$ remains as in Fig.32 also for other values of the complex refractive index. When

$$\frac{2\pi r}{\lambda} \ll 1 \tag{1.78}$$

(the particles being markedly smaller than the wavelength), the factors Q_{ex}, Q_s and Q_{abs} tend to zero. For the limiting case [eq.(1.78)], we have

$$Q_{ex} \sim \left(\frac{2\pi r}{\lambda}\right)^{-4}. \tag{1.79}$$

The maximum value of Q_{ex} is reached at

$$\lambda \approx 2\pi r.$$

As the particle size increases, the value of Q_{ex} fluctuates repeatedly in the neighborhood of $\frac{2\pi r}{\lambda} \approx 1$. For high $\frac{2\pi r}{\lambda}$ these fluctuations are damped and

$$Q_{ex} \to 2, \quad C_{ex} = 2\pi r^2$$

when

$$\frac{2\pi r}{\lambda} \to \infty.$$

Scattering at $\frac{2\pi r}{\lambda} \ll 1$ is known as Rayleigh scattering. The indicatrix of Rayleigh scattering, for total intensity, is

$$\varkappa(\cos\gamma) = \frac{3}{4}(1 + \cos^2\gamma). \tag{1.80}$$

Scattering involves polarization. In the case of Rayleigh scattering, we have

$$\left.\begin{aligned} \varkappa_\perp(\cos\gamma) &= \frac{3}{4}, \\ \varkappa_\parallel(\cos\gamma) &= \frac{3}{4}\cos^2\gamma, \end{aligned}\right\} \tag{1.81}$$

where $\varkappa_\perp$ is the component whose electric vector is at right angles to the source-particle-observer plane; $\varkappa_\parallel$ is the component whose electric vector is parallel

/68

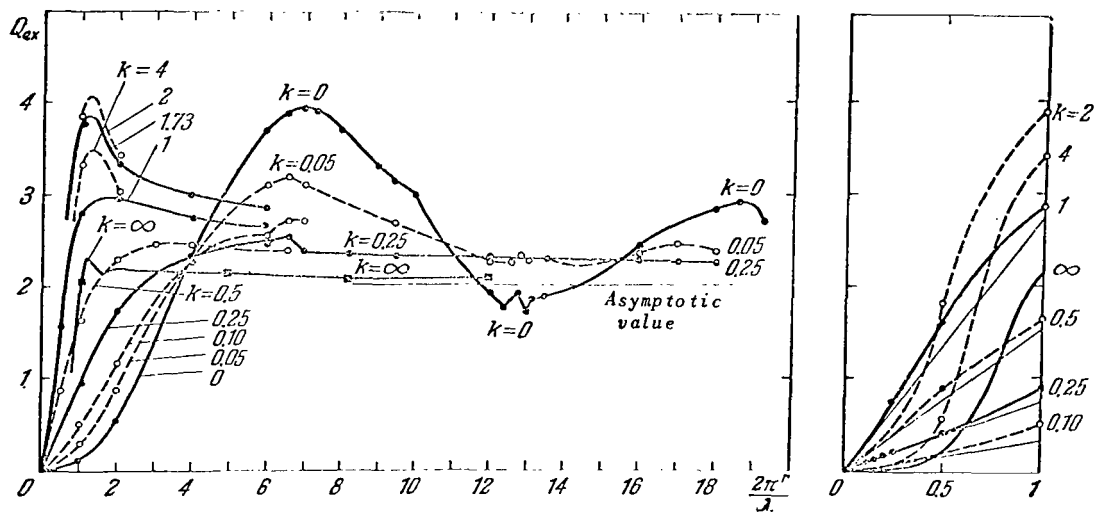

Fig.32 Extinction Factor Q_{ex} as a Function of Wavelength. Complex refractive index m = 1.29 (1 - ik) (Ref.52).

to this plane. The physical picture of occurrence of this polarization may be /69 interpreted as follows: Since the particle is much smaller than the wavelength, the wave causes an in-phase vibration of the electrons, so that they form an elementary oscillating emitter-dipole oriented at right angles to the direction of wave propagation. Since the dipole does not radiate in the direction in which it is oriented, the component $\varkappa_\parallel$ is zero when $\gamma = \frac{\pi}{2}$. In the equatorial plane the radiation of the dipole is independent of the direction and hence the component $\varkappa_\perp$ = const. The degree of polarization in Rayleigh scattering is

$$p = \frac{\varkappa_\perp - \varkappa_\parallel}{\varkappa_\perp - \varkappa_\parallel} = \frac{\sin^2\gamma}{1 - \cos^2\gamma}. \tag{1.82}$$

As the particle size increases, the polarization decreases and the indicatrix becomes more elongated (Fig.33). It is of interest that the extinction cross section for large particles is no longer equal to, but twice as large as their geometric cross section. This is due to the fact that the attenuation here is caused not just by shielding but also by diffraction.

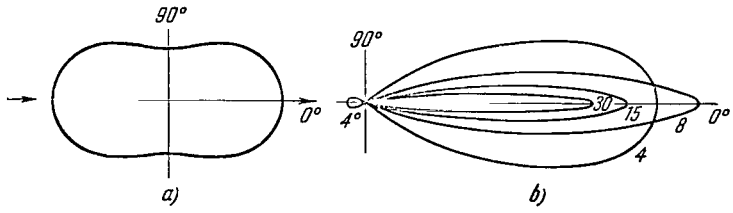

Fig.33 Scattering Indicatrices.
a - Rayleigh indicatrix; b - Scattering indicatrix for water droplets ($m = 1.33$ and $\frac{2\pi r}{\lambda} = 4, 8, 15, 30$) (Ref.53).

b) Gaseous Rayleigh scattering. Until now, we have discussed the scattering of light by particles which, though extremely small, still contain a large number of molecules. Scattering of light may also occur in a purely gaseous medium. Then, three fundamentally different effects are observed: 1) resonance scattering in lines (cf. Sect.1.4); 2) combination scattering (cf. Sect.1.1); 3) Rayleigh scattering at fluctuations in gas density. For a continuous spectrum, combination scattering merely leads to an insignificant redistribution of energies.

TABLE 13 /70

REFRACTIVE INDEXES OF GASES UNDER NORMAL CONDITIONS
($P = 1$ atm, $T = 293^{\circ}K$)

Gas	$m-1$, $\lambda=0.546\ \mu$	Gas	$m-1$, $\lambda=0.546\ \mu$
Air	$2.8\cdot10^{-4}$	He	$3.5\cdot10^{-5}$
N_2	$3.0\cdot10^{-4}$	CO_2	$4.5\cdot10^{-4}$
O_2	$2.7\cdot10^{-4}$	CH_4	$4.4\cdot10^{-4}$
H_2	$1.4\cdot10^{-4}$		

For molecular Rayleigh scattering

$$\sigma = \frac{32\pi^3 (m-1)^2}{3n\lambda^4}, \qquad (1.83)$$

where m is the refractive index of the gas. Table 13 presents the values of $m - 1$ for various gases under normal conditions. The dependence $\sigma \sim \lambda^{-4}$ accounts for the blue color of the cloudless sky. With the aid of a polaroid it is readily ascertained that, on a cloudless day, the polarization of the sky at an angular distance $\gamma = 90^\circ$ from the sun is nearly 100%, in accordance with eq.(1.82). Substituting in eq.(1.83) the value of $(m - 1)$ for air we have $\sigma \approx \approx 10^{-7}$ cm^{-1} at sea level.

The total optical thickness of the terrestrial atmosphere with respect to molecular Rayleigh scattering is

$$\tau_p = \sigma H = 10^{-7} \cdot 8 \cdot 10^5 = 0.08, \tag{1.84}$$

where $H = \dfrac{\int_0^\infty n(z)dz}{n(0)}$ is the altitude scale. Here, $n(z)$ is the concentration of molecules at the altitude z and $n(0)$ is the concentration at the surface. Radiation from any point source located outside the atmosphere, when observed from the earth's surface, will be attenuated $e^{-\tau_0 \sec z}$ times by atmospheric scattering, where z is the zenith distance. The quantity

$$p = e^{-\tau_0} \tag{1.85}$$

is called the transmission coefficient. Equation (1.84) gives the optical thickness only for molecular Rayleigh scattering. Actually, however, scattering and absorption by aerosols, as well as - in certain regions of the spectrum - absorption in molecular bands are just as essential. Consequently, the volume coefficient of extinction will be

$$\alpha = \sigma_m + \sigma_a + k_m + k_a, \tag{1.86}$$

where σ_m and σ_a are the molecular and aerosol scattering factors while k_m and k_a are the corresponding absorption coefficients. The total optical thickness is /71

$$\tau_0 = \alpha H. \tag{1.87}$$

In the infrared spectrum region ($\lambda > 1\ \mu$), we have

$$\sigma_a \gg \sigma_m$$

and, outside the molecular absorption bands,

$$\alpha = \sigma_a + k_a.$$

In the absorption bands for a cloudless atmosphere, we have

$$k_m \gg \sigma_a,$$

but in this case the formula

$$p = e^{-\tau}$$

is no longer sufficiently representative of observations since, as in the case of strong non-overlapping lines, the absorption is proportional to the square root of the air mass (cf. Sect.1.4). In the visible spectrum region (λ = = 0.55 μ), the Rayleigh transmission coefficient of the terrestrial atmosphere is

$$p = e^{-0.08} = 0.92.$$

Actually, observations at sea level as a rule indicate that $p \approx 0.8$.

c) Multiple scattering. An important question in the problem of the scattering of light by particles is whether their alignment is ordered. In a crystal, where the atoms exist in an ordered arrangement, interference by the waves scattered by these atoms leads to variations in the velocity of propagation of light, while scattering in the strict sense of this word is absent. Similar effects, associated with the regular arrangement of scattering centers and coherence of scattered light, are termed collective. In planetary atmospheres these effects are inessential.

Consider a layer of scattering particles having the optical thickness τ, on which radiation is incident. How will the variation in τ influence the intensity of the radiation scattered by this layer? So long as $\tau \ll 1$, it may be assumed that the total intensity of scattered light equals the sum of the intensities from each particle. However, as soon as τ comes close to 1, complications set in: a) The light of the external source is markedly attenuated with depth; b) in addition to the scattering of direct light from the external source, secondary scattering of the already scattered light occurs. The latter effect is known as multiple scattering. When $\tau < 0.1$, multiple scattering hardly affects the brightness of the scattering layer; when $0.1 < \tau < 0.3$, an allowance must /72 be made for second-order scattering, and when $\tau > 0.3$, an allowance must be made for higher-order scattering.

The mean number of successive scattering processes suffered by the quantum before it is absorbed or emerges toward the outside, is known as scattering multiplicity factor L. In an infinitely extended atmosphere we have $L = \infty$ if the scattering is conservative. For nonconservative scattering, the multiplicity factor depends on the albedo:

$$L = \sqrt{\frac{1}{1-a}}. \qquad (1.88)$$

If $a < \frac{1}{2}$, $L < \sqrt{2}$, higher-order scattering may be disregarded in first approximation.

In the theory of multiple scattering of light, two basic problems are distinguished: direct and inverse. In the direct problem, the specified characteristics of the medium [σ, k, $\varkappa$, (γ) which are the properties of the underlying surface (if it exists), etc.] are used for calculating the brightness and polarization of scattered light as a function of the angles of incidence and reflection. In the inverse problem, the characteristics of reflected radiation must be utilized for determining the characteristics of the medium. In planetary as-

trophysics, the inverse problem is more important than the direct problem, as is readily understood. Unfortunately, however, the inverse problem often has no unambiguous solution, unless major simplifying constraints are imposed. The direct problem has been rigorously solved only with respect to a few simple models. Nevertheless, in many cases a comparison of these findings with the observations at least permits a qualitative interpretation of the observed phenomena.

In this connection, an elementary model is represented by a semi-infinite homogeneous two-dimensional atmosphere - a medium of constant a bounded by a plane surface. Note that the ratio

$$a = \frac{\sigma}{\sigma + k} \tag{1.89}$$

does not only depend on the absorbing properties of the particles but also on those of the gas medium in which they are submerged.

For isotropic scattering, such a model will be

$$B = \frac{E}{\pi} \frac{\varphi(\mu_1)\varphi(\mu_2)}{\mu_1 + \mu_2} - \frac{a}{4}, \tag{1.90}$$

where $E = E_0\mu_1$ is the illumination at the boundary, from the external source (the beam being assumed as parallel); μ_1 and μ_2 are the cosines of the angles of incidence and observation, respectively; $\varphi(\mu)$ is the auxiliary function for which tables are given elsewhere (Ref.54, Table 4) and (Ref.55, Table XI). The ratio/73

$$\rho(\mu_1, \mu_2) = \frac{B\pi}{E} = \frac{B\pi}{E_0\mu_1} \tag{1.91}$$

is known as the brightness coefficient (E_0 being the illumination of an area oriented normal to the incident rays). For a surface reflecting the incident radiation uniformly in every direction without absorption, we have

$$\rho = 1. \tag{1.92}$$

Such a surface is known as "absolutely white" Lambert surface.

The nonspherical indicatrix in the scattering theory is usually represented by an expansion in a series of Legendre polynomials of the first kind

$$\varkappa(\cos\gamma) = \varkappa_0 + \varkappa_1 P_1(\cos\gamma) + \varkappa_2 P_2(\cos\gamma) + \ldots. \tag{1.93}$$

The more the indicatrix is elongated, the greater will be the number of terms to be considered. For the case of an elementary nonspherical indicatrix

$$\varkappa(\cos\gamma) = a(1 + \varkappa_1 \cos\gamma), \quad \varkappa_1 \leqslant 1 \tag{1.94}$$

the brightness coefficient is

$$\rho(\mu_1, \mu_2, \psi - \psi_0) = \frac{a}{4} \frac{\varphi_0^0(\mu_1)\varphi_0^0(\mu_2) - \varkappa_1 \varphi_1^0(\mu_1)\varphi_1^0(\mu_2)}{\mu_1 + \mu_2} +$$

$$+ \frac{a}{4} \varkappa_1 \frac{\varphi_1^1(\mu_1)\varphi_1^1(\mu_2)}{\mu_1 + \mu_2} \cos(\psi - \psi_0), \qquad (1.95)$$

where $(\psi - \psi_0)$ is the difference in the azimuths of the incident and reflected rays; $\varphi_0^0(\mu)$, $\varphi_1^0(\mu)$, $\varphi_1^1(\mu)$ are the auxiliary functions (Ref.54, 56a). In the book by Chandrasekhar (Ref.55) the solution in this case is expressed in other auxiliary functions.

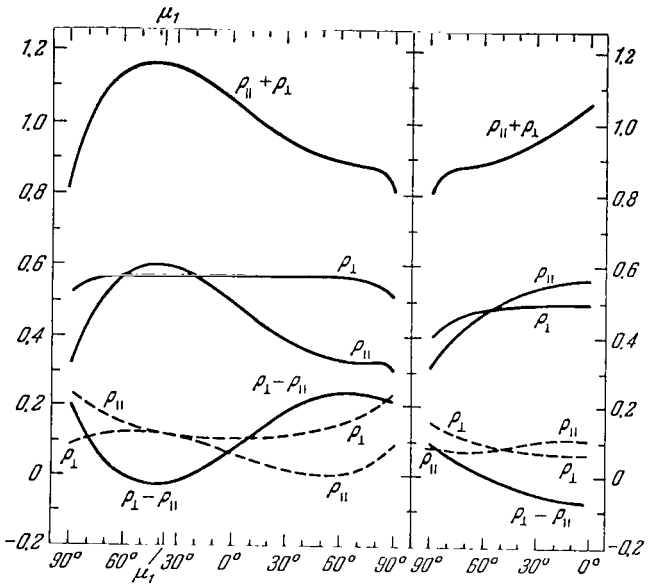

Fig.34 Law of Diffuse Reflection by a Semi-Infinite Atmosphere at Rayleigh Scattering.
The relation of the brightness coefficients $\rho_\perp$ and $\rho_\parallel$ to the reflection angle is shown for an angle of incidence corresponding to $\mu_1 = 0.8$ in the planes $\psi = \psi_0 = 0$ (left) and $\psi - \psi_0 = \frac{\pi}{2}$ (right). The brightness coefficients $\rho_\perp$ and $\rho_\parallel$ of light which suffered only single scattering (broken curve) are also given, as is the total brightness coefficient $\rho_\perp + \rho_\parallel$ (Ref.55).

If $\tau_0 \to \infty$, then $\rho_0 = \frac{\varkappa(\cos\gamma)}{4(\mu_1 + \mu_2)}$.

For Rayleigh scattering, a solution of the problem can be found elsewhere (Ref.55). This author gives the brightness coefficients for both polarization planes $\rho_\perp$ and $\rho_\parallel$, expressed by certain auxiliary functions as in eq.(1.95). The functions $\rho(\mu_1, \mu_2, \psi - \psi_0)$ have one common property regardless of the indicatrix, namely that of being symmetric with respect to μ_1 and μ_2. The points 1 and 2 on the planetary disk at which $\mu_1(1) = \mu_2(2)$ and $\mu_1(2) = \mu_2(1)$ are known as corresponding points. Their brightness coefficients are the same, and their brightness itself is proportional to the cosines of the angle of incidence. Minnaert showed that any homogeneous scattering atmosphere or homogeneous scattering solid surface satisfies this law (which is known as the principle of reciprocity).

For single scattering with/74 an arbitrary indicatrix $\varkappa(\cos\gamma)$ and a layer of an optical thickness of τ_0, the brightness coefficient is determined from the formula

$$\rho_0 = \frac{\varkappa(\cos\gamma)}{4(\mu_1 + \mu_2)}\left[1 - e^{-\tau_0\left(\frac{1}{\mu_1} + \frac{1}{\mu_2}\right)}\right]. \qquad (1.96)$$

All complex functions $\rho(\mu_1, \mu_2, \psi - \psi_0)$ tend to ρ_0 as $a \to 0$ or $\mu_1, \mu_2 \to 0$.

Figures 34 and 35 give the functions $\rho(\mu_2)$ calculated for a Rayleigh atmosphere with selected values of μ_1 and $\psi - \psi_0$. /75

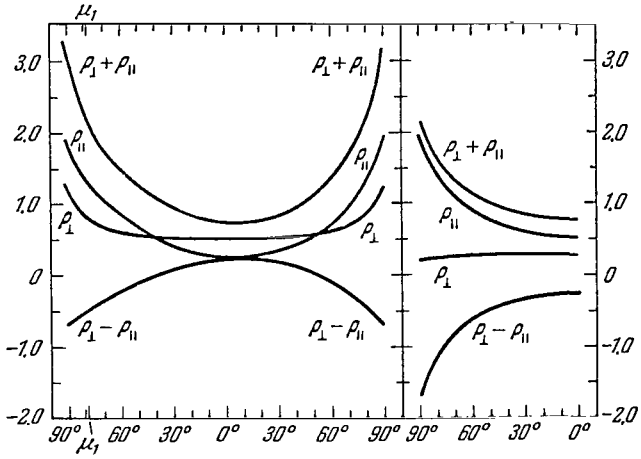

Fig.35 Same as in Fig.34, for $\mu_1 = 0.2$. The findings for single scattering are not included (Ref.55).

It can be seen from Fig.34 that, on taking multiple scattering into account, the total intensity is increased and the polarization characteristics of reflected radiation are qualitatively changed. When $\mu_1 = \mu_2$, singly-scattered radiation is not polarized, whereas when $\mu_1 - \mu_2 = \frac{\pi}{2}$ - this radiation is 100% polarized. Multiple scattering causes some (negative) polarization at $\mu_1 = \mu_2$ and sharply reduces the degree of polarization at $\mu_1 - \mu_2 = \frac{\pi}{2}$.

When the planet is in its full phase, we have $\mu_1 = \mu_2$ at any point on the disk. The law of limb darkening is then expressed by the formula

$$B = \mu\rho(\mu)\frac{E_0}{\pi}.$$

The function $\mu\rho(\mu)$ for certain simple indicatrices is given in Fig.36. According to Lambert's law, $\mu\rho = 0$ at the limb. From Fig.36 it can be seen that scattering by the atmosphere produces a finite brightness at the limb. The limiting value is determined from eq.(1.96) for $\mu_1 = \mu_2 \to 0$:

$$(\mu\rho)_{\mu\to 0} = \frac{1}{8}\varkappa(0). \tag{1.97}$$

When the albedo a decreases, limb darkening become less distinct. /76

For an atmosphere with a finite optical thickness, the brightness coefficients of reflected and transmitted radiation can also be calculated for a number of simple indicatrices. For isotropic scattering, we have

$$\left.\begin{aligned}\rho_{neg}(\mu_1, \mu_2) &= \frac{a}{4}\frac{\varphi(\mu_1)\varphi(\mu_2) - \psi(\mu_1)\psi(\mu_2)}{\mu_1 + \mu_2},\\ \rho_{trans}(\mu_1, \mu_2) &= \frac{a}{4}\frac{\varphi(\mu_1)\psi(\mu_2) - \varphi(\mu_2)\psi(\mu_1)}{\mu_2 - \mu_1},\end{aligned}\right\} \tag{1.98}$$

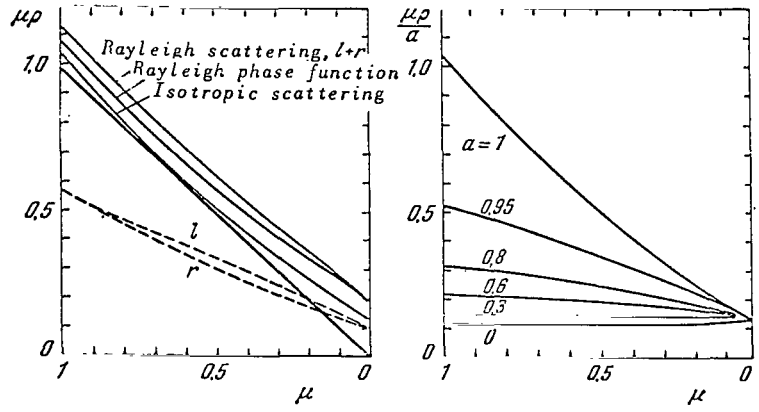

Fig.36 Curves for Darkening of the Disk toward the Limb of a Planet with a Semi-Infinite Atmosphere, as a Function of Various Scattering Indicatrices for a = 1 (Left) and for Isotropic Scattering in the Presence of Various a (Right) (Ref.64).
l and r - Different polarizations in the case of Rayleigh scattering.

where $\varphi(\mu)$, $\psi(\mu)$ are auxiliary functions [most complete function tables are given elsewhere (Ref.56)]. Similar relations have been derived for the indicatrix [eq.(1.94)]. Tables by other authors (Ref.57) give approximate values of the auxiliary functions, permitting a calculation of ρ_{neg} and ρ_{trans} for various values of τ, a, $\varkappa_1$ with respect to some moderately elongated scattering indicatrix which satisfies the relation

$$\left|\frac{3}{2}\int_0^{\pi}\varkappa(\cos\gamma)\sin\gamma\cos\gamma\,d\gamma\right|<1.5. \tag{1.98a}$$

The approximate formulas on which these tables are based were derived by Ye.G. Yanovitskiy (Ref.57a). /77

The next model is that of an atmosphere of finite thickness, bounded at the bottom by the subjacent surface. According to Sobolev (Ref.54) in this case, for a Lambert surface (ρ = const) with an albedo A_s, we have

$$\left.\begin{aligned}\rho_{neg}&=\rho'_{neg}+\frac{A_s}{1-A_sC}\,\mu(\mu_1)\,\mu(\mu_2),\\ \rho_{trans}&=\rho'_{trans}+\frac{A_s}{1-A_sC}\,\nu(\mu_1)\,\mu(\mu_2),\end{aligned}\right\} \tag{1.99}$$

where ρ'_{neg} and ρ'_{trans} are the brightness coefficients in the absence of an underlying surface; μ, ν, C are the auxiliary functions. For an arbitrary indicatrix

satisfying eq.(1.98a), the approximate values of auxiliary functions are given in other tables (Ref.57). For a Rayleigh indicatrix, this model has been calculated by Coulson (Ref.58).

In the case of an atmosphere of finite optical thickness (Mars), the optical thickness τ can be determined by comparing the observed dependence of the brightness coefficients $\rho(\mu_1, \mu_2)$ with the theoretical dependence. Assuming that the scattering is due solely to the gaseous component of the atmosphere, the concentration n of molecules near the surface and the pressure P = nkT can be found from eqs.(1.95) and (1.92). This method of determining the pressure is termed "photometric". To distinguish between the atmospheric and surface components of brightness, polarization of Rayleigh scattering (polarization method) may be employed. Polarization accompanying the scattering by solid materials depends on their chemical nature, degree of disintegration, and other factors. It may be utilized to identify the material of planetary surfaces and particles of the cloud layer, but the reliability of an identification of this kind often is inadequate.

Obviously, rigorous formulas for the brightness coefficients have a complex form even in the presence of extremely simple scattering indicatrices. For many problems, only approximate analytic solutions can be used. Numerical methods of solution of rigorous transport equations on high-speed computers also have been developed (Ref.59, 60). By means of approximate analytic and numerical methods, the transport problem can be solved even for extremely extended indicatrices whose representation requires as many as a hundred terms of expansion of Legendre polynomials. Indicatrices of this kind characterize the terrestrial cloud particles. A survey of the basic findings on the problem of radiation transport in the clouds is given elsewhere (Ref.61). In the limiting cases of large ($a \lesssim 0.5$) and small ($a \gtrsim 0.8$) absorption, one can resort to the approximate solutions by /78
G.V.Rozenberg (Ref.62) derived for any indicatrix on taking polarization effects into account. These solutions are written in the form

$$\rho(r', r) = \left\{ h(r', r)\, e^{-S(r', r)\, y} - \right.$$
$$\left. - g(r')\, g(-r) \frac{\sinh y}{\sinh by} \left[e^{-by} - \frac{A_s \sinh y}{\sinh by - A_s \sinh (b-1)\, y} \right] \right\} e^{-\tau_{out}\left(\frac{1}{\mu_1} + \frac{1}{\mu_2}\right)} \qquad (1.100)$$

for small absorption ($\rho \gtrsim 0.2$), and in the form

$$\rho(r', r) = \frac{f_{11}(r', r)\, \beta^{-1}}{4(\mu_1 + \mu_2)} e^{-\tau_{out}\left(\frac{1}{\mu_1} + \frac{1}{\mu_2}\right)} \qquad (1.101)$$

for large absorption ($\rho > 2$). The solutions (1.100) and (1.101) are derived from the following model: A plane homogeneous atmosphere of large optical thickness ($\tau \gg 1$) consists of scattering particles and an absorbing gas. The ratio is

$$\frac{k}{\sigma} = \beta = \frac{1-a}{a} = \text{const.}$$

A portion of the gas (optical thickness τ_{out} in absorption) is above the cloud layer. The atmosphere is bounded at the bottom by a surface having an albedo of $A_s \cdot y = \eta\sqrt{\beta}$, $b = \frac{\tau}{l} + 1$, where η and l are constants that depend on the type of the scattering matrix; $\mathbf{r}$ and $\mathbf{r}'$ are the directions of incidence and sighting. The functions $h(\mathbf{r}', \mathbf{r})$, $S(\mathbf{r}', \mathbf{r})$ and $g(\mathbf{r})$ are unknown and are subject to experimental determination or calculation; $f_{11}(\mathbf{r}', \mathbf{r})$ is the scattering indicatrix. There is reason to believe that, under real conditions, the functions h, S, and g depend weakly on the arguments and type of the scattering matrix and are of an order of magnitude close to unity. The coefficients η and l are expressed by the auxiliary quantity q

$$\eta \approx 4\sqrt{q}, \quad l \approx 4q,$$

where $q = \frac{1}{3}$ for Rayleigh scattering and $q = 1.5$ for cloud $\left(\frac{2\pi r}{\lambda} \approx 20\right)$.

For extremely weak absorption $\left(\eta\sqrt{\beta} \ll 1 \text{ and } \tau \ll \frac{l}{\eta\sqrt{\beta}}\right)$ eq.(1.100) can be simplified to

$$\rho(r', r)_{neg} = h(r', r) - \frac{g(r')\,g(-r)}{b + \frac{A_s}{1 - A_s}}. \tag{1.102}$$

For the same case at the surface we have /79

$$\rho_{trans} = \frac{\eta\sqrt{\beta}\, e^{-\eta\sqrt{\beta}\frac{\tau}{l}}}{1 - A_s}. \tag{1.103}$$

At $\eta\sqrt{\beta} \ll 1$, $\tau \gg \frac{l}{\eta\sqrt{\beta}}$, the surface illumination is virtually zero and an approximation of a semi-infinite atmosphere is realized

$$\rho(r', r) \approx h(r', r)\, e^{-S(r', r)\,\eta\sqrt{\beta} + \tau_{out}\left(\frac{1}{\mu_1} + \frac{1}{\mu_2}\right)}. \tag{1.104}$$

If the absorption lines observed in the spectrum of the reflected solar radiation form within the cloud layer, then the extent of absorption

$$R = \frac{\rho_{out} - \rho_{in}}{\rho_{out}}, \tag{1.105}$$

(where ρ_{in} and ρ_{out} are the brightness coefficients inside and outside the line, respectively) can be used as a criterion for determining only the parameter β - the ratio of the absorption coefficient k to the scattering coefficient σ. This is clearly illustrated by eqs.(1.100) - (1.104). In a continuous spectrum, eq.(1.102) can normally be utilized while eqs.(1.101) or (1.104) are applicable to absorption lines.

In eq.(1.104), the exponent consists of two parts. The first part describes absorption within the cloud layer and the second part gives that above the cloud layer. The gaseous mass above the cloud layer is determined by the formula

$$\tau_{out} = Hk,$$

where H is the altitude scale (cf. Sect.1.6) and k is the absorption coefficient. The profile of the spectral line forming in the atmosphere containing the cloud layer consists of two parts whose respective contributions to the equivalent width depend on the quantities H, k, μ_1, μ_2, σ and on the functions η and S. Under certain conditions (e.g., when $\sigma \to \infty$) the role of absorption within the cloud may become sufficiently minor so that conventional methods of quantitative spectral analysis, as described in Section 1.4, can be applied. Otherwise the quantity σ enters the growth curve as an independent parameter, and a quantitative analysis becomes highly complicated.

Note that all existing modifications of the multiple-scattering theory, convenient for practical application, presuppose that the ratio within the confines of the cloud layer is to be

$$\beta = \frac{k}{\sigma} = \text{const.} \qquad (1.106)$$

Moreover, the surface of the layer is assumed to be smooth (plane or spherical). In reality, the gas concentration and the absorption coefficient k usually de- /80 crease exponentially with altitude and the surface of the cloud layer may have a complex structure. Strictly speaking, eq.(1.106) can be applied only in the case in which the thickness of the layer, within which the major portion (e.g., 80%) of the reflected flux forms, is markedly smaller than H. In the case of weak absorption ($\beta < 1$), this condition apparently is not satisfied in the planetary atmospheres. The inhomogeneities can be disregarded only if their dimensions $d_1 \ll \frac{1}{\sigma}$. This condition also is rather improbable in reality.

In the case of an unresolved molecular band, the parameter β undergoes considerable variations within its confines. The mean absorption $\bar{R}$ can be found by a numerical method through averaging the monochromatic values of R_ν. This problem was examined by analytic methods in studies by King (Ref.63) for the case of isotropic scattering.

In concluding this Section, let us refer to two surveys [van de Hulst (Ref.64) and van de Hulst and Irvin (Ref.65)] as the starting points for the reader who desires to become more familiar with the problems of the scattering of light in planetary atmospheres. Detailed bibliographies are given in these surveys.

Section 1.6 Photometry

The elementary photometric characteristic of a planet is its stellar magnitude. Various investigators measured the stellar magnitudes of the planets by means of visual and photographic methods, but the most accurate results are ob-

tained by photoelectric observations. Observations of this kind are performed with the aid of electrophotometers, with comparison stars being used as the photometric standards. Extensive material on integral photometry and colorimetry of planets and satellites, largely based on original photoelectric observations, is presented in a survey by Harris (Ref.66).

The integral stellar magnitude of a planet varies in time owing to variations in the phase angle, distance from sun and earth, rotation of the planet, and effects on its surface. If the last two factors are disregarded, the observable stellar magnitude is

$$V = V(1, 0) + 5 \log rd + \Delta m(\varphi), \tag{1.107}$$

where r is the distance from the planet to the sun; d is the distance from the planet to the earth; V(1, 0) is the stellar magnitude of the planet for r = d = = 1 astronomical unit and $\varphi = 0$; φ is the phase angle, i.e., the sun-planet-earth angle; $\Delta m(\varphi)$ is the variation in stellar magnitude as a function of the phase /81 angle. The presence of the correction $\Delta m(\varphi)$ is due to two causes: First, the phase angle determines which part of the disk is illuminated and, second, the diffuse reflection of light by the planet's surface depends on the angles of incidence and reflection. For our further reasoning, it is convenient to employ the phase function, determined on the scale of illumination:

$$f(\varphi) = 10^{-0.4\Delta m(\varphi)}. \tag{1.108}$$

Knowing the stellar magnitude V(1, 0) of the planet and the phase function, it is possible to calculate the spherical albedo

$$A_c = \frac{\Phi}{\Phi_0}, \tag{1.109}$$

where Φ_0 is the flux incident on the planet; Φ is the flux reflected in every direction, while the geometric albedo is

$$p = \frac{E_0}{E_L}, \tag{1.110}$$

where E_0 is the illumination of the earth by the planet in full phase; E_L is the illumination that would be produced on earth by a plane absolutely white Lambertian screen of the same diameter as the planet, located in place of the planet. Obviously, at r = d = 1 a.u., the illumination of the earth would be

$$E(1, 0) = pE_L = pB_L \pi \rho^2 = pE_\odot(1)\, \rho_1^2, \tag{1.111}$$

where ρ_1 is the angular radius of the planet for d = 1, and $E_\odot(1)$ is the solar constant.

For other phase angles at d = 1 a.u., we have

$$E(1, \varphi) = pE_\odot(1)\, \rho_1^2 f(\varphi). \tag{1.112}$$

Let us now determine the spherical albedo. To this end, let us imagine that the planet is surrounded by a sphere having a radius of 1 a.u., let us isolate - on this sphere - a strip enclosed between cones of angles φ and $\varphi + d\varphi$, then calculate the flux incident on this belt. The illumination of the sphere is given by eq.(1.112) and is constant within the above belt. The area of the belt is

$$S = 2\pi \sin\varphi \, d\varphi$$

while the flux is equal to

$$\Phi_{\varphi,\,\varphi+d\varphi} = E(1.\,\varphi)\,S = 2\pi p \rho_1^2 E_\odot(1)\, f(\varphi) \sin\varphi \, d\varphi.$$

Integrating over the entire sphere, we find /82

$$\Phi = 2\pi p E_\odot(1)\,\rho_1^2 \int_0^\pi f(\varphi) \sin\varphi \, d\varphi.$$

Since $\Phi_0 = E_\odot(1)\,\pi\rho_1^2$, we have

$$A = \frac{\Phi}{\Phi_0} = pQ, \tag{1.113}$$

where $Q = 2\int_0^\pi f(\varphi) \sin\varphi d\varphi$. The quantity Q is designated as phase integral.

The geometric albedo can be determined for any planet or satellite

$$\log p = 0.4\,[V_\odot - V(1, 0)] - 2\log\rho_1, \tag{1.114}$$

where $V_\odot$ is the stellar magnitude of the sun. Equation (1.114) is derived from eq.(1.111) by means of elementary transformations. It is by no means always possible to determine the phase integral from observations. Its calculation requires knowing the function $f(\varphi)$ for any phase angle; this function can be calculated on the basis of ground observation only for the Moon, Mercury, and Venus. The maximum phase angle is 47° for Mars and 12° for Jupiter. In such cases, the function $f(\varphi)$ is extrapolated by analogy with other observational or theoretical phase functions. For Mars, the estimate can be made by means of Russell's empirical rule who found that, for all known observational and theoretical curves,

$$Q = 2.2 f(50^\circ). \tag{1.115}$$

However, even such an estimate cannot be made for the Jovian planets; for these, the phase function of an orthotropically scattering sphere is often employed

$$Q = 1.50.$$

The calculation of the equilibrium temperature of a planet (Sect.1.2) requires knowing the integral albedo

$$A_l = \frac{\int_0^\infty p(\lambda)\, Q(\lambda)\, E_\odot(\lambda)\, d\lambda}{\int_0^\infty E_\odot(\lambda)\, d\lambda}, \qquad (1.116)$$

where $E_\odot$ is the illumination of an area perpendicular to the solar rays at the top of the planetary atmosphere.

For a planet lacking an atmosphere, the quantities p, Q, $f(\varphi)$ depend sole- /83
ly on the optical properties of the surface; if there is an atmosphere, it also affects these quantities. If the planet has a very dense atmosphere, its integral optical properties will be determined by the atmosphere alone. On the basis of the theory of multiple scattering of light it is possible to calculate p, Q, and $f(\varphi)$ for various τ, scattering indicatrices, and single-scattering albedos (cf. preceding Section) and to compare the findings with observations; as a rule, this involves an excessive number of unknowns. The brightness distribution over the disk at various phase angles may provide substantial additional information, but normally it is greatly distorted by instrument errors (vibration, scattering of light in the instrument, etc.). Photometry of planetary disks and its interpretation has been studied in detail by N.P.Barabashev and coworkers (Ref.6).

The spherical albedo of a semi-infinite atmosphere at a moderately drawn-out indicatrix, satisfying the condition (1.98a), is equal to

$$A = 1 - 2\int_0^1 \varphi_1^0(\mu)\, d\mu \approx \frac{\sqrt{4 - x_1 a} - 2\sqrt{1-a}}{\sqrt{4 - x_1 a} + 2\sqrt{1-a}}$$

(see Ref.57a). When $x_1 = 0$, this yields a simpler formula

$$A \approx \frac{1 - \sqrt{1-a}}{1 + \sqrt{1-a}},$$

which is valid for isotropic scattering.

By analogy with the spherical albedo, one can introduce the concept of the albedo of a plane area

$$A(\mu_1) = \frac{\Phi}{E(\mu_1)},$$

where $E(\mu_1)$ is the illumination produced by a parallel beam incident at an angle μ_1 to the normal; Φ is the flux of scattered radiation. At a spherical scattering indicatrix, the "flat" albedo of a semi-infinite medium is equal to

$$A'(\mu_1) = 1 - \varphi(\mu_1)\sqrt{1-a}.$$

For the scattering indicatrix $1 + \varkappa$, cos γ, we have

$$A'(\mu_1) = 1 - \frac{1}{\mu_1}\varphi_1^0(\mu_1) \tag{1.117}$$

(see Ref.54). At a = 1, we always have A and A′ = 1. With increasing elongation of the indicatrix for a given a < 1, the quantities A and A′ decrease.

Section 1.7 Certain Problems of the Structure of Planetary Atmospheres /84

a) Barometric formula. A column of gas of thickness dz and cross-sectional area of 1 cm^2 has a weight of $\rho g\, dz$, where ρ is the density of the gas,

$$\rho = \sum n_i m_i = nm.$$

Here, n_i is the numerical concentration of molecules of molecular weight m_i; n is the total concentration; m is the mean molecular weight. The weight of an element of volume is compensated by the pressure difference

$$\rho g\, dz = -dP.$$

The equation of state of an ideal gas P = nkT permits integration of this relation. In general, temperature, acceleration due to gravity, and mean molecular weight are functions of the altitude

$$T = T(z),$$
$$g = g(z),$$
$$m = m(z)$$

and

$$P = P_1 e^{-\int \frac{m(z)\, g(z)}{kT(z)} dz} = P_1 e^{-\int \frac{dz}{H(z)}}, \tag{1.118}$$

where P_1 is the surface pressure; $H(z) = \frac{kT}{mg}$ is the local altitude scale or the altitude of a homogeneous atmosphere. This formula is known as the barometric formula. If m, g, and T are independent of altitude, then

$$n = n_1 e^{-\frac{z}{H}}, \quad P = P_1 e^{-\frac{z}{H}}, \tag{1.119}$$

$$\int_0^\infty n\, dz = n_1 H. \tag{1.120}$$

In the terrestrial atmosphere, H = 8 × 10^5 cm at sea level. In the lower layers of the atmosphere ($z \ll R_1$, where R_1 is the radius of the planet) we have g = = const and, as a rule, m = const. Only T changes markedly with altitude. In the upper layers of the atmosphere all three basic quantities T, m, and g vary

with altitude. If the altitude scale changes with altitude according to the linear law

$$H = H_1 + bz, \quad b = \frac{dH}{dz} = \text{const}, \tag{1.121}$$

then eq.(1.118) yields /85

$$n = n_1 \frac{m_1 g_1}{mg} \left(\frac{H}{H_1}\right)^{-\frac{1+b}{b}}. \tag{1.122}$$

In the same way,

$$\int_0^\infty n dz = n_1 H_1.$$

If T = const and m = const in the atmosphere and if the variation in H is due only to the variation in g with altitude, then the barometric formula becomes

$$n = n_1 e^{-\frac{\gamma M m (R-R_1)}{kTRR_1}} = n_1 e^{-\frac{R_1}{H_1} + \frac{R}{H}}, \tag{1.122a}$$

where R_1 is the radius of the planet; $R = R_1 + z$; H_1 is the altitude scale at the surface. This formula is no longer valid as soon as the values of R become extremely large, since the density calculated from this formula does not diminish to zero as $R \to \infty$. If an allowance is made for the interaction between the gaseous masses themselves (according to Milne), a more accurate relation is derived:

$$n = n_1 \left(\frac{R_1}{R}\right)^2 e^{-\frac{R-R_1}{R}\left(\frac{R_1}{H_1} - 2\right)}. \tag{1.122b}$$

The altitudes at which the difference between n determined from eq.(1.122a) and n determined from eq.(1.122b) becomes appreciable are normally so high that the molecules suffer practically no collisions and the hydrostatic equilibrium, on which the above relations are based, hardly exists there. Nevertheless, it can be shown that, in the absence of dissipation (see below), these relations will be valid in this region provided that the molecular velocity distribution remains Maxwellian.

Let us briefly consider the factors influencing the dependence m = m(z). So long as the relative concentration of the various constituent gases of the atmosphere and the mean molecular weight remain unchanged, the partial pressure of various kinds of molecules will show the same pattern of variation. A change in mean molecular weight may be caused by two factors: diffusion, which tends to establish a separate barometric distribution for every individual component

$$n_i = n_{1i} e^{-\frac{z}{H_i}}, \tag{1.123}$$

and dissociation of molecules.

At sufficiently high velocity of back reaction, the dissociation is appreciable only at altitudes at which /86

$$\tau = n_i s H \leqslant 1,$$

where s is the dissociation cross section of molecules of a concentration n_i. Taking $s = 10^{-19}$ cm^2 (cf. Fig.16) as the typical quantity and assuming that $H = 10^6$ cm, we have $n_i = 10^{13}$ cm^{-3} which is 3×10^6 times lower than at the earth's surface. For example, for O_2 molecules, this concentration is reached in the atmosphere at an altitude of 100 km.

The onset of diffusion equilibrium is counteracted by the process of mass mixing. The rate of mass motion in the atmosphere varies from several meters to tens of meters per second. Assuming that the mean velocity of mass motion is $v_s = 10^3$ cm $\cdot$ sec^{-1}, the effective mixing time at the earth's surface will be

$$t_s = \frac{H}{v_s} \approx 10^3 \text{ sec}.$$

If the time of establishment of diffusion equilibrium is determined in the same manner as the time used by a particle to travel a distance equal to the altitude scale, then

$$t_D = \frac{H^2}{2D}. \tag{1.124}$$

This is the well-known formula of Brownian movement derived by Einstein. Here D is the diffusion coefficient:

$$D = \frac{1}{3} Vl = \frac{V}{3\sqrt{2}\pi d_m^2 n}, \tag{1.125}$$

where V is the mean velocity of the molecules; d_m is the effective diameter; n is the concentration. At sea level, $n = 2.7 \times 10^{15}$ cm^{-3}. For O_2, we have $V = 4 \times 10^4$ cm $\cdot$ sec at $T = 300^\circ$K, $\pi d^2 \approx 5 \times 10^{-16}$ cm^2, whence at the sea level in the terrestrial atmosphere we have

$$t_D = \frac{(8 \cdot 10^5)^2}{2 \cdot 4 \cdot 10^4} \cdot 3\sqrt{2} \cdot 5 \cdot 10^{-16} \cdot 2{,}7 \cdot 10^{19} \approx 5 \cdot 10^{11} \text{ sec}.$$

Therefore, in the lower layers of the atmosphere, we have

$$t_s \ll t_D \tag{1.126}$$

and mixing processes predominate over diffusive separation. Here, the state of total mixing for which $m(z) = \text{const}$ sets in. However, t_D rapidly decreases with altitude, and for $n \approx 10^{11}$ cm^{-3} the characteristic times become equal. In the terrestrial atmosphere, this concentration corresponds to the altitude z = 130 km. A more rigorous analysis of the problem of diffusive separation is carried out with the aid of the diffusion equation [cf. for example (Ref.67)]; this is a means of determining the concentration distribution of various components over the altitude, in the transition zone. /87

By means of the barometric formula, T(z) can be determined if the altitude dependence of density and the molecular weight are known. Conversely, knowing the altitude scale and T, it is possible to estimate m. There exist two known methods of determining n(z) at high altitudes on the basis of optical observations: 1) according to the brightness of twilight airglow; 2) according to the extinction of a star during its occultation. At twilight, the sun illuminates the upper layers of the atmosphere. The farther from the terminator the higher will be the boundary of the shadow. If only first-order scattering is taken into account, the brightness of the scattered light becomes

$$B(z) \backsim \tau = \int_{z_0}^{\infty} n(z)\, C_s dz,$$

where C_s is the Rayleigh scattering coefficient, and z_0 is the altitude of the lower boundary of the illuminated zone. Obviously, n(z) can be readily determined by measuring the brightness B(z). The chief error involved in this method is due to the share of the aerosol component in B(z), since this component remains fairly high even at altitudes of 100 - 150 km. For observation of other planets from the earth's surface, the twilight method produces no reliable results owing to the scattering of light from the day portion of the planetary disk in the instrument. However, it may produce some results when used with onboard instruments of space vehicles, provided that steps are taken to exclude noise from the illuminated portion of the disk.

The second method is highly effective for ground-based observations (Ref.68, 69). When a star approaches the limb of a planetary disk, its light starts being attenuated. This attenuation is not caused by scattering (τ is still too low at the time the attenuation is observed) but by refraction: The light beam from the star no longer will be parallel (Fig.37). A quantitative examination shows that then the altitude scale is

$$H = \frac{f\left(\frac{E}{E_0}\right)}{\frac{dy}{dt}(t - t_0)}, \qquad (1.127)$$

where $\frac{E}{E_0}$ is the decrease in illumination; $\frac{dy}{dt}$ is the velocity of motion in the plane y (see Fig.37); t_0 is the instant of intersection of the x-axis by the star; t is the instant of observation; f is some known function (Ref.3). Along

with the altitude scale, the absolute density values of the atmosphere are determined. For planets such as Venus and Jupiter, distinct attenuation takes place already at densities of the order of $10^{13} - 10^{14}$ cm^{-3}. /88

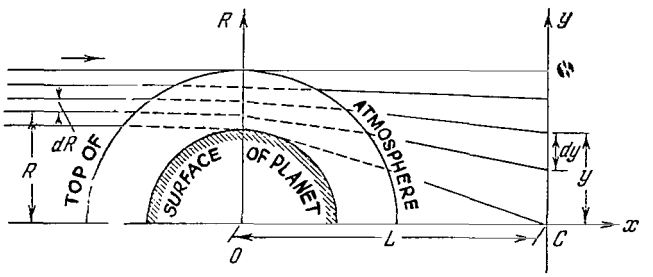

Fig.37 Course of Light Rays Responsible for the Gradual Attenuation of the Brightness of a Star during its Occultation by a Planet.

The density of the terrestrial atmosphere in its upper layers is currently determined by direct methods: a) from the retardation of artificial satellites (up to an altitude of ~ 1800 km) and b) from direct measurement with manometers (up to an altitude of ~ 500 km). In time, the launching of artificial satellites into the atmospheres of the other planets will permit the use of direct methods for the study of their structure; however, for the immediate future optical methods will retain their supremacy.

If the chemical composition of the atmosphere, the total pressure at the surface, the surface albedo, and the absolute energy distribution in the solar spectrum are all known, then the vertical structure of the atmosphere (dependence of T, n, P, m on z) can be calculated in theory, on the basis of solving the equation of heat balance from which the T(z) dependence is found:

$$\frac{dQ}{dt} = \frac{dq_{s.r}}{dt} + \frac{dq_{p.r}}{dt} + \frac{dq_{h.c}}{dt} + \frac{dq_c}{dt}, \qquad (1.128)$$

where $\frac{dQ}{dt}$ is the total amount of heat received in unit time by an element of volume of the atmosphere; $\frac{dq_{s.r}}{dt}$ is the heat influx due to solar radiation; $\frac{dq_{p.r}}{dt}$ is the heat influx due to planetary radiation (radiative exchange of heat with the surface and the adjoining elements of the atmosphere); $\frac{dq_{h.c}}{dt}$ is the heat influx due to heat conduction; $\frac{dq_c}{dt}$ is the heat influx due to convection.

In the presence of thermal equilibrium, /89

$$\frac{dQ}{dt} = 0. \qquad (1.129)$$

In reality, two or three terms of eq.(1.128) predominate at every given altitude while the other terms can be neglected. Problems of the heat balance of the terrestrial atmosphere have been considered in detail by K.Ya.Kondrat'yev (Ref.70, 71). Examples of calculation for the atmospheres of the other planets will be given in the following Chapters.

b) Dissipation of the atmosphere. The altitude at which the mean free path equals the altitude scale $l = H$, i.e.,

$$\frac{1}{\pi n d_m^2 \sqrt{2}} = \frac{kT}{mg}, \tag{1.130}$$

is known as the critical level z_c. In the upper layers of the terrestrial atmosphere ($z > 300$ km), we have $T \approx 1500^\circ$K in the years of peak solar activity (Ref.72). Then the density at the critical level, using $m = 16$ (atomic oxygen), will be

$$n_c = \frac{mg}{kT\pi d_m^2 \sqrt{2}} = \frac{1.67 \cdot 10^{-24} \cdot 16 \cdot 900}{1.38 \cdot 10^{-16} \cdot 1500 \cdot 5 \cdot 10^{-16} \sqrt{2}} \approx 2 \cdot 10^8 \ cm^{-3}.$$

Such a density is reached at an altitude of 500 km. Molecules and atoms moving toward the outside in the region of the critical level emerge from this level and subsequently travel along a ballistic trajectory without undergoing collisions. If the velocity is less than parabolic

$$V_p = \sqrt{\frac{2\gamma M}{R_1 + z_c}}, \tag{1.131}$$

the orbit will be elliptical and the molecule will return to the atmosphere. If the velocity is greater than parabolic, the molecule will totally escape from the atmosphere. At any temperature there exists a number of molecules whose velocity exceeds V_p.

Thus, the atmosphere is gradually scattered into outer space, due to the escape of molecules existing at the critical level. This process is known as dissipation of the atmosphere. The total flux of particles is equal to

$$N = \frac{n_c}{4} \int_{v_p}^{\infty} V P(V)\, dV \ cm^{-2} sec^{-1}, \tag{1.132}$$

where $P(V)$ is the Maxwellian velocity distribution of the molecules. The coefficient $\frac{1}{4}$ ("geometric factor") allows for the outward travel of one half of the molecules and the inward travel of the other half and for the fact that the mean direction of the outward-moving molecules is not at right angles to the surface of the critical level. Integration gives

/90

$$N = \frac{n_c \cdot c}{\sqrt{6\pi}} (1 + X_c) e^{-X_c}, \tag{1.133}$$

where $X_c = \frac{3}{2} \frac{V_s^2}{c} = \frac{R_c}{H_c}$, $c = \sqrt{\frac{3kT}{m}}$ is the mean-square velocity; $H_c = \frac{kT_c}{mg_c} =$

$= \frac{kT_cR_c^2}{\gamma Mm}$ is the altitude scale at the critical level; $R_c = R_1 + z_c$ is the radius of the critical level.

In all, the atmosphere, in unit time, loses $4\pi R_c^2 N$ molecules or atoms of mass m. If the altitude scale H at the ground surface, the radius R_c of the critical level, and the ratio $\frac{n_c}{n_1} = \alpha$ of density at the critical level to the density at the ground surface remain constant, then, as is readily seen, eq.(1.133) will yield

$$n_1 = n_{10}e^{-\frac{t}{t_0}}, \tag{1.134}$$

where

$$t_0 = \left(\frac{R_1}{R_c}\right)^2 \frac{H_1}{\alpha} \frac{\sqrt{6\pi}}{c} \frac{e^{X_c}}{1+X_c} = \left(\frac{R_1}{R_c}\right)^2 \frac{H_1}{\alpha} \sqrt{\frac{2\pi}{g_cH_c}} \frac{e^{X_c}}{1+X_c} \tag{1.135}$$

is the time of decrease in the amount of a given gas in the atmosphere by a factor of e ("lifetime of the atmospheric constituent"). If $T = T_c$ and $m = m_c$ throughout the atmosphere, then $g_cH_c = g_1H_1$ and, according to eq.(1.122a), $\alpha = e^{X_c - X_1}$ where $X_1 = \frac{R_1}{H_1}$. In such an isothermal atmosphere the lifetime is equal to

$$t_0' \approx \sqrt{\frac{2\pi H_1}{g_1}} \frac{e^{X_1}}{X_1} = \frac{c}{3g_1} \sqrt{6\pi} \frac{e^{X_1}}{X_1}, \tag{1.135a}$$

if $R_c \approx R_1$ and $X_1 \gg 1$. This formula gives a rough estimate of the lifetime even if there is very little information on atmospheric parameters. For the atmospheres of the planets in the terrestrial group it yields below-par estimates, since - so far as can be determined at present - the temperature in these atmospheres is higher at the critical level than in the lower layers of the atmosphere. Moreover, the formula is inapplicable for low t_0 when the rate of diffusion from the bottom restricts the concentration at the critical level so that it no longer satisfies eq.(1.122a).

Spitzer (Ref.4) introduced the correction factors $B = \frac{t_0}{t_0'}$ whose magnitude/91 depends on the real distribution pattern of H(z) in a given atmosphere. These factors are $10^6 - 10^7$ for the earth's atmosphere. The Spitzer coefficients were introduced for illustrative purposes, in order to show that eq.(1.135a) may lead to an error of several orders of magnitude. Generally, however, the rate of dissipation of atmospheric gases is quite accurately estimated directly from equation (1.135).

For oxygen in the terrestrial atmosphere (R_c = 6920 km, H_c = 110 km), we have, for example, $1/\alpha \approx 2 \times 10^{10}$, whence, according to eq.(1.134),

$$t_1 = 10^{29} \text{ years}.$$

Thus the amount of oxygen present in the earth's atmosphere could not markedly diminish over cosmogonic periods (5×10^9 years). For hydrogen, this calculation yields about 10^2 years. Hence hydrogen is being lost by the terrestrial atmosphere at an extremely rapid rate.

It is clear from these examples that dissipation must be a major process, regulating the composition of planetary atmospheres. However, the above theory must be approached with caution and is applicable only if the atmosphere does not receive new molecules that might compensate for the lost molecules. In the earth's atmosphere above 1800 km the principal constituents are hydrogen and helium. Their amount generally does not diminish in time, since the dissociation of H_2O continually compensates for the loss of hydrogen while radioactive decay in the earth's crust compensates for the loss of helium.

The region of the atmosphere above the critical level is known as the exosphere. The density distribution $n(z)$ in the exosphere in the presence of dissipation can be determined from the orbit and velocity distribution of the atoms leaving the critical level [see, for example (Ref.73, 74)].

c) General circulation of the atmosphere. The vertical structure of the atmosphere differs at various points on the planet. On the night side, there is no heating by solar radiation and, as a rule, the mean night temperature at every level is below the daytime temperature and the concentration at the higher altitudes decreases at night. In the terrestrial atmosphere this effect plays an essential role above 100 km. In the polar regions the altitude scale is lower than in the equatorial regions. If the planet rotates, the thermal equilibrium can be considered as being of the steady-state type only when averaged in time. In daytime, we have $dQ/dt > 0$ and at night $dQ/dt < 0$. The atmosphere reduces the temperature difference between the night and day sides of the planet as well as between the polar and equatorial regions. If the planet rotates /92
rapidly (Earth, Mars, Jovian planets), the fundamental mechanism smoothing out the temperature difference between day and night is correlated with the specific heat of the atmosphere. In daytime the atmosphere becomes heated, while at night it releases its heat to the subjacent surface.

Equilibration of temperature between equator and poles is accomplished by another process, namely circulation of the atmosphere. Air is heated at the equator, ascends, travels toward the poles and, on becoming cooled there, descends again. The return current travels close to the surface from the pole to the equator. Coriolis forces deflect this current from the meridional direction. If the heating at the equator is limited, the direction of the current is as shown in Fig.38 to the left. Such a regime of circulation of the atmosphere is termed symmetric or Hadleyan. If the heating at the equator and the cooling at the poles increases, the transport of heat will also increase. Symmetric circulation is able to transport only a limited amount of energy. Given a sufficiently strong heating, the symmetric regime of circulation is supplanted by a more /93
powerful regime, known as the wave regime (Fig.38, right).

On the earth, circulation is determined by the wave regime. On Mars, according to calculations by Mintz (Ref.75), a symmetric regime may be expected in summer and a wave regime in winter but the observational data are insufficient to confirm this hypothesis. If the planet rotates very slowly (Venus and Mer-

cury), the circulation may be of a completely different nature, with atmospheric currents directed from the subsolar point to the antisolar point and vice versa. In this case, the circulation equilibrates not only the latitudinal but also the longitudinal (the day-night difference) temperature distribution. A detailed discussion of the theory of the general circulation of planetary atmospheres is given elsewhere (Ref.75). The principal source of observational data on the circulation in the atmospheres of the other planets is the apparent structure of the cloud layer and the cloud movement.

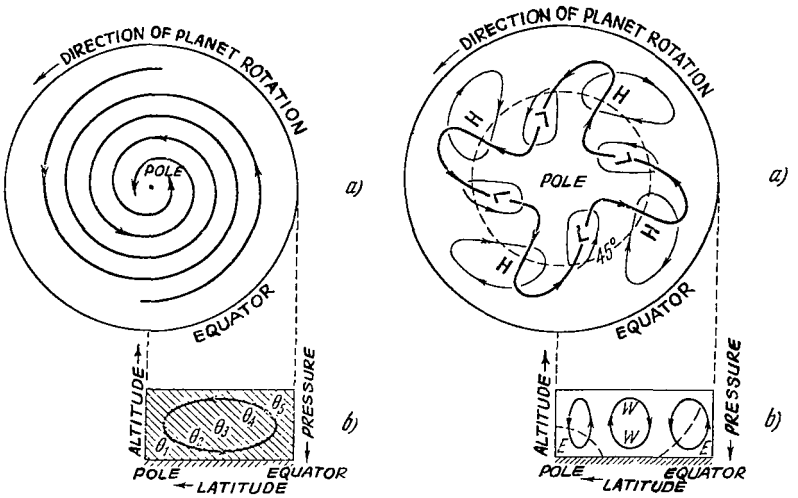

Fig.38 Two Regimes of General Circulation of the Atmosphere.
Left: Symmetric regime of general circulation. a - Streamlines in the upper layers; b - Cross-sectional view showing meridional projection of circulation and isotherms of potential temperature θ. Right: Wave regime of general circulation. a - Streamlines at the medium and upper levels (heavy curve) and near the surface (thin curve); L - low-pressure regions; H - high-pressure regions; b - Cross-sectional view of meridional circulation averaged over the zones and the averaged zonal wind; W - westerly wind; E - easterly wind.

Section 1.8 Radar

Within the confines of the solar system, heavenly bodies can be studied by radar methods. The received power of the reflected pulse is directly proportional to the power of the emitted pulse and to the cross-sectional area of the object and inversely proportional to the fourth power of distance. Hence the difficulties increase enormously with increase in distance. Radar sounding of the moon was first accomplished as far back as in 1946. Ten years had passed before a radar pulse could be bounced off Venus. And it is only in recent years that radar sounding of Mars, Mercury, and Jupiter has been successful. The ac-

cessibility of various bodies of the solar system to radar sounding is illustrated by the plot in Fig.39.

What are the purposes and possibilities of radar studies of the planets? The time between transmission and reception of a pulse, which can be measured very accurately, makes it possible to determine the distance to the planets with a much smaller error than that involved in optical observations. By determining more precisely the distance to Venus we can, by the same token, determine more precisely the length of the astronomical unit.

When the planet is rotating, sending a pulse of extremely narrow frequency will return a pulse blurred owing to the Doppler effect. The velocity of rotation of the planet can be determined from the width of the reflected pulse. Since different parts of the planet are located at different distances from the earth, the pulse duration also becomes blurred. Sufficiently large portions of the surface of the planet may display a lower or higher /94 radio-wave reflection coefficient, which leads to a diversification of the spectrum of the reflected pulse. Similar diversification has been observed in the spectrum of pulses bounced off Venus.

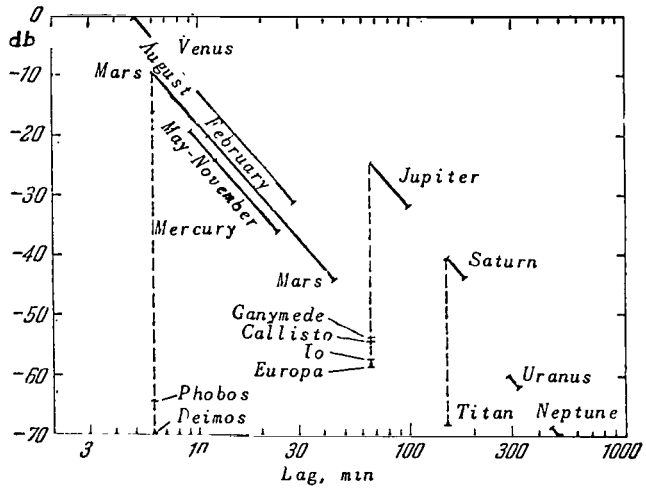

Fig.39 Relative Magnitude and Lag of Radar Signals Bounced Off the Planets and Satellites, Calculated for 1965.

A smooth spherical planet reflects earthward only a small portion of the power of the pulse sent toward it, since reflection takes place only from a central region of the disk (specular highlight). If the surface is densely covered with large - compared with the wavelength - inhomogeneities, then virtually the entire disk reflects and the duration of the reflected pulse is much longer. Thus, pulse duration is a criterion for determining the degree of surface smoothness.

If the velocity of rotation of a planet is known, a chart of the surface distribution of the reflection coefficient can be compiled by analyzing the frequency and duration of the received pulse. In that case, the width of the directional diagram is not essential. The radio-wave reflection coefficient depends on the physical properties of the planetary surface and particularly on the dielectric constant; thus, its measurement may provide important information on the material forming this surface.

By means of radar sounding at various frequencies, including sufficiently low frequencies, the critical frequency of the ionosphere and the height of the ionosphere above the surface can be determined. Once the critical frequency is

known, the electron density in the ionosphere can be determined. When polarized radio waves pass through a plasma in a magnetic field, their polarization plane is rotated, changing its orientation (Faraday effect). Thus, by comparing the polarization of the reflected and transmitted pulses it is possible to measure the intensity of the magnetic field. /95

TABLE 14

METHODS OF DETERMINING n AND P IN PLANETARY ATMOSPHERES

Method		Directly Determined Quantity	Additional Information Required	Application Field of Method
Spectroscopic	Directly according to line width	P	T and chemical composition	Lower atmosphere, $P \gtrsim 1$ atm
	According to growth curve			$P \gtrsim 10^{-3}$ atm (depending on intensity)
Photometric and polarimetric		τ	T and chemical composition (to determine H and refractive index)	Lower atmosphere, methods applicable when $\sigma_m \gg \sigma_a$
Observations of twilight regions		$\tau(z)$	"	Upper atmosphere, up to $n \approx 10^{12}$ cm^{-3}
Observation of stellar occultations		H n	Chemical composition (for refractive index)	Upper atmosphere at the level where $n \approx 10^{14}$ cm^{-3} /96
Direct measurements with manometers		P		Lower and upper atmosphere ($n > 10^{9}$ cm^{-3})
According to retardation of artificial satellites		$\rho = nm$		Upper atmosphere ($10^{10} > n > > 10^{4}$ cm^{-3})

The sensitivity of planet-sounding radar has been increasing rapidly in recent times. The world's largest radiotelescope, a 300-m hole-in-the-ground fixed paraboloid which was recently put into operation in Puerto Rico, was chief-

ly designed for the purpose of radar astronomy. Radar equipment mounted on interplanetary space platforms will make it possible to carry out studies with high spatial resolution.

TABLE 15

METHODS OF DETERMINING PLANETARY TEMPERATURES

Temperature	Method of Determination and Level of the Atmosphere or Ground, to which Temperature Refers
T_e - effective	Determined from conditions of thermal equilibrium with solar radiation [eq.(1.35) if T_e uniform over entire surface]
T_B - brightness	Determined from Planck's formula [eqs.(1.26) - (1.28)]. If $\tau_{atm} \gg 1$ in the atmosphere then T_B refers to the atmosphere at the level $\tau_{atm} \approx 1$; if $\tau_{atm} = 0$, T_B refers to the surface In the radio range (for $\tau_{atm} = 0$) T_B refers to a level at a depth as low as several meters below the surface
T_r - rotational	T_r refers to the effective level of formation of absorption bands in the atmosphere. A Boltzmann distribution of level populations is assumed
T_v - vibrational	The same
T_D - Doppler	Determined from the emission line width of night airglow and polar auroras. Refers to upper atmosphere
$T = \frac{Hmg}{k}$ - temperature calculated from altitude scale	Method suitable for determining the temperature of the atmosphere at any altitude for which the barometric formula is valid

Section 1.9 Review of Methodological Possibilities

Above, we discussed various methods of determining the basic physical characteristics of the planets. For convenience of the reader, we will now collate these methods. Table 14 enumerates the principal methods for determining the concentration n and pressure P of planetary atmospheres and specifies their /97 range of application. Table 15 enumerates the methods for determining planetary temperatures, and Table 16 gives methods for investigating the composition and structure of planetary surfaces. In the latter case, it is assumed that either the atmosphere has no influence on the measured characteristics or its influence

is precluded. As for the methods of determining the chemical composition of the atmosphere, the spectroscopic method is basic here but other estimate methods may prove useful on occasion [for example, the altitude scale (Ref.68)].

TABLE 16

METHODS OF INVESTIGATING THE COMPOSITION AND STRUCTURE OF PLANETARY SURFACES

Method	Quantities Directly Measured, and Determined Physical Characteristics
Photometric	$\rho(\mu_1, \mu_2)$ of the surface is measured and, by comparing with laboratory samples, both chemical composition (identification unreliable) and microstructure of the surface layer of several microns thickness are determined
Spectroscopic	The same, as above, except that a broader wavelength range is involved. Findings are more reliable, particularly in the presence of characteristic absorption bands
Polarimetric	Same characteristics, according to polarization in one or several wavelengths
Rate of variation in T_B (in radio and IR range) as a function of rate of variation in illumination (thermal inertia)	$K\rho c$ - product of specific heat (K), density (ρ) and heat conduction (c) of the surface layer of several meters thickness (as a function of λ)
Distribution of thermal radiation polarization over the disk	Dielectric constant of surface layer, under specific assumptions on surface smoothness
According to reflectivity for radar signals	Same characteristics
Duration of reflected radar signal	Mean inclination for surface sectors of a size exceeding the wavelength

CHAPTER II /98

MARS

Section 2.1 Introduction

Dark areas known as "seas" can be clearly distinguished on the disk of Mars even under conditions of moderate visibility. The light regions surrounding these patches are known as "continents" or land areas. The dark areas appreciably shift in position but their relative mutual alignment remains more or less constant. On reaching the west limb, they disappear beyond the rim and reappear within approximately 12^h on the east limb. This means that the rotation period of this planet is close to the terrestrial 24-hour day. The dark markings on the Martian surface had originally been observed some 300 years ago and their overall configuration has never changed. Hence there is reason to believe that they are on a solid surface and reflect the latter's geographic features. In the neighborhood of the limb, a small white area roughly coinciding with one of the poles can usually be observed. This is the polar cap. The polar caps (Fig.40) change their appearance in the course of the Martian year, shrinking in spring and spreading in fall, like their terrestrial counterparts. Occasionally both caps can be seen simultaneously. In spring, the contrast of the dark areas is greater. During the melting of the polar cap a wave of darkening, as it were, spreads toward the equator from the pole in the respective hemisphere. It appears likely that these seasonal periodic changes are associated with biological processes, but so far this cannot be proved.

The dark patches also undergo irreversible, secular changes. However, such changes were uncovered only by extremely thorough protracted studies, carried out with a maximum resolving power.

In addition to such patches stationary on the surface, visual and photographic observations of the Martian disk indicate shifting formations which at times cover the dark areas. Apparently, these are clouds.

The presence of clouds demonstrates that Mars has an appreciable atmosphere. The dark areas are distinguishable in greatest contrast in red light, whereas in blue light they virtually disappear. The polar caps and certain types of clouds, conversely, are clearly visible on photographs made with a blue filter. It /99
might be conceived that, in blue light, the natural contrast of the dark areas with respect to the continent becomes small, but this explanation cannot be correct. There are times (so-called "blue clearings") when the dark areas can also be observed through a blue filter. Hence the veiling of the dark areas in blue light must be caused by some agent present in the atmosphere and occasionally disappearing.

The conditions for observation of Mars vary markedly from one opposition to the other: The disk diameter is about $25''$ during favorable opposition and $14''$ /100
during the least favorable, aphelic opposition. However, the wide interest focusing on Mars during favorable oppositions is not fully justified. Many types

of physical observations can be carried out close to aphelic opposition with almost the same success as at favorable opposition. Figure 41 gives a diagram of the orbits of Mars and Earth on which the oppositions of Mars during the next 10 years are indicated. A table of oppositions until the end of the 20th Century can be found elsewhere (Ref.76).

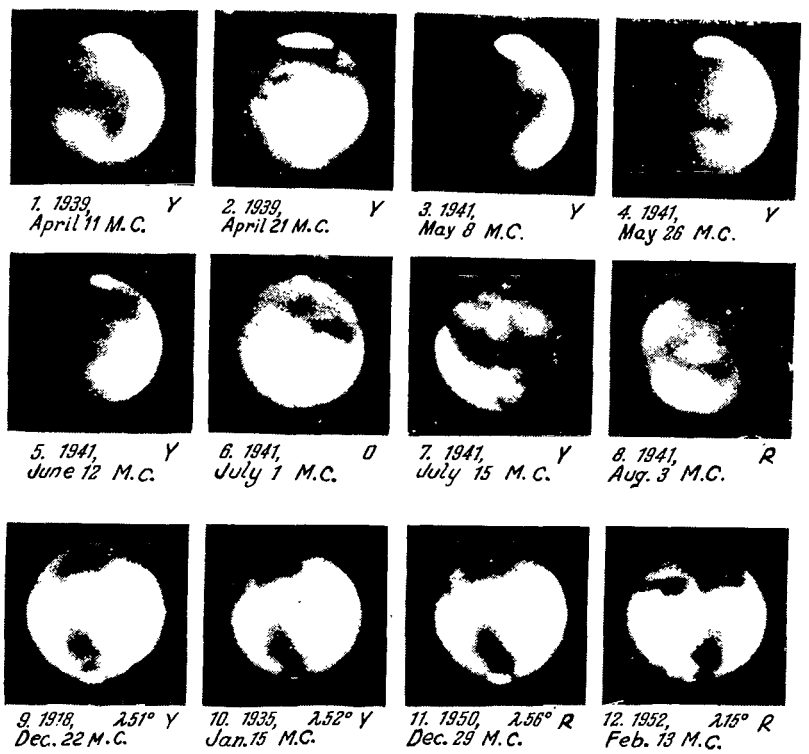

Fig.40 Seasonal Variations of the Polar Caps of Mars (Ref.86).
Dates are given in the Martian Calendar (M. C.). Letters Y, O, R - yellow, orange, and red filters, respectively. λ - longitude of the central meridian.

The visual stellar magnitude of this planet at the instant of favorable opposition is -2.6^m and during aphelic oppositions, -1.0^m. During the two months immediately preceding and following opposition, the brightness markedly decreases by about $1.3 - 1.6^m$. The irregular distribution of the dark areas causes slight fluctuations in the stellar magnitude, with a period equal to the period of rotation. The color index is $B-V = 1.36^m$, i.e., 0.71^m higher than for the sun (Ref.66).

The length of the Martian day has been determined with very high accuracy, based on the apparent displacement of the dark markings. This amounts to $24^h 37^m 22.62^s$. The Martian year lasts 687 days. The eccentricity of the orbit is 0.093, which is 6.5 times more than for earth. The inclination of the equator

to the elliptic is nearly the same as for the earth amounting to $23^{\circ}57'$. Hence, also the succession of seasons of the year is the same as on Earth, with the differences being due to the greater eccentricity of the orbit of Mars. The south pole of Mars is oriented sunward when the planet passes through its perihelion, so that the summer in the Southern Hemisphere is hotter and shorter than in the Northern. /101

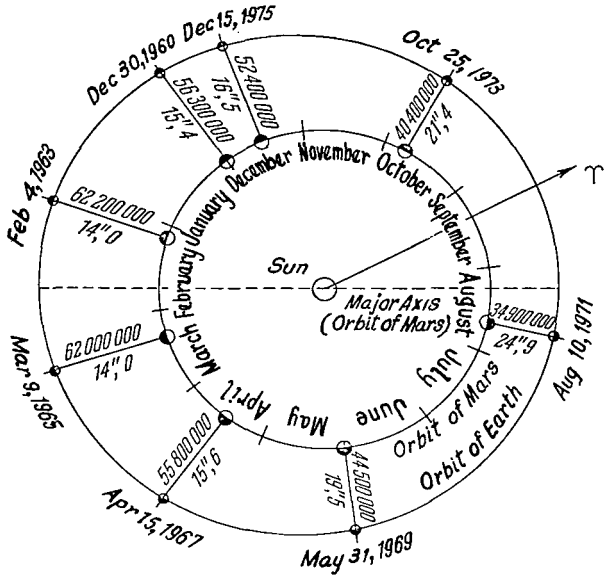

Fig.41 Oppositions of Mars during the 1960-1975 Period.

According to Brouwer and Clemence (Ref.77) the mass of Mars is

$$M_{\sigma} = \frac{M_{\odot}}{3083000 \pm 3000} = (0.10766 \pm 0.00010)\, M_{\oplus}.$$

Measurements of the trajectory of the spacecraft Mariner IV (Ref.634) point to a lower value

$$M_{\sigma} = \frac{M_{\odot}}{3098600 \pm 600}.$$

According to the survey by de Vaucouleurs (Ref.78), the equatorial diameter of Mars is

$$D_{\sigma} = 6828 \pm 8 \ km.$$

Radio observations of the occultation of Mariner IV by the planetary disk indicate a lower value

$$D = 6764 \pm 5 \ km.$$

The mean density of Mars

$$\rho_{\sigma} = 3.9 gm \cdot cm^{-3}$$

is markedly lower than that of Earth (5.5 gm $\cdot$ cm^{-3}); the acceleration due to gravity is

$$g = 370 \ cm \cdot sec^{-2},$$

and the parabolic velocity,

$$V = 5.2 \ km \cdot sec^{-1}.$$

The polar diameter is much smaller than the equatorial. The oblateness, according to de Vaucouleurs (Ref.78), is equal to

$$\varepsilon = \frac{D_{eq} - D_{tot}}{D_{eq}} = 0.012 \pm 0.002.$$

Trumpler (Ref.79) found a value of $\varepsilon = 0.0104 + 0.006$. Camichel (Ref.80) found $\varepsilon = 0.012$. These values were obtained by means of direct micrometric measurements. Oblateness can also be calculated in theory, by the methods of celestial mechanics, from the precession of the orbital plane and motion of line of apsides of the satellites of Mars (Ref.81). This quantity, known as dynamic oblateness, is much lower: $\varepsilon_0 = 0.0053$. The difference between ε and ε_0 greatly exceeds /102 the limits of errors of observation and theory. Öpik (Ref.82) assumes that the observed excessively high oblateness has to do with the properties of the atmosphere: The dense atmospheric haze on the equator may lead to an apparent increase in equatorial diameter.

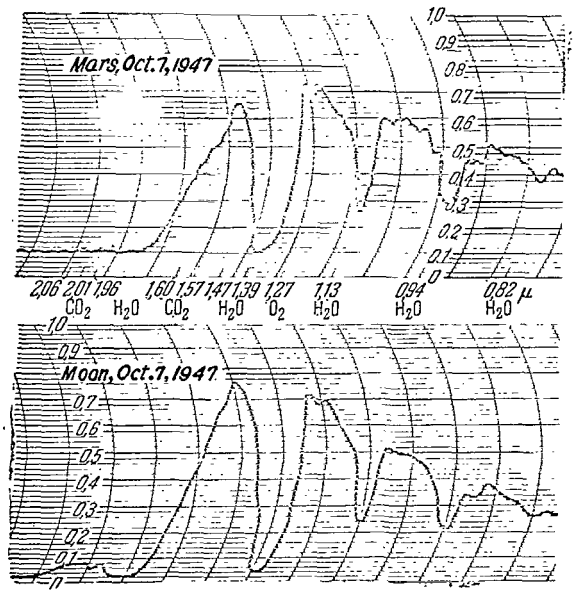

Fig.42 Spectrum of Mars and Moon in the Region λλ 0.8 - 2.5 μ according to Kuiper's First Observations (Ref.9).

Studies of Mars toward the end of the past Century had aroused enormous interest among the general public, because of the discovery of "canals" [Schiaparelli (Ref.83)] which are thin and fairly straight lines intersecting the planet's surface in various directions. Many assumed that the network of Martian canals was a manifestation of the activity of sentient beings. Naturally, this centered attention on visual and photographic observations of the Martian surface features, and nearly all that could be done in this direction has long ago been accomplished. Old visual observations were published by Antoniadi (Ref.84) and in the Lowell Observatory Bulletin (Ref.85), while more up-to-date observations (carried out at the Pic du Midi Observatory) were described by Dollfus (Ref.22). Exceptionally varied photographic material is contained in the books by Slipher (Ref.86, 87). Further progress can be expected only after scientific payloads can be carried aloft to outside the confines of the atmosphere (by balloons, space probes, and spacecraft). Recently, the first success in this direction has been achieved. Mars was successfully photographed by the American interplanetary spacecraft Mariner IV; the best of the photographs distinctly show lunar-like craters, montane regions, etc. (cf. Sect.2.9). These photographs which represent only the first experiment reveal the potential of that new weapon of the astronomer, namely outer space rockets.

In recent years, earth-based spectroscopic observations have produced a number of interesting findings, chiefly pertaining to the composition and struc-

ture of the Martian atmosphere. In the following Section, we will begin to examine these findings.

Section 2.2 CO_2 Content and Total Pressure in the Martian Atmosphere

The first attempts to investigate the chemical composition of the Martian atmosphere by spectroscopic methods were undertaken more than fifty years ago. Oxygen (electronic bands in the red portion of the spectrum) and water vapor were primarily sought. These gases could not be discovered at all, and no positive findings on the composition of the Martian atmosphere were obtained until as late as 1947 when Kuiper and his coworkers first obtained planetary spectra in the region of λλ 1 - 2.5 μ, using an infrared spectrometer with a PbS photovaristor. These observations revealed two CO_2 bands in the spectrum of Mars near 1.6 μ (λλ 1.573 and 1.606 μ) and later three more bands near 2 μ (λλ 1.95, 2.01, 2.06 μ). Carbon dioxide is also present in the earth's atmosphere; therefore, /103 in his search for CO_2 in the spectrum of Mars Kuiper also recorded the lunar spectrum at a time it was not far from Mars and at a close zenith distance. The intensity of CO_2 bands in the Martian spectrum proved to be much greater (Fig.42). The observations were carried out with the aid of the 82″ reflector at the McDonald Observatory. The resolving power of the spectrometer was rather limited, being $\frac{\lambda}{\Delta\lambda} = 80$.

To determine the CO_2 content of the Martian atmosphere, the solar spectrum for various air masses was recorded with the aid of the same spectrometer but without a telescope, using a scattering screen. Figure 43 gives the resultant dependence of total absorption on air mass, in the solar spectrum within the 1.575 and 1.606 μ bands. The point with the vertical bar represents absorption in the Martian spectrum for an air mass $M_\oplus = 1.1$. This corresponds to telluric absorption at $M_\oplus = 10$. Kuiper (Ref.4) estimated the amount of CO_2 as follows: /104 Mars accounts for 8.9 of the air mass, the mean value of the air mass for a uniformly illuminated disk is 4, and the amount of CO_2 in the atmosphere of Mars is $\frac{1}{4} \times 8.9 = 2.2$ times as high as in the earth's atmosphere above the McDonald Observatory or 1.8 times as high as above sea level. According to Allen (Ref.88), the reduced thickness of CO_2 in the terrestrial atmosphere above sea level is 2.60 m • atm, which gives 4.70 m • atm for the Martian atmosphere. It is quite obvious that this reasoning is valid only if the rotational lines in the CO_2 bands are unsaturated.

In the terrestrial atmosphere, the CO_2 bands are close to saturation. The photometric and polarization observations available at the time implied that pressure in the Martian atmosphere is at least one order of magnitude higher than in the terrestrial atmosphere (i.e., about 100 mb) and thus the Martian rotational lines must be more narrow than their terrestrial counterparts. Since their equivalent width is greater, they must be saturated which would mean that the observed intensity cannot serve as a yardstick for determining the amount of CO_2 and can be used only to find the mathematical product of the amount of carbon dioxide and pressure (cf. Sect.1.4) or, which comes to the same, the product of the relative concentration of carbon dioxide and the square of pressure. This

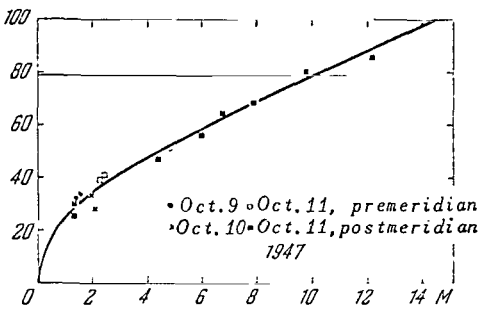

Fig.43 Relation of the Intensity of Telluric CO_2 Bands near λ 1.6 μ to Air Mass (Squares and Crosses) and Intensity of Martian CO_2 Bands according to Kuiper's Observations in 1947 for an Air Mass 1.1 (Straight Line Parallel to the Abscissa) (Ref.4).

parameter was calculated from Kuiper's observations eight years later, by Grandjean and Goody (Ref.42) who found

$$cP_1^2 = 160 \pm 50\, mb^2, \qquad (2.1)$$

where c is the relative volume concentration of CO_2 (it was assumed that the entire remaining atmosphere consisted of nitrogen); P_1 is the pressure at the surface. This corresponds to

$$u_{CO_2} P_1 = 3200\, m \cdot atm \cdot mb, \qquad (2.2)$$

or to the reduced thickness

$$u_{CO_2} = 32\, m \cdot atm, \qquad (2.3)$$

if P_1 = 100 mb.

Kuiper's observations in 1947 remained/105 for many years the only source of information on the intensity of CO_2 bands in the Martian spectrum. Sinton (Ref.89, 90) recorded the spectrum of Mars in the region from 1 to 4 μ, but the resolving power he had achieved in the interval from 1 to 2 μ, where the CO_2 bands are located, was lower than that obtained by Kuiper. Sinton and Strong (Ref.26) discovered several Martian CO_2 bands in the 8 - 13 μ region. These are difference bands; their intensity is greatly influenced by temperature and they are not even suitable for estimating the parameter $u_{CO_2} P_1$.

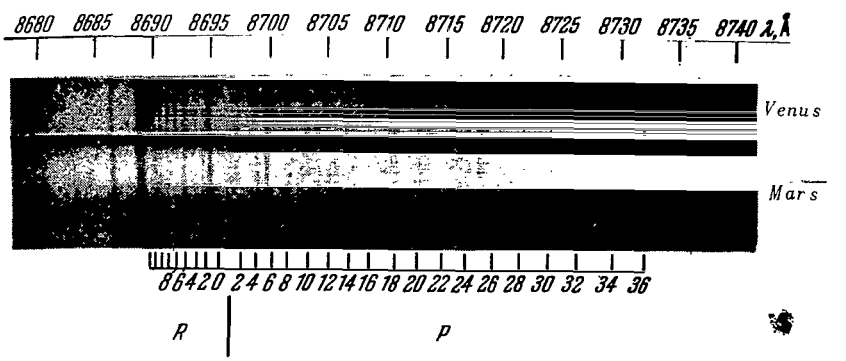

Fig.44 Spectrogram of Venus and Mars in the 8680 - 8740 Å Region.
The strong rotational $5\nu_3$ CO_2 lines in the spectrum of Venus exactly correspond in position to the very weak but perceptible Martian CO_2 lines. Dispersion of the original spectrograms, same in both cases: 5.6 Å/mm, but resolving power in the case of Mars higher.

To determine the CO_2 content independently of pressure, extremely weak absorption bands corresponding to the linear segment of the growth curve must be observed. For such observations a considerable resolving power is required, so that discrete rotational lines can be recorded. Spinrad, Münch, and Kaplan (Ref.91, 92), in the photographic infrared region, obtained Martian spectra with a dispersion of 5 Å/mm and a resolving power of $\frac{\lambda}{\Delta\lambda} \approx 10^5$ on the 100-inch reflector of the Mount Wilson Observatory. Their aim was to search for Martian H_2O lines; these lines were indeed discovered for the first time after numerous fruitless past attempts. We will discuss this in detail in Section 2.3, since we are now concerned more with another point, namely with the fact that the same spectrogram displayed traces of several rotational lines of an extremely weak $5\nu_3$ CO_2 band near λ 8700 Å (Figs.44 and 45). The equivalent widths of individual rotational lines of this band were only about 5 mÅ. Laboratory studies of this absorption band normally are performed with the aid of cells having a path length of about one kilometer (roughly 200 gm/cm^2). Consequently, on the basis of the report on the discovery of this band alone it could be concluded that the amount of carbon dioxide in the atmosphere of Mars is substantial. /106

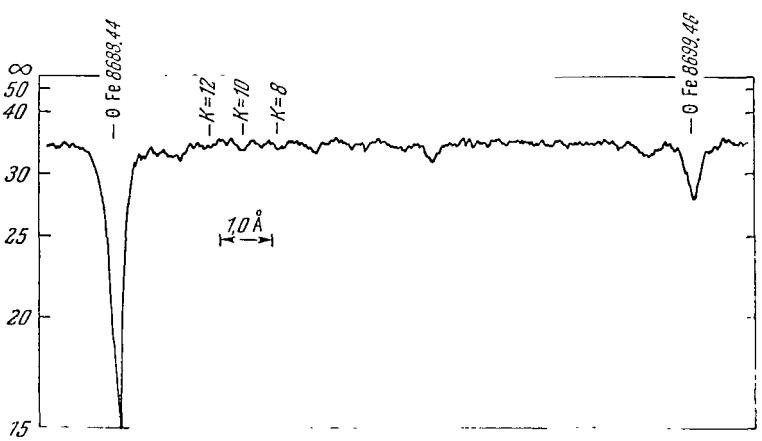

Fig.45 Microphotometric Trace of the R-Branch of the Martian $5\nu_3$ CO_2 Band. The lines K = 8, 10, 12, utilized for quantitative estimates and two solar lines were recorded. Ordinate: nonlinear scale of relative intensities.

Based on Rank's laboratory spectrograms, Kaplan, Münch and Spinrad (Ref.91) obtained

$$M_{\sigma} u_{CO_2} = 180\ m \cdot atm, \qquad (2.4)$$

where M_σ is the Martian air mass. Taking T = 230°K for the Martian atmosphere, these astronomers found that the temperature correction for the lines with K =

= 8, 10, 12 is approximately +10%. The air mass for the observed point on the disk is equal to

$$M_{\sigma} = \sec i + \sec z = 3.6,$$

whence

$$u_{CO_2} = 55\, m \cdot atm. \tag{2.5}$$

These authors estimated the indeterminacy of the above quantity as being ±40%. Owen (Ref.93) independently analyzed this spectrogram and, on the basis of his own laboratory measurements, found that /107

$$u_{CO_2} = 51 \pm 15\, m \cdot atm \quad at \quad T = 230^\circ K, \tag{2.6}$$
$$u_{CO_2} = 46 \pm 15\, m \cdot atm \quad at \quad T = 200^\circ K. \tag{2.7}$$

Owen also estimated u_{CO_2} by comparing the Martian spectrum with the solar spectrum for large air masses. He found that the telluric $5\nu_3$ CO_2 band equals its Martian counterpart in intensity if $M_{\oplus}$ = 30 ± 3, whence

$$u_{CO_2} = 73 \pm 7\, m \cdot atm. \tag{2.8}$$

Henceforth, we will use the estimate given in eq.(2.5). Together with eq.(2.2) the estimate (2.5) yields

$$P_1 = 60 \pm 30\, mb. \tag{2.9}$$

Allowing for observation errors, it can be concluded that the above pressure value is in agreement with photometric and polarization observations, which point to 80 - 100 mb (Ref.5). During the 1963 opposition, however, Moroz (Ref.94) and Kuiper (Ref.95) conducted new observations of saturated CO_2 bands, which showed that the parameter $u_{CO_2}P_1$ is much smaller than had been concluded by Grandjean and Goody from Kuiper's old observations. The new observations were distinguished by a much higher resolving power and accuracy. This had become possible because of the use of diffraction spectrometers and improvements in the sensitivity threshold of the sensors (PbS photovaristors). The latter, in part, was attained by cooling the photovaristors to the temperature of solid carbon dioxide (-73° C). The author repeated these observations during the 1965 opposition. Figures 46 - 47 present sample traces of the Martian spectrum recorded from the 1963 and 1965 observations in the USSR [Southern Station of the GAISh (State Astronomical Institute im. Shternberg) with a 125-cm reflector] and observations during 1963 in the United States (spectrometer of the Laboratory of the Moon and Planets, University of Arizona, and the 82-inch reflector of the McDonald Observatory).

A comparison of these traces with Fig.42 reveals the great increase in resolving power (in the new observations, from 500 to 1000). This increase in resolving power permitted the detection of numerous CO_2 bands that had not previously been observed in the Martian spectrum.

Table 17 gives the total list of absorption bands found in the spectrum of Mars by various investigators, with emphasis on identification and intensity.

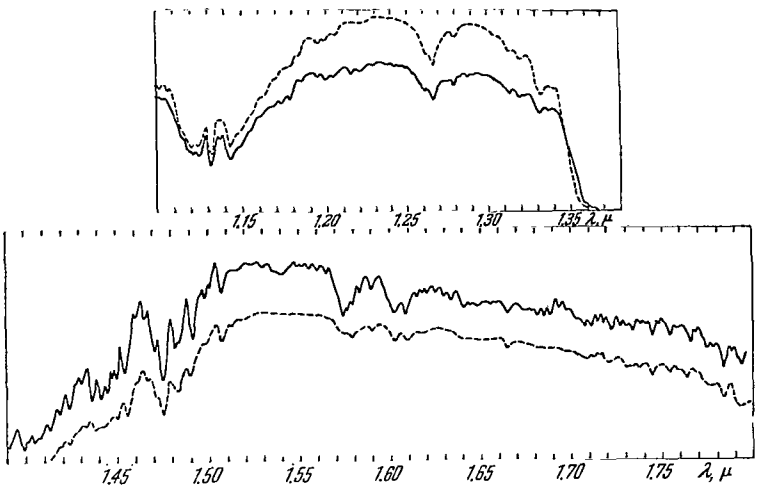

Fig.46 Spectrum of Mars in the λλ 1.1 - 1.8 μ Region, Averaged for Six Traces Recorded on April 4-5 and 6-7 1965 from Observations with the 125-cm Reflector of the GAISh Southern Station.
$\Delta\lambda \approx 17$ Å; recording speed 3 Å/sec; $\tau = 4.4$ sec; zenith distance from 36 to 47°; grating 600 rulings/mm.

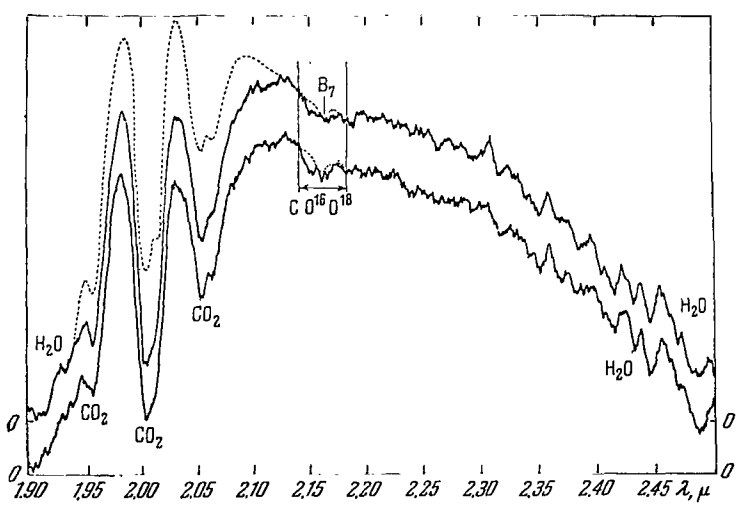

Fig.47 Spectrum of Mars in the 1.90 - 2.5 μ Region (Two Traces) according to Kuiper's Observations during the 1962 Opposition (Air Mass 1.05).
Broken curve - lunar spectrum.

TABLE 17

/109

ABSORPTION BANDS DISCOVERED IN THE MARTIAN SPECTRUM

Wavelength	Equivalent Width, Å	Identification	Resolving Power of Instrument	Reference*
8176.97 Å**	~0.004	211 H_2O	10^5	Kaplan et al. [91, 92]
8189.27 **	~0.004	211 H_2O	10^5	The same
8226.96 **	~0.004	211 H_2O	10^5	»
0.869 μ		005 CO_2	10^5	»
$K = 8$	0.0033	005 CO_2		
$K = 10$	0.0037	005 CO_2		
$K = 12$	0.0044	005 CO_2		
1.205 μ	5.7±0,8	103 CO_2	10^3	Moroz, 1965
1.215	2.5±0,5	023 CO_2	10^3	»
1.31	?	241 CO_2	$3 \cdot 10^2$	Moroz [94]
1.38	?	101 H_2O	10^2	Dollfus [115]
1.433	20?	003 CO_2	$3 \cdot 10^2$	Moroz [94]
1.528	6.3±0,5	301 CO_2	10^3	Moroz, 1965
1.578	18.8±2	221 CO_2	10^3	»
1.606	19.1±2,4	141 CO_2	10^3	»
1.646	12.3±0,5	061 CO_2	10^3	»
1.965	160?	201 CO_2	$3 \cdot 10^2$	Moroz [94]
2.009	250?	121 CO_2	$3 \cdot 10^2$	»
2.062	100±30	041 CO_2	$3 \cdot 10^2$	Moroz, 1965
2.0082	10?	$05^11—01^10$ CO_2	$3 \cdot 10^2$	Moroz [94]
2.102	20?	041 $C^{13}O_2^{16}$	$3 \cdot 10^2$	Moroz [94]
2.16	6.5±1	002 $C^{12}O^{16}O^{18}$		Kuiper [95]
2.7	2300	021 CO_2		Danielson et al. [43]
		101	$3 \cdot 10^2$	
3.43, 3.53, 3.59, 3.68 ***	?		50	Sinton [89, 90]
4.3	~5000	001 CO_2	$3 \cdot 10^2$	Danielson et al. [43]
4.8	~1500	110 CO_2		»
5.2	~500	03^10CO_2		»
9.4	~200	$00^01—02^00$ CO_2	10^2	Sinton and Strong[26]
10.4	200	$00^01—10^00$ CO_2	10^2	»
12.6	500	$11^00—02^00$	10^2	»

* Sources from which estimates of equivalent length are taken are specified.

** Wavelength of individual rotational lines.

*** It is suspected that these bands, which had for a long time been considered Martian, in reality are telluric (Ref.186).

It is obvious from this list that CO_2 bands represent the most prominent detail of the Martian spectrum throughout the observable wavelength range from 3000 Å to 13 μ. The CO_2 bands λ 2.7, 4.3, 4.8, and 5.2 μ were observed with the aid /110 of the balloon-borne telescope "Stratoscope II" (Ref.43). The newly discovered CO_2 bands include isotopic ($C^{13}O_2^{16}$ and $C^{12}O^{16}O^{18}$) and difference bands. All CO_2 bands discovered in the 1 - 2.5 μ region, even the weakest, are saturated or, expressed more accurately, consist of saturated rotational lines. Figure 48 presents the spectrum of Mars in the 8 - 13 μ region (Ref.26), which points to the presence of several hot CO_2 bands.

Below, we will attempt a new estimate of atmospheric pressure with the aid of the spectral method based on the totality of findings for the intensity of CO_2 bands. The bands most convenient for this purpose are 1.573, 1.606, and 2.05 μ. The bands 1.95 and 2.01 μ excessively overlap the telluric H_2O 1.9 μ band, while the 1.43 μ band overlaps the H_2O 1.38 μ band. The other bands within the 1 to 2.5 μ wavelength range are too weak, and their equivalent width cannot be measured with sufficient accuracy. Balloon observations are not sufficiently reliable, owing to the lack of comparison spectra. Tables 18 and 19 give the results of measurements of equivalent widths of CO_2 bands at 1.6 and 2.05 μ with respect to spectra obtained by us and by Kuiper. Sinton's findings (Ref.96) were not utilized in view of the comparatively low resolving power. The band intensities for λ 1.578 and 1.606 μ are closely adjacent, and Table 18 presents their average. In these tables, $\Delta\nu$ is the Doppler shift of the Martian lines with respect to the telluric lines, proportional to the velocity of Mars relative to the earth; $W_{\oplus+\sigma}$ is the observable equivalent width of CO_2 bands in the Martian spectrum, determined by total absorption in the terrestrial and Martian atmospheres; $M_\oplus$ is the air mass in the terrestrial atmosphere ($M_\oplus \approx \sec z$, where sec z is the zenith distance of Mars); $W_\oplus$ is the equivalent width of the telluric CO_2 band for a given value of $M_\oplus$; W_σ is the equivalent width of the CO_2 band in the spectrum of Mars. If the telluric and rotational lines of CO_2 had not overlapped each other and the Martian lines, the relation /111

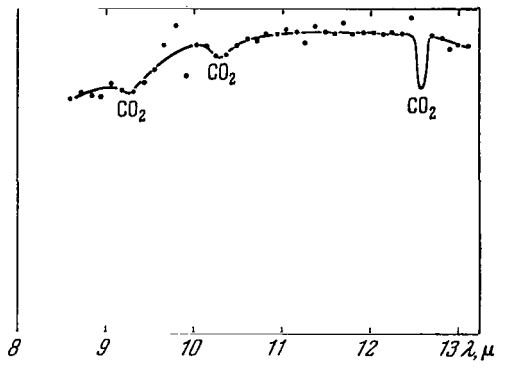

Fig.48 Spectrum of Mars in the λλ 8 - 13 μ Range, Corrected for Transmission through Terrestrial Atmosphere (Ref.26).

$$W_\sigma = W_{\sigma+\oplus} - W_\oplus, \tag{2.10}$$

would hold. If the telluric and Martian lines overlap, then

$$W_\sigma > W_{\sigma+\oplus} - W_\oplus. \tag{2.11}$$

If $\Delta\nu = 0$, the adjacent lines do not overlap and if, moreover, the telluric and Martian lines are saturated then we have, according to (1.56),

$$W_\sigma = \sqrt{W^2_{\sigma+\oplus} - W^2_\oplus}. \tag{2.12}$$

By numerical integration of the contours of the overlapping lines we obtain /112

$$\frac{W_\sigma}{W_{\sigma+\oplus} - W_\oplus} \tag{2.13}$$

TABLE 18

MEAN EQUIVALENT WIDTH OF THE BANDS λ 1.578 AND 1.606 μ IN THE MARTIAN SPECTRUM

Author	Date of Observations	Δν, cm^{-1}	$W_{\oplus+\sigma}$, Å	$M_\oplus$	$W_{\oplus+\sigma}-W_\oplus$, Å	W_σ, Å
Kuiper . .	Dec.8,1962	0.27	22	1.1	14.8	15.1
Moroz . . .	May 5,1963	0.31	31	1.4	14.0	14.3
Moroz . . .	April 4-7,1965	0.17	29	1.4	17.6	19.0
Mean . .						16±1 Å

TABLE 19

EQUIVALENT WIDTH OF THE λ 2.05 μ BAND IN THE MARTIAN SPECTRUM

Author	Date	Δν, cm^{-1}	$W_{\oplus+\sigma}$, Å	$M_\oplus$	$W_{\oplus+\sigma}-W_\oplus$, Å	W_σ, Å
Kuiper . .	Dec.14,1962	0.27	145	1.3	76±5	105
Moroz . .	March 5,1963	0.13	168	1.05	79±10	120
Moroz . .	April 8,1965		132	1.26	60±20	10
	April 19,1965	0.17	174	2.46	32±10	80
Mean . .						100±8 Å

at given Δν and $W_\oplus$. In the case of bands near 1.6 μ, this relation ranges from 1.01 (Δν = 0.31 cm^{-1}) to 1.06 (Δν = 0.17 cm^{-1}) at $M_\oplus \approx 1$, while for the band λ 2.05 μ it is roughly 1.5 at $M_\oplus \approx 1$ and 2.5 at $M_\oplus$ = 2.46.

Owen and Kuiper (Ref.16) made an extensive series of laboratory measurements of the equivalent widths of CO_2 bands (with a resolving power close to that used in astronomic observations) for various combinations of pressure, length of optical path, and relative concentrations of CO_2 (pure CO_2, 25% CO_2 and 75% N_2, 10% CO_2 and 90% N_2). Figures 49 and 50 show the equivalent widths of the 1.6 μ bands as a function of pressure at various path lengths, for pure CO_2 and for a mixture 10% CO_2 + 90% N_2.

In the presence of only small amounts of carbon dioxide u_{CO_2}, the equivalent width is almost independent of pressure; however, as u_{CO_2} rises the pressure dependence becomes increasingly stronger and ultimately tends to a quadratic dependence ($W \sim P^{0.5}$) if the overlap of neighboring lines is insignificant. Pure CO_2 gives greater equivalent widths than a mixture with N_2, for equal values of uP_1. A comparison of Figs.49 and 50 yields the correction for self-reversal broadening: /113

$$\frac{\alpha_{CO_2-CO_2}}{\alpha_{CO_2-N_2}} \approx 1.7, \tag{2.14}$$

which is somewhat higher than indicated in Table 9. The mean Martian air mass M_σ can be taken equal to 3, whence

$$M_\sigma u_{CO_2} = 165 m \cdot atm. \tag{2.15}$$

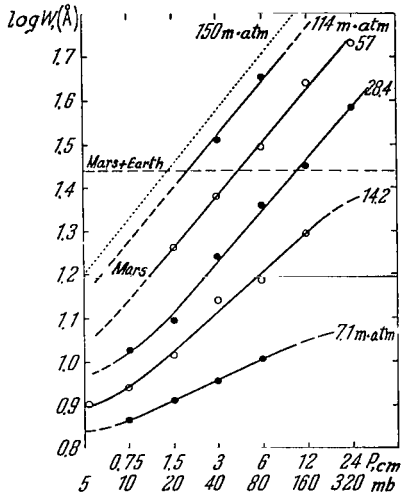

Fig.49 Mean Equivalent Width of the Bands λ 1.573 and 1.606 μ as a Function of Pressure for Pure CO_2 Gas Layers of Varying Thickness (Ref.16).

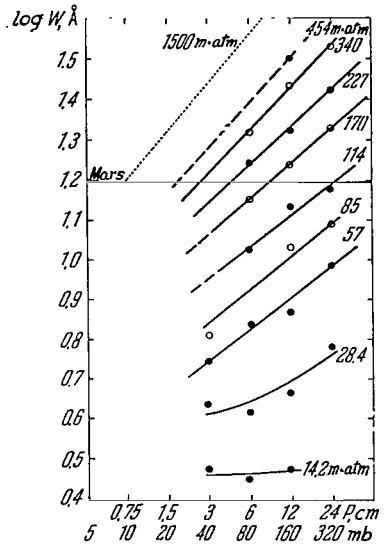

Fig.50 Same as in Fig.49, for an Atmosphere Consisting of 10% CO_2 and 90% N_2 (Ref.16).

Owen and Kuiper assumed a somewhat smaller value $M_\sigma u_{CO_2}$ = 150 m • atm (broken curve in Figs.49 and 50). The estimate (2.15) yields pressures of 4 and 7 mb, respectively, when compared with Figs.49 and 50). The pressure at the surface, according to eq.(1.72), must be twice as high

$$8 < P_1 < 15\ mb. \tag{2.16}$$

The upper limit is reached when CO_2 is a minor constituent and the lower limit is attained when the atmosphere is pure CO_2. At pressures $P_1 \approx 10$ mb and equivalent widths of ~ 15 Å, the data in Fig.47 can be expressed by the empirical formula*

$$\log W = 0.45 \log u M P_1 - 0.10, \tag{2.17}$$

* The analogous empirical formula (1) by Owen (Ref.16) was stated incorrectly. Apparently an arithmetic error was committed.

where the quantity uM is expressed in m • atm; P_1, in mb; W, in Å. For a mixture of 10% CO_2 and 90% N_2 at such pressures, no data are available but the correction for self-reversal broadening [eq.(2.14)] permits deriving the corresponding formula directly from eq.(2.17):

$$\log W = 0.45 \log uMP_1 - 0.20. \tag{2.18}$$

The estimate (2.16) is not corrected for the temperature effect. The equivalent width of saturated absorption bands decreases with temperature, since

$$W \sim \sum \sqrt{N_K}, \tag{2.19}$$

where N_K is the population of the K-th rotational level; ΣN_K = const. If N_K follows the Boltzmann distribution [eq.(1.17)], then $\Sigma \sqrt{N_K}$ decreases with a drop in temperature. Table 20 gives the temperature corrections of equivalent widths, calculated for CO_2 bands from eq.(2.19). The table shows that the temperature correction is sufficiently small. /114

For the 2.05 μ band in the presence of low relative concentrations of CO_2, we derived the following formula from Owen's findings (Ref.16):

$$\log W = 0.53 \log uMP_1 + 0.29. \tag{2.20}$$

Substituting W = 100 Å and uM = 165 m • atm, we have P_1 = 26 mb. The coefficient at log uMP in the above empirical formulas is close to 0.5. A quadratic approximation can be used if it is assumed that the coefficient is equal to 0.5. In this case, a determination of pressure yields P_1 = 21 mb with respect to the bands at 1.6 μ and P_1 = 28 mb with respect to the 2.05 μ band, at low relative concentrations of CO_2.

TABLE 20

TEMPERATURE CORRECTIONS FOR EQUIVALENT WIDTHS OF SATURATED CO_2 BANDS

T, °K	$\frac{W(T)}{W(300°\,K)}$
230	0.98
250	0.99
300	1.00

Finally, similar estimates can be obtained by comparing the equivalent widths of Martian CO_2 bands with their terrestrial counterparts. Figure 51 shows the dependence of the equivalent width of the telluric band λ 1.573 μ on the air mass, as obtained from observations of the sun. The diagram also gives a theoretical growth curve calculated for Elsasser's model by numerical integration for $\Delta\nu_c$ = = 0.04 cm^{-1}. The numerical integration was necessary since, in the presence of low air masses, the telluric lines are insufficiently saturated and are located on the intermediate segment of the growth curve. The median absorption R_{med} was determined, so that the contribution of the lines with an absorption $\bar{R}_\nu > R_{med}$ to the equivalent bandwidth would equal the contribution of the lines with an absorption $\bar{R}_\nu < R_{med}$. It can be shown that, for saturated lines, we have

$$R_{\text{med}} = 0.8 \frac{W}{d} \frac{\sqrt{N_{\max}}}{\sum \sqrt{N_K}}, \tag{2.21}$$

where d is the mean distance between the lines, and N_{max} is the population of the level corresponding to the maximum of the function (1.17). At 300°K,

$$\frac{R_{med}}{W} = 0.0141, \qquad (2.22)$$

if W is expressed in cm^{-1}. Then, $\frac{R_{med}}{W}$ is independent of λ.

A comparison of the theoretical and observational growth curves permits determining the mean intensity s per rotational line, which for the band λ 1.573 μ is 0.04 cm^{-1} $(m \cdot atm)^{-1}$, on the assumption that the amount of CO_2 above the observation site was 240 cm • atm at zenith. For large air masses, the theoretical curve plotted as a result of numerical integration is satisfactorily represented by the function (1.62). With a decrease in temperature the quantity $\frac{R_{med}}{W}$ increases, but this is accompanied by a change in s $\sim N_{max}$ and $\Delta\nu_c$ [$\Delta\nu_c$ is proportional to $T^{-0.5}$ according to eq.(1.46)]. At low temperatures, R_{med} can be calculated from eq.(2.22) with a correction taken from Table 20, on assuming that the values of s and $\frac{\Delta\nu_c}{P} = \alpha\left(\frac{T}{T_0}\right)^{-0.5}$ are as established for terrestrial temperatures. Considering that, at the effective level of formation of the lines in the terrestrial atmosphere (level corresponding to P = 0.5 atm), the temperature is 240 - 250°K, it is conceivable that this correction is only about 1%.

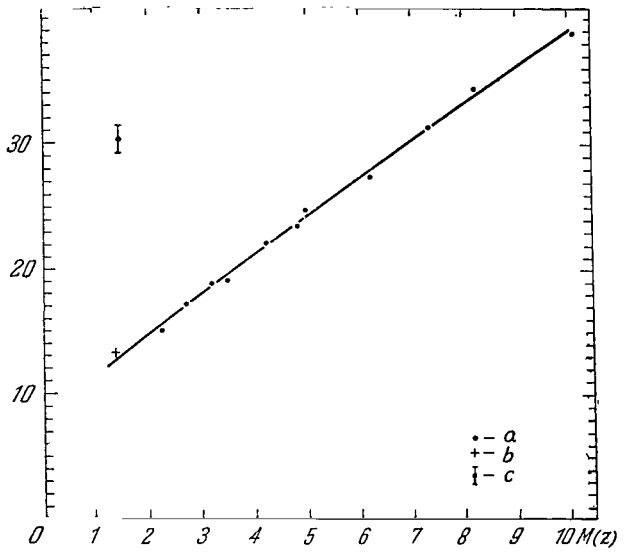

Fig.51 Equivalent Width of the Telluric Band λ 1.573 μ as a Function of Air Mass, according to Observations of (a) the Sun, (b) the Moon, (c) Mars. For observations of Mars the mean-square error is given (Crimean Observatory, April 6 1965).

Assuming that α = 0.07 cm^{-1}, s = 0.04 cm^{-1}, W_σ = 16 Å, we find with the aid of Elsasser's model [eqs.(1.56) and (1.58) when neglecting overlap or eq.(1.62) when taking overlap into account] that (uMP) = 1820 m • atm • mb for the λ 1.6 μ band, whence P_1 = 22 mb. Similar calculations for the 2.05 μ band yield P_1 = = 33 mb. The value of P_1 is calculated on the assumption that CO_2 is a minor constituent of the atmosphere and self-reversal broadening of the lines plays no role. In our opinion, the estimate P_1 = 22 mb (or, on the average, 20 mb) seems more reliable since the λ 2.05 μ band is overlapped by the neighboring CO_2

λ 2.01 μ band and it is precisely this that accounts for the higher value of P_1 calculated for the equivalent width λ 2.05 μ. Moreover, the correction for line overlap in the case of the λ 2.05 μ band is comparatively large (cf. Table 19) and the error of this correction also may influence the value of P_1.

Thus, if CO_2 is a minor constituent and the entire remaining atmosphere consists of nitrogen, then we have $P_1 = 20 \pm 5$ mb and the relative concentration is $c = \frac{28}{44} \cdot \frac{mg}{P_1} = 0.13$. Here, m is the mass of the vertical column of CO_2 (m = = 11 gm • cm^{-2}).

If an allowance is made for self-broadening, then P_1 must be higher. Moreover, the mean molecular weight of the atmosphere is actually greater than 28. Let us calculate P_1 and c taking self-broadening and the contribution of CO_2 to mean molecular weight into consideration. The correction for self-broadening will be taken as the mean of the data in Table 9 and the value calculated above [eq.(2.14)]:

$$\frac{\alpha_{CO_2-CO_2}}{\alpha_{CO_2-N_2}} = 1.5.$$

The mean weighted Lorentz half-width is

$$\alpha = c\alpha_{CO_2-CO_2} + \alpha_{CO_2-N_2}(1-c) = \alpha_{CO_2-N_2}(1 + 0.5c)$$

and

$$P_1' = P_1(1 + 0.5c),$$

where P_1' is the pressure calculated without taking self-broadening into account, and P_1 is the true pressure. The quantities

$$mP_1' = mP_1(1 + 0.5c) = b_1 \qquad (2.23)$$

and m are calculated from observations. On adding here the equation

$$c = \frac{P_{CO_2}}{P_1} = \frac{mg}{1000P_1}\frac{44c + 28(1-c)}{44} = \frac{mg(1 + 0.57c)}{1570P_1}, \qquad (2.23a)$$

we can determine c and P_1 separately. The combined solution of eqs.(2.23) and (2.23a) yields /117

$$c = b_2 - \sqrt{b_2^2 - 3.51}, \qquad (2.24)$$

where

$$b_2 = \frac{2760b_1}{m^2g} - 1.88$$

and

$$P_1 = \sqrt{\frac{b_1 g\,(1 + 0.57c)}{1570c\,(1 + 0.5c)}}. \qquad (2.24a)$$

This may be verified by means of the formula

$$m = \sqrt{\frac{1570 b_1 c}{g}\,\frac{1}{(1 + 0.5c)(1 + 0.57c)}}. \qquad (2.25)$$

Substituting b_1 = 220 gm • cm^{-2} mb and m = 11 gm • cm^{-2} into eqs.(2.24) and (2.24a), we have

$$c = 0.16, \quad P_1 = 18\ mb.$$

Thus the correction for self-broadening is insignificant, being only a fraction of the probable error in the determination of P_1.

It is not precluded (cf.Sect.2.3) that the Martian atmosphere might contain a large proportion of argon. Judging from the findings by Howard (Ref.32), it can be assumed that

$$\frac{\alpha_{CO_2\text{-}Ar}}{\alpha_{CO_2\text{-}N_2}} \approx 0.8, \qquad (2.26)$$

and the presence of argon will increase P_1 and reduce c. However, the increase in P_1 will be insignificant; even if the entire N_2 is replaced by Ar, it will not exceed a few millibars.

Owen and Kuiper (Ref.16), based on Kuiper's observations of the bands near λ 1.6 μ found P_1 = 17 ● 3 mb, when self-broadening is taken into account. The error here is given without considering the error in determining u_{CO_2}. Actually, this is of the order of 50%.

Kaplan, Münch and Spinrad (Ref.91) found P_1 = 25 ± 15 mb for the 2.05 μ band.

During the 1965 opposition, a number of American investigators carried out new observations of unsaturated CO_2 bands at 8600 and 10,470 Å. The 10,470 Å band was observed for the first time (Hanten). The estimated amount of CO_2 for this band, namely u_{CO_2} = 50 - 100 m • atm is in good agreement with eq.(2.5). Owen obtained u_{CO_2} = 55 ± 20 m • atm for the λ 8700 Å band. For the same band, Spinrad found u_{CO_2} = 80 m • atm from spectrograms obtained at Lick Observatory and u_{CO_2} = 84 m • atm from spectrograms obtained at McDonald Observatory. These findings were presented at the Pasadena Symposium on the Physics of the Moon /118 and Planets in Fall of 1965 and are cited from the report by A.D.Kuz'min who attended the Symposium.

Soon after its closest approach to Mars, "Mariner IV" passed behind the apparent limb of the Martian disk. The occultation of Mariner IV by Mars lasted

about one hour. During entry into occultation and exit from it, the phase changes in the radio signal from Mariner IV were recorded in detail in the hope of thus deducing any changes in the parameters of the ionosphere and troposphere. After allowing for numerous corrections, it was found that the total phase shift caused by the troposphere at the working wavelength λ 13 cm amounts to about 30 λ, and the phase shift caused by the ionosphere, to 10 λ (Fig.51a). The left minimum is due to the ionosphere, while the ascent of the curve at its right end is produced by the troposphere.

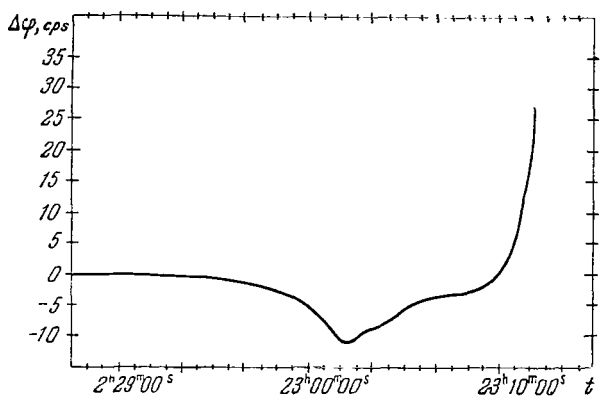

Fig.51a Variation in Phase of the Radio Signal of "Mariner IV" due to the Martian Atmosphere Prior to Occultation of the Spacecraft by the Planetary Disk (Ref.78a).

The findings during immersion and emersion differed widely. An essential factor was that immersion into occultation occurred on the day side of the planet whereas emersion from it occurred on the night side. On the curve of emersion the ionospheric minimum is absent and the tropospheric displacement is greater. The first of these phenomena is logical considering that the electron concentration decreases in the ionosphere at night, whereas the second phenomenon is not readily associated with the time of day. Below (Sect.2.7), we will demonstrate that no marked diurnal variations in pressure should take place in the atmosphere of Mars. Most likely, during immersion into occultation the beam accidentally passed over some local prominence of the alpine-plateau type.

TABLE 20a

/119

PRESSURE AND ALTITUDE SCALE IN THE MARTIAN ATMOSPHERE AS A RESULT OF OBSERVATION OF THE RADIO OCCULTATION OF "MARINER IV"

	Enter Occultation	Exit Occultation
Altitude scale at surface, km . .	9±1	12±1
Surface temperature °K		
100% CO_2	180±20	240±20
80% CO_2, 20% Ar	175±20	235±20
Surface pressure, mb		
100% CO_2	4.9±0.8	8.4±1.3
80% CO_2, 20%Ar	5.2±0.8	8.8±1.3

These measurements (Ref.78a) yielded certain parameters of the lower atmosphere (see Table 20).

The low altitude scale cannot be related to any appreciable relative concentration of nitrogen, for which reason CO_2 and Ar were assumed to be the major constituents of the atmosphere. The low total pressure would indicate a large relative concentration of CO_2 whereas, as pointed out above, purely spectroscopic data speak in favor of low relative concentrations of this gas. Table 20a indicates that the upper limit of pressure according to radio occultation overlaps the lower limit of pressure according to spectroscopic data; these limits correspond to approximately 10 mb.

What might be the reason for the fact that the overwhelming majority of older findings stipulated much higher values of total pressure? The old - photometric and colorimetric - methods are based on isolating, in some fashion or other, the brightness of the Martian atmosphere from the surface brightness and then ascribing, in toto or in a large measure, the brightness of the atmosphere to Rayleigh scattering. Photometric determinations reduce to representing the curves of limb darkening by theoretical formulas derived on the basis of a number of assumptions, namely that scattering in the atmosphere satisfies the Rayleigh law, that the surface scatters according to the Lambert law or according to some other specific law, and so on. However, the observed curves of limb darkening in themselves are not very reliable because of the effects of vibration, diffraction, aberrations, scattering of light in the emulsion, etc. The most detailed studies of this kind took into account multiple scattering and attempted to isolate the aerosol component (Ref.97, 98).

Some authors disregarded true absorption (Ref.100), while others attempted to estimate it from observations (Ref.82). The estimates by de Vaucouleurs /120 (Ref.101), based on the variation in visual contrast of the dark markings as a function of distance to the center of the disk, presuppose a dust-free atmosphere, and so do the polarization estimates (Ref.102). In the former method, aerosols are expected to enhance the observed effect and lead to an increase in the mass of the atmosphere, while in the latter method, conversely, they are expected to lead to a decrease in this mass (during dust storms, polarization decreases). Nevertheless, de Vaucouleurs and Dollfus, in applying this method, obtained nearly the same values (92 and 80 mb). Similar values were established with photometric methods by V.V.Sharonov [120 mb (Ref.103)] and N.N.Sytinskaya [46 - 86 mb (Ref.99)]. Based on the transmission coefficients calculated by N.P.Barabashev and I.F.Timoshenko (Ref.104) as well as by V.G.Fesenkov (Ref.97), de Vaucouleurs (Ref.5), with the use of photometric methods, established that $P = 114$ and 122 mb, respectively. Note that Lyot (Ref.105) who used the polarization method found a much lower value (24 mb) than Dollfus (Ref.102). N.P. Barabashev and B.Ye.Semeykin, in their 1934 study (Ref.106), also calculated from photometric observations a lower pressure (50 mb) than has subsequently been obtained with this method. It is interesting that these first findings apparently were closer to the truth than subsequent and more detailed studies. Specifically, there is the eminent study by Hess (Ref.107) who obtained a value of $P_1 = 80$ mb, on comparing the theoretical formulas for the altitude of formation of convection clouds, known from meteorology, with the observable altitudes of Martian clouds. However, this method, although inherently correct, is so susceptible to the variation in initial parameters that the results cannot be

seriously taken into consideration. Recently A.V.Morozhenko (Ref.107a) proposed an interesting modification for the polarization method of determining pressure, which permits a highly reliable exclusion of the surface effect. He found that the angle of inversion (the phase angle at which the polarization is reversed) in the polarization curves of Mars varies with the wavelength. The moon and terrestrial objects undergo no such variation. In the case of Mars, this change may be qualitatively and quantitatively attributed to the share of molecular scattering in the Martian atmosphere at $P_1 \approx 20$ mb. It should be noted, however, that this method is not free of the influence of aerosols (which, depending on the particle size, are capable of either reducing or increasing the polarization).

Of all optical methods in question, only spectroscopy permits determining the pressure without resorting to hypotheses on the law of light scattering in the atmosphere of Mars, the properties of its surface, the true absorption in the blue region of the spectrum, etc. Hence, when estimating the pressure, there is every reason for preferring spectroscopic findings as the most reliable, notwithstanding the scarcity of material. /121

TABLE 21

RELATIVE CONCENTRATION OF CO_2 AS A FUNCTION OF TOTAL PRESSURE

Total Pressure P_1, mb	5	10	20	30
Relative CO_2 concentration, %	100	50	13	6

Below, we will assume a pressure estimate of 20 ± 10 mb in some cases, since this book had been written prior to publication of the processing of the data on the radio occultation of Mariner IV. Currently, the most probable value seems to be 10 mb; 5 mb can be taken as the lower limit and 20 mb, as the upper.

Table 21 gives the relative volume concentrations of CO_2, calculated for four values of P_1: 5, 10, 20, and 30 mb. The concentrations and pressures were calculated with allowance for self-reversal broadening under the assumption that nitrogen is the principal constituent of the atmosphere.

Section 2.3 Chemical Composition of the Atmosphere

a) Possible content of nitrogen and argon. It is believed that carbon dioxide accounts for 5 - 50% of the Martian atmosphere. Most likely, the CO_2 content is less than 100%. There are no observational data on the other constituents of the atmosphere but the number of possible variants is limited since these must be relatively heavy and chemically inert gases.

This could be either N_2 or Ar. Argon-40, the principal isotope of argon which is present in the terrestrial atmosphere, is formed by β-decay of K^{40} in the earth's crust. The amount of Ar^{40} released from the crust into the atmosphere depends on the rate of soil erosion while the concentration of K^{40} in the crust near the surface is associated with differentiation processes in deeper strata. Unfortunately, neither nitrogen nor argon can be spectroscopically iden-

tified in the atmosphere of Mars, because their absorption bands lie in the far ultraviolet.

The total amount of Ar^{40} and N_2 is determined by the difference between the total pressure and the partial pressure of CO_2. Let us examine two hypotheses relative to the amount of argon: a) The amount of argon in the atmospheres of Earth and Mars is proportional to their surface area (in this case we have the same amount of argon per cm^2 of surface of Mars and Earth); b) the amount of argon is proportional to the mass. In the former case, we have P_{Ar} = 18 mb and in the latter, 2 mb. Table 22 gives the partial pressures of CO_2, Ar, and N_2 calculated for the hypotheses (a) and (b) (Ref.31). If the hypothesis (a) is valid, then argon rather than nitrogen is the principal constituent of the atmosphere. The relative concentrations of CO_2 given in Table 22 are somewhat lower than found above (Table 21).

/122

TABLE 22

PARTIAL PRESSURE OF MAJOR COMPONENTS OF THE MARTIAN ATMOSPHERE NEAR THE SURFACE ACCORDING TO KUZ'MIN (REF.31)

Pressure, mb		Lower Limit	Mean	Upper Limit
Total		10	20	30
CO_2		3	2	1.5
Ar^{40}	a)	7	18	19
	b)	2	2	2
N_2	a)	—	—	9.5
	b)	5	16	26.5

b) Oxygen and ozone. Carbon dioxide was discovered in the atmosphere of Mars from a direct comparison of the intensities of telluric and Martian absorption bands. In view of the relatively low resolving power available in the infrared spectrum region, accessible only to photovaristors, nothing further can be done in this direction. In the photographic infrared region (λ < 11,000 Å) the much more sensitive Doppler shift method can be used. This method is based on the premise that the absorption line formed in the Martian atmosphere must be displaced with respect to the telluric line. Consequently, given a large resolving power, the Martian lines can be detected even when they are hundreds of times less intense than the telluric lines of the same gas. This method has been applied in repeated attempts to detect electronic bands of O_2 in the red and near infrared regions of the Martian spectrum; however such bands were never found and it was possible only to estimate the upper limit of the O_2 content of the Martian atmosphere. The lowest value of this upper limit was found by Kaplan, Münch and Spinrad (Ref.91): $u_{O_2} < 70$ cm • atm, i.e., less than 5×10^{-4} of the O_2 content of the terrestrial atmosphere. Kozhevnikov et al. (Ref.108) attempted to raise the estimate of the upper limit of O_2 content in the Martian atmosphere by taking pressure into account, but this apparently stemmed from a misunderstanding since Martian lines are far from being saturated.

/123

An interesting possibility for an independent estimation of the upper limit of the O_2 content of the Martian atmospheres was pointed out by Petzold (Ref.109). The chain of reactions

$$(1) \qquad O_2 + h\nu \rightarrow O + O,$$
$$(2) \qquad O + O_2 + M \rightarrow O_3 + M,$$

$$O_3 + h\nu \rightarrow O + O_2, \quad (3)$$
$$O + O_3 \rightarrow O_2 + O_2, \quad (4)$$
$$O + O + M \rightarrow O_2 + M, \quad (5)$$
$$CO_2 + h\nu \rightarrow CO + O, \quad (6)$$
$$CO + O + M \rightarrow O_2 + M \quad (7)$$

should lead to the formation of ozone in the Martian atmosphere. Here, M is the third molecule entraining the excess energy and momentum. The first four reactions also govern ozone formation in the terrestrial atmosphere, while the last three reactions become significant when the O_2 concentration is small (< 0.001). Figure 52 shows the total amount of O_3 (reduced thickness, in cm • atm) as a function of the O_2 concentration in the atmosphere of Earth and Mars, as calculated by Petzold. Kuiper (Ref.4) estimated the upper limit of O_3 content in the Martian atmosphere at 0.005 cm • atm, meaning that the upper limit of the relative concentration of O_2 must be 10^{-4}. Assuming a total pressure in the Martian atmosphere of 100 mb, Petzold found the corresponding upper limit of O_2 content in absolute units

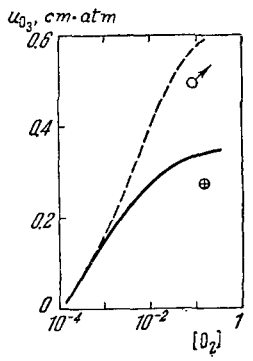

Fig.52 Total Amount of O_3 as a Function of Relative O_2 Concentration for the Atmospheres of Earth and Mars (Ref.109).

$$u_{O_2} < 300\, cm \cdot atm\,. \quad (2.27)$$

The decrease in pressure leads to a retardation in the rate of ozone formation, which will slightly augment the estimate of the upper limit u_{O_2}.

From the viewpoint of the existence of life, it is of extraordinary importance to know whether the Martian atmosphere absorbs ultraviolet radiation everywhere throughout the region $\lambda < 3000$ Å as is the case for the terrestrial atmosphere. In the region $\lambda < 1750$ Å, strong absorption of ultraviolet radiation by carbon dioxide takes /124 place (CO_2 dissociation limit). However, the processes within the 1750 - 3000 Å region are unknown. If the surface is not shielded from solar radiation in the given portion of the spectrum (in the terrestrial atmosphere such a shield is chiefly afforded by ozone), then all organic molecules on the Martian surface must be disintegrated by the ultraviolet, and it is doubtful that any form of life could withstand this. Early rocket observations by Dunkelman and Bogges (Ref.110) showed that the ultraviolet albedo of Mars in the neighborhood of 2700 Å is fairly high (0.24). In 1965, Evans (Ref.110a), as a result of observations, from a rocket carrying a grating spectrograph obtained the spectrum of Mars in the 2200 - 3400 Å region and found the albedo to be much smaller (the geometric albedo increases smoothly from approximately 0.04 near λ 3400 Å to 0.10 near λ 2200 Å) but without any perceptible traces of the ozone absorption band. Judging from these findings, the content of ozone and oxygen in the Martian atmosphere must be negligibly small. The upper limit of O_3 content is thus of the order of 10^{-3} cm • atm.

What could be the reason for the total or almost total absence of oxygen in the atmosphere of Mars? Three possible reasons exist: 1) The oxygen had dis-

sipated from the atmosphere; 2) the oxygen was absorbed due to oxidation of surface rocks; 3) the processes of formation of atmospheric oxygen proceed too slowly. Petzold (Ref.109) assumes that the first possibility holds, i.e., that of rapid dissipation of oxygen. However, a rather strong objection can be raised here. Above the level of CO_2 dissociation, the atmosphere of Mars must contain a large amount of atomic oxygen regardless of the concentration of molecular oxygen in the lower atmosphere. Were oxygen to dissipate rapidly, CO would accumulate in the planetary atmosphere. However, attempts to find the CO λ 2.35 μ absorption band proved unsuccessful (upper limit 1 cm • atm; see Table 22). It is obvious that the temperature of the upper atmosphere of Mars is sufficiently low, which would limit the rate of oxygen dissipation. Thus, this leaves the other two possibilities. If a small amount of oxygen exists in the lower atmosphere of Mars, then the ozone layer would directly adjoin the surface. This would accelerate the rate of oxidation reactions and reduce the equilibrium concentration of oxygen. In principle, a major source of oxygen may be the dissociation of H_2O (with subsequent dissipation of H), but the H_2O content of the Martian atmosphere is extremely small (see below). It is not impossible that the processes of oxygen formation in the Martian atmosphere have never been sufficiently rapid to raise the ozone layer above the surface. At /125 present it is virtually common consensus that the oxygen in the earth's atmosphere is of biogenic origin (Ref.4). The absence of oxygen means that terrestrial-type vegetation on any appreciable scale cannot exist on Mars.

c) Water vapor. The history of spectroscopic search for H_2O on Mars covers more than half a century. In 1908, Very (cf. Ref.5) compared the intensities of H_2O absorption bands in the spectra of Mars and Moon and found that the Martian absorption bands are more intense, which implied that the amounts of H_2O in the atmospheres of Mars and Earth are of a comparable magnitude. However, this was not corroborated by subsequent studies. Until recently, the findings have pointed increasingly toward a reduced value of the upper limit of H_2O content, in keeping with refinements in techniques and equipment. These studies were based on a method utilizing the Doppler shift. According to Dunham (Ref.111), the H_2O content of the Martian atmosphere does not exceed 0.0015 of the amount of H_2O in the terrestrial atmosphere in winter above Mount Wilson Observatory (i.e. 10 μ of precipitated water), but this estimate did not have a detailed analysis of spectrograms as basis and has been criticized repeatedly (Ref.112). In 1957, Kiess et al. (Ref.113) gave a more cautious estimate of the upper limit: about 8×10^{-3} gm • cm^{-2}. Spinrad and Richardson (Ref.114) analyzed the profiles of H_2O lines in the λ 7200 Å band on a spectrogram obtained in 1962 with a dispersion of 3.1 Å/mm, using the 122-cm reflector of Victoria Observatory. The spectrogram was obtained on an extremely dry night, but the Martian Doppler broadening was absent. With the aid of growth curves, an upper limit of $3.5 \times \times 10^{-3}$ gm • cm^{-2} or 35 μ of precipitated water was established. Spinrad and Richardson pointed out that the 8200 Å band would reduce the upper limit to 10 μ and the 11350 Å band, to 4 μ. In April 1963 Spinrad, Münch and Kaplan (Ref. 91, 92), with the 250-cm reflector of Mount Wilson Observatory, obtained a spectrogram of the H_2O λ 8200 Å band at a dispersion of 1.7 Å/mm, which indicated the presence of weak satellites of strong telluric lines of H_2O shifted in direction of longer wavelengths with respect to the main component (Fig.53). Measurements showed that the displacement is exactly equal to the Doppler shift. The H_2O content was estimated in a preliminary report (Ref.92), for 5 - 10 μ of precipitated water. Subsequent analyses yielded a somewhat higher value (Ref.91):

$$u_{H_2O} = (14 \pm 7)\,\mu \ . \qquad (2.28)$$

The discovery of water vapor in the atmosphere of Mars in 1963 was also reported by Dollfus (Ref.115), who found the mean H_2O content to be 2×10^{-2} gm/cm^2, i.e., 15 times as high as the estimate by Spinrad, Münch, and Kaplan. This finding seems dubious. Dollfus used the total intensity method. He observed the 1.38 μ absorption band with a special modulation photometer based on an interference-polarization filter. This device was calibrated so as to give direct readings in terms of the amount of H_2O along the line of sight. The observations were carried out on a dry and cold winter night at the Jungfrau Joch Alpine Observatory when the H_2O content of the terrestrial atmosphere did not exceed 10^{-2} gm · cm^{-2} vertical column. However, the very method of measuring the intensity of the H_2O band with the aid of a filter, at such small absorption, seems unreliable. Minor differences overlooked in the spectrum of Mars and Moon due to constant factors (e.g., the CO_2 bands on Mars) may produce a spurious signal. At such an amount of H_2O, the rotational lines of the λ 1.38 μ band must still be saturated and their equivalent width is determined by the product uP. Dollfus assumed that P = 85 mb. However, if we consider that the pressure is 4 - 5 times lower, Dollfus' estimate must be increased by a factor of 4 - 5, leading to 10^{-1} gm/cm^2. The estimate (2.28), obtained for unsaturated lines, seems more reliable.

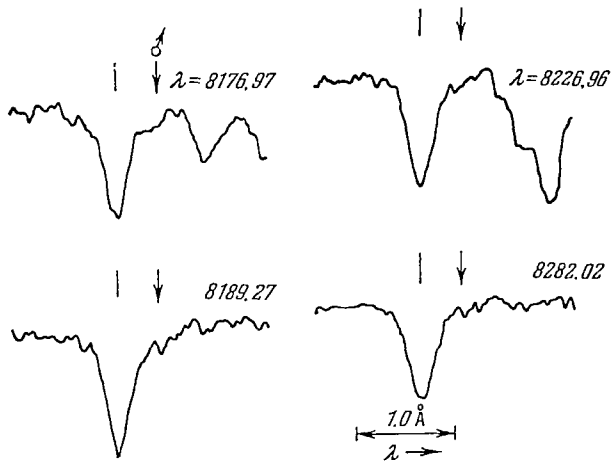

Fig.53 Four H_2O Lines with Weak Martian Satellite Lines, Shifted in Direction of Longer Wavelengths.

d) CO_2 isotopes and other gases. In addition to the bands of the main isotope $C^{12}O_2^{16}$ the spectrum of Mars, as mentioned previously (Sect.2.2, Table 17), also contains the bands $C^{13}O_2^{16}$ and $C^{12}O^{16}O^{18}$. An analysis of the relative isotope content is difficult because of the low intensity of these bands. Within the limits of errors of measurement (indeterminacy of 30 - 40% in the value of u) it may be assumed that the C^{12}/C^{13} and O^{16}/O^{18} ratios in the Martian atmosphere are the same as in the terrestrial atmosphere. Owen and Kuiper (Ref.16) assumed that the O^{16}/O^{18} ratio may be somewhat lower, but they do emphasize the tentative nature of this conclusion.

From the absence of the corresponding absorption bands, other authors (Ref.16, 94) estimated the upper limits of the content of molecules of CO, N_2O, NH_3, CH_4, C_2H_2, C_2H_4, C_2H_6, NO_2, HCHO, COS, $COCl_2$ in the Martian atmosphere. The maximum values of the reduced thickness are given in Table 22. These were ob-

tained on comparison with laboratory spectra or with absorption spectra of the terrestrial atmosphere. In addition to observations during the 1963 opposition, described elsewhere (Ref.94), spectra obtained by us in 1965 were utilized.

The laboratory spectra of CO_2, N_2O, and NH_3 described earlier (Ref.94) were recorded with the aid of a laboratory model of the diffraction spectrometer provided with a replica grating of 300 rulings/mm and an uncooled lead-sulfide photovaristor. The upper limits of the hydrocarbon content were found from tracing of the Martian spectrum in the region λλ 2.9 - 4.1 μ (Fig.54) obtained with a prism spectrometer on March 9, 1963. The upper limit of CH_4 content was determined from the absorption band λ 3.3 μ by comparison with the solar spectrum, while the estimates of the other hydrocarbons were based on the atlas of infrared absorption spectra (Ref.14). The study by Kuiper and Owen (Ref.16) was exclusively based on laboratory traces. Equivalent paths were multiplied by the coefficient 1/3 in order to make at least a rough allowance for the atmospheric mass. /129

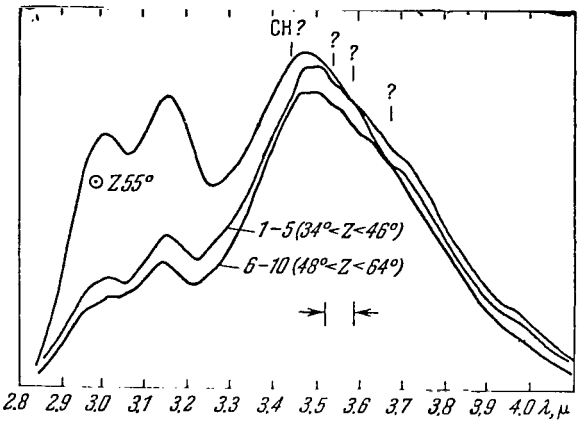

Fig.54 Spectrum of Mars λλ 2.8 - 4.1 μ, Obtained with a Prism Spectrometer with N_2-Cooled PbS Photovaristor. Two averaged traces (each averaged for five original traces), March 9, 1963; $34^\circ < z_\sigma < 64^\circ$, 2-mm Slits (Δλ 900 Å at 3.5 μ), rate 20 Å/sec, τ = 20 sec, $z_\odot = 55^\circ$.

e) Nitrogen oxides. Kiess, Corliss and Kiess (Ref.116) found a NO_2 band at 6200 Å on the spectrograms of Mars obtained with high dispersion, in the visible region. A study by Kiess, Karrer and Kiess (Ref.117) suggests that the Martian bands near λ 2 μ and in the region λ 3-4 μ may belong to NO_2. With respect to the bands near λ 2 μ, this hypothesis can be rejected at once, because of the sharp noncoincidence of the wavelengths. As for the 3.45 μ band (note that its existence is doubtful; cf. Sect.2.10), this can be identified with NO_2 but the amount of NO_2 here is no higher than 0.1 - 0.2 cm • atm. However, this suffices to create an appreciable absorption in the blue portion of the spectrum. The NO_2 molecule must polymerize and form N_2O_4 at sufficiently low temperatures

$$NO_2 \rightleftarrows N_2O_4.$$

Kiess, Karrer and Kiess (Ref.117) hold the properties of nitrogen oxides responsible for many effects observed on Mars. They regard the polar cap as a white precipitate of N_2O_4, and the color changes in the dark regions as the effects of chemical conversions of nitrogen oxides. Furthermore, they consider the yellow clouds to be clouds of NO_2 formed as a result of local surface heating. Sinton (Ref.118) and Huang (Ref.119) sharply objected to this interpreta-

TABLE 23

/128

CHEMICAL COMPOSITION OF THE ATMOSPHERE OF MARS

Molecule	u_{σ}, Content in Vertical Column, cm·atm (gm·cm^{-2} for H_2O)	Spectral Region μ	Laboratory Pressure, mm Hg	Reference	$u_{\oplus}$, Content in Vertical Column of Earth's Atmosphere, cm·atm
			Identified		
$C^{12}O_2^{16}$	5500	0.86	760	Kaplan et al. (31)	260
$C^{13}O_2^{16}$	55	2.11	*	Moroz, this book (1965 observations)	2.6
$C^{12}O^{16}O^{18}$		2.15	?		
H_2O	$1.4\cdot10^{-3}$	0.82		Kaplan et al. (31)	1
	10^{-2}	1.38	?	Dollfus (115)	
			Suspected		
N_2, Ar	40000				$6.4\cdot10^5$
			Spectroscopic Upper Limits		
NO_2	0.1	3.4		Moroz (94)	
O_2	70	0.76		Kaplan et al. (31)	$1.6\cdot10^5$
	2	2.35	760	Moroz, this book (1965 observation)	0.1
CO	1	2.35	760	Owen and Kuiper (16)	
	0.8	2.10	30	Owen and Kuiper (16)	0.4
N_2O	2	2.15	760	Moroz (94)	
	0.3	2.2 — 2.3	100	Owen and Kuiper (16)	—
NH_3	0.3	2.2 — 2.3	760	Moroz (94)	
	0.1	3.3		Moroz (94)	1.6
CH_4	0.1	2.25 — 2.3	*	Owen and Kuiper (16)	—
C_2H_2	0.03	2.9	59	Moroz (94)	—
C_2H_4	0.03	3.1	87	Moroz (94)	—
C_2H_6	0.02	3.2	50	Moroz (94)	—
H_2S	7.5	1.58	760	Owen and Kuiper (16)	—
NO	20	1.79	1000	Owen and Kuiper (16)	—
HCHO	0.3	2.27	760	Owen and Kuiper (16)	—
COS	0.2	2.44	760	Owen and Kuiper (16)	—

* Estimated from telluric lines.

tion. The spectrum and polarization of the polar caps are in good agreement with those of frozen water.

The presence of water vapor in the Martian atmosphere has been spectroscopically demonstrated, and the amount of H_2O thus determined is in satisfactory

agreement with the amount calculated from the equilibrium with the polar caps and with the nocturnal precipitation of hoarfrost. Had the polar cap consisted of solid N_2O_4, it would have been enclosed in dark conglomerates of absorbing gaseous nitrogen oxides, whereas actually the polar cap is the brightest feature of the Martian disk. The yellow clouds follow the polar caps in brightness and cannot represent accumulations of an absorbing gas. The dark bands or belts observed during the melting of the polar caps cannot consist of liquid nitrogen /130 dioxide, because the partial pressure of vapor above this liquid would be about 200 mb which is an order of magnitude greater than the total atmospheric pressure. Kiess, Karrer and Kiess (Ref.120) insisted on their hypothesis, referring chiefly to spectroscopic proofs of the presence of NO_2. Sagan (Ref.121) made detailed studies of available observations and concluded that the NO_2 content of the Martian atmosphere is less than 1 mm • atm. The spectrum by Kiess (Ref.116) apparently is associated with a temporary rise in the NO_2 content of the terrestrial atmosphere above the site of observation. In Sagan's opinion, the only Martian phenomenon that can be attributed to NO_2 is the blue haze (cf. Sect.2.6).

Section 2.4 Temperature of the Martian Surface

a) Effective temperature. The greater part of information on the surface temperature of Mars derives from measurements of the intensity of the characteristic radiation in the transparency window 8 - 14 μ. Recently, the brightness temperature has been measured on centimeter waves. The atmosphere of Mars - except for two relatively narrow intervals near λ 4.3 and λ 15 μ (CO_2 absorption bands) - should be transparent to the thermal radiation of the surface and apparently has practically no influence on the daytime temperature of the surface.

If we disregard the thermal conductivity of the soil and the atmospheric effect, the temperature at any point on the surface will be determined from the equation of instantaneous balance between absorption and emission. For the point above which the sun is at zenith (subsolar point), we have

$$\varepsilon\sigma T_s^4 = \sigma T_e^4 = \frac{E_0}{R^2}(1 - A_i). \qquad (2.29)$$

where the notation is the same as in eq.(1.35). Figure 55 gives the wavelength dependence of the quantity $\frac{\overline{B}_{\sigma\pi}}{E_\odot}$, obtained from observations by various authors ($\overline{B}_\sigma$ is the brightness at opposition, averaged over the disk). In the region λ < 0.9 μ, the absolute figures on the geometric albedo calculated by Woolley (Ref.122) and Harris (Ref.66) were utilized. In the region λλ 0.8 - 4 μ, only the curves of relative energy distribution (Ref.16, 94, 123) are available; however, since they adjoin the short-wave portion, the absolute scale can also be determined in this region. In the region λ < 2.5 μ, we have

$$\frac{\overline{B}_{\sigma\pi}}{E} = p$$

(here, p is the geometric albedo, $\overline{B}_\sigma$ is the mean brightness of the disk), but as soon as $\lambda > 3$ thermal radiation will become a definite factor. Woolley specified the farthest long-wave point at λ 6360 Å, in which $Q = 1.30$. For the infrared region, we will assume that

$$Q = Q\,(6360\text{Å}) = 1.30.$$

With the aid of the curve in Fig.55 eq.(1.116) yields

$$A_i = 0.26$$

which is nearly twice as high as the visual albedo. The same value (0.26 ± ± 0.02) was independently established by de Vaucouleurs (Ref.124). However, it should be noted that the curve of $p(\lambda)$ was plotted only tentatively and that the accepted hypothesis on Q in the infrared region may be far from reality.

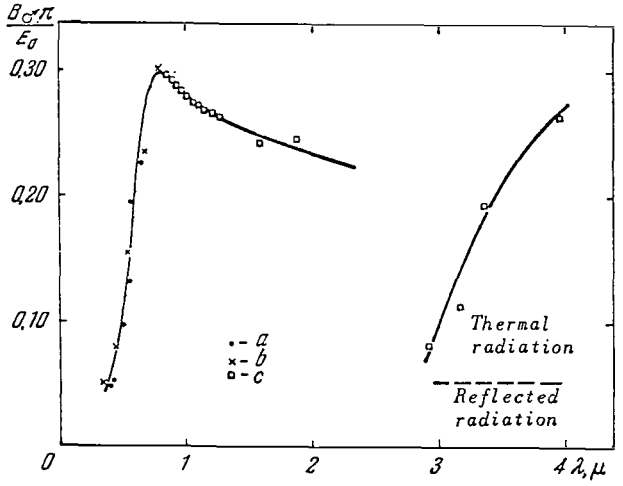

Fig.55 Intensity Ratio of Continuous Spectrum of Mars and Sun.
a - After Woolley (Ref.122); b - After Harris (Ref.66); c - This book. For reflected radiation, the curve shows the monochromatic albedo as a function of wavelength.

Table 24 gives the theoretical effective temperatures calculated from eq.(2.29) for the subsolar point, as well as the mean temperatures for the illuminated hemisphere and the average temperatures for the entire surface of the planet.

The circulation of the atmosphere and heat conduction from the soil must lead to a decrease in real temperature compared with the theoretical temperature, while the hothouse effect in the CO_2 band will lead to an increase.

b) Infrared brightness temperature. The brightness temperatures T_B of Mars were determined from the radiation in the 8 - 13 μ transparency window by Pettit and Nicholson (Ref.125), Coblentz and Lampland (Ref.126), and Sinton and Strong (Ref.26, 127). Table 25 gives the brightness temperatures of Mars according to Pettit and Nicholson. A comparison of Tables 24 and 25 shows that the measured temperatures of the subsolar point are about 10° lower than the theoretical temperatures. Note that all measurements of the brightness temperature pertain to the daytime hemisphere. The differences between T_B and T_e are within limits of the observational error. The intrinsic convergence of the observations by Pettit and Nicholson is fairly high (the discrepancy does not exceed 10°), but a comparison with the findings by other observers indicates that the absolute error may be higher.

TABLE 24

THEORETICAL TEMPERATURES OF MARS

	$\frac{E_0}{R^2}$, $\frac{erg}{cm^2 sec}$	T_e, °K		
		Subsolar Point	Illuminated Hemisphere	Planet-Average
Perihelion	$7.2 \cdot 10^5$	311	262	220
Aphelion	$4.9 \cdot 10^5$	283	239	194
Mean distance	$5.9 \cdot 10^5$	498	252	213

The brightness temperature T_B is below the real surface temperature T_s, since the emissivity is $\epsilon < 1$. Öpik (Ref.82) assumes that the emissivity of /133
the Martian surface is $\epsilon = 0.75$, based on data on the radiative properties of rocks. Of course, the real value of ϵ is unknown; however, to illustrate the possible effect of the corresponding correction, Table 25 also gives the temperatures T_s calculated from the premise that $\epsilon = 0.75$.

TABLE 25

TEMPERATURES OF MARS ACCORDING TO PETTIT AND NICHOLSON (REF.125)

	Subsolar Point		Limb	
	T_B, °K	T_s, °K ($\epsilon = 0.75$)	T_B, °K	T_s, °K ($\epsilon = 0.75$)
Perihelion	300	322	279	300
Aphelion	273	293	254	273
Mean distance	286	308	266	286

The observations by Pettit and Nicholson (Ref.125) as well as by Coblentz and Lampland (Ref.126) extended over many years, beginning with 1923 - 1924. Pettit and Nicholson worked with the 250-cm reflector at Mount Wilson Observatory, while Coblentz and Lampland worked with the 112-cm reflector at Lowell Observatory. Both teams used vacuum thermocouples as sensor. To distinguish between thermal and reflected radiation, the measurements were performed with a glass or water filter (which gave the intensity of only the reflected radiation) and without a filter (total radiation), after which one was deducted from the other.

Despite the similarity of the methods used, the results by Pettit (Ref.125) and Coblentz (Ref.126) are contradictory in some respects. The Lowell observations, in contrast to the Mount Wilson observations, show that the temperature /134

maximum does not coincide with the subsolar point and actually occurs 1 - 1½ hrs after midday (Fig.56a).

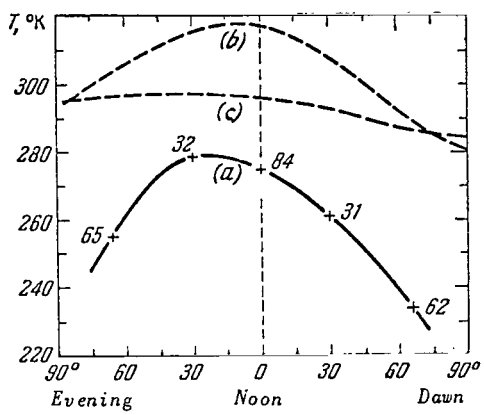

Fig.56 Mean Course of Temperature along the Martian Equator, Diurnal Temperature Course (a) (according to Observations by Coblentz and Lampland).
Next to each point, the number of averaged observations is given.
Curves b and c - diurnal temperature course in the Gobi desert, in the ground and in air 2 m above the ground surface (Ref.128).

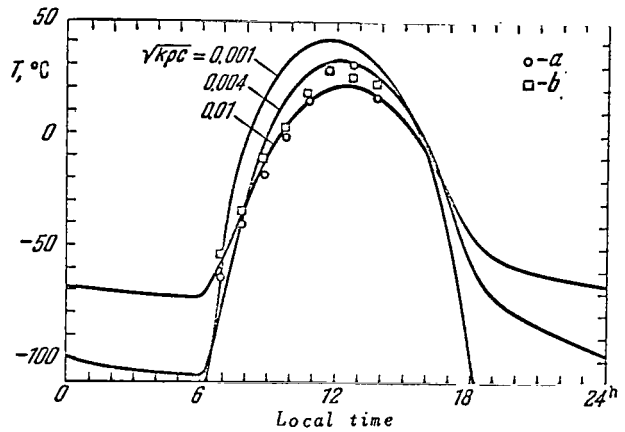

Fig.57 Theoretical and Observed Variations in the Temperature of the Bright Regions of Mars on the Equator.
a - Observations on July 20, No.8;
b - July 21, No.9 (cf. Fig.62).

Originally, it was assumed that the random effects associated with the position of the dark and light areas might be responsible for this displacement of the maximum in the diurnal temperature course. To verify this, Gifford (Ref.128) plotted the diurnal course for all these observations, whenever the longitude of the central meridian was within the limits from 100 to 300° (brighter side) and separately for all other cases (darker side). The results were the same. It was also shown that the dimensions and shape of the sensitive surface do not markedly distort the amplitude and phase of the diurnal curve.

It is interesting to note that the noon temperature of the atmosphere at a height of a few meters may be appreciably lower than at the surface. To illustrate this, Fig.56b and c gives the curves of the diurnal temperature course for the ground and for air 2 m above the surface of the Gobi Desert. At noon, this temperature difference may exceed 20°C. At the same time, a comparison of the curves (a) and (b) in Fig.56 shows that the diurnal temperature variation of the Martian surface in the equatorial zone is much broader than on Earth. During daylight, the variation in temperature exceeds 50° C; the nocturnal temperatures have not been measured. Some idea on nocturnal temperatures can be obtained /135 from the sequence of theoretical curves in Fig.57.

Figure 58 gives the mean temperatures along the meridian for various Martian seasons. The seasons pertain to the Southern Hemisphere. Spring is construed as the interval from the vernal equinox to the summer solstice, and so on. The winter curve is based on scanty and insufficiently precise data obtained during the unfavorable oppositions of 1935 and 1937 and does not seem reliable. The "sag" in the spring curve (latitude 16°S) also may be unreliable, in which case the real curve would correspond to the broken curve. Gifford considers this as real, stating that the majority of the spring observations corresponding to this point pertain to the bright Hellas area. Gifford assumes that the bright areas are colder since they represent elevated plateaus, but the difference in albedo also may account for the temperature difference of the order of 10°K between dark and bright areas. It could be that, by analogy with the diurnal course, there also exists an annual lag in temperature; however, for the summer season this lag seemingly does not exceed three weeks and its existence does not appear wholly evident.

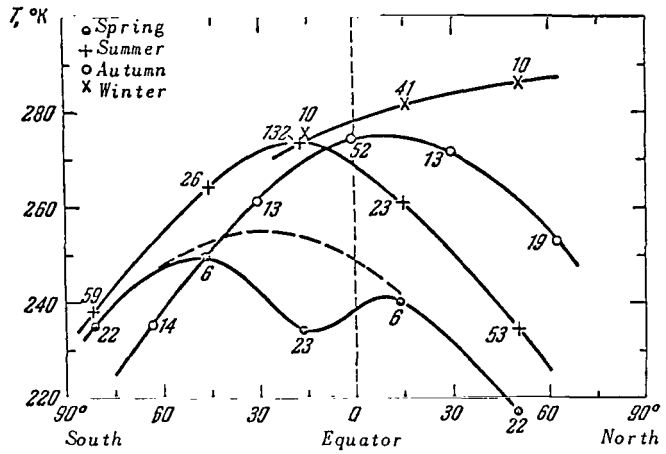

Fig.58 Mean Temperature Course along the Martian Noon Meridian for Various Seasons. Next to each point, the number of averaged observations is given [(Ref.128), after observations by Coblentz and Lampland].

/136

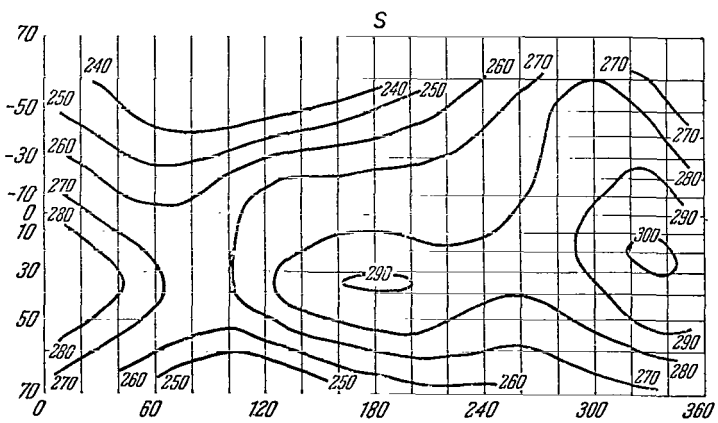

Fig.59 Mean Temperature Distribution on Mars during the Summer in the Southern Hemisphere (Ref.128); from Observations by Coblentz and Lampland.

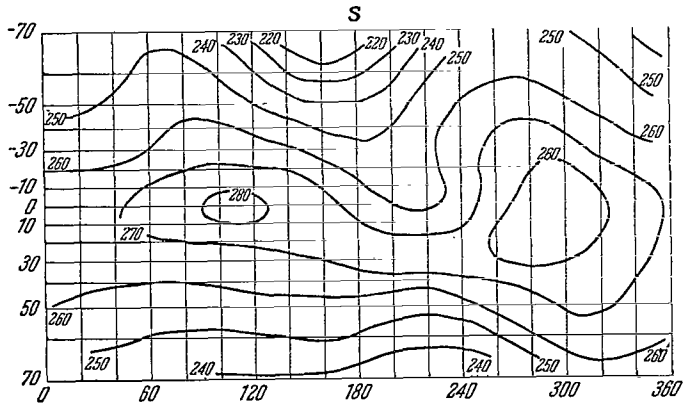

Fig.60 As in Fig.59, for Autumn in the Southern Hemisphere.

On the basis of early (1923 - 1926) observations by Coblentz and Lampland, Hess (Ref.107) plotted a chart of Martian isotherms for the summer season. Gifford repeated this operation on the basis of more voluminous data (1926 - 1943) for summer, autumn, and winter in the Southern Hemisphere; the data on the spring season proved to be insufficient. These charts are compiled according to sections along the central meridian. They show (Figs.59 - 61) a large number of details some of which can be identified with the better-known regions of Mars. /137

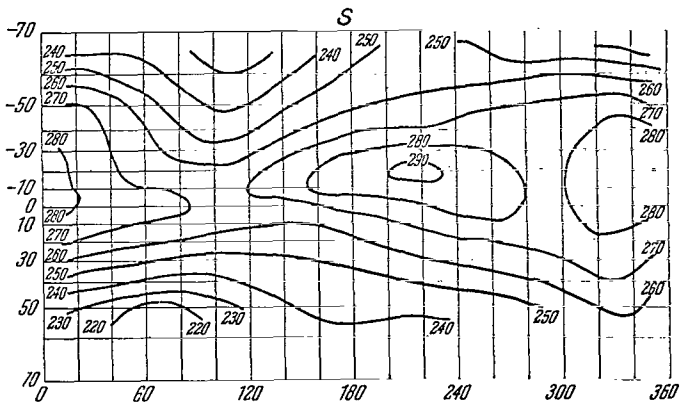

Fig.61 As in Fig.59, for Winter in the Southern Hemisphere.

For example, the 290° isotherm forms a characteristic ellipse on the summer chart in the neighborhood of Mare Cimmerium, while the 280° isotherm outlines the contour of Syrtis Major. On the autumn and winter charts, Mare Cimmerium shows as a relatively cold area, which apparently points to true seasonal temperature variations in this region. In a number of cases, the maxima on the isotherm charts are associated with atmospheric circulation rather than with the radiation

characteristics of the individual regions.

The summer temperatures (Fig.59) measured by Coblentz and Lampland pertain to the oppositions immediately following the favorable opposition (1926 and 1928), but the corresponding maximum temperatures are somewhat lower than those established by Pettit and Nicholson (cf. Table 25). Sinton (Ref.26, 127) used an apparatus he had developed in collaboration with Strong (an optico-acoustic converter and a silver-sulfide filter passing radiation of wavelengths $\lambda > 5\ \mu$) and

/138

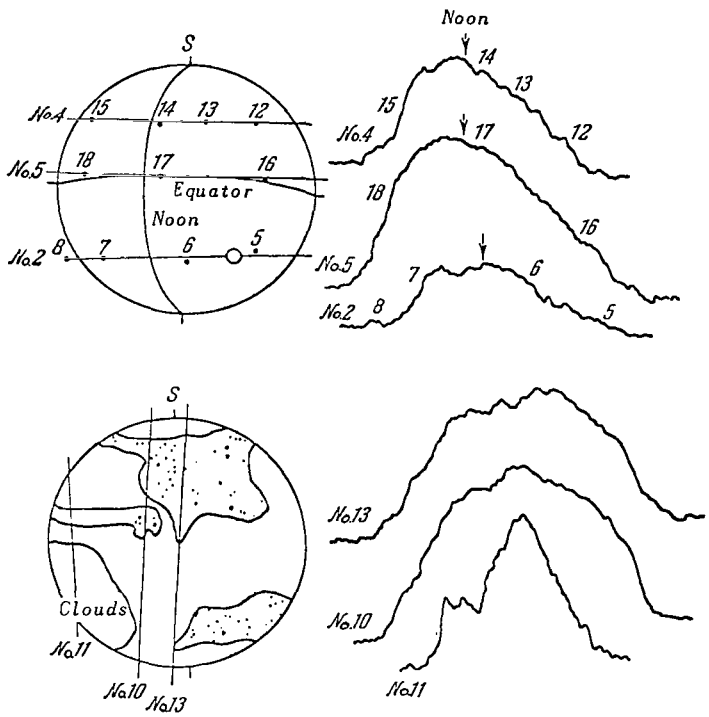

Fig.62 Brightness Distribution over the Martian Disk. Observations by Sinton and Strong on July 20, 1954 (Ref.26).

investigated, with the 250-cm reflector, the brightness distribution of thermal radiation over the Martian disk during the 1954 opposition (Fig.62). The observations were carried out with a resolution of 1.5″. The maximum temperatures found by Sinton are close to 300°K, i.e., are closer to the Pettit and Nicholson results. Sections 10 and 13 in Fig.62 intersect the dark region Sinus Meridiani where also some increase in brightness, corresponding to an 8° temperature rise, is observed. Of interest also are Sections 2 and 11 which intersect a yellow cloud and, in the corresponding area, indicate a decrease in brightness. According to these sections, the cloud temperature must be 25°C.

Sinton (Ref.127) compared his experimental curve of diurnal temperature vari-

ations with the theoretical curve calculated for a planet lacking an atmosphere, taking the thermal conductivity of the ground into consideration. The planetary surface is assumed as flat, semi-infinite, and homogeneous. Allowance is made for the equation of thermal conductivity

$$\frac{\partial T}{\partial t} = \frac{k}{\rho c}\frac{\partial^2 T}{\partial z^2},$$

where t is the time; z is a linear coordinate reckoned from the surface; k is the coefficient of heat conduction; ρ is the density; c is the specific heat. /139
The heat flux due to the thermal conductivity of the ground is

$$F = k\frac{dT}{dz}.$$

The following condition is satisfied on the surface

$$\sigma T^4 = I + F,$$

where σT^4 is the radiated energy; I is the energy received from the sun. It is assumed that

$$I = (1 - A)\,E\cos\frac{2\pi t}{P},$$

where P is the rotation period. For known values of P and A, the theory gives a series of curves T(f), dependent on $(k\rho c)^{1/2}$ which is the combination of surface properties known as thermal inertia (Fig.57). Figure 57 shows that the observational data agree best with the curve corresponding to $(k\rho c)^{1/2} = 0.004$ with respect to phase and with the curve corresponding to $(k\rho c)^{1/2} = 0.01$ with respect to amplitude. For terrestrial rocks, the thermal inertia is close to 0.05, while for sandy and dusty soils it is close to 0.01. It must be borne in mind that the atmosphere reduces the amplitude of diurnal temperature fluctuations and shifts the phase such that the value of thermal inertia $(k\rho c)^{1/2} \approx 0.004 - 0.01$ established for Mars becomes a maximum while, in reality, it should be lower. Hence, the Martian surface or at least its major portion is covered by finely pulverized material. Polarimetric and spectroscopic observations, pointing toward a similarity of the Martian surface characteristics with the characteristics of finely pulverized limonite (cf. Sect.2.9), do not contradict this conclusion. Coblentz assumed that, by analogy with the earth, SiO_2 is the principal constituent of Martian rocks and he even introduced into his measurements a correction for the decrease in emissivity in the region of the known band of specular reflection of quartz at λ 8.8 μ. On the spectra of Mars in the λλ 8 - 13 μ region, directly recorded by Sinton and Strong (Ref.26) with the aid of a 5-m reflector, this band was not detected (see Fig.48). In the emission spectrum of Mars such a band should be an absorption band. However, van Tassel and Salisbury (Ref.129) showed that, for quartz in a sufficiently finely divided state (particles a few microns in size), the λ 8.8 μ band virtually disappears. Coblentz' correction was superfluous, but the spectra given by Sinton and Strong cannot be regarded as a proof of the absence of SiO_2 in any amount from the surface of Mars. It is presently

possible to increase the accuracy of measurement of Martian temperatures by using cooled varistors and bolometers, as well as to obtain a spectrum with a higher resolution in the region λλ 8 - 13 μ, but so far this has not been done. /140

c) Radio emission of Mars. Radio emission of Mars was first discovered by Mayer, McCullough, and Sloanaker during the favorable 1956 opposition at λ 3.15 cm (Ref.130). The averaging of 70 discrete traces yielded a brightness temperature of T_B = 218 ± 50°K for the disk as a whole. In 1958, observations with greater sensitivity gave T_B 211 ± 20°K (Ref.131, 132). In 1962, Drake found T_B = 177 ± 17°K from radio emission at λ 10 cm (Ref.133). Thus, the brightness temperatures obtained in the centimeter range are lower than in the infrared region. It seems that, at the effective level of formation of centimeter radio waves which occurs at a depth of several λ, the diurnal temperature fluctuations are much smaller than at the surface and the radio temperature is closer to the mean temperature of the planet as a whole, whereas the infrared temperature pertains to the illuminated hemisphere. A similar situation exists with respect to radio emission of the moon.

TABLE 26

RADIO EMISSION OF MARS

λ, cm	T_B, °K	References
3.15	218 ± 50	Mayer et al. (Ref. 130)
3.14	211 ± 20	Giordmaine et al. (Ref. 131)
10	177 ± 17	Drake after (Ref. 133)
21	1124 ± 50	Davies (Ref. 134)
6	192 ± 28	Kellerman (Ref. 135)
11	162 ± 18	»
21	190 ± 41	»

At the 1964 Congress of the International Astronomical Union Davies (Ref.134) reported that the brightness temperature of Mars is much higher at λ 21 cm (T_B = = 1140 ± 50°K). He interpreted his observations, by analogy with Jupiter, as the effect of strong nonthermal radio emission of high-energy electrons captured in the radiation belts of Mars. However, further observations did not confirm this finding. Kellerman (Ref.135), at λ 6, 11, and 21 cm, obtained temperatures that were identical within the error limits (cf. Table 26) and were close to 200°K.

Section 2.5 Clouds and Winds; General Circulation /141

Figure 63 presents high-quality photographs of Mars obtained at a calm Martian atmosphere. The visibility of the dark markings often deteriorates owing to cloud formation. Several types of Martian clouds are distinguished depending on the color filter through which they can best be seen: yellow, white, and blue.

White and blue clouds are fairly similar in their conditions of formation and probably also in their physical properties, while the yellow clouds are markedly different.

De Vaucouleurs (Ref.5) called the white and blue cloud formations "clouds of type 1" and the yellow formations "clouds of type 2". Slipher (Ref.86) and Gifford (Ref.136) essentially adhered to the same classification, emphasizing

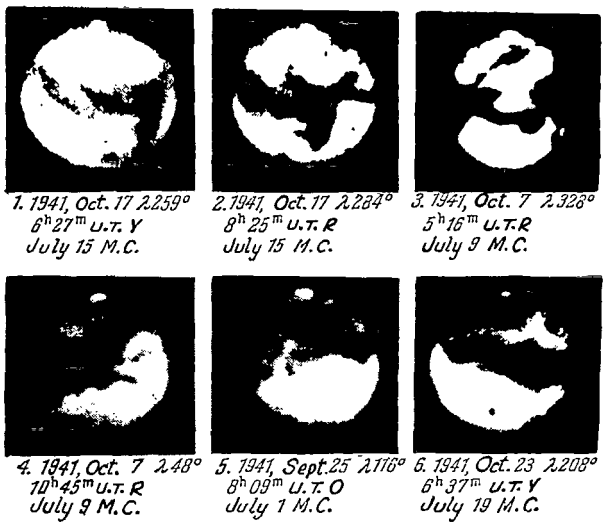

Fig.63 Photographs of Mars Obtained at a Calm Martian Atmosphere (Ref.86).

the similarity between white and blue clouds. All these types of clouds are brighter than the background against which they appear. Dark cloud formations are rarely encountered on Mars.

Yellow-orange clouds are observed throughout the disk, while whitish and bluish clouds normally are observed in the neighborhood of the limb and terminator; these might be called "limb" clouds, after Gifford. Extending to the terminator, the clouds jut out in tongues whose length can serve as a criterion for determining their altitude. The altitude of the /143 yellow clouds is 5 - 10 km and that of the blue and white clouds, 10 - 30 km going sometimes as high as 50 km. The relatively low altitude of the yellow clouds is in agreement with the altitude of the convection zone (cf. Sect.2.7).

TABLE 27

FREQUENCY OF OCCURRENCE OF MOVING MARTIAN CLOUDS AS A FUNCTION OF THE LATITUDE OF THEIR OBSERVATION (REF.136)

Latitude (North or South)	Yellow Clouds, %	"Limb" Clouds, %
60°	6	—
50 — 59	—	5
40 — 49	6	65
30 — 39	19	5
20 — 29	6	—
10 — 19	31	25
0 — 9	31	—
	(16 cases)	(20 cases)

White and blue clouds are most often observed on the morning side, but there exist some specific regions over which clouds of this type occur in the evening [groups of W-shaped clouds in the region of Tharsis in the neighborhood of Lacus Phoenicis (Ref.86); (Fig.64)]. The lifetime of the yellow clouds is long and their presence has nothing to do with any particular time of day. On measuring their displacement from night to night it is possible to estimate their mean rate of motion which is 8 - 10 m/sec (Ref.136), i.e., much slower than that of terrestrial clouds (30 m/sec). Occasionally, however, they travel at speeds that are several times as high.

A statistical analysis performed by Gifford (Ref.136) showed that yellow clouds occur most often in the equatorial regions. Blue clouds are chiefly located in the temperate latitudes (Table 27 and 28).

Similar analyses show that yellow clouds occur in regions of the highest temperature and blue clouds in relatively cold regions.

Clouds may form by two different processes: a) condensation of some gaseous

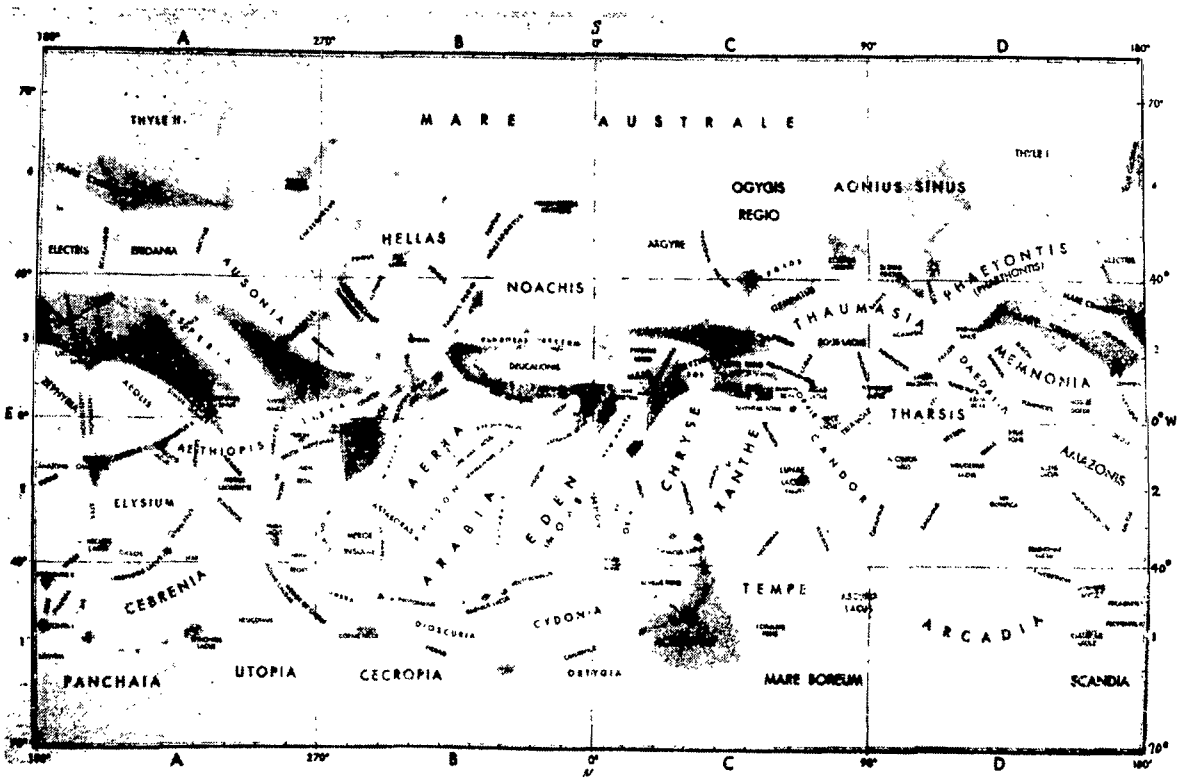

Fig.64 Chart of Mars according to Slipher (Ref.86).

TABLE 28

AS IN TABLE 27, FOR THE LATITUDE OF THEIR LAST OBSERVATION (REF.136)

Latitude (North or South)	Yellow Clouds, %	"Limb" Clouds, %
60°	6	5
50 — 59	—	5
40 — 49	12	50
30 — 39	25	10
20 — 29	31	10
10 — 19	19	15
0 — 9	6	5
	(16 cases)	(20 cases)

TABLE 29

FREQUENCY OF OCCURRENCE OF MOVING MARTIAN CLOUDS AS A FUNCTION OF MEAN SEASONAL TEMPERATURE AT THE FIRST OBSERVATION POINT (REF.136)

T, °K	Yellow Clouds, %	"Limb" Clouds, %
240—249	6	10
250—259	—	30
260—269	12	10
270—279	—	40
280—289	27	10
290—299	44	—
	(16 cases)	(20 cases)

/144

constituent of the atmosphere due to cooling; b) dust particles raised off the ground by turbulent motion. It is most likely that the "limb" clouds, both white and blue, are formed due to condensation caused by a temperature drop. This would fully account for their location, their relatively high altitudes, and their disappearance in daytime. The table of chemical composition of the Martian atmosphere (Table 23) implies that H_2O and CO_2 are the most logical materials for blue and white clouds. In Section 2.7 it will be shown that the condensation of H_2O is a more probable cause of the formation of "limb" clouds than CO_2. White clouds give roughly the same polarization as terrestrial fogs of ice particles, while the polarization of blue clouds resembles that of water droplets of a diameter of about 3 μ (Ref.102). The polarization curve (relation of degree of polarization to phase angle) of white clouds is given in Fig.65. It should be noted, however, that polarization observations in a single wavelength cannot be considered a definite proof since they do not admit of an unambiguous interpretation. /145

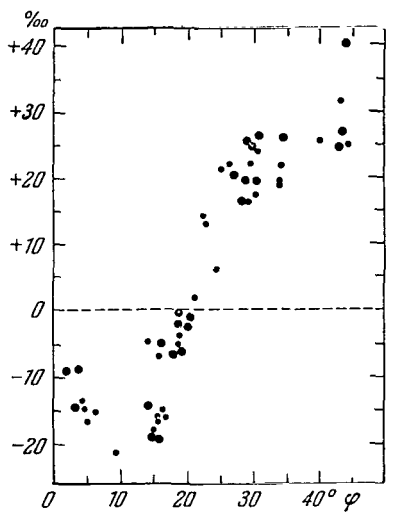

Fig.65 Polarization of Martian White Clouds and Haze in Equatorial and Temperate Zones (pro mille = ‰). The dimensions of the patches agree with the cloud nontransparency (Ref.102).

The polarization observed in white and blue clouds has the same sign as normal polarization at a given point on the disk. Figure 65 shows the excess polarization of the clouds compared with the polarization observed in their absence. This is of interest in view of the excessively high pressure values yielded by polarimetric and photometric methods. If the atmosphere contains some constant amount of an aerosol material analo-

gous to particles of blue and white clouds, this could result in an appreciable excess brightness and polarization.

/146

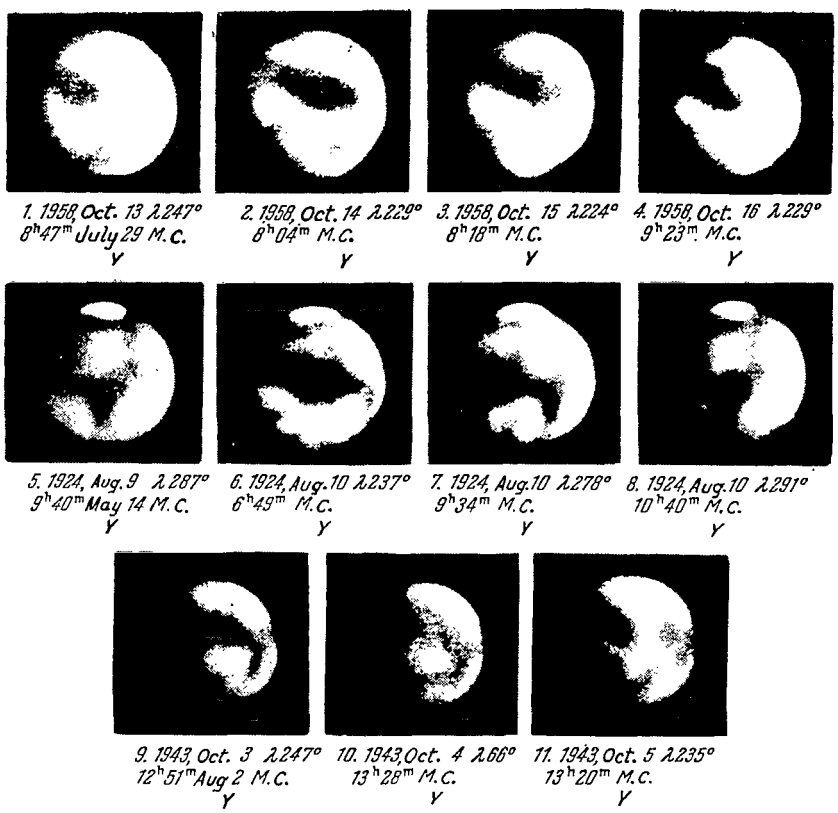

Fig.66 Growth of Yellow Cloud on Oct.13-16,1958 (Ref.86). 1 - Oct.13, cloud appears in the region of Isidis (northeast of Syrtis Major); 2 - Oct.14, cloud moves northward (regions of Toth-Nephentes, Libia); 3 - Oct.15, cloud spreads eastward; 4 - Oct.16, cloud enters the region of Hesperia (Ref.86). For comparison, photographs taken in 1924 and 1943 near the same longitudes of the central meridian are shown.

Yellow clouds readily occur in daytime and tend to appear in the warmest regions where the ascending currents must be stronger. Their altitudes are low. It seems that, unlike white and blue clouds, the yellow clouds are clouds of dust. They are generally observed as more or less isolated formations (Fig.66) but sometimes reach a global scale, encompassing nearly the entire planet. Global "dust storms" of this kind were observed during the favorable oppositions of 1922 and 1956 (Fig.67). The dust storm of 1956 commenced on August 24 with the appearance of a small bright cloud (Fig.67, Photo No.1, top left) and rapidly /148 - within a few days - spread over nearly the entire disk so that dark areas could be detected only at a few spots. In collaboration with A.V.Kharitonov (Ref.137) we made photoelectric measurements during the night of September 1-2 on the con-

trast between the yellow cloud then existing at Noachis and the neighboring continental regions (at that time, the cloud was still compact and very bright). The contrast was approximately 8% with a yellow filter (λ_e = 5450 Å) and 1% with a blue filter ($\lambda_e \approx$ ≈ 4495 Å). Normally, polarization sharply decreases during a dust storm.

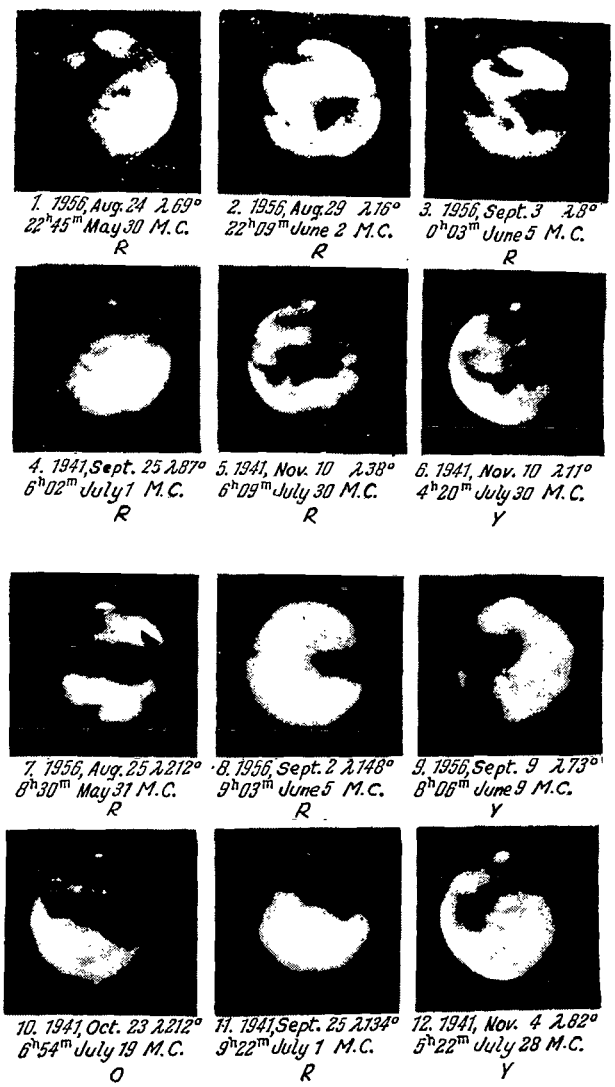

Fig.67 Growth of the 1956 Dust Storm. (For comparison, photographs taken in 1941 near the same longitudes of the central meridian are shown).

On the basis of aerodynamic considerations, Gifford (Ref.136) estimated the wind speeds required for raising dust particles off the surface of Mars and obtained a value close to that observed (about 10 m/sec). On earth, the comparable speed is 1 - 2 m/sec. The equatorial temperature sections (cf. Fig.57) and the spectral and polarization characteristics of the bright regions (Sect.2.9) indicate a finely pulverized structure of the Martian surface. Thus, the material necessary for the formation of dust clouds on Mars exists and the wind speed is sufficient for blowing this material off the surface. Both of these facts are important additional arguments in favor of the dust nature of the yellow clouds. However, not all observers are in agreement with Gifford's findings. The question of wind speeds and atmospheric pressure required for raising dust clouds from the Martian surface has also been discussed by Ryan [see (Ref.136a)] who found that at a pressure of 20 - 30 mb much higher wind speeds (50 - 100 m/sec) are needed, speeds that do not directly agree with the observations. However, it is not impossible that local temporary increases in wind speed might exist.

Examples of blue clouds observed in the neighborhood of the limb are presented in Fig.68. In some cases, these are comparable in brightness with the polar caps. They occur quite frequently near the limb, thus causing the brightness of the disk at the limb to increase in blue and violet light. Slipher also mentions a "limb glow" as a separate phenomenon which, however, most probably is associated with the clouds.

The shape and movement of such clouds constitute the sole observational source of information on the pattern of general circulation in the planetary atmosphere. The regime of general circulation depends on the amount of heat that must be transported by the atmospheric "heat engine" in unit time. Suppose that the average amount of heat per surface area in unit time at a latitude φ is $S(1 - A)$ where S is the time-averaged illumination and A the albedo, and suppose furthermore that the amount of heat radiated is $W = W_s + W_o$ where W_s is the surface radiation and W_o the radiation of the atmosphere (in CO_2 bands). The quantity $S(1 - A)$ is known as the mean diurnal insolation. The difference $\Delta Q = S(1 - A) - W$ represents the amount of heat that must be transported by the atmosphere. Figure 69 shows the latitude dependence of the quantities $S(1 - A)$ and W on Mars during the winter solstice in the Northern Hemisphere (Ref.75). To compensate for the difference $S(1 - A) - W$, the atmosphere must transport 2×10^{19} cal/day from the summer to the winter hemisphere. In the winter hemisphere, $\Delta Q_{45} = 1.36 \times 10^{19}$ /150 cal/day is transported across the latitude 45° and, in the summer hemisphere, $\Delta Q_{45} = -0.44 \times 10^{19}$ cal/day. After half a year, this pattern is reversed. If ΔQ exceeds some critical value ΔQ_{cr} then the symmetric regime becomes unstable and is superseded by a wave regime. As ΔQ increases further, the stability of the symmetric regime may be restored. Figure 70 shows the dependence of ΔQ_{cr} on the linear velocity of rotation of the planet $a\Omega$ (a being the radius of the planet) at the equator, calculated elsewhere (Ref.75). The symbol λ stands for the number of "loops" or waves in the circulation system (Fig.70); it is a function of ΔQ and $a\Omega$. As can be seen from Fig.70, the circulation of the Martian atmosphere in summer must have a symmetric regime while in winter it switches to a wave regime. In the neighborhood of the solstice, the regime may reverse with respect to the corresponding season. On earth the amount of heat transported by the atmospheric heat engine undergoes much smaller seasonal fluctuations and the circulation regime never changes (always being a wave regime). This difference is due to the fact that, on Earth, the average always decreases from the equator poleward, owing to the high specific heat of the oceans. On Mars the specific heat of the surface is low and the temperature continuously rises from the summer solstice to the winter solstice.

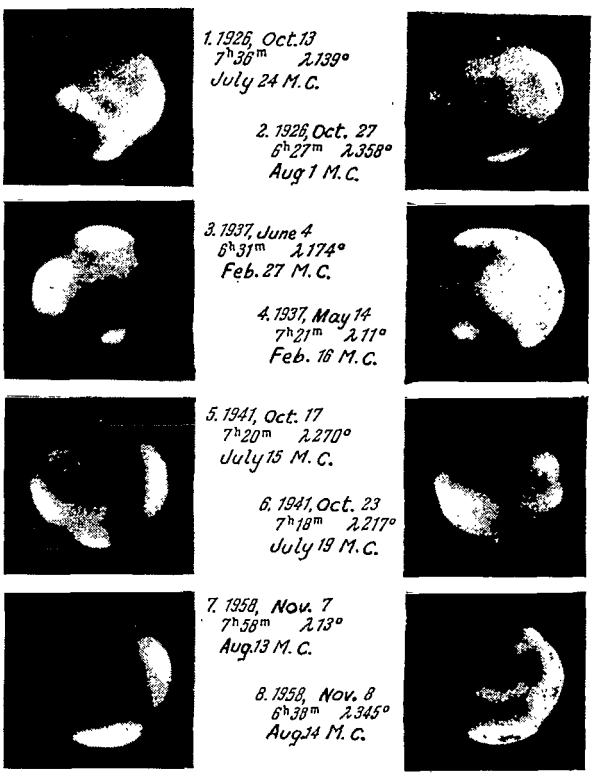

Fig.68 Photographs in Blue Light, Showing Blue Clouds and "Limb Glow" (Ref.86).

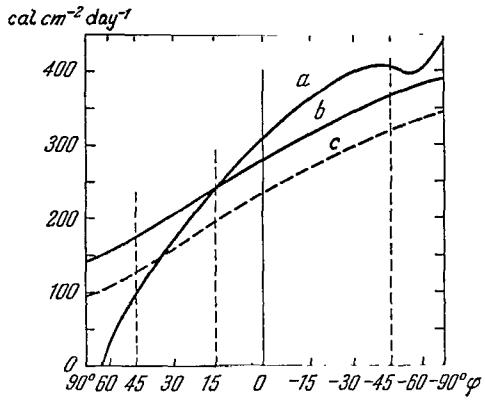

Fig.69 Radiation Balance of Mars during Winter Solstice in Northern Hemisphere. a - Effective insolation $S(1 - A)$ ($A = 0.26$); b - Sum of $W_s + W_0$ (W_s = radiation into space per unit surface in unit time, W_0 = radiation into space in CO_2 bands); c - W_s.

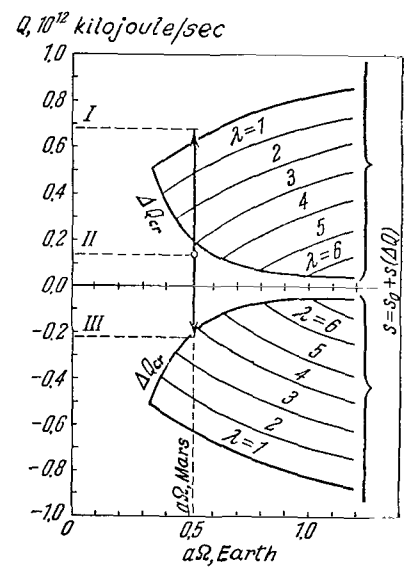

Fig.70 Circulation Regime of the Martian Atmosphere. ΔQ_{cr} and number of circulation "loops" as in (Ref.75). Here, $a\Omega$ (where Ω = angular velocity and a = radius) refer to the earth. I - Winter solstice; II - Early spring, late autumn; III - Summer solstice.

Miyamoto (Ref.138) noted that major dust storms on Mars may have to do with transition of the general circulation from the symmetric to the wave regime. During the symmetric regime it could be expected that the clouds will become elongated along parallels, forming cloud belts as on Jupiter. Slipher (Ref.86) actually observed such belts on photographs in blue light, but this is a very infrequent phenomenon. It is of interest that the published photographs, showing details of this type, were taken during the Martian spring when ΔQ is small and, according to the theory, a symmetric regime should actually be in force. Attempts to use the cloud movements as a criterion for the type of circulation were unsuccessful, but it must be borne in mind that the data on the movement of Martian clouds are very limited. Hess (Ref.107) analyzed 18 instances of cloud movement, chiefly for white and blue clouds, and Gifford (Ref.136) added 35 more instances, of which 16 pertain to yellow clouds. Thus, altogether only 53 cases of movement of Martian clouds have been studied, and it seems that both above observers utilized virtually all of the data available at present. On the basis of data on cloud movement and the observed temperature distribution, Hess plotted meteorological charts with isobars for various seasons, but the reliability of these charts is open to doubt.

/151

/152

Section 2.6 Transparency of the Martian Atmosphere; Blue Haze

The atmospheric pressure at the surface of Mars, according to spectroscopic data, is approximately 20 mb (cf. Sect.2.2). In this case, the number of molecules per vertical column of Martian atmosphere is

$$\frac{n_{\oplus} H_{\oplus}}{n_{\sigma} H_{\sigma}} = \frac{P_{\oplus} m_{\sigma} g_{\sigma}}{P_{\sigma} m_{\oplus} g_{\oplus}} \approx 20 \text{ times}$$

smaller than on earth. The molecular component of the optical thickness of the earth's atmosphere in scattering is $\tau_{0\oplus} = 0.08$ for λ 5600 Å (cf. Ref.184). Hence

for Mars, we have $\tau_{0\sigma} = 0.004$ on the same wavelength. The optical thickness at other wavelengths ($\tau \sim \lambda^{-4}$) is given in Table 30 for various values of the air mass M, based on the assumption of a total pressure of 20 mb which probably is somewhat exaggerated. In our calculations, we disregarded the excess scattering

TABLE 30

OPTICAL THICKNESS τ_s OF THE GASEOUS COMPONENT OF THE MARTIAN ATMOSPHERE IN SCATTERING

λ, Å	τ				τ_λ/τ_{5600}
	M=1	M=2	M=4	M=8	
9000	0.001	0.003	0.006	0.012	0.40
7600	0.002	0.004	0.008	0.016	0.51
5600	0.004	0.008	0.016	0.032	1.00
4500	0.006	0.012	0.025	0.050	1.55
3900	0.008	0.017	0.035	0.070	2.1
3550	0.010	0.020	0.040	0.080	2.5

power of CO_2. An examination of Table 30 reveals that, in the presence of molecular scattering alone, the transparency of the Martian atmosphere throughout the investigated range must be close to unity. It is well known, nevertheless, /153 that dark features are almost indistinguishable in the blue portion of the spectrum ($\lambda < 4500$ Å). The greatest contrast is observed on photographs made with red and infrared filters; in visible light, this contrast is smaller, while in blue light it normally is close to zero. The decrease in contrast is graphically illustrated by the curves of spectral reflectivity of the dark and bright areas

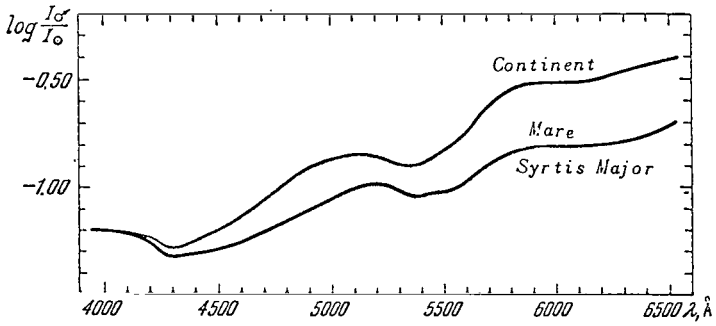

Fig.71 Apparent Reflectivity of the Continents and Seas as a Function of Wavelength (Ref.139). Ordinate: logarithm of the intensity ratios in an arbitrary continuous spectrum of Mars and Sun. The zero point was arbitrarily selected.

[Fig.71; after N.A.Kozyrev (Ref.139)]. This decrease, in contrast with the decrease in wavelength, either is a real property of the continents and seas or is ruled by the action of the atmosphere. The former assumption can be disproved since, during the so-called blue clearings, the contrast also becomes visible in blue light. A blue clearing lasts several hours and, at times, roughly a day, encompassing a considerable portion of the planet. Examples of photographs of Mars taken during blue clearings are presented in Fig.72. Most often a blue clearing is observed more or less at the time of a favorable opposition. The blue clearing phenomenon has been investigated photometrically by Pettit and Richardson (Ref.139a).

/154

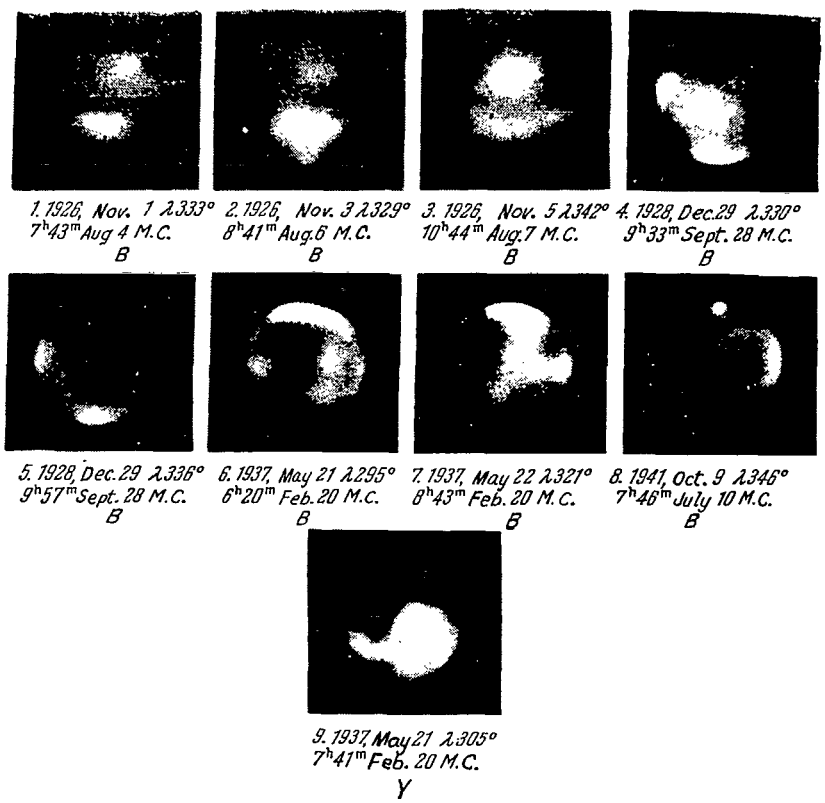

Fig.72 Photographs of Mars during Blue Clearings, Taken with Blue Filter (1-8); Photograph Taken with Yellow Filter (9); Ref.86.

It is obvious that Rayleigh scattering in a gaseous atmosphere could not account for the decrease in contrast with decrease in wavelength. Hence in the Martian atmosphere there should occur either true absorption by some unknown atmospheric gas or scattering (and perhaps also simultaneously absorption) on aerosol particles. In the earth's atmosphere, the real transmission coefficient is distinctly lower than the Rayleigh coefficient owing to scattering on aerosols. In the region $\lambda < 3500$ Å in the earth's atmosphere, true absorption (ozone) also commences to be a major factor. In the Martian atmosphere, there occur accumu-

lations of aerosols in the form of clouds. It is logical to expect that, in clear weather, the transparency of the Martian atmosphere, like that of the earth, is reduced by aerosols.

In the case of an optically thin atmosphere, the brightness of any point on the disk in opposition can be represented by the following formula [cf. for example (Ref.3)]:

$$B = \frac{E_0}{\pi}\left[\rho_s \mu q e^{-\frac{2\tau_0}{\mu}} + \frac{\varkappa(\cos\pi)}{8}\left(1 - e^{-\frac{2\tau_0}{\mu}}\right).\right] \qquad (2.30)$$

The first term in square brackets stands for the surface brightness coefficient and the second term, for the atmosphere brightness coefficient; ρ_s is the /155 brightness coefficient at the center of the disk in the absence of an atmosphere; μ is the cosine of the angle of incidence (during opposition, this equals the angle of reflection); $q \leq 1$ is the smoothness factor; τ_0 is the optical thickness of the atmosphere. For a smooth isotropically scattering surface (Lambert's law) we have $q = 1$, whereas for an uneven dissected surface we have $q < 1$, e.g., for the moon: $q = 0$. The factor $e^{-\frac{2\tau_0}{\mu}}$ describes atmospheric attenuation. The brightness of the atmosphere is derived from eq.(1.96) for $\mu_1 = \mu_2$, with $\varkappa(\cos\gamma)$ being the scattering indicatrix having the form (1.73) at $\gamma = \pi$. The magnitude of the second term increases with decreasing μ, while the magnitude of the first term decreases. The indicatrix $\varkappa(\cos\pi)$ equals a for isotropic scattering and $\frac{3a}{2}$ for Rayleigh scattering. Equation (2.30) correctly describes the brightness distribution for sufficiently small a and for any τ_0. If, on the other hand, $a \to 1$, the formula holds only for $\tau_0 \leq 0.1$. For large τ_0, an allowance must be made in this case for illumination of the surface by the atmosphere, multiple scattering in the atmosphere itself, and scattering - in the atmosphere - of the light reflected by the surface. A method of determining the optical parameters of the Martian atmosphere and surface, taking account of multiple scattering and anisotropy, is described in a paper by A.V.Morozhenko and E.G. Yanovitskiy (Ref.140).

On comparing the observed dependence $B(\mu)$ with eq.(2.30) or with a similar formula, it is possible to select the values of the parameters ρ_s, q, τ_0 such as to optimally represent the observations. The functions $B(\mu)$ were obtained by various observers using methods of visual, photographic, and recently also photoelectric photometry. Considerable photographic material was accumulated at Khar'kov Observatory during the 1956 opposition. Results of its analysis have been published in the form of a catalog [N.P.Barabashev and I.K.Koval' (Ref.141)]. Photographic observations permit a reliable tracing of $B(\mu)$ up to $\mu = 0.5$, which corresponds to 0.85 of the disk radius. Another author (Ref.142) made an attempt to determine the brightness distribution in the limb zone as far as 0.97 $r_\odot$ by the photoelectric method. The results are presented in Table 31.

The next to the last row in Table 31 gives the values of the geometric al-

TABLE 31

PHOTOELECTRIC OBSERVATIONS OF MARTIAN LIMB DARKENING
[1963 OPPOSITION (REF.142)]

r/r_{σ}	μ	$\frac{1}{\mu}$	λ, A									
			3550	3900	4200	4500	4750	5100	5600	6000	7600	9000
0.00	1.00	1.00	1.000	1.000	1.000	1.000	1.000	1.000	1.000	1.000	1.000	1.000
40	0.92	1.10	965	981	933	977	971	960	951	943	951	958
60	0.80	1.25	892	950	951	927	906	889	874	866	870	880
80	0.60	1.66	690	842	850	801	753	710	679	652	668	679
85	0.52	1.90	589	791	794	719	682	638	550	558	581	602
90	0.44	2.30	450	702	711	637	570	519	476	447	460	470
92	0.39	2.55	369	650	659	585	526	472	420	394	403	417
94	0.34	2.94	301	569	575	511	465	406	355	333	341	349
96	0.28	3.57	208	470	475	431	388	310	275	204	261	285
0.97	0.24	4.30	097	331	335	299	274	250	161	107	132	148
		p	0.052	0.058	0.065	0.080	0.090	0.115	0.150	0.200	0.305	0.320
		ρ_c	0.070	0.070	0.081	0.100	0.117	0.160	0.22	0.29	0.43	0.45

bedo p [interpolated from data by Harris (Ref.66) and Woolley (Ref.122) for the wavelengths specified in the table], while the last row gives the brightness coefficients at the center, calculated from these values and from the function of limb darkening specified in the table. The data of Table 31 are chiefly characteristic of the continents. According to Table 31, at λ 6000 Å Lambert's law /157 is roughly satisfied up to $r_\sigma = 0.94$ ($\mu = 0.34$). Photographic observations [cf. review in (Ref.143)] generally give the same results, although the scatter of the data is fairly wide. However, Koval' recently reported (Ref.143a) that a new analysis of the 1963 observations (presented in Table 31), making a more thorough allowance for the instrument profile, led to markedly lower values of the smoothness factor. For example, at λ 6000 Å, a smoothness factor of q = 0.5 was obtained. Apparently, the question of the smoothness factor needs further investigation. The method by which Koval' and his associates allowed for the instrument profile consists in that, parallel to sections of the planet, also the images of stars at zenith distances close to Mars are scanned. If the true intensity distribution over the Martian disk is $\Phi(x)$, then it is related to the observed distribution $F(x)$ by the integral equation

TABLE 32

BRIGHTNESS COEFFICIENTS ρ_s OF THE MARTIAN SURFACE (REF.144)

λ, Å	Continents	Maria	λ, Å	Continents	Maria
8400	0.410	0.312	5300	0.175	0.136
7500	0.330	0.203	4290	0.110	0.100
6470	0.254	0.180	3600	0.062	0.060

$$F(t) = \int_{-\infty}^{+\infty} G(t-x)\,\Phi(x)\,dx,$$

where $G(t - x)$ is the instrument profile which is determined from observations of the stars. This depends on the dimensions of the diaphragm and on the brightness distribution over the spurious disk. If the functions G and F are determined with sufficient accuracy from observations then, on solving the integral equation, $\Phi(x)$ can be calculated. This method is widely employed in radio astronomy and spectroscopy. It is conceivable that its use will also be of advantage in the photometry of planetary disks.

From the material of the Khar'kov photographic observations made during 1956, on assuming conservative scattering, N.P.Barabashev and I.K.Koval' (Ref.144) found a brightness coefficient ρ_s and the values of τ_0 given in Tables 32 and 33, which also present the values of vertical thickness of the Martian atmosphere from observations by these authors and the values of pressure from their calculations. In so far as can be determined from the figures in Table 33, the /158 pressures were calculated from the formula

$$P_\sigma = P_\oplus \frac{\tau_\sigma}{\tau_\oplus} \frac{(mg)_\sigma}{(mg)_\oplus},$$

which applies only if the optical thickness is conditioned by molecular scattering.

The optical thickness values given in Table 33 are about one order of magnitude higher than the molecular (Table 30) but are still too low to account for the decrease in the contrast of the seas and continents in the blue region of the spectrum. Similar findings have also been obtained by other observers who analyzed limb darkening on the assumption of conservative scattering (Ref.104, 145). De Vaucouleurs (Ref.5) even expressed the assumption that the above authors (Ref.104, 145) had made their observations during blue clearings, which apparently does not correspond to reality. These studies imply the logical conclusion that the observed energy distribution in the spectrum of Mars is governed by the true color of its surface, and that the contrast of the seas and continents in violet light is near-zero not per se but owing to the atmospheric effects [cf. for example (Ref.146)].

TABLE 33

OPTICAL THICKNESS OF THE MARTIAN ATMOSPHERE (REF.144)

λ, Å	$\tau_{\sigma'}$	$\tau_{\odot}$	$p_{\sigma'}$, mb
6470	0.014	0.16	34
5300	0.040	0.26	57
4290	0.062	0.42	57

An alternative hypothesis was offered by N.A.Kozyrev (Ref.139). He believes that the decrease in the Martian albedo as well as in the contrast of the seas and continents in proportion to the wavelength is due to true absorption. One of his arguments was that the spectrum of the seas and continents (cf. Fig.71) contains repetitive details. Since these details are common to both seas and continents, they must pertain to the atmosphere. However, observations at the Main Astronomical Observatory of the Academy of Sciences UkrSSR (Kiev, Goloseyevskaya Observatory) did not confirm the presence of these features (Ref.143b). Öpik (Ref.82), analyzed the observations of limb darkening from the premise of a Rayleigh scattering indicatrix, $a < 1$ and $q = 0$. The results of his calculations are presented in Table 34. Equation (2.30) was used as the working formula.

Thus, proceeding from roughly similar initial data, different observers /159
arrived at diametrically opposite conclusions concerning the qualitative and quantitative characteristics of the extinction due to the Martian atmosphere. Öpik's model is not based on an a priori assumption of conservative scattering but on other dubious hypotheses ($q = 0$, which conflicts with observations, and a Rayleigh indicatrix). On the whole, it must be stated that the question of the transparency of the Martian atmosphere is far from being solved. It may be that N.A.Kozyrev is right, after all, in maintaining that Mars is red because it is surrounded by an atmosphere which absorbs in the blue portion of the spectrum.

In other studies (Ref.143, 146), attempts were made to substantiate the hypothesis of conservative scattering but these cannot be considered convincing. For example, Koval' (Ref.143) regards the fact that the observed function $B(\mu)$ becomes more shallow with decreasing λ as an argument in favor of $a = 1$. It is true that, for small τ and $a = 1$, as is readily seen from eq.(2.30), the limb-to-center brightness ratio increases with increasing τ, but this also occurs at small a and large τ, i.e., in the presence of considerable true absorption. This

effect is illustrated in Fig.36 for a semi-infinite atmosphere, for decreasing a. One of the arguments by Sharonov (Ref.146) is that the clouds on "blue" photographs always look brighter than the background. However, these clouds (which most probably are ice clouds) do not necessarily represent accumulations of the blue haze substance. Slipher (Ref.86) gave photographs of Mars in blue light, showing dark clouds. This is a fairly rare phenomenon, but apparently it is exactly in this case that we are dealing with the aforementioned accumulations.

TABLE 34

OPTICAL THICKNESS τ_σ, SINGLE-SCATTERING ALBEDO a, AND MEAN SURFACE BRIGHTNESS COEFFICIENTS ρ_s ACCORDING TO ÖPIK (REF.100)

λ, A	4050	4250	4600	5200	5430	5800	6400
τ	2.97	2.13	1.10	0.62	0.51	0.37	0.30
a	0.13	0.15	0.20	0.22	0.23	0.24	0.20
ρ_s	—	—	0.246	0.289	0.335	0.405	0.528

Wright (Ref.147) discovered that the diameter of Mars on violet photographs is about 100 km greater than on red photographs. For a long time, this effect /160 had been attributed to the presence of a high-altitude absorbing or scattering layer, but subsequently N.P.Barabashev (Ref.148) and V.V.Sharonov (Ref.149) showed that this difference in diameters is of instrument origin. It seems that the agent responsible for the blue haze is centered in the lower layers of the atmosphere; if true absorption occurs, this agent would have to be located below the bright blue clouds which exist at altitudes of 10 - 30 km. Hess (Ref.107), Kuiper (Ref.2), and Schatzman (Ref.150) attributed the blue haze to scattering on particles with a strong forward-elongated indicatrix. Hess assumed that these are CO_2 particles; Kuiper, that they are ice particles; and Schatzman, that they are water droplets. However, elongated indicatrices as such, without the participation of true absorption, cannot account for the low reflectivity in blue light. When τ is large, pure scattering is anyway bound to result in excessive brightness, and when τ is small there is no blurring of contrast (Ref.151). Öpik (Ref.151) believes that all properties of the blue haze, including high opacity, bright clouds above the haze, etc., can be explained by assuming a two-layer model where the lower layer accounts for true absorption and opacity while the upper layer accounts for scattering, limb brightening, and bright clouds.

Absorption in the blue-violet spectrum region may be produced by various molecules; in an atmosphere rich in carbon dioxides the most probable are C_3O_2, $(C_3O_2)_n$, C_2, C_3, ..., C_n, which may form as a result of the photochemical reactions:

$$2CO + CO_2 + h\nu \rightarrow C_3O_2 + 2O, \quad (2.31)$$

$$C_3O_2 + h\nu \rightarrow C_2 + CO_2 \ (\lambda < 3250 \text{ Å}). \quad (2.32)$$

Absorption by gaseous C_2 can hardly account for the blue haze. Of necessity, C_2 must give distinct absorption bands (e.g., Swan's bands at λ 4737 and 5129 Å). Rosen (Ref.152) suggests that the blue haze may be due to continuous absorption by carbon particles. Polymerization of C_2 may lead to the formation of large particles, but part of the C_2 will retain its molecular form and will give Swan's bands. Another possibility involved in the reaction (2.31), namely the presence of C_3O_2, has not been analyzed in detail, since this suboxide rapidly decomposes (Ref.1).

Small amounts of NO_2 (of the order of several mm • atm) produce sufficiently strong absorption in the blue spectrum region. This explanation, proposed by Kiess, Corliss and Kiess (Ref.116), appears to be the most plausible of all those currently in fashion. Sagan (Ref.121) made a quantitative analysis of this interpretation and concluded that an abundance of NO_2 of the order of 1 mm • atm ensures the necessary degree of absorption. As the temperature of the atmosphere falls below 220°K, the polymerization /161

$$NO_2 \rightarrow N_2O_4$$

must lead to a decrease in absorption near λ 4000 Å. Absorption of NO_2 decreases in the $\lambda < 3800$ Å region. Table 31 shows that, on transition from 3900 to 3550 Å, the curve of limb darkening becomes more convex, as was to be expected at the increase in the parameter $a = \frac{\sigma}{k + \sigma}$ (see Fig.36).

An original theory of the blue haze and blue clearing was proposed by Urey and Brewer (Ref.153): They assumed that the absorption is due to the ions CO_2^+, N_2^+ and CO^+, with the ionization being sustained by solar wind; due to the absence of a magnetic field, the protons of the solar wind would directly penetrate into the atmosphere. The blue clearings would then occur owing to random temporary diminutions of the flux. The correlation with the oppositions was attributed to shielding by the terrestrial magnetic field. However, Sagan (Ref.154) demonstrated that the production of the necessary number of ions requires a particle flux of 10^{11} cm^{-2} sec^{-1} with energies of more than 2 Mev. In reality, the energies of the particles of the solar wind are several orders smaller and the flux is $10^8 - 10^9$ cm^{-2} sec^{-1}. Lastly, to justify attributing the blue clearings to shielding effects, the intensity of the magnetic field in interplanetary space would have to be 10^{-8} gauss which is four orders of magnitude smaller than observed. Thus, the Urey-Brewer hypothesis cannot be seriously considered.

Hess (Ref.107) assumes that the blue clearings are due to a gravitational deposition of particles. However, a clearing of this kind sometimes takes several hours, and such an explanation would require excessively large particles (measuring several tens of microns). The correlation with favorable oppositions is not explained within the framework of this hypothesis.

Another possibility is that the absorbing (or scattering) agent disappears owing to a phase transition or a reversible chemical reaction caused by a change in temperature. The correlation with favorable oppositions fits such an explanation since these coincide with the transit of the planet across the perihelion, but this involves another difficulty: It is not clear why the temperature would all at once become equal to the temperature of the phase transition over a large

portion of the planet.

The polar cap (cf. Sect.2.8) is clearly visible on blue photographs throughout all seasons of the year. In the opinion of many observers, during the autumn-winter period the apparent polar cap consists of an accumulation of clouds, whereas in summer it actually is a snow cover overlying the surface. If the latter is correct, it would mean that the blue haze either is completely absent in the polar regions or at least that its opacity is greatly reduced in /162 these regions compared with the equatorial and temperate zones. At first glance it might seem that this confirms the hypothesis of phase transition, but in reality it involves a contradiction: In the polar regions outside the polar cap the temperature during summer would then have to be higher than in the temperate zone of the winter hemisphere (Fig.69).

Section 2.7 Vertical Structure of the Atmosphere

Repeated attempts have been made to construct a model of the atmosphere of Mars, i.e., to find the dependence of temperature, density, pressure, and chemical composition on altitude (Ref.107, 155-159). Hess (Ref.107) attempted to calculate the altitude of the convection zone in the Martian atmosphere by proceeding from an analogy with the terrestrial atmosphere. A.I.Lebedinskiy (Ref.155) showed that this calculation was based on a fallacious premise since, in the terrestrial atmosphere, a major role is played by the processes of the condensation and evaporation of H_2O whereas in the Martian atmosphere the amount of H_2O is small and cannot markedly influence the heat balance of the atmosphere.

A.I.Lebedinskiy (Ref.155) and Goody (Ref.156) calculated models of the Martian atmosphere, by solving the equations of radiative transfer in the CO_2 λ 15 μ band. These models fit only up to the dissociation level of CO_2. Chamberlain (Ref.157) and Shimizu (Ref.160) calculated the altitude of the CO_2 dissociation level and the altitude dependence of the concentration of CO_2 and of its dissociation products (CO, O, and O_2).

Chamberlain (Ref.157) and Öpik (Ref.82) considered the problem of the heat balance of the upper atmosphere of Mars. Above its dissociation level in the upper Martian atmosphere CO_2 is substituted by CO and O. The ionization of atomic oxygen by the ultraviolet radiation of the sun must heat the upper atmosphere of Mars just as it heats the terrestrial atmosphere. The earth's upper atmosphere is cooled by the downward transport of the absorbed energy due to heat conduction, and its temperature is determined by the balance between the influx of ultraviolet radiation and the downcoming heat flux. Chamberlain and Öpik independently pointed out that, in the heat balance of the Martian upper atmosphere, a major role is played by one more process: radiation in molecular CO bands. In the earth's atmosphere this process is not essential in view of the small amount of CO_2. Bates' (Ref.161) study of the temperature of the earth's upper atmosphere proved highly important to theoretical calculations of the heat regime of the upper atmospheres of the planets. The work by Chamberlain (Ref.157) and Öpik (Ref.82) essentially represents an application of Bates' findings to the upper atmosphere of Mars.

Naturally, any model of the planetary atmosphere depends on certain initial

parameters: density, chemical composition near the surface, surface albedo. /163
Shilling (Ref.158, 159), bearing in mind the engineering needs of astronautics, calculated a series of models based on a sufficiently broad range of initial conditions. In particular, a pressure range from 40 to 200 mb was assumed. It would seem that such a range is sufficiently wide to encompass real initial conditions. However, it is obvious from the foregoing that the pressure determined by spectral method is at least twice as low as the lower limit assumed by Shilling.

Below we will construct three models of Mars: maximum, median, and minimum, proceeding from the following initial conditions (Table 35).

TABLE 35

INITIAL DATA FOR CONSTRUCTING MODELS OF THE MARTIAN ATMOSPHERE

	Maximum Model	Median Model	Minimum Model
Pressure at surface, mb	20	10	5
Chemical composition . .	10% CO_2, 90% N_2	50% CO_2, 25% N_2, 25% Ar	100% CO_2
Effective surface temperature, °K	270	250	225
Mean molecular weight below the CO_2 dissociation level . . .	29.6	39	44
Mean molecular weight above the dissociation level	26	27	22
Temperature gradient above the dissociation level, °K/km	1	2	0

The initial conditions are so selected that the minimum and maximum models would give the minimum and maximum mass densities at any altitude.

Let us assume, by analogy with the earth, that total mixing in the Martian atmosphere occurs up to the level at which the total concentration is $n = 10^{12}$ cm^{-3}, i.e., approximately 10^6 times smaller than at the surface. Below this altitude, the barometric formula is applicable, which includes the mean molecular weight; the latter, however, may change with altitude owing to the /164
dissociation of CO_2. Furthermore, we will show that the dissociation level corresponds to the partial concentration $n(CO_2) \approx 10^{13}$ cm^{-3}. Below the dissociation altitude, we can assume m = const. Moreover, at the altitudes $z \ll R$ where R is the radius of the planet, the dependence g(z) can be disregarded. Hence, up to the CO_2 dissociation level, the vertical structure of the atmosphere depends only on the temperature distribution T(z) with altitude. If we have the function T(z), then the dependence of the density of the atmosphere on altitude can be calculated from eq.(1.118).

a) Lower atmosphere and mesosphere. The altitude dependence of temperature is determined by the heat regime of the atmosphere. The lower atmosphere is chiefly warmed by the thermal radiation of the surface. Heat transport takes place by radiation and convection. Heat conduction in the lower atmosphere can be completely disregarded. In fact, the transport of heat flux due to heat conduction is

$$q = c\frac{dT}{dz}\ erg\cdot cm^{-2}\,sec^{-1}, \tag{2.33}$$

where c is the coefficient of heat conduction

$$c = 180\sqrt{T}\ erg\cdot cm^{-1}\ deg^{-1}sec^{-1} \tag{2.34}$$

for N_2 (Ref.162). If T = 250°K and the gradient equals the adiabatic gradient $\frac{dT}{dz} = 4°K/cm$, then q = 0.1 erg • cm^{-2} sec^{-1}. In this connection, the Martian atmosphere absorbs ~3 × 10^4 erg • cm^{-2} sec^{-1} in the CO_2 λ 15 μ band in daytime.

Consequently radiative transport must play a highly essential role. If radiative transport leads to a gradient that exceeds the adiabatic gradient in absolute value

$$\left|\frac{dT}{dz}\right|_{rad} > \left|\frac{dT}{dz}\right|_{ad}, \tag{2.34a}$$

then a convection zone will develop in the atmosphere. The convection will maintain the gradient very close to the adiabatic wherever the condition (2.34a) is satisfied. Since $\left|\frac{dT}{dz}\right|_{rad}$ in the real conditions of the lower atmosphere decreases with z in absolute value, the convection zone will extend as far as some limiting altitude z_a. Below z_a, the gradient $\frac{dT}{dz}$ is adiabatic whereas above z_a it is determined by radiative transport. The convection zone near the surface is usually called the troposphere and the region near z_a the tropopause. Let us estimate the adiabatic gradient for the atmosphere of Mars /165

$$\frac{dT}{dz} = -\frac{g}{c_p}, \tag{2.35}$$

where g is the acceleration due to gravity, and c_p is the specific heat at constant pressure. At the surface of Mars, g = 360 cm • sec^{-2}, c_{p_1} = 1.03 × 10^7 erg • • gm^{-1} • deg^{-1} for N_2 at 20°C and 0.523 × 10^7 erg • gm^{-1} • deg^{-1} for Ar at 15°C (Ref.162). For CO_2, we have c_p = 0.9 × 10^7 in the same units of measurement. For the assumed three models (maximum, medium, and minimum), we have c_p = 1.0 ×

$\times 10^7$, 0.84×10^7 and 0.9×10^7 erg $\cdot$ gm^{-1} $\cdot$ deg^{-1} and, correspondingly, $\frac{dT}{dz} =$ $= -3.6$, 4.5, and 4.0 deg km^{-1}.

Let us then calculate the altitude distribution of temperature in the atmosphere of Mars, by initially assuming that only radiative transport takes place. From the condition

$$\left|\frac{dT}{dz}\right|_{\substack{rad \\ z=z_0}} = \left|\frac{dT}{dz}\right|_{ad} \tag{2.36}$$

we determine z_a. Among the radiation-absorbing constituents of the lower atmosphere of Mars, CO_2 incontestably plays the dominant role. H_2O in an amount of 14 μ of precipitated water at a pressure P = 20 mb absorbs too little energy compared with CO_2 and, being an infrared absorber, water vapor cannot play a substantial role in the Martian atmosphere. If the blue haze has to do with true absorption, then it must be considered in the heat balance of the atmosphere. Since no sufficiently definite data on the nature of the blue haze are available, we will disregard its effect on T(z), but it must be borne in mind that true absorption in the blue portion of the spectrum, if it occurs at all, might sharply alter the temperature profile of the lower atmosphere of Mars.

The CO_2 absorption spectrum consists of two extremely strong fundamental bands - ν_1 λ 4.3 and ν_2 λ 15 μ as well as of overtones and compound frequencies located within the range of 0.8 - 5 μ, and also "hot" bands scattered throughout the 1 - 17 μ range. The radiation of the planet surface in the 4.3 μ band region is of much lower intensity than in the 15 μ region. Hence, the contribution of the 4.3 μ band to integral absorption is much less than that of the 15 μ band. The energy of solar radiation absorbed by the overtones is by one order of magnitude lower than the energy of the planetary surface radiation in the 15 μ band. Thus, the question of temperature distribution can be solved by taking into account, to a first approximation, only the CO_2 λ 15 μ band.

The band ν_2 λ 15.0 μ ($01^10 - 00^00$) overlaps the "hot" bands $11^10 -$ /166
$- 02^20$ λ 13.5 μ, $10^00 - 01^10$ λ 13.9 μ, $02^00 - 01^10$ λ 16.2 μ, $03^10 - 02^20$ λ 16.7 μ. As a result, a gas layer of a thickness of (for example) 0.5 m $\cdot$ atm is opaque from 13 to 17 μ, even at a pressure of 10 mb. The frequency dependence of the generalized absorption coefficient for the CO_2 band system in the 13 - 17 μ range is shown in Fig.31; this can be used to calculate the total equivalent width of all the bands.

The transport of long-wave radiation in the atmosphere can be studied by various methods (Ref.61, 70, 71, 164). We will use here one of the simplified methods, namely the method of resolution into isothermal layers as previously employed by Mintz (Ref.165). We will divide the entire lower atmosphere (up to the CO_2 dissociation level) into 10 plane layers each of which contains the same amount of CO_2: 1.1 gm $\cdot$ cm^{-2} or 550 cm$\cdot$atm (Fig.73). We will assume each of these layers to be isothermal. The amount of energy radiated by the i-th layer depends on its temperature and pressure:

$$Q_i = Q_i(T, P),$$

and, in the presence of thermal equilibrium,

$$\left.\begin{aligned} -2Q_1 + Q_2 &= 0, && (1)\\ +Q_1 - 2Q_2 + Q_3 &= 0, && (2)\\ &\cdots\cdots\cdots\cdots\\ +Q_{i-1} - 2Q_i + Q_{i+1} &= 0, && (i)\\ &\cdots\cdots\cdots\cdots\\ +Q_9 - 2Q_{10} + Q_{g,\,CO_2} &= 0, && (10)\\ E(1-A) + Q_{10} - Q_g &= 0, && (11)\\ Q_1 + Q_{10} = Q_{g,\,CO_2} &= rQ_g. && (12) \end{aligned}\right\} \qquad (2.37)$$

where Q_g is the total surface radiation; Q_{g,CO_2} is the part of surface radiation absorbed by the atmosphere; E is the integral illumination of the surface; A is the integral albedo. Solving the system of equations (2.37) it is possible to find the unknowns $Q_1, \ldots, Q_{10}, Q_g, Q_{g,CO_2}$ if E and A are known. These quantities are given in the second column in Table 37. In the maximum model, the initial temperature is calculated as the mean equilibrium temperature of the day hemisphere. As the mean normal illumination of the day hemisphere, we assumed

TABLE 36

PRESSURE DEPENDENCE OF EQUIVALENT WIDTH OF THE λ 15 μ BAND

P, *mb*	20	5	1.25
W, cm^{-1}	122	108	93

$$E = \frac{\pi r^2 E_\odot}{2\pi r^2} = \frac{E_\odot}{2} \approx 3\times 10^{-2}\ \ w\cdot cm^{-2}, \qquad (2.38)$$

where $E_\odot$ is the solar constant adjusted to the mean distance between Mars and Sun. /167

The function Q(t) can be defined as

$$Q(T) = W(P, u, T)\, I_{15}(T), \qquad (2.39)$$

where W(P, u, T) is the equivalent width of the λ 15 μ band, calculated from the curve $^1\nu$ plotted in Fig.31; $I_{15}(T)$ is the monochromatic radiation intensity of a perfect black body at the temperature T. In the calculations, it was assumed that u = 1.1 gm • cm^{-2} (5.5 m • atm), P = 5 mb, and T = 290°K. From Table 36 it follows that W is weakly dependent on P. The temperature dependence of W also is found to be weak, despite the presence of "hot" bands, clearly owing to the low relative intensity of these bands. At a pressure of 1.25 mb, the value of W (300°K) is only 30% higher than that of W (150°K). Disregarding the temperature dependence of equivalent width, we assumed that W (5.5 m • atm) = const = = 108 cm^{-1}. The function Q(t) calculated for this value of W is given in Table 37.

Table 38 (third column) gives the temperatures T_i of isothermal layers found from Q with the aid of the function Q(T). Each layer in the maximum model (together with N_2) creates a pressure of 2 mb, so that the pressures P_i at the layer boundaries correspond to the values given in the fourth column. Knowing the altitude scale H_i for each layer (fifth column) it is now possible from eq.(2.20)

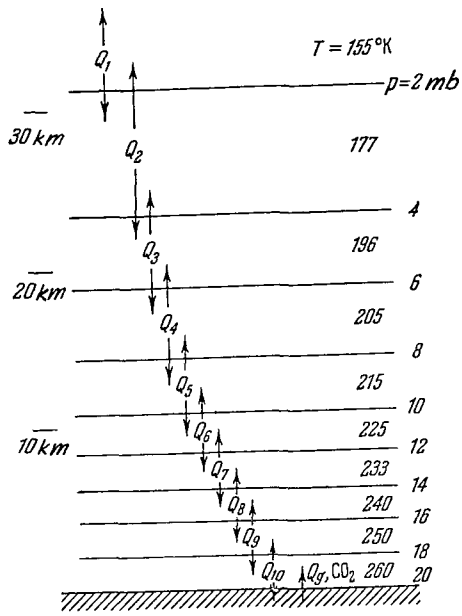

Fig.73 Calculating a Model of the Martian Atmosphere; Division into Plane-Parallel Layers.

TABLE 37 /168

FUNCTION Q(T) FOR THE CO_2 λ 15 μ BAND

T, °K	Q (T), $w \cdot cm^{-2}$	T, °K	Q (T), $w \cdot cm^{-2}$
100	8.5×10^{-6}	220	1.6×10^{-3}
120	4.2×10^{-5}	240	2.4×10^{-3}
140	1.4×10^{-4}	260	3.0×10^{-3}
160	3.4×10^{-4}	280	4.2×10^{-3}
180	6.3×10^{-4}	300	5.4×10^{-3}
200	1.0×10^{-3}		

to determine the altitude z_1 (sixth column) corresponding to each value of T_1.

When knowing Q_{g,CO_2}, it is possible to determine the brightness temperature of the surface. This temperature is adjusted for the hothouse effect of carbon dioxide. It is 15° higher than the temperature calculated without /169 taking CO_2 into account (cf. Table 24). The true surface temperature exceeds the brightness temperature, since the radiation coefficient $\epsilon < 1$ (cf. Tables 24 and 25).

Let us now find the limit toward which tends the temperature T as $\tau \to 0$. At the bottom of the first layer, T = 171°K and $\tau = 4$. Assuming a roughly gray atmosphere, we have

$$Q(T) = \frac{Q(T_e)}{2}\left(1 + \frac{3}{2}\tau\right), \quad (2.40)$$

where Q(T) is the flux of outgoing radiation, and τ is the optical thickness, whence

$$T \to 140° \text{K}.$$

This limiting temperature is reached at an altitude of approximately 60 km in a $N_2 - CO_2$ atmosphere and of 50 km in an $Ar - CO_2$ atmosphere. Figure 74

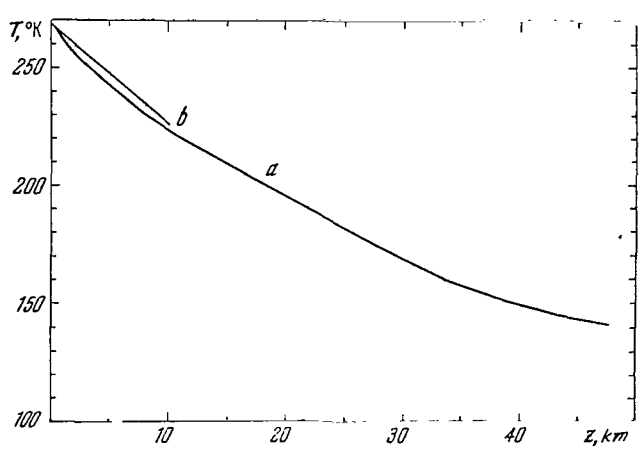

Fig.74 Temperature Distribution in the Lower Atmosphere of Mars (Maximum Model). a - Radiative equilibrium; b - Convective equilibrium.

presents the established patterns of T(z) in graphic form as well as the line corresponding to the adiabatic gradient $\frac{dT}{dz}$. It can be seen from Fig.74 that the condition (2.36) is satisfied for the maximum model at an altitude z_a = 7 km.

TABLE 38

CONSTRUCTING THE MAXIMUM MODEL OF THE LOWER ATMOSPHERE OF MARS

i	Q_i, $w \cdot cm^{-2}$	T_i, °K	P_i, mb	N_2—CO_2	
				H_i, km	z_i, km
			0		∞
1	3.1×10^{-4}	155		11.5	
			2		31.4
2	6.2×10^{-4}	177		13	
			4		23.4
3	9.3×10^{-4}	196		14	
			6		18.9
4	1.2×10^{-3}	205		15	
			8		14.5
5	1.6×10^{-3}	215		16	
			10		11.1
6	1.9×10^{-3}	225		17	
			12		8.2
7	2.2×10^{-3}	233		17.5	
			14		6.6
8	2.5×10^{-3}	240		18	
			16		4.2
9	2.8×10^{-3}	250		19	
			18		2.1
10	3.10×10^{-3}	260		19.5	
			20		0
g, CO_2	3.4×10^{-3}	267			

Thus, the convection zone in the Martian atmosphere is smaller than in the terrestrial. Apparently it develops more or less intensely at the noon hour, appearing in the morning and disappearing in the evening. /170 The presence of convective transport in daytime is of fundamental significance for the selection of initial temperatures in the model of the atmosphere. Owing to the presence of convection, the atmosphere is heated rapidly in daytime and its T(z) distribution then corresponds to the daytime conditions. At night there is no convection and the atmosphere is cooled only owing to radiation, and at altitudes of 10 - 15 km the night temperature differs little from the day temperature. Since the surface is about 100° colder at night than in daytime, a temperature inversion must occur at night in the surface layer. If there is no convective transport and if the temperature of the atmosphere is determined only by radiative transport, the initial temperature will be $\sqrt{2}$ times as small, since then the surface radiation is averaged over the entire sphere. This condition corresponds to an initial temperature of 225°K, assumed in the minimum model. In the medium model we assumed 250°K.

TABLE 39

ATMOSPHERE OF MARS; MEDIAN MODEL

Altitude, km	Temp., °K	Pressure, mb	Quantitative Concentration, cm^{-3}	Density, $gm \cdot cm^{-3}$	Local Altitude Scale for Pressure, km	Remarks
0	250	10	2.9×10^{17}	1.8×10^{-5}	13	Surface
5	225	6.5	2.0×10^{17}	1.2×10^{-5}	12.5	Tropopause
10	205	4	1.5×10^{17}	9×10^{-6}	11.5	
15	185	2.5	1.0×10^{17}	6×10^{-6}	11	
20	170	1.5	6×10^{16}	3.7×10^{-6}	9.5	
30	150	0.6	2.7×10^{16}	1.7×10^{-6}	9	
40	140	0.2	1.0×10^{16}	6.0×10^{-7}	8	
50	130	6×10^{-2}	3.5×10^{15}	2.2×10^{-7}	7.5	
60	120	1.6×10^{-2}	1.0×10^{15}	6.0×10^{-8}	7	
70	120	3.5×10^{-3}	2.0×10^{14}	1.2×10^{-8}	7	
80	120	8×10^{-4}	4.7×10^{13}	2.9×10^{-9}	7	
90	120	2×10^{-4}	1.2×10^{13}	8×10^{-10}	7	CO_2 dissociation
100	130	6×10^{-5}	4×10^{12}	3×10^{-10}	12.5	
110	140	2×10^{-5}	1.5×10^{12}	1×10^{-10}	14.5	
120	150	1×10^{-5}	6×10^{11}	4×10^{-11}	15	
130	160	6×10^{-6}	3×10^{11}	2×10^{-11}	16	
140	170	3.5×10^{-6}	1.5×10^{11}	1×10^{-11}	18.5	

TABLE 40

/171

ATMOSPHERE OF MARS; MAXIMUM MODEL

Altitude, km	Temp., °K	Pressure, mb	Quantitative Concentration, cm^{-3}	Density, $gm \cdot cm^{-3}$	Local Altitude Scale for Pressure, km	Remarks
0	270	20	5.4×10^{17}	2.7×10^{-5}	20	Surface
5	245	15.5	4.5×10^{17}	2.2×10^{-5}	18	Tropopause
10	230	11.4	3.6×10^{17}	1.8×10^{-5}	17	
15	215	8.7	2.9×10^{17}	1.4×10^{-5}	16	
20	200	6.2	2.2×10^{17}	1.1×10^{-5}	15	
30	175	3.0	1.2×10^{17}	6×10^{-6}	13	
40	155	1.3	6.3×10^{16}	3.2×10^{-6}	12	
50	140	0.5	2.7×10^{16}	1.4×10^{-6}	10	
60	130	0.2	1.0×10^{16}	5×10^{-7}	10	
70	130	7×10^{-2}	3.8×10^{15}	1.9×10^{-7}	10	
80	130	2×10^{-2}	1.4×10^{15}	7×10^{-8}	10	
90	120	10^{-2}	5×10^{14}	2.5×10^{-8}	9	
100	120	3×10^{-3}	2×10^{14}	1.1×10^{-8}	9	CO_2 dissociation
110	140	1×10^{-3}	7×10^{13}	4×10^{-9}	11	
120	160	6×10^{-4}	3×10^{13}	2×10^{-9}	13.5	
130	180	3×10^{-4}	1.2×10^{13}	6×10^{-10}	14	
140	200	1.5×10^{-4}	5×10^{12}	3×10^{-10}	16	
150	220	9×10^{-5}	3×10^{12}	1.5×10^{-10}	18	
160	240	5×10^{-5}	1.5×10^{12}	8×10^{-11}	20	
170	260	2.5×10^{-5}	7×10^{11}	4×10^{-11}	21	
180	280	1.2×10^{-5}	3×10^{11}	2×10^{-11}	22	

The following simple calculation proves that radiative cooling cannot appreciably affect the night temperature of the atmosphere. The specific heat of the atmosphere in the maximum model is taken as

$$\frac{5}{2} nhII = 2.5 \times 5.4 \times 10^{17} \times 1.38 \times 10^{-16} \times 2 \times 10^{6} = 3.72 \times 10^{8} \cdot \frac{erg}{deg \cdot cm^2}.$$

Approximately 10^{11} erg $\cdot$ cm^{-2} = 10^{4} w $\cdot$ cm^{-2} sec are stored in the atmosphere during the daytime. Since $Q \approx 3 \times 10^{-3}$ w $\cdot$ cm^{-2}, then over a time of 4×10^{4} sec (average duration of the night) the heat energy stored in the atmosphere during the daytime cannot diminish by more than 1%.

The low altitude of the convection zone also means that the daytime distribution of T(z), found from the condition of radiative equilibrium, is relatively undistorted by convection, and the true temperature distribution that takes into account both these effects can be obtained on displacing the curves of T(z) by several degrees, so that the "convective" and "radiative" curves of T(z) will merge at the point z_a. This method was used to set up Table 40 for the maximum model; the median (Table 39) and minimum (Table 41) models were constructed on the same principle.

TABLE 41 /172

ATMOSPHERE OF MARS; MINIMUM MODEL

Altitude, km	Temp., °K	Pressure, mb	Quantitative Concentration, cm^{-3}	Density, gm$\cdot$cm^{-3}	Local Altitude Scale for Pressure, km	Remarks
0	225	5	1.7×10^{17}	1.3×10^{-5}	11	Surface
5	200	2.7	1.1×10^{17}	8×10^{-6}	10	Tropopause
10	180	1.8	7×10^{16}	5.2×10^{-6}	9	
15	160	1.0	4.7×10^{16}	3.5×10^{-6}	8	
20	145	0.6	3.0×10^{16}	2.2×10^{-6}	7	
30	130	0.13	7×10^{15}	5.2×10^{-7}	7	
40	125	3.1×10^{-2}	1.6×10^{15}	1.2×10^{-7}	7	
50	120	7.5×10^{-3}	3.8×10^{14}	2.8×10^{-8}	6	
60	120	1.5×10^{-3}	7.5×10^{13}	5.5×10^{-9}	6	
70	120	3×10^{-4}	1.5×10^{13}	1.1×10^{-9}	6	CO_2 dissociation
80	120	5×10^{-5}	2.5×10^{12}	1.8×10^{-10}	6	
90	120	10^{-5}	5×10^{11}	4×10^{-11}	6	
100	120	2×10^{-6}	10^{11}	7×10^{-12}	6	

Hess (Ref.107) found a tropopause altitude of z_a = 40 km but proceeded from an incorrect analogy to the terrestrial atmosphere. A.I.Lebedinskiy calculated z_a = 2 km starting from the exact solution of the transport equation in the λ 15 μ band. Goody (Ref.156), using a similar method, found z_a = 8.5 km and T_∞ = 134°K (above z = 90 km). Lebedinskiy and Goody made use of the old estimates of CO_2 content and total pressure. It is easy to show that the increase in the amount of CO_2 has led to no appreciable change in T_∞ and in the altitude of the convection zone.

In calculating T(z) above the level of the tropopause, it is assumed that the atmosphere is in a state of local thermodynamic equilibrium and that radiation is transported solely owing to processes of true absorption and emission and furthermore that resonance scattering can be neglected. Goody (Ref.166) found that the vibrational relaxation level above which the processes of resonance scattering predominate over the processes of true absorption for the CO_2 λ 15 μ band exists at an altitude of approximately 75 km where the total concentration is $n \approx 10^{15}$ cm^{-3}. Above this level, the role of radiative transport in the heat regime of the mesosphere decreases sharply. Here the absorption of a quantum is followed by reradiation at the same frequency rather than by transmission of energy to another molecule as is the case in true absorption. Above the vibrational relaxation level the atmosphere is intensively cooled by radiation in the λ 15 μ band, whereas its heating is relatively weak.

According to Table 39 (Median Model), the level $n = 10^{15}$ cm^{-3} in the atmo- /173
sphere of Mars is at an altitude of z = 60 km. It is logical to assume that this altitude constitutes the vibrational relaxation level in the Martian atmosphere. The volumetric radiance above the vibrational relaxation level is (Ref.161)

$$R(z) = n^2 c \eta h\nu e^{-\frac{h\nu}{kT}}, \tag{2.41}$$

where c is the relative volume concentration of CO_2 (c = 0.1), and η is the deactivation coefficient ($\eta \approx 2.5 \times 10^{-15}$ cm^3 sec^{-1}).

At an altitude of 90 - 100 km, CO_2 is dissociated by the ultraviolet radiation of the sun:

$$CO_2 + h\nu \rightarrow CO + O, \quad \lambda < 1700\,\text{Å}. \tag{2.42}$$

This process is balanced by ternary recombination

$$CO + O + M \rightarrow CO_2 + M, \tag{2.43}$$

and, owing to the process

$$O + O + M \rightarrow O_2 + M \tag{2.44}$$

there forms a certain amount of molecular oxygen which retards the dissociation of CO_2, since it absorbs ultraviolet radiation

$$O_2 + h\nu \rightarrow O + O, \quad \lambda < 1750\,\text{Å}. \tag{2.45}$$

The rates of reaction (2.42) - (2.45) are known functions of the concentration and flux of ultraviolet radiation. This makes it possible to calculate the altitude dependence of the concentration of n(O), n(CO), $n(CO_2)$, and $n(O_2)$. The procedure is described in detail in Section 3.5; here, we will merely discuss the CO_2 dissociation altitudes, calculated in this manner for the atmosphere of Mars (cf. Tables 39-41).

The temperature at altitudes of 80 - 100 km can be found from the equilibrium condition

$$\int_{z_1}^{z_2} R(z)\,dz = \int_{z_1}^{z_2} B(z)\,dz, \qquad (2.46)$$

where B(z) is the energy of ultraviolet radiation absorbed between the levels z and z + dz. This condition yields T = 110 - 120°K. The photochemical equilibrium permits a correct determination of the dissociation level and of the density distribution of $n(CO_2)$, n(CO), n(O) and $n(O_2)$ below the dissociation level. However, the concentration of CO_2 and O_2 above the dissociation level may be much higher than calculated, because of the upward diffusion of CO_2 and O_2. Such a /174

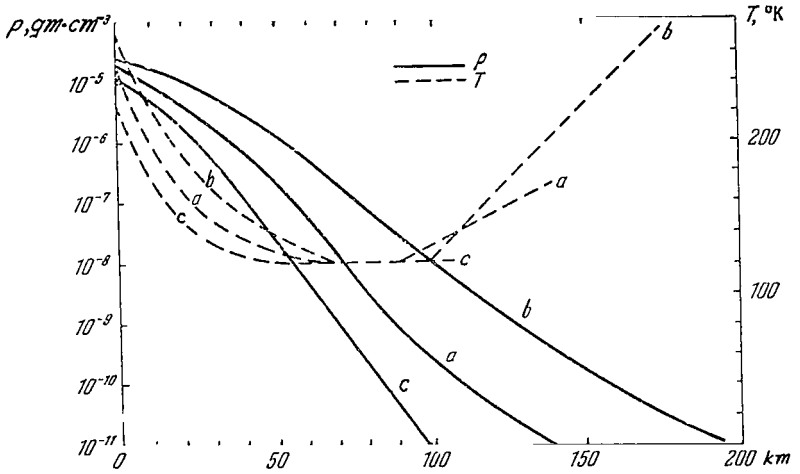

Fig.75 Distribution of Temperature and Density in the Atmosphere of Mars for Three Models: a - Standard Model; b - Maximum Model; c - Minimum Model.

pattern can be satisfactorily traced, for example, for molecular oxygen in the earth's upper atmosphere: At an altitude of 250 km, the ratio $O_2/O = 0.1$ although, in theory, it would follow from photochemistry that there should be virtually no O_2 at this altitude. Thus, it might be that, above 100 km, the temperature of the Martian atmosphere continues to decrease owing to luminescence in the CO_2 λ 15 μ band. The zone of temperature minimum above the mesosphere is termed the mesopause. Above the mesopause the temperature increases due to downward heat flow from the ionosphere. A reliable estimation of the mesopause temperature is practically impossible so long as the real distribution of CO_2 above the dissociation level remains unknown. If, below the mesopause minimum, the temperature gradient becomes sufficiently large (in absolute value), a second convection zone may arise in the mesopause. This was first suggested by Chamberlain (Ref.157).

In our model, we assumed the temperature of the mesopause minimum to be 120°K (100 < z < 120 km). It should be noted that the temperature distribution in the region of the Martian mesosphere differs substantially from the terrestrial

(Fig.75). In the terrestrial mesosphere the temperature course reaches a maximum in the neighborhood of the ozone layer. On Mars a small amount of O_3 forms near the O_2 dissociation level, but the absence of oxygen at lower altitudes /175 warrants the assumption that ozone cannot influence the temperature profile of the Martian atmosphere.

TABLE 42

SATURATION PRESSURE OF CO_2

T, °K	P, mb	T, °K	P, mb
100	2.3×10^{-4}	150	8.5
125	0.12	160	36
135	0.72	175	216
140	1.7		

If Ar is the main constituent of the Martian atmosphere, then the dissociation level will be lower since in such an atmosphere the altitude scale is smaller and since, moreover, Ar as the third body is less effective in the reactions (2.43) and (2.44); (Ref.167). The profile of such an atmosphere will be close to that obtained for the minimum model. All three models presented are reduced to the level at which the quantitative concentration is of the order of 10^{11} cm^{-3}. In the maximum model, this concentration occurs at an altitude of about 190 km and in the minimum model, at 100 km. Note that in the earth's atmosphere the concentration of 10^{11} cm^{-3} is reached at an altitude of about 140 km, which is roughly the same as in the median Martian model.

In the thermodynamics of the earth's troposphere a major role is played by the heat of condensation of H_2O. According to Section 2.3, the relative volume concentration of H_2O in the atmosphere of Mars is close to 10^{-5} and the partial pressure of H_2O near the underlying surface is approximately 2×10^{-3} mb. Tables 42 and 43 give the temperature dependence of saturated vapor pressure for CO_2 and H_2O according to Danilov (Ref.168). Let us compare these with Tables 39 and 41. If the mesopause temperature does not drop below 100°K, no CO_2 will condense even in the mesopause. If the relative volume concentration of H_2O does not decrease with altitude, then the partial pressure of H_2O near z = 30 km will be close to saturation pressure and there the water vapor must condense and form clouds even in daytime. At night, when the surface temperature falls to 150 - 180°K, condensation will also definitely occur in the surface layer of the atmosphere. Apparently, the blue and white clouds observed in the atmosphere of Mars are precisely a result of H_2O condensation (cf. Sect.2.5).

TABLE 43

SATURATION PRESSURE OF H_2O VAPOR AT LOW TEMPERATURES

T, °K	P, mb	T, °K	P, mb
100	3×10^{-17}	200	3×10^{-3}
120	2×10^{-12}	220	4×10^{-2}
130	9×10^{-11}	250	1.0
150	5×10^{-8}	273	6.1
180	9×10^{-5}		

So far, we have disregarded the thermodynamic effects of condensation and /176 evaporation of H_2O in the atmosphere of Mars, but they obviously must be taken into account in a more precise examination. The latent heat of evaporation of H_2O at 0°C is 2500 joules · gm^{-1} and the evaporation of 10^{-4} gm/cm^2 H_2O will cause an energy expenditure of 0.25 joule. For a time scale of 10^3 - 10^4 sec, this corresponds to a thermal capacity commensurate with the values of Q_1 (cf. Table 38).

b) Upper atmosphere. Direct photodissociation of N_2 is ineffective; dissociative recombination seems the principal mechanism of dissociation of these molecules (cf. Sect.1.1) since the flux of ultraviolet quanta beyond the ionization limit is sufficiently small and the velocity of back reaction is high. As a result, in the earth's atmosphere the nitrogen molecule is weakly dissociated even at high altitudes. This probably also applies to the Martian atmosphere, and that not only for N_2 but also for CO, which resembles N_2 in the structure of its electronic terms. Apparently, the main constituents of the atmosphere above the CO_2 dissociation level are O, CO, N_2, and Ar, with the concentration of O decreasing more slowly with the altitude than that of CO and N_2. In sufficiently high layers, oxygen must be the main constituent. As already mentioned in Section 2.3, the lower atmosphere of Mars does not contain much CO: Table 15 indicates only the upper limit. If the lifetime of CO_2 in the Martian atmosphere would substantially exceed the cosmogonic scale ($\sim 5 \times 10^9$ years), then carbon monoxide should have been accumulating in that atmosphere. It is also not excluded that certain specific chemical processes may result in the escape of CO (Ref.1), since the CO molecule is chemically active. The simplest explanation, however, is that proposed in Section 2.3: Oxygen does not dissipate from the Martian atmosphere. Let us discuss the conditions which this proposal imposes on the temperature and altitude of the dissociation level.

TABLE 44

/177

LIFETIME OF OXYGEN IN THE MARTIAN ATMOSPHERE

T_c, °K / z_c, km	500	800	1000	1200	1500	2000
500	10^{20}	3×10^{13}	3×10^{10}	6×10^{9}	6×10^{8}	3×10^{7}
1000	3×10^{8}	6×10^{11}	10^{10}	5×10^{8}	2×10^{7}	3×10^{6}
1500	3×10^{16}	3×10^{11}	3×10^{9}	3×10^{8}	10^{7}	10^{6}
2000	5×10^{14}	3×10^{10}	3×10^{8}	5×10^{7}	3×10^{6}	5×10^{5}

Table 44 gives the lifetime t_o of oxygen (in years) in the Martian atmosphere, as calculated from eq.(1.135) for four different values of the altitude of the critical level (dissipation level) z_c (from 500 to 2000 km) and for six values of temperature (from 500 to 2000°K). The integral $\int_0^c n(z)dz$ encloses the entire oxygen existing in the Martian atmosphere, including the oxygen bound in CO_2. In the calculations it was assumed that the dissociation of CO can be neglected so that each molecule of CO_2 would be a potential supplier of one oxygen atom. It was also assumed that atomic oxygen is the main constituent of the Martian atmosphere at the critical level. In fact, in the region of the diffusive separation the Martian atmosphere consists of N_2, CO, and O and the concentration of O decreases with altitude more slowly than that of N_2 and CO.

The dissipation of oxygen from the Martian atmosphere can be neglected if

$$t_0 \geqslant 10^{10}\ years. \qquad (2.47)$$

Comparing this condition with Table 42, we see that the temperature at the critical level should not be higher than 1000°K even if this level were at an altitude of 500 km. The real temperature of the upper atmosphere is determined by the processes of heating and cooling. This region is heated by the ultraviolet and corpuscular radiation of the sun and cooled by heat conduction and radiation.

Harris and Priester (Ref.72), based on an analysis of density data obtained with artificial earth satellites and taking diurnal variations into account, found that the effective heat flux during the solar activity maximum is 2 erg cm^{-2} sec^{-1}.

The maximum daytime temperature of the earth's upper atmosphere in the isothermal zone would then be 1760°K. An analysis of diurnal variations established that, in addition to ultraviolet radiation, there exists an auxiliary source of heating of the upper atmosphere, which accounts for about 50% of the total heat flux. The above authors conditionally termed this "corpuscular" although it may be of a different nature. For Mars it is natural to assume half as large a flux: 1 erg cm^{-2} sec^{-1}. /178

TABLE 44a
CHARACTERISTICS OF THE MARTIAN ATMOSPHERE ($z_\odot$ = 70°) ACCORDING TO OBSERVATIONS OF THE RADIO OCCULTATION OF MARINER IV (REF.634)

Electron density at ionization maximum	$9 \pm 1 \times 10^4\ cm^{-3}$
Altitude of maximum	120—125 km
Electron scale of altitudes above the maximum	20—25 km
Temperature	< 200°K at altitudes 120 to 200 km

In first approximation, it can be assumed that, in the Martian thermosphere, the temperature gradient is close to 1 - 2 deg/km and the maximum temperature is several hundred degrees. The coefficient of heat conduction for atomic hydrogen, according to Nicolet (Ref.162), is

$$c = 270\sqrt{T}\ erg\ cm^{-1}\ sec^{-1}\ deg^{-1}. \qquad (2.48)$$

Hence heat conduction may drain a flux of 0.05 - 0.1 erg cm^{-2} sec^{-1}; to heat conduction one must add the cooling due to infrared radiation of CO in the vibrational band λ 4.7 μ and in the rotational lines. The volume radiance or radiant emittance in λ 4.7 μ is given by eq.(2.41); Chamberlain (Ref.157) gave $\eta = 10^{-14}$. According to Bates (Ref.161), the volume radiant emittance in the rotational lines is

$$R^r_{CO} = 6.4 \times 10^{-17} f(CO)\, n\ erg\ cm^{-3}\ sec^{-1} \qquad (2.49)$$

at T = 1500°K, whereupon $R^r_{CO} \sim T^2$.

Chamberlain (Ref.157) and Öpik (Ref.82), based on these findings, examined the problems of heat balance of the upper atmosphere of Mars and obtained fairly high temperature values, close to the upper limit found above.

However, observations of the radio occultation of Mariner IV (Table 44a) disproved these expectations. It was found that the temperature of the ionosphere, calculated on the electronic altitude scale from observations of the immersion of Mariner IV into occultation, is very low; the altitude of the ionization maximum also points to a low temperature of the upper atmosphere, of the /179 order of 200°K. It appears that the upper atmosphere of Mars is subject to some powerful cooling factor which had not been considered in the theoretical calculations. Most likely, this factor is the radiation of CO_2 molecules which, owing to diffusion, penetrate into the region above the dissociation level.

It is of interest that, during observations of the emersion of Mariner IV from occultation (i.e., on the night side) no ionosphere was detected. The upper level of electron density on the night side is 10^4 cm^{-3}. The magnitude of daytime ionization closely agrees with theoretical calculations (Ref.82, 157, 168).

It is essential that the onboard magnetometer and high-energy particle counters of Mariner IV detected no traces of a Martian atmosphere. The magnetic field of Mars is at least 3000 times smaller than that of the earth (Ref.23). It would be highly important to study the theoretical problem of the interaction between solar wind and atmosphere of a planet lacking a magnetic field, both from the viewpoint of accretion and of excitation of emission in its upper layers. This problem is becoming particularly urgent considering that Venus also appears to lack a magnetic field.

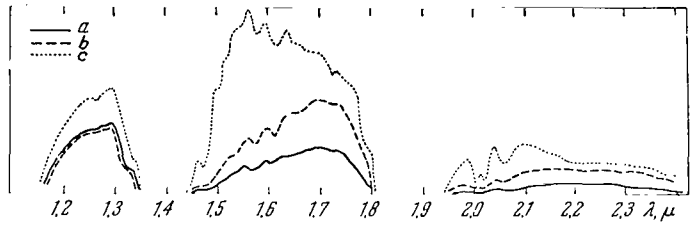

Fig.76 Spectral Dependence of the Reflection Coefficient of: a - Snow and b - Hoarfrost (Crystals $\lesssim$ 0.1 mm), Multiplied by the Solar Spectrum (c).

The outermost layers of the earth's atmosphere consist of helium and hydrogen. The source of helium is radioactive decay in the earth's crust, while the source of hydrogen is currently considered by most investigators to be the photodissociation of H_2O. The rate of dissipation of helium and hydrogen from the Martian atmosphere is many times as great as that from the earth's atmosphere. If helium and hydrogen were supplied only from the bottom up, one could be certain that the concentration of these gases in the Martian exosphere would be negligible. However, accretion of interplanetary plasma (solar wind) may produce, in the upper layers of the Martian atmosphere, concentrations of H and He comparable to the terrestrial (cf. Sect.4.2). It is not precluded that Mars, like Earth, is surrounded by an extended hydrogen corona.

Section 2.8 Polar Caps

The polar caps - the most notable features on the disk of the planet - were first observed by Cassini in 1666. It is probable that to an observer on Mars the earth's polar caps would also appear as the outstanding feature of our planet. In fact, in winter the earth's northern polar cap spreads to approximately 90° latitude and the inhabitants of the temperate zone spend a large part of the year within it. In the summer the cap shrinks to the dimensions of the Arctic zone, i.e., to 25 - 30° latitude.

On Mars during the winter maximum the south polar cap reaches an even greater latitudinal extent (as much as 100°). The maximum corresponds to late February and early March of the Martian calendar*. The extent of the north polar cap is much smaller - about 53° at the maximum. This is due to the fact that for the Southern Hemisphere aphelion occurs in winter and the polar cap forms during a period of 382 days (autumn + winter in the Southern Hemisphere), whereas the north polar cap forms when the planet is at perihelion (the combined duration of autumn and winter in the Northern Hemisphere is 305 days). /180

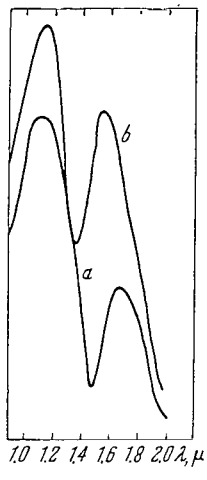

Fig.77 Spectra of Polar Cap (a) and Disk of Mars (b) in the Region 1 - 2 μ. Prism spectrometer; PbS cooled with CO_2; averaged from three traces; entrance slit 0.15 × × 0.3 mm; exit slit 2 mm (Δλ 1800 Å); rate 70 Å/sec, τ = 2.2 sec.

Since during summer in the Southern Hemisphere the planet passes through its perihelion, the south polar cap shrinks at a faster rate than the north cap and disappears completely. The north polar cap during summer in the Northern Hemisphere does not entirely disintegrate, shrinking to a minimum of the order of 6°.

Spectral and polarization observations of the polar caps indicate that they consist of frozen water. Figure 76 presents the spectra of coarse-grained snow and fine-grained hoarfrost, obtained under laboratory conditions. These differ from the spectrum of water vapor in that the absorption bands are shifted approximately 0.1 μ in the direction of longer wavelengths. The albedo in the region λ 1.3 μ is 0.8 - 0.85 but beyond the absorption band of ice λ 1.5 μ it decreases by a factor of 1.5 - 2. The intensity of the absorption bands of ice is greater for large crystals (snow) and smaller for very small (frost). Kuiper (Ref.4) found that the intensity minimum at λ 1.4 μ, characteristic of telluric H_2O absorption, is displaced toward 1.5 μ in the spectrum of the polar cap and that the albedo markedly decreases in the direction of longer wavelengths. This finding was confirmed by us in 1963 (Ref.94). Figure 77 shows averaged spectra of the polar cap in the central portion of the disk, obtained by us with an infrared prism spectrometer of a resolving power Δλ ≈ ≈ 0.2 μ. Such observations are made very difficult by atmospheric jitter, but the finding appears fairly reliable. /181

* Martian dates correspond to terrestrial dates provided that $l_\odot = l_\sigma - 84°$ where $l_\odot$ is the earth's heliocentric longitude, l_σ is the heliocentric longitude of Mars at a given moment.

G.A.Tikhov (Ref.169) compared the color characteristics of the polar caps and ice in the photographic region and found satisfactory agreement.

Dollfus (Ref.102) plotted the polarization curve of the polar cap and showed that the polarization of the polar cap during its melting is the same as the polarization of ice crystals sublimating when heated by a strong source of infrared radiation. The polarization curve of the polar caps corresponds to the characteristic porous structure formed during sublimation of ice crystals. The disappearance of the polar caps undoubtedly occurs at a temperature below 0°C (cf. Sect.2.4). Thus, we are not dealing here with thawing as such but with sublimation (absence of liquid-phase stage).

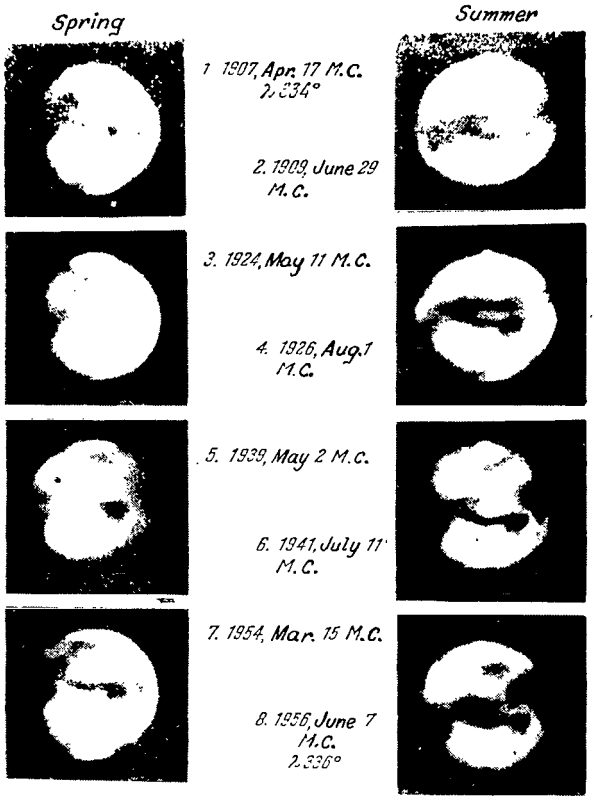

Fig.78 Seasonal Variations in Dark Areas and Melting of the Polar Cap (Ref.86).

Sublimation of the polar caps is closely related with other phenomena observed on the surface of Mars and primarily with the darkening of the seas (Fig.78). Before the process of sublimation comes to an end, the polar caps break up into several regions of varying brightness, with the isolated fragments always being observed in the same portion of the planet. The last fragment of the south polar cap is always observed in a zone located roughly 6° from the pole ($\varphi = 83°.5$, $\lambda = 30°$). The north polar cap also is displaced with respect to the pole, but much less [by roughly 1° (Ref.86)]. These shifts indicate that the Martian relief is not smooth, at least not in the polar regions.

Mitchell's Mountains - the very small bright spots observed at latitude -73° after the south polar cap has shrunk beyond the confines delineated by this parallel - represent an even clearer proof of the unevenness of Martian relief /182 (Fig.79). There is no doubt that these are elevated regions on which the "thawing" is delayed owing to lower temperatures.

Many observers point to the presence of a dark fringe along the boundaries of the polar cap during the sublimation. It has been suggested that this is a consequence of the contrast effect associated with the great brightness of the cap, but observations with a red filter (with which the relative brightness of the polar cap decreases greatly) indicate the reality of this fringe. Earlier it had been assumed that the dark fringe is a belt of liquid water left after

thawing of the polar cap, but measurements of pressure and temperature disproved this. Apparently this fringe represents a belt of moistened ground. /183

Figure 80 shows the width of the south polar cap in relation to seasons of the year according to observations by various investigators. During the summer solstice, this width is still as large as 11 - 12°, completely disappearing in the second half of summer. Depending on the rate of fragmentation of the polar caps and the turbidity of the atmosphere (at the time when the substance of the polar caps undergoes sublimation), A.I.Lebedinskiy and G.I. Salova (Ref.170) estimated the thickness of the polar cap at 10^{-3} - 10^{-1} gm · cm^{-2}. At such a surface density, it would be impossible for snow or frost to form a uniform cover of the cap without bulges and depressions. In this respect, nonuniformities of this kind should have caused the visual albedo of the polar cap to be much lower than the observed albedo (0.7 - 0.8). Some authors (Ref.170) assume that the polar caps, at least in part, represent stable cloud formations of ice crystals. A similar opinion is held by N.A.Kozyrev (Ref.139), in view of the good visibility of polar caps in blue light as distinct from the seas and other dark markings. However, the blue haze veiling the seas that are chiefly located in the equatorial and temperate belts may be absent or more transparent in the polar regions (cf. Sect.2.6).

Fig.79 Mitchell's Mountains at the Edge of the Polar Cap to the Left (Ref.86).

Some investigators (Ref.86, 171) assume that, in spring and summer, the polar cap is a true snow cover blanketing a surface which, in autumn and winter, is covered with clouds resembling the clouds near the morning limb of the disk (cf. Sect.2.5). In confirmation of this viewpoint, two objective arguments could be cited: 1) The albedo /185 of the polar cap is much lower in winter and autumn than in spring and summer; 2) in winter and autumn, the size of the polar cap is greater in blue light than in red light, whereas in spring and summer it is the same. These arguments, of course, are not conclusive. It is not impossible that, in spring and summer, the clouds do not disappear but that their altitude and albedo undergo changes.

It is highly doubtful, however, that the material of the polar caps exists entirely in suspended state, since then it would be extremely difficult to account for their stability as well as for the strict regularity of waxing and waning of these caps. Most likely, the polar caps are indeed due to a deposit of snow or hoarfrost covering the surface, over which a fog of ice particles is suspended in the atmosphere.

Spectroscopic observations do not contradict the "cloud" hypothesis of polar

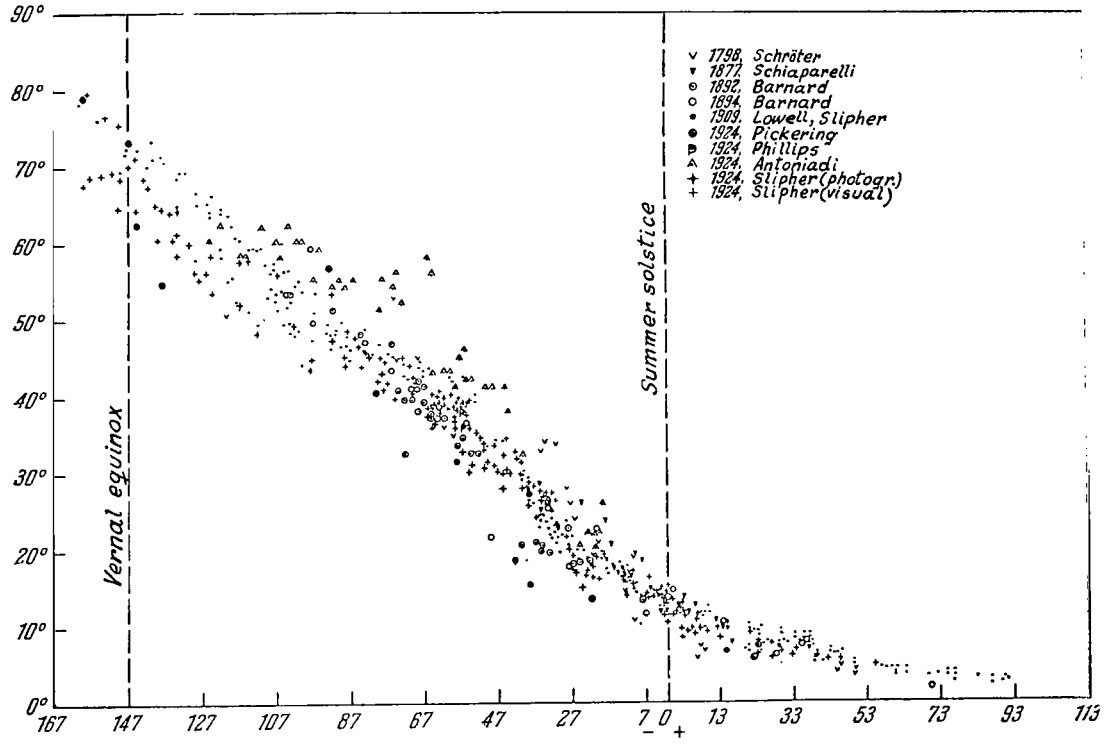

Fig.80 Seasonal Variation in the Width of the South Polar Cap according to Observations by Various Authors.
Abscissa: interval of time before (or after) the summer solstice, in Martian days.

caps. The reflection spectrum of ice-crystal clouds must contain ice absorption bands, and observations of terrestrial cirrhus clouds confirm this (Fig.81).

With respect to polarization observations, it is quite impossible that they could fit both the surface snow deposit and the ice crystal fog. Dollfus identified his polarization curve of the polar cap with sublimating frost rather than with fog. Dollfus' observations pertain to the spring-summer period, when the polar cap is quite free of clouds (although, possibly, not completely). /186

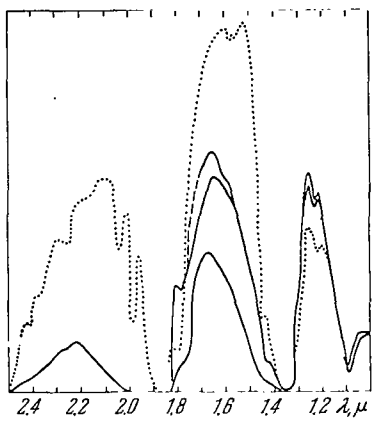

Fig.81 Spectrum of Solar Radiation Scattered by Terrestrial Ice Clouds (Cirrhus Clouds) in the 1 - 2.5 μ Region (Crimea, 125-cm Reflector of the State Astronomical Institute im. Shternberg, Diffraction Spectrometer, June 1964). Solid curves - traces of cloud spectra recorded at various times; broken curve - trace of the solar spectrum.

Occasionally, outside the polar caps in the morning hours, bright white spots appear in the colder regions of the planet, which subsequently disappear without change in position. Slipher (Ref.86), like many other authors, assumed that these spots are a result of the deposition of frost on the surface of the planet. The white deposits usually appear in the bright areas and are much less frequently encountered in the dark areas. Long ago, this led to the suspicion that the dark areas are warmer than the bright areas and probably are also lower in level. The first of these assumptions was confirmed by measurements of the infrared brightness temperature (Sect.2.4).

Section 2.9 Continents

Lunar maria are shallow depressions while the continents are mountainous regions. With respect to the Martian continents, there is reason to believe that they constitute some high ground. This was discussed at the end of the preceding Section.

Slipher (Ref.86) pointed out that the boundary of the dark areas is always concave, at the terminator; however, this phenomenon hardly can serve to determine the depth of the Martian seas or oceans. Instead, it seems attributable to their lower albedo.

Photometric observations in the red spectrum region indicate a smoothness factor q from 0.5 to 1 (cf. Sect.2.6), which would imply a comparatively level relief, at any rate more level than that of the moon (q = 0). Earth-based observations do not permit a direct detection of any rugged feature of the Martian surface; in difference to the moon, there is no observable shadow cast by the mountains. On this basis, the literature often mentions 750 m as the maximum estimate of the height of Martian mountains. Tombaugh [cf.(Ref.1)] showed that this estimate, made by Lowell, contains an error of about one order of magnitude: the actual upper limit is 5 km. The geographic deviation of the summer

vestiges of the polar caps from the poles as well as the pattern of waning of the south polar cap can most probably be attributed to some sort of relief, but so far no conclusions have been drawn as to the height of such features.

The best of the photographs transmitted by "Mariner IV" (Figs.82 - 83) /187 show annular mountains similar to lunar craters and irregular bright formations greatly resembling lunar mountain chains. Thus, the above-mentioned difference in smoothness apparently is of a quantitative nature. The qualitative similarity between the shapes of lunar and Martian relief is obvious. An analysis of several photographs transmitted by Mariner IV no doubt will provide more information on the nature of the Martian relief than all preceding ground observations taken together. In all, the photographs transmitted by Mariner IV contain more than 70 detectable craters measuring from 4 to 120 km in diameter. Considering that Mariner IV photographed approximately 1% of the Martian surface, it can be assumed that Mars has about 10,000 craters with a diameter of more than 4 km. Particularly intriguing is the photograph No.11 which reveals a large bright arc, probably the wall of a collapsed crater measuring about 120 km in diameter. The slope of the crater walls is about 10° according to Leighton et al. (Ref.171), which would mean that the "shadows" clearly visible on many photographs are not really shadows but merely sectors of greater illumination (the zenith distance on the photographs varies from 24 to 71°). However, as estimated by the above authors (Ref.171), the depth of the craters reaches several hundred meters. The coordination between the photographs and the coordinate grid is not sufficiently precise for determining the morphological differences between the dark and bright areas.

/188

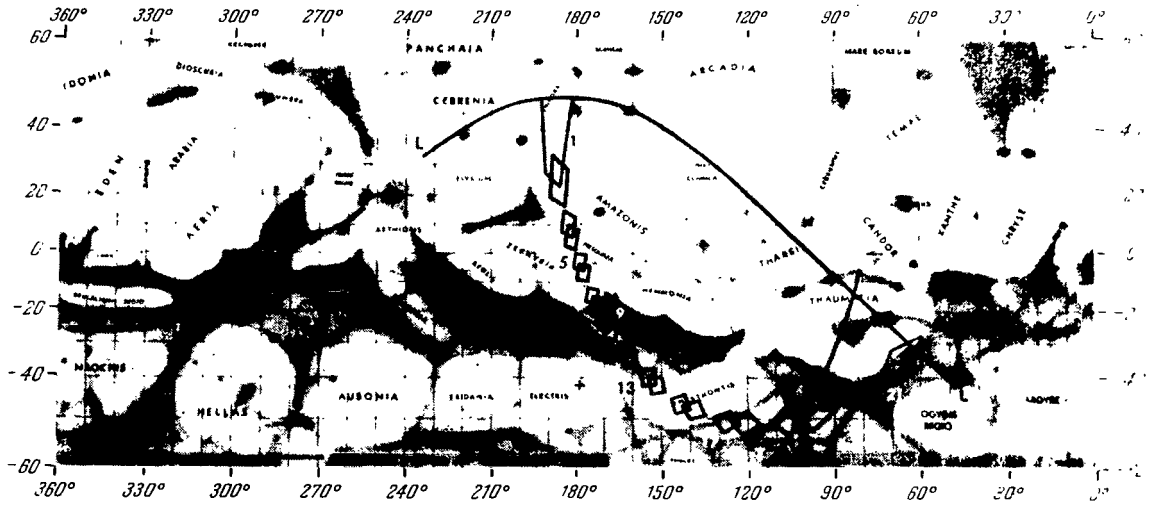

Fig.82 Chart of Mars, Showing the Location of Sectors Photographed by Mariner IV.

The continents, unlike the seas (Sect.2.10), are not subject to variations in brightness or color. According to Kuiper's observations (Ref.4), the con-

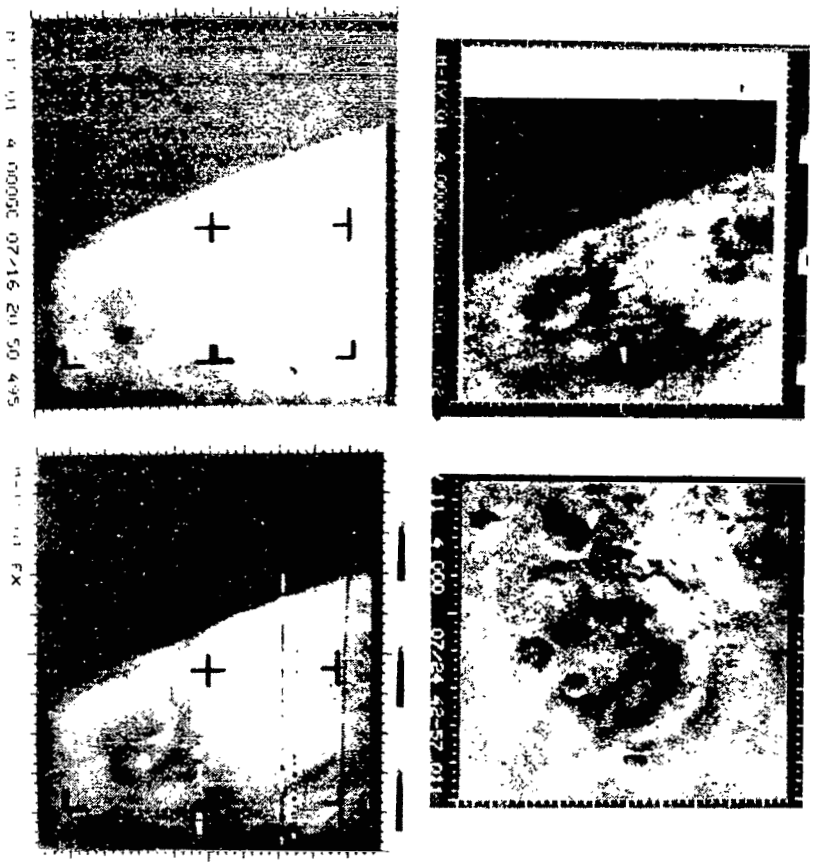

Fig.83 The Two Left and the Upper Right Photographs Represent Frame No.1 from the Series of Photographs of the Martian Surface Taken on July 14,1965 by Mariner IV. Distance to surface: 17,000 km. A limb sector of 650 km length was photographed. Position: Latitude 35°N, longitude 172°E. Orange filter. Upper left photograph - frame without supplementary work-up, in the form in which it was directly transmitted by Mariner IV. Left bottom - same frame after preliminary work-up on July 15,1965. Right top - final processed variant, with a roughly doubled contrast. Right bottom - frame No.11. Approximate location - latitude 31°S, longitude 197°E (Atlantis, between Mare Sirenum and Mare Cimmerium). Distance to surface; 12,500 km. North at top. Zenith distance of the sun: 47°. Green filter. Contrast magnification 4 ×. Dimensions of photographed region: 270 (N - S) × 240 (E - W) km.

trast between the continents and seas in the λλ 0.6 - 2.5 μ range does not vary, so that the wavelength dependence of the mean geometric albedo of Mars p(λ) within this range (cf. Fig.55) can be used for identifying the material of the Martian surface. The region in the direction of shorter wavelengths is masked by the blue haze effect. The curve of p(λ) has a highly characteristic slope; it has its maximum in the region λλ 1.2 - 1.6 μ and drops steeply in direction of shorter wavelengths (apparently along the initial segment of this descent, atmospheric absorption is not yet a major factor); this is followed by a gentle downward slope of the curve in the region λλ 1.8 - 2.5 μ and an ascent in the region λλ 3 - 4 μ. Thus, near λ 2.5 - 3 μ a wide absorption band appears; unfortunately, its central portion cannot be traced owing to superposition by the strong telluric H_2O λ 2.7 μ band.

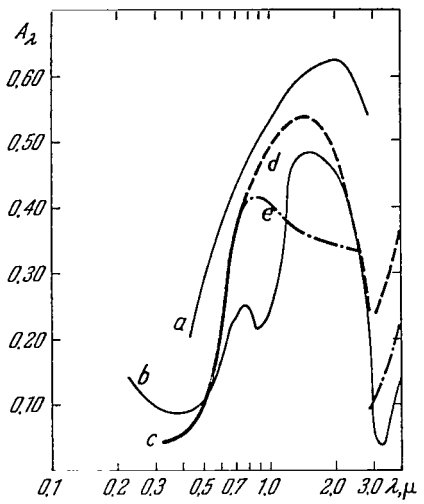

Fig.84 Comparison of the Spectral Reflectivity of Mars and Limonite.
Albedo of limonite according to Sagan et al. (Ref.173) - curve a; according to Hovis (Ref.173a) - curve b. Albedo of Mars according to Harris (Ref.66) - curve c; according to Sinton in the infrared region - curve d; according to us - curve e.

Such an absorption band normally exists in the spectra of rocks and minerals containing water of crystallization. The sharp decrease in reflectivity in the direction of shorter wavelengths is characteristic of iron oxides. The curve of p(λ) greatly resembles /190 the curve of the spectral reflectivity of brown hematite or limonite $Fe_2O_3 \cdot nH_2O$ (Fig.84). Other authors (Ref.94, 172-174), based on this similarity, independently concluded that the Martian soil may contain large quantities of limonite. The high absolute value of the albedo near λ 1.5 μ indicates that Martian limonite would exist in a finely divided state, at least in the surface layer. The relatively low brightness radiotemperature of Mars (200°K; cf. Sect.2.4) suggests that this pulverized surface layer is at least 10 cm thick. Kuiper (Ref.4), on the basis of his earlier observations of the infrared spectrum of Mars (λλ 0.7 - 2.3 μ), assumed the surface material to consist of the silica rock, felsite. Of course, anhydrous silica rocks that do not give the λ 3 μ water of crystallization band have been eliminated from the picture by present-day investigators, but it is worthwhile to seriously consider other possibilities, since the presence of a large amount of finely divided brown hematite on the surface of Mars is difficult to explain.

Sinton and Strong (Ref.26) voted against silica rocks (Fig.48) because of absence of the λ 9 μ band; however, as mentioned above, if the material is sufficiently pulverized, this band may also disappear for the silicas (Ref.129).

Long before methods of infrared spectroscopy made this possible, Dollfus identified the Martian surface rocks as limonite, on the basis of an interpreta-

tion of polarization studies (Ref.102). He examined several hundred specimens of various terrestrial rocks, of which not a single one - except for limonite - satisfactorily fitted the Martian polarization curve. Sharonov (Ref.175) similarly interpreted photometric and colorimetric observations in the region $\lambda < 0.7\ \mu$, but his approach is the least reliable because of the possible influence of the Martian atmosphere on the albedo and color of the planet. /191

From the velocity of the reversible reaction

$$Fe_2O_3 \cdot H_2O \rightleftarrows Fe_2O_3 + H_2O$$

it is possible to estimate the equilibrium concentration of H_2O in the atmosphere. This was done by Adamchik (Ref.176). The equilibrium content of H_2O in the Martian atmosphere ranges within the limits from 2×10^{-4} to 6×10^{-2} gm $\cdot$ $\cdot$ cm^{-2}, according to observations which give a value of 1.4×10^{-3} gm $\cdot$ cm^{-2} (Sect.2.3). The rate of decomposition of limonite is an exponential function of temperature, and the equilibrium pressure of H_2O must be greater in regions where the temperature is higher.

Öpik (Ref.82) mentioned meteoritic iron as a possible source of limonite on the surface of Mars. Mars moves in the immediate neighborhood of the asteroid belt so that the fall of meteoritic materials in comparatively recent epochs may have had a greater influence on the formation of the surface of Mars than on that of the earth. The Martian craters detected on the photographs, taken at close quarters by the Mariner IV interplanetary spacecraft, are most likely of meteoritic origin. Lastly, it might well be that the process of gravitational differentiation of elements has been slower on Mars than on earth and that thus its crust has become enriched in iron. On earth, limonite is formed by the interaction between the weathering products of silica rocks and water and free oxygen. It might seem that, on the Martian surface, the rate of formation of limonite should be much slower, but this question requires a painstaking study. For example, the presence of even minute amounts of ozone near the surface may accelerate the rate of formation of limonite.

Section 2.10 Dark Areas

The largest of the Martian dark areas are termed seas (Mare). Smaller areas are known as lakes (Lacus) or oases (Oase). Canals intersect at the oases. Dark spots of low contrast are termed bogs (Palus) and triangular protrusions of the seas are called bays (Sinus). The dark areas have their own names, like the continents. The nomenclature of the Martian regions had been updated by Schiaparelli. The International Astronomical Union recently introduced certain new names, but in general the changes are minor.

An observer who first views Mars through a telescope normally will experi- /192
ence disappointment. He can distinguish between the polar caps, discern the Syrtis Major (if the proper side of Mars faces him), but that is usually the end of it. To identify even the largest of the seas, a certain skill is required. Figure 63 presents six photographs of Mars, that may be of some assistance to tentative orientation. These photographs generally differ by 60° in longitude

of the central meridian and were taken under roughly identical conditions of visibility and transparency of the Martian atmosphere. Let us examine these photographs by referring to the chart (Fig.64). On the first photograph, Mare Erythraeum is at the center. To the left of it, at the bottom, there is the triangular Sinus Margaritifer. Adjoining the apex of this triangle is Oxia Palus. At the north limb there appears the darkish Mare Acidalium, separated from Mare Erythraeum by the bright regions Chryse and Xanthe. To the left, in the southeastern part of the limb, we have Eden (Moab). The Southern Mare Australe is separated from Mare Erythraeum by the continents Argyre and Ogygis Regio. The bright region Thaumasia, at whose center there lies a dark spot Solis Lacus linked to Mare Erythraeum by the Nectar Strait, stands out distinctly. A similar comparison of the other photographs with the chart is left to the reader's discretion. Note that, in visual observations, a perception on the disk of as many details as are shown by these photographs is possible only at extremely good visibility. Anything more than that requires an excellent image and first-class optics.

It can be seen from the chart and the photographs that the seas are chiefly concentrated in the southern portion of the disk. It is here that they merge, with the darkest of them - Mare Sirenum, Mare Cimmerium, Mare Tyrrhenum, Syrtis Major, Sinus Sabaeus - forming a belt extending over the latitudes from 0° to 30°. The triangular bays whose apices chiefly face north are noteworthy. The maria in the northern portion of the disk are much smaller in area and more isolated. The largest of them, Mare Acidalium, has the shape of a triangle whose apex faces south.

The average contrast between seas and continents was already discussed in Sections 2.6 and 2.9 (cf. Table 32). Visual contrast undergoes marked seasonal as well as random fluctuations (the latter are associated with variations in transparency of the Martian atmosphere. Most observers, including such experienced ones as Tombaugh, Slipher, and Barabashev, assess the color of the maria as bluish. Some of these (for example, Kuiper) consider their hue as neutral. Objective spectrometric (Ref.139) and colorimetric data [e.g.(Ref.144)] show /193 that the energy distribution in the spectrum of the seas and continents is similar but that the curve for the continents is somewhat steeper (Fig.71 and Table 32). It is thought that the hues which are sometimes acquired by the Martian dark areas and which the writer also observed during the favorable opposition of 1956, are not real but caused by some physiological effects (Ref.121).

Physiological effects probably also govern the question of the canals. Schiaparelli and Lowell saw them as straight. They also discovered a number of geminations of such canals. Schiaparelli and Lowell were sure that the Martian canals are, if not artificial structures, then at least strips of vegetation extending along true water arteries. French observers, beginning with Antoniadi, insisted that these lines are no "canals" at all and are instead composed of mottlings and spots irregularly scattered throughout the disk, existing just at the threshold of vision, owing to imperfections of the eye, perceived as a grid of straight lines. The visual sketches by Antoniadi showed better resolution than Lowell's sketches and the lively dispute on the canals which flourished at the turn of the Century culminated in the victory of the French school. Recently, Slipher (Ref.86) advanced a new argument in defense of the reality of the canals. He agrees that the canals may have a definite fine structure but

emphasizes that they represent real rectilinear features. Slipher's book includes inserts of direct photographic prints of a number of negatives of Mars, which distinctly show canals. Alongside the photographs, he gives visual sketches. By far not all canals shown on the sketches are visible on the photographs, but the opposite is also true.

The photographs taken by the cameras of "Mariner IV" show no rectilinear features that could be interpreted as canals. Thus, canals in the sense in which they had been construed by Schiaparelli and Lowell do not in fact exist. However, the Mariner IV photographs cover only a very small portion of the planetary surface and do not rule out the possible presence of beaded chains of dark spots measuring several tens of kilometers in diameter, stretching along the great circles, and perceived in ground observations as straight lines. Patches of this kind may be fields of lava that had formed along the fault lines of the continental crust. Gifford (Ref.178) assumes that the "canals" are dunes intersecting the Martian deserts, but this does not explain why such dunes should be dark, unless they are narrow (several kilometers) ridges with appreciable declivities. The latter assumption must be rejected, since narrow straight features of this kind would have been definitely visible on the photographs taken by Mariner IV. /194

Fig.85 Sketches of the Syrtis Major Region and of the Double Canals Thoth and Nilosyrtis according to Observations with the 60-Inch Reflector at Pic du Midi. a - Medium image quality; b - Excellent quality (Ref.22).

The low atmospheric pressure precludes the existence of open water bodies on Mars, but it might be a priori conceivable that the Martian maria are not filled with water but with some other fluid having a low saturated vapor pressure. This also cannot be; a detailed analysis of the best photographic negatives as well as careful visual observations show that the maria have a fine structure (Fig.85) so that their surface must be nonuniform. Moreover, V.G. Fesenkov (Ref.177) noted that an open liquid surface, measuring more than 300 m in diameter, would reflect perceptible highlights. The polarization curve of the seas hardly differs from that of the continents (Ref.137).

By way of a working hypothesis it may be assumed that the nature of the

soil in the Martian seas and on the continents is the same (limonite) but the surface of the maria is one-third covered with patches having an extremely low albedo. This would account not only for the identical polarization but also for the wavelength independence of contrast in the red and infrared spectrum regions.

Even one and the same observer never sees Mars exactly the same as he had seen it previously. The quality of the image changes, as do the angular dimensions of the disk and the conditions of illumination of the features. Naturally, a comparison of the findings of different observers is a difficult task and not infrequently results in contradictions; the problem of the canals is an explicit example. Nevertheless, the changes in brightness and configuration of the Martian features are so distinct that generally the observers arrive at compatible conclusions concerning this question. Three types of changes are observed: regular seasonal changes, which recur each Martian year; unstable seasonal changes, with the appearance of the same regions differing each year in the spring; and sudden distinct changes, which persist over prolonged periods of time. /195

Fig.86 Seasonal Variation of Syrtis Major (Ref.84).

As a prominent example of seasonal changes, Slipher mentioned Pandorae Fretum (Fig.78). This region is at its darkest in summer, when it occupies an area of millions of square kilometers, roughly the same as that occupied by Sinus Sabaeus which runs parallel to it. In autumn and winter, this area cannot be distinguished against the background of the surrounding bright regions. Similar changes in contrast, more or less distinct, have also been observed for other dark areas. Not only the brightness but the outline varies. Thus, Syrtis Major is more narrow at perihelion (ABC) (Fig.86) while, during winter in the Northern Hemisphere, it bulges eastward at aphelion (ADC).

The darkening of each region occurs later the lower its latitude, with the wave of darkening propagating at a roughly constant rate (about 30 km/day). De Vaucouleurs (Ref.5) and Focas (cf. Ref.22) investigated this process in detail. In the equatorial zone two waves of darkening are observed: one, during the melting of the south polar cap and the other, during the melting of the north polar cap. As a result, the dark areas near the equator show the greatest contrast. The dark areas in the high and temperate latitudes may reach the same contrast as the equatorial areas, but only for a short time; following the passage of the wave, they become brighter.

During each Martian year, the seasonal wave changes the appearance of the Thoth, Casius, Utopia, Nepenthes Regio (Ref.22). The contour of Solis Lacus often changes (Ref.84). These constitute changes of the second type: semiregular. Lastly, pronounced irreversible changes sometimes encompass vast regions of the planet. Until 1950, Laestrygonum Sinus had been classified as a bay of Mare Cimmerium. However, subsequently part of Mare Cimmerium south of Laestrygonum

Sinus suddenly became bright and now Laestrygonium Sinus (if the few canals linking it to this mare are disregarded) is isolated from Mare Cimmerium (Ref.86). /196
Generally, however, the outlines of the dark areas remain constant. It is astonishing that the intense dust storms usually produce no changes in these outlines; after a dust storm is over they are exactly as they had been prior to its onset.

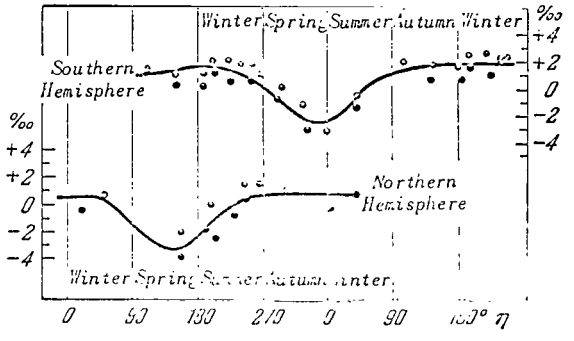

Fig.87 Seasonal Changes in Polarization of the Dark Areas; the Difference in Polarization between the Seas and Continents is Given as a Function of the Heliocentric Longitude of Mars (Ref.102).

Dollfus (Ref.102) found seasonal changes in the polarization of dark and bright areas. Figure 87 shows the difference in the polarization of the dark and bright areas as a function of the heliocentric longitude. In spring, an anomalous negative polarization takes place, which disappears again toward the end of summer. This anomaly may be interpreted as the effect of a temporary increase in the size of the light-scattering grains or perhaps as the effect of the formation of larger grains.

When the wave of darkening reaches the equator, the dimensions of the polar cap start shrinking but its sublimation apparently commences much earlier. Spectroscopic and polarization observations (cf. Sect.2.8) show that the polar cap consists of snow or frost. On the other hand, recent spectroscopic observations by Spinrad, Münch and Kaplan (Ref.92) directly detected water vapor in the atmosphere of Mars. Apparently the seasonal wave of darkening is associated with the circulation of H_2O in the Martian atmosphere, which increases during sublimation of the polar cap. Darkening and the change in polarization may be associated either simply with the increase in moisture content of the surface material or with activity of a biosphere. Dollfus investigated the polarization of various plants and compared it with the polarization of the dark areas. There was no resemblance /197
with the higher plants in general. However, it was found that slight changes in polarization similar to those observed may also be exhibited by microorganisms scattered like dust over a given surface. Many types of microorganisms are highly adaptable. A brightly colored pigment may afford some protection from sharp changes in temperature. The algae Nivalis, which inhabit alpine snows, stain large areas during certain seasons. It may be that the apparent changes in coloration of the Martian seas are of similar origin. On the other hand, seasonal changes in polarization may, of course, be attributed to the presence of minute hygroscopic particles which increase in size (or in refractive index) when moist and which change in color as well.

Attempts at a spectroscopic comparison of the reflectivity of the Martian seas with that of terrestrial vegetation have been made repeatedly. Slipher (Ref.179) and G.A.Tikhov (Ref.180) attempted to detect chlorophyll bands in the Martian spectrum but failed. Kuiper's spectrophotometric studies of the dark areas in the infrared spectrum indicate that the spectra of the maria do not

show the increase in reflectivity in the region $0.7 < \lambda < 1.4$ μ which is characteristic of higher terrestrial plants (Fig.88). G.A.Tikhov (Ref.181) found that the infrared reflection maximum is greatly attenuated in the reflection spectrum of terrestrial vegetation belonging to the flora of Arctic or alpine regions with a harsh climate. The lower plants, such as mosses, algae, fungi, or lichens, lack this maximum. The reflectivity of these plants is low and virtually constant within the limits from 0.5 to 2.5 μ. There is nothing surprising about the absence of higher plants. Plants similar to terrestrial vegetation with high water content of the tissue (which, incidentally, accounts for the decrease in reflectivity in the region $\lambda > 1.5$ μ and the absorption bands at 1.4 μ and 2.0 μ; cf. Fig.88) would be unable to survive in the Martian climate with its low nocturnal temperatures. /198

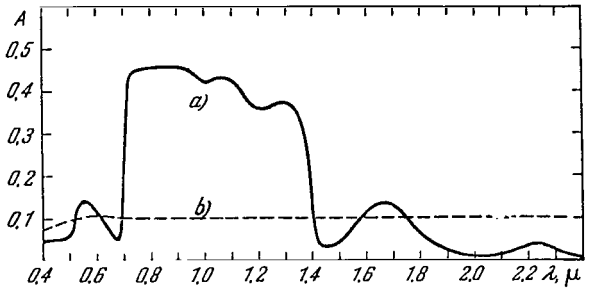

Fig.88 Typical Curves of Reflectivity of: a - Higher Plants; b - Lichens. Ordinate: albedo in arbitrary units (Ref.4).

Lichens - the hardiest plants on earth - exhibit a highly characteristic feature in the reflection spectrum: the λ 3.43 μ absorption band. This band represents the fundamental vibrational frequency of the CH chain, a chain which is an elementary constituent of hydrocarbon molecules. Depending on the nature of the molecule, the wavelength may vary within specific limits. For simple molecules it is somewhat longer (about 3.3 μ for CH_4) and for complex molecules, shorter.

In the 3 - 4 μ interval, the earth's atmosphere is sufficiently transparent, but the intensity in the spectrum of Mars near λ 3.5 μ is comparatively low since this is exactly where the boundary runs between the regions of reflected and natural radiation (cf. Fig.20). Hence the spectrum of Mars in the 3 - 4 μ intervals could be obtained only with a limited resolution $\left[\frac{\lambda}{\Delta\lambda} \approx 80\right.$ in Sinton's studies (Ref.89, 90, 182) and $\left.\frac{\lambda}{\Delta\lambda} \approx 40\right.$ in our own study (Ref.94)]. According to Sinton (Ref.89, 90), three absorption bands exist in the spectrum of the dark markings (λ 3.43, 3.56 and 3.67 μ) in the 3.4 - 3.7 μ region; the spectrum of the continents does not contain these bands. Details with similar wavelengths but of a weaker nature have been detected in the spectrum of the entire disk by us (Ref.94). The reality of these bands has long been considered irrefutable, and they had been regarded as a strong argument in favor of the existence of lower plants on Mars. Sinton assumed that they pertain to all three bands, but some observers [cf. for example (Ref.183-185)] were of a different opinion. Special experiments were made and extensive literature was accumulated. Recently, however, Sinton, in an article co-authored by Rea and O'Leary (Ref.186), essentially abandoned his discovery, declaring that the comparison spectra were insufficiently reliable since the continents and seas had been observed on dif-

ferent nights and that the bands in the 3.4 - 3.7 μ region might be telluric and pertain to water enriched with deuterium (mixture of HDO and D_2O). In fact, random variations in moisture content might lead to an error of this kind. Similar doubts could also be voiced with respect to the spectrum published by us (Ref.94, 187), since the sun was used as the comparison source (although it was observed also on the morning following the observations of Mars). New observations, with careful coordination of reckoning with the moon or stars at the same zenith distance and on the same night, are needed. It would also be highly important to increase the spectral resolution.

Even if Sinton's bands are rejected, four arguments in favor of the existence of a biosphere on Mars still remain: 1) seasonal variations in contrast of the dark markings in relation to the continents; 2) ability of the dark markings to return to their original appearance following strong dust storms; 3) seasonal variations in polarization of the dark markings; 4) greenish-blue hues of the dark markings. /199

Argument (2) seems fairly convincing. The frequent dust storms should have covered the planetary surface with a thick and uniform layer of yellowish dust if there were no vegetation to restore the appearance of the dark regions. On earth there exist arid desert regions without vegetation but nevertheless markedly differing in coloration. However, the earth's deserts are isolated regions surrounded by regions of greater moisture which absorb the pulverized material transported from the rocky plateaus. If the dark areas are lowlands, it would be difficult to conceive how they could avoid becoming covered by dust unless they are blanketed with vegetation. If the recovery of the appearance of the dark areas is unrelated to vegetation, it must be assumed that they are elevated rocky plateaus. However, polarization observations show that the surfaces of the continents and seas are of a similar nature.

V.G.Fesenkov (Ref.188), in denying the existence of a Martian biosphere, pointed to the extremely severe climatic conditions characteristic of the Martian surface: low pressures, extremely low temperatures in winter and at night in summer (cf. Sect.2.4), extremely low content of water in the atmosphere, and lack of oxygen. Opik (Ref.82) noted that low temperatures may be a favorable factor, since they promote the extraction of water from the Martian atmosphere; at night during the sharp temperature drop, the water would then deposit on the surface in the form of hoarfrost and could there be assimilated by the Martian organisms. A number of studies (Ref.189, 190) showed that under near-Martian conditions, at low temperatures and in the absence of oxygen and water, certain anaerobic soil bacteria not only do not die but even proliferate. Any sample of terrestrial soil taken at random contains a certain number of such bacteria (Ref.191). Clearly, the specific Martian microorganisms which, under corresponding conditions, may have traveled the lengthy path of evolutionary development and natural selection, would have had more chances to adapt themselves to the Martian conditions and it is not impossible that complex life forms may exist on Mars although most likely not resembling terrestrial forms of life [cf. for example the book by K.A.Lyubarskiy (Ref.292)].

Various authors made an attempt at accounting for the complex entity of the properties of the Martian dark areas, without presupposing the existence of a biosphere. One such hypotheses was developed by McLaughlin (Ref.192, 193). /200

He mentioned the distinctive shape of the dark areas in the Southern Hemisphere, extending from southeast toward southwest. Their orientation generally correlates with the direction of movement of the clouds during summer in the Southern Hemisphere. Another important detail is constituted by the triangular bays at

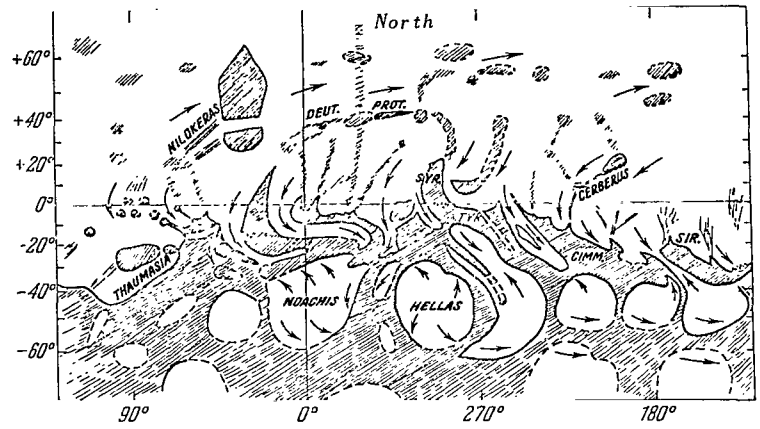

Fig.89 Relationship between Position of the Maria and Principal Wind Direction, according to McLaughlin (Ref.152).

the northern boundaries of the maria. McLaughlin assumes that the maria are coated with dark volcanic ash ejected by volcanoes located at the apices of the triangular bays and transported by tradewinds to the south, since the system of tradewinds corresponding to summer in the Southern Hemisphere is more powerful than the inverse system occurring during summer in the Northern Hemisphere. The reason for this lies in the fact that summer in the Southern Hemisphere corresponds to the perihelion. Figure 89 illustrates the pattern of formation of the maria according to McLaughlin. The general outlines and position of the seas remain constant, since they are determined by continually active volcanoes and by the principal direction of the tradewinds. Variations in the rate of volcanic eruptions may cause numerous irregular changes. Certain types of seasonal changes are satisfactorily explained by changes in wind direction. As pointed out above, the eastern boundary of Syrtis Major shifts periodically, somewhat /201 receding after perihelion and bulging outward after aphelion. Figure 90 shows how this effect might be explained by a seasonal change in principal wind direction. It is assumed that the volcano, representing the source of the igneous material, is located at point A. During winter in the Northern Hemisphere ash is transported from point A toward the southwest. Near the equator the wind - and along with it the flux of ash - veers south, occupying the area between the lines ABC and ADE. During the same period, the region between AFE and ADE becomes covered by the red dust transported from the region G. With the advent of summer in the Northern Hemisphere the wind direction changes, ash is transported to the region between AFE and ADE, and Syrtis Major expands in area.

McLaughlin's hypothesis satisfactorily accounts for the position, shape,

and certain types of variation in the dark areas but does not adequately explain the seasonal wave of darkening. It is incomprehensible that an insignificant humidification of volcanic ash should cause these phenomena. For example, consider how distinct these phenomena are in the region of Pandorae Fretum (Fig.79). Polarization curves and reflection spectra in the infrared region differ markedly for volcanic ash and limonite, and yet the polarization and infrared spectrum of the dark and bright areas are the same, except for some peculiarities such as the excess polarization in the dark areas in summer and, of course, the lower albedo of these areas. The close fit between spectrophotometric and polarimetric characteristics can be explained only on the assumption that volcanic ash does not form a continuous blanket over the surface.

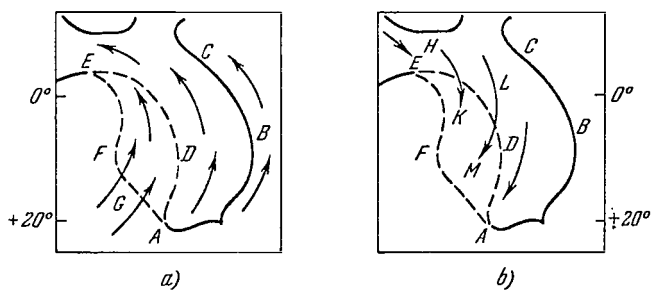

Fig.90 Interpretation of Seasonal Variations in Syrtis Major, according to McLaughlin (Ref.192).
a - At perihelion (summer in the Southern Hemisphere); b - At aphelion (winter in the Southern Hemisphere).

B.M.Vladimirskiy and K.A. /202 Lyubarskiy (Ref.193a) objected to McLaughlin's hypothesis also on the ground that it is impossible to discover any ions or groups of ions determining the coloration of the minerals (so-called chromophores) that could account for the observed coloration of the maria and its variations on the planetary scale. They arrived at this conclusion after examining all possible chromophores formed by the comparatively most abundant elements of the Periodic Table.

Volcanic activity may be a major factor in the formation of a microclimate particularly favorable to the development of a biosphere: higher temperatures, possibility of extraction of water from the soil (whereas, in the other regions, this is blocked by the permafrost). Lastly, soil fertility may increase owing to the admixture of volcanic ash (Ref.194). Combining the volcanic hypothesis with the hypothesis of vegetation furnishes a satisfactory explanation of the shape, orientation, and seasonal variations of the maria. Vegetation in itself cannot account for the shape and orientation of the dark areas, while the volcanic hypothesis alone cannot account for the seasonal wave of darkening.

The scale of volcanic activity required for this interpretation need not greatly exceed the terrestrial. For a major change in the albedo, it is sufficient to coat the surface with a layer of ash averaging 1 mm in thickness. The blanketing of an area measuring 1000 × 1000 km^2 requires one cubic kilometer of volcanic ash. During major volcanic eruptions on earth, an even greater amount of volcanic ash is sometimes ejected. The distances over which the ash is carried by winds during terrestrial eruptions also are comparable in scale to the dimensions of the Martian seas. During the strong eruptions of Vesuvius in 472 and 1631, ash was deposited as far away as Constantinople, a distance of 1200 km. In 1932 following the eruption of four volcanoes in the Andes, considerable

masses of ash fell on Buenos Aires.

V.V.Sharonov (Ref.195) attempted to account for the properties of the seas without resorting to either vegetation or volcanoes. He believed that the maria are regions in which weathering processes are highly active and a great deal of pulverized material is formed. The weathering products are periodically carried off by tradewinds. In summer, when the amount of the weathering products is at a minimum, fresh dark surface is laid bare, leading to the occurrence of a slightly anomalous polarization. Such an interpretation is extraordinarily attractive, since it introduces a minimum of unproved assumptions. However, it does not account for the presence of a seasonal wave of darkening and its relationship to the melting of the polar caps. It is unclear why the bright areas fail to react to the wave of darkening if they were to consist of the same material as the dark areas.

Attempts to attribute the amazing phenomena observed on the surface of /203
Mars to a biosphere, volcanoes, or certain wind roses are largely based on terrestrial analogies. Nevertheless, it is not excluded that the dark areas actually harbor some processes that are specific to Mars alone.

A.I.Lebedinskiy (Ref.155) and V.D.Davydov (Ref.195a) assumed that extensive water reserves may be stored underneath the apparent surface of Mars. V.D. Davydov proposed a hypothesis according to which part of the Martian surface is covered by an ocean with an extremely thick (1 - 1.5 km) ice cover, concealed by the weathering products of the continents. The photographs transmitted by Mariner IV show a large number of irregular terrain features, including ring-shaped mountains; this renders V.D.Davydov's hypothesis on a Martian ocean completely invalid. However, it might be that large amounts of H_2O exist as permafrost below the Martian surface. It is probable that a thick stratum of permafrost would retard the emergence of H_2O from the bowels of Mars to the surface, which might thus account for the low concentration of H_2O in the atmosphere.

Radar soundings of Mars carried out by the United States (Ref.196) and the USSR (Ref.197) yielded a reflection factor k = 0.02 - 0.1 (ratio of signal power measured to signal power obtained if the signal were to bounce off an ideally smooth conducting sphere of the same diameter). According to Goldstein (Ref.196), the seas exhibit a larger reflection coefficient than the continents. Statistical analysis of radar observations shows that the surface of Mars, on decimeter waves, is smoother than that of the moon.

Section 2.11 Phobos and Deimos

The Martian satellites Phobos and Deimos were discovered by Asaph Hall during the 1877 opposition. These move along near-circular orbits close to the equatorial plane of Mars. The distance (center-to-center) between Phobos and Mars is 9400 km and its synodic period is 7^h40^m; for Deimos the distance to Mars is 23,500 km and the synodic period is 30^h21^m. Phobos is the only known satellite to revolve about a planet more rapidly than the latter rotates about its own axis. Once every $5^h.5$ Phobos rises in the West of the Martian sky and sets in the East. At first, Hall believed that he was seeing not one but several internal satellites. Phobos is so close to Mars that its angular diameter visible

at its zenith from the surface of Mars is 1.5 times as large as at the horizon.

Phobos is a body of $+11^m.6$ and Deimos, a body of $+12^m.8$ (at an average opposition) (Ref.66). The color index B - V for both satellites is $0^m.6$, i.e., within the limits of error it coincides with the solar index. Hence, unlike most other satellites, these reflect solar light neutrally. The dimensions of Phobos and Deimos can be estimated only according to their brightness. For example, Phobos is 12^m weaker than Mars, which means that - at such an albedo - its radius must be 250 times smaller than the Martian radius, i.e., be equal to /204

$\frac{3400}{250} = 14$ km. The radius of Deimos, calculated by the same method, is 11 km.

I.S.Shklovskiy (Ref.198) drew attention to Sharpless' discovery of the phenomenon of secular acceleration of the motion of Phobos. He considered various effects that might account for this acceleration and found that the only possible cause would be a retardation in the exosphere (similar to the acceleration of artificial earth satellites). However, for this the mean density of Phobos would have to be 0.001 gm/cm^{-3}. This is possible only if this Martian satellite is hollow, i.e., if it is an artificial body. Shklovskiy's hypothesis was met with derision, although there is no reason to doubt that the creation of artificial heavenly bodies of such dimensions is basically feasible. V.P.Vinogradova and V.V.Radziyevskiy (Ref.199) demonstrated that the observed acceleration could be also attributed to bremsstrahlung, provided that the shape of Phobos is not spherical. A non-spherical shape should lead to fluctuations in brightness, which makes it mandatory to check whether the stellar magnitudes of both Phobos and Deimos do remain constant. Considering present conditions on Mars, it is doubtful whether intelligent life exists on the planet, but the possibility of its existence in the past cannot be precluded. From this viewpoint, it is important to estimate the age of the Martian craters. Should old craters of an age of $(1 - 2) \times 10^9$ years be discovered on Mars, this would mean that the Martian atmosphere had been rarefied in the distant past and that there had never existed any large amounts of H_2O on Mars. Otherwise, this might leave the possibility that, in the past, Mars had a developed biosphere and a civilization of high technological level. We consider it not unlikely that the satellites of Mars might represent relics of such a civilization.

CHAPTER III /205

VENUS

Section 3.1 Introduction

Figure 91 presents photographs of Venus in various phases. Since its orbit lies within earth's orbit, the phase angle φ varies from 0 (superior) to 180° (inferior conjunction). Between quadrature ($\varphi = 90°$) and inferior conjunction, Venus appears as a sickle. With approach to a conjunction, the crescent becomes more narrow and its horns or cusps elongate (phenomenon of elongation of horns); at $\varphi \approx 180°$, the crescent changes to an annulus. The elongation of horns and formation of an annulus at inferior conjunction can be explained only by the presence of an atmosphere (twilight illumination). When Venus lies exactly on the earth-sun line at inferior conjunction, it will pass in transit across the solar disk, but this occurs quite rarely. At the moment of contact between Venus and the solar disk, the latter extends, as it were, in the direction of the planet owing to refraction in the atmosphere of the planet. This effect was first observed - and correctly interpreted as a proof for the existence of an atmosphere on Venus - by M.V.Lomonosov in 1761. It became known as the Lomonosov effect. Elongation of the horns was discovered thirty years later (Schröter, 1790). The interval between two successive inferior or superior conjunctions (the synodic period of rotation) of Venus is 584 days. The true (sidereal) period of rotation is 224.7 days.

In visual observation, it is difficult to discern any surface features on Venus. Their contrast is extremely low and, moreover, the observations are impeded by the considerable gradient of brightness between limb and terminator. Dollfus (Ref.22) distinguished between markings of two types: 1) regions somewhat darker than the background, which apparently are real and 2) shadows along the limb, which probably are due to physiological characteristics of the eye. Occasionally, one or several low-contrast features are seen but markings are usually absent. Figure 91 gives composite photographs of Venus, prepared by Camichel from plates obtained with the 38-cm reflector at Pic du Midi. These photographs show a strong contrast. Presumably, the observed features are clouds, although Dollfus points out that a comparison of drawings made on successive /206 days shows that the positions of the features coincide more often than could be expected of a random distribution. It is intriguing that these diffuse dark shadings, alternately disappearing and reappearing, remain in a roughly constant position with respect to the terminator.

The extremely poor visibility of markings on the disk of Venus suggests that the atmosphere of the planet has a considerable optical thickness. The instability of the markings indicates substantial dust pollution of the atmosphere. This is also apparent from the yellowish color of the planet (cf. Sect.3.2); if Rayleigh (gas) scattering would predominate, Venus would have to be blue. The cloud-bound nature of the planet makes it virtually inaccessible to optical observations.

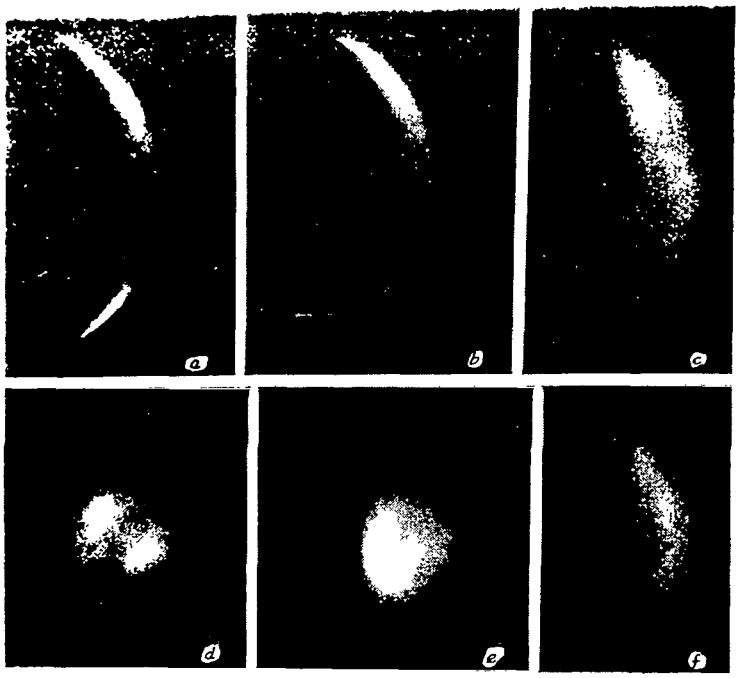

Fig.91 Composite Photographs of Venus in Yellow Light.
a - Oct.3,1943, k = 0.189 (illuminated part of the disk);
b - Oct.9,1943, k = 0.242; c - Nov.6,1943, k = 0.446;
d - Sept.17,1942, k = 0.963; e - July 26,1942, k = 0.866;
f - Nov.22,1943, k = 0.534 (Ref.22).

Photographs of Venus in ultraviolet light ($\lambda_e \approx 3500$ Å) distinctly show /207
systems of bright patches and roughly parallel bands (Fig.92). These markings probably are due to scattering in higher and more tenuous clouds. They are much more stable than the visually observed markings.

Measurements of the diameter of Venus naturally refer to the top of the cloud layer rather than to the solid body of the planet. To exclude the distorting effect of phase, the diameter is usually measured at phase angles close to 0° and 180°. In the former case, the accuracy is less since the distance to the planet is maximal, the irradiation effect (apparent displacement of the boundary of the bright field in direction of the dark background) is considerable, and the phase remains appreciable. In the latter case, the diameter of the annulus is measured or, during transit across the solar disk, the diameter of the dark planet against the background of the photosphere is measured; in this case, a different type of interference occurs: for example, during transit across the disk the diameter decreases owing to refraction in the atmosphere of Venus (Lomonosov effect). De Vaucouleurs (Ref.78), in analyzing measurements made with various methods, found that the radius of Venus is

$$R_\varphi = 6120 \pm 8\,km. \qquad (3.1)$$

Measurements at inferior conjunction usually give a larger diameter. For example Smith (Ref.202) obtained

$$R_{\varphi} = 6155 \pm 3\,km \tag{3.2}$$

Observations of the occultation of a star by Venus also can be used for determining the diameter. D.Ya.Martynov (Ref.201) in observing the occultation of Regulus derived a value which, in satisfactory agreement with eq.(3.1), is

$$R_{\varphi} = 6100 \pm 34\,km. \tag{3.3}$$

/208

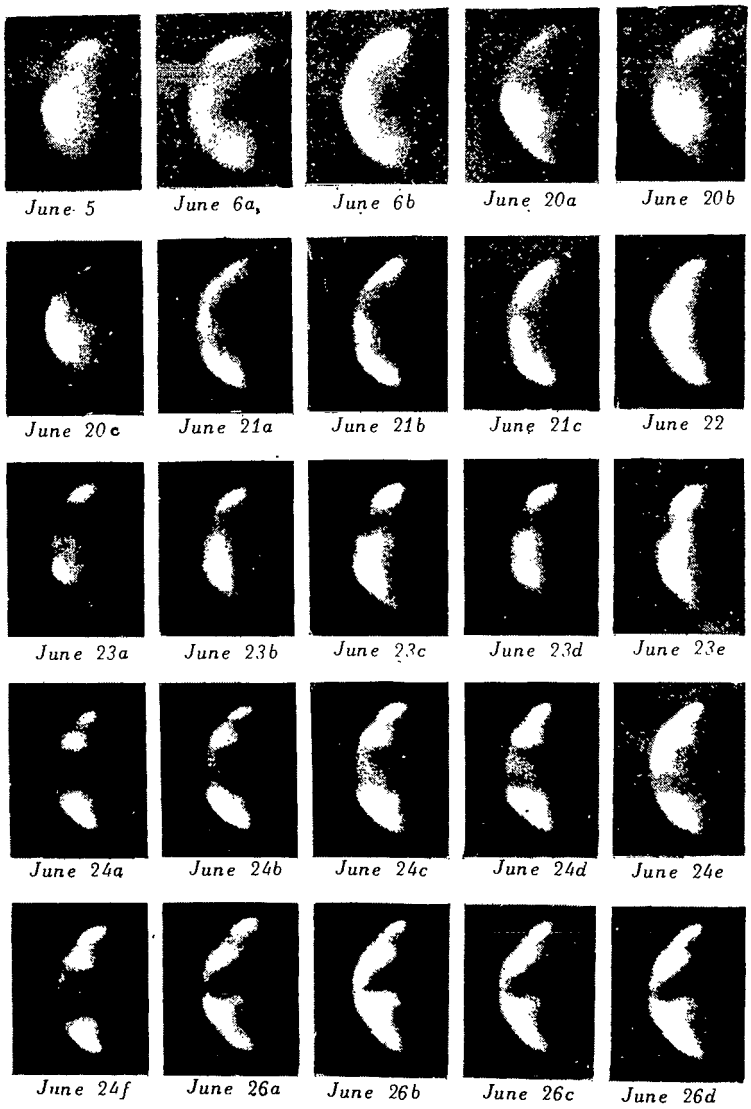

Fig.92 Photographs of Venus in Ultraviolet Light (Ref.200).

The considerable difference between eq.(3.2) on the one hand and eqs.(3.1), (3.3) on the other can be attributed to real properties of the cloud layer of Venus. If the cloud layer lacks a sharp boundary (as also indicated by other data), the forward-extended scattering indicatrix may lead to a marked displacement of the apparent top of the cloud on transition from $\varphi = 0^\circ$ to $\varphi = 180^\circ$

Determination of the mass of a planet without satellites is a rather difficult problem. This is usually based on studies of the perturbation exerted on the motion of other planets. The mass of Venus was determined more accurately by measuring the trajectory of the American spacecraft "Mariner II" which in December 1962 flew past at a distance of 32,000 km from the planet's surface. According to Brouwer and Clemence (Ref.77), the mass of Venus is /209

$$M_\varphi = \frac{M_\odot}{408\,600 \pm 200} = (0.81366 \pm 0.00040)\, M_\oplus. \tag{3.4}$$

An investigation of the trajectory of Mariner II (Ref.203) indicates the mass to be

$$M_\varphi = (0.81485 \pm 0.00015)\, M_\oplus. \tag{3.5}$$

Taking the altitude of the apparent cloud top as $z_1 = 60$ km (see below), eqs.(3.1) and (3.5) will yield the mean density

$$\rho_\varphi = 5.25\, gm \cdot cm^{-3} \tag{3.6}$$

and the acceleration due to gravity at the subjacent surface

$$g_\varphi = 880\ cm \cdot sec^{-2}. \tag{3.7}$$

Thus, Venus is very close to Earth in diameter, mass, and mean density. For a long time it had been assumed that this analogy also extends to other characteristics. Recently, however, this was found not to be so. The cloud layer greatly complicates studies of the physical characteristics of the atmosphere and surface of Venus. Hence our knowledge of Venus is even more schematic than that of Mars. However, the use of radio astronomy methods (including radar sounding) and of methods of infrared engineering has yielded a number of more credible data on the properties of the atmosphere and surface of Venus.

Section 3.2 Determination of the Rotation Period and Other Results of Radar Sounding of Venus

The absence of sufficiently distinct features on the planetary disk prevents a reliable estimation of the period and direction of rotation from a displacement of such markings. Dollfus (Ref.22), assuming that the perceptible dark shadings with their occasional low contrast pertain to the surface, found that the rotation is direct and the period of rotation of Venus equals its period of revolution about the sun ("synchronous rotation"), i.e., the planet keeps the same face turned permanently toward the sun. Schiaparelli and Antoniadi also assumed that Venus rotates synchronously. The basis for this conclusion was that

the dark shadings tend to occupy roughly the same position with respect to the terminator. However, as Dollfus himself mentioned, these dark markings may represent clouds connected with the topography of the terminator.

Ross (Ref.200), from the displacement of individual markings on photographs in ultraviolet light, estimated the period of rotation as being 10 - 30 days. Kuiper (Ref.204), assuming that the bands on these photographs are parallel to the equator, found the inclination of the plane of the equator to the plane of the ecliptic to be approximately 40°. A new estimate of the rotation period was derived from photographs in ultraviolet light by Boyers and Camichel (Ref.205): they found a period of four days. /210

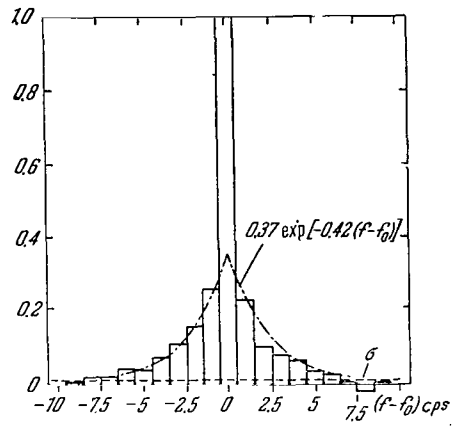

Fig.93 Spectrum of Radar Pulse Bounced Off-Venus. Ordinate: reflected power in relative units (Ref.210).

Attempts to utilize the Doppler effect to determine the rotation period of Venus have been made repeatedly, but only a lower limit could be established: A.A.Belopol'skiy obtained $T \geq 2$ weeks (Ref.206). Richardson (Ref.207) arrived at roughly the same value: $T > 14$ days if the rotation is direct and $T > 5$ days if the rotation is retrograde. Slipher (Ref.208) found $T \geq 30$ days.

In 1956, the Lincoln Laboratory of the Massachusetts Institute of Technology carried out the first radar sounding of Venus (Ref.209). In subsequent years the experiment was repeated by both this organization and by many others: Jodrell Bank Observatory in Great Britain, Institute of Radio Engineering and Electronics of the Academy of Sciences USSR, Laboratory of Reactive Motion of the California Institute of Technology, and Radar Observatories in Arecibo (Puerto Rico) and Jicamarca (Peru).

Results from radar soundings of Venus in the wavelength range of 3.6 to 780 cm have recently been published (Table 45). Originally, the purpose of this radar sounding was a more precise determination of the astronomical unit, but beginning with 1961 the emphasis in studies was shifted to determination of the physical characteristics of the planet itself and primarily of its rotation period. /211

The frequency of a monochromatic pulse, bounced off the surface of Venus, will blur due to rotation of the planet (Fig.93) owing to the Doppler effect. The period of rotation can be estimated from the frequency bandwidth of the reflected pulse. The peak with zero frequency shift in Fig.94 is produced by specular reflection from the central portion of the planetary disk. With increasing distance from the center, the power of the reflected signal will decrease more or less rapidly depending on the degree of roughness of the planet. This complicates the estimation of the total frequency bandwidth, particularly for low signal-to-noise ratios. Therefore, first attempts to determine the rotational velocity according to the frequency bandwidth of the bounced pulse led

TABLE 45

/212, /213

RESULTS OF RADAR STUDIES OF VENUS

Year	λ, cm	Rotation: Period, Days	Rotation: Direction	Rotation: North Pole α	Rotation: North Pole δ	Rotation: Inclination of Equator to Ecliptic	Reflection Coefficient, K	Dielectric Constant ε	Mean Inclination of Reflecting Sector of Surface	Observatory	Ref. Source	Remarks
1956	68	—	—	—	—	—	1	—	—	M	(209)	
1958	76	—	—	—	—	—	0.02	—	—	JB	(226)	
1958	68	—	—	—	—	—	0.052	—	—	M	(227)	
1961	68	225^{+275}_{-110}	Direct	—	—	—	0.11	—	—	M	(211)	Rotation was investigated according to spectrum width
1961	38	9	»	—	—	—	0.1	—	—	IRE	(212)	»
1961	12.5	200—400	»	—	—	—	0.10—0.15	—	—	C	(216)	»
1962	73	225	»							JB	(216a)	»
1962	43	200—300	Retrograde	—	—	0	0.12—0.18	—	—	IRE	(210)	»
1962	12.5	250	»	21^h16^m	69°	18°	0.0975	3.75	4°—7°	C	(214)	Rotation was determined according to displacement of the spectral component and according to spectral width, with discrimination by distance
1962	12.5	250	»	$16^h44^m \pm$ $\pm 1^h$	78 ±15°	16				C	(215)	
1962	3.6	—	—	—	—	—	0.009±0.003	—	—	M	(217)	Smoothness factor q = 0
1962	600	230±50	—	—	—	—	0.2	—	—	J	(218)	Smoothness markedly greater than for the moon
1962	780	—	—	—	—	—	0.2	—	—	C	(219)	
1964	12.5	249±7	Retrograde	17^h04^m	+67°	4	0.115±0.01	—	—	C	(219a)	New components discovered in the spectrum
1964	70	247±5	»	$18^h11^m \pm$ $\pm 15^m$	+71° 5±4°	6	—	—	—	C	(219a)	
1964	43	230±25	»	—	—	—	0.19			IRE	(220a)	
1964	73	200±100	»	—	—	—	—	—	—	JB	(216a)	

Notation: M - Massachusetts Institute of Technology (United States); C - California Institute of Technology (United States); JB - Jodrell Bank (Great Britain); IRE - Institute of Radio Engineering and Electronics, Acad. Sci. USSR; J - Jicamarca Observatory (Peru).

to contradictory results: During the inferior conjunction of 1961 the Lincoln Laboratory (Ref.211) derived direct rotation with a period of approximately 220 days whereas the Institute of Radio Electronics (IRE) obtained a period of 9 days (Ref.212). This discrepancy could not be attributed to the difference in the wavelengths employed since the American sounding was made at λ 68 cm and that of the Soviet Union at λ 43 cm (Ref.213).

/214

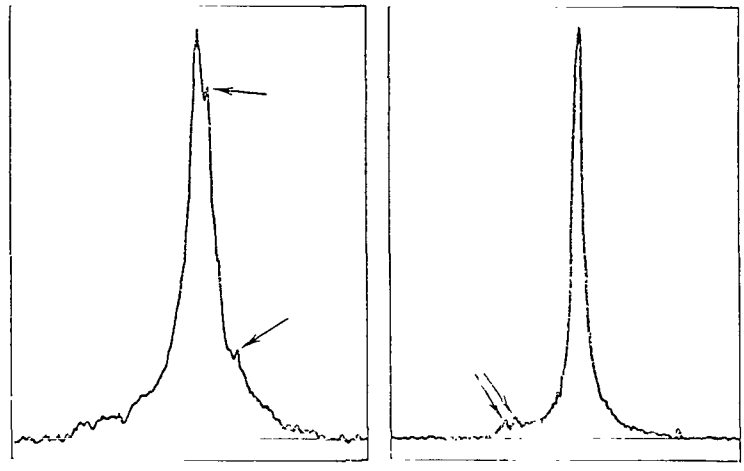

Fig.94 Components of Spectra of the Bounced Pulse. The left spectrum was obtained on May 19,1964 and the right spectrum on July 8.

During the inferior conjunction of 1962 the front of research became greatly broadened. The sensitivity of radar was increased greatly, and new facilities were put into operation. The periods determined in 1961 proved to be erroneous. The most reliable results were obtained at the California Institute of Technology [Carpenter (Ref.214) and Goldstein (Ref.215)] for λ 12.5 cm. The transmitter power was only 13 kw. A parabolic antenna of 25 m diameter was used. The study was carried out virtually in the regime of continuous emission: The transmitter radiated a monochromatic wave for several minutes, after which the system was switched to reception. The spectrum of reflected emission was investigated with a high resolving power, which made it possible to study its fine structure. It was found that the spectrum of the reflected signal contains a constant component whose spectral position changes gradually. The rate of displacement of this component can be used to estimate the sidereal period, which is found to be 1200 days if the rotation is direct and 230 days if it is retrograde. The frequency bandwidth of the reflected signal does not fit the first assumption but satisfactorily fits the second.

Apparently the component in the spectrum of the reflected pulse is due to bouncing off some feature of surface relief or off a sector with a higher reflection factor. Since the apparent rotation due to the relative orbital motion of Venus and Earth and the axial rotation of Venus occur differently before and after inferior conjunction, the direction of rotation can be assessed from the

change in the frequency bandwidth. This method has been used independently in the experiment by the California Institute of Technology, also yielding a retrograde rotation with a period of ~250 days. To enhance the accuracy, use was made of discrimination by distance, which precluded the peak in specular reflection. On 1962, the Soviet IRE team (Ref.210) arrived at a retrograde rotation with a period of 200 - 300 days, according to the shape of the frequency band. Goldstein (Ref.215) and V.A.Kotel'nikov et al. (Ref.210) also found that the plane of the Venus equator is roughly parallel to the plane of the ecliptic. According to Carpenter and Goldstein, the inclination of the plane of the equator to the plane of the ecliptic is $\epsilon = 17 \pm 15^{\circ}$.

Experiments performed in 1964 (Ref.119) at the California Institute of Technology yielded an even more accurate value of the period of rotation: 249 ± 7 days. The inclination was found to be 6°. Lastly, observations with the 300-m antenna in Puerto Rico gave 247 ± 9 days and an inclination of 4°. Retrograde rotation also was definitely confirmed. /215 The experiments of the California team revealed new components of the spectrum of the reflected pulse (Fig.94) and led to compilation of a chart of regions with higher reflection coefficients (Fig.95). The sidereal period of 248 days corresponds to a solar day of 120 days. During a single revolution of Venus about the sun the latter rises and sets twice.

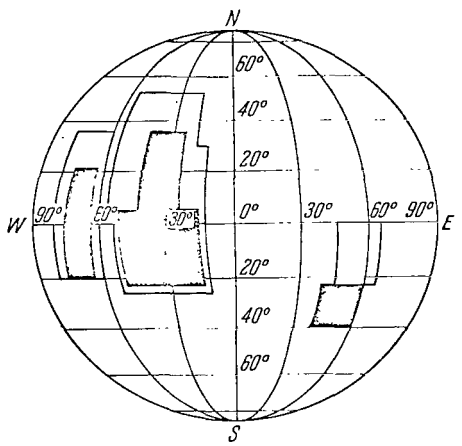

Fig.95 Chart of Regions with Higher Reflection Coefficient.

In the first experiment (Ref.209), the radar reflection coefficient at λ 68 cm proved unexpectedly high: ~1. Subsequently, however, this result was not confirmed. During the experiments in 1961, it was found that k = 0.11 at λ 68 cm (Ref.211), k = 0.1 at λ 38 cm (Ref.213) and k = 0.10 - 0.15 at λ 12.5 cm (Ref.216). During the 1962 experiments, the values obtained were k = 0.0975 at λ 12.5 cm (Ref.214) and k = 0.12 - 0.18 at λ 38 cm (Ref.210). Apparently, within the decimeter wave range it can be assumed that everywhere

$$k = 0.12 \pm 0.03 \qquad (\lambda = 12 \div 68\ cm).$$

The low values of k obtained in 1958 (Jodrell Bank, k = 0.02; Lincoln Laboratory, k = 0.052; cf. Table 45) probably can be disregarded. During the 1962 inferior conjunction, the radar reflection coefficient of Venus was measured at centimeter wavelengths [λ 3.6 cm (Ref.217)] and at meter wavelengths [λ 6 m (Ref.218) and λ 7.8 m (Ref.219)] and was found to be one order of magnitude lower at centimeter wavelengths than within the decimeter wavelength range:

$$k = 0.009 \pm 0.003 \qquad (\lambda = 3.6\ cm),$$

while at meter wavelengths it was somewhat higher:

$$k \approx 0.2 \qquad (\lambda = 6 - 7.8m).$$

The radar reflection coefficient depends on the dielectric constant and the dimensions of the surface inhomogeneities compared with the wavelength. Using as the criterion the observed dependence of reflected power on the distance to /216 the center of the disk (or, which comes to the same, the discrimination by distance), the mean inclination and the dielectric constant can be separately determined as a function of k. Carpenter (Ref.214) found $\varepsilon \approx 3.75$ from observations at λ 12.5 cm, which corresponds to an extremely arid sandy or rocky soil. The mean-square inclination is $\alpha = 4 - 7^\circ$, i.e., is appreciably higher than for the moon. Muhleman (Ref.220) made a statistical analysis of the radar observations and found $\alpha = 2^\circ.3 - 7^\circ.4$ at λ 12.5 cm (with the lower values predominating) and $\alpha = 2^\circ.3 - 2^\circ.9$ at λ 68 cm. At meter wavelengths, Venus is smoother than the moon. Figure 96 gives the time curve of the pulse bounced off Venus and off the moon at λ 6 m (Ref.218): Venus showed a smaller pulse rise time. For Venus, the greater portion of the power transmitted at λ 6 m is reflected from 1/40 of the apparent disk, and for the moon - from 1/20. Thus, at decimeter and meter wavelengths Venus is also smoother than the moon. A completely different picture is obtained at centimeter wavelengths: at λ 3.6 cm, the specular peak (similar to that shown in Figs.93 - 94) is absent and the shape of the reflected emission spectrum indicates that the entire surface of the planet is covered with inhomogeneities commensurate with this wavelength. At λ 3.6 cm, Venus displays the same reflection pattern as the moon in the optical region (smoothness factor q = 0). The low reflection coefficient at λ 3.6 cm cannot be attributed to surface roughness. For such a low reflectivity the surface material or the atmosphere must absorb radio waves in the centimeter range.

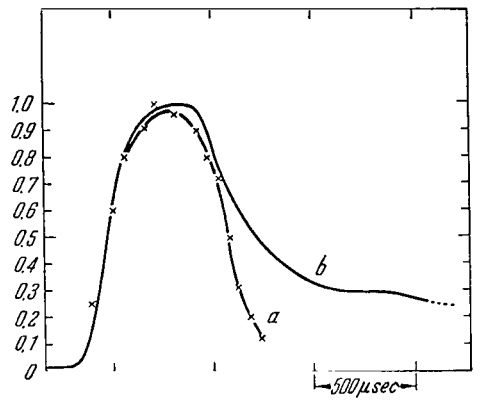

Fig.96 Radar Pulse Rise Time (λ 6 m), Reflected from Venus (a) and from the Moon (b), Allowing for Difference in Radii. Ordinate: reflected power in relative units (Ref.218).

Levi and Schuster (Ref.224) attempted to extract additional information on the smoothness from the depolarization of reflected emission. The ratio of the power of the signal reflected with an opposite polarization to the power of the signal reflected with the same polarization as that of the transmitted signal is 11.5 db, i.e., approximately as much as for the moon. /217

Some of the early hypotheses assumed that Venus is entirely covered with a purely aqueous ocean (Ref.221) or with a watery ocean with an overlay of hydrocarbons (Ref.222). The absence of ideal smoothness does not contradict these hypotheses (waves are able to persist on the surface of an ocean), but the dielectric constant determined by radar sounding is much lower than that of water (ε = 80) and somewhat higher than that of liquid hydrocarbons (ε = 2 - 3). Ap-

parently, the hypothesis of a watery ocean is completely out of the question. Kuz'min and Clark (Ref.223) found $\epsilon = 2.5$ from observations of the polarization of the natural radio emission of Venus. This value of ϵ may fit the hydrocarbon hypothesis, but other data (high temperature) speak for a definite rejection of any "oceanic" hypotheses.

During the 1962 inferior conjunction, an attempt was made (Ref.224) to detect Faraday rotation in the reflected signal (rotation of the plane of polarization during passage across a plasma in a magnetic field). Compared with the earth's ionosphere, no excess rotation was detected. The authors (Schuster and Levi) point to three possible causes: 1) The intensity of the magnetic field of Venus is markedly lower than the intensity of the earth's magnetic field; 2) the electron density is lower than in the earth's ionosphere; 3) the orientation of the magnetic axis is unfavorable. Apparently the first cause is the most significant, since the onboard magnetometer of Mariner II, during its flyby of Venus, failed to record any increase in the intensity of the magnetic field compared with the interplanetary intensity. These observations showed that the magnetic moment of Venus is at least 20 times lower than that of the earth (Ref.225).

Section 3.3 Albedo, Phase Curve, Polarization

The visual spherical albedo of Venus is close to 0.7 - 0.8, but observations by various authors show a fairly large scatter. Table 46 presents values of the geometric albedo p for three wavelengths, calculated by Harris (Ref.66) from the results of visual photometry by Danjon (Ref.228) as well as from his own colorimetric observations in the system U, B, V. The visual phase integral (cf. Sect.1.6) is $Q = 1.296$ according to Danjon (Ref.228), so that the visual spherical albedo is $A_V = 0.76$.

TABLE 46

GEOMETRIC ALBEDO OF VENUS IN THE U, B, V SYSTEM, ACCORDING TO HARRIS (REF.66)

	λ_e, Å	p
U	3530	0.353
B	4480	0.492
V	5540	0.586

TABLE 47

/218

GEOMETRIC AND SPHERICAL ALBEDO OF VENUS IN THE U, B, V SYSTEM ACCORDING TO OBSERVATIONS AT LOWELL OBSERVATORY [KNUCKLES, SINTON AND SINTON (REF.229)]

	p	Q	A
U	0.810	0.649	0.53
B	1.026	0.763	0.78
V	0.925	0.888	0.87

Photoelectric photometry of Venus in the system U, B, V carried out at Lowell Observatory [Knuckles, Sinton and Sinton (Ref.229)] led to widely differing findings (cf. Table 47) and, in particular (Ref.229), to

$$A_V = 0.87.$$

Figure 97 gives visual phase curves of Venus obtained by various authors, while Table 48 shows the visual stellar magnitudes adjusted to unit distance (cf. Sect.1.6) for $\varphi = 0$ and 50°, together with the values of the phase integrals. The mean $V(1; 0^\circ) = -4, 40$. Hence, eq.(1.114) yields $p = 0.65$ and $A_v = 0.70$, assuming $V_\odot = -26^m.81$ and applying the estimate (3.1) of the radius of Venus.

TABLE 48

VISUAL MAGNITUDES $\overline{V}(1; 0^\circ)$, $\overline{V}(1, 50^\circ)$ AND PHASE INTEGRAL Q ACCORDING TO VARIOUS INVESTIGATORS

Author	$V(1; 0^\circ)$	$V(1; 50^\circ)$	Q
Müller (Ref.230)	$-4^m.16$	$-3^m.44$	(1.194)
Müller (Ref.231)	—	—	1.078
King (Ref.232)	—	−3.50	—
Danjon (Ref.228)	−4.27	−3.71	1.296
Knuckles, et al. (Ref.229)	−4.76	−3.69	0.888
Mean	−4.40	−3.58	1.087

All colorimetric and spectrophotometric observations point to a decrease in reflectivity in the blue and ultraviolet spectrum regions, but the quantitative findings diverge greatly. For example, observations by N.A.Kozyrev (Ref.233) show this decrease to be much sharper than observations by I.N.Glushneva (Ref.234) and Spinrad (Ref.249). In all three studies, spectrographs of low dispersion /219 were used. It might be that the albedo in the violet and ultraviolet spectrum regions undergoes marked fluctuations associated with the formation, dissolution, and movement of "ultraviolet clouds". V.V.Avramchuk and I.K.Koval' (Ref.234a) showed that the decrease in reflectivity in the ultraviolet spectrum region is consistently lower near the terminator than in the subsolar zone. Apparently, the difference in phases and in orientation of the slit on the disk also may partially account for the difference in findings.

Figure 98 gives the wavelength dependence of the Venus-to-Sun intensity ratio, plotted from data on infrared spectrophotometry performed near superior conjunction by the author (Ref.235, 236) in the region $\lambda\lambda$ 1-4 μ. Results on relative spectrophotometry in the region $\lambda\lambda$ 0.7-1.0 μ are presented elsewhere (Ref.123). The curve in Fig.98 is continued in direction of shorter wavelengths according to the observational findings of other authors and so calibrated that, for $\lambda = 5550$ Å, it would give the geometric albedo $p = 0.65$. Thus this curve can be regarded as the dependence of the geometric albedo on the wavelength. Assuming $Q = 1.087$ for all wavelengths, the integral spherical albedo [cf. eq.(1.116)] will be

$$A_i = 0.73.$$

In the near infrared region, the albedo decreases owing to the presence of strong CO_2 absorption bands.

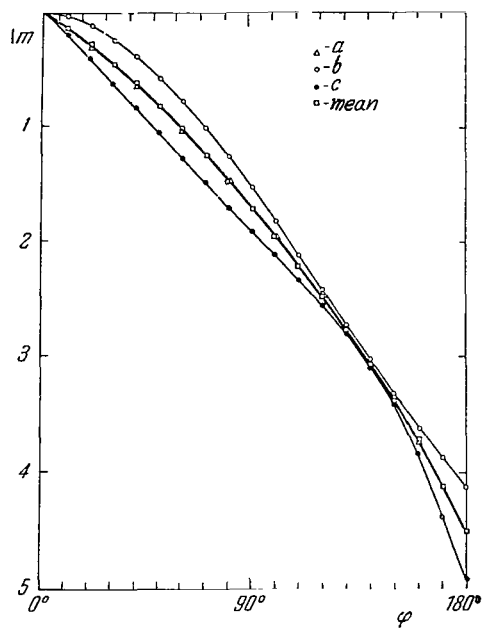

Fig.97 Phase Curves of Venus according to Müller (a), Danjon (b), Knuckles, Sinton and Sinton (c).

A semi-infinite atmosphere with pure scattering has a spherical albedo of A = 1. The monochromatic albedo of Venus always is less than unity, which may be attributed /220 to two factors: 1) presence of true absorption in the continuous spectrum; 2) finite optical thickness of the atmosphere. It is not excluded that both effects operate simultaneously, but more probably either one predominates. In addition to CO_2 bands, true absorption definitely predominates in the region $\lambda > 2.8\ \mu$, where the albedo of Venus drops to nearly 1% (in the neighborhood of λ 2.5 μ, $p \approx 0.40$ and the scattering coefficient cannot change greatly at such a minor change in λ). Apparently, true absorption also predominates in the region $\lambda < 4500$ Å. It would be of interest to clarify whether true absorption occurs in the broad intermediate region of $0.45 < \lambda < 2.50\ \mu$.

V.V.Sobolev, Horak, Harris, N.P.Barabashev and V.I.Yezerskiy (Ref.237, 238, 239, 66, 240) regarded the atmosphere as semi-infinite and calculated the albedo a of a unitary scattering process.

V.V.Sobolev and other authors (Ref.240, who used Sobolev's method) directly determined the scattering indicatrix from the observations. Horak presupposed isotropic scattering, while Harris assumed a Rayleigh phase function. Table 48a presents the results of these calculations. The indicatrices given elsewhere (Ref.237, 238, 240) are similar. One of these (Ref.238) is presented in Fig.99. From Table 48a it follows that the calculated albedo of the unitary scattering process decreases with a reduction in the elongation of the indicatrix, as was to be expected (cf. Sect.1.6).

G.V.Rozenberg's theory (cf. Sect.1.5) gives the following brightness coefficient for a semi-infinite atmosphere

$$\rho = he^{-S\eta\sqrt{\beta}}, \qquad (1.104a)$$

where /221

$$\beta = \frac{k}{\sigma} = \frac{1-a}{a},$$

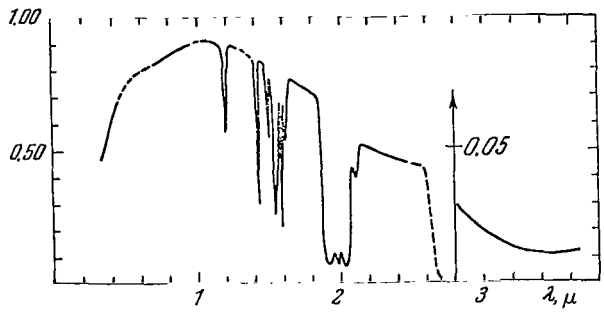

Fig.98 Venus-to-Sun Intensity Ratio as Function of Wavelength.

TABLE 48a

VISUAL ALBEDO "a" OF THE UNITARY SCATTERING PROCESS, ASSUMING A SEMI-INFINITE ATMOSPHERE

Author	Indicatrix	a
V.V.Sobolev (Ref.237)	Empirical	0.989
V.V.Sobolev (Ref.238)	»	0.987
N.P.Barabashev and V.I.Yezerskiy (Ref.240)	»	0.995
Harris (Ref.66)	$\frac{3}{4}(1+\cos^2\gamma)$	0.975
Horak (Ref.239)	1	0.95

S and h are angle functions close to unity; η is a parameter dependent on the indicatrix. For not too high an angle to the normal, we have $S\eta \approx 2$ for isotropic and Rayleigh scattering and a value of 5 for very extended indicatrices corresponding to $\frac{2\pi r}{\lambda} = 20$ at m = 1.3 (terrestrial clouds). Putting $\rho = p = 0.65$ and h = 1, we have $\beta = 0.045$, a = 0.95 for isotropic and Rayleigh scattering and $\beta = 0.008$, a = 0.99 for a very extended indicatrix.

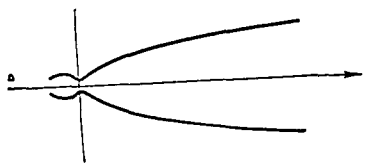

Fig.99 Scattering Indicatrix in the Atmosphere of Venus (Ref.238).

V.V.Sobolev's method utilizes only the first two terms in the expansion of the indicatrix in Legendre polynomials. Checking this method against terrestrial aerosols shows that the indicatrices calculated in this manner may differ greatly from real indicatrices. The indicatrix shown in Fig.99 is much less extended than the scattering indicatrices in terrestrial clouds [cf.(Ref.61)]. The asymmetry of the indicatrix is characterized by the quantity $\varkappa_1$ of the second term in its expansion in Legendre polynomials. According to Sobolev (Ref.238), $\varkappa_1 = 1.43$, and the tables by Clark et al. (Ref.241) gave $\frac{2\pi r}{\lambda} \approx 2$ if the refractive index is m = 1.3. There is reason to believe (see below) that, actually, the parameter $\frac{2\pi r}{\lambda}$ is higher and comes close to 10 - 20, i.e., to values typical of terrestrial clouds.

Now let us consider another possibility: Scattering in the visible and near infrared regions of the spectrum is conservative and the albedo of the planet is always less than unity owing to the finite optical thickness of the atmosphere. Then, from eq.(1.102) it is possible to estimate the total optical /222

thickness τ_0:

$$\rho = h - \frac{g(\mu_1)\, g(\mu_2)}{\frac{\tau_0}{l} + \frac{A_s}{1 - A_s}}, \qquad (1.102a)$$

where l varies from 1.3 for isotropic and Rayleigh scattering to 6 for scattering in clouds with $\frac{2\pi r}{\lambda} = 20$. Putting $\rho = p = 0.65$, $h = g = 1$, and $A_s = 0$, we have

$$\tau_0 = \frac{l}{0.35}, \qquad (3.8)$$

whence

$$4 < \tau_0 < 20. \qquad (3.9)$$

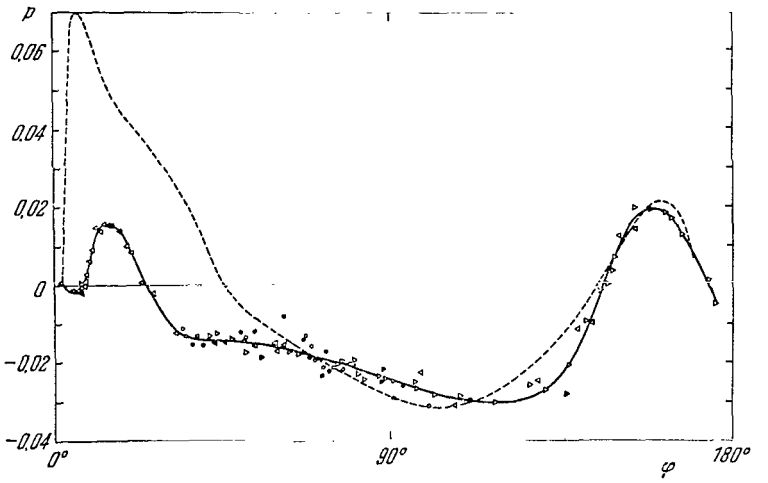

Fig.100 Visual Polarization Curve of Venus according to Lyot (Ref.242).
The broken line represents the laboratory curve for water droplets of 2.5 μ diameter.

The underlying surface reduces this estimate, but if its albedo is low ($A_s < 0.2$) then the effect of the subjacent surface can be neglected in the adopted approximation. If the hypothesis considered is true, then the dependence $p(\lambda)$ in the region 0.45 - 2.5 μ is attributable to the wavelength dependence of the mean /223 scattering coefficient and τ_0. The maximum value of $p(\lambda)$ is reached at $\lambda \approx 1$ μ. The wavelength dependence of the scattering coefficient is described by a curve of the kind shown in Fig.32. It may be assumed that the peak of the curve $\left(\frac{2\pi r}{\lambda} \approx 6\right)$ corresponds to the maximum $p(\lambda)$. Then, $r \approx 1$ μ and in the visible

region $\frac{2\pi r}{\lambda} \approx 12$ and $\tau_0 \approx 15 - 20$.

Figures 100 - 102 give the polarization curves of Venus plotted by various authors [Lyot (Ref.242), Kuiper (Ref.243), Gehrels and Samuelson (Ref.244)]. Lyot's curve was obtained from visual observations and Kuiper's, from observations in the infrared region. Gehrels and Samuelson worked with a set of filters from 3250 to 9900 Å. Lyot established that a mist of water droplets of 1 μ radius each would give a visual polarization curve greatly resembling the Venusian. Conversely, Kuiper (Ref.243) found that, in the infrared region, no such resemblance exists. A possible reason for this discrepancy might be that the droplets or crystallites constituting the Venusian clouds, in this portion of the spectrum, have an absorption coefficient different from H_2O.

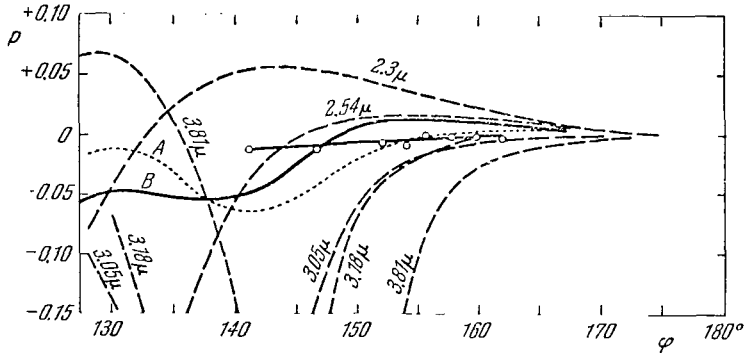

Fig.101 Polarization Curve of Venus for λ 2 μ (Circles) and Theoretical Polarization Curves for Water Droplets of Various Diameters (Ref.243).

It is difficult to make a choice between the two above hypotheses on the basis of photometric data alone. The relative intensities of weak CO_2 lines (cf. Sect.3.4) indicate conservative scattering in the near infrared region. Lastly, the presence of conservative scattering in the visible and near infrared regions is implied by the greenhouse model of the atmosphere, without which it /224 appears impossible at present to account for the high brightness radio temperatures. Note that the albedo of the unitary scattering process, a = 0.99 for τ = = 20 and $2\pi r/\lambda \approx 10 - 20$ in itself reduces the flux of solar radiation transmitted by the atmosphere by a factor of several units. The greenhouse model stipulates $a \lesssim 10^{-3}$. This requirement is more than satisfied in terrestrial clouds: in the visible region of the spectrum, these clouds have an albedo of $a \approx 10^{-7}$.

These considerations can be summed up as follows: Most probably, scattering in the atmosphere is conservative in the interval λλ 0.45-2.5 μ and is due to transparent particles with a mean radius $r \approx 1$ μ at m = 1.3. If m markedly differs from 1.3, the radius may be different, but the indicatrix and wave dependence of the scattering coefficient will be the same as for $2\pi r/\lambda \approx 10 - 20$ (for λ 0.55 μ) and $m \approx 1.3$.

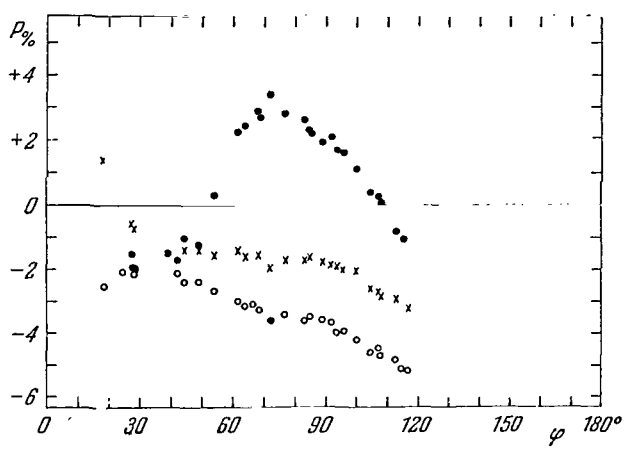

Fig.102 Photoelectric Polarization Curves of Venus in the Range λλ 3250-9900 Å (Ref.244).

N.P.Barabashev (Ref.6) discovered that maximum brightness is displayed by those sectors of the planet for which the angles of incidence and reflection are mutually equal and lie on different sides of the normal. Similar results were obtained by V.I.Yezerskiy (Ref.245). Originally, this effect was ascribed to the influence of the underlying surface which thus should exhibit certain specular properties. These observations were even interpreted as an argument in favor of a /225 Venusian planetary ocean. In reality, this phenomenon apparently has nothing to do with the subjacent surface. As shown by corresponding calculations [cf. (Ref.61)] and observations, clouds consisting of particles with elongated indicatrices may themselves produce a specular effect of this kind.

Note that for $\tau_0 = 20$ and an elongated indicatrix ($l = 6$), large and sufficiently contrasting surface features of dimensions greatly exceeding the height of the clouds can be discerned on the planet disk, although only up to a point. In fact, eq.(1.102a) yields $\rho = 0.72$ at $A_s = 0.20$ and $\rho = 0.70$ at $A_s = 0.05$. The contrast amounts to 3%. In isolated instances, the contrast of the diffuse markings observed on the disk of Venus attains 10 - 12% (Ref.252).

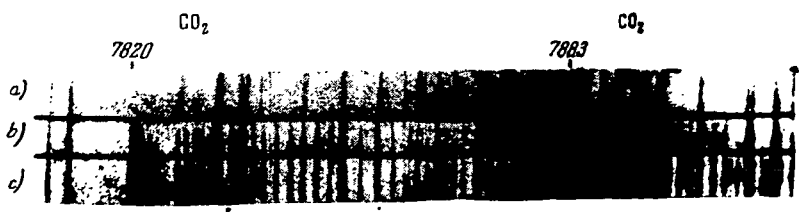

Fig.103 Spectrum of the Sun (a) and Venus (b) and (c) in the Infrared Region according to Dunham (Ref.111). (c - Spectrum recorded with broadening.)

Section 3.4 Carbon Dioxide Absorption Bands

a) Identification of CO_2 bands and their relative intensity. In 1932, Dunham and Adams (Ref.111) photographed the spectrum of Venus in the region of near λ 8000 Å, with the object of searching for H_2O lines. They found no H_2O lines but, on the other hand, discovered two unknown absorption bands near λ 7820 and λ 7883 with clearly discernible heads and a regular structure characteristic

TABLE 49

/226

ABSORPTION BANDS DISCOVERED IN THE SPECTRUM OF VENUS
(REF.15, 38, 233, 235, 236, 246, 248, 249)

λ_{meas}, μ	W, Å	Identification	λ_{lab}	Remarks
(0.4120)		—	—	Observed by N. A. Kozyrev (Ref. 223); not confirmed by other observers (Ref. 249)
(0.4372)		—	—	
0.7158		$C^{12}O_2^{16}$ $12^05—00^00$	0.7158	(236)
0.7820	1	$C^{12}O_2^{16}$ $10^05—00^00$	0.7820	(236)
0.7883		$C^{12}O_2^{16}$ $02^05—00^00$	0.7883	(236)
0.8689	1.6	$C^{12}O_2^{16}$ $00^05—00^00$	0.8689	(248)
0.8736		$C^{12}O_2^{16}$ $01^15—01^10$	0.8736	(236)
1.0362		$C^{12}O_2^{16}$ $20^03—00^00$	1.0362	(236)
1.0462	3.5	$C^{12}O_2^{16}$ $12^03—00^00$	1.0462	(236)
1.0627		$C^{12}O^{81}$ $04^03—00^00$	1.0327	(236)
1.138		H_2O	1.138	Discovered by Strong et al. owing to observations from a balloon (274)
1.206	.42	$C^{12}O_2^{16}$ $10^03—00^00$	1.206	W according to (Ref. 15)
1.220	30	$C^{12}O_2^{16}$ $02^03—00^00$	1.221	W according to (Ref. 15)
1.229	12	$C^{12}O_2^{16}$ $03^13—01^10$	1.229	(236)
1.235	10	$C^{13}O_2^{16}$ $10^03—00^00$	1.236	(236)
1.253	3	$C^{13}O_2^{16}$ $02^03—00^00$	1.253	(236)
1.263	6.7	$C^{12}O_2^{16}$ $40^01—00^00$	1.263	W according to (Ref. 15)
1.293	16	$C^{12}O_2^{16}$ $32^01—00^00$	1.293	»
1.314	27	$C^{12}O_2^{16}$ $24^01—00^00$	1.317	»
1.335	15	$C^{12}O_2^{16}$ $16^01—00^00$	1.340	»
1.38		H_2O		(236)
1.433	129	$C^{12}O_2^{16}$ $00^03—00^00$	1.434	W according to (Ref. 15)
1.47	34	$C^{13}O_2^{16}$ $00^03—00^00$	1.475	(236)
1.493	11	$C^{12}O_2^{16}$ $11^02—00^02$	1.497	(236)
(1.520)	5	—	—	(236)
1.529	13	$C^{12}O_2^{16}$ $31^00—01^00$	1.530	(236)
1.538	34	$C^{12}O_2^{16}$ $30^01—00^00$	1.538	W according to (Ref. 15)
1.549	0.7	—	—	(236)
(1.556)	0.7	—	—	(236)
1.562)	0.5	—	—	(236)
1.576	122	$C^{12}O_2^{16}$ $22^01—00^00$	1.575	W according to (Ref. 15)
(1.588)	2	—	—	(236)
1.607	154	$C^{12}O_2^{16}$ $14^01—00^00$	1.606	W according to (Ref. 15)
1.630	14	$C^{13}O_2^{16}$ $14^01—00^00$	1.634	(236)
1.645	72.5	$C^{12}O_2^{16}$ $06^01—00^00$	1.646	W according to (Ref. 15)
1.663	3	$C^{12}O_2^{16}$ $07^00—00^00$	1.661	(236)
1.681	0,5	$C^{12}O_2^{16}$ $06^01—0^00^0$	1.680	(236)

TABLE 49 (cont'd)

/227

λ_{meas}, μ	W, Å	Identification	λ_{lab}	Remarks
1.701	3	—	—	(236)
1.960	300	$C^{12}O_2^{16}$ 20^01—00^00	1.961	(236)
1.987	7	$C^{12}O_2^{16}O^{18}$ 04^01—00^00	1.983	(236)
2.007	300	$C^{12}O_2^{16}$ 12^01—00^00	2.009	(236)
2.036	10	$C^{12}O^{16}O^{18}$ 20^01—00^00	2.039	(236)
2.047	20	$C^{13}O_2^{16}$ 12^01—00^00	2.046	(236)
2.060	300	$C^{12}O_2^{16}$ 04^01—00^00	2.061	(236)
2.082	30	$C^{12}O_2^{16}$ 04^01—00^00	2.080	(236)
2.095	30	$C^{12}O_2^{16}$ 06^21—02^20	2.097	(236)
2.110	40	$C^{13}O_2^{16}$ 04^01—00^00	2.106	(236)
2.125	20	$C^{13}O_2^{16}$ 05^01—01^10	2.124	(236)
2.133	2	$C^{13}O_2^{16}$ 06^01—02^20	2.134	(236)
2.142	12	$C^{12}O_2^{16}$ 00^02	2.140	(236)
2.125	70	$C^{12}O^{16}O^{18}$ 00^02—00^00	2.156	(236)
(2.173)	10	—	—	(236)
(2.223)	4	—	—	(236)
2.35	20	CO 2—0	2.35	(236)
11.2	—	C_3O_2(?)	—	(25)

*Numerals in parentheses refer to Ref.

Note: The wavelengths in the region $\lambda < 1.1\ \mu$ are given for band edges and in the region $\lambda > 1.1\ \mu$, for zero frequencies. The parentheses pertain to bands whose presence requires further verification.

of R- and P-branches. At that time it was not possible to identify these bands by direct comparison with known bands, owing to the inadequate level of laboratory research. However, when the rotational constant was determined from the inter-line distance, it was found that it was very close to the rotational constant of CO_2. Soon a third CO_2 band was discovered at λ 8689 Å, followed by the discovery of the group of bands near λ 1.05 μ. In 1947 when Kuiper (Ref.4) recorded the spectrum of Venus up to λ 2.5 μ by means of a spectrometer with a hydrogen sulfide varistor, groups of strong bands were discovered at $\lambda\lambda$ 1.6 and 2 μ. Observations in recent years (Ref.235, 236, 15, 246) resulted in the discovery in the region 1.1 - 1.2 μ of a large number of bands of medium intensity. Nearly all of these are identifiable with various transitions of CO_2. On the /227 other hand, all sufficiently intense laboratory CO_2 bands known within this range are also present in the spectrum of Venus. No CO_2 bands can be detected in the 8 - 13 μ range. The reasons for this will be discussed in Section 3.7.

Figures 103 - 107 present spectrograms and photoelectric traces of the spectrum of Venus obtained by various investigators. Table 49 gives a list of the absorption bands pertaining to Venus, discovered from these observations. Certain CO_2 bands are "hot", i.e., are formed on absorption from the fundamental level./230 There exists a fairly large number of isotopic $C^{13}O_2^{16}$ bands, several $C^{12}O^{16}O^{18}$ bands, and one $C^{13}O^{16}O^{18}$ band. Figure 108 shows the relationship between the

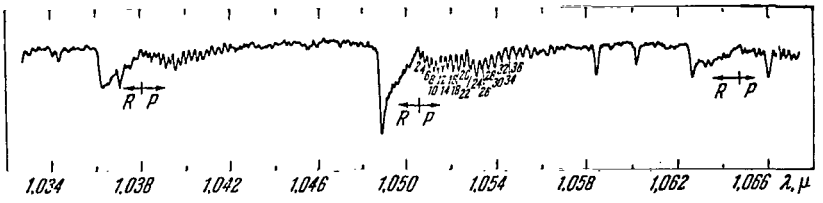

Fig.104 Photomicrogram of Spectrum of Venus near 1.05 μ.

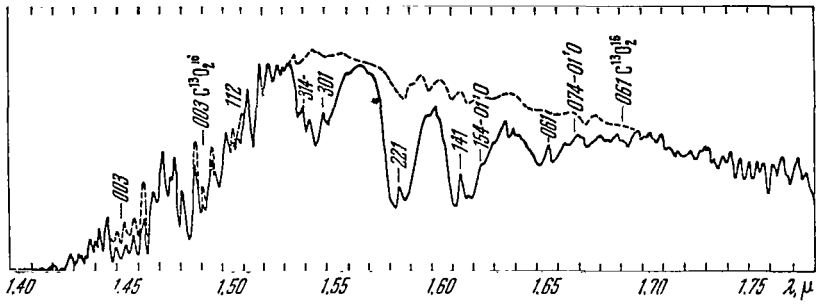

Fig.105 Spectrum of Venus in the Region λλ 1.4-1.8 μ. 125-cm Reflector of Southern Station of the GAISh (State Astronomical Institute im. Shternberg), CO_2-cooled PbS diffraction spectrometer, averaged from three traces recorded on Sept.20, 1964; slits 0.7 mm (Δλ = 12 Å); rate 1.8 Å/sec. Broken line - solar spectrum.

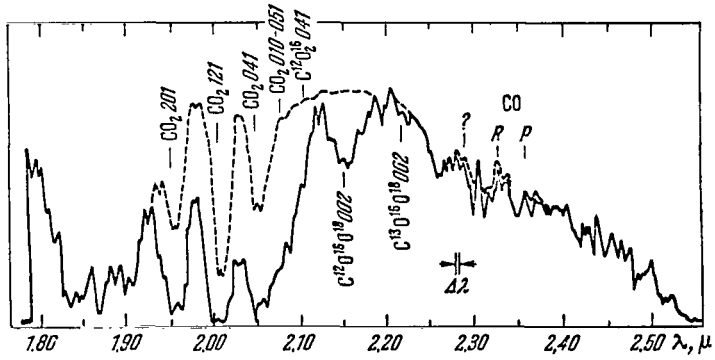

Fig.106 Spectrum of Venus in the Region λλ 1.78-2.55 μ. 125-cm Reflector of Southern Station of the GAISh, CO_2-cooled PbS diffraction spectrometer; March 5,1963; z = = 64°, slits 1 mm (40 Å), rate 7.3 Å/sec; τ = 4.4 sec. Broken line - solar spectrum.

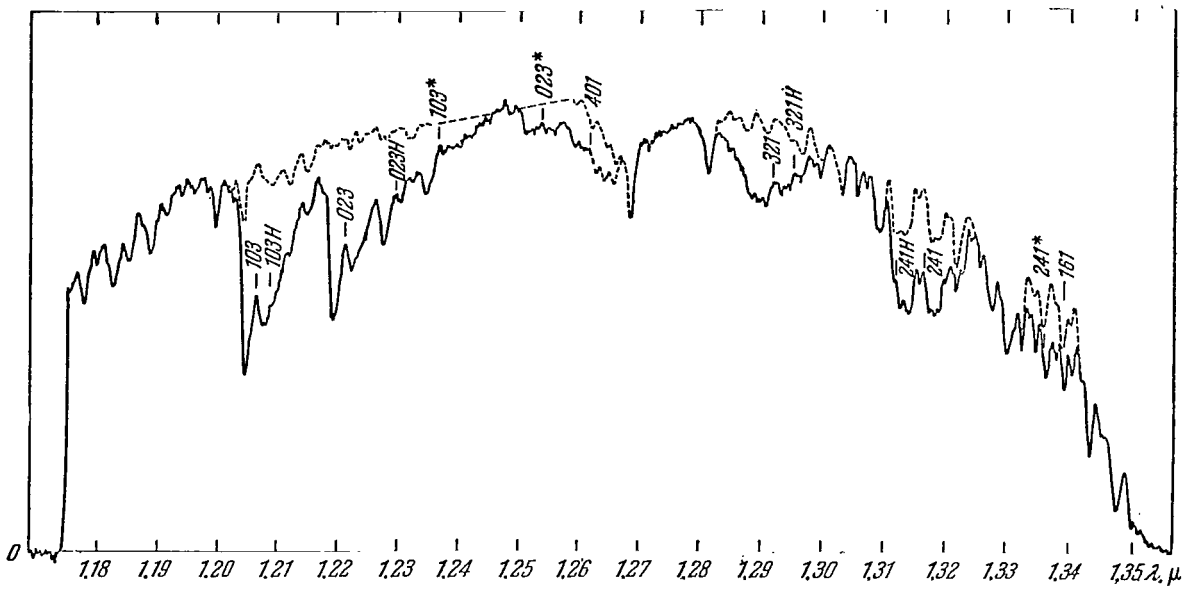

Fig.107 Spectrum of Venus in the Region 1.18 - 1.35 μ according to Observations at McDonald Observatory [Kuiper (Ref.15)]. Resolving power $\frac{\lambda}{\Delta\lambda} \approx 1500$, τ = 3 sec. Diffraction spectrometer, PbS, cooled with CO_2. Broken line - solar spectrum.

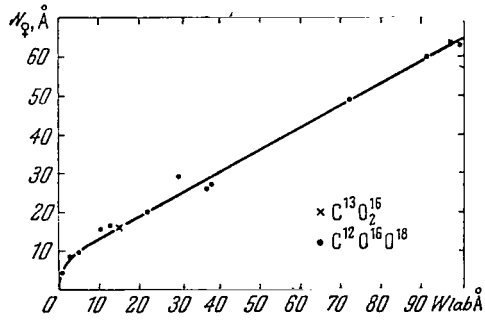

Fig.108 Equivalent Width of CO_2 Bands in Spectrum of Venus in Relation to Laboratory Equivalent Widths (Ref.15).

equivalent widths of Venusian CO_2 bands and their laboratory counterparts. The isotopic bands do not exceed the confines of the overall scatter of points, which means that the relative content of the isotopes $C^{12}:C^{13}$ and $O^{16}:O^{18}$ on Venus is the same as on the earth.

The relative intensities of "hot" and normal CO_2 bands can be used for determining the vibrational temperature, while the relative intensities of the allowed (bands in the region λλ 0.7-1.1 μ) rotational lines can be used for determining the rotational temperature. These questions will be discussed in more detail in Section 3.7. For now, we will only note that a determination of vibrational temperature is complicated by the marked difference between the relative intensities of normal bands in the spectrum of Venus and their laboratory counterparts - the weak bands in the Venusian spectrum are comparatively stronger, as clearly indicated in Fig.108. /231

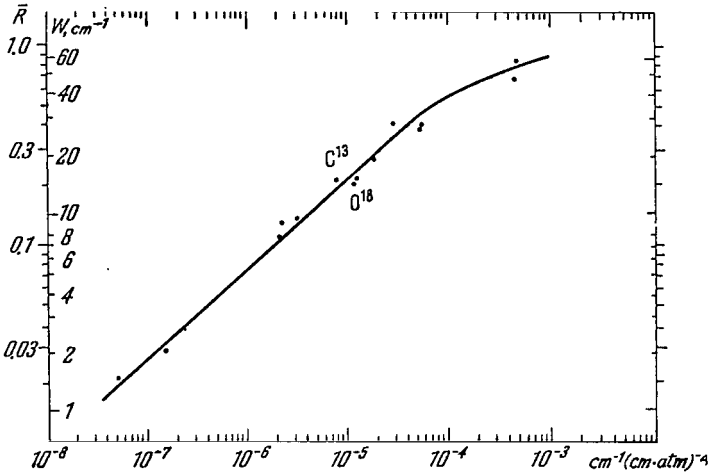

Fig.109 Equivalent Width of Venusian Bands, as a Function of the Integral Absorption Coefficient.

Figure 109 gives the equivalent widths W and mean absorptions $\overline{R}$ of the Venusian CO_2 bands as a function of the specific integral absorption coefficient. The integral absorption coefficient for bands in the region $\lambda > 1.0\ \mu$ was calculated from laboratory measurements by Kuiper (Ref.15); the absorption coefficient of the weakest bands λ 7820 and 8689 Å was taken from the study by Rank et al. (Ref.247). Kuiper's measurements were analyzed on the basis of Elsasser's model (cf. Sect.1.4). The equivalent widths of the Venusian CO_2 bands were taken from other papers (Ref.38, 148, 246). It follows from Fig.109 that the equivalent widths of even the weakest Venusian lines, unlike their laboratory counterparts, obey the square law ($W \sim \sqrt{s}$). It is this that accounts for the qualitatively different slope of the curve in Fig.108. The values of s used in plotting the curve in Fig.108 are given in Table 50.

TABLE 50

MEAN SPECIFIC INTEGRAL ABSORPTION COEFFICIENT OF CO_2 LINES

λ, μ	Upper Level	s, $cm^{-1}(cm \cdot atm)^{-1}$	λ, μ	Upper Level	s, $cm^{-1}(cm \cdot atm)^{-1}$
0.782	105	4×10^{-8}	1.340	161	1.6×10^{-5}
0.869	005	1.5×10^{-7}	1.475	003(C^{13})	9×10^{-6}
1.051	123	2×10^{-6}	1.538	301	3×10^{-5}
1.206	103	2×10^{-5}	1.575	221	4×10^{-4}
1.221	023	1.4×10^{-5}	1.606	241	4×10^{-4}
1.293	321	3×10^{-6}	1.646	061	3×10^{-5}
1.317	241	6×10^{-6}	2.156	002(O^{18})	8×10^{-6}

b) Variation in intensity of CO_2 bands. The intensities of CO_2 vary substantially in time (Ref.248-250). We can mention two types of variations in in-

tensity: 1) systematic variations with phase angle; 2) random variations from day to day. Table 49 presents averaged values of these variations for small phase angles ($\varphi \approx 40 - 50^\circ$).

TABLE 51

/232

INTENSITY OF CO_2 λ 1.6 μ BANDS IN THE SPECTRUM OF VENUS AS A FUNCTION OF PHASE

Phase Angle, φ	$M=\frac{2}{\cos\frac{\varphi}{2}}$	Illuminated Part of Disk, k	Mean Equivalent Width of the Bands λ 1.575 and 1.606 μ, w, cm	Date
32°	2.08	0.924	51	Oct. 27-30, 1961
44	2.16	0.860	43	May 7, 1963
54	2.24	0.793	59	June 19-21, 1962
55	2.26	0.785	5	June 22-23, 1962
78	2.56	0.612	41	Sept. 20, 1964
84	2.70	0.545	52	April 2, 1964
100	3.18	0.412	39	Sept. 17, 1962
136	3.78	0.140	17	Jan. 4, 1966
147	6.60	0.081	14	June 5, 1964
149	7.40	0.073	16	Jan. 11, 1966
162	12.50	0.024	13	Jan. 19, 1966
166	16.70	0.016	10	Jan. 21, 1966

Examples of intensity variations for a number of bands in the region λλ 1.5-2.2 μ are given in Table 51. Figures 110 and 111 present the intensities of the bands λ 0.7820 μ according to Spinrad (Ref.38) and 1.575 + 1.606 μ (total equivalent width) according to Moroz (Ref.250), as a function of phase.

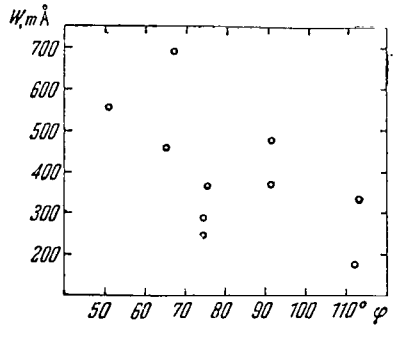

Fig.110 Phase Dependence of the Equivalent Width of the P-Branch of λ 7820 Å Band.

It can be seen from Figs.110 and 111 that, with approach to inferior conjunction, the equivalent width of the absorption bands decreases, notwithstanding the increase in the mean secant of the angles of incidence and reflection $\left(\text{which equals } \frac{1}{\cos\frac{\varphi}{2}}\right)$.

c) Conditions for Formation of CO_2 bands in the atmosphere of Venus. In a number of studies (Ref.4, 38, 14, 41, 111, 236, 246, 247, 253, 254) it was assumed that the cloud layer of Venus has a sharp and clearly delineated boundary at the top, similar to a solid surface, and that absorption bands occur in the atmosphere above the cloud layer. Nearly all existing estimates of the amount of CO_2 in the atmosphere of Venus are based on this primitive model (which we will call a simple-reflection model). The observed phase dependence of the intensity directly contradicts this model, since absorption in a cloudless atmosphere must in-

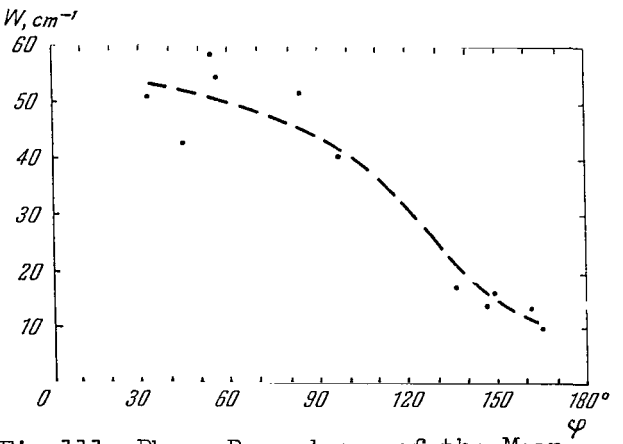

Fig.111 Phase Dependence of the Mean Intensity of the Bands λ 1.575 and 1.606 μ.

crease with any increase in the angles of incidence and reflection. Chamberlain and Kuiper (Ref.248) showed that in a semi-infinite homogeneous - i.e., having a constant ratio of absorption coefficient to scattering coefficient $\beta = \frac{k}{\sigma}$ - /233 scattering atmosphere the dependence of absorption on the angle of incidence is roughly in agreement with observations if β is sufficiently low.

The CO_2 absorption bands in the spectrum of Venus originate within the cloud layer. The intensity of the absorption bands forming in a scattering medium obeys laws that are totally different from those in a medium with pure absorption. In particular, the degree of absorption depends not on the absolute amount of the absorbing substance but on the ratio $\frac{k}{\sigma}$ (cf. Sect.1.5).

Consider weak lines for which everywhere $\beta \ll 1$. In the absence of absorption in a continuous spectrum and at a Lorentz form of the absorption coefficient [cf. eq.(1.47)], eq.(1.104) yields

$$R_\nu = 1 - e^{-S\eta\sqrt{\frac{k_\nu}{\sigma}}} \approx S\eta\sqrt{\frac{k\Delta\nu_C}{\pi\sigma}}\frac{1}{\sqrt{(\nu-\nu_0)^2+\Delta\nu_C^2}}, \qquad (3.10)$$

where k is the integral volume coefficient of absorption. The equivalent width is

$$W = \int_{-\infty}^{+\infty} R_\nu d\nu.$$

This integral diverges if R_ν is specified by eq.(3.10). To avoid divergence, /234 we shall restrict the limits of integration to some quantity $\nu_m \gg \Delta\nu_C$. Then,

$$W = S\eta\sqrt{\frac{k\Delta\nu_C}{\pi\sigma}}\int_{-\nu_m}^{+\nu_m}\frac{d\nu}{\sqrt{(\nu-\nu_0)^2+\Delta\nu_C^2}} \approx \approx 2S\eta\sqrt{\frac{k}{\sigma}\frac{\Delta\nu_C}{\pi}}\ln\frac{2\nu_m}{\Delta\nu_C}. \qquad (3.11)$$

Putting $2\nu_m = d = 1.56$ cm^{-1} (mean distance between individual rotational lines in CO_2 bands), the logarithmic multiplier will vary from 5.1 for $\Delta\nu_c = 0.01$ cm^{-1} (pressure of approximately 0.1 atm) to 2.8 for $\Delta\nu_c = 0.1$ cm^{-1} (pressure of approximately 1 atm). The equivalent width of the faint lines forming in a scattering medium is proportional to $\sqrt{k\Delta\nu_c}$, like saturated lines in a medium with pure absorption. Thus, the observed quadratic dependence of the equivalent widths of Venusian CO_2 bands is satisfactorily explained by the model of a semi-infinite homogeneous scattering atmosphere.

If the coefficient of absorption k_c in a continuous spectrum exceeds the coefficient of absorption in a line k_ν, then eqs.(3.10) and (3.11) no longer apply. In this case,

$$R_\nu = 1 - e^{-S\eta\left(\sqrt{\frac{k_\nu + k_c}{\sigma}} - \sqrt{\frac{k_c}{\sigma}}\right)} \approx \frac{S\eta k_\nu}{2\sigma\sqrt{\beta_c}}, \tag{3.12}$$

and the equivalent width obeys the linear law

$$W = \frac{S\eta k}{2\sigma\sqrt{\beta_c}}, \tag{3.13}$$

where $\beta_c = \dfrac{k_c}{\sigma}$.

The function $S(\mu_1, \mu_2)$ is lower at glancing angles of incidence than at normal incidence. The phase angle $\varphi = 150^\circ$ corresponds on the average to $\mu_1 = \mu_2 = \cos\dfrac{\varphi}{2} = 0.25$. To account for the observed phase course of the intensity of CO_2 bands, it must be assumed that $S\eta \approx 2$ at $\mu \approx 0.25$ if $S\eta \approx 6$ at $\mu = 1$. Experiments with suspensions simulating scattering clouds of large particles $\left(\dfrac{2\pi}{\lambda} \approx \right.$ $\left. \approx 10 - 20\right)$ are in agreement with these values of $S\eta$. Chamberlain (Ref.251), assuming isotropic scattering, found that /235

$$W \sim \mu_1 + \mu_2. \tag{3.14}$$

According to eq.(3.10),

$$\Delta\nu_c = \frac{1}{\sqrt{3}}\Delta\nu_{meas}, \tag{3.15}$$

where $\Delta\nu_{meas}$ is the measured half-width. The only known investigation of the width of Venusian lines was carried out by Spinrad (Ref.38). His measurements give

$$\Delta\nu_c \approx 0.10\ cm^{-1} \tag{3.16}$$

with fluctuations of roughly twice as much in both directions. Hence, assuming that N_2 is the principal constituent of the atmosphere (below, we will see that the relative concentration of CO_2 is small), eq.(1.46) can be used for estimating the pressure, which then is found to be 1.6 atm. The variations in $\Delta\nu_c$ apparently reflect real variations in effective pressure, depending on the mean depth at which the lines take form. The mean equivalent width of individual rotational lines of the 8689 Å band in the presence of low phase angles is 0.05 cm^{-1} according to Chamberlain (Ref.251). Substituting in eq.(3.10) this value of W, $\Delta\nu_c = 0.1$ cm^{-1}, and $S\eta = 6$, we then find the parameter β for the line center

$$\beta_0 = \frac{k}{\pi\sigma\Delta\nu_C} = \left(\frac{W}{2S\eta \ln \frac{2\nu_m}{\Delta\nu_C}}\right)^2 \frac{1}{\Delta\nu_C^2} \approx 2.5\times10^{-4}. \qquad (3.17)$$

Since weak lines in the spectrum of Venus obey the square law, the parameter β in the continuous spectrum must be lower than β_0:

$$\beta_c < 2.5\times10^{-4}. \qquad (3.18)$$

It follows that true absorption is not the reason why the albedo of Venus differs from unity, since we then would have $\beta_c \approx 0.01$. Apparently, this difference is due to the limited optical thickness of the atmosphere. In the preceding Section it was shown that in this case $\tau_0 \approx 20$, if $\frac{2\pi r}{\lambda} \approx 10 - 20$. To verify the extent to which this model fits the spectroscopic observations, we calculated the dependence $W(\beta)$ from eq.(1.100), assuming that the surface albedo $A_s = 0.1$; $\tau_0 = 20$; $S\eta = 6$ at $\mu = 1$ and $S\eta = 2$ at $\mu = 0.25$. The results are presented in Fig.112 for two values of $\Delta\nu_c = 0.1$ and 0.01 cm^{-1} (pressures of 1.6 and 0.16 atm). Plotted along the abscissa are the mean values of absorption /236

$$\overline{R} = \frac{W}{d}.$$

Overlap between adjacent lines was not taken into account. When $\rho < 0.2$, eq.(1.100) is unsuitable, and in such cases we utilized the $\rho(\beta)$ dependence calculated by L.M.Romanova for particles with $\frac{2\pi r}{\lambda} = 20$, $m = 1.3$, by the exact numerical method described by Romanova (Ref.59). The observed dependence $\overline{R}(s)$ is located between the curves for $\Delta\nu_c = 0.1$ and 0.01 cm^{-1} in such a manner that, as was to be expected, weak bands correspond to somewhat higher pressures than strong bands (see the dots in Fig.112).

Hence a scattering atmosphere of finite thickness satisfactorily accounts also for the observed relative intensities and phase dependence. Figure 112 presents the curve f calculated for a semi-infinite atmosphere with limited continuous absorption ($\beta_c = 0.005$ or $a_c = 0.995$). As is readily seen, this curve cannot account for the observed relative intensities. /237

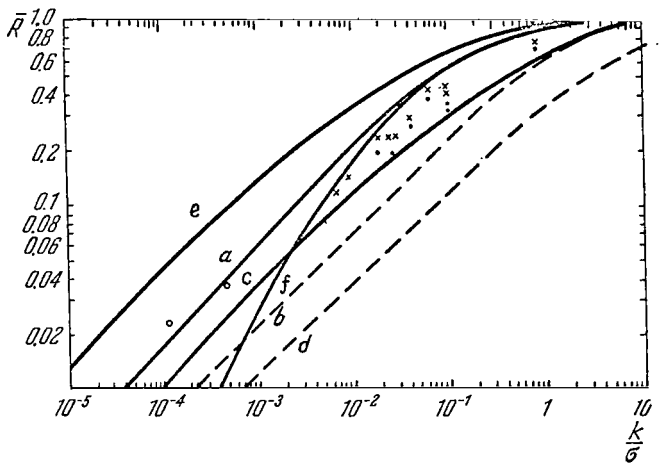

Fig.112 Theoretical Correlation of the Intensity of CO_2 Bands with k/σ for Various Parameters of the Scattering Layer. a - $\tau_0 = 20$, $A_s = 0.1$ $k_c/\sigma = 0$, $\Delta\nu_c = 0.1$ cm^{-1}, normal angles of incidence and observation ($\mu = 1$); b - Same, for 75° angles of incidence and observation ($\mu = 0.25$); c - Same, for $\Delta\nu_c = 0.01$ cm^{-1}, $\mu = 1$; d - Same for $\Delta\nu_c = 0.01$ cm^{-1}, $\mu = 0.25$; e - $\tau_0 = \infty$, $\mu = 1$, $\Delta\nu_c = 0.1$ cm^{-1}, $k_c/\sigma = 0$, f - Same for $k_c/\sigma = 0.005$.

Curve e in Fig.112, calculated for a semi-infinite atmosphere without absorption in the continuous spectrum, lies substantially above curve a, even at $\bar{R} = 0.5$ ($\tau_0 = 20$, with all other parameters remaining the same). This means that not only weak but also strong CO_2 bands will form at considerable optical depths. In the case of strong bands, these great depths account for most of the absorption in the line wings.

To estimate the amount of CO_2 in the atmosphere, a specific scattering coefficient σ or, for a given total optical thickness τ_0, a specific linear thickness Δz of the optical layer must be known. In terrestrial stratus clouds the coefficient is $\sigma \approx 3 \times 10^{-4}$ cm^{-3} (Ref.61). Assuming the same scattering coefficient for Venusian clouds, we have

$$\Delta z = \frac{\tau_0}{\sigma} \approx 1 \text{ km}. \qquad (3.19)$$

It is doubtful whether a cloud layer of an average thickness of about one kilometer could constantly envelop the entire planet without occasionally showing some major rents and gaps. Apparently, Δz must be at least one order of magnitude higher. The upper limit of Δz is determined by the altitude of the apparent cloud top above the underlying surface of the planet:

$$\Delta z \approx 5 \times 10^6 \text{ cm, whence } \sigma \approx 4 \times 10^{-6} \text{ cm}^{-1}.$$

The absolute concentration of CO_2 and the absorption coefficient both decrease exponentially with altitude

$$k = k_0 e^{-\frac{z}{H}},$$

where H is the altitude scale. The assumption of a fixed $\frac{k}{\sigma}$ ratio means that the scattering coefficient obeys the same law

$$\sigma = \sigma_0 e^{-\frac{z}{H}}$$

and the total optical thickness is

$$\tau_0 = \sigma_0 H,$$

where σ_0 is the scattering coefficient at the base of the cloud layer. Consequently, /238

$$\sigma_0 = \frac{\tau_0}{H} = \frac{20}{10^6} = 2 \times 10^{-5}. \tag{3.20}$$

Putting $\Delta\nu_c = 0.1$ cm^{-1} at the level where $p \approx 1.5$ atm,

$$\bar{\sigma} = 10^{-5}\ cm^{-1},$$

we have, for the λ 8689 Å band ($\bar{R} = 0.03$, $\frac{k}{\sigma} \approx 3 \times 10^{-4}$; cf. Fig.112),

$$\bar{k} = 3 \times 10^{-9} cm^{-1}.$$

According to Table 51, the specific integral absorption coefficient for this band is

$$\bar{s} = 1.5 \times 10^{-7}\ cm^{-1}\ (cm \cdot atm)^{-1},$$

so that the CO_2 content must be

$$r_{CO_2} = 0.02\ cm \cdot atm \cdot cm^{-3} \tag{3.21}$$

or the relative concentration at P = 1.5 atm,

$$c \approx 0.015. \tag{3.22}$$

If the pressure is P = 10 atm at the surface (cf. Sect.3.9), the total amount of CO_2 in the Venusian atmosphere will be

$$u_{CO_2} = 3 \times 10^5\ cm \cdot atm. \tag{3.23}$$

The reduced thickness u'_{CO_2} within the cloud cover is

$$u'_{CO_2} = 2 \times 10^4\ cm \cdot atm. \tag{3.24}$$

The model of simple reflection (Ref.4, 39, 111, 247, 249, 254) implies the presence of one to several km • atm of CO_2 above the cloud layer, according to the weak bands at λ 0.8 μ, and several hundred m • atm according to the strong bands at λ 1.6 μ (Ref.236) as well as a relative CO_2 concentration of about 10%.

The assumption that $\sigma = \sigma_0 e^{-\frac{z}{H}}$ appears fairly artificial in view of our knowledge of terrestrial clouds, whose tops always are sharply delineated. It would be intriguing to consider a model in which k varies exponentially while σ, for example, retains a certain constant value of

$$\sigma = \sigma_0$$

up to an altitude $z = z_0$, and a value of $\sigma = 0$ when $z > z_0$. Investigation of such a model with a variable $\frac{k}{\sigma}$ ratio would be impossible without complex calculations on electronic computers. We considered another model /239

$$\frac{k}{\sigma} = \beta_0 = \text{const}$$

up to an altitude $z = z_0$, while at $z > z_0$,

$$\sigma = 0,$$
$$k = k_0 e^{-\frac{z}{H}},$$

where H is the altitude scale. It turned out that, in such a model, the phase effect qualitatively agrees with the observations (W decreases with decreasing μ) only when

$$\sigma \leqslant 10^{-6}\ cm^{-1}.$$

At $\sigma \approx 10^{-5}$ cm^{-1} the effect of the air mass in the atmosphere above the cloud already compensates the effect of damping of the intra-cloud component of the lines. A scattering coefficient of 10^{-6} cm^{-1} would be definitely too low. Moreover, for such a low σ, it is meaningless to speak of a sharply delineated boundary of the cloud layer since then the mean free path of the quantum would exceed the altitude scale.

This means that the Venusian cloud mantle lacks a sharply defined boundary. The aerosol concentration gradually decreases with altitude, apparently even more slowly than the gas density. This is indicated by the phase effect of the strong bands at λ 1.6 and λ 2 μ. According to the curves a and b in Fig.112, the equivalent width of the λ 2.06 μ band should decrease by only 30 - 40% on transition from $\mu = 1$ and $\mu = 0.25$ but actually decreases by about a factor of 3. Presumably, this is due to the fact that, close to $\mu = 0.25$, the band forms in higher layers of the atmosphere where the $\frac{k}{\sigma}$ ratio is lower. In addition to the smooth variation in $\frac{k}{\sigma}$ with altitude, inhomogeneities of another type such as cloud structure and relief of the cloud surface, also may be a factor.

Let us sum up briefly the foregoing: The relative concentration of CO_2 in the atmosphere of Venus is approximately 1.5% with an indeterminacy of 2 - 3 times or more depending on the actual closeness of the adopted model of the cloud layer ($\tau_0 = 20$; scattering indicatrix corresponds to $\frac{2\pi r}{\lambda} \approx 10 - 20$; the $\frac{k}{\sigma}$ ratio does not change with altitude). The totality of observations points

to a cloud layer of extended height, which lacks a distinct boundary and has a scattering coefficient close to 10^{-5} cm^{-1}.

Let us discuss, in some detail, the question of atmospheric pressure. The half-width of the λ 7820 Å band lines as determined by Spinrad yields /240

$$P \approx 1.5 \ atm, \qquad (3.25)$$

which is roughly half as much as indicated by Spinrad himself (Ref.38); the difference is due to the difference in models [a simple-reflection model was assumed in his paper (Ref.38)]. This pressure is somewhat averaged over the height of the cloud layer. It is difficult to fix the altitude of the level for this particular pressure, in accordance with its ratio to the surface pressure and, particularly, to the apparent top of the cloud layer. The first of these ratios can be defined from available data on rotational temperatures but only within the framework of a specific model of the atmosphere, while it is virtually impossible to determine the second ratio. It must be emphasized that the concept of "top of the cloud layer", which often figures in studies of Venus, has no true physical meaning; not one of the parameters known from observations can be tied to this concept. An exception is the determination of the pressure and altitude scale at the level at which the eclipse of Regulus occurs (Ref.69). By extrapolating the findings to the apparent limb, it becomes possible to determine the pressure at the corresponding altitude. However, any further downward extrapolation would be extremely unreliable, since all of the other physical parameters are measured in the central portion of the disk (cf. Sect.3.9).

Section 3.5 CO and Dissociation of CO_2

In 1961, Sinton (Ref.255, 256) discovered the CO λ 2.35 μ absorption band (first overtone) in the spectrum of Venus. He estimated the equivalent path as 79 cm • atm at a pressure of 7.1 cm in the spectrometer cell (without correction for double passage and secant). On the basis of observations performed in the summer of 1962 (Ref.235), we found only extremely unreliable traces of planetary absorption in the λ 2.35 μ band and estimated the equivalent path of CO as 5 cm • atm at normal pressure. Kuiper, during observations in the summer of 1962 (Ref.15, 257), detected no absorption in the λ 2.35 μ band and estimated the upper limit as 10 cm • atm at atmospheric pressure.

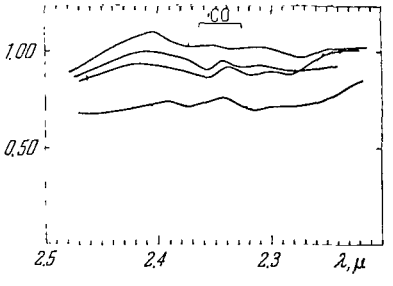

Fig.113 Smoothed Curves Plotted by Dividing the Intensities in the Spectrum of Venus by the Intensities in the Spectrum of the Sun in the Region λλ 2.2-2.5 μ.

In the region λ 2.35 μ, fairly strong absorption is displayed by the edge of the telluric band ν_3 H_2O (the X band which, in ground-based observations, completely obscures the range λλ 1.55-2.80 μ). Hence it was essential to repeat the observations in winter at sufficiently low temperatures when the absolute moisture content and the telluric absorption of H_2O are small. We did this on March 5,1963 [Fig.107 (Ref.236)] when the ambient air temperature was about -10°C. Of the

14 spectral traces recorded on that day we selected the eight best, divided them into four pairs, averaged the spectra for each pair, and divided each of the four averaged spectra by the solar spectrum observed on the same day. Smoothed curves representing the result of these operations are shown in Fig.113. All four curves exhibit a characteristic depression with a peak near λ 2.35 μ and with two minima corresponding to the R-and P-branches of the 2 - 0 CO band. For comparison, Fig.114 presents a laboratory spectrum plotted by us with an 85-mm long spectrometer cell. The slits, in the laboratory experiment, were more narrow than in the observations of Venus (0.5 mm instead of 1 mm) but the λ 2.35 μ band is very wide so that this difference is hardly significant. At λ 2.28 μ, the Venusian spectrum contains yet another minimum of roughly the same depth. Its nature is still obscure.

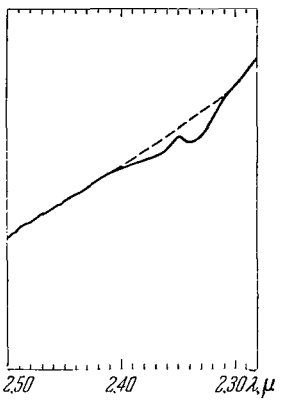

Fig.114 Laboratory Spectrum of CO in the Region of the First Harmonic. P = 1 atm, cell 85 mm, Δλ = 20 Å.

From the laboratory spectrum in Fig.114, with the aid of Elsasser's model, we can estimate

$$s \approx 2\times10^{-2}\ cm^{-1}\ (cm\cdot atm)^{-1}, \tag{3.26}$$

for the spectrum of Venus $\bar{R} \approx 0.05$, so that the mean equivalent width of an individual rotational line of CO will be $\bar{W} = \bar{R}d = 0.2\ cm^{-1}$. In the case of CO_2, such an equivalent width would imply $\bar{R} = \frac{0.2}{1.6} = 0.12$; $\Delta\nu_c$ for CO under normal conditions is 0.13 cm^{-1}. Curve a in Fig.112 in the region $\bar{R} < 0.2$ may be represented by the formula

$$\log \bar{W} = \log \bar{R}\, d = 0.56 \log \frac{k}{\sigma} + 0.66, \tag{3.27}$$

and curve b, by the formula

$$\log \bar{W} = 0.53 \log \frac{k}{\sigma} + 0.10. \tag{3.27a}$$

From eq.(3.27), we have

$$\left(\frac{k}{\sigma}\right)_{CO} = 4\times10^{-3}$$

and, putting $\sigma = 10^{-5}\ cm^{-1}$, we find that

$$k = 4\times10^{-8}\ cm^{-1}. \tag{3.28}$$

From eqs.(3.28) and (3.26) we find the content

$$r_{CO} \approx 2 \times 10^{-6}\ cm \cdot atm \cdot cm^{-3}.$$

If P = 1.5 atm, the relative concentration will be

$$c = 1.5 \times 10^{-6}$$

and the ratio of concentrations of CO and CO_2,

$$[CO] : [CO_2] = 10^{-4}. \tag{3.29}$$

It seems probable that photodissociation of CO_2 by solar ultraviolet radiation may be a source of CO in the atmosphere of Venus. Let us try to estimate the amount of CO that may be produced by such photodissociation. We will assume that the photochemical equilibrium of CO_2 is determined by the chain of reactions (cf. Sect.2.5)

$$CO_2 + h\nu \rightarrow CO + O, \quad \lambda < 1700\ \text{Å}, \tag{2.42}$$

$$CO + O + M \rightarrow CO_2 + M, \tag{2.43}$$

$$O + O + M \rightarrow O_2 + M, \tag{2.44}$$

$$O_2 + h\nu \rightarrow O + O, \quad \lambda < 1750\ \text{Å}. \tag{2.45}$$

As a reaction inverse to the reaction (2.42), except for (2.43), a considerable role may be played by recombination of CO with an excited oxygen atom

$$O\,(^3P) + CO \rightarrow CO_2, \tag{3.30}$$

but, to simplify the calculations, we will disregard this. Thus, our final equilibrium values of CO concentration may be exaggerated.

The velocity of reaction of the photochemical decomposition of CO_2 (3.42) is

$$\frac{dn\,(CO_2)}{dt} = -\frac{n\,(CO_2)}{t_{CO_2}}, \tag{3.31}$$

where

/243

$$t_{CO_2} = \frac{1}{\int_0^\infty s_{\lambda, CO_2} F_\lambda d\lambda}, \tag{3.32}$$

Here, s_λ is the photodissociation cross section; F_λ is the radiant flux. The

velocity of the back reaction (2.43) is

$$\frac{dn(CO_2)}{dt} = n(CO) \cdot n(O) \cdot n(M) \cdot C_1, \tag{3.33}$$

where C_1 is the rate constant of the reaction. According to Bates (Ref.258)

$$C_1 = 10^{-36}\, cm^6 \cdot sec^{-1}. \tag{3.34}$$

Part of the oxygen atoms, owing to the ternary-recombination reaction (2.44), is linked to the molecules at a rate of

$$\frac{dn(O_2)}{dt} = n(O) \cdot n(O) \cdot n(M) \cdot C_2, \tag{3.35}$$

where, according to Penndorf (Ref.259),

$$C_2 = 10^{-32}\, cm^6 \cdot sec^{-1}. \tag{3.36}$$

The velocity of the back reaction is

$$\frac{dn(O_2)}{dt} = -\frac{n(O_2)}{t_{O_2}}, \tag{3.37}$$

where

$$t_{O_2} = \frac{1}{\int_0^\infty s_{\lambda, O_2} F_\lambda d\lambda}. \tag{3.38}$$

Under equilibrium conditions, eqs.(3.31) and (3.33) yield

$$n(CO_2) = n(CO) \cdot n(O) \cdot n(M) \cdot C_1 \cdot t_{CO_2} \tag{3.39}$$

while eqs.(3.35) and (3.37) give

$$n(O_2) = n(O) \cdot n(O) \cdot n(M) \cdot C_2 \cdot t_{O_2}. \tag{3.40}$$

In addition, under equilibrium conditions,

$$n(CO) = n(O) + 2n(O_2). \tag{3.41}$$

Let us assume the initial chemical composition to be 98.5% N_2 and 1.5% CO_2. According to Koval' (Ref.252), the molecules of N_2 are 1.5 times less effective, in their quality as third body, than O_2 and CO_2.

Since the velocity of reaction is correctly known only in order of magnitude, the difference in effectiveness can be disregarded and it may be assumed /244 that

$$n(M) = n_0,$$

where n_0 is the total initial concentration. In addition,

$$n(CO) + n(CO_2) = 1.5 \times 10^{-2} n_0. \tag{3.42}$$

Equations (3.39) - (3.42) represent a system with four unknowns: $n(CO_2)$, $n(CO)$, $n(O_2)$, and $n(O)$. The integral terms of eqs.(3.32) and (3.38) include a quantity determined from the formula

$$F_\lambda = F_{0\lambda} e^{-\tau \sec z}, \tag{3.43}$$

where $F_{0\lambda}$ is the extra-atmospheric flux; τ is the optical thickness at a given level in a given wavelength. Outside the atmosphere, the lifetimes of CO_2 and O_2 molecules are, respectively,

$$t_{CO_2} = 10^6 \text{ sec},$$
$$t_{O_2} = 3 \times 10^4 \text{ sec}.$$

When calculating t_{CO_2} and t_{O_2} from eqs.(3.32) and (3.38), the integrals are substituted with sums of the type of

$$\sum s_{\lambda_{i+1}-\lambda_i} F_{\lambda_{i+1}-\lambda_i} \Delta\lambda.$$

For this, the values of s_λ and $F_{0\lambda}$ (extra-atmospheric flux) given in Table 52 are used. The dissociation cross sections of CO_2 were taken from Wilkinson (Ref.260) and the dissociation cross sections of O_2, from Watanabe (Ref.261).

Extra-atmospheric fluxes of ultraviolet radiation at various wavelengths /245

TABLE 52

ASSUMED PHOTODISSOCIATION CROSS SECTIONS AND SPECTRUM OF SOLAR ULTRAVIOLET RADIATION

λ, Å	F_0, $\frac{quantum}{cm^2 \cdot sec}$ [262]	σ_{CO_2}, cm^2 [260]	σ_{O_2}, cm^2 [261]
2400—2200	2.6×10^{14}	0	5×10^{-24}
2200—2000	1.1×10^{14}	0	7×10^{-24}
2000—1900	2.6×10^{13}	0	9×10^{-24}
1900—1800	1.1×10^{13}	0	1.5×10^{-23}
1800—1700	7×10^{12}	0	4×10^{-19}
1700—1600	3.2×10^{12}	10^{-19}	2×10^{-18}
1600—1500	1.4×10^{12}	3×10^{-19}	8×10^{-18}
1500—1400	5.2×10^{11}	3×10^{-19}	1.5×10^{-17}
1400—1300	1.6×10^{11}	—	1.5×10^{-17}

were taken from Hinteregger's study (Ref.262) and adjusted to the distance of Venus by multiplying by 2. Figures 115 and 116 show t_{O_2} and t_{CO_2} as a function of the amount of O_2 and CO_2 above a specific level.

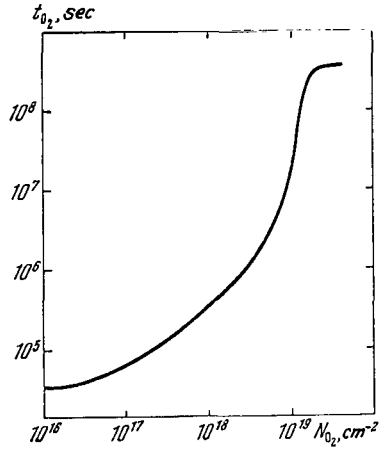

Fig.115 Lifetime of O_2 Molecules as a Function of the Amount of O_2 above a Given Level of the Atmosphere.

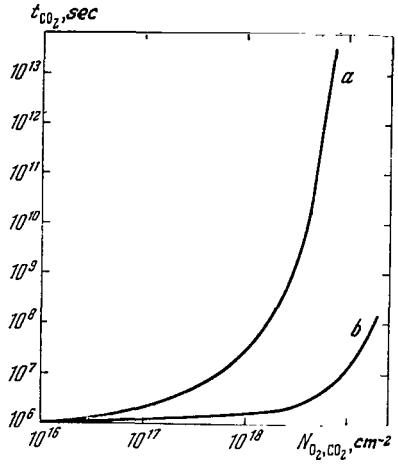

Fig.116 Lifetime of CO_2 as a Function of the Amount of O_2 (a) and CO_2 (b) above a Given Level of the Atmosphere.

The system of equations (3.39) - (3.42) can be reduced to a single equation of the third degree

$$n(O) = \frac{10^{36}}{x n_0 t_{CO_2}} = -\frac{2.5\times10^{31}}{n_0 t_{O_2}} + \sqrt{\frac{6.25\times10^{62}}{n_0^2 t_{O_2}^2} + \frac{7.5\times10^{29}x}{(1+x)\,t_{O_2}}} \qquad (3.44)$$

with respect to the variable

$$x = \frac{n(CO)}{n(CO_2)}. \qquad (3.45)$$

Upward of the dissociation level of O_2 in eq.(3.44), the second term of the radicand becomes much smaller than the first. In this region, we have

$$x = \frac{6.6\times10^{37}}{n_0^2 t_{CO_2}} \qquad (3.46)$$

and

/246

$$n(O) = 1.5\times10^{-2} n_0, \qquad (3.47)$$
$$n(CO) = 1.5\times10^{-2} n_0, \qquad (3.48)$$

$$n(CO_2) = 2.25 \times 10^{-40} n_0^3 t_{CO_2}, \quad (3.49)$$
$$n(O_2) = 2.25 \times 10^{-36} n_0^3 t_{O_2} \quad (3.50)$$

Below the O_2 dissociation level, the first term of the radicand in eq.(3.44) is much smaller than the second. Neglecting the first term, we have

$$x = 1.1 \times 10^{14} \sqrt[3]{\frac{1}{n_0^2} \frac{t_{O_2}}{t_{CO_2}^2}} \quad (3.51)$$

and

$$n(O) = \frac{10^{22}}{\sqrt[3]{n_0 t_{CO_2} t_{O_2}}}, \quad (3.52)$$

$$n(CO) = 1.5 \times 10^{12} \sqrt[3]{n_0 \frac{t_{O_2}}{t_{CO_2}^2}}, \quad (3.53)$$

$$n(CO_2) = 1.5 \times 10^{-2} n_0, \quad (3.54)$$

$$n(O_2) = 10^{12} \sqrt[3]{n_0 \frac{t_{O_2}}{t_{CO_2}}}. \quad (3.55)$$

Thus, the position of the CO_2 dissociation level is determined by the amount of molecular oxygen produced by the reaction (2.44) and by the position of the dissociation level of oxygen. Molecular oxygen forms a protective layer retarding the dissociation of CO_2 and raising the altitude of its dissociation level. It can be seen from Figs.115 and 116 that the values of t_{O_2} and t_{CO_2} also increase sharply when the total amount of O_2 above a given level reaches a critical value. It is thus obvious that the transition region, where $x \approx 1$, must be narrow. We solved eq.(3.44) for a descending series of discrete altitudes spaced by 10 km in the region of $x \gg 1$ and later, on approach to the dissociation level, spaced by 5 km. Below the dissociation level, the spacing was increased again. The start of reckoning was taken as the level at which the 1960 occultation of Regulus occurred. At the altitude of that level, according to Menzel and de Vaucouleurs (Ref.69), we have

$$P = 2.60 \pm 0.13 \times 10^{-3}\ mb, \quad H = 6.8 \pm 0.2\ km. \quad (3.56)$$

It was assumed that, at the level,

$$n_0 = \frac{P}{m_H \mu g H} \approx 8 \times 10^{13}\ cm^{-3}.$$

According to de Vaucouleurs (Ref.69), the logarithmic gradient of the altitude /247 scale is as follows:

$$\frac{1}{H} \frac{dH}{dz} = 0.010 \pm 0.002. \quad (3.57)$$

We disregarded the presence of this gradient and assumed that H = 6.8 km everywhere. The results of the calculation are given in Table 53 and Fig.117. It can be seen from Table 53 that the thickness of the layer within which x in-

creases from 0.3 to 3 is very limited (about 5 km), i.e., the transition layer is very narrow and the presence of a sharp CO_2 dissociation level is quite conceivable. It is logical to assume that the height of this level is the altitude at which $x = 1$ ($z = -18$ km). Actually, the dissociation level is blurred by diffusion and mixing. Owing to these processes, the concentration of CO_2 and O_2 above the dissociation level may be much higher than calculated in theory. Below the dissociation level, the diffusion rate is sufficiently low and mixing accounts for the downward transport of dissociation products. It follows from Table 53 that, in the region where $P \approx \approx 1$ atm ($n \approx 10^{19}$ cm^{-3}), the calculated relative concentration

$$[CO] : [CO_2] \approx 10^{-6},$$

is two orders of magnitude smaller than observed. However, at a level only 20 km higher it reaches an order of 10^{-4}.

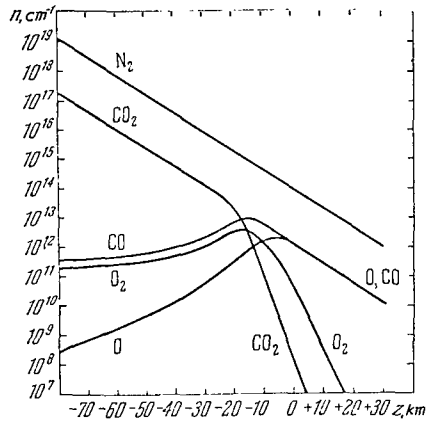

Fig.117 Photochemical Equilibrium of CO_2 in the Atmosphere of Venus.

The lifetime of CO molecules within this altitude interval is about 10^9 sec while the characteristic diffusion time (cf. Sect.1.7) is $10^{11} - 10^{12}$ sec; thus, in accordance with the above, diffusion is unable to cause an appreciable redistribution of the dissociation products. The effect of mixing is difficult to estimate quantitatively, but it is doubtful whether it could augment the relative concentration of CO by two orders of magnitude. That would require a virtually constant absolute concentration of CO below the dissociation level ($\sim 10^{13}$ cm^{-3}). It must be stated that the hypothesis of the photochemical origin of CO involves major discrepancies. It appears that the CO present in /248 the Venusian atmosphere is of different origin.

The photochemical equilibrium of CO_2 in the atmosphere of Venus had been considered earlier by Shimizu (Ref.263) and by us (Ref.236), but these studies referred to excessively high relative concentrations of CO_2 derived from the simple-reflection model. The dissociation level in these studies was assumed as about 15 km higher; it roughly coincided with the level at which the eclipse of Regulus occurs.

Section 3.6 Chemical Composition of the Atmosphere and Cloud Layer

a) Nitrogen and oxygen. In Section 3.4 it was shown that the relative concentration of CO_2 is far below 100%. Apparently, we lack observational data on the nature of the greater part of the atmosphere, since all other identified molecules represent incontestably minor constituents of the atmosphere. In 1954, Kozyrev (Ref.264) first photographed the spectrum of the Ashen Light of Venus and discovered a series of emission bands which he identified with the emission of N_2 and N_2^+.

TABLE 53

CONCENTRATION OF CO_2, CO, O, AND O_2 IN THE UPPER LAYERS OF THE VENUSIAN ATMOSPHERE (PHOTOCHEMICAL EQUILIBRIUM)

z*	Concentration				
	Total	CO_2	O_2	O	CO
30	9.7×10^{11}	2×10^{2}	6×10^{4}	1.4×10^{10}	1.4×10^{10}
20	4.2×10^{12}	1.7×10^{4}	5×10^{6}	6.3×10^{10}	6.3×10^{10}
10	1.8×10^{13}	1.3×10^{6}	4×10^{8}	2.7×10^{11}	2.7×10^{11}
0	8×10^{13}	1.1×10^{8}	3.4×10^{10}	1.2×10^{12}	1.2×10^{12}
—5	1.7×10^{14}	3×10^{9}	4×10^{11}	1.7×10^{12}	2.5×10^{12}
—10	3.6×10^{14}	1×10^{11}	1.8×10^{12}	1.7×10^{12}	5.3×10^{12}
—15	7.6×10^{14}	3×10^{12}	4×10^{12}	7×10^{11}	9×10^{12}
—20	1.6×10^{15}	1.8×10^{13}	3×10^{12}	2.5×10^{11}	6×10^{12}
—25	3.4×10^{15}	4.7×10^{13}	2×10^{12}	10^{11}	4×10^{12}
—30	7.1×10^{15}	1.1×10^{14}	10^{12}	5×10^{10}	2×10^{12}
—40	3×10^{16}	3×10^{14}	5×10^{11}	1.5×10^{10}	10^{12}
—60	6.2×10^{17}	9.3×10^{15}	3×10^{11}	2×10^{9}	6×10^{11}
—80	1.2×10^{19}	1.8×10^{17}	2×10^{11}	3×10^{8}	4×10^{11}

* The altitude of the level of the occultation of Regulus (Ref.69) is taken as the start of reckoning.

Warner (Ref.265) confirmed this identification, but mentioned that /249
part of the bands may refer to O_2 and O_2^+. However, despite numerous subsequent attempts by N.A.Kozyrev and other investigators [see, e.g. (Ref. 266, 267)], no other photographs of these bands could be obtained. G.P.Polyakova, Ya.M.Fogel', and Ch'iu Yu-Mei (Ref.268) showed that all of the bands discovered by Kozyrev are present in the CO_2 emission excited by a 38-Kev proton beam and that no positive conclusions as to the presence of nitrogen and free oxygen in the Venusian atmosphere can be drawn from Kozyrev's spectrum. Apparently, in 1954 Kozyrev obtained his spectrogram during an intense bombardment of Venus by a solar corpuscular flux, i.e., he had observed a polar aurora on Venus.

It is normally assumed that nitrogen is a major constituent of the Venusian atmosphere, but it must be stressed that the only ground for this assumption is an analogy with the earth. In the case of Mars, we also considered another possibility, namely argon or a mixture of argon and nitrogen. On Venus, the relative concentration of inert gases can hardly be significant since the total pressure at the surface is quite high.

Repeated attempts have been made to detect molecular oxygen in the atmosphere of Venus. In 1962, V.K.Prokof'yev and N.N.Petrova (Ref.269-271) announced their discovery of weak Venusian Doppler satellites in the wings of the lines of the telluric bands of oxygen A (λ 7660 Å). On discrete spectrograms and photomicrometric traces these satellite lines are not visible; they could be detected only by averaging a large number of spectra. The displacement of the satellite lines varied in accordance with the expected Doppler shift. Spinrad and Richardson (Ref.272), who used an instrument with a high resolving power, failed to find

these satellites, but they did not use averaging so that their findings can hardly be considered a conclusive refutation.

V.K.Prokof'yev and N.N.Petrova gave no estimate on the intensity of these satellite lines or on the O_2 content. Spinrad and Richardson estimated the upper limit of equivalent width, as

$$W_{O_2} < 0.008 \text{ Å}$$

and of the amount of O_2, as

$$u_{O_2} < 70 \ cm \cdot atm$$

from the simple-reflection model. In the above-adopted scattering-atmosphere model, we have

$$\frac{k_{O_2}}{\sigma} < 10^{-4}$$

and /250

$$k_{O_2} < 10^{-9} \ cm^{-1}.$$

According to Spinrad et al. (Ref.272), s = 3×10^{-5} cm^{-1} $(cm \cdot atm)^{-1}$ and the content is

$$r_{O_2} < 3 \times 10^{-5} \ cm \cdot atm \cdot cm^{-3};$$

while the relative concentration is

$$r_{O_2} < 2 \times 10^{-5}.$$

This is 20 times as much as obtained from calculations of photochemical equilibrium, but mixing may increase the relative concentration of O_2 above its theoretically calculated amount. In the direct-reflection model, the relative concentration is 10^{-4} if the pressure above the cloud layer is taken as 0.3 atm (Ref.236). For our estimate, we used eq.(3.27) with somewhat altered constants, in view of $\alpha_{O_2} \approx 0.04$ cm^{-1} (cf. Table 9) and, at P = 1.5 atm, $\Delta\nu_c \approx 0.06$ cm^{-1}. It was assumed, as before, that $\sigma \approx 10^{-5}$ cm^{-1}.

b) Water vapor. The first indications of the presence of H_2O in the atmosphere of Venus were derived from observations by Strong, Ross, and Moore (Ref.273, 274), carried out from a balloon at an altitude of 25 km by means of a reflector with a photoelectric spectrometer in the region of the absorption band λ < 11,300 Å. The guiding was manual and somewhat inaccurate so that the records became slightly distorted and, although the presence of Doppler satellites was recorded, it was difficult to estimate the absorption. In February 1964 (Ref.275, 276), the observations were repeated with a more refined apparatus equipped with automatic homing and guiding attachments, and the extent of absorption was measured accurately to within ±5%. The intensity of the Venusian absorption bands proved one order of magnitude greater than that of the telluric bands at an altitude of 25 km. On the basis of the simple-reflection model,

Strong and his coworkers estimated the equivalent path of H_2O in the Venusian atmosphere as 1.1×10^{-2} gm • cm^{-2} (2.9×10^{-3} gm • cm^{-2}, taking the air mass into account) at a pressure of 600 mb or as 4.7×10^{-2} gm • cm^{-2} at a pressure of 90 mb. Earlier, Dollfus (Ref.277) obtained a rather similar estimate as to the amount of H_2O in the Venusian atmosphere but this had been subject to doubt, since, for Mars, the same study had specified a clearly exaggerated amount of H_2O.

Spinrad (Ref.278), using the Doppler shift method, searched for planetary lines of H_2O near λ 8180 Å on plates that gave high rotational temperatures and high pressures with respect to the band λ 7820 Å. It was assumed that the atmosphere on the corresponding days was at its most "translucent" in the investi- /251 gated spectrum region. Spinrad found no Doppler satellites and gave an estimate of 10^{-5} for the upper limit of the relative concentration of H_2O. Observations by Strong's team specified the relative concentrations of H_2O above the cloud layer as 3×10^{-5} for a pressure of P = 600 mb and as 10^{-4} for P = 90 mb. Thus, within the scope of the simple-reflection model, the upper limit derived by Spinrad conflicts with Strong's results.

It is unclear whether this discrepancy also applies to the scattering-atmosphere model. Spinrad's estimate is based on the lines of the band λ 8200 Å. Taking an equivalent width of 0.01 Å as the upper limit in the case of Spinrad's study, eq.(3.27) will yield

$$\frac{k}{\sigma} < 4 \times 10^{-5}$$

or, at $\sigma = 10^{-5}$ cm^{-1},

$$k < 4 \times 10^{-10}.$$

According to Kaplan et al. (Ref.91) for these lines $s = 1$ cm^{-1} • gm^{-1}, so that the absolute volume concentration of H_2O is below 4×10^{-10} gm • cm^{-3} and the relative concentration, below 3×10^{-6}.

Strong's measurements were not calibrated in equivalent widths. The present writer, by extrapolating the Bottema growth curves (Ref.276), attempted to perform such a calibration and obtained the mean band absorption $\bar{R} \approx 0.02 - 0.05$, whence

$$\frac{k}{\sigma} \approx 10^{-4} \text{ to } 5 \times 10^{-4}.$$

The intensity of H_2O lines varies in a complex manner along the band. Assuming, on the average, $\bar{s} = 2 \times 10^{-3}$ cm^{-1} $(cm \cdot atm)^{-1}$, we have the relative concentration

$$c_{H_2O} \approx 7 \cdot 10^{-7} \text{ to } 3 \times 10^{-6}, \qquad (3.58)$$

which is much lower than for the simple-reflection model.

c) Other atmospheric gases. The photochemical reaction

$$CO_2 + H_2O + h\nu \rightarrow CH_2O + O_2$$

must lead to the formation of formaldehyde HCHO in the Venusian atmosphere (Ref.279), but apparently the H_2O concentration is too low to produce amounts of formaldehyde sufficiently large to be detected by methods of absorption spectroscopy. From spectra in the photographic ultraviolet, Wildt (Ref.279) derived an upper limit of 3 mm • atm (equivalent path with consideration of the air mass; simple-reflection model). In the emission spectrum of the night part of the /252
disk, N.A.Kozyrev detected bands which he identified with HCHO (Ref.280), but no

TABLE 54

CHEMICAL COMPOSITION OF THE VENUSIAN ATMOSPHERE

Molecule	Model of Scattering Atmosphere, P = 1.5 atm		Model with Simple Reflection*		Remarks	Relative Concentration in Terrestrial Atmosphere, %
	Relative Concentration, %	Partial Pressure, mb	Equivalent Path, cm·atm	Relative Concentration, %		
CO_2	1.5	22	$1-2\times10^5$	10÷20	The ratios $C^{13}:C^{12}$ and $O^{18}:O^{16}$ are the same as on earth	3×10^{-4}
(N_2)	98.5	1480	1.2×10^6	80—90	Spectroscopically not identified	78.1
H_2O	10^{-6}	1.5×10^{-3}	120 **	10^{-4}		1 ***
O_2	$<2\times10^{-5}$	$<3\times10^{-4}$	<70	$<5\times10^{-5}$	Correctness of identification (Refs. 269-271) disputed (Ref. 272)	20.1
CO	1.5×10^{-6}	2×10^{-3}	1.5	10^{-6}	Correctness of identification (Refs. 236, 256) disputed (Ref. 15)	10^{-5}
HClO	?	?	<0.3	$<2\times10^{-7}$	Identified only on the basis of a single emission spectrum (Ref. 280)	—

* Corrected for air mass.
** Namely, 1.2×10^{-2} gm • cm^{-2}.
*** Near surface.

quantitative estimates are available. Moreover, it must be noted that the spectra of the night side of Venus are generally distinguished by their poor reproducibility. N.A.Kozyrev systematically photographed spectra of the night side of Venus near inferior conjunction and found that, as a rule, the appearance of these spectra changed greatly from one conjunction to the other. The ratio of day brightness to night brightness was about 10^4. Hence, scattered light from the bright crescent is a hazardous source of every possible kind of errors, including spurious lines.

The various results on the chemical composition of the Venusian atmosphere

are integrated in Tables 54 and 55. Table 54 presents information on the identified molecules, and Table 55 gives data on the upper limits of the content of certain unidentified molecules that are of interest as possible constituents of the atmosphere or of the cloud layer. In certain cases, the upper limits given are substantially lower than those found by Kuiper (Ref.4).

TABLE 55 /253

UPPER LIMIT OF THE CONTENT OF CERTAIN MOLECULES IN THE VENUSIAN ATMOSPHERE*

Molecule	Equivalent Path, cm·atm	Spectral Region, μ	Laboratory Pressure	Reference	Reduced Thickness in Terrestrial Atmosphere, cm·atm
H_2	5×10^5	0.8	?	(278)	0.5
N_2O	4	2.26	*atm*	(236)	0.4
NH_3	3	2.3	17 *mm*	(236)	—
C_3O_2	2	2.25	67 *mm*	(236)	—
CH_4	2	2.35	*atm*	(236)	1.6
CH_2CH_2	3	2.32	*atm*	(236)	—
CH_3CH_3	2	2.35	70 *mm*	(236)	—

* Simple-reflection model, corrected for air mass.

d) Chemical Composition of cloud layer. The partial pressure P_{H_2O} is too low for saturation to be reached at the temperature of the cloud layer ($T \gtrsim$ $\gtrsim 220^\circ K$; cf. Sect.3.7). At $T = 220^\circ K$, the saturated vapor pressure is $4 \times$ $\times 10^{-2}$ mb (cf. Table 44), whereas observations yield $P_{H_2O} \approx 1.5 \times 10^{-3}$ mb (cf. Table 54). In the model with simple reflection the partial pressure of H_2O is higher, but this model is known to be incorrect.

At such a partial pressure, saturation is reached near $T \approx 180^\circ K$. This temperature is too low for the cloud layer of Venus. In October 1964, Bottema, Strong, and Zander (Ref.281, 282) recorded the spectrum of Venus in the region 1.7 - 3.4 μ with balloon-borne instruments. They identified the bands at $\lambda = 2$ and $\lambda = 2.7$ μ with the absorption bands of ice, but considering the low resolving power they used (800 Å) there exists the danger that this coincidence was fortuitous: Strong bands of CO_2 exist exactly at these wavelengths. Other authors (Ref.281) introduced corrections for CO_2 and H_2O absorption and, as a result, obtained a good fit between the reflectivity curves of Venus and ice clouds, but the validity of this correction is also open to doubt. In one way or another, one of the two findings of Strong's team is erroneous; either the magnitude of H_2O absorption is greater or the clouds do not consist of ice crystals.

Earth-based observations also conflict with the ice-crystal hypothesis. Spectra recorded from the earth's surface are distorted by the superposition of telluric H_2O bands, but their resolution is much higher (10 - 15 Å). The ice /254 bands are shifted approximately 1000 Å with respect to the position of water vapor bands. Such spectra, for example, would distinctly show the bands λ 1.5

and 2.0 μ if these had been present. However, no traces of such bands have been detected (Ref.15, 235). Already several years ago (see Fig.98) Sinton (Ref.255) proposed the hypothesis of ice-crystal clouds to account for the low reflectivity at λ 3.5 μ, but the absence of bands at λ 1.5 and 2.0 μ in spectra recorded from the earth has so far remained a convincing counterargument. It would be highly important in solving this problem to record spectra with a higher resolution by means of balloon-borne apparatus.

Lyot (Ref.242) assumed that the visual polarization curve of Venus is a weighty argument in favor of water clouds. The polarization of infrared radiation, as pointed out above, does not fit the hypothesis of water-droplet clouds (Ref.243). It is unclear whether the spectrum of radio radiation of Venus in the millimeter-wave range can be matched with clouds consisting of ice crystals or water droplets. Some authors answer this question in the negative (Ref.283) and others, in the affirmative (Ref.284, 285).

A number of other hypotheses has been proposed concerning the chemical nature of the clouds:

1) CO_2; recently this hypothesis was supported by Mintz (Ref.165) who claims that adiabatic cooling of CO_2 during vertical updrafts may lead to condensation of CO_2. To achieve this, however, the temperature must drop to 170°K. If the temperature of the upper layer of cloud would actually be that low, the amount of H_2O would have been much less than found by Strong and Dollfus.

2) C_3O_2 - carbon suboxide. This hypothesis was first formulated by Kuiper (Ref.243) referring to an unpublished study by Grot and Hartek. Carbon suboxide must form as a result of the photochemical reaction

$$2CO + CO_2 + h\nu \rightarrow C_3O_2 + O_2; \qquad (3.59)$$

C_3O_2 polymerizes and forms a yellowish powder $(C_3O_2)_n$. The reaction is independent of temperature and thus this hypothesis explains, as it were, why polarization is the same at different points of the disk and why the polarization curve of Venus is stable, recurring from year to year. Sinton and Strong (Ref.25) discovered absorption in the spectral region λλ 8-13 μ which may be ascribed to $(C_3O_2)_n$. Nevertheless, other spectroscopic findings conflict with this hypothesis. The monomer C_3O_2 displays very strong absorption bands in the region /255
λλ 2-2.5 μ and near λ 3350 Å. I.N.Glushneva (Ref.234) obtained the spectrum in the ultraviolet region near the transmission boundary of the earth's atmosphere. This spectrum showed no sharp increase in absorption beyond λ 3350 Å. From the λ 2.25 μ band we estimated (Table 55) the upper limit $(C_3O_2)_n$ content as 2 cm • • atm, which corresponds to a relative concentration of 10^{-6} and a partial pressure of 3×10^{-3} mb, whereas the saturated vapor pressure of C_3O_2 is about 60 mb at -50°C and 1 mb at -100°C. Thus, the $(C_3O_2)_n$ hypothesis seems quite improbable.

3) Hydrocarbons. This hypothesis, proposed by Hoyle and prompted by cosmogonic considerations (Ref.222) was recently supported by Kaplan (Ref.286). It is unlikely, however, that an atmosphere rich in hydrocarbons should lack such molecules as CH_4, C_2H_2, C_2H_4, and other elementary hydrocarbon molecules. Never-

theless, the spectroscopic upper limit for these molecules is extremely low (cf. Table 55). The cloud layer itself should consist of more complex compounds with a sufficiently low saturated vapor pressure, but complex hydrocarbons also display strong absorption bands in the region $\lambda < 2.5\ \mu$ (Ref.14). Kaplan assumes that hydrocarbons are a definite factor in the greenhouse effect. Still, the 700°K surface temperature presupposed by the greenhouse effect must be accompanied by cracking reactions resulting in the release of elementary hydrocarbon compounds. Thus, the hydrocarbon hypothesis also contains contradictions, but there is as yet no reason to reject it conclusively.

4) Mineral dust. All preceding hypotheses were predicated on the condensation of clouds from some gaseous constituent of the atmosphere. This satisfactorily explains the continuous and stable nature of the cloud mantle. The mineral dust hypothesis abandons this convenient explanation. To assume that the clouds consist of mineral dust means postulating for Venus some highly stable yet turbulent system of circulation which maintains the atmosphere in an extremely dust-laden state up to the higher altitudes. Opinions of this kind have been advanced by Öpik [aeolosphere hypothesis; cf. (Ref.41)], but neither Öpik nor any one else has ever constructed a detailed picture of circulation in such an atmosphere.

It must be stated that, at present, we have no satisfactory hypothesis on the nature of Venusian clouds. Most likely, these clouds represent a condensate. The theory of ice-crystal clouds is very attractive but not all observational /256 data support it. The hypothesis of solid carbon dioxide can be completely discarded, and the hydrocarbon and $(C_3O_2)_n$ hypotheses are not too plausible.

e) Chemical interaction between atmosphere and the surface. The high temperature (about 700°K) that apparently exists at the surface of Venus (cf. Sect. 3.8) will of necessity influence the chemical composition of the atmosphere. In particular, it is not precluded that the high temperature has to do with the relatively large amount of CO_2 in the atmosphere of Venus, which is substantially higher than the already abundant amount of carbon dioxide on the earth and on Mars. Urey (Ref.287, 288) suggested that the amount of CO_2 on a planet with liquid water on its surface is governed by the reaction between carbonates and silicates (Urey equilibrium):

$$\underset{\text{magnesite}}{MgCO_3} + \underset{\text{quartz}}{SiO_2} \rightleftarrows \underset{\text{enstatite}}{MgSiO_3} + CO_2, \tag{3.60}$$

$$\underset{\text{calcite}}{CaCO_3} + \underset{\text{quartz}}{SiO_2} \rightleftarrows \underset{\text{wollastonite}}{CaSiO_3} + CO_2. \tag{3.61}$$

The liquid water in this reaction plays the role of a catalyst accelerating the course of the reaction from right to left. The large amount of CO_2 in the atmosphere of Venus initially seemed to be a consequence of a disturbance in the Urey equilibrium due to either the absence of liquid water on the surface or, conversely, to the presence of an ocean covering the entire surface and thus preventing the interaction between atmosphere and surface. At a temperature of 700°K, the presence of an ocean is out of the question so that only the former possibility remains. Adamchik and Draper (Ref.289) calculated the velocities of reactions (3.60) and (3.61) for various temperatures in the absence of H_2O. They

supplemented the reactions (3.60) and (3.61) by a third reaction that should be significant when O_2 is totally or almost totally absent from the atmosphere:

$$FeCO_3 + \frac{1}{2} SiO_2 \rightleftarrows \frac{1}{2} Fe_2SiO_4 + CO_2. \tag{3.62}$$

The dependence of the equilibrium pressure of CO_2 on temperature, calculated by others (Ref.289), is shown in Fig.118. For T = 700°K, the partial pressure of CO_2 is excessively high; it even exceeds the estimates of total pressure ($P < 10$ atm; cf. Sect.3.9). Thus, the Urey equilibrium is upset in the Venusian atmosphere, but in a completely different direction: The CO_2 pressure is lower than given by the reactions (3.60) - (3.62). Apparently, carbonates are chemically unstable on the surface of Venus and the entire oxidized carbon is present in the atmosphere. Müller (Ref.290) independently calculated the rates of the processes (3.60) and (3.61) as well as of certain other similar reactions and, in particular, /257

$$\underset{\text{dolomite}}{CaMgC_2O_6} + 2\underset{\text{quartz}}{SiO_2} \rightleftarrows \underset{\text{diopside}}{CaMgSi_2O_6} + 2CO_2, \tag{3.63}$$

$$\underset{\text{diopside}}{CaMgSi_2O_6} + \underset{\text{calcite}}{CaCO_3} \rightleftarrows \underset{\text{akermanite}}{Ca_2MgSi_2O_7} + CO_2. \tag{3.64}$$

These last reactions give a lower equilibrium pressure of CO_2. An appreciable pressure ($P_{CO_2} \approx 1.5$ atm) is implied by the reaction of the thermal decomposition of magnesite

$$MgCO_3 \rightleftarrows MgO + CO_2. \tag{3.65}$$

Müller also presented weighty arguments against the possibility of the presence of large amounts of hydrocarbons in the atmosphere of Venus at a surface temperature of 700°K. Such temperatures already are accompanied by rather rapid reactions of hydrocarbon cracking.

Section 3.7 Temperatures of Venus Determined from Emission in the Optical Range

a) Equilibrium temperature. Owing to its high albedo, Venus receives only about half as much energy as the earth, despite the fact that it is closer to the sun. By virtue of eq.(1.36) the effective equilibrium temperature of the planet is

$$T_e = \frac{280 \sqrt[4]{1 - A_1}}{\sqrt{R}} = 238 \pm 16^\circ \text{K}$$

(for $A_1 = 0.73 \pm 0.07$). Equation (1.36) presupposes the same effective temperature at every point on the planet and, as we will see below, this is true in first approximation. The indeterminacy of the specified integral albedo probably

exceeds 10% and the error in temperature may be greater than specified.

b) Temperature at the level of occultation of Regulus. According to Menzel and de Vaucouleurs (Ref.69) the scale height of the atmosphere at the level of occultation of Regulus is

$$H = \frac{kT}{mg} = 6.8 \pm 0.2 \ km \qquad (3.56)$$

while the logarithmic gradient of the scale height is /258

$$\frac{1}{H}\frac{dH}{dz} = 0.010 \pm 0.002. \qquad (3.57)$$

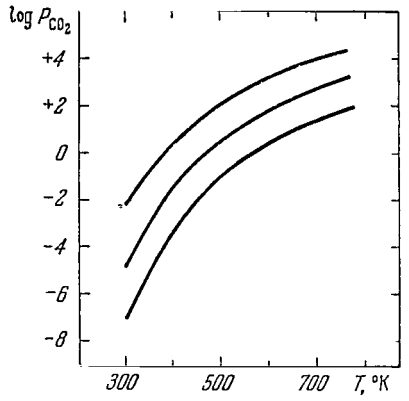

Fig.118 Temperature Dependence of CO_2 Pressure in the Presence of Urey Equilibrium (Ref.289). Upper curve: reaction (3.62); middle curve, reaction (3.61); lower curve, reaction (3.60).

D.Ya.Martynov and M.M.Pospergelis (Ref.291) derived H = 6 km from the same observations (probable error not specified). Let us use the estimate (3.56). Assuming that nitrogen is the principal atmospheric constituent, we have at the level of the occultation

$$T = 200 \pm 6 \ °K. \qquad (3.66)$$

The acceleration due to gravity is here taken as 860 $cm^{-1} \cdot sec^{-2}$. The calculated temperature refers to the upper layers of the atmosphere; the density there is the same as at an altitude of 90 km above the earth's surface. Equation (3.57) yields

$$\frac{dT}{dz} = 2 \ °K / km. \qquad (3.67)$$

The increase in temperature with altitude may mean that the level of occultation is located above the mesopause, with the latter probably coinciding with the dissociation region of CO_2. In Section 3.5 it was shown that the dissociation region is located 15 - 20 km below the level of the occultation.

c) Brightness and color temperatures determined from infrared radiation. The intensities of the natural thermal and reflected radiations of Venus become comparable near 4 μ (cf. Fig.20). In the region λ > 5 μ, reflected radiation can be virtually disregarded. On the night side of the planet thermal radiation can also be measured at shorter wavelengths.

If the effective temperature of radiation is close to 240°K, the peak in the spectral energy distribution must be near λ 12 μ in accordance with Wien's law. Hence, if the emission coefficient is close to unity, the brightness temperature measured according to emission in the 8 - 13 μ transparency window should be close to equilibrium temperature, which indeed is true.

The brightness temperature of Venus was measured in the 8 - 13 μ window by Pettit and Nicholson as far back as in the 1920s (Ref.125); they obtained T_B = = 240°K in the central part of the disk, i.e., a temperature exactly coinciding with the equilibrium temperature. The indeterminacy of this figure is 1 - 2%. Sinton and Strong (Ref.25, 127) confirmed the findings of Pettit and Nicholson. Their observations partly pertained to a more narrow band ($\Delta\lambda \approx 1.5$ μ, near λ 11.9 μ). In addition to photometric observations, they also made spectral observations (with a resolution of about 0.1 μ). Pettit and Nicholson worked with a 2.5-m reflector, while Sinton and Strong worked with the 2.5-m and 5-m reflectors of Mount Wilson and Mount Palomar Observatories. /259

TABLE 56

INFRARED BRIGHTNESS TEMPERATURE OF VENUS

Author	Wavelength Range, μ	T_B, °K	
		At Disk Center	Mean
Pettit and Nicholson (Ref.297)	8—13	250	—
Pettit and Nicholson (Ref.298)	8—13	237	—
Pettit and Nicholson (Ref.125)	8—13	241	—
Sinton and Strong (Refs.127, 25). . . .	8—13	234	226
Sinton (Ref.256)	3.75	237	—
Chase, Kaplan and Neugebauer (Ref.293)	8.4 & 10.4	240	—
Murray, Wildey and Westphal (Ref.294)	8—13	215 *	—
Murray, Wildey and Westphal (Ref.295)		215	—

* With correction published in (Ref.296).

During the Venus flyby of "Mariner II" the radiation intensity of Venus in bands approximately 1 μ wide, centered at λ 8.4 and λ 10.4 μ, was measured with an onboard infrared photometer. These measurements, for both wavelengths, yielded

$$T_B = 240° \text{ K}, \tag{3.68}$$

but the probable error (±10%) is markedly higher than for earth-based observations (Ref.293).

An appreciably lower temperature was recently derived by Murray, Wildey, and Westphal (Ref.294, 295) [see also the correction in (Ref.296)]: T_B = 215°K correct to within ~5%. The above authors (Refs.294, 295) mentioned that their values of T_B may be underestimated owing to indeterminacy of the assumed transmittance of the telescope optics. If, on the other hand, the brightness temperature is indeed 215°K then the integral albedo of Venus must be increased to approximately 0.80 - 0.85. Measurements of the brightness temperature of Venus are collated in Table 56.

Sinton obtained T_B = 237°K near λ 3.75 μ with the aid of a spectrometer

(Ref.260). Thus the color temperature in the λλ 4-10 μ range nearly equals the brightness temperature. In the 8 - 13 μ range, the same equality is observed (Ref.292). It follows from this that the emission coefficient ε in the region λ ≈ 3.5 μ is close to unity and the brightness temperatures are close to the /260
kinetic temperature of the emitting medium. In the interval λλ 3-4 μ, the closeness of ε to unity is directly implied by the low albedo (cf. Fig.98).

All above observations indicate a nearly identical brightness temperature on the day and night sides and the existence of a distinct limb darkening. The best spatial resolution was achieved by Murray, Wildey, and Westphal, namely ~1/40 of the diameter near inferior conjunction. All other observations (including observations from Mariner II) were carried out with a resolution no better than 1/10. The record-breaking spatial resolution in the studies by Murray and coworkers was accomplished by using a sensor with increased sensitivity (mercury-doped germanium cooled with liquid hydrogen); in all other observations, thermal sensors were used.

Figure 119 presents the isophots or, more exactly, the isotherms of Venus with a high spatial resolving power obtained by Murray, Wildey, and Westphal in 1962 and 1964. The pattern of the isotherms changes greatly in the course of a day. The temperature maximum often shifts in the direction of the antisolar point with respect to the center of the disk. The 1962 isotherms were appreciably compressed in - apparently - the direction of the equator. If this is true, then the pattern of this compression can be regarded as a proof of low inclination of the equator. In the isotherms of 1964 this compression is less evident, and on some days (April 14, near quadrature) it is completely absent. A possible reason for this difference may be the fact that the 1962 observations pertained to the sunrise side whereas those in 1964 referred to the sunset side. Isolated local anomalies, some of them displaying a stable nature, also are observed. Thus, on December 15, 1962 a distinct local maximum was observed near the South Pole. The isotherms of 1964 are greatly extended in direction of the South Pole.

The extent of limb darkening, determined by various observers, is roughly the same and may be expressed as

$$T(\mu) = T_0 \mu^{\frac{1}{8}} \tag{3.69}$$

or

$$I = \sigma T^4 \infty \mu^{\frac{1}{2}}, \tag{3.70}$$

where I is the brightness integrated over all wavelengths; μ is the cosine of the angle between the normal to the planet surface and the direction of observation. Suppose the source of emission in the λ 8-13 μ region is the atmosphere. Let us proceed from the premise that the absorption coefficient in this spectral region is much higher than the scattering coefficient. For pure absorption ($k/\sigma \to \infty$, /261
$a \to 0$), the transport equation is

$$\mu \frac{dI_\nu}{d\tau_\nu} = I_\nu - J_\nu(T), \tag{3.71}$$

where $J_\nu(T) = \frac{1}{2}\int_{-1}^{+1} I_\nu(\mu)d\mu$ is the mean intensity; I_ν is the intensity at the optical depth τ. In the presence of local thermodynamic equilibrium $J_\nu \equiv B_\nu$, where B_ν is the Planck function. For outgoing radiation the solution of eq.(3.71) is represented by the function

$$I_\nu(\tau_\nu = 0, \mu) = \int_0^\infty B_\nu(T)\, e^{-\frac{\tau_\nu}{\mu}} \frac{d\tau_\nu}{\mu} \tag{3.72}$$

or, assuming that k_ν = const (gray atmosphere),

$$I(\tau = 0, \mu) = \int_0^\infty B(T)\, e^{-\frac{\tau}{\mu}} \frac{d\tau}{\mu}. \tag{3.73}$$

Within a limited range of values of τ and T we may put

$$B \backsim \tau^\alpha, \tag{3.74}$$

in which case eq.(3.73) yields

$$I(\mu) = I_0 \mu^\alpha. \tag{3.75}$$

A comparison of eqs.(3.70) and (3.75) yields

$$\alpha = 0.5. \tag{3.76}$$

If the mass absorption coefficient $\varkappa$ is independent of pressure and temperature, then

$$\tau = \varkappa\rho H = \varkappa\rho \frac{kT}{m_H \mu g} = \frac{\varkappa P}{g}, \tag{3.77}$$

where ρ is the density; H is the scale height; P is the pressure; m_H is the mass of hydrogen atom; μ is the mean molecular weight. Assuming a linear dependence of temperature on altitude, eqs.(1.122), (3.70), (3.74), and (3.77) will give

$$T^4 = T^{-\frac{\alpha}{\beta}},$$

where /264

$$\beta = \frac{dT}{dz}\frac{k}{m_H \mu},$$

whence

$$\frac{dT}{dz} = -\frac{\alpha m_H \mu g}{4k} = -4\times10^{-5}\ deg\cdot cm^{-1}. \tag{3.78}$$

This gradient (4 deg/km) must apply in the region of $\tau \approx 1$. It is much smaller

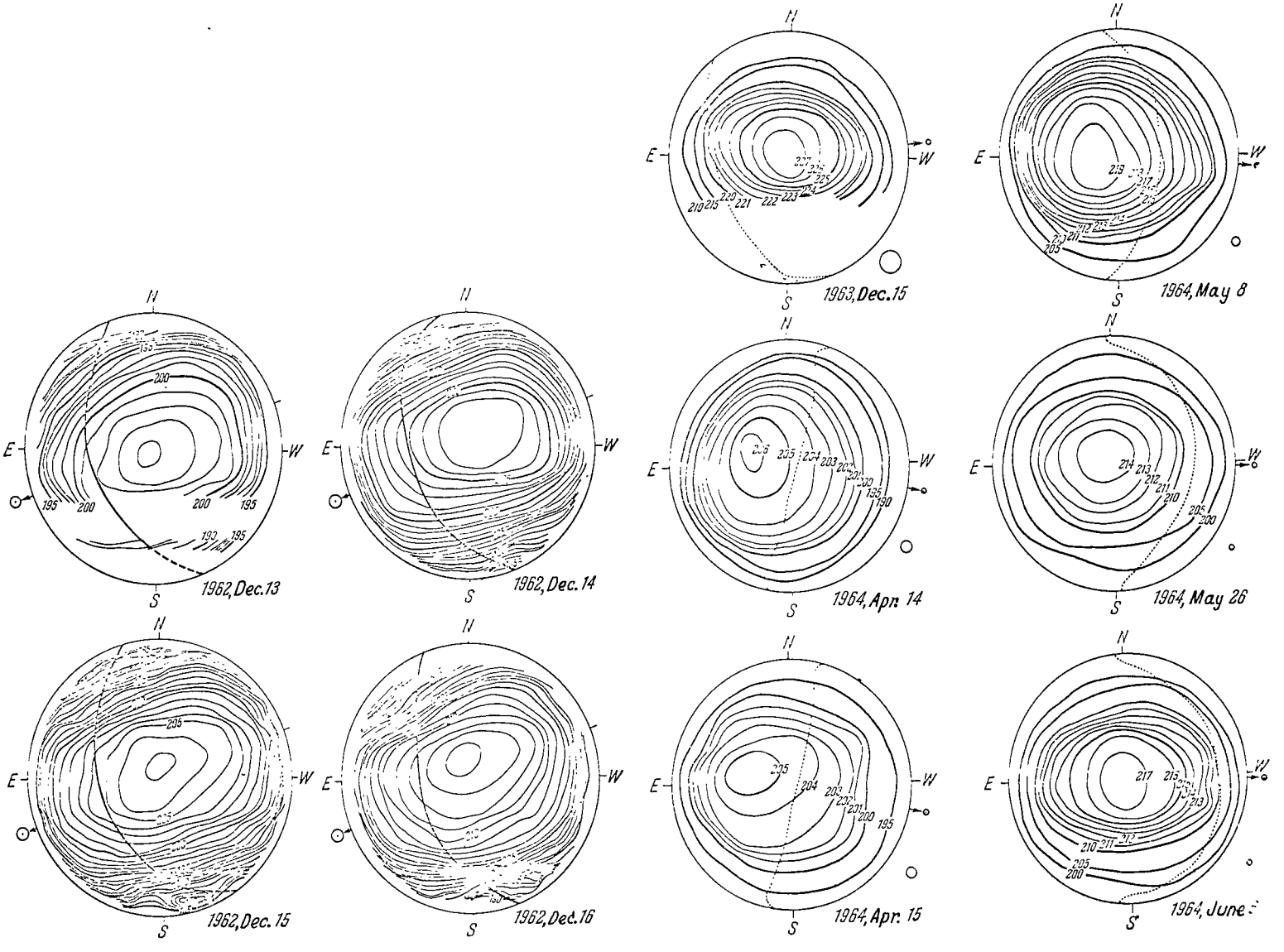

Fig.119 Isophots of Thermal Emission of Venus according to Murray, Wildey, and Westphal (Ref.294, 295); 5-m Reflector of Mount Palomar Observatory.
Circles indicate dimensions of the diaphragm and arrows give orientation to the sun. The isophots are given in °K. The broken line or the heavy solid line refer to the terminator.

than the adiabatic gradient

$$\frac{dT}{dz} = -\frac{g}{c_p} = -8.5\times10^{-5}\ deg\cdot cm^{-1}.$$

If the mass absorption coefficient is proportional to the pressure, as is the case in the line wings, then

$$\tau = \frac{c_0 P^2}{g} \tag{3.77a}$$

and

$$\frac{dT}{dz} = -\frac{\alpha m_H \mu g}{2k} = -8\times10^{-5}\ deg\cdot cm^{-1}, \tag{3.78a}$$

which is much closer to the adiabatic gradient.

Such an interpretation of the observed limb darkening is possible only on condition that $\frac{k}{\sigma} \gg 1$. Moreover, this presupposes an absorption independent of wavelength and also the boundary conditions

$$B \to 0, \quad T \to 0 \quad at \quad \tau \to 0,$$

as well as the approximation $B(\tau) \sim \tau^{\alpha}$, which is of an empirical nature.

In the presence of radiative equilibrium it would be more correct to use, for example, Eddington's approximation

$$T^4 = \frac{1}{2} T^4_{\tau=0}\left(1 + \frac{3}{2}\tau\right). \tag{3.79}$$

Pollack and Sagan (Ref.299) employed this approximation, putting

$$f = \frac{\varkappa_W}{\varkappa_R} \neq 1, \tag{3.80}$$

where $\varkappa_W$ is the mean coefficient of absorption in the range 8 - 13 μ; $\varkappa_R$ is the mean coefficient of absorption according to Rosseland [cf. for example (Ref.300)]. On substituting eqs.(3.79) and (3.80) into eq.(3.72), they obtained

$$I(\mu) = B_W(\tau=0)\left[1 + \left(\frac{3}{2}\right)^2 \frac{\mu}{f} + \left(\frac{3}{2}\right)^{5/2} \pi^{1/2}\left(\frac{\mu}{f}\right)^{3/2} e^{\frac{2f}{3\mu}} \times \right.$$
$$\left. \times \left\{\frac{1}{2} - \varphi\left[\left(\frac{4f}{3\mu}\right)^{1/2}\right]\right\}\right], \tag{3.81}$$

where

$$B_W = \int_{8\mu}^{13\mu} B_\lambda\, d\lambda.$$

/265

It was assumed that $B_w \sim T^6$ within the temperature range in question. The observations actually encompass the interval of $0.5 < \mu < 1$. Within this interval, eq.(3.81) can be roughly represented by eq.(3.70) if f = 2.25. Thus in the region $\lambda > 14\ \mu$, the transparency and hence also the brightness temperature of Venus must be greater than in the region 8 - 13 μ, if the assumption of the absence of scattering (or $a \to \tilde{0}$) is correct.

If, along with absorption, scattering also is a major factor ($a \neq 0$), then the transport equation, according to some other authors [e.g.(Ref.55)], will have the form

$$\mu \frac{dI_\nu}{d\tau_\nu} = I_\nu - (1-a) B_\nu - \frac{a}{2} \int_{-1}^{+1} I \varkappa (\cos \gamma)\, d\mu, \tag{3.82}$$

where $\varkappa$ (cos γ) is the scattering indicatrix (1.73). For a = 0, eq.(3.82) is transformed into eq.(3.71). The emission coefficient is

$$\varepsilon = 1 - A_s(\mu),$$

where $A_s(\mu)$ is the plane-layer albedo. For the indicatrix $1 + \varkappa_1 \cos \gamma$ we have from eq.(1.117)

$$\left.\begin{aligned} \varepsilon(\mu) &= \frac{1}{\mu} \varphi_1^0(\mu), \\ I(\mu) &= B\varepsilon(\mu). \end{aligned}\right\} \tag{3.83}$$

A close angular dependence was experimentally established elsewhere (Ref.302). In isotropic scattering $\varkappa_1 = 0$, a pattern of limb darkening close to the observed value is obtained if we assume a = 0.85 (Ref.301). When $\varkappa_1 = 1$ (indicatrix 1 + + cos γ) the pattern will fit if a = 0.80 (Fig.120). For more extended indicatrices, the value of a will be still lower.

Pollack and Sagan considered a cloud layer with scattering and absorption in the presence of a temperature gradient from two premises: convective equilibrium and radiative equilibrium. The pattern of limb darkening in the presence of high albedos differs little from eq.(3.83) whereas for low albedos it asymptotically approaches eq.(3.81). The results of calculations by Pollack and Sagan are presented in Fig.121. Here, curve a corresponds to a model with pure absorption presupposing $B \sim \tau^a$, while curve b corresponds to eq.(3.81) and curves c and d to combined models for a = 0.8 and 0.99.

At a = 0.8, μ = 1, $\varkappa_1$ = 0, eq.(3.83) yields ε = 0.7, whence the temperature of the cloud layer, to an isothermal approximation, will be /266

$$T = \frac{240}{\sqrt{\varepsilon}} = 260^\circ \text{ K}.$$

If this were true, the brightness temperature in the region of λλ 3-4 μ

(where ϵ is higher) would be close to 255°K and the intensity would greatly exceed the observed intensity, which means that the isothermal layer hypothesis cannot be valid. Apparently, the approach of $a \to 0$ in the region λλ 8-13 μ corresponds to reality.

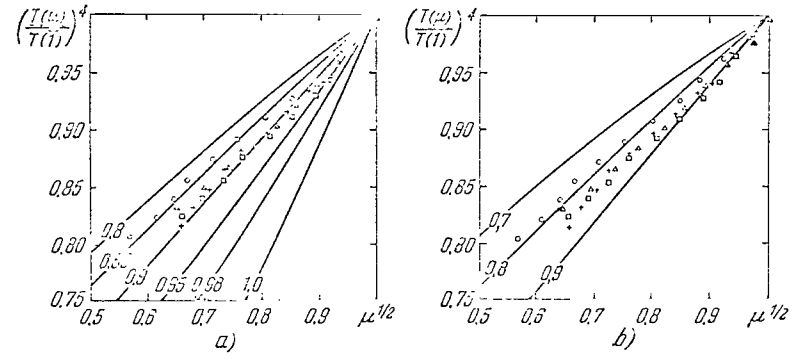

Fig.120 Limb Darkening of Venus in the Region 8 - 13 μ. Circles, triangles, etc. refer to observations by Murray et al. (Ref.294), while the lines represent theoretical curves for an isothermal scattering cloud layer with a specified albedo of the unitary scattering process (a - isotropic scattering; b - indicatrix 1 + cos γ).

Unfortunately, the observable range of μ is too narrow to warrant a substantiated choice between the various theories as to the nature of the observed limb darkening, on the basis of the pattern of $I(\mu)$ alone. The range of μ could be broadened by photometry of the Venus disk at close distance, but this would require a much greater resolving power than was available for the experiment carried out with Mariner II. At any rate, the estimates of the temperature gradient (3.78) and (3.78a) can be taken as the upper limit. If scattering is taken into account, this could only reduce, but not increase, these estimates.

The foregoing is based on the assumption that the atmosphere is the source of infrared radiation. This hypothesis was adopted on the generally intuitive grounds that the surface is shrouded by clouds in the visible portion of the /267 spectrum. In this connection, a purely scattering atmosphere that is optically thick in the region λ 0.5 μ may be optically thin near 10 μ. However, other temperatures (rotational temperature and the temperature determined from radio emission) are known and these, judging from the totality of data, pertain to deeper-lying levels. Undoubtedly, radiation in the region λλ 8-13 μ originates at a considerable height above the surface.

The theory of limb darkening implies that the albedo of the unitary scattering event is $0 < a < 0.8$. Most likely, it is closer to the lower than to the upper limit. The strong absorption in the infrared region is directly visible in the region λ 3-4 μ, where the albedo does not exceed 10% and the parameter

$a \lesssim 0.8$ for an indicatrix $\frac{2\pi r}{\lambda} = 20$ and $a \lesssim 0.5$ for an indicatrix $1 + \cos\gamma$.

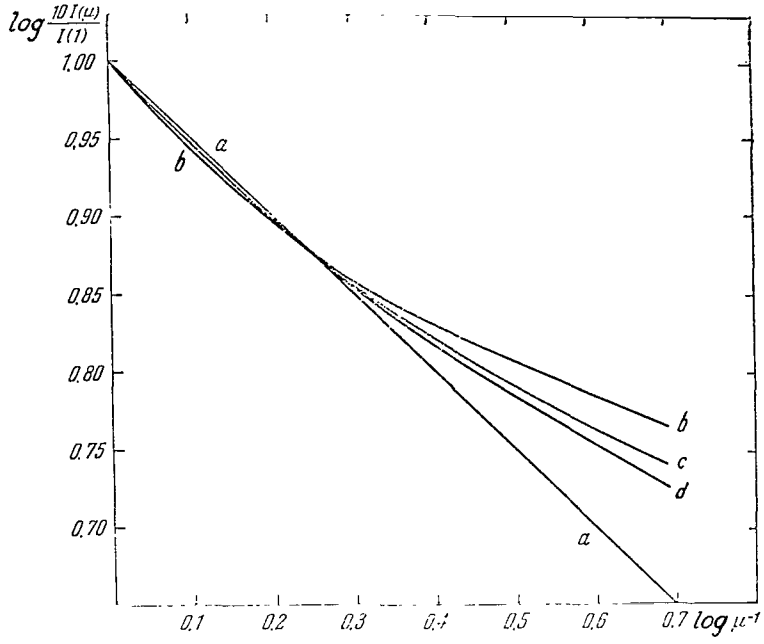

Fig.121 Theoretical Curves of the Limb Darkening of Venus (Ref.299).
a - Pure-scattering model, T = 0 for a = 0; b - Same, T ≠ 0 for a = 0; c - Radiation with scattering for a = 0.8; d - Same, for a = 0.99.

These estimates of the albedo, however, point to a major discrepancy between /268
our own observations (Ref.236) and those by Sinton (Ref.256). We specified A ≈ ≈ 0.01 whereas Sinton gave A ≈ 0.15. The reasons for this discrepancy are unclear, particularly if it is considered that, for Mars, both authors obtained similar findings within this range. If A = 0.01 then a = 0.2 even for elongated scattering indicatrices. At such an albedo of the unitary scattering event, the atmosphere can be considered as purely absorbing. The equality of the brightness temperatures at λ 3.75 μ and λ 10 μ indicates that absorption in these wavelengths is of a comparable extent. The strong absorption in the infrared spectrum region, along with pure scattering in the visible region, is a major argument in favor of the greenhouse model of the atmosphere, which will be examined below.

The spectrum of Venus in the λλ 8-13 μ region, observed with the 5-m reflector by Sinton and Strong (Fig.122), shows no details except a depression at λ 11.2 μ which, as has been assumed, may pertain to C_3O_2 (cf. Sect.3.6). It appears that no substance in the gas phase is capable of giving a continuous absorption spectrum over such a wide interval. It may turn out that the resolving power was insufficient to detect details and that actually there exists a specific fine structure, but this is rather doubtful. Most likely, the absorption is due to a substance in the solid phase such as particles of the cloud layer. It is not precluded, of course, that in the deep-seated layers of the atmosphere

the same radiation-absorbing substance exists in the gas phase.

One of the two channels (λ 10.4 μ) of the infrared photometer on board the Mariner II spacecraft was focused in wavelength on the absorption band CO_2 ($00^0 1 - 10^0 0$; cf. Table 2) and the other, outside the CO_2 absorption bands. Observations revealed no differences in the brightness measured in both channels. In the spectrum obtained by Sinton and Strong (cf. Fig.122) this band also is absent.

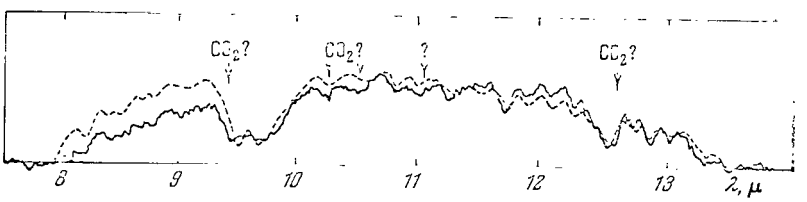

Fig.122 Spectrum of Venus (Solid Line) and Moon (Broken Line) in the Region 8 - 13 μ; 5-m Reflector, Mount Palomar Observatory, Diffraction Spectrometer (Ref.25).

The isothermal scattering layer, in view of the higher emission coefficient compared with a continuous spectrum, should give emission in spectral lines, while the atmosphere with a temperature gradient but without scattering should give absorption. The absence of the λ 10.4 μ band may mean that the temperature gradient compensates for the scattering effect, but this question has not been quantitatively investigated. /269

d) Rotational temperature. The relative intensities of unsaturated rotational lines of linear molecules in the direct-reflection model are determined from eqs.(1.17) and (1.18). In the model of the scattering atmosphere the square law

$$I_K \sim \sqrt{N_K}, \tag{3.84}$$

obviously must apply in lieu of eq.(1.18). Substituting in eq.(1.17) the molecular constants of CO_2 we obtain, for the first model,

$$\log \frac{W(K)}{(2K+1)^2} = \text{const} - \frac{0.244K(K+1)}{T_r}, \tag{3.85}$$

and, for the second model,

$$\log \frac{W(K)}{(2K+1)^2} = \text{const} - \frac{0.122K(K+1)}{T_r}, \tag{3.86}$$

where W(K) is the equivalent width of the line with the rotational quantum number K; T_r is the rotational temperature. In both cases, the atmosphere is assumed to be isothermal.

TABLE 57

/270

ROTATIONAL TEMPERATURE OF VENUS

Author	Band	Model	Method	Temperature, °K
Adel (Ref. 303)	7820Å CO_2	Direct reflection	From number of most intense line	320 (unitary spectrum)
Dunham (Ref. 111)	7820 Å	»	»	300±50
Chamberlain and Kuiper (Ref. 248)*	7820 Å and 8689 Å	Scattering atmosphere	From all lines eq. (3.94)	285±9
Chamberlain (Ref. 251) from material of (Ref. 248)	8689 Å	»	»	291±10
»	8689 Å	»	From all lines on assuming an adiabatic gradient [eq. (3.95)]	272±9
»	8689 Å	»	The same, on assuming a gradient of 0.35 of the adiabatic	283±9
»	8689 Å	Direct reflection	From all lines [eq. (3.93)]	317±14
Spinrad (Ref. 38)	7820 Å	»	»	From 214 to 445 on various days
»	7820 Å	Scattering atmosphere	»	From 142 to 433 on various days
Kaplan (Ref. 286)	7820 Å, unitary spectrum	Direct reflection	From number of most intense line	Two maxima, 325 and 700°K
Moroz (Ref. 246)	1.22; 1.54; 1.61; 1.64 μ	Direct reflection	From distance between maxima of R and P	250±50 (unitary spectrum)
Sinton (Ref. 304)	2.35 CO	»	»	210±75
Moroz (Ref. 246)	2.35 CO	»	»	190±50

* The rotational temperature for the band 8689 Å (T = 286 ± ± 13°K) is given erroneously; for corrected value see line below.

For a semi-infinite scattering atmosphere with a temperature gradient, Chamberlain (Ref.251) found

$$\log \frac{W(K)}{(2K+1)^2} = \text{const} - \frac{1}{K + \Delta K} \frac{0.122K(K+1)}{T_M}, \qquad (3.87)$$

where

$$\Delta K = \frac{b}{2}\left[\frac{K(K+1)}{M(M+1)} - 1 - 2\ln\left(\frac{2K+1}{2M+1}\right)\right],$$

while M is the rotational quantum number of the most intense line in the band;

b is the gradient of the scale height (assuming that $\tau \sim P \sim T^{-\frac{1}{b}}$). The quantity

$$\Delta K = \frac{T_K}{T_M} - 1,$$

where T_K and T_M are the "effective" temperatures corresponding to the lines with the rotational numbers K and M. Equation (3.87) was derived on condition that $\Delta K \ll 1$, i.e., on the assumption that the relative variation in temperature in the region of band formation is limited. If the gradient is less than or equal to the adiabatic ($b \leq 0.3$), the temperatures T_r and T_M, calculated from eqs.(3.86) and (3.87) also will not differ much (Table 57). Equation (3.87) gives lower temperatures than eq.(3.86) while eq.(3.85) gives higher temperatures, but in either case the deviation normally does not exceed 10%.

In Sections 3.3 and 3.4 it was shown that the cloud layer of Venus has a finite optical thickness and that CO_2 bands form throughout this layer, beginning at its base. Equation (3.92), and along with it eqs.(3.86) and (3.87), then still apply if the relative variation in temperature within the confines of the layer is small. The rotational temperature, like the pressure calculated from line widths, is an averaged characteristic of the cloud layer. It would be logical to refer both of these characteristics to the same level in the atmosphere, but this question requires further investigation. /271

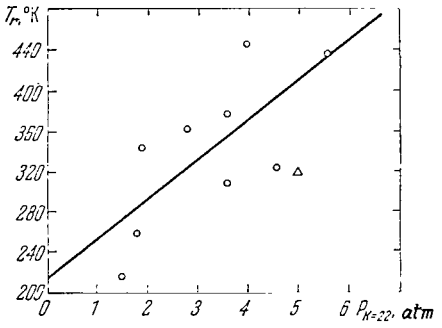

Fig.123 Correlation between Rotational Temperature and Pressure Measured from Lines of the λ 7820 Å Band. The straight diagonal was plotted by the method of least squares (Ref.38).

If the individual rotational lines are not resolved but the overall band contour is recorded with a sufficient accuracy, such that the R- and P-branches are clearly discernible (see, e.g. Fig.106), it is possible to estimate the rotational temperature as a function of the distance between their maxima with the aid of eq.(1.19). By determining the number of the most intense line from the allowed bands, the rotational temperature can be estimated "by eye".

Rotational temperatures were chiefly determined from the CO_2 bands λ 7820 and 8689 Å. This method of estimating the temperature of the Venusian atmosphere was first proposed by Adel (Ref.303). Chamberlain and Kuiper (Ref.248) modified it for the case of a scattering atmosphere. The rotational temperatures display considerable fluctuations from day to day, correlating with variations in pressure and line intensity (Fig.123). There is no systematic phase dependence. Table 57 presents the figures on measurements of rotational temperature by various authors.

The mean rotational temperature of the bands λ 7820 and λ 8689 may be taken as

$$T_r = 285^\circ \text{ K}$$

in the scattering-atmosphere model. Table 58 presents Spinrad's results on variations in rotational temperature and pressure, as based on an analysis of 10 spectrograms obtained in the 1930s by Adams and Dunham with the 250-cm reflector at a dispersion from 2.8 to 5.6 Å/mm. The orientation of the slit with respect to the disk was not given. It is essential that, on some days, the rotational /272 temperature increases above 400°K. Spinrad (Ref.38) and Kaplan (Ref.286) adhere to the opinion that on these days the cloud layer is most transparent so that one can look through to the subjacent atmosphere. From the viewpoint of a scattering atmosphere, the reverse also seems possible, namely that the clouds become thicker exactly at this time and that their lower boundary dips into denser and hotter gas. At any rate, the occasionally observable high rotational temperatures are a weighty argument in favor of the hypotheses postulating an elevated temperature of the planetary surface (cf. Sect.3.8).

TABLE 58

ROTATIONAL TEMPERATURES AND PRESSURES DETERMINED FROM THE LINES OF THE 7820 Å BAND (REF.38)

Plate	Phase of Venus	T, °K		Pressure (atm) in the Direct-Reflection Model		
		Direct Reflection	Multiple Scattering	K=6	K=22	K=33
Cc1720	51°	361±19	305± 23	2.2	2.8	4.0
1745	65	257±12	183± 13	1.4	1.8	6.1
3028	67	434±21	433± 59	3.8	5.6	
1753	74	342±21	328± 31	1.5	1.9	
1756	74	214± 6	142± 5	1.1	1.5	
2292	76	445±31	388± 45	1.8	4.0	
2310	91	322±38	258± 37	1.2	4.6	
2307	91	307±19	270± 33	3.2	3.6	
489	112	376±45	377±100	2.4	3.6	
492	113	319±28	281± 53	2	5	
Mean		337±21	296±25	2.1	3.4*	

* Mean pressure for the first two rows is 2.8 atm. In the model with multiple scattering, this decreases by a factor of $\sqrt{3}$ [cf. eq.(3.15)], i.e., to 1.6 atm.

e) Vibrational temperature. On comparing the ratio of the observed intensities of "hot" to normal CO_2 bands in the spectrum of Venus and their laboratory counterparts, it becomes possible to estimate the vibrational temperature on assuming that the population of the ground level of the hot band is proportional to the Boltzmann factor /273

$$N_v \backsim e^{-\frac{E}{kT}}.$$

If, for a given pair of bands (one of which is hot), the laboratory measurements give a population ratio of α_{lab} whereas observations of Venus give α_{φ}, then the Venusian vibrational temperature will be

$$T_{\kappa} = \frac{E}{k} \frac{1}{\frac{E}{kT_{lab}} - 2.3 \log \frac{\alpha_{\varphi}}{\alpha_{lab}}}, \qquad (3.88)$$

where T_{lab} is the laboratory temperature. Here, it must be considered that on Venus the equivalent width is $W \sim \sqrt{N_{vs}}$ for all bands consisting of non-overlapping lines, whereas in the laboratory this applies only to saturated lines. The ratio of the equivalent widths of the bands λ 1.220 μ ($02^{0}3 - 00^{0}0$) and λ 1.229 μ ($03^{1}3 - 01^{1}0$) is 2.7, whence $\alpha_{\varphi} \approx 2.7^{2} = 7.3$.

/274

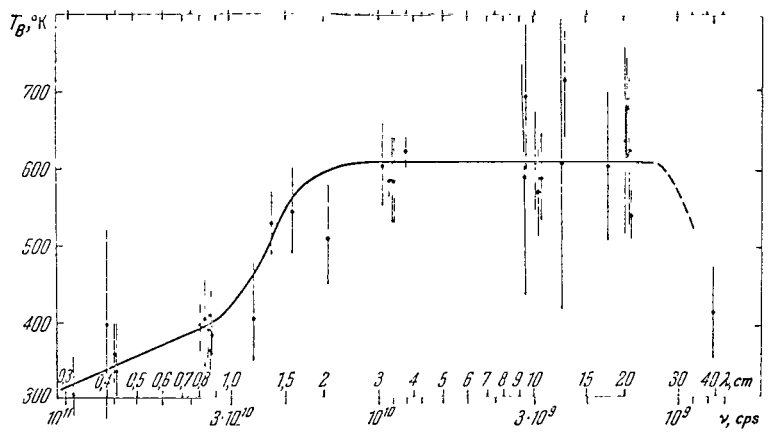

Fig.124 Radio Emission Spectrum of Venus.

In the laboratory spectrum obtained by Kuiper (Ref.243) at a pressure of 5 atm, the hot band is unsaturated and the normal band lies on the intermediate segment of the growth curve. Our estimate shows $\alpha_{lab} \approx 7$ for these bands so that

$$T_{\varphi} \approx T_{lab} \approx 300^{\circ}\ \mathrm{K}.$$

Kuiper himself emphasized that, for the λ 1.229 μ band, T_{φ} is definitely higher than T_{lab}. The discrepancy is attributable to his failure to allow for the difference in growth curves for the Venusian and laboratory spectra.

Section 3.8 Radio Emission of Venus

a) Spectrum of radio emission. Radio emission of Venus was first observed by Mayer, McCullough, and Sloanaker (Ref.130) in 1956 at the 9530-mc frequency (λ 3.15 cm) with the aid of the 15-m precision reflector of the US Naval Research Laboratory. They discovered that the flux of radio emission from Venus is unexpectedly large. The mean brightness temperature calculated from eqs.(1.40) and

TABLE 59

MEAN BRIGHTNESS RADIO TEMPERATURES OF VENUS NEAR INFERIOR CONJUNCTION*

λ	T, °K	Year of Observations	Author
3.2 *mm*	300^{+57}_{-27}	1962	Tolbert and Straiton [cf. Ref. (308,&331)]
3.2	290±50	—	Epstein (cf. Ref. 31)
4	390±120	1961	Kislyakov, Kuz'min and Salomonovich (Ref. 308, 309)
4.3	350^{+50}_{-30}	1961	Grant, Corbett and Gibson (Ref. 310)
4.3	330^{+56}_{-36}	1962	Tolbert and Straiton [cf. Ref. (308,&331)]
8	394±30	1962	Vetukhnovskaya, Kuz'min, et al. (Ref. 311)
8.35	395±60	1962	Thornton and Welch (Ref. 312)
8.5	380^{+72}_{-34}	1962	Linn, Mecks, and Sohigian (Ref. 313)
8.6	410^{+30}_{-20}	1959	Gibson (Ref. 314)
8.6	353±10 **	1962	Copeland and Tyler (Ref. 315)
8.6	375±53	1962	Tolbert and Straiton [cf. Ref. 308,&331)]
1.18 *cm*	395^{+75}_{-55}	1962	Staelin, Barrett, and Kusse (Ref. 316)
1.35	520±40	1962	Gibson and Corbett (Ref. 317)
1.6	535±60	1962	Vetukhnovskaya, Kuz'min, et al. (Ref. 311)
2.07	500±70	1962	McCullough and Boland (Ref. 318)
3.15	595±55	1956	Mayer, McCullough, and Sloanaker (Ref. 130)
3.15	547±5**	1961	Mayer, McCullough, and Sloanaker (Ref. 319)
3.37	575±58	1958	Alsop, Giordmaine, et al. (Ref. 320)
3.75	616±40	1962	Haddock and Dickel [cf. (Ref. 338)]
9.4	580±160	1956	Mayer, McCullough, and Sloanaker (Ref. 130)
9.6	690±100	1961	Bibinova, Kislyakov, et al. (Ref. 322)
10.0	533±60 **	1962	Vetukhnovskaya, Kuz'min, and Salomonovich [cf. (Ref. 31)]
10.0	581±10	1962	Drake (Ref. 323)
10.2	600±65	1959	Mayer, McCullough, and Sloanaker (Ref. 324)
10.7	580±60	1962	Clark and Spencer (Ref. 325)
10.6	560±60	1964	Kuz'min and Clark (Ref. 223, 326)
11.3	605±30	1964	Kellerman (Ref. 411)
12.5	600±200	1962	Stel'zrid and Schuster [cf. (Ref. 327)]
13.0	712±80	1962	Boischot et al. (Ref. 328)
18	596±100	1962	Clark and Spencer (Ref. 325)
21	630±130	1962	Lilley (Ref. 329)
21	674±70	1962	Boischot et al. (Ref. 328)
21	616±100	1962	Clark and Spencer (Ref. 325)
21	596±6 *)	1964	Davis [cf. (Ref. 308)]
21.3	590±30	1964	Kellerman (Ref. 411)
21.4	528±33	1962	Drake (Ref. 323)
31	510±50	1964	Kellerman (Ref. 411)
40	400±60	1962	Drake (Ref. 323)
48	505±100	1964	Kellerman (Ref. 411)

* The observational findings of (Ref.332, 333) near λ 1 cm are separately given in Table 60.

** Only the intrinsic accuracy of observation is given.

(1.32) proved to be

$$T_B = 595 \pm 55^\circ \text{ K}, \tag{3.89}$$

which is substantially higher than the temperatures determined from infrared emission. If the surface of the planet is the source of the radio emission then the brightness temperature should be independent of the wavelength. Hence, on obtaining this result near the inferior conjunction of 1956 at λ 3 cm, Mayer et al. (Ref.130) rapidly switched to another wavelength (9.4 cm); they found the temperature to be almost the same

$$T_B = 580 \pm 160^\circ \text{ K}. \tag{3.90}$$

Mayer, McCullough, and Sloanaker theorized on this basis that the surface of Venus is heated to ~600°K and hence is a waterless desert unfit for the existence of life. This was a rather bold hypothesis, considering that nothing of the kind could be predicted on the basis of previously available data: Venus is very close to the earth in diameter and mass and even receives less heat from the sun than does the earth. Astronomers working on Venus [cf. for example (Ref.6, 221, 222, 264, 306, 307)] had earlier believed that the physical conditions on its surface resemble the terrestrial. Naturally, the problem of radio emission of Venus aroused great interest, and in subsequent years Venus was repeatedly observed at the radio astronomy observatories of various countries. Table 59 and Fig.124 present the brightness temperatures measured near inferior conjunction at various wavelengths, from 3 mm to 48 cm. The accuracy of the measurements is limited by scatter of the test points due to the various signal-to-noise ratios as well as by errors in the absolute instrument calibration and primarily in the determination of antenna parameters. The error in absolute calibration normally is 10 - 20% and, in favorable cases, 5% although the intrinsic accuracy may be much higher (within 1%). Figure 125b shows sample traces of the transit of Venus across the directional /276 diagram, obtained at λ 1.6 and 3 cm with the 22-m reflector of the Radio Astronomy Station of FIAN (Physics Institute, Acad. Sci. USSR) in Serpukhovo (Ref.311).

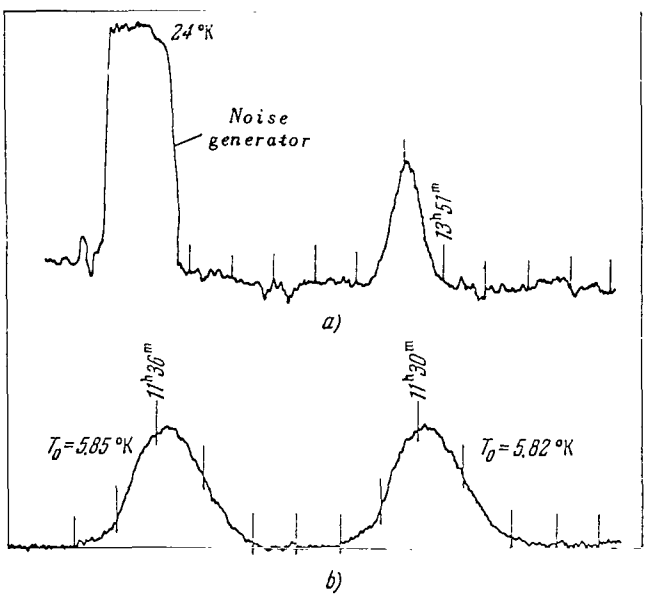

Fig.125 Sample Traces of Transit of Venus across the Directional Diagram of the 22-m Paraboloid at the Physics Institute, Academy of Sciences USSR.
a - λ 1.6 cm, Nov.5,1962; b - λ 3.3 cm, Nov.18,1962 (Ref.311).

As shown, the signal from Venus is recorded very reliably. As the wavelengths increase, the difficulties of measurement also increase since the flux $E \sim \lambda^{-2}$ if T_B = const [cf. eqs.(1.40) and (1.32)]. Moreover, the increase in wavelength is accompanied by a decrease in antenna directivity and gain. For these reasons, very few data have been obtained in the region $\lambda > 21$ cm. At millimeter waves, the accuracy is reduced by the relatively low sensitivity of the instruments.

As can be seen from Table 59 and Fig.124, two main parts may be isolated within the spectrum of radio emission despite the considerable scatter of points: λ 0.3-1.2 cm, where $T_B \approx 380 - 390^\circ$K (but not higher than 410°K) and λ 3-21 cm, where $T_B \approx 600^\circ$K. Presumably, the jump in temperature from $T_B = 395^\circ$K at wavelength λ 11.8 mm (Ref.316) to $T_B = 520^\circ$K at λ 13.5 mm (Ref.317) seems so sharp because of observational errors, but it is not precluded that the transition /277 from the region of $T_B = 400^\circ$K to $T_B = 550 - 600^\circ$K has a fairly steep slope, becoming abrupt in the region $\lambda\lambda$ 12-15 mm. It would be extremely important to determine the real shape of the spectrum in this transition region.

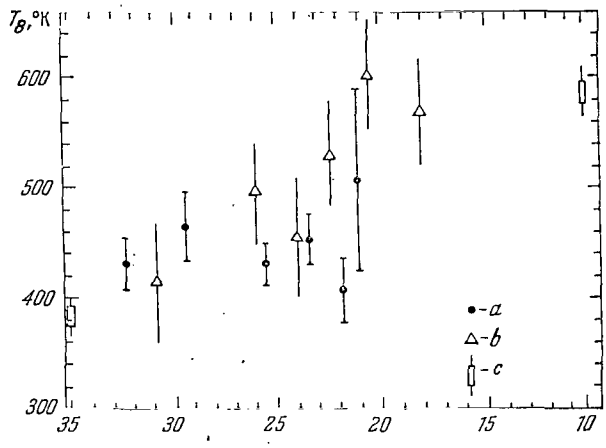

Fig.126 Observational Findings on Venus in the "Transition" Region of its Radio Emission Spectrum.
a - Observations by Staelin and Barrett (Ref.331); b - Welch and Thornton (Ref.332); c - Results of a large number of earlier observations (cf. Table 59).

Attempts at solving this problem were made during the 1964 inferior conjunction by Staelin and Barrett (Ref.330, 331) and Welch and Thornton (Ref.332). Staelin and Barrett observed Venus with a 5-channel receiver which essentially represented five separate radiometers linked to a common antenna. Five traces were simultaneously recorded at $\lambda\lambda$ 1.37, 1.28, 1.18, 1.01, and 0.926 cm. In addition, measurements at λ 1.42 cm were performed with a separate radiometer. Welch and Thornton used a single radiometer which they successively adjusted to wavelengths of 1.653, 1.456, 1.350, 1.245, 1.158, 0.971, and 0.835 cm. The findings are presented in Table 60 and Fig.126. In the region of $\nu > 25$ gigacyles ($\lambda < 1.2$ cm), both series of observations give different results: There are either narrow spectral components or the errors are greater than specified by the authors. The presence of narrow spectral components in this spectrum region is generally not precluded, but it seems strange that the observations by Welch and Thornton, when considered separately, indicate a gradual increase in T_B with wavelength, whereas Staelin and Barrett found a temperature which was uniform - within the error limits - throughout the range of wavelengths from /278 0.926 cm (32.4 cycles) to 1.37 cm (21.9 cycles) and a sharp increase at λ 1.42 cm (21.1 cycles). The observations by Staelin and Barrett encompass a much broader interval of time than those by Welch and Barrett who made observations on only a few days in late July. It is interesting that on these days, at frequencies of

less than 25 Gc, Staelin and Barrett found a higher temperature than the mean, close to the results of Welch and Barrett. If this coincidence is not random, the spectrum of the radio emission of Venus near λ 1 cm would be variable. Further observations in the region λ 1 cm are needed before any serious consideration can be given to such a conclusion. So far it still is impossible to determine what exactly we are dealing with in the transition region of the spectrum - a sharp jump in T_B, a smooth variation with wavelength, or spectral components of a more complex shape.

TABLE 60

SPECTRUM OF RADIO EMISSION OF VENUS IN THE "TRANSITION" REGION [NEAR λ 1 cm (REF.330)]

λ, cm	ν, Gc	T_B, °K	Date	Observer*
1.653	18.15	560±51	July 24	WT
1.456	20.60	505±50	July 25	WT
1.42	21.1	502±80	July 15, 17, 8	SB
1.37	21.9	464±36	**	SB
1.350	22.22	530±45	July 26, 31	WT
1.28	23.5	450±23	**	SB
1.245	24.10	451±53	July 27	WT
1.18	25.5	428±20	**	SB
1.158	25.92	455±50	July 30	WT
1.01	29.5	408±32	**	SB
0.971	30.9	412±55	July 19	WT
0.926	32.4	430±24	**	SB
0.835	35.9	390±45	July 20	WT

* WT - Welch and Thornton (Ref.332); SB - Staelin and Barrett (Ref.331).

** The observations covered 13 days between June 5 and July 30.

Of special interest is the 22.22-mc frequency (1.35 cm) which is the frequency of the rotational resonance line of H_2O. Gibson and Corbett (Ref.317) found $T_B = 520 \pm 40°K$, which indicates the absence of any appreciable absorption. A similar finding was made by Welch and Thornton ($530 \pm 45°K$). On the other hand, Staelin and Barrett (cf. Fig.126) found a distinct minimum of T_B at the 22.22-mc frequency. To resolve this contradiction, further observations are /279 needed. Since the spectrum may vary in time, a multichannel or scanning radiometer must be used for such observations.

b) Variations in intensity. Near superior conjunction, the number of observations has been very small. A.Ye.Basharinov, Yu.N.Vetukhnovskaya, et al. (Ref.333) found the following value at λ 8 mm near superior conjunction:

$$T_B = 490° \pm 50° K,$$

which is approximately 100°K higher than measured with the same radiotelescope

at inferior conjunction (Ref.311). According to other authors (Ref.333), the dependence of T_B on the phase φ at λ 8 mm can be approximated by the formula

$$T_B = 427^\circ + 41^\circ \cos(\varphi - \varphi_0), \tag{3.91}$$

where $\varphi_0 = 21^\circ$ is the angle of lag (the minimum sets in after inferior conjunction). Earlier, A.D.Kuz'min and A.Ye.Salomonovich (Ref.308), for the brightness temperature at λ 8 mm, gave the formula $T_B = 387 + 375$ k where k is the illuminated part of the disk, but this was obtained for $k < 0.6$ and, moreover, as pointed out elsewhere (Ref.311) the calibration was insufficiently reliable. Copeland and Tyler (Ref.315) did not corroborate the considerable phase effect found earlier (Ref.308). According to Copeland (Ref.315),

$$T_B = 353^\circ + 53^\circ k \tag{3.92}$$

for $k < 0.172$ which, within the error limits, does not contradict Vasharinov et al. (Ref.333).

The phase effect at λ 4 mm also is unclear. A.G.Kislyakov, A.D.Kuz'min and A.Ye.Salomonovich (Ref.308, 309) reported that at λ 4 mm the phase course is close to that observed at λ 8 mm. Grant, Corbett, and Gibson found that the brightness temperature at 4.3 mm is independent of phase (Ref.310).

Extensive observational series over a broad range of phase angles were carried out at λ 3.15 (Ref.319) and λ 10.0 cm (Ref.323). For the λ 3.15 cm range, Mayer, McCullough, and Sloanaker (Ref.319) found

$$T_B = 621^\circ (\pm 7) + 73^\circ (\pm 9) \cos[\varphi - 11^\circ.7 (\pm 33^\circ)]. \tag{3.93}$$

Haddock and Dickel (Ref.485) obtained a similar curve at λ 3.5 cm. At λ 10.0 cm, Drake (Ref.323) observed

$$T_B = 622^\circ (\pm 6) + 41^\circ (\pm 12) \cos[\varphi - 21^\circ (\pm 9^\circ)]. \tag{3.94}$$

At λ 10 cm, several points were obtained near superior conjunction and the phase course was derived without extrapolating.

A.D.Kuz'min in his observations made in 1964 in the United States found no phase effect at λ 10 cm (Ref.334). He also analyzed the observations of other authors and showed that the phase effect found earlier at λ 3 and λ 10 cm may be a consequence of a disregarded systematic error (relation of antenna parameters to zenith distance). Thus, the question of the phase effect at centimeter /280
waves cannot be considered even qualitatively solved. It is interesting that the displacement of the minimum of T_B with respect to the time of inferior conjunction (the minimum occurs after conjunction), according to American observations at λ 3 and λ 10 cm, is exactly as it should be for retrograde rotation; however, this may be a random coincidence. A.D.Kuz'min and A.Ye.Salomonovich, in their early observations at λ 3 cm, found a shift in the opposite direction, pointing toward direct rotation (Ref.335).

A.D.Kuz'min and A.Ye.Salomonovich (Ref.308) observed variations in T_B at λ 10 cm from day to day, reaching several hundred degrees. This fact was considered as a proof that the radio emission, at least at λ 10 cm, does not originate at the planetary surface. Other observers (Ref.323), however, found no variations at λ 10 cm that could be considered real, and Kuz'min et al. (Ref.308) subsequently also did not confirm this finding. Most likely, the variations observed by the latter (Ref.308) are due to instrument errors.

/281

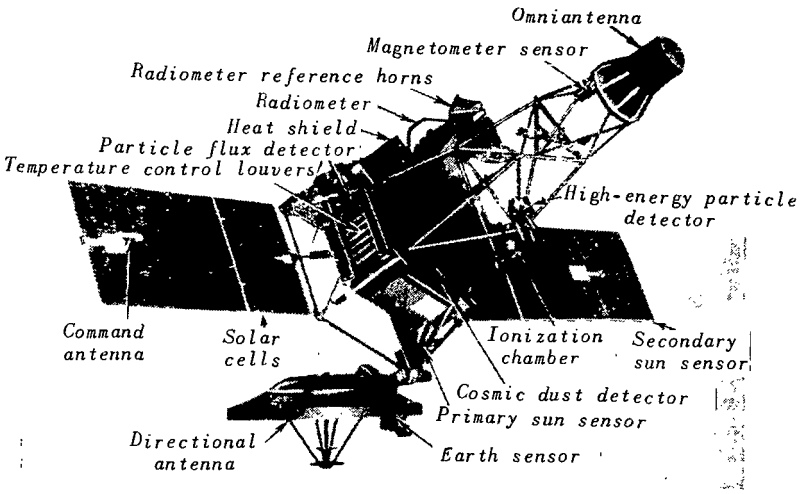

Fig.127 Mariner II Interplanetary Spacecraft.

c) Brightness distribution over the disk. A difficult yet important problem is the investigation of the distribution of brightness temperature over the disk. Comparisons of brightness temperatures at inferior and superior conjunctions can be used only to determine the difference in mean temperature on the dark and illuminated hemispheres. However, the brightness radio temperature may be a function of latitude and may also display a peculiar pattern at the limb, as in the case of the infrared brightness temperature. Lastly, the dimensions of the emitting regions, generally speaking, may exceed the dimensions of the disk. If this actually were the case, we would have a direct proof that the source of emission is not the surface of the planet but the upper layers of the atmosphere. The radio brightness distribution over the planet disk can be obtained in earth-based observations only if one uses a single extremely large antenna or interferometer. The same problem could be solved with the aid of a small radiotelescope mounted on a spacecraft making a close flyby of the planet.

Mariner II (Fig.127) carried a 2-channel radiotelescope at λ 1.35 and 1.9 cm with a paraboloid of a diameter of 48.5 cm. On December 14,1962, during the closest approach of the spacecraft to Venus, the antenna scanned the planet disk three times: once on the illuminated hemisphere, once on the dark hemisphere, and once across the terminator. Figure 128 presents the transmitted traces (a) and the position of each section on the planet disk (b). The authors of the experiment [Barath, Barrett, Copeland, Jones, and Lilley (Ref.336)] pub-

lished only the peak values of brightness temperature corresponding to each section. These are given in Table 61.

TABLE 61

PEAK TEMPERATURES OF THREE RADIOMETRIC SECTIONS OF THE VENUS DISK, OBTAINED DURING FLIGHT OF MARINER II (REF.336)

No. of Section	Distance to Center of Venus, km	Angular Extent of Section	T_B, °K	
			λ 1.9 *cm*	λ 1.35 *cm*
1	46800	10°	480	393
2	44300	15	590	400
3	42500	10	460	396

At λ 1.9 cm, the sections 1 and 3 give a much lower peak brightness temperature than the section 2 and, moreover, the peak brightness temperatures for sections 1 and 3 are almost the same. Thus, it can be stated that at λ 1.9 cm a) limb darkening occurs; b) the temperatures of the dark and illuminated side are virtually the same. At λ 1.35 cm, limb darkening is absent but Barath et al. (Ref.336) do not attach great importance to this, since the precision of measurements at λ 1.35 cm was much lower than at λ 1.9 cm (cf. Fig.128). The probable/283 error is estimated as 5% for the channel at λ 1.9 cm and as 25% for the channel at λ 1.35 cm.

At present, there exists no antenna with a directional diagram of a width smaller than the angular dimensions of Venus (about 1′ at inferior conjunction), but the brightness distribution of the extended source influences the shape of the trace even in cases where the width of the directional diagram is several times as large as the width of the source. Naturally, the transit of the source across the directional diagram must be recorded with high accuracy, and the diagram itself should be clearly defined. Using this method, D.V.Korol'kov, Yu.N. Pariyskiy, G.M.Timofeyeva, and S.E.Khaykin (Ref.337), in observations with the antenna of the Pulkovo Observatory during the inferior conjunction of 1962, found that at λ 3 cm the brightness temperature of Venus does not increase from center to limb (i.e., it either decreases or remains constant). These results are in qualitative agreement with the data acquired by Mariner II.

During the same inferior conjunction, Clark and Spencer observed Venus at λ 9.5 cm with a variable-base two-mirror radio interferometer at Owens Valley (Fig.25) and came to a diametrically opposite conclusion: They found that the brightness temperature either increases toward the limb or remains constant, but in the latter case the dimensions of the radiating region must exceed the dimensions of the apparent disk itself (Ref.325). However, the observations were limited to a narrow range of variation of the base and the results seems unreliable. At any rate, similar observations made in 1964 (during the next conjunc-

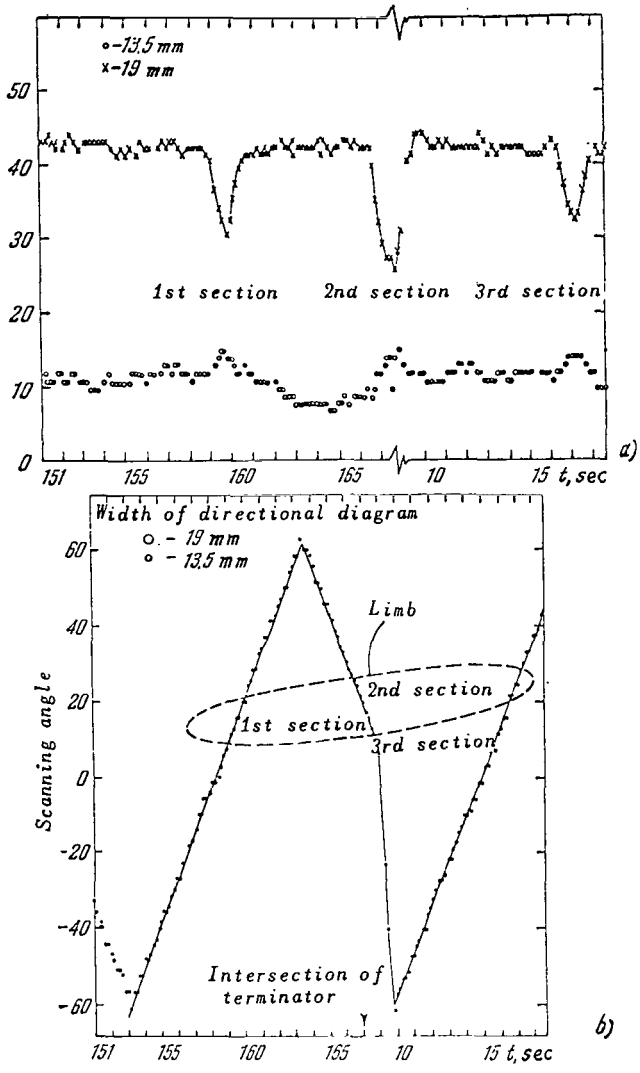

Fig.128

a - Telemetric signal from radiometers at λ 1.35 mm and λ 1.9 cm, received from Mariner II during approach to Venus. The abscissa gives the time reckoning, each unit corresponding to an interval of 120.96 sec. The ordinate gives the signal magnitude.
b - Trajectory of antenna beam in space. Normal scanning rate 0.1°/sec, but switching to "rapid" rate of 1°/sec toward the end of the second sweep; as a result, the third sweep did not extend past the disk (Ref.337).

tion) with the same interferometer by Kuz'min and Clark did not confirm this finding. These observations were carried out on the basis of a more comprehensive program and included polarization measurements. /282

Kuz'min and Clark (Ref.223, 326) found that, along the equator at inferior conjunction, limb darkening is either absent or extremely small (< 2% at the limb compared with the center); limb brightening along the equator is possible and exists, but is not unambiguously implied by the observations. A totally different brightness distribution is obtained along the central meridian: There, a distinct decrease in brightness temperature toward the limb occurs. At the poles, the temperature is 25 - 30% lower than at the antisolar point (center of disk during inferior conjunction). The position of the "pole of cold" established from observations coincides within the limits of error with the position of the pole of rotation found by radar sounding. As for the radius of the radiating region, this proved to be very close to the optical (0.7 ± 0.9% smaller).

A decrease in temperature at the poles on inclination of the axis of rotation to the ecliptic would lead to periodic variations in the mean brightness temperature from one inferior conjunction to another, but this is not observed. This circumstance was pointed out by Pollack and Sagan (Ref.338). The invariability of the mean brightness temperature (at the observed decrease in T_B at the poles) gives the upper limit of the inclination $\epsilon \leq 8^\circ$. /284

d) Nature of radio emission.

The nature of the observed radio emission spectrum has long been disputed and no common consensus has as yet been achieved. Radio waves in the centimeter and decimeter ranges should freely pass through the atmosphere, provided that it is not greatly ionized. In the millimeter range, molecular absorption may occur. Thus, one of the possibilities is that the source of radio emission in the λλ 1.5-21 cm range is a solid surface while that in the λλ 0.4-1.5 cm would be a certain height in the atmosphere. The finding that the brightness temperature, within the limits of accuracy of measurement, is virtually the same at any wavelength beginning with λ 1.5 cm has a natural explanation when interpreted from the viewpoint of this hypothesis. Another problem is the possible cause of the heating of the surface. Two heating mechanisms have been suggested:

a) greenhouse effect [Sagan, cf. (Ref.1)],
b) friction heating [Öpik (Ref.41)].

Below we will discuss these mechanisms in detail. In principle, also the internal heat of the planet may play an appreciable role [A.D.Kuz'min (Ref.339)], but this seems unlikely. At any rate, whatever the heating mechanism, the marked difference between radio temperatures means that the atmosphere must be highly opaque in the infrared region, roughly from 2 μ to 40 μ. This hypothesis also means (again irrespective of the heating mechanism) that the convection zone of the Venusian atmosphere lies at a much lower level than its terrestrial counterpart and that the pressure at the surface is much higher (cf. Sect.3.9).

The hot-surface hypothesis paints a picture of rigorous, inhospitable physical conditions on the surface of Venus, highly dissimilar to our terrestrial environment. Many authors rejected this hypothesis and attempted to find other explanations for the radio emission of Venus. This immediately encountered the obstacle that the radio emission spectrum of Venus is typically thermal. Hence, nonthermal mechanisms such as magnetic bremsstrahlung of electrons of relativistic or subrelativistic energies must be rejected. Scarf (Ref.340) suggested plasma oscillations in the ionosphere as a possible source of this radio emission, but such a process also cannot adequately account for the observed spectrum. Jones (Ref.341, 342) and later other authors considered thermal radio emission /285 of the ionosphere as a possible mechanism. We will examine this mechanism in greater detail.

e) The ionosphere model and its critical evaluation. The absorption coefficient of electromagnetic radiation in plasma is

$$\varkappa = \frac{1}{2c\mu\varepsilon}\,\frac{4\pi e^2}{m}\,\frac{n_e\nu}{\omega^2+\nu^2}, \tag{3.95}$$

where n_e is the electron density; ω is the radiation frequency; ν is the collision frequency; μ is the magnetic permeability; ε is the dielectric constant. If $\omega \gg \nu$, then the absorption coefficient is proportional to the square of the wavelength. In the upper atmosphere this condition is satisfied. Since $\nu \infty n_e$, the optical thickness of the ionosphere can then be written as

$$\tau_\lambda = c(T)\,\lambda^2 \int_0^\infty n_e^2\,dz, \tag{3.96}$$

where c(T) is a weak temperature dependence. At $T = 600^{\circ}K$, $c(T) \approx 6 \times 10^{-27} cm^3$. The brightness temperature T_B is composed of the surface brightness temperature reduced by absorption in the ionosphere and of the brightness temperature of the ionosphere itself

$$T_B = T_{Bs} e^{-\tau_\lambda} + T_e (1 - e^{-\tau_\lambda}), \tag{3.97}$$

where T_{Bs} is the surface temperature; T_e is the ionosphere temperature. The T_B of the ionosphere is $T_e (1 - e^{-\tau_\lambda})$. At $\tau_\lambda \gg 1$

$$T_B = T_e,$$

while at $\tau_\lambda \ll 1$

$$T_B = T_{Bs}.$$

The ionosphere hypothesis assumes that $\tau \approx 1$ at $\lambda \approx 1.5 - 2$ cm and that the surface radiates at shorter wavelengths while the ionosphere radiates at longer wavelengths. This accounts for the relatively low temperature in the region $\lambda > 1.5$ cm and the high temperature in the region $\lambda > 1.5$ cm. Substituting $\tau_\lambda = 1$ into eq.(3.96), we have

$$\int_0^\infty n_e^2 dz = 5 \cdot 10^{25} cm^{-5} \tag{3.98}$$

and, assuming that the ionosphere is a homogeneous region of 5×10^7 cm thickness,

$$n_e = 10^9 cm^{-3}, \tag{3.99}$$

which is 1000 times as much as for the earth's ionosphere. To produce such a high electron density, either the ionization source must be extremely powerful /286 or the recombination coefficient in the atmosphere of Venus must be extremely low [(Ref.1), cf. also (Ref.342)].

This very serious obstacle is not the only one. As pointed out in Section 3.2, within the range λλ 12 cm to 7.8 m the radar reflection coefficient is virtually independent of the wavelength and is approximately 0.1 - 0.2. However, for $n_e = 10^9$ cm^{-3} the critical frequency is

$$\nu_{cr} \approx 10 \sqrt[4]{n_e} \approx 300 \ mc, \qquad \lambda_{cr} \approx 100 \ cm \tag{3.100}$$

which means that, in the range λλ 10 - 100 cm, such an ionosphere can neither reflect (i.e., $\lambda < \lambda_{cr}$) nor transmit (since $\tau \gg 1$) radar signals. In the region $\lambda_{cr} \approx 100$ cm, the reflection coefficient must increase sharply. Assuming that the ionosphere reflects everywhere in the region $\lambda > 10$ cm, it would have a completely improbable vertical structure that simultaneously satisfies two conditions:

$$\lambda_{cr} \leqslant 10\,cm, \tag{3.101}$$

$$\int_0^\infty n_e^2\,dz = 5\times10^{25}\,cm^{-5}. \tag{3.102}$$

Condition (3.109) gives $n_e = 10^{11}\,cm^{-3}$ for $\lambda_{cr} = 10$ cm, whence eq.(3.110) would indicate an ionosphere thickness of 3×10^3 cm. Assuming that the ionosphere partially transmits radio waves ($\tau \lesssim 1$), this will be in disagreement with the observed spectrum of radio emission (T_B = const for $\lambda > 3$ cm).

Lastly, the ionosphere hypothesis assumes that $\tau \approx 1$ at $\lambda \approx 1.5$ cm, whence it follows that the brightness temperature near this wavelength must increase toward the limb. As pointed out above, observations with a high resolving power at λ 1.9 and λ 3 cm do not indicate such limb brightening.

An interesting experiment was proposed by Kuz'min and Clark (Ref.223, 326) in order to decide between the hot-surface hypothesis and the ionosphere hypothesis. It is known that, at oblique incidence, the coefficient of reflection from a smooth interface between two media with different refractive indexes depends on the polarization. Hence, by virtue of Kirchhoff's law, the thermal emission of a sphere whose surface represents such an interface must be partially polarized along the edges (Ref.341). Polarization is absent if the emission source is an amorphous medium lacking a distinct boundary - the ionosphere, the cloud layer, etc.

The integral polarization averaged over the disk must then be extremely small. A resolving power sufficient for isolating the effect for different portions of the disk is required. This may be accomplished by means of a variable-base interferometer. During transit of a discrete source of radio emission /287
across the multilobe directional diagram of a two-aerial interferometer, a sine-wave signal is recorded at the receiver output; the amplitude of this signal depends on the relation between angular diameter of the source and the base, with the length D of the base determining the angular width of the diagram lobes: $\Delta\varphi \approx \frac{\lambda}{D}$. The dependence of the signal amplitude on the base length is termed the visibility function. If the Fresnel-Aragon laws of reflection are applicable at the disk limb, then, at a certain sufficient length of the base, the visibility function $F_\perp$ in the polarization plane at right angles to the base must be greater than the visibility function $F_\parallel$ in the polarization plane parallel to the base. If $F_\perp = F_\parallel$, this will mean that the Fresnel polarization is zero and the emission source is an amorphous medium lacking a distinct boundary.

Polarization observations with an interferometer were carried out at a value of λ 10.6 cm by Kuz'min and Clark during the above-mentioned studies (Ref.223, 326). They found that $F_\perp > F_\parallel$, as should be expected if the emitter is a hot surface. Figure 129 shows the difference $F_\perp - F_\parallel$ they plotted as a function of the effective base

$$\beta = \frac{D}{\lambda} r_\odot, \tag{3.103}$$

where D is the base length; λ is the wavelength; $r_\odot$ is the ephemeridal angular radius of Venus. The diagram also presents calculated values of this difference with respect to a number of values of the dielectric constant of the surface. The best fit between experimental and theoretical findings, as determined by the method of least squares, occurs when

$$\varepsilon = 2.2 \pm 0.2, \tag{3.104}$$

which is somewhat lower than given by radar sounding data (cf. Sect.3.2). The asymmetry in the distribution of brightness temperature, as found in this experiment, should lead to a marked polarization of the integral emission. This does actually occur and the degree of polarization is p = (0.8 ± 0.5)% according to Kuz'min and Clark (Ref.223, 326). Earlier, Seielstad et al. (Ref.345) found p = = (0.6 ± 1.1)% at the same wavelength.

The dielectric constant (3.112) corresponds to an emissivity of 0.911 ± ± 0.010. From this quantity, Kuz'min and Clark derived the true temperature averaged over the entire disk surface /288

$$\overline{T} = 615 \pm 65^\circ \text{ K}. \tag{3.105}$$

The temperature at the equator is 680 - 720°K and at the pole, 425 - 465°K, depending on which pattern of planet-wide surface temperature distribution is assumed.

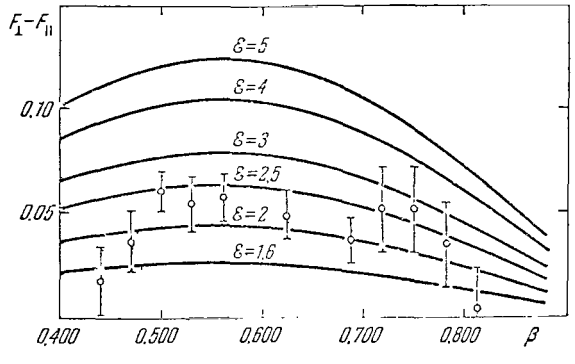

Fig.129 Results of Polarization Observations of Venus with a Variable-Base Interferometer: Difference between Visibility Functions in Directions Perpendicular and Parallel to the Interferometer Base (Ref.326).

Recently, some authors attempted to revise the ionosphere model so that it would not contradict the radar signatures (Ref.346-351). Two hypotheses were proposed: the so-called "sieve" ionosphere (Ref.346 to 350) and the "semitransparent" ionosphere (Ref.349-351). The "sieve" ionosphere would consist of discrete clouds where $n_e \approx 10^9 - 10^{10}$ cm^{-3} and the electron temperature $T_e \geq$ ≥ 1000°K. Radio emission is due to the combined emission of the surface through the gaps between the clouds and of the clouds themselves. Radar signals are reflected from a surface whose true reflection coefficient is higher than measured.

The "semitransparent" ionosphere is located in the lower atmosphere where the collision frequency is so high that τ is independent of λ in the region $\lambda \geq 2$ cm, with the optical thickness being small there: $\tau \ll 1$. At shorter wavelengths, the collision frequency becomes lower than the emission frequency and τ decreases in inverse proportion to the square of the frequency. Radio emission in the centimeter and decimeter wave ranges is the totality of the surface emission escaping through the ionosphere and of the ionosphere itself; in the

millimeter range, only the surface emits - as in the model of the sieve iono- /289
sphere. The low optical thickness ensures passage of radar signals and the condition $\omega < \nu$ guarantees independence of the brightness of the ionosphere emission component of λ, in the centimeter and decimeter ranges. Such an unusual ionosphere must have a moderate electron density ($n \approx 10^7$ cm^{-3}) but is located at a very low altitude: the pressure of the neutral molecules is 0.1 atm. The electron temperature must be fairly high ($T_e \approx 1000^\circ$K).

Both these models do not formally contradict either the radar or the polarization observations (polarization is ascribed to the surface component) but their basic premises seem highly artificial. The dense ionosphere clouds required by the sieve model could be detected in radar experiments as regions in which there is no reflection, by analogy with the previous detection of clouds with higher reflection coefficients. If the dimensions of the clouds were much smaller than the radius of the planet, they should rapidly disintegrate owing to diffusion. A semitransparent ionosphere located in the lower layers of the atmosphere would require some unusual ionization source, since the ultraviolet and corpuscular radiation of the sun does not penetrate into such dense layers. V.M. Vakhnin and A.I.Lebedinskiy (Ref.351), as well as Tolbert and Straiton (Ref.352) suggest electric discharges in the lower atmosphere as the emission source but, as is readily shown, the attendant release of heat would have been incredibly large, comparable with the influx of energy from the sun. A.D.Kuz'min proposed the hypothesis of a superhigh radioactivity on the surface of Venus, maintaining the required ionization of the lower atmosphere (Ref.350). However, in addition to ionization, this would require a mechanism ensuring a high electron temperature.

A correlation has been established between distance to Venus, measured by means of radar sounding at λ 68 cm, and the flux of solar radio emission at λ 10.7 cm [Whipple, cf. (Ref.353)] and λ 20 cm (Ref.348): As the solar activity increases, the measured distance shrinks. This may be attributable to the increase in the density of the ionosphere with increasing solar activity. A value of $n_e < 10^8$ cm^{-3} (in the normal ionosphere at $\nu \gg \omega$) would suffice for an interpretation of the observed effect [Muhlman (Ref.353)]. Thus, the above correlation cannot be viewed as an argument in favor of the ionosphere model.

f) The greenhouse model. This makes it clear that the high brightness temperature of Venus in centimeter and decimeter waves cannot be attributed to iono- /290
spheric radio emission unless fantastic assumptions as to properties of the ionosphere are made. On the other hand, the hot-surface hypothesis is supported by major observational proofs from optical astronomy (cf. Sect.3.7):

1) The rotational temperatures of weak CO_2 bands sometimes are extremely high, as much as 400 - 450°C, and correlate with the width and total intensity of the bands.
2) In the region $\lambda > 2\ \mu$, and particularly $\lambda > 3\ \mu$, the albedo of Venus decreases substantially. If the atmosphere of Venus absorbs the infrared radiation of the sun then the natural radiation of the planet also must be absorbed, and this must lead to heating of the surface.

As pointed out above, two mechanisms have been proposed to account for the high surface temperature: the greenhouse model and the aeolosphere model. First, the greenhouse model presupposes a sufficient transparency of the Venusian cloud

layer with respect to solar radiation, despite the great optical thickness of that layer, and the absorption by the planetary surface of the radiation passing through the layer. Note that in Sections 3.3 and 3.4 it was shown that true absorption in the visible and near infrared regions is absent and that nearly all of the radiation that does not rebound into space reaches the surface. Second, the greenhouse model presupposes an extremely great opacity of the lower atmosphere with respect to the natural thermal radiation of the planet in the region $\lambda > 2.5\ \mu$. This assumption also fits the observations, as we have seen. According to the greenhouse hypothesis, the small amount of sunlight absorbed by the surface heats it to a temperature of 650 - 700°K owing to the opacity of the atmosphere to infrared radiation.

Since CO_2 cannot ensure the necessary opacity over the broad range from 2 to 40 μ, it was assumed in the initial variant of the greenhouse model [Sagan (Ref.1)] that the Venusian atmosphere contains a fairly large amount of H_2O (10 - 100 gm • cm^{-2}). This would quite probably mean that the cloud layer consists of water droplets and ice crystals. In Section 3.6, we saw that some spectroscopic data do not fit such a composition of the clouds. In a later study, Sagan (Ref.354) no longer insisted on large amounts of H_2O and, furthermore, pointed to the well-known fact that CO_2 absorption increases at the relatively high pressures assumed for the surface. A small amount of H_2O (e.g., up to 5 gm • • cm^{-2}) also is not precluded and may even be an appreciable factor. Sagan and Kellogg (Ref.355) assumed that these constituents definitely suffice to produce a strong greenhouse effect. However, the totality of present-day results sug- /291 gests that the atmosphere of Venus contains some other constituents which absorb infrared radiation and may also be responsible for formation of the cloud layer.

The greenhouse model requires transparency of the cloud layer with respect to visible radiation. Öpik (Ref.41) worked out the so-called aeolosphere model of the Venusian atmosphere, to which this requirement does not apply. Its basic idea is that a planetary system of strong winds continually is active in the lower atmosphere, with the atmosphere being extensively dust-laden. Owing to the excessively low content of water vapors, the purifying effect of moisture and rainfall is absent from this atmosphere. The dust layer is virtually impenetrable to solar rays and to the natural infrared radiation of the surface. Owing to this last factor, the relatively small amount of heat generated by friction suffices to heat the surface to a high temperature. The apparent top of the clouds is simply the surface of a perpetually turbulent dust mantle.

The aeolosphere hypothesis encounters two significant objections: 1) It contradicts the observed optical properties of the clouds (as shown in Sect.3.4, absorption in clouds in the visible and near infrared regions is negligibly small); 2) solar radiation in this model is only an indirect source of heating of the surface (its role consists in maintaining the circulation) in which case the radio temperature should be the same at every point on the surface (Ref.41), which is not in agreement with observations. These objections appear sufficient to preclude the aeolosphere hypothesis from further consideration.

A.D.Kuz'min suggested (Ref.339) the internal heat of the planet as the source of heating. He rejected the greenhouse model on the ground that the atmosphere has a great optical thickness. However, he apparently disregarded the fact that an optically thick atmosphere with conservative scattering does not absorb radiation.

It is perfectly obvious that the flux of internal heat must be comparable with the solar heat input so that, for a given surface temperature, the atmosphere would display at least the same characteristics as in the greenhouse model. If the heat influx is smaller, then, at the same surface temperature, there must be either a lower radiative and turbulent heat conduction or a greater thickness of the atmosphere. Moreover, in the presence of such high heat fluxes, the temperature gradient below the surface would reach an absolutely fantastic magnitude. If, according to Kuz'min (Ref.339), the internal heat flux is taken as 2×10^{-4} cal $\cdot$ $cm^{-2} sec^{-1}$ (20 times smaller than the solar heat flux) and /292 the coefficient of heat conduction of the surface layer is assumed as equal to the terrestrial, namely 6×10^{-3} cal $\cdot$ $deg^{-1} cm^{-2} sec^{-1}$, then we have a gradient of 3×10^{-2} deg $\cdot$ cm^{-1} or 3000° per kilometer. In other words, at a depth of 2 km below the surface, the temperature of Venus must be equal to the temperature of the solar photosphere. Obviously, such a model can also be precluded from consideration.

In the hot-surface hypothesis, the interpretation of the decrease in intensity in the mm-wave region in the spectrum of the radio emission of Venus is not directly related to the surface heating mechanism. Such a decrease in intensity can be explained only by true absorption in the gaseous or aerosol constituent of the atmosphere. Scattering there can influence the spectrum only in the case of very large particles. Barrett and Staelin (Ref.327) found that this requires particles of a diameter measuring fractions of a millimeter. Particles of this size will rapidly deposit on the surface.

In the millimeter range at high pressures (10 atm), induced absorption of CO_2 occurs. This possibility was first considered by Barrett (Ref.356) and subsequently by certain other authors [(Ref.357), see also (Ref.327)]. According to Barrett and Staelin (Ref.327) for an atmosphere consisting to 10% of CO_2 and to 90% of N_2, the interpretation of the observed decrease requires a pressure of at least 100 atm. As shown in Section 3.4, the relative concentration of CO_2 is substantially smaller (by at least one order of magnitude) and thus the lower limit of pressure must be increased to 300 atm. As we will demonstrate below, such high pressures are entirely out of the question for the lower layers of the Venusian atmosphere.

The effective cross section for absorption of particles extremely small compared with the wavelength, according to van de Hulst (Ref.52), is as follows:

$$C_{ab} = -\frac{4\pi k a^3}{\lambda} \operatorname{Im}\left(\frac{m^2 - 1}{m^2 + 1}\right), \tag{3.106}$$

where k is the absorption coefficient; m is the complex refractive index; a is the particle radius. If m does not markedly vary with the wavelength, we have

$$\tau \backsim C_{ab} \backsim \frac{1}{\lambda}, \tag{3.107}$$

and the variation in T_B in the theoretical spectrum will be too smooth (Ref.326, 339). Polar liquids (H_2O, many organic compounds) exhibit a sharp variation in

m in the neighborhood of the frequency

$$\nu = \frac{1}{2\pi\tau_r}, \tag{3.108}$$

where τ_r is the relaxation time of the molecule. Here, /293

$$\tau \sim C_{ab} \sim \frac{1}{\lambda^2}, \tag{3.109}$$

so that the steepness of the spectrum is closer to that observed. From the cut-off frequency $\nu \approx 3 \times 10$ cps, we have

$$\tau_r \approx 5 \times 10^{-12}\ sec. \tag{3.110}$$

This is roughly one order of magnitude higher than for water. A.D.Kuz'min (Ref.339) found that the observed spectrum of radio emission is satisfactorily explained by the absorption by droplets of a polar fluid in an amount of 0.2 – 0.3 gm cm^{-2} for $\tau_r \approx 3.5 \times 10^{-12}$ sec.

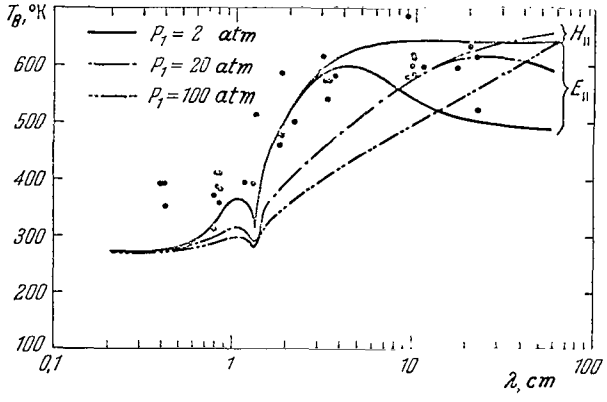

Fig.130 Theoretical Spectrum for an Atmosphere Containing Water Vapor and Clouds.

The water content of the cloud layer is 10^{-6} gm • cm^{-3} and P_{H_2O} = 25 mb at the bottom boundary of the cloud layer. Thickness of the clouds, 6 km; temperature at cloud top, 300°K; at cloud bottom, 270°K; surface temperature, 700°K; temperature gradient, 4.8 deg • km^{-1}. Brightness temperatures, calculated for two narrow zones of the planet surface (one parallel to the electric vector and the other, to the magnetic vector) (Ref.326).

In a watery cloud, absorption by vapors in equilibrium with the liquid phase at the temperature T = 270°K in the millimeter range predominates over droplet absorption. Barrett and Staelin calculated the effect of absorption by H_2O droplets and vapors for the following model (Ref.327): surface temperature 700°K, temperature gradient 4.8 deg/km; cloud layer located between the levels T = = 300°K and 270°K (and only 6 km thick); water content of the clouds 10^{-6} gm • cm^{-3}; vapor in the clouds in equilibrium with the liquid phase (partial pressure /294 P_{H_2O} = 25 mb at the lower boundary); relative vertical concentration of H_2O in the space between the bottom of the clouds and the planet surface roughly constant. The surface pressures of 2, 20, and 100 atm correspond to relative concentrations of 0.8, 0.3, and 0.08. Figure 130 presents the results of the calculations. A rough agreement with observations is obtained

only for the surface pressure $P_1 = 2$ atm. The temperatures at millimeter waves are too high for all three variants, but the fit may become better if the temperature of the cloud bottoms were higher (Ref.283). Unfortunately, the relative concentration of H_2O required by this model greatly exceeds the spectroscopic estimates.

Thus, it is as yet impossible to define the particular molecule responsible for true absorption in the millimeter range, but some of its properties can be predicted. It is highly probable that we are dealing here with droplets of a polar liquid of a relaxation time $\sim 5 \times 10^{-12}$ sec, but gaseous constituents also may make a definite contribution. Absorption by mineral dust, which is characterized by the dependence (3.107), is precluded.

Section 3.9 Vertical Structure of the Atmosphere

Above, we have considered estimates of the chemical composition, temperature, and pressure in the atmosphere of Venus, obtained by various methods. It is logical to attempt to integrate these data into some model of the atmosphere. No doubt such a model would be of an extremely tentative and sketchy nature. Attempts in this direction have been frequent and such models may be found, e.g. in the book by Kellogg and Sagan (Ref.1) which gives three models: greenhouse, aeolosphere, and ionosphere each of which is considered equally probable. Since then certain new observational results have been obtained and we now have grounds for selecting one of these models, namely the greenhouse model, as a working hypothesis of greater probability than all the others. However, even with this hypothesis the atmosphere model remains extremely tentative, since the absorbing agent has not been identified.

a) Structure of an atmosphere of great optical thickness. Let us assume at the outset, as we have done already with respect to the Martian atmosphere, that convection is absent and that the heat transport is due to radiation. Let us further assume that $\frac{k}{\sigma} \gg 1$ for thermal radiation everywhere in the atmosphere and that scattering can be disregarded, and also that the absorption coefficient k is independent of the wavelength. Given these assumptions and the boundary condition /295

$$I(0, \mu) = 0 \qquad (0 > \mu \geqslant -1) \tag{3.111}$$

the solution of the transport equation (3.79) for a semi-infinite atmosphere in Eddington's approximation yields

$$\left.\begin{aligned} J(\tau) = B(\tau) &= \tfrac{3}{4} F\left(\tau + \tfrac{2}{3}\right) \\ T^4 &= T_e^4\left(\tfrac{3}{4}\tau + \tfrac{1}{2}\right), \end{aligned}\right\} \tag{3.112}$$

where T_e is the effective temperature, determined by the ratio

$$\pi F = \sigma T_e^4.$$

with πF being the radiant flux and $J(\tau)$, the intensity averaged over all directions and equal to the Planck function $B(\tau)$ in the presence of a local thermodynamic equilibrium. The flux is constant and directed upward, which means that there are no energy sources in the atmosphere. In the greenhouse model, this condition is satisfied since this model presupposes the scattering of solar radiation without absorption. A portion A of the solar radiation rebounds into space and a portion 1-A reaches the surface and is absorbed by it. In this case,

$$\pi F = (1 - A) E_{\odot},$$

where $E_{\odot}$ is the solar constant at the distance of Venus. As was shown in Section 3.7, $T_e \approx 240^{\circ}K$, which satisfactorily fits the infrared brightness temperature.

For an atmosphere of finite optical thickness [see, for example (Ref.358)], a second boundary condition at the lower edge applies:

$$I(\tau_1, \mu) = \frac{\sigma}{\pi} T_B^4, \tag{3.113}$$

where T_B is the brightness temperature of the surface. The total flux (Ref.55) is

$$\pi F(\tau) = 2\pi B(T_B) E_2(\tau_1 - \tau) + 2\int_{\tau}^{\tau_1} J(\tau') E_2(\tau' - \tau) d\tau, \tag{3.114}$$

where $E_n(x)$ is the integral exponential function /296

$$E_n(x) = \int_1^{\infty} e^{-xt} \frac{dt}{t^n}.$$

General physical considerations suggest that the Eddington approximate solution obtained for a semi-infinite atmosphere [eq.(3.112)] will, with adequate accuracy, also apply to a finite atmosphere of sufficiently large optical thickness. The boundary condition (3.111) also is valid at $\tau = 0$; the second boundary condition (3.113) remains to be added. To this end, we substitute eq.(3.112) into eq.(3.114) and equate, in this equation, the surface flux $\pi F(\tau_1)$ with the flux πF. We then have

$$F\left[\frac{3}{4}\tau_1 + 1 - E_3(\tau_1) + \frac{3}{2} E_4(\tau_1)\right] = B(T_B) \tag{3.115}$$

or, for $\tau_1 \gg 1$,

$$F\left(\frac{3}{4}\tau_1 + 1\right) \approx B(T_B), \tag{3.116}$$

whence

$$\tau_1 = \frac{4}{3}\left[\left(\frac{T_B}{T_e}\right)^4 - 1\right].$$

According to Section 3.8, for the unilluminated side of Venus we can assume

$$T_B \approx 600^\circ \text{ K}.$$

On the illuminated side the temperature is apparently higher. Let us assume that

$$\overline{T}_B = 650^\circ \text{ K} \tag{3.117}$$

averaged over the disk and, furthermore, that the emission coefficient in the infrared region is the same as in the radio range (~0.9). Then,

$$\tau_1 = 70. \tag{3.118}$$

A roughly similar optical thickness is shown in the range of 3 - 100 μ by a 1-mm thick layer of liquid water (Ref.359, 360). This does not mean that a cloud layer of H_2O having a density of 0.1 gm • cm^{-2} would suffice to account for the greenhouse effect. It is clear, however, that the necessary large optical thickness is not inadmissable. Osteriker (Ref.358) compared the solution (3.118) with the exact solution of the problem for an atmosphere of finite thickness. The error in temperature decreases with increasing τ_1. At $\tau_1 = 50$, this error is at most 0.5%, if $\frac{\tau}{\tau_1} > 0.02$. The Chandrasekhar method of successive approximations (Ref.55) is highly accurate but in view of the schematic nature of the premises of our calculations, the solution (3.118) can be considered quite satisfactory. /297

As $\tau \to 0$, the temperature, according to eq.(3.112), tends to the limit

$$T = T_0 = \frac{T_e}{\sqrt[4]{2}} = 0.84 T_e = 200^\circ \text{ K} \tag{3.119}$$

which is in excellent agreement with the estimate (3.66) of the temperature of the upper atmosphere of Venus, derived from observations of the occultation of Regulus. It follows that the upper layers of the Venusian atmosphere ($\tau \lesssim 1$) exist in radiative equilibrium.

At the interface of atmosphere and surface the temperature is

$$T(\tau_1) = T_B \left(\frac{\tau_1 + \frac{2}{3}}{\tau_1 + \frac{4}{3}} \right)^{1/4} = T_B \left[1 - \frac{1}{2} \left(\frac{T_e}{T_B} \right)^4 \right]^{1/4}. \tag{3.120}$$

We see that, at the very surface, the temperature dependence of τ undergoes a discontinuity: the temperature of the lower boundary of the atmosphere is lower than the brightness temperature of the surface. A physical explanation for this discontinuity is the fact that the atmosphere is not a perfect black body. This

discontinuity is also present in the exact solution. Its extent depends on τ_1. At $\tau_1 = 70$, the discontinuity is 5%. The discontinuity between the true surface temperature and the temperature of the atmosphere is even greater. As a result, the narrow surface layer of the atmosphere ($\tau_1 - \tau \ll 1$) is the seat of a strong superadiabatic temperature gradient which might be maintained by the ineffectiveness of convection in such a thin layer.

Assume that the mass absorption coefficient $\varkappa = \frac{k}{\rho}$ is independent of pressure and temperature:

$$d\tau = \frac{\varkappa dP}{g}. \tag{3.121}$$

Differentiating eq.(3.120) and substituting $d\tau$, we obtain

$$T^3 \frac{dT}{dP} = \frac{3\varkappa T_e^4}{16g}. \tag{3.122}$$

Let us integrate this equation for the boundary conditions

$$T \to T_1 \quad at \quad P \to P_1,$$
$$T \to T_0 \quad at \quad P \to P_0 = 0.$$

The first integration within the limits from T to T_1 yields /298

$$T_1^4 - T^4 = \frac{3T_e^4}{4g}(P_1 - P)\varkappa, \tag{3.123}$$

and the second, from T_0 to T_1, taking eqs.(3.119) and (3.120) into account, furnishes

$$P_1 = \frac{4g}{3T_e^4}(T_1^4 - T_0^4)\frac{1}{\varkappa} = \frac{4g}{3}\left[\left(\frac{T_B}{T_e}\right)^4 - 1\right]\frac{1}{\varkappa} = \frac{g\tau_1}{\varkappa}. \tag{3.124}$$

Taking into consideration the equation of hydrostatic equilibrium

$$dP = -\rho g\, dz$$

and of the ideal gas

$$P = \frac{\rho RT}{\mu},$$

eq.(3.122) can be transformed into

$$P = -\frac{16R}{3T_e^4\mu} T^4 \frac{dT}{dz}\frac{1}{\varkappa}, \tag{3.125}$$

and from eqs.(3.123) - (3.125) we have

$$\frac{4R}{\mu g} T^4 \frac{dT}{dz} + T^4 - T_0^4 = 0. \tag{3.126}$$

Integrating eq.(3.126) with the boundary condition $z \to 0$ as $T \to T_1$, we obtain

$$z = \frac{4R}{\mu g}\left\{T_1 - T + \frac{1}{4} T_0\left[\ln\left(\frac{T+T_0}{T-T_0}\right) + 2\,tan^{-1}\left(\frac{T}{T_0}\right) - L\right]\right\}, \tag{3.127}$$

where

$$L = \ln\left(\frac{T_1+T_0}{T_1-T_0}\right) + 2\,tan^{-1}\frac{T_1}{T_0}. \tag{3.128}$$

Figure 131 (curve a) gives the altitude dependence of temperature calculated from eq.(3.127) for

$$T_B = 650°\ \mathrm{K}, \quad T_1 = 618°\ \mathrm{K}, \quad T_0 = 200°\ \mathrm{K},$$
$$\mu = 28, \quad g = 870\ cm^{-1} \cdot sec^{-2}.$$

In the region of $\tau > \frac{2}{3}$, $T > T_e$, the temperature varies with altitude almost linearly with a gradient of 7 deg/km for $\tau \to 0$, $T(\tau) \to T_0$. Equation (3.126) implies that the maximum of the absolute value of the radiative temperature gradient is

$$\left|\frac{dT}{dz}\right|_{\max \mathrm{rad}} = \frac{\mu g}{4R}\left[1 - \left(\frac{T_0}{T_1}\right)^4\right] \leqslant \frac{\mu g}{4R}. \tag{3.129}$$

The adiabatic gradient is /299

$$\frac{dT}{dz} = \frac{g}{c_p} = \frac{\mu g}{R}\frac{\gamma - 1}{\gamma}, \tag{3.130}$$

where $\gamma = \frac{c_p}{c_v}$. If $\gamma > \frac{4}{3}$, then the adiabatic gradient is smaller than the radiative gradient and radiative equilibrium will exist in the atmosphere. If $\gamma < \frac{4}{3}$, we are dealing with convective equilibrium. For diatomic molecules, $\gamma = 1.4$ and the gradient is below the adiabatic (cf. curves a and b in Fig.131). This conclusion presupposes, however, that the mass absorption coefficient is independent of pressure. Absorption in a gaseous medium normally is a function of pressure. Putting

$$\varkappa = \varkappa_0 P, \quad k = \varkappa_0 \rho P, \quad d\tau = \frac{\varkappa_0 P dP}{g}, \quad \tau = \frac{\varkappa_0 P^2}{2g}, \tag{3.77a}$$

as is the case in the line wings, the coefficient for $\frac{dT}{dz}$ in eq.(3.126) may decrease to half. Then,

$$z = \frac{2R}{\mu g}\left\{T_1 - T + \frac{1}{4}T_0\left[\ln\left(\frac{T+T_0}{T-T_0}\right) + 2\,tan^{-1}\left(\frac{T}{T_0}\right) - L\right]\right\}, \qquad (3.131)$$

and the radiative gradient

/300

$$\left|\frac{dT}{dz}\right|_{max\ rad} \approx \frac{\mu g}{2R}\left[1 - \left(\frac{T_0}{T_1}\right)^4\right]$$

will then also be twice as high.

In this case, an atmosphere consisting of diatomic molecules will exist in convective equilibrium only up to the altitude of $\tau \approx 1$, and the radiative gradient will exceed the adiabatic. Exactly such a situation appears to exist in the atmosphere of Venus. If $\varkappa$ markedly increases with temperature, as occurs e.g. for the absorption coefficient of water vapor in the earth's atmosphere owing to near-saturation, the radiative gradient will become even higher.

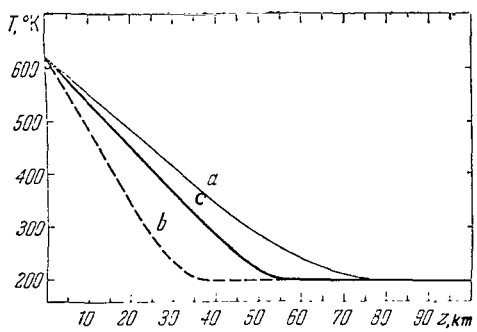

Fig.131 Theoretical Temperature Distribution in the Atmosphere of Venus.
a - Eddington's approximation, volume absorption coefficient $k = \varkappa\rho$; b - Same, $k = \varkappa_0 \rho P$; c - Convective model.

In view of the above, we must expect convective rather than radiative equilibrium for the Venusian atmosphere in the region of $\tau > 1$. It should also be noted that, without convection, it would be difficult to explain how a constant and extremely thick cloud mantle would persist. If, as we assume here, N_2 is the principal constituent of the atmosphere, then the adiabatic gradient would be $\frac{dT}{dz} =$

$= -8.4$ deg $\cdot$ km^{-1}.

In the region of $T \approx T_e$, the temperature gradient is roughly 4 deg/km if $k = \varkappa\rho$ and 8 deg/km if $k = \varkappa_0 \rho P$. Observations of limb darkening suggest the same values of the gradient as above, which indicates an insignificant effect of scattering of the thermal radiation of the atmosphere by particles of the cloud layer (cf. Sect.3.7).

In principle, it is not difficult to solve the same problem for selective absorption if a specific frequency dependence of the absorption coefficient is considered. In the presence of sectors in which k_ν and τ_ν are much higher than in neighboring regions, radiative transport occurs chiefly in these transparency windows. If the mass absorption coefficient can be represented as the product

of two functions [see (Ref.361)],

$$k_\nu = \Phi(P, T)\Psi(\nu, T), \tag{3.132}$$

then the temperature gradient will be

$$\frac{dT}{dz} = \frac{F}{\frac{4}{3}\rho\Phi(P, \overline{T})\int_0^\infty \Psi(\nu, \overline{T})\frac{dI_\nu}{dT}d\nu}. \tag{3.133}$$

The quantity in the denominator is analogous to the conventional coefficient of heat conduction. If we denote by $\overline{\tau}_1$ the total optical thickness of the atmosphere derived from the assumption of gray absorption, then for selective absorption we have $\tau_1 < \overline{\tau}_1$ in the transparency windows and $\tau_1 > \overline{\tau}_1$ between these windows. For example, if we put $\Phi = 1$ and

/301

$$\frac{\Psi(\lambda < 2.5\ \mu)}{\Psi(\lambda > 2.5\ \mu)} = 2 \times 10^{-2},$$

then $\tau = 170$ in the region $\lambda > 2.5\ \mu$ and $\tau = 3.4$ in the region $\lambda < 2.5\ \mu$.

G.M.Strelkov (Ref.362) worked this problem by assuming that the transport takes place in the window $\lambda\lambda$ 8–13 μ (transparency window of water vapor; the windows $\lambda\lambda$ 3–4 μ and $\lambda\lambda$ 2–2.5 μ were not considered). He additionally assumed that the atmosphere is bounded upward by the cloud layer considered as a perfect black body of a specified temperature T. At $T = 300^\circ K$, we then have the following optical thickness in the window $\lambda\lambda$ 8–13 μ

$$\tau_1 \approx 8. \tag{3.134}$$

The optical thickness outside this window was not calculated, but of necessity it must be very large. The estimate (3.134) corresponds to the water vapor content

$$u_{H_2O} \approx \frac{80}{P_1}\ gm \cdot cm^{-2},$$

where P_1 is the total pressure at the surface. At $P_1 = 10$ atm, the estimate (3.134) requires a relative H_2O concentration of 10^{-3} and at $P = 1$ atm, a concentration of 10^{-1}. Spectroscopic estimates give approximately 10^{-6} and in no case more than 10^{-5}. Of course, owing to condensation the H_2O content may be much lower in the cloud layer than at the surface, but the required concentration still seems much too high.

It may be that scattering by aerosol particles reduces the required optical thickness in absorption, but this question has not been quantitatively investigated. Clearly, the albedo of an individual scattering event must be quite close to unity if this mechanism is to reduce τ_1 to an appreciable extent. Ohring

and Mariano (Ref.363) studied the greenhouse effect in the presence of a cloud layer, considered as a perfect black surface of slight porosity. In the absence of porosity, the temperature of the cloud layer must equal the surface temperature and the required optical thickness between them must be zero. The greater the porosity, the higher the required optical thickness. This approach does not settle the basic issue: The problem of radiative transport is merely transferred from the atmosphere below the cloud to the cloud layer. Of a similar nature is the study by Sagan and Pollack (Ref.364), which mainly differs from Ohring's paper (Ref.363) in that Sagan and Pollack considered the cloud layer as continuous but of finite transmittance and albedo.

b) Working models of the atmosphere. Leaving aside the question of the /302
nature of the absorbing substance, which requires further experimental studies, let us now examine in greater detail the basic characteristics of the atmosphere stipulated by the greenhouse model. Solar radiation will directly heat only the illuminated portion of the surface. The temperature of the unilluminated portion, which is observed during inferior conjunction, can be maintained only by thermoluminescence of the atmosphere; if this is sufficiently great, the heat may be retained throughout the night owing to specific heat (see below). Moreover, the heat margin is complemented by the circulation. In one way or another, convection near the surface in a layer with an optical thickness of the order of unity must cease at night. Sagan (Ref.354) assumed that on the night side convection is generally absent throughout the thickness of the atmosphere and a subadiabatic gradient sets in throughout the atmosphere, but this seems doubtful. During the night, the atmosphere of Venus loses such a small portion of its heat (see below) that any marked diurnal variation in its characteristics can hardly be considered (even though the day is roughly equal to four terrestrial months). Hence we shall proceed in our further calculations from the premise that the convective distribution of temperature considered above (Fig.131, curve b) represents the mean diurnal (and mean annual) distribution.

Only two more or less reliable estimates of pressure in the atmosphere of Venus are available. One was derived by de Vaucouleurs and Menzel from observations of the occultation of Regulus and pertains to the upper layers of the atmosphere (Ref.69). At the level where the radiation influx from Regulus decreased in half, there was

$$P = 2.60 \pm 0.13 \times 10^{-3}\ mb. \qquad (3.135)$$

The other estimate was derived by Spinrad from the line widths of the CO_2 λ 7820 Å band (Ref.38). For the direct-reflection model, this amounts to P = 2.8 atm and for the model with multiple scattering in the cloud layer (cf. Sects.3.4 and 3.7), to

$$P = 1.6\ atm. \qquad (3.136)$$

Dollfus (Ref.102), from polarization observations, derived P = 90 mb "at the top of the cloud cover" but this figure is not credible since in the case of Venus it is impossible to distinguish between Rayleigh and aerosol polarizations by any method whatever. The present writer (Ref.236), using the direct-reflection model, derived P = 300 mb "at the top of the cloud cover" from the relative in- /303
tensities of CO_2 bands, but subsequent observations near inferior conjunction

showed that the original model was incorrect and hence this estimate also is meaningless.

The estimate (3.135) pertains to an altitude 62 ± 10 km above the top of the cloud cover, but we do not know the point on the curve of T(z) where this boundary lies (Fig.131). One possibility is to identify the apparent top of the cloud layer with the effective level $\left(\tau = \frac{2}{3}\right)$ of the thermal radiation of the cloud layer, but there exist no direct grounds for this assumption. As pointed out above, the concept of "apparent top of cloud layer" is extremely vague. The temperature at the level of the occultation is known with satisfactory accuracy, but this also does not make it possible to relate the pressure to some altitude above the surface, since an isothermal segment of the curve of T(z) occurs there.

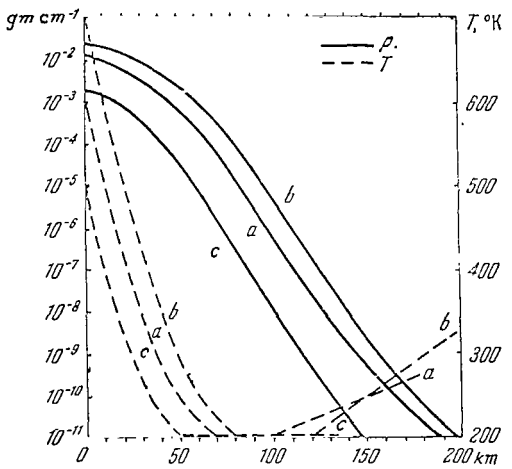

Fig.132 Models of the Atmosphere of Venus.
a - Standard; b - Maximum; c - Minimum.

There remains the estimate (3.136) based on the CO_2 line width, which logically refers to the same altitude as the rotational temperature. It would be highly important to investigate the accuracy of this assumption, but so far this has not been done. Since line width and rotational temperature vary from day to day, the temperatures derived by Spinrad himself (cf. Table 58) must be employed. The mean of his estimates

$$T = 296 \pm 25^\circ \text{K} \qquad (3.137)$$

within the error limits fits the temperature T = 291 ± 10°K found by Chamberlain from the λ 8689 Å band [(Ref.251), cf. Table 57]. The estimate (3.137) was derived on the assumption of an isothermal atmosphere. In an adiabatic atmosphere (cf. Sect.3.7), this must be reduced by 7%, whence

$$T_{ad} = 296 \times 0.93 = 275^\circ \text{K}. \qquad (3.138)$$

The parameter b in the barometric formula (1.122) in the case of an adiabatic atmosphere is as follows:

$$b = \frac{R\left(\frac{dT}{dz}\right)_{ad}}{Mg} = \frac{Rc_p}{M} = 0.29.$$

It seems reasonable to assume, for the level T = 300°K, a pressure of P_1 = = 1 atm for the median model of the atmosphere, 2 atm for the maximum model, and 0.5 atm for the minimum model. Correspondingly assuming surface temperatures of

TABLE 62

MODELS OF THE ATMOSPHERE OF VENUS

Altitude z, km	Temperature T, °K	Pressure P, atm	Quantitative Concentration n, cm^{-3}	Density ρ, $gm \cdot cm^{-3}$	Local Scale Height for Pressure, H	Remarks
			a) Medium Model			
0	600	23	$2,8 \times 10^{0}$	1.4×10^{-2}	19	Surface
10	515	13	$1,6 \times 10^{20}$	8×10^{-3}	16	
20	430	6.7	$1,1 \times 10^{20}$	5×10^{-3}	13	
30	345	2.8	6×10^{19}	3×10^{-3}	11	
40	280	1.0	3×10^{19}	1.5×10^{-3}	9.0	
50	230	0.3	1×10^{19}	5×10^{-4}	7.5	Tropopause
60	210	0.1	4×10^{18}	2×10^{-4}	7.0	Apparent limb
70	200	2×10^{-2}	8×10^{17}	4×10^{-5}	6.5	
80	200	4×10^{-3}	2×10^{17}	1×10^{-5}	6.5	
100	200	2×10^{-4}	8×10^{15}	4×10^{-7}	6.5	
120	220	1×10^{-5}	4×10^{14}	2×10^{-8}	7	CO^2 dissociation
140	240	7×10^{-7}	2×10^{13}	1×10^{-9}	8	Occultation of Regulus
160	260	7×10^{-8}	2×10^{12}	1×10^{-10}	8.5	
180	280	8×10^{-9}	3×10^{11}	1.5×10^{-11}	9.0	
			b) Maximum Model			
0	700	40	5.0×10^{0}	2.5×10^{-2}	23	Surface
10	615	31	3.7×10^{20}	1.8×10^{-2}	20	
20	530	18,4	2.5×10^{0}	1.2×10^{-2}	17	
30	445	10,0	1.6×10^{20}	8×10^{-3}	14	
40	360	4,8	1.0×10^{20}	5×10^{-3}	11.5	
50	280	2,0	5×10^{19}	2.5×10^{-3}	9.0	
60	230	0,8	2.5×10^{19}	1.2×10^{-3}	7.5	Tropopause
70.	210	0.2	7×10^{18}	4×10^{-4}	7.0	
80	200	5×10^{-2}	2×10^{18}	1×10^{-4}	6.5	Apparent limb
100	200	2×10^{-3}	7×10^{16}	4×10^{-6}	6.5	
120	200	1×10^{-4}	4×10^{15}	2×10^{-7}	6.5	
140	210	5×10^{-6}	2×10^{14}	1×10^{-8}	7	CO^2 dissociation
160	260	4×10^{-7}	1.5×10^{13}	7×10^{-10}	8	Occultation of Regulus
180	300	5×10^{-8}	1×10^{12}	5×10^{-11}	10	
200	340	7×10^{-9}	1.5×10^{11}	7×10^{-12}	11	
			c) Minimum Model			
0	500	3,0	4.3×10^{19}	2.1×10^{-3}	18	Surface
10	415	1,6	2.8×10^{19}	1.4×10^{-3}	13	
20	330	0.7	1.5×10^{19}	7.5×10^{-4}	11	
30	260	0,3	8×10^{18}	4×10^{-4}	8.5	
40	220	8×10^{-2}	3×10^{18}	1.5×10^{-4}	7.0	Tropopause, apparent limb
50	200	2×10^{-1}	7×10^{17}	3.5×10^{-5}	6.5	
60	200	4×10^{-3}	1.5×10^{17}	7.5×10^{-6}	6.5	
70	200	8×10^{-4}	3×10^{16}	1.5×10^{-6}	6.5	
80	200	2×10^{-4}	7×10^{15}	3.5×10^{-7}	6.5	CO^2 dissociation
100	200	8×10^{-6}	3×10^{14}	1.5×10^{-8}	6.5	Occultation of Regulus
120	200	4×10^{-7}	1.5×10^{13}	7.5×10^{-10}	6.5	
140	200	2×10^{-8}	7×10^{12}	4×10^{-11}	6.5	
160	200	10^{-8}	4×10^{12}	2×10^{-12}	6.5	

600, 700, and 500°K, eq.(1.122) yields surface pressures of approximately 20, 50, and 3 atm. Tables 62a, b and Fig.132 present these models in greater detail. The mean molecular weight in every case is taken as $\mu = 28$. Kaplan (Ref.365) /304 constructed similar models based on the pressure at the level of occultation of Regulus and derived a surface pressure of 5-10 atm. Such a narrowing of the pressure range can hardly be substantiated.

For all three models, we assumed a convective gradient up to altitudes at which $\tau \approx 1$ in gray absorption.

The amount of heat contained above 1 cm^2 of surface in an atmosphere consisting of diatomic molecules is

$$Q = \frac{5}{2} k \int_0^\infty n(z)\, T(z)\, dz = \frac{5}{2} k \int_0^\infty n_1 \left(\frac{T}{T_1}\right)^{-\frac{1+b}{b}} T\, dz = \\ = \frac{5}{2} P_1 \frac{RT_1}{Mg} = \frac{5}{2} P_1 H_1, \tag{3.139}$$

where n_1, P_1, T_1, H_1 are the concentration, pressure, temperature and height scale, respectively, at the surface. Substituting the figures from Table 61 for the standard model, we have

$$Q = 10^{14}\ erg \cdot cm^{-2}.$$

The length t of the solar day on Venus equals 120 terrestrial days. During the night (one-half of this period) the atmosphere loses /306

$$\frac{t}{2} \sigma T_e^4 \approx 1.3 \times 10^{12}\ erg,$$

i.e., only about 1% of its energy margin. This means that the atmosphere of Venus hardly cools during the night and the nocturnal temperature distribution differs little from the daytime. This may possibly account for the phase independence of the brightness temperature in the region λλ 8-13 μ.

Note, however, that these considerations cannot be exploited as an argument in favor of a high surface pressure [as was done elsewhere (Ref.354)]. First, circulation may largely compensate for that insignificant part of heat lost by the atmosphere during the Venusian night, even at very moderate wind velocities (Ref.366). Second, it is well known that the effective radiation temperature of the earth differs little in the polar and equatorial latitudes. This is due to the fact that the height of the effective level of radiation in the earth's atmosphere (tropopause) decreases with increasing latitude. A similar situation may also exist on Venus, if the cloud layer were to consist of some condensate; the tropopause on the night side would then move farther down. A more substantial proof in favor of a considerable mass of the atmosphere would be a low phase effect in the radio temperature; here, however, the experimental findings are contradictory. If the phase effect at millimeter waves established by the FIAN (cf. Sect.3.8) is confirmed, this would indicate a relatively low pressure.

CHAPTER IV

/307

MERCURY

Section 4.1 Surface

Mercury is the planet nearest to the sun. The semimajor axis of its orbit has a length of 0.387 a.u. and the maximum elongation (apparent recession from the sun) is only about 20°. Near that position Mercury is clearly visible at dawn or at twilight. Not all transits of maximum elongation are equally favorable for observation. The orbital eccentricity is 0.2 and the distance from the sun at perihelion shrinks to 0.308 a.u. whereas at aphelion it reaches 0.467 a.u. Owing to its considerable orbital eccentricity, the stellar magnitude of this planet near maximum elongation varies from $-0^m.3$ to $+0^m.6$. Under sufficiently good atmospheric conditions Mercury can be observed through a telescope in the daytime as well, particularly at periods when transit across maximum elongation coincides with the perihelion.

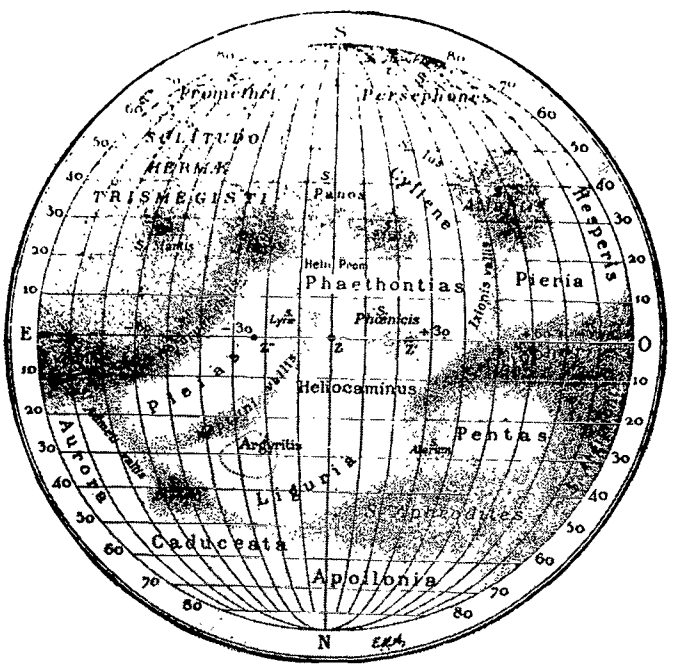

Fig.133 Chart of Mercury according to Antoniadi (Ref.370).

Measurements of the diameter of Mercury give a considerable scatter: from 6".2 to 6".8 at a distance of 1 a.u. De Vaucouleurs (Ref.78) suggests as the most reliable figure $6''.73 \pm 0''.02$ - the mean of the results obtained during the transit of Mercury across the solar disk on November 7, 1960. Transits across the solar disk are particularly important in measuring the diameter of Mercury, since near the customary conjunctions, the diameter is virtually unobservable while at other times the shape of the disk is greatly distorted by the phase. An ingenious method of measuring the Mercurian diameter with a high degree of accuracy was proposed by Hertzsprung: An accurately calibrated diaphragm and, in back of it, a photocell are mounted at the telescope focus during transit across the solar disk on the path of travel of Mercury. The dark disk of Mercury damps the flux from the photosphere and the extent of this damping is used as criterion for accurately calculating the ratio of the angular radii

of diaphragm to planet. With this method Camichel, Hugon, and Rösch (Ref.367) obtained an angular diameter of 6″.84 ± 0″.03 at the distance of one astronomical unit. This corresponds to the linear diameter

$$D_{\mathbb{Q}} = 4960 \pm 20 \text{ km}$$

The mass of Mercury, calculated by Rabe (Ref.368) from perturbations of Eros, is

$$M_{\mathbb{Q}} = \frac{M_{\odot}}{6120500 \pm 43000} = (0.0543 \pm 0.0004)\, M_{\oplus}, \qquad /308$$

whence, if the estimate of diameter is accepted, the mean density will be d = = 5.09 ± 0.07 gm • cm^{-3}, the acceleration due to gravity g = 352 cm sec^{-2}, and the parabolic velocity V_p = 4.2 km • sec^{-1}.

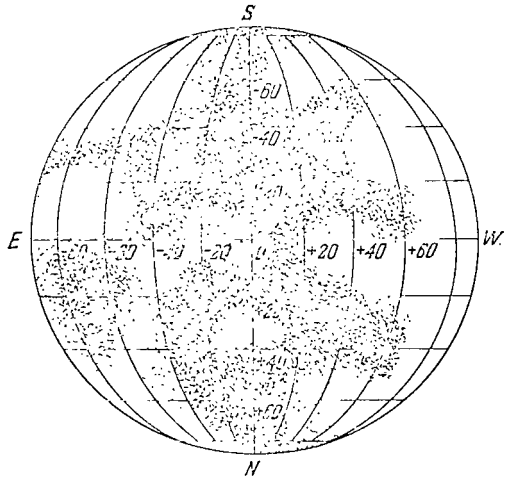

Fig.134 Chart of Mercury, Reproducing the Patches Observed on Ten Composite Photographs Obtained by Lyot and Camichel (Ref.22).

Surface features on the disk of Mercury are discernible only when the visibility is particularly good. Figure 133 gives a chart compiled by Antoniadi from observations with the 33″ refractor at Meudon Observatory, while Fig.134 shows a similar chart derived from photographs by Lyot and Camichel (Pic du Midi, 38″ refractor). In the latter case, a composite printing method was used to enhance the contrast. A comparison of these charts reveals certain common features but on the whole they coincide very little. On comparing the mark- /309 ings observed at various times, Schiaparelli - and later Antoniadi (Ref.369-370) and Dollfus (Ref.22) - concluded that the period of rotation of this planet equals its period of revolution (88 terrestrial days).

However, recent radar soundings cast doubt on this classical conclusion. In 1965, radar soundings of Mercury with a 300-m radiotelescope at Arecibo (Puerto Rico) gave a sidereal rotation period of 59 ± 7 days [Fig.135 (Ref.371)]. The rotation is direct and the axis of rotation is roughly perpendicular to the axis of the ecliptic. The length of a Mercurian solar day is about 180 terrestrial days. This means that roughly two Mercurian years elapse between two successive sunrises.

Other authors (Ref.371a) mentioned that a simultaneous repetition of phase and of the distribution of dark patches over the disk may occur not only in synchronous rotation. Such a repetition may take place also for the rotation period

$$T = \frac{t}{n + \frac{\theta}{360}}, \qquad (4.1)$$

where t is the time interval between observations; n is the number of complete rotations of the planet about its axis; θ is the mean angular displacement of Earth and Mercury with respect to the stars during the time t. On examining 59 drawings made by various observers, McGovern, Gross, and Rasool (Ref.371a) found that the observable repetitions may be explained by periods of 50.1, 58.4, 70.2, and 88 days. The second of these values, namely 58.4 ± 0.4 days, is in good agreement with the period obtained from radar soundings. The visual observations do not contradict the radar signatures. /310

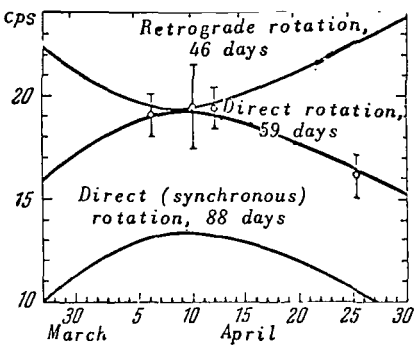

Fig.135 Theoretical Width of Radar Pulse Reflected from Mercury, as a Function of Position near the 1965 Inferior Conjunction. Results of radar soundings of Mercury at λ 70 cm (300-m reflector at Arecibo). Length of vertical segment - extent of probable error (Ref.371).

Colombo (Ref.371b) noted that the rotation of Mercury with a period equal to two-thirds of the period of revolution (58.65 days) should be stable since then, during each transit across the perihelion, the minor axis of the ellipsoid of inertia is roughly directed along the radius vector. Most likely, the rotation period of Mercury indeed equals two-thirds of its period of revolution.

Earlier radar studies of Mercury were carried out in the USSR [Institute of Radio Engineering, Acad. Sci. USSR, team headed by V.A. Kotel'nikov (Ref.372)] at λ 43 cm and in the United States [California Institute of Technology, Carpenter and Goldstein (Ref.373)] at λ 12.5 cm. In these experiments, the reflected signal was too weak to determine the velocity of rotation. Both studies established that the radar reflection coefficient of Mercury is roughly the same as that of the moon (≈ 0.06). Radar soundings at λ 70 cm performed in Arecibo produced a similar result (Ref.374). This gives reason to believe that the surface of Mercury resembles the lunar surface so far as smoothness is concerned. Of course, this refers to surface features comparable to or greater than the wavelength.

Theoretical characteristics of Mercury also greatly resemble those of the moon. Its visual albedo is 0.056 (0.067 for the moon) (Ref.66). For the moon, the albedo monotonically increases with wavelength up to at least λ 1.6 μ (Ref.375). Beyond this limit, the dependence on $p(\lambda)$ no longer is traceable, since then the contribution of thermal emission becomes appreciable. Lastly, the visual phase curves also display a marked similarity for both Mercury and the moon; in both cases, the mean brightness increases rapidly with approach to $\varphi = 0$ [cf. (Ref.66)]. The polarization characteristics of both bodies also are similar. The similarity of optical characteristics points to similarity of the microstructure, if not of the surface material. /311

Nearness to the sun and the low albedo result in high surface temperatures. According to our earlier result (Ref.375), the integral albedo of Mercury is 0.09. Disregarding heat conduction and the effect of the atmosphere, we obtain for the illuminated portion of the disk,

$$E = E_0 \cos\theta = \sigma T_e^4 (1 - A_i)^{-1}, \tag{4.2}$$

from the condition of heat balance between absorbed and emitted energies, where θ is the zenith distance of the sun; T_e is the effective temperature; σ is the Stefan-Boltzmann constant; E_0 is the illumination integrated over the entire solar spectrum at normal incidence

$$E_0 = \frac{E_{0\odot}}{R^2}, \tag{4.3}$$

with R being the distance in a.u. and $E_{0\odot}$, the solar constant. Equations (4.2) and (4.3), for any point on the illuminated portion of the disk, furnish

$$T_e = \frac{395 \sqrt[4]{(1 - A_i)\cos\theta}}{\sqrt{R}}. \tag{4.4}$$

The mean effective temperature of the illuminated portion of the disk can be derived from the ratio

$$\pi r^2 E_0 = 2\pi r^2 \sigma \bar{T}_e^4 (1 - A_i)^{-1}. \tag{4.5}$$

This is equal to

$$\bar{T}_e = \frac{322 \sqrt[4]{1 - A_i}}{\sqrt{R}}. \tag{4.6}$$

The maximum temperature is reached at the subsolar point ($\theta = 0$); it is determined from eq.(2.29). As is readily seen,

$$T_e(\theta = 0) = \sqrt[4]{2}\, \bar{T}_e. \tag{4.7}$$

Table 63 presents values of the effective equilibrium temperature of Mercury, $\bar{T}_e$ and $T_e(\theta = 0)$, calculated for three distances: median, at perihelion, and at aphelion. Owing to the considerable eccentricity, the distance from aphelion to perihelion varies by a factor of 1.5 and the illumination, by a factor of 2.3. Hence T_e also varies substantially; here, the eccentricity effect is much greater than in the case of Mars. On the unilluminated part of the disk, in this approximation, we have $T = 0$.

Pettit and Nicholson (Ref.125), from observations with the 250-cm reflector of Mount Wilson Observatory (equipped with a radiation thermocouple) in the transparency window 8 - 13 μ at the subsolar point, obtained a value of /312

$$T_B(\theta = 0) = 613^\circ \text{K}$$

for the median distance. This nearly coincides with the calculated value (Table 63), although the slight difference may be of real significance. The temperature distribution over the disk was not directly investigated by Pettit and

TABLE 63

EQUILIBRIUM TEMPERATURE OF MERCURY

Distance, a.u.		Mean	At Subsolar Point
Mean	$R = 0.387$ . . .	505° K	618° K
Perihelion	$R = 0.308$ . . .	565	693
Aphelion	$R = 0.467$ . . .	460	563

Nicholson (this is difficult to accomplish owing to the small angular dimensions of the planet due to atmospheric jitter). They calculated $T_B(\theta = 0)$ on the assumption that

$$T_B(\theta) = \sqrt[4]{\cos\theta}\, T_B(\theta = 0) \qquad (4.8)$$

on the illuminated side and

$$T_B = 0 \qquad (4.9)$$

on the unilluminated side.

We obtained spectra of Mercury in the λλ 1-4 μ region with the 125-cm reflector of the GAISh Southern Station (Ref.375) by means of the infrared spectrometers described in Section 1.3. Direct comparison with the solar spectrum (Fig.136) shows that already in the region $\lambda \approx 2\ \mu$ thermal radiation is more intense than reflected radiation. According to measurements performed on October 14 (R = 0.333) the mean brightness temperature at λ 2.2 μ is $\overline{T}$ = = 590 ± 20°K. In calculations of the brightness temperature, it was assumed that the albedo at λ 2.2 and λ 1.6 μ is the same. Assuming that eq.(4.8) is valid, we have everywhere /313

$$T_B(\theta = 0) = 650 \pm 25^\circ\,\mathrm{K},$$

which is somewhat below the theoretical value of T_e for this distance R. The color temperature

$$T_B = 670^\circ \pm 20^\circ\,\mathrm{K}.$$

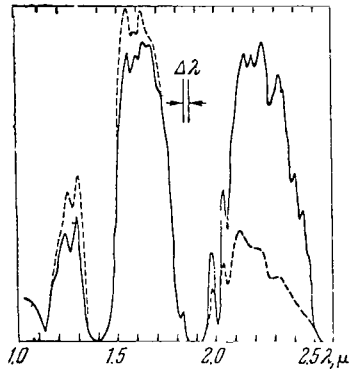

Fig.136 Diffraction Spectrum of Mercury in the Region λλ 1.0-2.5 μ. Sample of unitary trace on Oct.2,1963, z = 77°, slits 0.6 and 5.0 mm ($\Delta\lambda \approx 200$ Å), rate 29 Å/sec, τ = 2.2 sec. Broken line - solar spectrum seen with the same slits, z = 77°.

was derived from the ratios between intensities at λ 2.2 and λ 3.4 μ as observed on October 4 (R = = 0.308, perihelion). Since, in the spectral region satisfying Wien's law, the brightness largely depends on the temperature, the region around the subsolar point furnishes the greatest contribution to the observed radiation. Hence, the color temperature is close to $T_B(\theta = 0)$ and not to $\overline{T}$.

Pettit and Nicholson also derived the phase dependence of the mean brightness of thermal emission of Mercury in the window λλ 8-13 μ. This satisfactorily agrees with the dependence calculated theoretically from eqs.(4.8) and (4.9) (Fig.137). However, this does not imply that the temperature of the night side of Mercury is close to absolute zero. From Fig.137 it can be concluded that

$$\overline{B}_n \leqslant 0.02 - 0.03\overline{B}_d \approx 2 \times 10^{-3}\ \ w \cdot cm^{-2} \cdot sterad^{-1},$$

where $\overline{B}_n$ and $\overline{B}_d$ are the mean brightness values of the night and day sides of the disk, respectively. Table 64 indicates that this corresponds to the following upper limit of the mean night temperature:

$$\overline{T}_n \leqslant 250^\circ \text{K}.$$

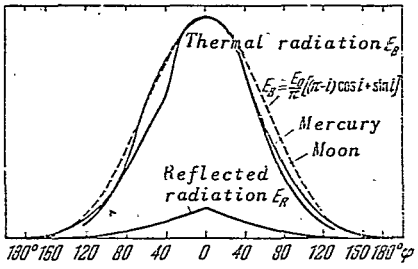

Fig.137 Radiation of Mercury and Moon as a Function of Phase Angle and Theoretical Curve for a Smooth Slowly Rotating Perfect Black Sphere (Ref.125).

Measurements of the integral flux of infrared emission of Mercury will not give any more definite data on the temperature of the non-illuminated portion of the disk. The reason is obvious: The temperature dependence of the infrared brightness is extremely great so that the contribution by the night side is very small, even at comparatively high "terrestrial" temperatures.

Despite this fact, it had been assumed until quite recently that the temperature on the dark side of Mercury does not exceed several tens of degrees on the Kelvin scale. Thus /314 Walker (Ref.376), assuming that the rate of heat release at the interior of Mercury is the same as for chondrites (flux 22 erg · cm^{-2} · sec^{-1}) and disregarding heat conduction, found a value of T = 25°K for the night side and a value of T = 28°K when allowing for heat conduction, under stipulation of synchronous rotation. The heat flux from the earth's interior is several times as large. Assuming that the heat flux from Mercury's interior equals the terrestrial flux (64 erg · $cm^{-2}sec^{-1}$) and disregarding heat conduction, the temperature will be 33°K. If the findings

TABLE 64

BRIGHTNESS IN THE 8 - 13 μ INTERVAL IN RELATION TO BRIGHTNESS TEMPERATURE

T_B, °K	Brightness, $w \cdot cm^{-2} \cdot sterad^{-1}$	T_B, °K	Brightness, $w \cdot cm^{-2} \cdot sterad^{-1}$
100	8×10^{-7}	350	6.2×10^{-3}
140	2.8×10^{-5}	400	1.3×10^{-2}
180	2.3×10^{-4}	450	2.4×10^{-2}
220	8.9×10^{-4}	500	3.3×10^{-2}
260	2.3×10^{-3}	550	4.5×10^{-2}
286	3.4×10^{-3}	600	5.7×10^{-2}
300	4.8×10^{-3}	650	6.9×10^{-2}

obtained in Arecibo are correct and Mercury does not rotate synchronously, the theoretical temperature of the dark side must be higher. The temperature of the moon during eclipses decreases to 160 - 180°K within one hour. If the heat inertia of Mercurian rocks is close to that of lunar rocks, then the temperature on the night side of the rotating Mercury (at absence of an atmosphere) must be

comparable to the dark side of the moon (100 - 120°K).

Since the brightness is proportional to the first degree of temperature on the Rayleigh segment of the Planckian curve, the night side must make a comparatively large contribution to the radio emission. Radio emanation from Mercury was first discovered in 1961 by Howard, Barrett, and Haddock (Ref.330, 377) at λλ 3.45 and 3.75 cm. Near quadrature, the mean brightness temperature was found to be $T_B = 400 \pm 80°K$. The observations were not sufficiently accurate to determine the phase dependence of the radio temperature. Assuming that the temperature distribution over the disk is described by eqs.(4.4), the brightness radio temperature at the subsolar point must be markedly higher than its infrared counterpart: $T_B(\theta = 0) = 1100 \pm 300°K$ (at median distance).

Field (Ref.378) mentioned that this estimate can be greatly reduced and reconciled with the infrared observations on assuming /315

$$\bar{T}_n \approx 200 - 300° K,$$

Barrett (Ref.330) gave a more exact estimate:

$$\bar{T}_n = 270° K.$$

Kellerman (Ref.379), during May to June 1964, observed the radio emission of Mercury at λ 11.3 cm with the aid of the 68-m radiotelescope at Parker, Australia. This study was carried out over a broad range of phase angles from 29 to 145° but, within the accuracy limits of measurement, no phase dependence was established (Fig.138). The mean brightness temperature over the disk is $\bar{T}_B = 293 \pm 13°K$. These results also can be considered as indicating a comparatively high (200 - 300°K) temperature of the unilluminated side of Mercury. Welch and Thornton (Ref.332) found $\bar{T}_B = 465 \pm 115°K$ at λ 1.53 cm for a mean phase angle $\varphi \approx 120°$ (illuminated portion of the disk, k = 0.25). The temperature distribution over the disk can be represented by the general formula

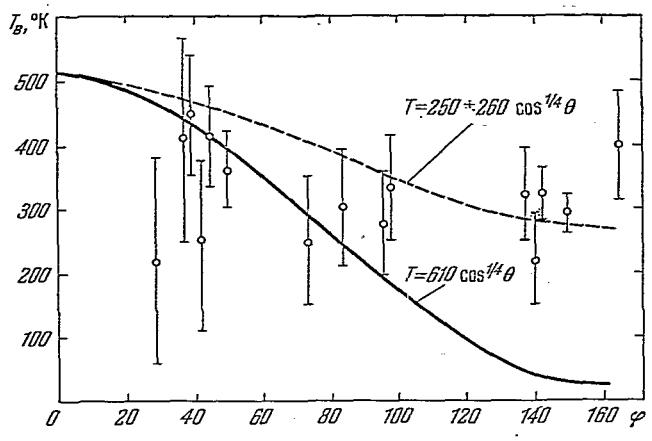

Fig.138 Brightness Temperature of Mercury at λ 11.3 cm according to Kellerman's Observations with 68-m Australian Reflector.

$$T_B = T_0(\cos\theta)^n + T_n, \qquad (4.8a)$$

where T_0 is the temperature at the subsolar point, T_n is the temperature of the unilluminated part (assumed to be identical at every point of that portion). /316
Putting $T_n = 0$, $T_0 = 620°K$, $n = 0.5$, for $k = 0.25$ we have

$$\bar{T}_B = 100° K.$$

To reconcile the theoretical $\overline{T}_B$ with the observed $\overline{T}_B$ (465°K), we must assume that

$$T_n = 440° \text{ K}.$$

The high temperatures on the dark side, established at centimeter waves, do not refer to the surface but to some effective radiation-generating level located at a depth of several wavelengths. In synchronous rotation the temperature of that level differs little from the surface temperature, while in some opposite case the rotation-induced temperature fluctuations may become smoothed out due to thermal inertia, as is the case for the moon. As is known, the brightness temperature of the moon at λ 10 cm is independent of the phase. Another possible explanation (the only one in the case of synchronous rotation) would be the effect of an atmosphere. For the atmosphere to release heat to the surface on the unilluminated side of the planet, it must contain molecules absorbable in the infrared spectrum region.

The effect of the thermal inertia of the ground must decrease with the wavelength. The radio temperatures of the moon exhibit an appreciable phase dependence; beginning with λ 3 cm, the oscillation amplitude increases in keeping with the transition to shorter wavelengths. In this connection, the observations of Mercury at λ 8 mm, performed with the aid of the 22-m antenna of the FIAN (Physics Institute of the Acad. Sci. USSR) by Kutuza, Losovskiy, and Salomonovich (Ref.380) are of special interest. These observations give $T_B(\theta = 0) = 660 \pm 120°$K if we put $n = \frac{1}{4}$ and $T_n = 0$ in eq.(4.8a), and $T_B = 540 \pm 85°$K if $n = 0$ and $T_n = 0$. Moreover, the idea of the possible existence of a phase dependence (increase in T_B with approach to full phase) is advanced, although not too confidently. In the light of these findings, it seems probable that the relatively high brightness temperature of the dark side at centimeter waves may be attributed to rotation of the planet, but this question still needs quantitative investigation. The experimental results also cannot be considered exhaustive. It would be extremely important to measure the temperature from infrared emission on the dark side. If that temperature were to prove comparable with the temperature determined at centimeter waves, we would have an indisputable proof of the existence of an atmosphere capable of transporting heat from the illuminated side to the dark side and transmitting it to the surface.

Section 4.2 Hypothetical Atmosphere of Mercury /317

Antoniadi (Ref.370, 381) interpreted the variable visibility of discrete dark and bright spots on the disk of Mercury as the possible effect of haze and clouds in the atmosphere. Observations of markings on the surface of this planet are extremely difficult, and variations of the above kind can naturally not be considered a valid argument for the existence of a Mercurian atmosphere. More significant in this respect is the result obtained by Dollfus (Ref.102) who discovered that the polarization at the center of the disk is greater in green light than in red, and greater near the cusps than at the center. According to Dollfus, the observed anomalies in polarization may be attributed to Rayleigh scattering in a gaseous atmosphere containing approximately 3 gm $\cdot$ cm^{-2} of air in

the vertical column. This interpretation is not without ambiguity, considering the small magnitude of the effect.

The parabolic velocity at the surface of Mercury is low (4.2 km • sec^{-1}) and the proximity to the sun suggests high temperatures at the critical level. Hence the lighter gases - H, He, O_2, N_2 - must completely disappear from such an atmosphere over the geological times (cf. Sect.4.3). Heavy polyatomic molecules apparently also cannot persist, owing to dissociation and subsequent dissipation of their component elements. All this implies that the atmosphere of Mercury, if it does exist would consist of inert gases chiefly of argon since this is the most abundant inert gas on the earth. Synchronous rotation has often been mentioned as an additional factor interfering with the formation of a dense atmosphere, since it must cause the freezing-out of the atmosphere on the dark side. However, this process may be inoperative even at synchronous rotation, owing to the heating of the dark side by the atmosphere itself. Moreover, the temperature of the Mercurian atmosphere may be lower, in principle, than that of the earth. This temperature is determined from the correlation between solar energy absorption and processes leading to energy losses of the upper atmosphere molecules. The influx of energy to Mercury is greater but, correspondingly, also the cooling processes - under certain assumptions - may be more effective (see below). Generally, there is no cogent reason for a priori rejecting the possibility of a molecular atmosphere on Mercury, similar to the atmospheres of other planets in the terrestrial group.

We made an attempt to compare the CO_2 absorption band intensities near λ 1.6 μ in the Mercurian and lunar spectra (Ref.375). These intensities were greater in the spectrum of Mercury. This observation was made at the sensitivity threshold, which makes it desirable for other observers to confirm the reality /318 of this intensification. At first [in 1963, cf. (Ref.382)] the sun was used as the comparison standard, but in the spring of 1964 it was found that a consistent difference exists between the equivalent widths of CO_2 bands in the spectra of both sun and moon. The reason for this difference has not been defined. There is some basis for assuming that it has nothing to do with diurnal variations in the amount of CO_2 in the atmosphere or with nonlinearity of the receiver. In one way or another, since this difference does exist and since the equivalent widths in the lunar spectrum are greater, it was decided to use only the moon for comparison. Both Moon and Mercury were observed under highly similar conditions, with the same light grasp of the lenses, identical slits and equal magnification, whereas during comparisons with the sun the first and third conditions were not satisfied.

Figure 139 shows the total equivalent widths of CO_2 bands at λ 1.575 and 1.606 μ in the Mercurian and lunar spectra as a function of zenith distance, derived from observations on March 30 and 31,1964. Each of the two points for Mercury represents the mean of all measurements made during the same day.

On comparing observations of the sun in various months we established the existence of a slight seasonal variation in the equivalent width of the CO_2 absorption bands. In October they were broader than in March (by 10%), while in May they returned to their October level. For this reason, the spectra of Mercury obtained in October were compared with spectra of the moon obtained in May. In Fig.140 the equivalent widths of the bands at λ 1.6 μ in the spectrum of Mer-

cury obtained on October 14 are compared with morning observations of the moon on May 29. In all, 35 spectra from the observations on October 14 were analyzed, divided into several groups, and averaged for each group. The curves in Figs.139 and 140 confirm the strengthening of the CO_2 λ 1.6 μ bands in the spectrum of Mercury. Observations made in September 1964 produced the same result. As is known, the CO_2 content of the surface layer of the earth's atmosphere is at its highest just before dawn; consequently, the use of morning observations of the moon for a comparison with Mercury apparently does away with the possibility of a spurious effect due to diurnal variations in CO_2. /319

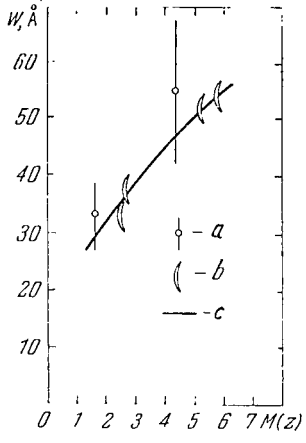

Fig.139 Total Equivalent Width of Carbon Dioxide Bands λ 1.57 and 1.61 μ in the Spectra of Mercury (a) and Moon (b), March 30-31,1964, from Spectra with Resolution of 100 Å (Recording Rate 14.5 Å/sec, Theoretical growth curve (c). The length of the vertical segment represents the mean-square error. Abscissa: air mass.

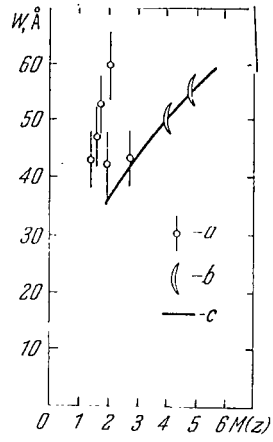

Fig.140 Same as in Fig.139; from Observations of Mercury on October 14,1963, and of the Moon on May 25,1964. (According to observations of the sun the CO_2 content of the terrestrial atmosphere was the same during these periods).

In Figs.139 and 140, observations of the moon are interpolated and extrapolated with the aid of Elsasser's growth curve. From solar observations it was verified that the air-mass dependence of the equivalent widths of CO_2 bands at λ 1.6 μ is satisfactorily represented by this theoretical growth curve.

The CO_2 content can be calculated with the method used for Mars in Chapter II. The theoretical growth curve for Mercury must be plotted with allowance for Doppler broadening, which becomes appreciable already at pressures of the order of 1 mb and at temperatures of 600°K in the observed absorption ($\bar{R}$ = = 0.02 ± 0.01). Under these conditions, the overlap of rotational lines of CO_2 can be disregarded and the growth curve for mean absorption in the band can be replaced by a growth curve for a single line. The absorption observable in the

spectrum of Mercury refers to the logarithmic segment of the growth curve, so that the amount of CO_2 along the line of sight can be correctly determined only to within one order of magnitude. This content ranges from 1 to 25 gm • cm^{-2}. The amount of CO_2 above 1 cm^2 of surface may range from 0.3 to 7 gm • cm^{-2} or from 1.5 to 35 m • atm. If we are to believe the polarimetric observations which indicate the total mass of the atmosphere as being 2 - 3 gm • cm^{-2} (Ref.102), then the relative concentration of CO_2 must lie within the limits from 10 to 100%.

Owing to the high temperature, the hot bands of CO_2 must be stronger in the spectrum of Mercury. In the interval λλ 1.1-2.5 μ a number of transitions exist for which the ground levels are 010 (667 cm^{-1}) and 020 (1286 cm^{-1}). The relative intensities of the former must increase 20 times and those of the latter 60 times, on transition from T = 250°K to T = 600°K, but they all either blend with other CO_2 bands and telluric H_2O bands or remain too faint. The band 001 to 100 λ 10.4 μ must become stronger by two orders of magnitude (initial level, 1385 cm^{-1}) and its anticipated equivalent width is approximately 0.1 μ. In /320 September 1964, the author obtained the spectrum of Mercury in the region λλ 8-13 μ with a resolving power of $\frac{\lambda}{\Delta\lambda}$ = 20, but the accuracy proved insufficient for either confirming or refuting the presence of the λ 10.4 μ band with an equivalent width of ~0.1 μ.

The above-described observations of λ 1.6 μ bands indicate some likelihood of CO_2 in the atmosphere of Mercury, but the possibility of a systematic error cannot be completely precluded. This identification still needs confirmation by other observers. An irrefutable proof would be the discovery of hot bands, but these have not yet been detected. Spinrad, Field, and Hodge (Ref.383) attempted to find the weak band $5\nu_3$ CO_2 (λ 8690 Å) in the spectrum of Mercury but failed. They estimated the upper limit of CO_2 content in the atmosphere of Mercury as 57 m • atm, which does not contradict the estimates based on the λ 1.6 μ bands.

An atmosphere of the order of 1 gm • cm^{-2} is already sufficient to protect the surface of a planet from meteoritic bombardment. In the earth's atmosphere meteors burn out at an altitude of about 80 km, above which approximately 10^{-2} gm • cm^{-2} of matter exists. This raises the question why all known characteristics of the Mercurian surface resemble those of the lunar surface whose formation is thought to have been largely influenced by meteoritic erosion. In this connection, Spinrad et al. (Ref.383) mention that marked density fluctuations of the Mercurian atmosphere over geological times are not entirely out of the question.

The main constituents of the atmospheres of Mars and Venus (cf. Chapt.I and II) are CO_2 and, apparently, N_2 at a ratio of roughly 1:1 to 2:100. The terrestrial atmosphere may originally have had a similar composition, but owing to photosynthesis most of the carbon dioxide was converted to the bound state, with the attendant release of oxygen into the atmosphere. An additional amount of oxygen could come from the dissociation of H_2O. If the identification of CO_2 in the spectrum of Mercury is correct, it might possibly be that the composition of its atmosphere does not differ qualitatively from that of the atmospheres of other terrestrial planets. Below, we will consider the properties that should

be displayed by the atmosphere of Mercury if it would contain a large amount of carbon dioxide.

A CO_2 molecule is dissociated by ultraviolet radiation at $\lambda \leq 1700$ Å. The absorption coefficient is approximately 10^{-19} cm^2 and it can be shown that the number of O atoms and CO molecules above the dissociation level must be close to 10^{19} although part of the O atoms will be combined into O_2 molecules. If the altitude of a homogeneous atmosphere in the dissociation region is taken as 10^6 cm, the concentration there must be close to 10^{13} cm^{-3}. The energy of ultraviolet radiation absorbed owing to dissociation (approximately 500 erg/cm^2) is /321 released by recombination. It may be that this energy is the principal source of heating of the atmosphere in the neighborhood of the dissociation level. Cooling occurs owing to radiation in the resonance band CO_2 λ 15 μ. The dissociation region is located above the level of vibrational relaxation of CO_2, and the rate of cooling is directly determined by volumetric luminance in this band, which can be calculated from eq.(2.41). The equilibrium temperature is about 200°K for an atmosphere of pure CO_2 and 150°K for an atmosphere consisting of 10% CO_2 and 90% N_2.

At an altitude where the total number of O atoms and CO molecules is $N < < 10^{18}$ cm^{-2}, the ionosphere begins. The ionization limit of O and CO is close to 900 Å. At Mercury's distance from the sun, the flux of solar ultraviolet radiation in the region $\lambda < 900$ Å is approximately 15 $erg/sec \cdot cm^2$ according to Hinteregger (Ref.262). Part of this energy is released during recombinations and directly converted into heat in the thermosphere, and part is transported downward by the diffusion of ions and electrons so that it does not directly participate in the heating of the thermosphere. The earth's thermosphere absorbs approximately 2 $erg/sec \cdot cm^2$, and - as estimated by various authors - releases from 5 to 50% of that energy. Taking a thermal effectiveness of 15% for Mercury, we find that its flux of approximately 2 - 2.5 $erg/sec \cdot cm^2$ must be released in its thermosphere. Cooling of the thermosphere may proceed in three ways: 1) by radiation in the CO λ 4.5 μ band and in the rotational lines; 2) by radiation in the forbidden line λ 63 μ; 3) by heat conduction.

In the earth's atmosphere, the third process predominates. Below 200 km, a certain role is played by transport of radiation in the λ 63 μ line. In the atmosphere of Mercury - if it contains a large amount of carbon dioxide - a major role should be played by CO radiation, and it would seem that the higher the relative concentration of CO in the thermosphere the lower should be temperature. However, more detailed estimates show that this is not so. If only CO and O are present in the thermosphere, then the absorption of ultraviolet radiation takes place in a region where the collision frequency at any temperature is too low to compensate for the heating due to CO radiation at the same altitude. Radiation occurs at much lower altitudes than absorption, and the absorbed energy can be transmitted downward only by heat conduction. It is readily shown that the thermosphere would then become heated to an extremely high temperature (more than 10,000°K) which would be accompanied by rapid dissipation. If, in addition to CO and O, some neutral constituent of the N_2 or Ar type were present, then dissipation would cease once the relative concentration of CO and O (CO_2 in the lower atmosphere) would become sufficiently low, the absorption region would descend to a zone of sufficiently high mean density and collision frequency, and its temperature would decrease. The decrease in temperature would be aided by /322

a slower dissipation of CO compared with O. An identical location of the regions of emission and absorption would require reducing the relative concentration of CO_2 to at least 10%. Consequently, the lower limit of the relative concentration of CO_2 (10 - 100%) which we derived from observations of the range seems plausible.

Henceforth we will assume that the atmosphere of Mercury consists of 10% CO_2 and 90% N_2 and that the total mass of the gas column is 3 gm $\cdot$ cm^{-2}. If the atmosphere of Mercury can retain CO_2 (which, at the dissipation level, is completely dissociated), then it can also retain N_2.

Owing to the high surface temperature and intense radiation in the CO_2 λ 15 μ band at high altitudes, the temperature gradient between the surface and the mesopause ($z \approx 130$ km) on the illuminated side of the planet is near-adiabatic and the convection zone probably extends from the surface to the very dissociation level of CO_2. At the surface of Mercury, the concentration of molecules is as low as it is on the earth at an altitude of 50 km but decreases more slowly with increasing altitude so that, on the whole, the atmosphere extends farther up. In the CO_2 dissociation region atomic oxygen is present, and the ternary collision reaction

$$O + O + M \rightarrow O_2 + M$$

also produces a certain amount of O_2. In the presence of photochemical equilibrium, the ratio of total CO_2 molecules to their dissipation products is

$$CO_2 : CO : O : O_2 = 1 : 2\times10^{-3} : 10^{-3} : 5\times10^{-4}. \qquad (4.9a)$$

The photochemical equilibrium was calculated in the same way as in Chapter III for the atmosphere of Venus.

The temperature of the thermosphere is about 1500°K at the level at which one-half of the ultraviolet flux $\lambda < 900$ Å is absorbed. This temperature is calculated from the balance between the absorbed energy, emission in the CO bands, and heat conduction. At the top of the absorbing region, the temperature apparently is close to 2000°K.

The temperature of the thermosphere is of special interest since it affects the dissipation rate, but it is exactly this question that is the most unsettled even when considered within the framework of the specified model, not to mention the possibility that the above-assumed initial chemical composition may differ from the true composition. For example, we had assumed a "thermal effectiveness" of 15% arbitrarily and solely by analogy with terrestrial conditions.

If CO_2 is actually present in the atmosphere of Mercury, then the critical/323 level cannot be very far from the surface (2000 - 2500 km) and its temperature cannot be higher than 800°K. If the critical level is at an altitude of 2500 km, then at a temperature of 800°K the "lifetime" of the atmosphere (as restricted by the dissipation of oxygen) will be about 10^6 years. Assuming that a continuous replenishment of the atmosphere from the bottom up (owing to the release of CO_2 by rocks) compensates for its dissipation rate, this would mean that the CO_2

in the atmosphere of Mercury would by now have been renewed 10^3 times. There is nothing improbable in this assumption, since the total amount of CO_2 released during the geological history will in this case be approximately 1 kg • cm^{-2}. This is not very much when we consider that large amounts of CO_2 still remain bound in the earth's sedimentary rocks. If the altitude of the critical level is 2000 km and the temperature is 600°K, the dissipation of oxygen can be disregarded in general. The calculation results for a model of the hypothetical atmosphere of Mercury are presented in Fig.141. In this calculation, it was assumed that N_2 and CO molecules are not dissociated at every altitude.

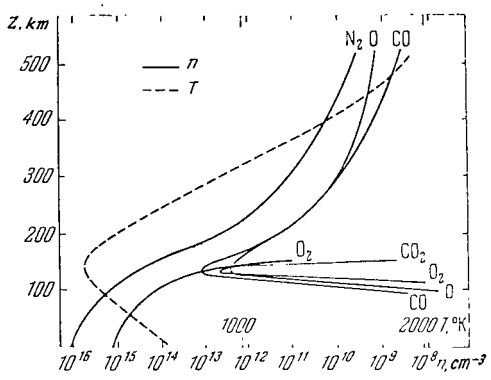

Fig.141 Model of the Atmosphere of Mercury.

Thus, the temperature of the critical level is apparently lower than the temperature of the thermosphere calculated in our model. This means that either the temperature of the thermosphere of Mercury is lower than calculated or the temperature decreases with altitude above the level of effective heating (unlike in the earth's atmosphere). The reason for this discrepancy may lie, e.g., in the fact that Mercury is a slowly (and perhaps synchronously) rotating planet. In the atmosphere of such a planet, an appreciable transport of heat from the illuminated to the unilluminated hemisphere must occur at various levels, and this will reduce the temperature of the illuminated hemisphere. It can be shown, e.g., that in the exosphere the exchange of molecules moving in elliptical orbits between the illuminated and unilluminated hemispheres will result in a heat leak of the order of 1 erg • cm^{-2} • sec^{-1}. The heat transfer coefficient above Mercury's thermosphere, in view of its assumed chemical composition (atomic oxygen) and T = 2000°K, is ~0.2 erg • km • cm^{-2} • sec^{-1} • deg^{-1}. Hence the supply of a flux of ~1 erg • cm^{-2} • sec^{-1} to the exosphere requires a high temperature gradient and the total heat drop between the thermosphere and the exosphere may reach several thousand degrees. This means that the temperature at the critical level and the dissipation rate may be much lower than in the model with an isothermal temperature variation above the thermosphere. /324

If eq.(4.9a) is correct, then it is impossible to detect CO or O_2 in the Mercurian atmosphere with methods of absorption spectroscopy. However, the photochemical equilibrium is disturbed by diffusion and mixing, so that eq.(4.9a) may not correspond to reality. Moreover, CO may accumulate owing to a more rapid dissipation of O. Nevertheless, the CO λ 2.35 μ absorption band could not be detected. Table 65 presents the upper limits of the content in the Mercurian atmosphere of CO and of certain other compounds, derived from the author's observations (Ref.375).

N.A.Kozyrev (Ref.384) obtained spectrograms of Mercury in the visible and near ultraviolet spectrum regions in late April and early May and then in October 1963, using the 122-cm reflector of the Crimean Astrophysical Observatory. He discovered that the profiles of the hydrogen lines H_β, H_γ, H_δ in the spectrum

of the solar radiation reflected from the illuminated hemisphere of the planet differ somewhat from the profiles of the same lines in the solar spectrum. The difference is close to the sensitivity threshold but is consistent, recurring /325 on many spectrograms. N.A.Kozyrev attributes this to planetary hydrogen emission with a brightness of about 1 erg $\cdot$ cm^{-2} $\cdot$ sec^{-1} $\cdot$ sterad^{-1}, i.e., to approximately 10^{12} quanta $\cdot$ cm^{-2} $\cdot$ sec^{-1} $\cdot$ sterad^{-1}. Weak H_α emission is present in the spectrum of the terrestrial night light, and moreover H_β and H_γ are present in the auroral spectrum of the earth, but in this case the brightness is very much smaller (nocturnal emission of H_α, approximately 10^6 quanta $\cdot$ cm^{-2} $\cdot$ sec^{-1} $\cdot$ $\cdot$ sterad^{-1}). The nocturnal emission of H_α is due to the scattering of solar

TABLE 65

SPECTROSCOPIC ESTIMATES OF THE UPPER LIMIT OF CONTENT OF CERTAIN MOLECULES IN MERCURY'S ATMOSPHERE

Molecule	Equivalent Path, cm-atm	Spectral Region, μ	Laboratory Pressure, atm	Content in Vertical Column of Earth's Atmosphere, cm·atm
CO	10	2.35	1	0.1
N_2O	2	2.12 and 2.26	1	0.4
NH_3	1	2.26—2.32	1	—
CH_4	0.3	3.3	*	1.6

* The solar spectrum was used as the comparison spectrum.

L_β-quanta in the earth's hydrogen corona, resulting in the conversion of L_β-quanta to L_α and H_α owing to cascade transitions. The upper atmosphere of Mercury should contain some amount of hydrogen owing to accumulation of solar corpuscular fluxes, but the brightness of hydrogen emission that can be produced by such a mechanism in the case of Mercury is completely insufficient.

Auroral hydrogen emission is attributable to charge exchange between the protons of solar corpuscular fluxes and the neutral atoms of oxygen. This mechanism in the case of Mercury - in the presence of oxygen in its upper atmosphere (see below) - possibly could be responsible for the brightness values comparable with the observed values, but the emission lines are smeared out and substantially shifted owing to the great velocity of the corpuscular fluxes (~1000 km/sec). Hence, this can hardly account for N.A.Kozyrev's observations. It would be very important to investigate as accurately as possible the profiles of lines of the Balmer series in the spectrum of Mercury and to elucidate the shape and displacement of the emission center, if its existence is confirmed. N.A.Kozyrev draws far-reaching conclusions from his observations, claiming that hydrogen is the principal constituent of the Mercurian atmosphere. There exists no justification for such a claim since the mechanism of excitation is unknown and only the number of atoms at the ground level can be derived from observations. Spinrad and Hodge (Ref.385) mentioned that on Mercurian spectrograms the superposition of light scattered from the twilight sky may result in the occurrence of Fraun-

hofer-line satellites that undergo Doppler shift and that Kozyrev's observations may be attributed to this effect.

Section 4.3 General Problems of Interiors of the Terrestrial Planets

Each of the three planets in the terrestrial group considered above represents a complex entity of problems and enigmas.

First we dealt with comparatively well-investigated Mars and then with extremely enigmatic Venus and lastly with Mercury. As regards Mercury, nothing /331 really definite can be said about it, beginning with its rotation and ending with the chemical composition of its atmosphere whose very existence has not been proved either. Much work, chiefly of the observational type, has yet to be done before the problems posed by these planets can be solved. Table 66 represents an attempt to present in compact form the principal available data on the terrestrial planets. The picture is still too incomplete to warrant a unified and consistent interpretation of the observed effects.

Below, we will consider two problems of the same type but far from fully clarified: 1) internal structure of planets of the terrestrial group; 2) nature of their atmospheres.

a) Internal structure. The masses of the terrestrial groups roughly range from 2×10^{-7} to 3×10^{-6} $M_\odot$. The atmospheres account for a negligible fraction of this total. The nature of the solid planetary interiors can be interpreted only by analogy with the earth and general physical laws. A large portion of the earth's surface is covered by the hydrosphere. The other planets have no hydrosphere, which undoubtedly must influence their principal features (structure of surface, composition of atmosphere, etc.).

The yield point of terrestrial rocks is reached at a depth of several tens of kilometers. At considerable depths, the shearing strength is too low for maintaining a major pressure difference at any one level. Consequently, the earth and other planets can be regarded as bodies existing in hydrostatic equilibrium. In the presence of hydrostatic equilibrium, a body of revolution assumes the shape of an oblate ellipsoid. If the ratio of centrifugal to gravitational acceleration

$$q = \frac{\omega^2 R^3}{\gamma M} \tag{4.10}$$

is low, as is the case for planets of the terrestrial group (0.0035 for the earth, 0.0046 for Mars, and much lower for Venus and Mercury) then the shape or, as it is known, the equilibrium configuration of such a body is close to spherical.

At the interior of a spherical body, we have

$$\frac{d\bar{P}}{dr} = -\left[g(r) - \frac{2}{3}\omega^2 r\right]\rho(\bar{P}), \tag{4.11}$$

TABLE 66

/326

COMPOSITE TABLE OF PRESENT KNOWLEDGE ON THE PHYSICAL CONDITIONS OF THE TERRESTRIAL PLANETS

Method of Observation	Findings and Interpretations		
	Mercury	Venus	Mars
Visual and photographic observations: Cloud layer: structure of cloud, circulation of cloud	Isolated reports on changes in the visibility of surface markings	Distinct structure of the type of parallel streaks in the ultraviolet. Low-contrast blurred markings in visible light	White and blue clouds observed most often near limb and terminator. Apparently, ice clouds. Above the deserts, yellow cloud formation sometimes covering large expanses. Assumed to be dust storms. Surface markings normally not visible in the blue and violet spectrum regions (blue haze phenomenon). Occasionally, clearing of the haze ("blue clearing" phenomenon) permitting observation of the markings also in these spectrum regions
Surface markings, principal topographic features	Dark and bright regions discernible on surface. No photographic mapping was made. Visually compiled maps with a resolution of several hundred kilometers are available	Surface not discernible in visible light owing to compact opaque cloud mantle	Distinct bright and dark areas, polar caps. Seasonal variations in albedo, color, and shape of the dark areas. Secular variations of the albedo and extent of the dark areas. Seasonal variations in polar caps. Photographs acquired by Mariner IV revealed lunar-like craters. Rotation period $24^h 37^m 23^s$ /327
Photometry: Reflectivity of disk depends on topography, wavelength, and phase angle. Used for deter-	Visual albedo 0.056; integral albedo approximately 0.09	Visual albedo 0.70; integral albedo 0.73. Wavelength dependence of the albedo indi-	Ultraviolet albedo 0.05; visual albedo 0.12 in dark areas, 0.15 in bright areas; integral albedo 0.26

(cont'd)

TABLE 66 (cont'd)

Method of Observation	Findings and Interpretations: Mercury	Venus	Mars
mining nature of the cloud layer and surface and for calculating the heat balance		cates size of the cloud layer particles to be several microns	
Occultations of stars and eclipses of satellites indicate scale height, scale-height gradient, and pressure at the altitude of eclipse	No observations	Occultation of Regulus: 55 ± ± 15 km above the cloud layer, height scale 6.8 ± ± 0.2 km. Pressure at the level of occultation: $2.6 \times 10^{-3} \pm \pm 1.3 \times 10^{-4}$ mb	No observations
Limb effects: brightness gradient in direction of the limb as a function of wavelength provides information on the structure of the atmosphere and on the altitude and nature of clouds and haze	Instances of veiling of markings are more frequently reported for the Western than for the Eastern Hemisphere	Elongation of cusps near inferior conjunction indicates high-altitude clouds or a layer of haze	Limb darkening in visible region; smoothness factor $0.5 < q < 1$, near λ 6000 Å. Limb darkening decreases with decreasing wavelength
Polarimetry: Degree of polarization as a function of topography, wavelength, and phase angle; may be used for determining	Atmospheric pressure at the surface, about 1 mm. Surface covered with minute opaque particles and resembling	Clouds consist at least partially of transparent particles several microns in size. Water droplets and certain minerals	Surface apparently covered with small, quasi-opaque particles; seasonal variations in degree of polarization observed in the dark regions, apparently due to seasonal variations in particle size. Polarization (cont'd)

/328

TABLE 66 (cont'd)

Method of Observation	Findings and Interpretations: Mercury	Venus	Mars
atmospheric pressure and nature of the scattering particles	lunar surface	roughly (but not fully) agree with observed polarization curves	of polar caps, white clouds, and haze on the *morning* limb indicates hoarfrost. Polarization of bright areas indicates limonite
Spectroscopy: Visible and infrared spectra of reflected or scattered sunlight provide the following information: a) analysis of chemical composition of the atmosphere at the effective scattering level as based on an identification of bands and lines; b) temperature of the atmosphere near the effective scattering level according to the intensity distribution of rotational lines; c) atmospheric pressure above the effective scattering level, according to line broadening. Some information on chemi-	The λλ 1.57 and 1.61 μ bands in the Mercurian spectrum seem stronger than the telluric CO_2 content 1.5-35 m • atm	The CO_2 7820 Å band indicates variations in temperature and pressure; increase in pressure accompanied by increase in temperature. Mean pressure, about 1.5 atm at the level where $T \simeq \simeq 300^{\circ}K$. Relative CO_2 concentration about 2%. Chemical nature of the remaining atmosphere portion unknown but apparently N_2 plus a small quantity of Ar. Small amounts of H_2O (about 10^{-2} gm • cm^{-2}) and CO (about 5 cm • atm) present	Relative volume concentration of CO_2, from 10 to 50%. Chemical nature of the remaining atmosphere portion unknown, but apparently N_2 and Ar. Traces of H_2O absorption present. Absorption in the 8200 Å band indicates water vapor content of 10^{-3} gm • cm^{-2}. Reflection spectra of polar cap near λ 1.5 μ indicate frost but not solid CO_2. Spectrum of bright areas fits limonite

/329

(cont'd)

TABLE 66 (cont'd)

Method of Observation	Findings and Interpretations		
	Mercury	Venus	Mars
cal composition of surface and cloud layer possible, but spectral characteristics of fluids and solids less clearly associated with chemical composition than those of gases			
Spectra in the far infrared, i.e., of natural radiation of the atmosphere, clouds, and surface, may provide information on chemical composition, temperature, and pressure, but the data are difficult to interpret	Observations of the natural emission spectrum in the region λλ 2-4 μ indicate, near perihelion, a color temperature of ~670°K and a brightness temperature of ~630°K at the subsolar point	Discovery of an absorption band at λ 11.2 μ with a time-variant intensity. Tentatively identified as $(C_3O_2)_n$ or carbonates. CO_2 bands existing in the region λλ 8-13 μ, not detected in Venusian spectrum	CO_2 absorption bands λ 10.4 and 9.4 μ
Radiometry: Infrared: absolute intensity measurements with wide filters in the 8-14 μ optical window and in other windows give temperature of the radiating layer	Mean temperature in the 8-13 μ window at the subsolar point, T_B = = 600°K. Fairly broad variations due to orbital eccentricity. No data available on the unilluminated hemisphere	Brightness temperature 220 to 240°K in the 8-13 μ window, same on illuminated and unilluminated hemispheres except for transient temperature rise probably due to gaps in clouds. Marked limb darkening. Isotherms	All observations within the region λλ 8-13 μ. Mean annual temperature averaged over the entire disk, 200°K. Maximum temperature about 300°K. Diurnal equatorial variation of temperature, 90°K; seasonal (for middle latitudes) variation, 60°K;

(cont'd)

TABLE 66 (cont'd)

Method of Observation	Findings and Interpretations		
	Mercury	Venus	Mars
		occasionally flattened toward equator. Thermal charts indicate discrete cold and hot regions. In the 3-4 μ window on the dark side $T_B = 236^\circ \pm 8^\circ K$.	
Microwave: absolute measurements of mean brightness in the interval λλ 3 mm to 70 cm useful for determining brightness temperatures at certain effective radiation levels. Presence of absorption components possible. Limb effects may give information on the mechanism of generation	Within the λλ 0.8-11 cm range, mean brightness temperatures varied from 200 to 400°K. Dependence of T on λ or phase course impossible to determine within the error limits. Brightness temperature of unilluminated side in the range λλ 3-11 cm, $T_n \approx 200\text{-}300^\circ K$	Brightness temperature 350-400°K within the λλ 3-10 mm range and 600°K within λλ 2-21 cm. At longer wavelengths, tendency of T_B to decrease. Apparently, the surface itself radiates in the 2-21 cm range. The high temperature at 1.35 cm would indicate the absence of substantial amounts of H_2O in the lower atmosphere. Decrease in T_B at millimeter waves, most probably attributable to an unidentified absorbing substance	Observations in the λλ 3-21 cm range give $T_B \approx 200^\circ K$ /330
Radar: Delay time of reflected pulse	Comparable in reflectance to	Reflectance near inferior	Reflectance comparable to lunar (0.06). Reflection (cont'd)

TABLE 66 (cont'd)

Method of Observation	Findings and Interpretations		
	Mercury	Venus	Mars
useful not only for determining distance to the planet but also for information on rotation and the surface character according to duration, amplitude, and frequency spectrum of the echo. A sufficiently extensive ionosphere would influence amplitude and length of pulse	the moon (0.06). Rotation period 59 ± 7 days	conjunction, k ≈ ≈ 0.10 within λλ 12-70 cm and 0.2 (with marked fluctuations) at λλ 6 and 7.8 mm; 0.01 at λ 3 cm. Rotation retrograde, with a period of 248 + + 7 days. Inclination of equator to the ecliptic, < 10°. Markings of high reflection coefficient present on the surface. Surface generally smoother than on the moon.	factor of dark areas (at λ 12.5 cm), markedly above disk-wide average.

$$g(r) = \frac{\gamma M(r)}{r^2} = \frac{4\pi\gamma}{r^2}\int_0^r \rho(x)\, x^2\, dx, \qquad (4.12)$$

where g(r) is the acceleration of gravity; $\frac{2}{3}\omega^2 r$ is the mean radial compon- /332

ent of the centrifugal force; M(r) is the mass of the interior of a sphere of radius r; $\rho(\overline{P})$ is the equation of state. The density distribution inside an ellipsoid may also be reduced to the same form if the compression ϵ is introduced into the definition of the parameter r.

Knowing the function $\rho(P)$ and the central pressure P_0 it is possible to unambiguously determine the total mass M and radius R of a planet. However, in general, fixed values of M, R, and of the equation of state may correspond to various values of P_0. A rough estimate of P_0 can be made on assuming that the density ρ of the planet everywhere equals the mean $\overline{\rho}$. In this case, eq.(4.11) yields

$$P_0 = \frac{3}{8\pi}\frac{\gamma M^2}{R^4}. \qquad (4.13)$$

Since the crystal lattice has a high compressive strength, the density can in-

crease only by a factor of a few units, even at pressures of millions of atmospheres. Thus, the estimate (4.13) gives values with an accuracy to within an order of 2.

The lower limit of the central density ρ_0 can be obtained from the observed characteristics of a planet on assuming that its main mass is concentrated in a small core of radius a and density ρ_0. Then, the moment of inertia is

$$I > \frac{2}{5} \cdot \frac{4\pi}{3} \rho_0 a^5$$

and

$$\rho_0 a^3 = \bar{\rho} R^3,$$

whence

$$\rho_0 \geqslant \left(\frac{5}{2} \frac{I}{MR^2}\right)^{-\frac{3}{2}} \bar{\rho}. \tag{4.14}$$

This estimate naturally presupposes a monotonic increase in density ρ toward the center. The Rado-Darwin classical theory shows that the factor of the moment of inertia is equal to

$$f = \frac{I}{MR^2} = \frac{2}{3} - \frac{4}{15}\left(\frac{15\pi}{2\gamma\rho t\varepsilon} - 1\right)^{1/3}, \tag{4.15}$$

where t is the rotation period; $\varepsilon = \frac{R_e - R_p}{R_e}$ is the equatorial compression. For a homogeneous sphere, f = 0.4. With the aid of eq.(4.15) it is possible to obtain the moment of inertia of a planet I. For determining the moment of inertia, the use of geometric compression should be replaced by dynamic compression which can be derived from an analysis of motion of satellites. An attempt to substitute into eq.(4.15) the geometric compression for Mars (~1/100) causes the quantity in parentheses to become lower than zero. The use of dynamic compression (~1/190) yields a plausible value of $f \approx 0.35$. In the case of Mars, the value of the geometric compression is most likely influenced by the atmosphere, but even if that were not so it is more justified to use the dynamic compression since it characterizes the planet as a whole rather than just its surface. Table 67 contains estimates of P_0 and ρ_0 derived for planets of the terrestrial group with the aid of eqs.(4.13) and (4.14). No estimates of ρ_0 for Mercury and Venus are available, since these planets lack satellites of their own so that their dynamic compression and moment of inertia are unknown.

The heat flux from the earth's interior to the surface and the data on the heat conduction of rocks provide an idea of the earth's abyssal temperatures. It was shown (Ref.386) that these temperatures reach 3000 - 5000°K in the earth's core and apparently nowhere exceed this limit. There is no reason to believe that the situation should be much different on the other terrestrial planets. The change in density on a 1000-degree increase in heating is roughly the same as a change of 10^9 dyne $\cdot$ cm^{-2} in pressure, whereas the pressure at the earth's interior is close to 10^{12} dyne $\cdot$ cm^{-2}. Obviously, the temperature dependence of

pressure can be disregarded; this justifies writing the equation of state as $\rho = \rho(P)$ instead of the more general $\rho = \rho(P, T)$, which greatly facilitates the problem.

TABLE 67

ESTIMATES OF CENTRAL PRESSURE AND DENSITY FOR TERRESTRIAL PLANETS AND THE MOON

	g	Mass $M/M_\oplus$	Mass $M_\odot/M$	$\bar{R}$, km	$\bar{R}/\bar{R}_\oplus$	ρ, gm·cm^3	f	P_0, 10^{12} dyne × cm^{-2}	$\rho_0/\bar{\rho}$
Mercury	3.24×10^{26}	0.0543	6120000	2480	0.389	5.1	—	0.220	—
Venus	4.86×10^{27}	0.8137	408000	6060*	0.950	5.25	—	1.28	—
Earth	5.98×10^{27}	1	318000	6378	1	5.52	0.333	1.7	>1.32
Mars	6.06×10^{26}	0.1077	3088000	3414	0.534	3.9	0.389	0.25	>1.04
Moon	7.34×10^{25}	0.0123	25800000	1738	0.272	3.34	0.397	0.05	>1.01

* Micrometric measurements give 6120 km; height of apparent limb above the surface is assumed to be 60 km (Sect.3.9).

Earthquakes and powerful explosions generate seismic waves which, on undergoing refraction and reflection deep at the earth's interior, are recorded on seismographs. There exist two basic types of seismic waves: longitudinal or P and transverse or S waves. Their velocity depends on the state of the medium in which they propagate. Transverse waves cannot propagate in fluids, since fluids do not resist shear compression. When transverse waves are recorded, it can be concluded that the lithosphere is solid down to extremely great depths. However, early in this Century it was shown that, beginning with a depth of approximately 3000 km, transverse waves cannot propagate farther downward. From this, it was concluded that a fluid core exists within the lithosphere. Later studies showed that within the fluid core itself there exists a denser and, most likely, solid innermost core (radius approximately 1300 km). /334

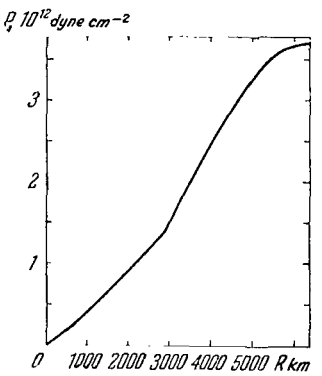

Fig.142 Depth Dependence of Pressure at the Earth's Interior, Calculated by Bullard from Seismic Data (Ref.387).

The earth's solid envelope is inhomogeneous - having a sharp discontinuity at a depth of 40 km (Mohorovicic boundary). The comparatively thin surface zone above this boundary is termed the crust. The region between the Mohorovicic boundary and the liquid (outer) core is termed the mantle. The mantle also is inhomogeneous and divided into zones. One of the principal interfaces within the mantle is the Golitsyn boundary (~400 km) which divides the mantle into upper and lower.

Figure 142 shows the depth dependence of the pressure in the earth's interior, as calculated by Bullard from seismic data. Figure 143 gives the analogous pressure dependence of density. Both curves have a marked inflection point at the boundary between mantle and core and a less sharp inflection point at the Golitsyn boundary. These boundary surfaces divide the earth into three regions in each of which the bulk modulus

$$k = \rho \frac{dP}{d\rho} \tag{4.16}$$

can be represented by the linear dependence

$$k = a + b\rho, \tag{4.17}$$

where a and b are constants. In each of these regions the equation of state /335 is

$$P = \frac{a}{b}\left[\left(\frac{\rho}{\rho_u}\right)^b - 1\right], \tag{4.18}$$

where ρ_u is the density corresponding to P = 0. The physical nature of the discontinuities at the earth's interior has not yet been defined. Many investigators assume that the core consists of metals, chiefly of iron, and that the chemical composition changes at its interface with the mantle. Another possibility is that the chemical composition of the core does not differ from that of the mantle (silicates of iron and magnesium) and that the discontinuity is due to a phase transition, to "metallization" of the silicates.

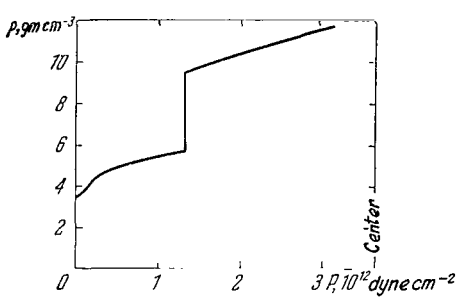

Fig.143 Pressure Dependence of Density at the Earth's Interior (Ref.387).

Nearly all investigators agree that the earth and the other planets came into being as a result of the merging of smaller bodies. The gravitational energy released in the process of this merger was sufficiently rapidly reradiated, and during this primordial era not even partial melting occurred (Ref.388). The duration of this period was relatively short [10^8 years, cf. (Ref.389)]. Subsequently, heating by radioactive elements gradually raised the temperature of the earth's interior, resulting in the formation of a molten core whose dimensions gradually increased. Had the earth undergone the stage of complete melting, this would have resulted in stratification of elements, with the heavier elements sinking downward and the lighter elements being displaced to the uppermost strata. Later calculations (Ref.389), however, showed that complete melting did not occur and that, apparently, the substance of the mantle had never existed in a molten state.

Consequently, there is reason to believe that the substance of the mantle

has remained unchanged ever since the earth acquired its present-day mass. It is not precluded that, originally, the mantle had extended downward to the very center of the earth. Proceeding from this hypothesis, Littleton (Ref.390) calculated the earth's radius for the primordial epoch. The equation of state was used in the form of eq.(4.18). He took the constants a, b, ρ_u as calculated from seismic data for the present-day mantle. The radius of the "primordial" earth was then found equal to R' = 6730 km, which is 350 km (~5%) larger than /336 at present. If this is indeed correct, it would mean that the dimensions of the earth shrank in subsequent geologic epochs owing to the formation of the molten core.

The compression of the earth resulted in folding of the earth's crust, i.e., in orogeny. Littleton showed that the mean altitude of the mountains is estimated as

$$h \leqslant \frac{E\eta}{3\rho_s g}, \qquad (4.19)$$

where E is Young's modulus (10^{12} dyne • cm^{-2}); ρ_s is the density of the crust (2.7 gm • cm^{-3}); g is the acceleration of gravity; η is the contraction coefficient [over the surface area - $(0.05)^2 \approx 0.002$]. Substitution of numerical values gives h ≈ 2.5 km, which is in good agreement with the true height of the earth's mountains.

Returning to Table 67, we see that at the interior of Mars and Mercury the pressure at the center P_0 is lower than at the interface between mantle and molten core of the earth (cf. Fig.143). If Mars and Mercury had originally been formed of the same material as the earth, they must lack a molten core (and thus also must lack mountains on their surface). Magnetohydrodynamic processes in the earth's molten core apparently were the source of its magnetic field [cf. for example (Ref.391, 393)]. Therefore, it must be expected that neither Mercury nor Mars have any appreciable magnetic field. Venus resembles the earth in mass and radius and thus must have a molten core and the course of its orogenic processes must resemble those of the earth. The low magnetic moment of Venus (less than 1/20 of that of the earth) apparently is attributable to its slow axial rotation.

Littleton (Ref.392) showed that the hypothesis of identical composition of the interiors of the terrestrial planets holds at least for Mars and the moon. The same equation of state (4.18) was used to calculate a set of models of the internal structure of Mars, assuming that it consists of two zones: inner and outer. The first zone was calculated on the basis of the parameters a, b, ρ_u derived from seismic data for the lower mantle of the earth and the second zone, from the same parameters for the upper mantle. The mass of the planet was specified, and various values of the radius of the inner zone r_c were taken. For r_c = 2800 km, the radius of the planet, the density, and the moment of inertia fit the observations within the error limit. For the moon, the central pressure is lower than at the Golitsyn boundary at the earth's interior for which reason a simpler single-zone model with parameters corresponding to the earth's upper mantle was selected for the moon. The calculated lunar radius then coincided /337 with the observed radius with an accuracy to within 1 km; at the same time, cor-

rect values of mean density and moment of inertia were obtained.

The mean density of Mercury seems too high for its size. Either it has a different chemical composition (for the possible reason that it was originally formed closer to the sun than the other planets) or its mass and radius have been largely miscalculated.

Early results by Jeffreys (Ref.393) and Bullen (Ref.394, 395), who assumed the existence of a small core in Mars, seem unconvincing. Bullen, for example, employed the quadratic formula

$$k = a + b\rho + c\rho^2,$$

which gave a model with an extremely low concentration at the center, thus implying an unacceptably low dynamic compression. To bypass this difficulty he had to assume a heavy core. However, it is difficult to understand why, considering the relatively low central pressure characteristic of Mars, this planet should have a core if its interior structure resembles that of the earth, as is assumed in the theories of Jeffreys and Bullen. A linear representation of the pressure dependence of the bulk modulus does not lead to such a contradiction.

b) Nature of the atmospheres. The mass of the earth's atmosphere accounts for approximately 10^{-6} of the total mass of the earth. For Venus, this proportion is one order of magnitude higher and for Mars, one order of magnitude lower. The composition and origin of the atmosphere and lithosphere are closely interrelated. If the lithospheres of the planets of the terrestrial group are similar, this is bound to result in a similarity of the characteristics of their atmospheres, and observations indeed reveal a number of common features: For example, for the planets of the terrestrial group, complete or almost complete lack of hydrogen is typical, while in all CO_2 has been detected. The hydrogen deficiency of planets of the terrestrial group is one of their more striking properties. The sun, the stars, the interstellar medium, and the Jovian planets consist to 99% of hydrogen and helium. The amount of carbon, nitrogen, and oxygen in the medium of the Universe is on the whole 10^4 times lower than the amount of hydrogen, while the iron and silicon content is 10^5 times lower. Thus, the terrestrial planets are anomalous bodies with respect to their chemical composition. A particularly distinct anomaly is represented by the earth and its oxygen-rich oxidizing atmosphere.

The chemical composition of the lithosphere has remained constant once its formation was completed, whereas the atmosphere doubtlessly has changed. In fact, the composition of the atmosphere is influenced by numerous processes that play different relative roles on different planets and may have changed in the course of cosmogonic time.

These processes include: /338

1) dissipation of atmospheric gases;
2) liberation of gases from the lithosphere owing to volcanic activity;
3) dissociation of complex molecules owing to solar ultraviolet radiation;
4) chemical reactions between atmospheric gases and material of the crust;

5) interaction with the biosphere (absorption of some gases, liberation of others);
6) accretion of interplanetary medium.

The rate of dissipation depends on the temperature of the exosphere and on the parabolic velocity, with the latter being determined by the mass and mean density of the planet. Table 68 presents the lifetimes of H, He, O, N_2, and CO in the atmospheres of the planets of the terrestrial group, calculated from eq.(1.135). The temperature of the Venusian exosphere is taken as 2000°K - somewhat higher than the earth's since Venus is closer to the sun. For Mars the temperature of the exosphere was taken as the upper temperature limit, based on the fact that oxygen is retained on that planet (in the form of CO_2). A similar estimate has also been made for Mercury. Note again that the temperature of the exosphere largely depends on the phase of solar activity and the time of day; for example, in the earth's exosphere the temperature at night during the solar activity minimum drops to 700°K. The dissipation rate can be estimated on the basis of maximum temperature, but then it must be considered that the corresponding lifetimes must be increased by roughly one order of magnitude. This correction was not made in Table 68. Moreover, extremely short lifetimes t_o ($\lesssim 10^3$ years) do not seem realistic, since the diffusion rate of the upward-transported molecules is limited. For comparison, Table 68 presents the results of similar calculations of the dissipation of hydrogen from the atmosphere of Jupiter, assuming a distinctly exaggerated temperature of Jupiter's exosphere (1000°K). The dissipation rate for Mercury was calculated for two different assumed temperatures and altitudes of the critical level (cf. Sect.4.2). Note that the identification of CO_2 in the spectrum of Mercury, on which these assumptions were based, must be considered tentative. If this is not confirmed, the temperature at the critical level may be higher.

Table 68 shows that the terrestrial planets (unlike Jupiter) may have lost tremendous quantities of hydrogen and helium during the lifetime of the solar system, and indicates that during primordial times the atmospheres of these /339
planets had been rich in light gases. At first glance, it seems probable that the original composition of the planets of the terrestrial group had been the same as that of the sun and of the superior planets but the dissipation of the lighter gases from their atmospheres had taken place at a more rapid rate, thus resulting in the present-day difference in their chemical composition. This view was advocated, in particular, by Kuiper (Ref.307, 396), However, all above estimates of the time t_o were derived with the aid of eq.(1.134) which presupposes that the radius R_c of the critical level and the scale height H_c remain constant during the dissipation. If the dissipation of a large portion of the entire mass of a planet is involved, these conditions are not satisfied and eq.(1.134) no longer applies. I.S.Shklovskiy (Ref.397, 398) showed that, in this case, the lifetime is virtually independent of the original mass of the planet and very weakly dependent on temperature and that - in any case - it is many orders of magnitude higher than the age of the solar system. It is true that, in addition to conventional heat-induced dissipation, dissipation due to corpuscular radiation also may have played a major role in primordial times (Ref.396), but this mechanism has been little investigated, and it is difficult to assess the extent to which it is really effective.

It is probable that the terrestrial planets, unlike the giant planets, never

have been "hydrogen" planets, but it may be that at the outset of their evolutionary path their atmospheres had been richer in hydrogen than they are now. Hydrogen is a powerful reducing agent and it is known in this respect (Ref.399, 400) that it is exactly in an atmosphere with reducing properties that synthesis of complex organic molecules takes place most effectively. Conversely, in an oxidizing atmosphere, such as the present-day terrestrial atmosphere, reactions of this type are greatly inhibited (Ref.400-402). Thus the formation of the /340 terrestrial biosphere is an indirect argument in favor of an originally high content of hydrogen in its atmosphere.

TABLE 68

DISSIPATION RATE OF CERTAIN ATMOSPHERIC GASES

Planet	T_c, °K	z_c, km	t_0, years			
			H	He	O	N_2, CO
Mercury	800	2480	0.1	3	10^6	10^{10}
	600	2000	—	—	—	—
Venus	2000	600	10	10^5	2×10^{21}	10^{38}
Earth	1800	550	50	10^7	10^{29}	3×10^{50}
Mars	1000	1000	0.4	10^2	10^{10}	10^{17}
Jupiter*	1000	500	3×10^{86}	3×10^{376}	10^{1561}	10^{2073}

* For Jupiter the calculations are based on eq.(1.135) which gives only the lower limit of t_0 for real atmospheres. The actual values of t_0 for Jupiter are many orders of magnitude higher than given in the table.

There exist geological data pointing to a lower content of oxygen in the Archean era compared with the present. Thus, in sedimentary rocks of an age $\geq 2 \times 10^9$ years, uranium oxides are encountered exclusively in the form of UO_2, whereas U_3O_8 predominates in more recent rocks (Ref.403). Other similar instances exist. At the same time, Chamberlain (Ref.404) postulated that oxygen has always existed in the earth's atmosphere, even if its quantity in the past may have been smaller than it is at present. This is indicated by the Archeozoic iron ores (hematite, Fe_2O_3).

The transition from a reducing to an oxidizing atmosphere took place as a result of the action of two processes: photodissociation of H_2O due to solar ultraviolet radiation, and organic photosynthesis. The former process probably predominated in the past, whereas the latter is now prevalent. The long-wave limit of the dissociation continuum of H_2O is close to 1860 Å. In the region $\lambda < 1860$ Å, the flux of solar radiation is 10^{12} quanta $\cdot$ cm^{-2} $\cdot$ sec^{-1} and, in the absence of other absorbing substances, a total of 10^{12} molecules of water would be dissociated per second above each cm^2 of the earth's surface.

Actually, however, the rate of photodissociation is many orders of magnitude less, since strong Schuman-Runge bands and the continuum of molecular oxygen

shield this region of the spectrum. The amount of hydrogen lost per second owing to thermal dissociation is 10^7 to 10^8 atoms $\cdot$ cm^{-2}. Obviously, the rate of formation of oxygen molecules per second is only one-fourth as great. Conversely, photosynthesis produces approximately 10^{14} $cm^{-2} \cdot sec^{-1}$ molecules of O_2. It is clear that, at present, the photodissociation of H_2O can be disregarded as a source of oxygen. Photodissociation of H_2O as well as of CO_2 (long-wave limit, 1760 Å) may have played a role only as a mechanism of primordial accumulation of oxygen.

TABLE 69 /341

CONTENT OF INERT GASES IN RELATION TO SILICON ON EARTH (REF.405) AND IN THE COSMOS (REF.406)

Gas	Atomic Weight, μ	$C_\oplus$		C_c	$F = \frac{C_\oplus}{C_c}$
		Lower Bound	Upper Bound**		
Ne	20	1.1×10^{-10}	8.1×10^{-10}	10	3×10^{-11}
Ar	36*	2×10^{-10}	8×10^{-10}	0.1	3×10^{-9}
Kr	84	6.0×10^{-12}	4.4×10^{-11}	6×10^{-5}	3×10^{-7}
Xe	131	4.9×10^{-13}	3.6×10^{-12}	3×10^{-6}	5×10^{-7}

* The isotope Ar^{40}, which accounts for 99.7% of the earth's argon, is of radiogenic origin (decay of K^{40}).

** The lower bound was derived on taking only atmospheric gases into account; the upper bound includes gases occluded in rocks. It is assumed that the relative content of inert gases at any depth is the same as in the crust.

Of special interest is the content of nonradiogenic isotopes of inert gases in the earth's atmosphere. Owing to the high atomic weight of inert gases and their inability to enter into chemical reactions, their relative and absolute content has probably remained constant ever since the formation of the earth's atmosphere and of the earth herself. Table 69 gives values of C - the ratio of the terrestrial content of rare gases to silicon as a function of the atomic number. Silicon was selected, because its quantity no doubt has remained constant ever since the earth has been formed. The table also presents cosmic contents (C_c) of inert gases, again in relation to silicon.

Table 69 indicates clearly that the terrestrial content of inert gases is much lower than in outer space: The values of F given in the last column range from 10^{-6} to 10^{-10}. These are designated as coefficients of deficiency (or "coefficients of fractionation"). The coefficients of deficiency of the inert gases systematically increase with increasing atomic weight.

According to Kuiper (Ref.307), the deficiency coefficients can be represented by the empirical formula

$$\log F(\mu) = -6.4 - 12.4e^{-0.055\mu} \tag{4.20}$$

or

$$F = F_0 e^{-\frac{\Delta t}{t_0}}, \tag{4.21}$$

where

$$\left.\begin{aligned} F_0 &= 4\times 10^{-7}, \\ \frac{\Delta t}{t_0} &= \frac{28.6}{e^{0.055\mu}}. \end{aligned}\right\} \tag{4.22}$$

Equation (4.21) has exactly the same form as eq.(1.134) for the rate of thermal dissipation. Comparing eq.(4.22) with eq.(1.135), we have

$$\frac{R_c}{H_c} = \frac{\gamma_m M}{kT_c R_c} = 0.055\mu,$$

whence, on substituting the numerical values of the constants and putting R_c = /342 = R, it follows

$$T_c \approx 10^5 \frac{M}{M_\oplus}\frac{R_\oplus}{R}, \tag{4.23}$$

where $M_\oplus$ and $R_\oplus$ are the present-day mass and radius of the earth. Thus, the correlations between the deficiency factors can be formally attributed to the effect of thermal dissipation. Putting $M = M_\oplus$ and $R = R_\oplus$ and taking, for example, the Spitzer coefficient (cf. Sect.1.7) $B = 10^7$ (as in the contemporary terrestrial atmosphere), we have

$$\Delta t \approx 10^4 \text{ years}.$$

Already at $\mu \approx 100$, the exponential term of eq.(4.20) ceases to play a significant role in the deficiency coefficient. The absolute values of the deficiency coefficients remain extremely low ($< 10^{-6}$). Thus, thermal dissipation alone cannot account for the deficiency coefficients. It might well be that the thermal dissociation was augmented by hydrodynamic dissociation, which eliminated all gaseous matter at the same rate regardless of atomic weight. Equation (4.23) is susceptible to the most varied interpretations [cf. (Ref.400)]:

1) $M = M_\oplus$, $R = R_\oplus$, and $T \approx 10^5$ °K. In this case, either an intense corpuscular heating of the atmosphere occurred over a period of 10^4 years or the luminosity of the sun had been much greater in the past than it is now (in the same interval of time). Modern theories of stellar evolution do not preclude such a possibility.

2) Small mass of Protoearth of equal mean density. In this case, eq.(4.23) will be satisfied for moderate temperatures of the exosphere. This explanation would be satisfactory if, for example, the earth had come into existence by merg-

ing of bodies roughly as large as the moon. There exist independent arguments in favor of this theory but, to avoid digression, we will not dwell on them here.

3) Small mean density of Protoearth of equal mass:

$$\frac{M}{R} \approx 10^2 \frac{M_\oplus}{R_\oplus}.$$

Lastly, it is not impossible that fractionation (i.e., preferential dissipation of lighter gases) had occurred as early as in the pre-planetary stage. /343 Iokipii (Ref.407), from this point of view, discussed the cosmogonic hypothesis by Hoyle (Ref.408, 409). Hoyle's hypothesis, as is known, stipulates that the transport of angular momentum from the sun to the protoplanetary nebula is due to the intermediary of a magnetic field. During break-up of the protoplanetary nebula, the neutral and ionized atoms would escape from the Protosun in the plane of the ecliptic. Ionized atoms would be captured by the magnetic field. The lower the ionization potential the higher the probability of capture, so that elements of low ionization potential (metals) would concentrate chiefly in the central portion of the protoplanetary nebula. It is known that inert gases have high ionization potentials, increasing in the sequence Xe, Kr, Ar, Ne. Iokipii showed that ambipolar diffusion in the magnetic field of the protoplanetary nebula would account for the observed deficiency coefficients if the temperature of the nebula were about 10^6 °K.

The above demonstrates how important it would be to know the content of inert gases in the atmospheres of the other planets. Their spectroscopic detection (in any case, in observations from the earth's surface) does not seem feasible, leaving as the only possible method a direct mass-spectrometric analysis with the aid of soft-landing interplanetary probes.

If, however, fractionation did occur during the formative stage of the planets rather than in the protoplanetary nebula as assumed by Iokipii, then it is clear that the present-day main constituents of the terrestrial atmosphere could not have existed in gaseous form during the formative stage of the earth. In fact, for nitrogen we have $F \gtrsim 10^{-5}$ and for oxygen, $\gtrsim 10^{-6}$ (even if considering only the atmospheric oxygen) although their atomic weights are lower than that of neon. It appears that the contemporary atmosphere is of secondary origin, i.e., that it was released by the lithosphere only after the earth had already been formed.

The liberation of N_2, CO_2, and H_2O from the lithosphere owing to volcanic activity takes place in a continuous process. Oxygen is not liberated directly since the terrestrial rocks are incompletely oxidized; instead, oxygen is produced by photosynthesis. It is probable that throughout the earth's geologic history, the composition and total pressure of the atmosphere underwent certain fluctuations. However, the presence of traces of glaciation in ancient rocks (Ref.404) shows that, in the past, no climate resembling the Venusian had ever existed on earth. The amount of buried carbon dioxide bound in carbonates (and released by them into the atmosphere) is extremely large (approximately 10 kg $\cdot$ $\cdot$ cm^{-2}) but such an amount of CO_2 has never been present in the atmosphere all at once; if it had, it would have produced a strong greenhouse effect.

The question of the accretion of interplanetary medium as a factor in the present-day formation of planetary atmospheres remains relatively uninvestigated. The solar wind at a distance of 1 a.u. gives a proton flux of $N \approx 2 \times 10^8$ cm^{-2} $\cdot$ $\cdot$ sec^{-1}; if we disregard the effect of magnetic fields and assume that all the solar corpuscles arriving at the top of the atmosphere get absorbed by the atmosphere, then we may calculate the equilibrium density of hydrogen at the critical level with the aid of eq.(1.133) on putting /344

$$N = \frac{2 \times 10^8}{r^2} cm^{-2} \cdot sec^{-1},$$

where r is the distance to the sun. Here, it is assumed that none of the other sources of hydrogen are significant factors. Assuming the values of T_c and z_c given in Table 69, the equilibrium densities for Mercury, Venus, and Earth are roughly the same and are close to 10^4 cm^{-3}, while the equilibrium density for Mars is about 10^3 cm^{-3}.

Exactly such an amount of hydrogen exists at the critical level in the earth's atmosphere, but this coincidence most likely is accidental, since the magnetic field deflects an overwhelming majority of the solar protons. Studies of paleomagnetism [cf. for example (Ref.386)] show that the earth's magnetic field has repeatedly changed in polarity so that, in the history of the earth, there were times at which this field passed through zero. Sagan (Ref.400) assumed that, during about 2% of its entire time of evolution, the earth had no magnetic field. In this case, the amount of hydrogen present in the earth's upper atmosphere could not be attributed to accretion, whereas even such a small proportion of time would suffice to account for the helium content. Assuming a 10% helium content, we have a mean flux

$$\bar{N}_{He} = 2 \times 10^8 \times 0.1 \times 0.02 = 4 \times 10^5 cm^{-2} \cdot sec^{-1},$$

which is close to the amount lost by thermal dissipation. According to Table 68, $t_0 = 10^7$ years for helium. Altogether, the atmosphere contains 10^{20} cm^{-2} helium atoms (5×10^{-6} by volume), so that the dissipating flux is $N = 3 \times 10^5$ cm^{-2} $\cdot$ $\cdot$ sec^{-1}. Estimates of the rate of release of helium from the earth's interior give approximately 10^6 cm^{-2} $\cdot$ sec^{-1} (Ref.410).

On Mercury, Venus, and Mars there apparently is no magnetic shield and the accretion of interplanetary plasma in their atmospheres may be the principal source of hydrogen and helium in the upper layers of their atmospheres. The possibility of an accretion of solar wind in the Mercurian atmosphere was first mentioned by N.A.Kozyrev (Ref.385). The accretion of inert gases over the intermediary of the solar wind is insignificant - at least in the earth's atmosphere.

Apparently, the accretion of meteoritic matter in the contemporary epoch also plays a role in the formation of the atmosphere. Rocket and artificial satellite studies of micrometeorites showed that the actual rate of accretion of meteoritic matter may be extremely high, much higher than had been assumed earlier. It is not precluded that this rate attains 10^6 tons daily, with the overwhelming majority of this matter being captured by the atmosphere. If these estimates are correct, then the accretion of meteoritic matter plays an enormous /345

role in the balance of our atmosphere (and of the atmospheres of the other planets of the terrestrial group): In 10^7 to 10^8 years, the atmosphere would become augmented by a mass equal to its present-day mass.

Tilles (Ref.400) showed that the accretion of heavy gases, promoted by interplanetary dust, may take place much more effectively than the direct accretion from solar plasma.

Thus, we arrive at the conclusion that the role of various factors influencing the formation of planetary atmospheres in many cases requires further theoretical research and new observational data. So far we can answer only certain specific questions, while in general the problem of the origin of the planetary atmosphere is far from solved, and surprising discoveries in this respect can be expected.

/346

CHAPTER V

THE GIANT PLANETS

Section 5.1 Introduction

The giant planets - Jupiter, Saturn, Uranus, and Neptune - largely resemble each other and markedly differ from the planets of the terrestrial group. Their masses greatly exceed the mass of the earth and amount to 10^{-4} - 10^{-3} $M_\odot$, while conversely their mean densities are lower than those of the terrestrial planets, ranging from 0.7 gm • cm^{-3} for Saturn to 2 gm • cm^{-3} for Neptune. Correspondingly, their radii are comparatively long, with the equatorial radius of Jupiter being R_e = 11.2 $R_\oplus$. All these planets rotate rapidly; their periods range from roughly 10^h to 15^h. The rapid rotation is associated with a pronounced equatorial compression. The parabolic velocity and gravity on planets of this kind are such that there is virtually no escape of hydrogen and, a fortiori, of helium from their atmospheres (cf. Table 68). Hence it is conceivable that on the giant planets the composition and extent of the atmosphere have remained unchanged ever since the solar system first came into existence; in other words, they retained their primordial atmosphere. The depth of the gaseous atmospheres of the giant planets is extremely large, attaining at least 10^3 km. It is not excluded that this accounts for a significant proportion of the planetary radius. Along with the gaseous component, the atmospheres of the giant planets contain large aerosol formations (clouds). Owing to the considerable distance from the sun, the amount of heat received from the sun is small and there exist grounds for assuming that the internal heat flux plays an appreciable role in the thermodynamics of the atmospheres of these distant planets.

The giant planets are relatively little investigated compared with the planets of the terrestrial group. The obstacles to their investigation are due both to the great distances (poor spatial resolution) and to the radical difference between their principal physical characteristics and those of the terrestrial planets, a difference which prevents resorting to analogies with the earth. Jupiter, the nearest of the giant planets, is relatively the best-investigated of these planets and may be considered as their typical representative. Hence these are sometimes termed Jupiter-type planets or Jovian planets. The major portion of this Chapter deals with the results obtained on Jupiter, /347 since we know more about it than about the three other giant planets taken together.

Jupiter moves in an orbit whose semimajor axis has a length of 5.2028 a.u. and a fairly large eccentricity - 0.0483. At its mean distance from the sun, Jupiter receives 27 times less energy per unit area than the earth. Its sidereal period is 11.86 years and its synodic period, 398.9 days.

The linear equatorial radius of this planet is R_e = 71,800 ± 100 km according to a survey of micrometric and heliometric observations made by Rabe (Ref.412). The polar radius is R_p = 67,900 ± 120 km.

Allen's manual (Ref.88) gives a radius R_e differing substantially from that derived by Rabe: 71,350 km, without specifying the probable error. This value is given in the annual publications and was obtained also by Sampson from observations of satellite occultations. Struve, who observed occultation of the star BD 6°6191, found R_e = 71,470 km. It is unclear which method to prefer. For the time being, we can only mention the existence of a systematic discrepancy, reaching 500 km.

The compression of Jupiter is $\epsilon = 0.061$. The compression derived from direct measurements of the angular diameter virtually coincided with the compression derived from the motion of the satellites.

The mass of Jupiter, according to the findings of Newcomb, which were adjusted to a lower figure by Clemence (Ref.2), is equal to

$$\frac{M_\odot}{1047.39 \pm 0.03} = 318.4 M_\oplus = 1.88 \times 10^{30}\ gm,$$

while the mean density is

$$\bar{\rho} = 1.3\ gm \cdot cm^{-3}.$$

The inclination of the equator to the orbit is extremely slight, being 3°05′. Manifestations of seasonal changes are virtually absent on Jupiter. The acceleration of gravity at the equator (g_e = 2360 cm · sec^{-2}) is markedly smaller than at the poles (g_p = 2600 cm · sec^{-2}) owing to the rapid rotation and considerable compression of this planet. We will assume g = 2500 cm · sec^{-2} in our calculations of the physical characteristics of the atmosphere. The markings observable on the disk have to do with the cloud cover, but they include a sufficiently large number of compact and persistent formations to be used as points of reference for determining the period of rotation. Since atmospheric currents whose velocity may differ at different latitudes also contribute to the observed rotational effect, it is natural to expect that the mean period thus derived will somewhat depend on the latitude, and this indeed is the case. A.A.Belopol'skiy (Ref.413) established that the spots in the equatorial zone within the limits /348 of the latitudes ±5° have a rotation period of 9^h50^m whereas within the latitudes from 10 to 45° this period is 9^h55^m. The rotational speeds at various latitudes will be considered in greater detail in the next Section. The periodicity of the bursts of Jupiter's radio emission in the decameter wave range is close to the rotation period in the temperate latitudes without being exactly equal to it.

In this connection, three longitude systems have been adopted to denote coordinates on Jupiter: system I (equatorial); system II (for temperate latitudes) and system III (according to bursts of decameter radio emission); the corresponding sidereal periods are

I	9^h	50^m	$30^s.003$
II	9	55	40. 632
III	9	55	29. 37.

The initial meridians for these systems were selected conditionally and are not associated with any definite markings observable on the disk. At the instant of 1897, July 14.00, Julian day 2414120.0, the initial meridian of the system I had the longitude $43^{\circ}.31$; that of the system II, the longitude $96^{\circ}.58$; the initial meridian of the systems III and II coincided on January 1, 1957 at 0^{h} Greenwich time. Latitudes and longitudes on Jupiter are termed zenographic (from Zeus, the Greek name of the planet).

The theory of the internal structure of Jupiter implies that the bulk of the planet is in the solid state, which naturally raises the question as to which of the above periods is closest to the period of rotation of the solid body of the planet. It may be expected that near the equator the atmospheric currents have a greater influence on the rotational velocity of the spots. If the radio emission source in the decameter range is associated with a solid surface (directly or over a magnetic field), then the period in the system III must be taken as the "true" period. This is indicated by the exceptional stability of the period of repetition of the radio bursts.

Reese (Ref.414) attempted to derive the probable longitude of the source of perturbations ("volcano") and its rotation period on the basis of observations of bursts of optical activity in the South Equatorial Belt. Making use of the data on five disturbances of this kind (between 1919 and 1952) he derived a period of $9^{h}55^{m}42^{s}.66$, close to the system II, but the differences between the observations and the calculated position of the source in the longitude system with this new period are as great as $\pm 10^{\circ}$, which exceeds the observational error [cf. (Ref.415)].

The visual stellar magnitude of Jupiter at mean opposition is $-2^{m}.4$ and its geometric albedo, 0.445 (Ref.66). Since the phase angle of Jupiter varies within limits of only 12°, a determination of the phase integral from observations seems impossible. As will be demonstrated below, the atmosphere of Jupiter, from the optical point of view, can be considered as a semi-infinite atmosphere without constraints. At isotropic scattering, such an atmosphere /349

gives $Q = 1.45$ if $a = \frac{\sigma}{\sigma + k} = 1.0$ and $Q = 1.52$ if $a \approx 0.95 - 0.97$, which corresponds to reality. Harris increased the value of Q to 1.60 in order to allow for a probable anisotropy of scattering. Then $A_c = 0.71$, which is close to the corresponding value for Venus. High albedos are typical of any planet having an optically thick atmosphere.

Section 5.2 Markings and Phenomena Observable on the Disk of Jupiter

The disk of Jupiter (Fig.144) is striated with dark-reddish belts (sometimes termed streaks). The intervals between the belts are termed zones. The overall pattern of distribution of the belts and zones and their shape, contrast, and fine structure vary in time. Various authors used different notations for the belts and zones. Henceforth, we shall employ the nomenclature given in /350 the monograph by the British amateur astronomer Peek (Ref.415) which represents the most exhaustive survey of the markings and phenomena observed on the disk of

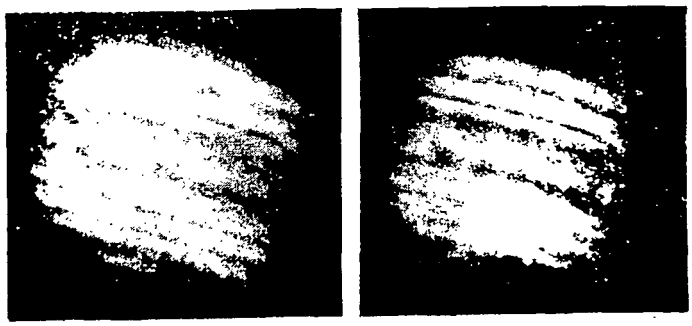

Fig.144 Photographs of Jupiter Acquired with a Record-High Resolution (0".25) at the Pic du Midi Observatory (Ref.415). Print scale: 1" - 2 mm. Left photograph taken on Nov.22, 1964 at $23^h 25^m$; right photograph, on Nov.25, 1964 at $0^h 05^m$, yellow filter, $0^s.8$ exposure. Real variations in the "microstructure" of the belts and zones are discernible. Right top: the Great Red Spot.

Jupiter. It is worth noting that observations of Jupiter by amateurs (some of which, such as Peek's own studies, have been carried out systematically over tens of years) are the most important source of information on the changes observable on the disk of this planet. Owing to the exceptionally large angular dimensions of its disk and its principal markings, Jupiter is much easier to observe than, for example, Mars and interesting results can be obtained with small amateur instruments even under the mediocre astroclimatic conditions characteristic of the British Isles or the Moscow Region.

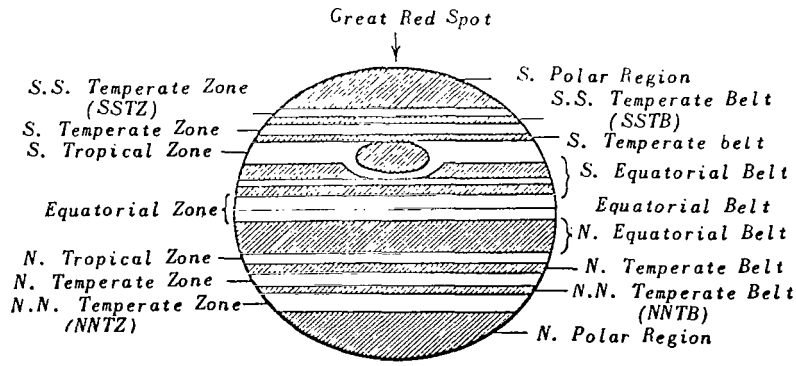

Fig.145 Nomenclature of Belts and Zones on Jupiter.

The principal markings and their nomenclature are given in Fig.145 (compare with Fig.144). Along the equator extends the bright Equatorial Zone (E.Z.). At its center a thin dark streak is occasionally observed. Dark belts are located on both sides of the Equatorial Zone: the South Equatorial Belt (S.E.B.) and the

North Equatorial Belt (N.E.B.). The South Equatorial Belt consists, as a rule, of two components - the northern and the southern (N. comp. S.E.B. and S. comp. S.E.B.). Other belts also often have two components. North of the N.E.B. lies the North Tropical Zone (N. Trop. Z.) and beyond this the North Temperate Belt (N.T.B.). North of the N.T.B. the belts N.N.T.B.; N.N.N.T.B.; and so on, can be discerned. The intervals between these belts are termed N.N.T.Z.; N.N.N.T.Z.; and so on. As the latitude increases, the contrast between the zones and belts decreases and near 45° there commences the Polar Region with its uniform gray coloration. /351

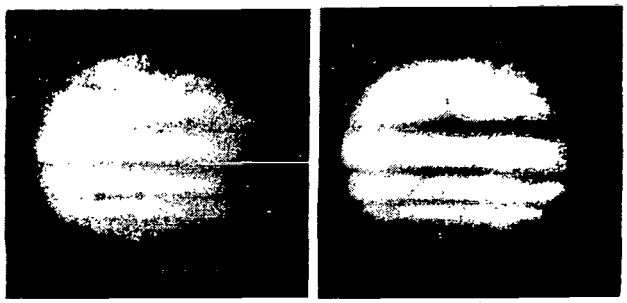

Fig.146 Photographs of Jupiter in Blue (Right) and Red (Left) Light. On the red photograph, the belts show greater contrast; the contrast of the South Equatorial Belt is particularly distinct.

A similar structure is displayed by the Southern Hemisphere, but this has certain features of its own. In the South Tropical Zone, an oval-shaped more or less dark object - the Great Red Spot (G.R.S.) is discernible around which the southern boundary of S. comp. S.E.B. curves back forming the so-called Red Spot Hollow or Bay. The Spot sometimes fades until completely invisible, but the Bay always remains observable. Between the years 1901 and 1940, a darkening of part of the S. Trop. Z. had been observed. This darkening was termed the South Tropical Disturbance. The N.E.B. is the reddest of all the other belts (Fig.146).

Normally there are four main belts and five zones on Jupiter, but their number may increase or even decrease at times. For example, the S.E.B. periodically becomes very blurred while the N.E.B. and N.E.Z. shift southward. The fine structure of the belts and zones (dark and bright spots, "bays" and promontories, etc.) varies to an even greater extent. Isolated formations of this kind may persist for months and years (a record of constancy is held by the Great Red Spot and the Red Spot Hollow), but in some cases the changes are of a catastrophic nature and may occur at enormous speeds so that the appearance of discrete markings as much as 10^4 km in extent may change within 10^3 sec. Along with the variations in contrast, shape, and position of the markings, there are also variations in their color.

The periodicity of variations in the latitude and width of the belts has been investigated by many authors [see, e.g., (Ref.6, 415-418)]. Table 70 and Fig.147 give the results obtained by Focas (Ref.418) from an analysis of visual and photographic observations from 1885 to 1961. A period of 12-16 years is typical, but there also exist isolated sharp deviations: The southern edge of the S.E.B. and the northern edge of the N.E.B. display a shorter period of variation in latitude (about 5 years). With respect to the N.E.B., this finding was confirmed by Mourão (Ref.419) who established that the width of the belt varies with a period of 4 - 6 years. A broad belt encompassing the entire latitude /352

TABLE 70

PERIODICITY OF VARIATIONS IN LATITUDE OF BELTS ON JUPITER

Belt	Period, years	Latitude Variation
Southern Hemisphere		
S. S. T. B.	12—15	6—8°
S. T. B.	14—16	3—4
S.E.B. south. edge	4—6	3—4
Equatorial Zone		
S.E.B. north. edge .	12—16	3—4
N.E.B. south. edge	12—16	3—4
Northern Hemisphere		
N.E.B. north. edge	3—6	3—6
N. T. B.	10—14	3—4
N. N. T. B.	12?	4—8

region from the northern boundary of the N.E.B. to the southern boundary of the S.E.B. occasionally forms along the equator. Such a phenomenon was observed in 1878-1879 and it recurred in 1962-1963 (Ref.420-421). This /353 indicates the possible existence of an activity cycle lasting about 90 years. The concept of activity on Jupiter includes the shape and contrast of the belts, the presence of rapidly shifting spots, etc. During maximum activity, the contrast is greatest; blobs of dark and bright matter are clearly discernible in the belts, and rapid movements are often observed. Focas found that activity minima recur once every 20 - 22 years, but it was exactly in 1962, when the next decrease in activity had been expected, that intense perturbations were observed that changed the appearance of the disk.

As mentioned above, rotation periods determined according to long-enduring spots are greater in the temperate latitudes than in the equatorial. This points to a certain - but far from complete - analogy with the sun. On the sun, the diurnal displacement of spots is a smooth function of the latitude φ. It amounts to

$$\xi = 14^\circ.38 - 2^\circ.96 \sin^2 \varphi.$$

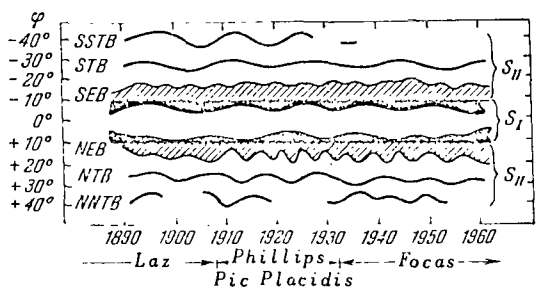

Fig.147 Variations in Latitudes of the Bands.

For Jupiter, no such smooth function can be selected. The equatorial markings generally shift more rapidly, but the greatest velocities are observed at the latitude +23° (Table 70). The velocity distribution outside the equatorial region displays an irregular pattern and differs in the Northern and Southern Hemispheres. Prolonged observations show that the rate of motion of the long-enduring markings abruptly changes with latitude, while remaining constant within certain more or less narrow latitude ranges. This points to the existence of certain atmospheric fluxes directed along the parallels. The concept of these fluxes or currents was introduced by the British amateur astronomer Williams (Ref.422) and is now generally accepted. The latitudinal localization of the currents is more stable than the localization of the belts, and the boundaries of the currents do not always coincide with the boundaries of the belts and zones. Rotation periods corresponding to the various currents are given in Table 71, which was taken from Peek's monograph (Ref.415). On the whole, the rotation period of the Southern Hemisphere is somewhat shorter than that of the Northern. Peek's book presents detailed data on the morphological features

TABLE 71

/354

ATMOSPHERIC CURRENTS OBSERVABLE ON THE DISK OF JUPITER

Position and Designation of Current	Approximate Latitude	Variation in Longitude, in 30 Days	Period of Rotation	Number of Oppositions Used in the Calculation
North Polar Current	fr. +90 *to* +47°	+1°	$9^h55^m42^s$	19
N.N.N.T.B. (Temperate Current N.N.N.)	+43	−15	9 55 20	9
N.N.T.B. and N.N.T.Z. (N.N. Temperate Current B)	fr. +40 *to* +36	+1	9 55 42	35
Southern edge of N.N.T.B. (N.N. Temperate Current B)	+35	−78	9 53 55	6
Northern edge of N.T.B. and southern edge of N.T.Z. (North Temperate Current A)	fr. +33 *to* +29	+18	9 56 05	24
Center of N.T.B. (North Temperate Current B)	+27	−105	9 53 17	6
Southern edge of N.T.B. (North Temperate Current C)	+23	−62	9 49 07	6
N.T.Z. and northern part of N.E.B. (North Equatorial Current)	fr. +22 *to* +14	−9	9 55 29	52
Center of N.E.B. 1898-1900	?	−6	9 55 32	2
1927-1940	+13	−67	9 54 09	7
Southern edge of N.E.B. and northern edge of E.Z. (northern branch of Great Equatorial Current	fr. +10 *to* +3	−4	9 50 24*	47
Center of Z.E. (middle branch of Great Equatorial Current)	fr. +3 *to* −3	−4	9 50 24*	14
Northern edge of S.E.B. and southern edge of E.Z. (southern branch of Great Equatorial Current)	fr. −3 *to* −10	−3 +38	9 50 26* 9 51 21	39 11
Southern edge of S.E.B. (normal spots)	−19	−1	9 55 39	13
Southern edge of S.E.B. (northern branch of Circulating Current	−19	+132	9 58 43	6
S. Trop. Z.	fr. 21° *to* −26°	−3°	$9^h55^m36^s$	7
Great Red Spot, northern edge	−22	−2	9 55 38	64
of S.T.B. (southern branch of Circulating Current)	−27	−116	9 53 02	5
S.T.B. (South Temperate Current)	−29	−15	9 55 20	47

/355

TABLE 71 (cont'd)

Position and Designation of Current	Approximate Latitude	Variation in Longitude, in 30 Days	Period of Rotation	Number of Oppositions Used in the Calculation
South edge of S.T.B. and S.S.T.Z. (S.S. Temperate Current)	fr. —31 *to* —45	—25	9 55 07	42
S.S.S.T.B. and South Polar Region	fr. —45 *to* —90	—8	9 55 30	5

* Although these three periods generally are almost identical, in some years they differ markedly.

and velocity of motion of the dark and bright formations observed in the various currents.

We will dwell in greater detail on the Great Red Spot and the South Tropical Disturbance. The Red Spot has been attracting special attention of observers ever since 1879. Denning (Ref.423), analyzing old drawings of Jupiter dating from the Seventeenth Century, discovered the Red Spot on some of these charts. The first ever to observe this formation probably was Hooke (1664) followed by Cassini in 1665. However, these early observers failed to isolate the Spot /355 from other formations, apparently because of its low contrast. In 1879-1882 the Great Red Spot turned unusually dark and was the most noticeable marking on the disk. If Denning is right, the Red Spot is most likely more than 300 years old. In general, the Red Spot is a stable marking on the disk of Jupiter, and its only constant marking at that.

In 1879-1882 the Red Spot had the shape of an ellipse whose major axis extended 33°.7 (40,000 km) in longitude and 10° (13,000 km) in latitude. In subsequent years, its apparent dimensions shrank and fluctuated irregularly. Thus, during the period from 1927 to 1943, it reached its greatest longitudinal extent (30°) in 1935 and its shortest extent (21°) as little as a year thereafter. In 1936, the Spot was very dark (probably nearly as dark as in 1881). In 1919-1920, its edges were blurred but the overall extent occasionally reached 40°.

The Red Spot almost never merges with the S. comp. S.E.B., and the boundary between the "shores" of the Red Spot Hollow or Bay and the Red Spot itself is normally distinct. The N. comp. S.E.B. remains parallel to the equator. The Hollow is particularly distinct when the Red Spot is blurred. Both markings have never yet disappeared simultaneously. The depth of the Red Spot Hollow /356 is not associated with temporary variations in the width of the Red Spot. The southern edge of the Red Spot occasionally adjoins the S.T.B. and is overlapped by the latter, but sometimes the Hollow takes shape.

The configuration of the Red Spot and the Hollow differs in different years (Fig.148). Peek described three characteristic shapes of the Great Red Spot:

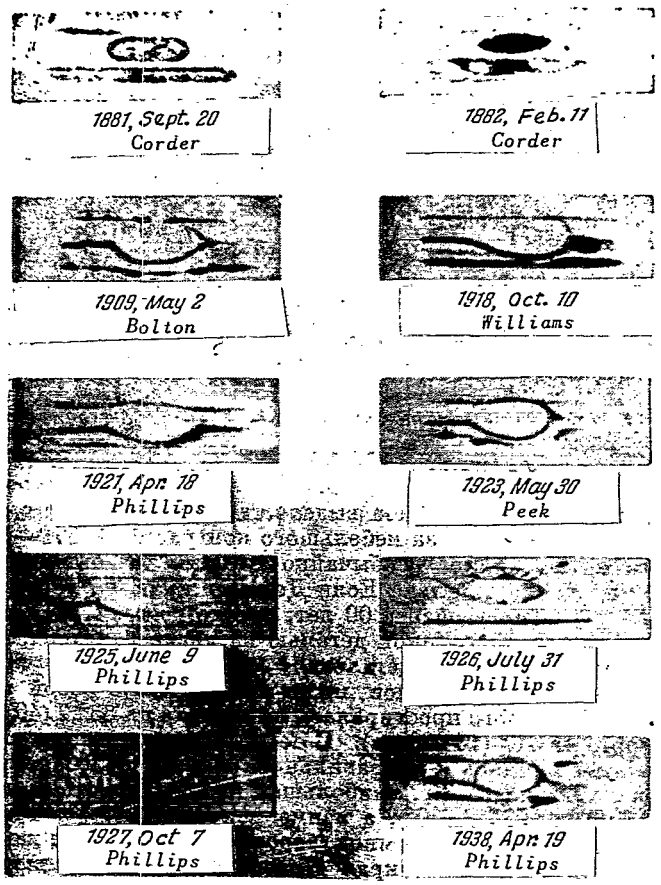

Fig.148 Characteristic Appearance of the Great Red Spot and Hollow in Various Years (Ref.415).

1) dark-red contrast formation. A dark border is often visible along the edge. The brightness distribution is hardly ever uniform, and then exactly during maximum contrast of the Spot (1879-1882). 2) Boundaries almost completely blurred, contrast low, with only a faint haze visible in the Hollow. 3) Contrast low, but "whiskers" indicating the boundaries of the Red Spot radiate from the edges of the Hollow: the Hollow has no gaps along its periphery. The Spot then may not be visible at all. An unbroken elliptical shape of the Hollow is usually observed at moments of conjunction with the South Tropical Disturbance. /357

The change in contrast and color displays a certain periodicity. Thus, in 1879-1882 the contrast was high; in 1890 it was low, and in 1893-1894 it was high again and the Red Spot was clearly visible until 1907, after which it faded. Good visibility of the Red Spot was recorded in 1914, 1927-1928, 1936, around 1950, and last in 1962-1964. Peek emphasizes that the variations in contrast may be at least partially attributable to the increase in brightness of the ambient bright material of the S. Trop. Z. rather than to changes in brightness

of the Spot itself. In 1927-1928 and in 1936, the South Tropical Zone was extremely bright.

The zenocentric latitude of the Red Spot fluctuates within the limits of 3°. Maximum latitude (about 23°) was observed in 1912 and 1925 and minimum (about 20.5 - 21°), in 1908-1909, 1917-1918, 1929-1930. The period of variation in latitude is close to 12 years. On variation in latitude from +22 to 23°, the radius of rotation increases by 0.7%. Were the Red Spot a solid and had its angular momentum remained constant, the period would have increased by 1.5% or 9 min. Actually, however, the maximum variation in the rotation period of the Great Red Spot does not exceed 12 sec and is in no way associated with variations in its latitude.

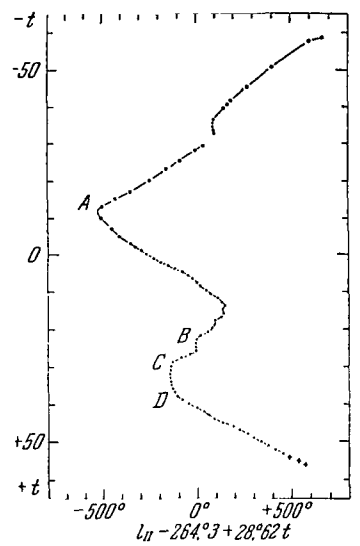

Fig.149 Longitudinal Drift of the Great Red Spot between 1831 and 1955 (Ref.415).

The mean rotation period of the Red Spot is $9^h55^m37^s.58$ according to observations from 1831 until 1955. Its variations have been investigated in detail by Peek. They are shown in Fig.149 where the longitude in the system corresponding to the mean rotational velocity of the Spot is plotted along the abscissa while the time (in units /358 equal to the interval between two oppositions - 398.88 days) is plotted along the ordinate. The points A, B, C, and D indicate the moments of sudden variation in the velocity of the Great Red Spot (1880, 1919, and 1936). They all coincide with moments of excellent visibility of the Spot. A similar variation in velocity has recently been discovered by Smith and Tombaugh (Ref.424). Until November 10, 1963 the period was $9^h55^m43^s$, 1 ± 0.2, whereas after that date it changed to $9^h55^m41^s$, 7 ± 0.3. In 1959, the rotational velocity of the Red Spot again underwent an abrupt change. It was at roughly the same time, too, that the rotational velocity of the source of bursts of radio emission in the decameter range also had changed (cf. Sect.5.8).

The South Tropical Disturbance (Fig.150) was discovered in 1900 in the form of a series of dark humps extending from the southern edge of the S.E.B. within the confines of the S. Trop. Z. On February 28, 1901, the mass of dark matter joined the S.E.B. with the S.T.B. and bright spots occurred at its ends. This mass trailed the Red Spot at a distance of approximately 90° Long., but the rotation period of the Disturbance was shorter ($9^h55^m20^s$) so that the gap between them shrank gradually. Although the movement of the South Tropical Disturbance slowed in subsequent months, it reached the Red Spot Hollow in 1902.

Not long before making contact with the Red Spot, the velocity of the leading edge of the South Tropical Disturbance increased. Observers impatiently waited for the moment of coalescence. Nothing special happened. In any case, the appearance of the Red Spot remained completely unchanged. Six weeks later

the leading edge of the Disturbance appeared on the other side of the Hollow. The Hollow was seen as a bright elliptical spot against a dark background. The Spot itself displayed much less contrast than the Disturbance. Everything seemed to indicate that the South Tropical Disturbance had passed underneath the Red Spot. After three months, the conjunction came to an end.

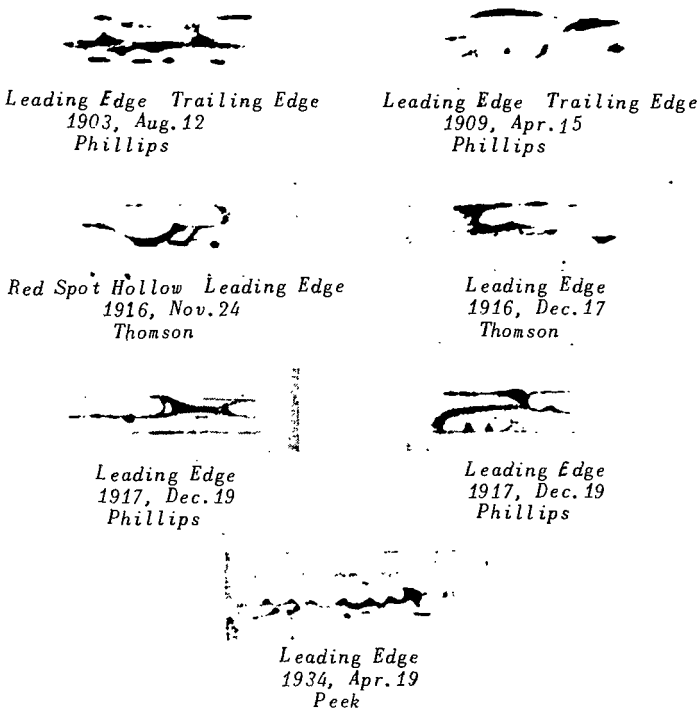

Fig.150 Characteristic Appearance of South Tropical Disturbance in Various Years (Ref.415).

Conjunctions between the South Tropical Disturbance and the Great Red Spot also have been observed in 1904 and 1906 as well as in subsequent years. These have been becoming increasingly longer in time (the ninth conjunction lasted 10 years, from 1928 to 1938) since the rotation period of the South Tropical Disturbance has been approaching that of the Red Spot, and its physical extent has been gradually increasing from several degrees in 1900 to 230° in 1935. At the same time, the Disturbance has been growing fainter and was apparently last observed in 1940. A marking similar to the South Tropical Disturbance was discovered in 1955, but there is no certainty that it can be identified with it. Similar doubts also arise with respect to a drawing of the early XIX Century on which there is a similar darkening in the South Tropical Zone.

The effect of the Red Spot on the rate of motion of the dark material of /359 the South Tropical Disturbance had been extremely distinct during the early conjunctions. The leading and trailing edges of the dark mass moved faster on

coming close to the Red Spot Hollow and slower once they had passed the Hollow. Not all observers give an identical description of the phenomena accompanying the conjunctions. Thus, V.G.Fesenkov (Ref.416) emphasized that the "veil", as he termed the South Tropical Disturbance, alters the configuration of the Red Spot Hollow and the South Temperate Belt during conjunction with the Red Spot.

As mentioned above, all of the belts vary in intensity. Normally, a gradual variation in brightness of the entire belt takes place. Sometimes, however, local darkening occurs which subsequently spreads throughout the belt. Effects of this kind are particularly distinct in the South Equatorial Belt (S.E.B.). /360 Peek gave a detailed description of five strong disturbances in the S.E.B.: in 1919-1920, on August 10, 1928; on December 17, 1942; on February 11, 1943; in July 1949; in October 1952. A recent disturbance (September 24, 1963) was described by Smith and Tombaugh (Ref.424). Such disturbances commence with the appearance of compact and occasionally numerous dark spots which subsequently are smeared out into thin streaks. At times, bright spots suddenly appear. Often these spots travel at great velocities. At night, extremely rapid movements of the disturbances and appreciable variations in the appearance of the disk are a rare but repeatedly observed phenomenon (for example, in October 1920 during a major equatorial disturbance). Figure 151 shows typical photographs of eruptive effects in the South Equatorial Belt. Within two days, the shape of the spots in the neighborhood of the Great Red Spot had changed substantially. Smith and Tombaugh attributed the change in velocity of the Red Spot on November 10, 1963 to the autumn equatorial disturbance. Both emphasized that, roughly about that time, three bright spots approached the trailing edge of the Red Spot.

The Circulating Current exhibits remarkable properties (see Table 71). In February 1920, two spots (A and B) arose in the S. comp. S.E.B. spaced 60° apart and began traveling in retrograde direction (period of A, $9^{h}57^{m}59^{s}$; period of B, $9^{h}57^{m}52^{s}$). On reaching the South Tropical Disturbance they disappeared, but a month later they reappeared in the near latitudes; this time their rotation was direct and amounted to $9^{h}53^{m}29^{s}$ and $9^{h}53^{m}20^{s}$, respectively. Later, similar phenomena have been observed in this region.

During 1940-1941, very small but extremely dark spots, measuring about 1" in area and moving in a peculiar manner had been observed in the South Tropical Zone. Their movement indicated the superposition of a damping oscillation on smooth longitudinal displacement. A similar effect was observed in 1941-1942. The oscillatory period of these spots (which were termed "oscillating" by Peek) was about 2 months (Ref.415, 425).

Thus, along with many-year periods there occur local periods of much smaller atmospheric activity on Jupiter. The main cycle is not related either to solar activity or to period of revolution about the sun but rather characterizes the periodicity of quasi-volcanic processes within the planet itself. We cannot use the full term "volcanic", since the Jovian structure differs too much from the terrestrial structure to expect a close similarity between the tectonic activities in these planets. B.M.Rubashov (Ref.426) found correlations of /361 secular (averaged over 10-year intervals) variations in the period of different currents in the atmosphere of Jupiter and slow variations in solar activity, but such correlations, as is known, may be of an extremely complex and circumstantial

character. Even correlations between solar activity and terrestrial meteorological effects generally have no clear physical explanation, and this is even more so the case for Jupiter.

1928, Oct. 5, 08^{h}10^m UT λ=317°

1928, Oct. 7, 09^{h}58^m UT λ=324°

Fig.151 Rapid Relative Movements of Bright and Dark Spots in the South Equatorial Belt.

Focas and Baños (Ref.420) introduced the concept of photometric index of the atmospheric activity of Jupiter. The photometric index of some square or of some latitudinal region on the Jovian disk is proportional to the decrease in its brightness compared to some standard quantity. Focas and Baños did not /362 use absolute standardization in determining the photometric index; instead, they calculated the standard brightness on the assumption that there always exists some sector in the unperturbed state on the disk. It would be essential to supplement the procedure of determining photometric indexes with absolute standardization of brightness, but even so the photometric index in its present form is of interest as a quantitative characteristic of the state of the Jovian atmosphere. Figure 152 shows the variation in the photometric index of activity of the equatorial regions of Jupiter from 1956 to 1963. The changes in brightness of the belts and zones should lead to variations in the stellar magnitude of Jupiter, which actually is the case (Ref.66, 421).

The brightness distribution over the disk of Jupiter and the absolute values of the brightness coefficients have been measured repeatedly, chiefly

by photographic means. A review of the photometric studies can be found in the book by N.P.Barabashev (Ref.6) and in the article by V.N.Lebedinets (Ref.427). All these authors agree that the observed brightness distribution along the equator of intensity is satisfactorily represented by the theoretical distribution derived for isotropic scattering in a semi-infinite atmosphere (Fig.36), for various values of the parameter $a = \frac{\sigma}{k + \sigma}$. V.G.Teyfel' (Ref.428) derived the values of a given in Table 72 from the curves of limb darkening for the S.T.Z. and the Great Red Spot. The contrast between the Red Spot and the S.E.B. is extremely slight so that the values of a for the belts may be taken practically the same as those for the Red Spot. The values of "a" given here can be considered as the lower limit, since anisotropic scattering with a forward-extended indicatrix requires high values of a in order to obtain the same value of albedo of the atmosphere, other conditions being equal.

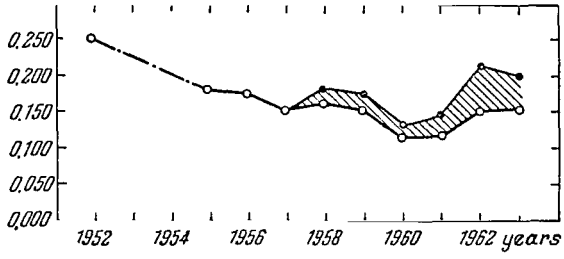

Fig.152 Variation in the Photometric Index of Jupiter in the Jovian Equatorial Regions, from 1956 to 1963 (Ref.420).

The decrease in a with wavelength indicates that Rayleigh scattering does not markedly contribute to the general photometric characteristics of the atmosphere. These are determined by scattering on aerosols, and it is to be expected that the mean scattering indicatrix is greatly elongated. /363

TABLE 72

CONTRAST AND ALBEDO OF UNITARY SCATTERING IN THE S.T.Z. AND THE GREAT RED SPOT (REF.428)

λ	Contrast at Center	a	
		Zone	Spot
6250	0.92	0.97	0.96
5300	0.77	0.95	0.92
4200	0.68	0.93	0.88

Polarization observations [cf. (Ref.102, 434)] yield some additional information on the characteristics of the Jovian atmosphere. Lyot and Dollfus discovered a considerable increase in the degree of polarization at the poles where it attains 8%, and its plane is oriented perpendicularly to the limb. It is not excluded that the polarization is due to the gaseous component of the atmosphere. Another possible explanation is that of a haze, consisting of small-diameter particles and located above the main layer of clouds (Ref.435). The former of the above interpretations means that the upper cloud boundary is lower in the polar than in the equatorial regions, as is the case in the terrestrial atmosphere (owing to the decrease in mean surface temperature with latitude). Rayleigh polarization at a phase angle of 0° may arise only owing to multiple scattering; and if it actually were due to the gaseous layer, then the optical thickness τ_g of that layer must be sufficiently great. Gehrels and Teska (Ref.434) estimated the possible limits of τ_g near the poles as 0.4 to 0.8. Spectroscopic observations (cf.

Sect.5.3) often reveal an increase in the intensity of CH_4 bands in the polar regions, but this also cannot be unambiguously interpreted as a result of an increase in the thickness of the gaseous layer. The wavelength dependence of the polarization of the polar regions is not in agreement with the dependence implied by Rayleigh scattering (Fig.153). This increases rapidly with decrease in wavelength between λ 10,000 and λ 5000 Å, after which it either becomes constant or decreases. It is interesting that, in the equatorial region, polarization /364 monotonically increases with decreasing wavelength. Note that in the case of Venus, the photometric data may in principle be explained by both true absorption and the effect of finite thickness of the atmosphere. Models of the internal structure of Jupiter give an extremely high linear thickness of the atmosphere, making it almost certain that this alternative does not apply to Jupiter; the photometric characteristics of Jupiter apparently are determined only by the properties of its atmosphere.

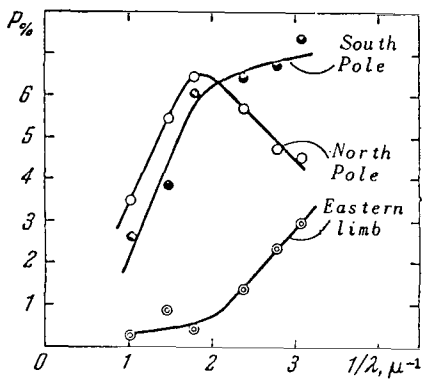

Fig.153 Polarization at the South Pole, North Pole and Eastern Limb of Jupiter, as a Function of Wavelength. Observations performed with a 4″-diaphragm in April 1960. (Ref.434).

Since the albedo of the atmosphere and the limb darkening point to the presence of true absorption, it is of interest to estimate the level at which a marked attenuation of solar radiation occurs. Such an estimate would also characterize the critical depth at which the markings observable on the disk are able to exist. Experiments with optical cloud models indicate that, at $\tau = 40$ and $a = 0.99$, a 10-fold attenuation takes place if the elongation of the indicatrix is characterized by the parameter $\delta \approx 30$, and a 20-fold attenuation if $\delta = 15$ (δ being the ratio of forward-scattered flux $0 < \gamma < \frac{\pi}{2}$ to backscattered flux $\frac{\pi}{2} < \gamma < \pi$). The attenuation increases as the shape of the indicatrix approaches a spherical form; under the same conditions, $a = 0.95$ gives a 30- to 100-fold attenuation. Similar estimates can be obtained on the basis of Rozenberg's approximation theory. Assuming that the depth at which solar radiation suffers a 10-fold attenuation represents the limiting depth, it appears that the corresponding optical thickness would be $\tau_{lim} < 40$, with the upper limit being reached only for extremely elongated indicatrices; for a spherical indicatrix, a corresponding attenuation is reached at $\tau_{lim} < 3$.

We take $\tau_{lim} = 10$, bearing in mind that the actual value may differ by a factor of 2 - 3 from the adopted value. To determine the corresponding linear depth, the scattering coefficient σ must be known. Spectroscopic observations (Sect.5.4, Subsect.2) show that, for the indicatrix $\frac{2\pi r}{\lambda} \approx 20$, we have a value of σ that is at least 5×10^{-6}, whence the sought linear depth of penetration is

$$z_{lim} = \frac{\tau}{\sigma} \leqslant 20\ km$$ /365

A roughly similar value of z_{lim} is also derived for a spherical indicatrix.

The limited intensity variation of CH_4 bands along the equator indicates that, on the average, the altitude of the cloud layer does not vary by more than a few kilometers, but the spatial resolving power of spectroscopic observations (1″, i.e., 4×10^3 km) is too small to preclude the presence of major local variations in the altitude of the cloud top. However, the extent of these variations hardly exceeds the scale height of the Jovian atmosphere ($\sim$ 20 km). Thus, the vertical scale of the region of optical effects considered here does not exceed 40 km. This scale also determines the depth within whose limits the hydrodynamic effects in the atmosphere can be directly related to solar radiation.

The variable appearance of the markings observed on the Jovian disk means in itself that, at least in most cases, we see only the clouds floating in the atmosphere of this planet. An estimation of z_{lim} convincingly shows that clouds are about the only feature of Jupiter we can see in general, since the depth of its atmosphere is $\gtrsim$ 1000 km (cf. Sect.5.11).

A special problem is presented by the nature of the Great Red Spot since, unlike all other markings on Jupiter, this spot is almost always present. At various times, three hypotheses have been advanced. At first it had been assumed that the Red Spot represented an expulsion of material from a permanent volcano. However, the variations in the rotation period of the Red Spot cast doubts on this hypothesis and it was then assumed that the Red Spot is an island floating in the viscous semi-liquid lower atmosphere of Jupiter. This hypothesis is supported by Peek (Ref.415). It is clear from the foregoing that we would never be able to see this island. Moreover, Sagan (Ref.429) on the basis of considerations of dynamics, showed that - if this hypothesis were correct - the considerable longitudinal drift should be accompanied by a similar latitudinal drift, which is not the case. Instead, similarity between the curves of limb darkening of the Red Spot and the belts (Ref.428, 430) indicates that the Red Spot is of a gaseous nature. The third hypothesis was postulated by Hyde (Ref.431, 432) who showed that a moderately substantial inhomogeneity of the planetary surface around which the atmosphere circulates could generate a system of vertical currents (Taylor's column) of considerable height. Such an inhomogeneity might be either a depression or an elevation (plateau). The /366 vertical extent of this inhomogeneity must exceed a certain critical limit

$$h_c = \alpha d \frac{u}{\Omega L},$$

where $\alpha \approx 1$; d $\approx$ 1000 km is the thickness of the atmosphere; u is the velocity of hydrodynamic motion at the surface; $\Omega = 1.5 \times 10^{-4}$ rad $\cdot$ sec^{-1} is the angular velocity of rotation of the planet; L is the linear dimension of inhomogeneity. If L = 25,000 km and u = 10 m/sec, then h_c = 2.5 km. This law was experimentally verified.

Hyde's hypothesis seems more logical than the volcanic hypothesis, but has the same basic shortcoming: Its acceptance makes it necessary to assume that the rotation period of the solid body of the planet is variable. At the same time, Hyde's hypothesis accounts for the short-lived dark spots (increase in wind velocity) as well as for the pattern of currents around the Great Red Spot and, particularly, for the presence of the Red Spot Hollow: experiments show that, on the equatorward side of the column, the flow must be laminar.

On the whole, the hydrodynamics of Jupiter are still largely uninvestigated. At the equator, the rotational speed is greater than in the temperate latitudes. On transition to the temperate latitudes at the boundary of the equatorial zone, the velocity changes by a value of $\Delta v \approx 1$ km/sec, which is close to the speed of sound. This change occurs within a latitudinal zone not more than 3° wide. What is the reason for the presence of this discontinuity? Lastly, the rotational speed of the solid body of the planet is considered close to the period of the system III (which differs only little from the system II, associated with the optical markings in the temperate latitudes). The basis for this opinion is the high degree of constancy of the period of repetition of bursts in the decameter range. However, according to the law of conservation of angular momentum, the gaseous masses floating up at the equator must decrease rather than increase in angular velocity, so that the rotation period of the solid body of the planet must be shorter rather than longer than the period of the system I. If the depth of the atmosphere is 1000 km then, in view of the conservation of angular momentum, the difference must be about 20^{m}, which gives a rotation period of $9^{h}30^{m}$ for the solid body of the planet. However, such short periods are in no way manifest.

The general circulation of the atmosphere of the giant planets is difficult to interpret on the basis of terrestrial analogy, since the depth of their atmospheres is too great. The atmosphere of Jupiter cannot be considered as a thin film covering the surface, as is done in theories of the general circulation of the earth's atmosphere. Moreover (and this is an even more important difference), the circulation on the giant planets is apparently determined by internal energy sources rather than by solar heating. In fact, solar radiation penetrates only to a depth of the order of 20 km, whereas the total depth of the atmosphere is at least 50 times as great. In one way or another, had the circulation on Jupiter been due to solar heating, a distinct meridional component would have been present in the observed movements, whereas actually meridional displacements on Jupiter are comparatively slow and of low amplitude. /367

Clouds located at such heights above the surface and having such a high albedo undoubtedly consist of condensation products rather than of particles uplifted from the surface, although in isolated instances ejections of a volcanic nature may be a factor. Presumably, most of the variations observed on Jupiter represent the effects of condensation and sublimation associated with small temperature fluctuations, variations in concentration of condensing gases, and changes in the number of condensation nuclei (the role of particles rising from the surface may be particularly large in this respect). Meteorological effects of this kind require no major expenditure of energy. During the disturbances on Jupiter, however, there are accelerated movements of isolated clouds which are difficult to attribute to anything other than real hydrodynamic displacement, in which case the energy expenditure may be substantial.

The data presented in Table 71 give the impression that dark belts take shape at the boundaries between hydrodynamic currents of differing velocities: the S.E.B. at the boundary between the southern branch of the Great Equatorial Current and the South Temperate Current; the N.E.B. between the northern branch of the Great Equatorial Current and the North Equatorial Current, etc. The activity in the belts is generally much higher than in the zones; the belts represent the more disturbed regions of Jupiter. The physical meaning of this apparently lies in the fact that the belts are the boundary regions between currents, in which phenomena of large-scale turbulence develop.

TABLE 73

/368

ABSORPTION BANDS IN THE SPECTRA OF GIANT PLANETS ACCORDING TO OBSERVATIONS AT SMALL DISPERSION (VISIBLE REGION) (REF.436,437)

λ, Å	Presence and Estimates of Equivalent Widths, Å*				Identification
	Jupiter	Saturn	Uranus	Neptune	
4861	*absent*	*absent*	(3)	(10)	CH_4 $8\nu_3$
5093	»	»	*present*	(20)	CH_4 $7\nu_3 + \nu_4$
5210	»	»	*absent*	(5)	CH_4 $6\nu_3$
5340	»	»	»	*present*	CH_4 $15\nu_4$
5376	»	»	»	»	CH_4 ?
5428	(5)	(10)	(50)	(100)	CH_4 $7\nu_3$
5571	*absent*	*absent*	*absent*	*present*	CH_4 $6\nu_3 + \nu_2$
5762	*present*	*present*	(25)	(50)	CH_4 $6\nu_3 + \nu_4$
5973	*absent*	*absent*	*present*	*present*	CH_4 $5\nu_3 + \nu_1$
6190	20	(50)	(100)	(150)	CH_4 $6\nu_3$
6407	*absent*	*absent*	*present*	*present*	CH_4
6427	»	»	»	»	H_2
6470	(5)	»	*absent*	*absent*	NH_3 $5\nu_1$, $4\nu_1 + \nu_2$
6498	—	—	»	*present*	CH_4
6561	—	—	»	»	CH_4 $5\nu_3 + \nu_2$
6613	—	—	»	»	CH_4 $2\nu_4$
6677	*present*	*present*	»	»	CH_4 $5\nu_3 + \nu_4$
6812	»	»	»	»	CH_4
7020	»	»	»	**	CH_4
7190	»	»	**	**	CH_4 $11\nu_4$
7260	»	»	**	**	CH_4 $4\nu_1 + \nu_2$, $3\nu_1 + 2\nu_3$
7500	*absent*	»	**	**	CH_4
7820	»	»	**	**	CH_4 $3\nu_1 + \nu_3 + \nu_4$, $2\nu_1 + \nu_2 + \nu_4$

* The estimates of equivalent width - except for λ 6190 Å which was taken from the work by V.G.Teyfel' and N.V.Priboyeva (Ref.438) - were tentatively derived from a visual examination of reproductions.

** Total absorption in the given spectrum region; individual bands cannot be isolated.

The above comments on the possible interpretation of phenomena observed on Jupiter are of an extremely tentative and approximate nature. If we are right in our appraisal of the role of internal energy sources in the general circulation of the Jovian atmosphere, then the apparatus for its theoretical descrip-

tion might be sought in the hydrodynamics of the sun rather than in terrestrial meteorology.

Section 5.3 Qualitative Chemical Analysis of the Jovian Atmosphere

The planetary absorption bands in the spectrum of Jupiter and other giant planets have been discovered with primitive methods of visual spectroscopy as far back as the 1870s (Secchi, Rutherford, Huggins and Miller, LeSueur). Early in the XX Century, the spectra of the giant planets already were photographically investigated with small and medium dispersion by Slipher, who found a large number of absorption bands in the visible region (Table 73). Some of these are common to all four planets, while others are present only in Jupiter's spectrum. Most bands gain in intensity on transition from Jupiter to Saturn and so on; /369 bands that are strong in the spectrum of Neptune often are extremely weak or even imperceptible in the spectrum of Jupiter (Fig.154).

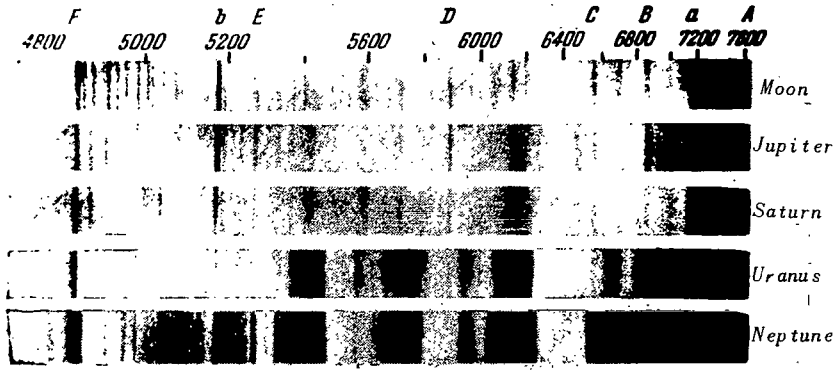

Fig.154 Spectra of Giant Planets and Moon in the Visible Region [according to Slipher (Ref.437)].

In 1931, Wildt (Ref.439) obtained the spectrum of Jupiter in the region λλ 7000-9000 Å with a lens prism and discovered three strong bands near λλ 7900, 8650, and 9000 Å. He identified two of these (the first and third) with NH_3. In addition, Wildt examined Slipher's list (reproduced in Table 73) and identified part of the bands with CH_4 and NH_3. The region λλ 8000-10,000 Å in the spectrum of Jupiter was independently investigated by Slipher with the aid of a slit-type spectrograph (Fig.155). Slipher found six bands (Table 74), all of which subsequently were identified with CH_4 and NH_3. The identification of bands in the spectra of the giant planets was the subject of many joint studies by Adel and Slipher (Ref.453, 454). Nearly all the bands pertain to CH_4 and NH_3; distinct NH_3 bands have been identified only for Jupiter; in the spectrum of Saturn the NH_3 bands are either nonexistent or extremely weak. Uranus and Neptune completely lack such bands. Conversely, CH_4 bands increase in strength on transition from Jupiter to the more distant members of the group of giant planets. The probable reason is that CH_4 condenses at lower temperatures than NH_3 (for NH_3, the equilibrium pressure of 3 mb occurs at T = 170°K; and for CH_4, at 70°K).

TABLE 74 /370

ABSORPTION BANDS IN THE SPECTRUM OF JUPITER (REGION 8000-10,000 Å), ACCORDING TO SLIPHER (REF.437)

λ, Å	Equivalent Width, Å	Identification	λ, Å	Equivalent Width, Å	Identification
7830	(10)	CH_4	8630	(50)	CH_4
7920	(10)	NH_3	8800	200	$CH_4 + NH_3$
8400	(5)	CH_4	10150	400	$CH_4 + NH_3$

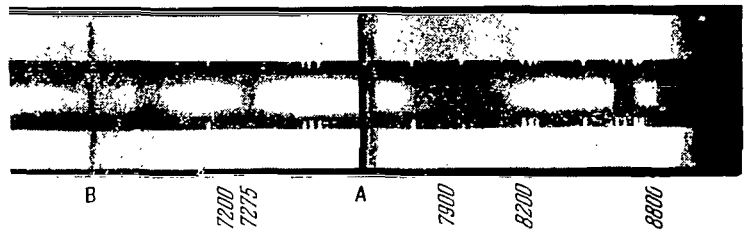

Fig.155 Spectrum of Jupiter in the Region λλ 8000-10,000 Å [according to Slipher (Ref.437)]. At the ends: spectrum of the sun. The emission lines represent laboratory calibration (spark discharge).

Both CH_4 and NH_3 show strong absorption bands in the region λλ 1 - 3 μ. In 1947, Kuiper (Ref.4, 440) derived spectra of Jupiter and Saturn up to 2 μ with the aid of a lead-sulfide varistor and a prism spectrometer of a resolving power $\frac{\lambda}{\Delta\lambda} = 80$. In fact, he discovered strong bands which he tentatively identified with CH_4 and NH_3. This identification was convincingly confirmed by Adel (Ref.441) who recorded the spectrum of sunlight passed through cells containing CH_4 and NH_3. As recently as in the 1960s the present author (Ref.442 and 443) and Kuiper (Ref.444) independently studied the spectrum of Jupiter in the region λλ 1 - 2.5 μ with the aid of diffraction spectrometers, achieving a resolving power of $\frac{\lambda}{\Delta\lambda} \approx 500$. The list of absorption bands discovered within this range is given in Table 75, and sample (discrete and averaged) traces of the spectrum are presented in Figs.156-159. In 1964, the spectrum of Jupiter in the region λλ 1 - 3 μ was recorded during a flight of the US balloon "Stratoscope II". The resolving power was low (the spectral width of the slit being /372 300 Å, i.e., $\frac{\lambda}{\Delta\lambda} \approx 60$ at λ 1.8 μ), but the absence of telluric absorption bands is a definite advantage (Fig.160). Debouille, Roland, and Gebbi (Ref.446) recorded the spectrum of Jupiter in the region λλ 1 - 2.5 μ using the method of

TABLE 75

/371

IDENTIFICATION OF PLANETARY ABSORPTION BANDS IN THE SPECTRUM OF JUPITER ($\lambda\lambda$ 0.97-2.5 μ)

Measured Wavelength, μ	Measured Equivalent Width, Å	Identification	Laboratory Wavelength, μ	Remarks
0.97—1.03	400	CH_4 $2\nu_1+\nu_2+\nu_3$, $\nu_1+\nu_2+2\nu_3$ NH_3 $3\nu_3$	0.98 1.028	Per equivalent width, NH_3 occupies not more than 20%
1.063	2	—	—	Extremely weak bands found on 1963 traces
1.085	2	—	—	Absent in (Ref. 444), possibly owing to inadequate signal-to-noise ratio
1.094	7	CH_4 $3\nu_3$, R (8)	1.095	Relatively free of telluric overlaps
1.12--1.18	800	CH_4 $\nu_1+2\nu_3$, $3\nu_3$	1.12	Overlapped by telluric band of H_2O λ 1.13 μ
		CH_4 $2\nu_1+\nu_3$ CH_4 $2\nu_3+2\nu_4$ CH_4 $2\nu_2+2\nu_4$ NH_3 $2\nu_3+\nu_4$	1.16 1.18 1.19 1.18	In the region $\lambda > 1.15\ \mu$, negligibly low intensity of NH_3
1.20	5?		—	Overlapped by the band 1.12-1.18 μ
1.23	25?	NH_3 $2\nu_1+\nu_4$ CH_4 H_2, $2-0(Q)$	1.23 1.23 1.23	Overlapped by the band 1.12-1.18 μ
1.26	10	NH_3 $2\nu_3+\nu_4$	1.258	Overlapped by the telluric band λ 1.28 μ
1.28—1.35	200	NH_3 $2\nu_1+\nu_3$ CH_4 $\nu_2+2\nu_3$	1.29 1.33	Overlapped by the telluric band λ 1.38 μ
1.45—1.49	250?	CH_4	1.47	Overlapped by the telluric band λ 1.38 μ
1.49—1.56	400	NH_3 $2\nu_1$, $2\nu_3$, $\nu_1+\nu_3$	1.52	Virtually free of telluric overlaps
1.54	10?	—	—	Overlapped by the band λ 1.49-1.56 μ
1.58	20	NH_3	1.58	Possible contribution by CO_2

/372

TABLE 75 (cont'd)

Measured Wavelength, μ	Measured Equivalent Width, Å	Identification	Laboratory Wavelength, μ	Remarks
1.60—1.80	Nearly total absorption	CH_4, $2\nu_2$	1.606	
		CH_4 $\nu_1 + \nu_2 + \nu_3$, $\nu_2 + \nu_3 + \nu_4$	1.72	
		NH_3 $\nu_2 + \nu_3 + \nu_4$	1.66	Low relative contribution by NH_3
1.9—2.5	Nearly total absorption	CH_4 $2\nu_2$	2.43	Substantial contribution by induced absorption of H_2 (band 0.1)
		CH_4 $\nu_2 + 2\nu_4$	2.40	
		CH_4 $\nu_1 + \nu_4$	2.37	
		CH_4 $\nu_3 + \nu_4$	2.32	
		CH_4 $\nu_2 + \nu_3$	2.20	
		NH_3 $\nu_3 + \nu_4$	1.98	
		NH_3 $\nu_2 + \nu_3$	2.26	
		NH_3 $\nu_1 + \nu_2$	2.33	
		NH_3 $\nu_2 + \nu_4$	2.38	

interference modulation, but their resolution was smaller than that obtained with diffraction spectrometers. The overall pattern of the spectrum of Jupiter in the region λλ 1.0-2.5 μ is well illustrated in Fig.156 which presents an averaged trace recorded at high speed (29 Å/sec) with a relatively wide slit (spectral width of the order of 200 Å). The region λλ 1.9-2.5 μ was recorded with an amplification factor 10 times as high as the region λλ 1.0-1.9 μ. The solar spectrum is recorded with a fixed amplification factor throughout the interval λλ 1.0-2.5 μ. Figure 156 indicates that the telluric bands in the region λλ 1.1-1.7 μ in the Jovian spectrum are markedly broadened by absorption of planetary origin, while the emission of the planet in the region λ > 1.6 μ is so weak that it was just barely recorded during the 1960 observations (Ref.442).

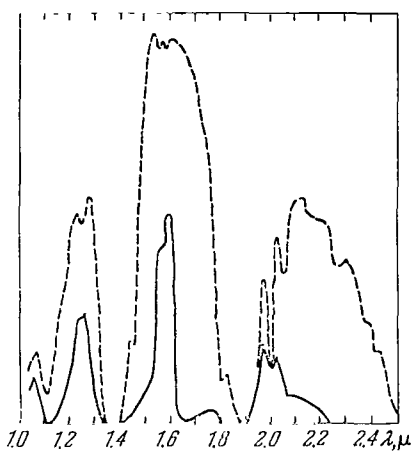

Fig.156 Spectrum of Jupiter in the Region λλ 1.0-2.5 μ. Averaged from four traces recorded on September 30, 1963, Ellis reflector, diffraction spectrometer, grating 300 rulings/mm, slits 2 and 5 mm (Δλ = 200 Å), recording speed 29 Å/sec, τ = 4.4 sec, z = 42 - 44°. Broken line - solar spectrum. In the region λλ 1.9-2.5 μ, the amplification factor in the recording of Jupiter is 10 times higher than in the region λλ 1.0-1.9 μ.

Figures 157 - 159 present more distinct traces recorded with a narrow slit (30 Å) and at low speeds (7.3, 3.7, 2.2 Å/sec). These show much greater detail. In Fig.161 the telluric bands are eliminated since the spectrogram shows the ratio of the intensity /373 in the Jovian spectrum to the intensity in the solar spectrum. In the photographic region, the spectrum of Jupiter contains a large number of CH_4 and NH_3 lines. In the region λ > 1 μ, CH_4 and

NH_3 give strong absorption bands. The spectrograms present positions of these bands according to Herzberg (Ref.10). They roughly correspond to the observed planetary bands in the spectrum of Jupiter. Direct recordings of laboratory spectra of CH_4 and NH_3 (Ref.441, 444, 447 - 450) confirm this correspondence. Examples of laboratory traces (Ref.444) are given in Fig.162; the resolution roughly corresponds to the spectra of Jupiter in Figs.157 - 159 and 161. A detailed comparison convincingly shows that nearly all absorption bands in the region λλ 0.9-1.6 μ in the Jovian spectrum, both strong and weak, are identifiable with CH_4 and NH_3 (Table 75). It is suspected that, in some cases, the absorption of other atmospheric constituents is superimposed on the CH_4 and NH_3 bands. For example, in the region λλ 2-2.5 μ as well as near λ 1.23 μ, induced dipole absorption of H_2 (see below) must be a factor. The NH_3 band at λ 1.58 μ may be intensified by CO_2, but there is no proof for this supposition.

/374

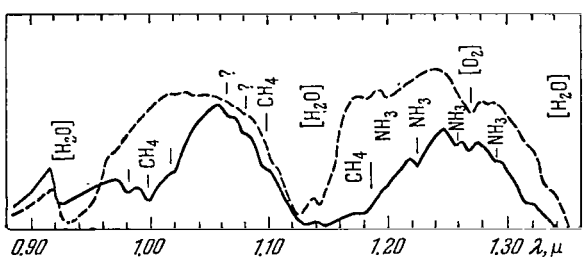

Fig.157 Spectrum of Jupiter in the Region λλ 0.90-1.30 μ. Averaged from six traces recorded on October 7, 1963, Ellis reflector, diffraction spectrometer, replica 600 rulings/mm, slits 1.5 mm (Δλ = = 30 Å), recording speed 7.3 Å/sec, τ = 4.4 sec, z = 40 - 43°. Broken line - solar spectrum.

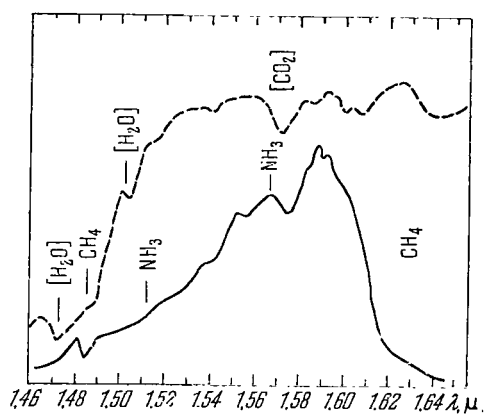

Fig.158 Spectrum of Jupiter in the Region λλ 1.45-1.65 μ. Averaged from 6 traces taken on October 1, 1963, Ellis reflector, diffraction spectrometer, grating 300 rulings/mm, slits 1 mm (Δλ = = 40 Å), recording speed 3.7 Å/sec, τ = 4.4 sec, z = 41 - 44°. Broken line - solar spectrum.

Sagan (Ref.451), in his investigation of laboratory models of the atmospheres of the giant planets, arrived at the conclusion that these may contain a considerable amount of vapors of hydrocyanic acid HCN. In his opinion, the weak unidentified absorption at λ 1.54 μ may pertain to HCN.

Along with the advances made in the relatively far infrared, observations of Jupiter have recently been undertaken, with high dispersion and high resolving power in the visible and photographic infrared spectrum regions. Such /376
spectra had first been obtained as far back as the 1930s by Dunham who used a spectrograph in the 100"-Coudé focus of the Mount Wilson reflector (Ref.111). Dunham's high-dispersion observations confirmed the identification of certain previously known bands as CH_4 and NH_3, but the results were not published in

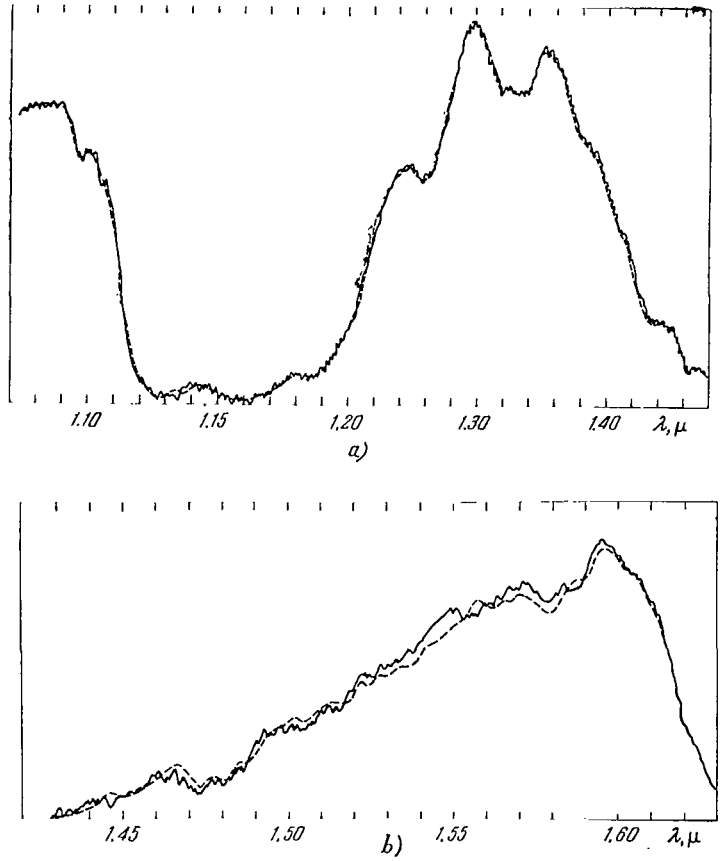

Fig.159 Spectrum of Jupiter from Observations on September 19, 1964.
a - In the region λλ 1.08-1.34 μ; b - In the region λλ 1.42-1.63 μ. Solid line - discrete trace, broken line - mean of several traces (four in the region λλ 1.1-1.3 μ; six in the region λλ 1.4-1.6 μ). Ellis reflector, grating 600 rulings/mm, slits 2.2 and 2.5 mm ($\Delta\lambda \approx 40$ Å), recording speed 2.2 Å/sec, τ = = 4.4 sec, z = 28 - 40°.

detail. For a long time, this particular study remained the only one in existence until finally, as late as toward the end of the 1950s, Kiess, Corliss, and Kiess (Ref.452) obtained a series of spectrograms of Jupiter with a dispersion from 2 to 5 Å, using a collimating lens of extremely modest dimensions and a concave-grating spectrograph. These authors made detailed comparisons of various bands in the Jovian spectrum, with the laboratory spectra of CH_4 and NH_3 in the interval 6200 - 8000 Å and arrived at a new and exceptionally important result: They found quadrupole lines of the 3 - 0 band of molecular hydrogen (Table 76).

The low mean density of Jupiter and the indisputably relict, primeval /378 character of its atmosphere have long furnished a justification for many authors

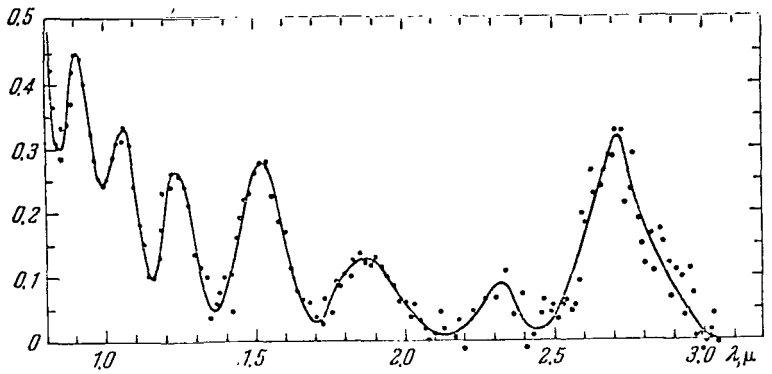

Fig.160 Spectrum of Jupiter Recorded with Balloon-Borne Telescope, Project "Stratoscope II" (Ref.445).

TABLE 76

QUADRUPOLE LINES OF THE (3,0) H_2 BAND IN THE SPECTRUM OF JUPITER (REF.452)

Notation	Laboratory Wavelengths, Å	Wavelengths in Jovian Spectrum
(3, 0) Q (1)	8497.49	8497.52
(3, 0) S (0)	8272.69	8272.60
(3, 0) S (1)	8150.68	8150.66
(3, 0) S (2)	8046.44	8046.44

to defend the hypothesis of a substantial amount of hydrogen and helium on Jupiter. Baum and Code (Ref.68) plotted the curve of attenuation of σ Arietis during the occultation of that star by the Jovian disk and derived from it the scale height

$$H = 8.3^{14.2}_{2.1}\ km. \qquad (5.1)$$

The limits given above are extreme, and the probable error appears to be smaller. This quantity pertains to comparatively high altitudes ($P < 10^{-3}$ mb). Following Kuiper (Ref.307), Baum and Code assumed $T = 86^{\circ}K$ for Jupiter's atmosphere whence the mean molecular weight of the atmosphere would be $\mu = 3.3 \pm 1.1$. Thus, the hypothesis of the considerable content of the light gases in the Jovian atmosphere has been observationally confirmed. It would be extremely important, however, to further substantiate this confirmation with spectroscopic observations. Long ago, Herzberg mentioned the fundamental possibility of utilizing quadrupole lines as a means of detecting molecular hydrogen in the atmosphere of the giant planets [cf. (Ref.4)] and this was ultimately accomplished in the study by Kiess, Corliss, and Kiess. Spinrad and Trafton (Ref.455) measured the equivalent widths of the lines S(1) and S(0) shown in Table 77 and found yet another H_2 line belonging to the (4-0) band, namely S(1) λ 6367.80 Å. Its

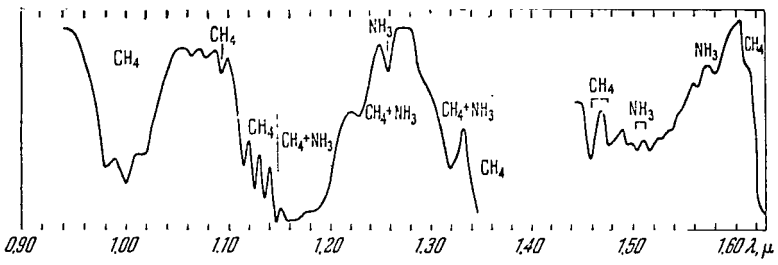

Fig.161 Ratio of Spectral Intensities for Jupiter and Sun from Traces Recorded with Grating and Replica 600 Rulings/mm.

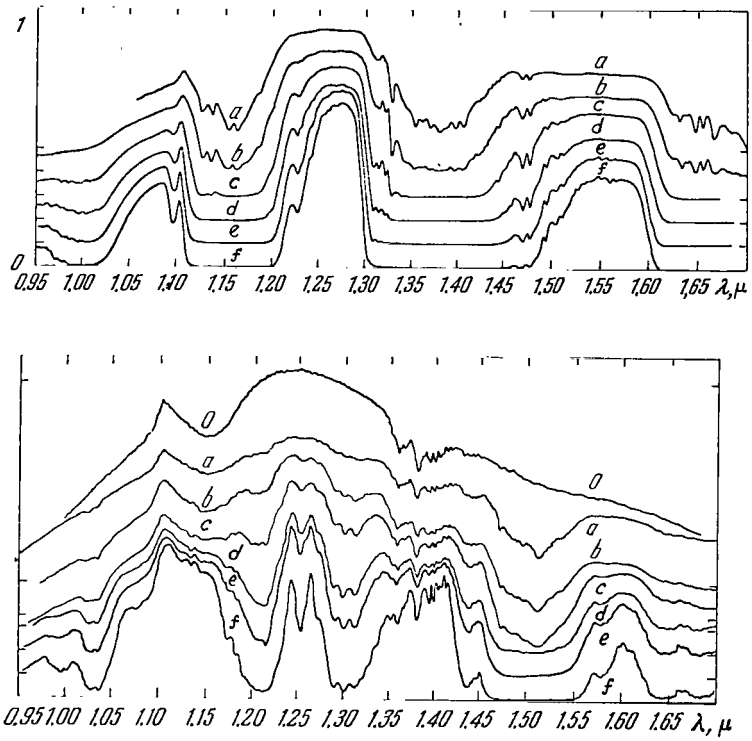

Fig.162 Laboratory Spectra of CH_4 and NH_3 in the Region λλ 0.95-1.70 μ.
Top: CH_4, equivalent path 80 m and pressures of (a) 10 mm Hg; (b) 28 cm Hg; (c) 1.0 atm; (d) 2.0 atm; (e) 3.4 atm; (f) 5.0 atm.
Bottom: NH_3, reduced thickness of 0.5 (a), 1.0 (b), 2.5 (c), 5 (d), 10 (e) and 20 m · atm (f), (0) - free cell.

equivalent width is 8 ± 2 Å. The line S(1) (4-0) is weaker, but on the other hand it is free of overlap by the telluric absorptions which complicate an exact determination of the line intensity of the band (3-0).

TABLE 77

EQUIVALENT WIDTHS OF THE LINES S(1) AND S(0) OF THE BAND (3-0) H_2 (in m Å) (REF.455)

Object	S (1)	S (0)	Remarks
Laboratory (45 km.atm)	14	—	Temperature T = 300°K
Jupiter (1957)	80	40	Zabriskie's measurements from the plates of Kiess, Corliss, and Kiess
Jupiter (1962)	40	31	Central meridian
Jupiter (1962)	28	—	Equator

Quadrupole lines are very weak and their detection under laboratory conditions requires paths attaining several tens of kilometers in length. Obviously, the presence of quadrupole lines of H_2 in the spectrum of Jupiter is possible /379 only if the molecular hydrogen is the basic, or one of the basic, constituents of the atmosphere. However, the quantitative estimates differ substantially. Thus Zabriskie (Ref.456) estimated the equivalent path of H_2 in Jupiter's atmosphere as approximately 5 km • atm, whereas Spinrad and Trafton, on the basis of 1962 observations, estimated it as 27 ± 9 km • atm. These estimates were derived from lines of the band (3-0). The value derived by Spinrad and Trafton seems reliable, since it was derived empirically by comparison with laboratory spectrograms (mean air mass for Jupiter was taken as M = 4); Zabriskie, on the other hand, proceeded from theoretical values of intensity. Foltz and Rank (Ref.457) found that detection of the line S(1) (4-0) requires an amount of hydrogen one order of magnitude greater than that specified by Spinrad and Trafton, but Foltz and Rank based their conclusion on theoretical relative intensities of (4-0) and (3-0). Note that the presence of the line S(1) (4-0) was confirmed by Herbig [cf. (Ref.247)]. The study by Rank, Fink, Foltz, and Wiggins (Ref.247) gives the integral absorption coefficient for the line S(1) of the band (3-0). They obtained 1.1×10^{-3} cm^{-1}/atm • km. According to Table 77, the mean equivalent width of S(1), as measured by Spinrad and Trafton, is 50 ± 15 mÅ or $(7.5 \pm 2.5) \cdot 10^{-2}$ cm^{-1}, whence the equivalent path in the atmosphere of Jupiter will be

$$l \approx \frac{(7.5 \pm 2.5)\,10^{-2}}{4 \times 1.1 \times 10^{-3}} = 17 \pm 6 \ km \cdot atm \qquad (5.2)$$

which, within the error limit, is in agreement with the estimate by Spinrad and Trafton.

According to Rank et al. (Ref.247), the anticipated intensity ratio under

laboratory conditions is

$$t_{lab} = \frac{I(3-0)}{I(4-0)} = 15, \tag{5.3}$$

whereas observations on Jupiter give

$$t_{obs} = \frac{I(3-0)}{I(4-0)} = 4^{+5}_{-2}, \tag{5.4}$$

i.e., the amount of H_2 derived from the line S(1) (4-0) is four times as high as the amount derived from S(1) (3-0). Considering that the air-mass estimate adopted by Spinrad and Trafton apparently is somewhat exaggerated, we derive from this line S(1) (4-0) an equivalent path of ~ 90 km • atm with an indeterminacy of the order of 2. In the calculations, the mean air mass M was taken as 3. The discrepancy between eqs.(5.3) and (5.4) is not as large as had been found in the early study by Foltz and Rank (Ref.457) but still remains fairly substantial. This contradiction may be due to one of the following factors /380 (or to both): 1) The line S(1) (3-0) in the spectrum of Jupiter comes close to saturation, in which case the estimate of approximately 90 km • atm, derived from the line S(1) (4-0), is closer to reality; 2) the lines form in the cloud layer during multiple scattering on aerosols. The latter factor seems more likely. In Section 3.4 it was shown that, in the presence of multiple scattering, the following relation must apply to weak lines

$$t_{obs} \backsim t^{1/2}_{lab}, \tag{5.5}$$

if absorption in the line greatly exceeds true absorption in a continuous spectrum.

According to Kuiper (Ref.4), the equivalent path of CH_4 in the atmosphere of Jupiter is 150 m • atm and that of NH_3, 7 m • atm. These estimates were derived from the relatively weak bands in the visible spectrum region. Earlier (Ref.442, 443), we derived much lower values of the equivalent path of NH_3 than did Kuiper, namely ~ 1 m • atm. The reasons for this discrepancy will be discussed below. All above estimates of the content of various molecules should not be literally construed as referring to values of reduced thickness, as done occasionally. The term "equivalent path" was used here (as earlier) solely with respect to the amount of gas which, under normal conditions, gives the same absorption as the observed absorption. A determination of the real values of reduced thickness of various gases in the atmosphere of Jupiter would require making an allowance for the role of scattering in the formation of the lines, as well as for the pressure and temperature effects. It should be noted that the relative line intensities in the CH_4 and NH_3 bands in the Jovian spectrum differ from their laboratory counterparts owing to the lower temperature of the former (Ref.111, 452, 455).

Recently, Owen made a detailed analysis of high-dispersion spectrograms of Jupiter with the object of detecting any previously unknown lines. He published his results only with respect to the region λλ 7800-11,200 Å (Ref.458, 459). In addition, Owen, Richardson, and Spinrad described a new NH_3 band near λ 7650 Å (Ref.460). The equivalent path for the weakest lines of this band is markedly

greater than 7 m • atm. In the interval 9000 - 11,200 Å, no fundamentally new identification could be made but, from a comparison with the laboratory spectra of a number of compounds recorded with a similar dispersion, Owen derived the upper limits of their quantitative abundance in the atmosphere of Jupiter. The values of these upper limits are given in Table 78. To this must be added the upper limit of the abundance of CO_2 (1 m • atm) derived earlier (Ref.443).

TABLE 78 /381

UPPER LIMITS OF ABUNDANCE OF CERTAIN GASES IN JUPITER'S ATMOSPHERE (REF.460)

Gas	Band, Å	Upper Limit of Equivalent Path*, in m•atm	Gas	Band, Å	Upper Limit of Equivalent Path*, in m•atm
C_2H_2	10372	3	CH_3D	9936	20
C_2H_4	8715	2	HCN	10385	2
C_2H_6	9060	4	SiH_4	9738	20
CH_3NH_2	10325	3	HD	7377,7464	500

* Assuming that $\bar{M} = 3$.

Kiess, Corliss, and Kiess (Ref.452) assumed that the decrease in the albedo of Jupiter with decreasing wavelength in the blue portion of the spectrum may be attributed to the presence of NO_2. Peek (Ref.415) and certain other authors suggested solid particles of NO_2 as the agent responsible for the red color of the bands. It is doubtful whether nitrogen dioxide actually exists in the Jovian atmosphere. In the region λ 2700 Å, Bogges and Dunkelman (Ref.110) found, on the basis of rocket observations, that Jupiter's albedo is 0.26, which would indicate extremely strong NO_2 absorption. Recent spectroscopic observations by Stecher (Ref.484) confirmed the comparatively high albedo of Jupiter in the far ultraviolet. Moreover, the decrease in albedo with wavelength in the near ultraviolet actually is much slower than had been derived by Kiess, Corliss, and Kiess [cf. (Ref.234)].

When the slit of the spectrograph is set parallel to the equator, the spectral lines on the limb are shifted in various directions owing to the Doppler effect induced by rotation of the planet. As a result, the lines start slanting, and their angle of slant can be used to measure the rotational velocity. As is readily ascertained, the angle of slant of the lines forming in the atmosphere of the outer planets must be half as wide as the angle of slant of Fraunhofer lines if absorbing gases rotate at the same velocity as scattering clouds. Spinrad and Trafton (Ref.455) found that the inclination of the NH_3 lines is smaller than expected, which formally may be attributed to the slower rotation of NH_3 masses compared with the rotation of the clouds; the difference in rotational velocities must attain 4 km/sec. Considering that the clouds appear to consist largely of condensed NH_3 (see below), this seems highly surprising. Other authors [cf. (Ref.461)] who, following the publication of the study by Spinrad

and Trafton, attempted to detect the phenomenon of anomalous inclination, were unsuccessful. It may be that this phenomenon is of a labile nature, but it /382
is more likely that Spinrad and Trafton's conclusion (Ref.455) concerning the presence of anomalous inclination was due to some overlooked instrument errors. Note that the widths of NH_3 lines greatly exceed the widths of Fraunhofer and CH_4 lines.

Section 5.4 Quantitative Interpretation of the Spectra of Jupiter (Chemical Composition and Pressure)

a) Variations in intensity from center to limb. The simplest model from the viewpoint of quantitative analysis is the direct-reflection model: The cloud layer has a sharp boundary which is optically equivalent to a solid surface above which lies the "supracloud" atmosphere. Applying the same techniques of analysis as those in Chapter II for Mars, this model can be used for determining, from the unsaturated lines, the amount of absorbing gases above the cloud layer and, from the saturated lines, the mathematical product of this amount and the total pressure at the cloud top. For Venus, this model obviously does not fit the actual physical picture: The phase course of the intensity of CO_2 bands in the Venusian spectrum cannot be matched with the direct-reflection model.

The phase angle of Jupiter varies only within narrow limits so that it is impossible to use the phase course of the intensity of absorption bands as a criterion for applicability of the model. Conversely, in view of the considerable angular dimensions of the disk, variations in intensity from center to limb may be used as such a criterion.

The intensity distribution of CH_4 and NH_3 bands over the disk has been investigated by various authors. A survey of early studies (Elvey and Farley, Yeropkin, Bobrovnikov, Slipher) is given in the paper by Hess (Ref.462). All of these investigators mentioned the absence of variations in the intensity of CH_4 bands; as regards the NH_3 bands, the conclusions were somewhat contradictory. Hess himself found that the CH_4 bands λ 6190 Å and λ 6490 Å become somewhat weaker toward the limb in the equatorial region and markedly stronger on transition from the equatorial to the temperate and polar regions; the intensity variations along the equator as derived by Hess also do not exceed the error limit, and although Hess himself considered them real, we can hardly agree with him. V.G.Teyfel' (Ref.463), in his study of spectra with lower dispersion (143 Å/mm at H_γ) but greater in number than those investigated by Hess, found no marked variations in the band λ 6190 Å along the equator. The meridional distribution was slightly nonuniform but less so than found by Hess. Apparently, the intensity of the CH_4 band λ 6190 Å on the equator does not vary over a distance of 0.9 R_o (where R_o is the apparent radius) from the center of the disk. This discrepancy can be conclusively settled only with methods of photoelectric spec- /383
trophotometry which are able to greatly increase the accuracy of the results. Münch and Younkin (Ref.464), using a photoelectric spectrometer, found that the intensity of the band λ 6190 Å actually decreases somewhat along the equator from the center toward the limb, but they gave no numerical estimates in their preliminary report. According to Hess, this variation lies within the limits of 5% over a distance of 60° Long. from the center. A similar result (slight decrease in intensity toward the limb) was obtained for the bands λ 6450 Å and

λ 7900 Å. In the direct-reflection model, the intensity at a distance of 60° should be twice as high as at the center for the case of unsaturated lines, and $\sqrt{2}$ times as high for the case of saturated lines. The lines of the quadrupole band (3-0) H_2 display no variations with longitude or latitude. The strong CH_4 band 8900 Å markedly increases in intensity with latitude but its intensity decreases again near the poles, and bright polar caps are observed on Jupiter for this wavelength. V.G.Teyfel' (Ref.465) independently found that the intensity of the bands λλ 7250, 8860, and 9900 Å increases in the temperate latitudes (Fig.163). The increase in band intensity may be due to the decrease /384 in altitude of the cloud top on transition to higher latitudes. (This, however, does not account for the anomalous polarization; see above.) The "polar caps" probably represent high-altitude clouds which may consist of frozen methane. Münch and Younkin found that the CH_4 and NH_3 absorption bands are stronger in the zones than in the belts - a result that could not be obtained with methods of photographic spectrophotometry.

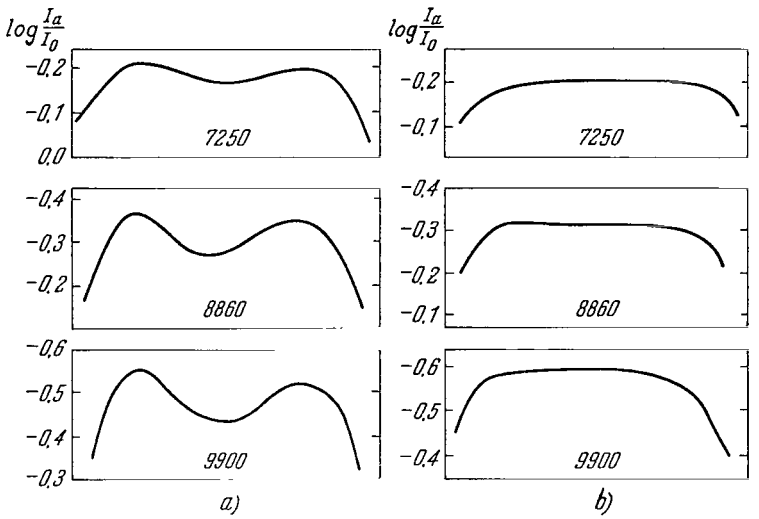

Fig.163 Variation in Intensity of the Bands λλ 7250, 8860, and 9900 Å along the Central Meridian (a) and Equator (b) of Jupiter (Ref.465).
I_a - Intensity of absorption band at center; I_o - Intensity of continuous spectrum.

Other authors (Ref.464) assumed that the absence of variations in H_2 lines over the disk is due to saturation of these lines. That is a doubtful assumption. Individual CH_4 lines in strong bands display equivalent widths that are many times greater than those of H_2 lines; there is no doubt that they are saturated, and yet these bands exhibit marked variations. Apparently, the negligible dependence on position on the disk is a characteristic feature of all weak lines and has to do with the conditions of their formation. Concerning the H_2 lines, it must be particularly emphasized that the accuracy of measurement of intensities of these lines in the work by Münch and Younkin could not be high considering that their observations, as reported, were carried out with a resolution of 10 Å.

It is obvious that only the variations in intensity along the equator are a suitable tool for analyzing the conditions of line formation on the basis of the center-to-limb effect. Meridional variations are at least partially due to latitudinal differences, whereas on the equator similar effects appear to be absent. On the equator, as we have seen, center-to-limb variations are either completely absent or just barely discernible, a result which cannot fit the elementary hypothesis of a dense cloud layer with a smooth and sharp boundary located at a constant altitude. Three hypotheses have been proposed to account for the insignificant extent of center-to-limb variations:

1) Hess (Ref.462): The altitude of the cloud layer increases from the subsolar point (which virtually coincides with the center) toward the limb of the disk owing to variations in temperature; the greatest evaporation rate exists at the center and it is there that the cloud top lies lowest.

2) Squires (Ref.472): The cloud top has an intricate relief such that the atmosphere is more transparent at the center of the disk.

3) Sharonov (Ref.3): The lines form within the cloud layer at multiple scattering and, since the albedo of the individual scattering event in a line is higher, limb darkening within the line is smoother than within a continuous spectrum (cf. Fig.36). Then the equivalent width must decrease with approach to the limb. If part of the absorbing gas is located above the cloud, then, depending on the extent of its contribution, we may either have a center-to-limb or a limb-to-center effect. This explanation is also supported by Teyfel' (Ref.465).

The hypothesis of multiple scattering seems most logical, but the two /385
other hypotheses also do not meet with serious objections. Squires criticized Hess' hypothesis on the grounds that it requires an excessively low density of the disperse phase. Within the several hours that elapse between sunrise and noon on Jupiter, the altitude of the cloud layer, according to this hypothesis, would have to vary by about 10 km (somewhat less than the scale height). During that period 10^{-3} gm $\cdot$ cm^{-2} NH_3 may evaporate so that the density of the disperse phase must be 10^{-9} gm $\cdot$ cm^{-3}. Such a density is two orders of magnitude lower than in terrestrial clouds (10^{-7} gm $\cdot$ cm^{-3}). It is on this basis that Squires rejects Hess' hypothesis. As will be shown below, the multiple-scattering model does give a relatively low density of the disperse phase. Hence, when using this model as basis, the possible influence of variations in the altitude of the cloud layer must be borne in mind. V.G.Teyfel' and N.V.Priboyeva discovered fairly extensive variations in the equivalent width of the CH_4 band 6190 Å at the center of the disk, from one night to another, sometimes reaching 15% (Ref.438).

Thus the center-to-limb effect is not a conclusive criterion for deciding between the various models and hypotheses. The hypotheses of Hess and Squires merely represent modifications of the direct-reflection model and, in calculations to a first approximation, make it possible to employ all the mathematical apparatus inherent in this model. Owen (Ref.459), arguing in favor of the direct-reflection model, mentioned that the agreement between the theoretical and observed intensity distribution in the methane band $3\nu_3$ 11,057 Å will merely deteriorate with transition to the multiple-scattering model.

Below we shall consider the problem of quantitative chemical analysis of the Jovian atmosphere for both models (direct reflection and multiple scattering). However, first we will discuss the estimates of total pressure in the Jovian atmosphere according to line width.

b) Line widths in the spectrum of Jupiter. The width of absorption lines is the most direct source of information on pressures in planetary atmospheres, but its measurement is a difficult experimental problem. It should be noted that the line width is not greatly influenced by the particular model selected, whether this is the multiple-scattering or the direct-reflection model. Given a sufficiently strong true absorption in the continuous spectrum, the widths of weak lines coincide for both models whereas in the absence of such absorption these widths differ by a factor of $\sqrt{3}$ (cf. Sect.3.4). Unfortunately, the observational material is extremely limited; only Spinrad and Trafton (Ref.455) gave estimates of the widths of CH_4 and NH_3 lines in the spectrum of Jupiter. For the lines of the CH_4 band λ 6190 Å, Spinrad and Trafton specified the upper limit of the half-width as $\Delta\lambda \leq 0.03$ Å or $\Delta\tilde{\nu} \leq 0.08$ cm^{-1}. Assuming, in accordance with Table 9, that /386

$$\alpha_{CH_4-H_2} = 0.1\ cm^{-1},$$

and also that

$$T = 170^\circ\,\mathrm{K}$$

(cf. Sect.5.5), then eqs.(1.46) and (1.72) yield the upper limit of pressure at the "surface" of the cloud layer:

$$P_1 \leqslant \frac{2\Delta\tilde{\nu}}{\alpha}\left(\frac{T}{300}\right)^{1/2} = 1.3\ atm. \qquad (5.6)$$

If an appreciable proportion of helium is present, this value may be increased, since $\alpha_{CH_4-He} \approx 0.06$ cm^{-1}. However, in the direct-reflection model, we apparently may assume $P_1 < 2$ atm. Spinrad and Trafton derived a somewhat higher value ($P_1 < 2.8$ atm) for that model, since they assumed lower values of α and T (0.04 cm^{-1} and 150°K, respectively).

The half-widths of NH_3 lines in the Jovian spectrum are much greater. Spinrad and Trafton measured a large number of lines in the band λ 6450 Å. The scatter of the values was wide, but on the whole the measurements give 0.43 cm^{-1} with an error of roughly ±0.1 cm^{-1}. According to Table 9 and eq.(5.6) we thus have $P_1 = 4$ atm, but, owing to condensation, the scale height for NH_3 should be greatly below average, which means that the coefficient of 2 in eq.(5.6) is excessive and $P_1 = 2$ atm is obtained for the direct-reflection model. Of course, this estimate does not allow for the possible distortion of the profiles of NH_3 lines in the band λ 6450 Å due to inversional doubling. In one way or another, the quantity

$$P_1 = 3\ atm \qquad (5.7)$$

is the upper limit of pressure at some effective level of formation of the CH_4 and NH_3 lines, irrespective of whether direct reflection or multiple scattering

is assumed. In the direct-reflection model, such a pressure pertains to the "surface" of the cloud layer, whereas in the multiple-scattering model it refers to deeper strata of this layer.

c) Quantitative analysis in the direct-reflection model. In this model, the intensity of unsaturated lines that arise due to absorption from the ground level is independent of temperature, pressure, and extraneous impurities. It is directly proportional to the quantity of the absorbing substance, and estimates of equivalent width derived from these lines may be regarded as values of reduced thickness. It is obvious that the weakest lines must be utilized, since the accuracy of such estimates increases with increasing distance from saturation. Accordingly, the line S(1) of the band (4-0) H_2 must be preferred over /387 the lines of the band (3-0); seen from the viewpoint of this model, the discrepancy between their relative and theoretical intensities can be explained only by saturation. Thus, the reduced thickness of H_2 may be taken as

$$u_{H_2} = 9 \times 10^6 \ cm \cdot atm = 800 \ gm \cdot cm^{-2}.$$

In Section 5.3, we calculated this quantity as the equivalent path for the line S(1) of the band (4-0) according to observations by Spinrad and Trafton, making use of the absorption coefficient given by Rank et al (Ref.247). If hydrogen is the main constituent of the atmosphere and the temperature of the cloud layer is 170°K (cf. Sects.5.5 and 5.6) then the height scale will be

$$H = \frac{kT}{mg} = \frac{1.38 \times 10^{-16} \times 170}{1.67 \times 10^{-24} \times 2 \times 2500} = 28 \ km \qquad (5.8)$$

and the pressure,

$$P = nkT = ug = 2 \ atm, \qquad (5.9)$$

which is in good agreement with the estimate (5.7). However, a pure hydrogen atmosphere hardly fits the conclusions derived from the occultation of σ Arietis, discussed in Section 5.3. To have the results agree, the temperature at the level of occultation must be assumed as $T \approx 50°K$, which is too low. Öpik (Ref.466) in examining (incorrectly, by the way; cf. Sect.5.5) the question of temperature at the occultation level, derived $T = 112°K$, from which he found $\mu = 4.3 \pm 0.5$ based on the scale height calculated by Baum and Code from observations of the occultation. Öpik assumed that the atmosphere of Jupiter consists almost entirely of helium. Since, at that time, quadrupole lines of H_2 had already been discovered, such an assumption implied extremely high pressures at the surface, even when using the then only known and excessively low Zabriskie estimate of the amount of H_2 (5 km • atm). According to Öpik, the ratio of content of He to H_2 is

$$He : H_2 \approx 50.$$

If, as Öpik assumed in accordance with Zabriskie, u_{H_2} = 5 km • atm, then the total pressure will be ≈ 10 atm, which already is too high [see paragraph b) of this Section]. However, present-day estimates of the amount of H_2 are 20 times as high implying a pressure of 200 atm, which definitely is unlikely. Assuming 3 atm as the upper limit of pressure [see paragraph b)], the proportion of helium will be fairly insignificant. Spinrad and Trafton assumed a ratio of

$$He : H_2 = 0.6 \qquad (5.10)$$

according to the number of molecules. This gives a scale height of 19 km and /388 partial pressures of

$$P_{H_2} = 3.2 \ atm, \quad P_{He} = 1.9 \ atm .$$

Then the total pressure would be 5 atm which is still too high, and eq.(5.10) may be regarded as a firm upper limit of the relative content of He. The lower limit may be the mean cosmic propagation ratio He/(He + H) = 0.15. Taking into account the molecular state of hydrogen, this gives

$$He : H_2 = 0.36. \qquad (5.11)$$

Some additional information on the H_2 content on Jupiter can be derived from an analysis of its spectrum in the region λλ 2-2.5 μ. In addition to the narrow quadrupole lines of H_2 it can be expected that the Jovian spectrum will contain extremely broad (several hundred Å) lines induced by pressure at the fundamental vibrational frequency (region λλ 2-2.5 μ) and at the first-harmonic frequency (1.1-1.2 μ). Unfortunately, both these regions show considerable overlap by absorption of other gases, but some useful estimates are still possible. Near λ 1.97 μ, the CH_4 and NH_3 absorption is small compared with the adjoining regions. According to Fig.156 the residual intensity here is 5%. If the total absorption near λ 1.97 μ is ascribed to the fundamental pressure-induced vibrational-rotational band of H_2, then the upper limit of the amount of H_2 can be estimated. According to other authors (Ref.467, 468), the coefficients of induced absorption at T = 300°K for this wavelength amount to s = 7 × × 10^{-7} cm^{-1} • $amagat^{-2}$ (H_2 - H_2) and 3 × 10^{-7} cm^{-1} • $amagat^{-2}$ (H_2 - He). Here, the amagat is a density unit corresponding to normal conditions. Thus, 1 amagat = 2.69 × 10^{19} molecules • cm^{-3}. Induced absorption is proportional to the square of pressure. The wavelength 1.97 μ corresponds to the lines S(3), whose intensity in a pure rotational spectrum decreases by a factor of 6 - 7 on cooling to 85°K (Ref.468). Hence, for Jupiter we assumed lower values of the absorption coefficient: 3 × 10^{-7} cm^{-1} • $amagat^{-2}$ and 1.2 × 10^{-7} cm^{-1} • $amagat^{-2}$. In reality, these values are probably somewhat higher. The optical thickness of the isothermal atmosphere for a quadratic density dependence of the absorption coefficient, as readily ascertained, is equal to

$$\tau = \frac{1}{2y} s n_1^2 H \overline{M}, \qquad (5.12)$$

where s is the absorption coefficient; n_1 is the density of H_2 at the base of /389 the atmosphere; H is the scale height; $\overline{M}$ is the mean air mass.

$$y = \frac{n(H_2)}{n(H_2) + n(He)}.$$

Assuming that $\overline{M}$ = 2 (the observations pertain to the central portion of the disk), we calculated τ along the line of sight for several values of $u_{H_2} = n_1 H$ and y. These are given in Table 79. The column y = 0.7 corresponds to the cosmic abundance of H and He.

The residual intensity of 5% is equivalent to τ = 3. In view of possible

errors in the estimation of the absorption coefficient and τ [note that Debouille et al. (Ref.446) give an even lower value of τ, namely about 1.5], it may be assumed that

$$\left.\begin{aligned} 10 < u_{H_2} < 45\ km \cdot atm, \quad if \quad y \geqslant 0.7, \\ 5 < u_{H_2} < 22\ km \cdot atm, \quad if \quad y = 0.5. \end{aligned}\right\} \tag{5.13}$$

Any lower values of relative concentration are precluded, since they would give too high a value of optical thickness. Note again that, by ascribing the total observed absorption to molecular hydrogen, the upper limit of its content can be determined. Obviously, the discrepancy between estimates based on induced absorption and on quadrupole absorption cannot be eliminated even at y = 1, but it has its minimum at such values of y. In the Jovian spectrum, induced absorption in the region of the Q-branch of the first harmonic [cf. Ref.468, 470)] must amount to 5 - 10% near λ 1.23 μ, and the contribution of H_2 to the intensity of the planet band observed at this wavelength may be quite substantial.

TABLE 79

OPTICAL THICKNESS OF HYDROGEN IN INDUCED DIPOLE ABSORPTION, λ 1.97 μ

u_{H_2}, km·atm	$y = n(H_2)/[n(H_2) + n(He)]$				
	1	0,7	0,5	0,1	0,02
135	16	23	32	120	420
90	10	14	20	80	280
45	5	7	11	40	140
22.5	2.6	3.8	5.5	20	70
11	1.3	1.8	2.7	10	35

Let us now analyze the lesser constituents of Jupiter's atmosphere, /390 namely, CH_4 and NH_3. Despite the numerous studies made on the Jovian spectrum, the literature contains practically no data on the equivalent paths of these gases other than the already mentioned estimates by Kuiper: 150 m · atm and 7 m · atm, respectively. It is not known from which lines - strong or weak, saturated or unsaturated - these estimates were derived. Consequently, it is only logical for us to attempt to extract additional information on the CH_4 and NH_3 content from photoelectric traces of the Jovian spectrum in the region $\lambda\lambda$ 1-2.5 μ. These traces record only the envelopes of the absorption bands; the rotational lines are not resolved, but the total equivalent band widths can be measured with sufficient accuracy.

On comparing the intensities of the bands observed in the spectrum of Jupiter with their laboratory counterparts, it is of importance to consider primarily the effect of temperature as well as the influence of extraneous gases. For bands formed due to absorption from the ground level, two temperature effects are essential: the temperature dependence of the Lorentz half-width

$$\Delta\nu_c \sim T^{-1/2},$$

and the temperature dependence of the population of the rotational levels. The effect of extraneous gases is determined by the dependence of the Lorentz half-width on the effective collision cross sections. Let us first consider CH_4. The half-width for CH_4 - CH_4 collisions is 1.4 times as large as for CH_4 - N_2 collisions (see Table 9). For CH_4 - H_2 and CH_4 - N_2 collisions the damping constant is roughly the same, whereas for CH_4 - He collisions it is lower (0.6 $\alpha_{CH_4-N_2}$, according to Table 9). Assuming that hydrogen and helium are the principal constituents of the atmosphere, we have

$$\frac{\alpha_{24}}{\alpha_{CH_4-CH_4}} \approx 0.7.$$

It is interesting that this correction more or less compensates for the temperature coefficient ($\alpha T^{-0.5}$) in the Lorentz half-width: if we assume T = 200°K for Jupiter, this coefficient will be approximately 1.2. Thus, the damping constant of CH_4 lines in the Jovian atmosphere will differ from its laboratory counterpart only due to pressure differences.

If the variation in the damping constant is disregarded, the vibrational-rotational bands must become increasingly more narrow and deeper with decreasing temperature. If the rotational lines are unsaturated, the equivalent band width remains constant, while if they are saturated, it decreases. The rotational /391 structure of the CH_4 bands is complex, and it can be expected that the above effect will be fairly weak. To verify this, we compared the central intensities of CH_4 bands in the spectrum of Jupiter with their laboratory standards, at the same equivalent widths. It was found that the central intensities coincide within the error limit.

On comparing the CH_4 bands in the spectrum of Jupiter with a set of laboratory spectra obtained for various values of equivalent path and pressure, the effective pressure in the Jovian atmosphere can be directly determined, if the cloud layer is regarded as a sharply delineated reflecting surface. In a number of cases, as can be seen from Fig.162, the CH_4 and NH_3 bands overlap and are difficult to use for quantitative estimates. The following CH_4 bands are virtually free of overlap: ($2\nu_1 + \nu_2 + \nu_3$, $\nu_1 + \nu_2 + \nu_3$) λ 1.0 μ and ($2\nu_1 + \nu_3$, $\nu_1 + 2\nu_3$) λ 1.12 μ. The adjoining band CH_4 ($2\nu_3 + 2\nu_4$, $2\nu_2 + 2\nu_4$) λ 1.18 μ is overlapped by the band NH_3 ($2\nu_3 + \nu_4$). The CH_4 band at λ 1.16 μ is slightly overlapped by NH_3, but considerable local distortions may be introduced by telluric absorption. The wing of the strong CH_4 absorption band at λ 1.62 μ is free of overlap, as is the wing of $3\nu_3$ [lines R(4) - R(8), forming the component at λ 1.094 μ]. All of the above bands that are relatively free of overlap are saturated, and their intensity is determined as the product uP. From a comparison with laboratory spectra, we obtain

$$uP\overline{M} \approx 150 \pm 50\ m \cdot atm^2. \qquad (5.14)$$

According to Kuiper (Ref.4),

$$u_{CH_4} = 150\ m \cdot atm \qquad (5.15)$$

in the vertical column. Assuming that $\bar{M} = 2$ (the observations refer to the disk center), the effective pressure will be

$$P_e \approx 0.5 \ atm, \tag{5.16}$$

or, at the top of the cloud layer,

$$P_1 = 2P_e \approx 1 \ atm. \tag{5.17}$$

This value is below the partial pressure of H_2 (derived from quadrupole lines) even at total absence of He. Most likely, Kuiper's estimate [eq.(5.15)] is too high. Owen (Ref.459) presented spectrograms of Jupiter with a high resolution in the region 9700 - 10,500 Å, together with the spectrum of 170 m • atm CH_4. The intensity of weak lines in the Jovian spectrum, as a rule, is much lower than in the comparison spectrum. Thus, it seems that Kuiper's /392 estimate must be reduced to at least half, i.e.,

$$u_{CH_4} \approx 75 \ m \cdot atm, \tag{5.18}$$

$$P_1 = 2 \ \ atm. \tag{5.19}$$

Assuming that the estimate (5.18) is correct and contains the equal sign, we obtain the partial pressure of methane

$$P_{CH_4} \approx 1 \ mb \tag{5.20}$$

and the relative concentration

$$c = 5 \times 10^{-4}. \tag{5.21}$$

A quantitative analysis of NH_3 in the Jovian atmosphere is complicated by two circumstances.

1) The Lorentz width of NH_3 lines is highly susceptible to impurities. It averages 0.6 cm^{-1} • atm for NH_3 - NH_3 collisions whereas for NH_3 - He and NH_3 - H_2 collisions it is 10 and 20 times smaller, respectively.

2) At the temperatures in the Jovian cloud layer, ammonia of necessity condenses and must exist in equilibrium with liquid and solid phases. Hence, it is assumed that Jupiter's cloud layer consists chiefly of ammonia particles (cf. Sect.5.5). Within the range of 130 - 160°K a decrease in temperature of 3°K corresponds to a decrease of roughly two-thirds in the amount of gaseous ammonia. The adiabatic gradient for an atmosphere consisting to 50% of He and to 50% of H_2 is 2.8 deg/km. If the cloud layer is sustained by convection, then the gradient near its top cannot be much less than the adiabatic, which would mean that the scale height for ammonia (cf. Sect.5.5) is approximately 2 × × 10^5 cm, i.e., greatly below the mean. There is no doubt that the NH_3 mass responsible for absorption is mixed with particles of the cloud layer, in which case the direct-reflection model of the atmosphere cannot correspond to reality.

Table 80 presents equivalent paths of NH_3 derived from bands of various intensities. The weakest band gives an equivalent path of about 20 m • atm,

from which (cf. Table 83) follows the partial pressure

$$P_{NH_3} \approx 0.5 - 5 \; mb,$$

depending on the temperature gradient. The relative concentration is

$$c_{NH_3} \approx 2 \cdot 10^{-4} - 2 \cdot 10^{-3}. \qquad (5.22)$$

Clearly, these estimates are of an extremely formal nature, since c_{NH_3} rapidly /393 increases with depth. The relative intensity of the strong and weak bands is substantially lower than in laboratory spectra. This applies especially to the band λ 1.52 μ. Note that, in the direct-reflection model, the relative intensities of NH_3 bands in the Jovian spectrum cannot be attributed to the effects of temperature, pressure, and impurities.

TABLE 80

EQUIVALENT PATH OF NH_3 IN THE JOVIAN ATMOSPHERE ACCORDING TO ABSORPTION BANDS OF VARIOUS INTENSITY ($\bar{M}$ = 2)

Band, μ	Equivalent Width, Å	Equivalent Path, m·atm	Laboratory Pressure, atm	$u_{NH_3}P$ in Laboratory, m·atm^2
0.755	*	~20 [460]	?	
0.645	1.2 [462]	7 [4]	0.58	4
1.26	9	3	0.03	0.09
1.58	20	2.5	0.03	0.08
1.52	250	0.4	0.006	0.0024

* Equivalent width not known exactly, but definitely smaller than for the band λ 0.615 μ.

Summing up, it should be noted that CH_4 and NH_3, taken together, account for approximately 10^{-3} of the entire volume of the observable portion of the atmosphere and thus cannot greatly influence its mean molecular weight.

The C/H ratio in the Jovian atmosphere is close to 3×10^{-4}, judging from the partial-pressure values given above. The table of cosmic abundance of elements gives nearly the same value [4×10^{-4}, cf. (Ref.406)] and, although spectroscopic observations are not necessarily characteristic of the C/H ratio for the entire atmosphere of Jupiter, this is hardly a chance coincidence. It gives reason to believe that the C/H ratio in Jupiter's atmosphere is the same as the cosmic ratio. In our further discussion, we will make use of the following "working model" of the chemical composition of Jupiter's atmosphere (cf. Table 81).

The mean molecular weight 2.6 is less than that derived from observations of

σ Arietis (3.3 or, with Öpik's correction, 4.3). However, the observations of σ Arietis and the assumptions underlying their analysis are not sufficiently reliable to warrant the presence of such an excessive amount of inert gases, as has been done elsewhere (Ref.455, 471), or to assume an extremely high content of helium. It is more expedient to estimate the temperatures of the upper atmosphere from the scale height based on observations of the occultation, /394
assuming a specific molecular weight rather than vice versa. The molecular weight $\mu = 2.6$ at $T = 170^{\circ}K$ corresponds to the scale height

$$H = 22\ km.$$

The total pressure $P_1 = 3.8$ atm exceeds the estimates derived from the line broadening and relative intensity of the CH_4 bands, but the difference does not exceed the error limit.

TABLE 81

CHEMICAL COMPOSITION OF THE JOVIAN ATMOSPHERE (WORKING MODEL)

Molecule	μ	% By Volume	Partial Pressure, atm	Density, Amagat	Reduced Thickness, m·atm
H_2	2	70	2.6	4.5	100000
He	4	30	1.1	1.6	36000
CH_4, NH_3	16	5×10^{-4}—5×10^{-3}	2×10^{-3}—2×10^{-2}	3×10^{-3}—3×10^{-2}	70—700
		$\bar{\mu}=2.6$—2.8	$P_1=3.8$		

d) Consideration of multiple scattering. The apparatus of quantitative chemical analysis employed in Section 3.4 apparently cannot be applied in toto to the atmosphere of Jupiter. First, scattering in the continuous spectrum by the Jovian cloud layer cannot be considered conservative (cf. Sect.5.2). Second, we have no information on the scattering indicatrix other than assumptions that may be derived from analogies with terrestrial and Venusian clouds. Moreover, the information on line widths is extremely limited. For H_2, no observational data are available while for CH_4 only the upper limit is known, and in the case of NH_3 the data on widths may be distorted by inversional doubling.

On Venus, as we have seen in Section 5.3, the layer above the cloud furnishes practically no contribution, and all spectroscopic observations can be interpreted on the assumption that the ratio $\frac{k}{\sigma}$ does not change with altitude. Then, the intensities of weak lines must be proportional to $\sqrt{\frac{k}{\sigma}}$ if continuous absorption can be neglected and to $\frac{k}{\sqrt{\sigma}}$ if that absorption is stronger than /395
the line absorption. As we have seen in paragraph a) of this Section, the

relative intensities of the quadrupole H_2 lines of the bands (3-0) and (4-0) are proportional to $\sqrt{k}$, which may be interpreted as a sign of a negligibly small contribution of the layer above the cloud and a low degree of continuous absorption.

On the other hand, the weak lines of H_2, CH_4, and NH_3 show no appreciable center-to-limb effect, whereas in the model with constant $\frac{k}{\sigma}$ the line intensity regularly decreases with approach to the limb: The function S which enters eqs.(3.11) amd (3.13) is proportional to the cosine of the angle between the ray and the normal. It appears logical to attribute the observed absence of the center-to-limb effect to the compensating influence of the supracloud layer (Sharonov-Teyfel' hypothesis). Note that this is not the only possible explanation. If the clouds have a complex relief (e.g., cumulus clouds) the center-to-limb effect predicted by the model of a semi-infinite atmosphere without a supracloud layer may be greatly attenuated. Nevertheless, the compensation hypothesis admits of a simple quantitative interpretation of the observations. Without denying the possibility of other explanations, we will next examine the conclusions as to the chemical composition and pressure implied by this hypothesis.

For a semi-infinite atmosphere, eq.(1.100) can be rewritten in the form

$$\rho_\nu = h(r', r)\, e^{-S\eta\sqrt{\frac{k}{\sigma}} - \frac{2Hk_\nu}{\mu}}, \qquad (5.23)$$

where $k = k_\nu + k_{co}$ is the total absorption coefficient; k_ν is the coefficient of line absorption; k_{co} is the coefficient of absorption in a continuous spectrum. The monochromatic line intensity per unit continuous spectrum is

$$R_\nu = 1 - \frac{\rho_\nu}{\rho_{co}} = 1 - e^{-S\eta\left[\sqrt{\frac{k_\nu + k_{co}}{\sigma}} - \sqrt{\frac{k_{co}}{\sigma}}\right] - \frac{2Hk_\nu}{\mu}} \qquad (5.24)$$

The function S is proportional to μ and, at certain values of k_ν, k_{co}, H, and σ within a limited range of variations in μ (e.g., from 1 to 0.5), a decrease in the first term of the exponent may be compensated by an increase in the second. If $k_{co} = 0$ or $k_{co} \ll k_\nu$ then the compensation, for given values of H and σ, is possible only for a single value of k_ν. However, k_ν varies considerably within the confines of the line profile (which would be even more so in different lines of a band or in different bands). Consequently, at $k_{co} \ll k_\nu$ the compensation of the center-to-limb effect for the lines and bands is not feasible. The /396 situation is different if $k_\nu \ll k_{co}$. Then,

$$R_\nu = 1 - e^{-\frac{S\eta k_\nu}{2\sigma\sqrt{\beta_{co}}} - \frac{2Hk_\nu}{\mu}} \qquad (5.25)$$

and compensation becomes possible for a broad range of values of k_ν. Assuming

isotropic scattering for Jupiter, we would have $\beta_{c_0} = 0.03$ in the red spectrum region [(Ref.428) cf. Sect.5.2]. For isotropic scattering, $S\eta$ is 2.3 at $\mu = 1$ and 1.15 at $\mu = 0.5$. If the spherical indicatrix is replaced by an elongated indicatrix corresponding to particles of $\frac{2\pi r}{\lambda} = 20$, then $S\eta$ will be 6 and 3, respectively, and to keep the brightness coefficients in the continuous spectrum from varying, we must assume $\beta_{c_0} = 0.005$.

An elementary calculation based on these parameters shows that, for $R_\nu <$ < 0.8, the extent of R_ν hardly varies within the range of $0.5 < \mu < 1$ if σ equals 5×10^{-6} cm^{-1} in the case of an elongated indicatrix and 10^{-6} cm^{-1} in the case of a spherical indicatrix. A volume coefficient of scattering amounting to 10^{-6} cm^{-1} seems too low since then the mean free path of the quantum ($\approx$ 10 km) would be comparable with the scale height and the concept of the layer of gas above the cloud would become meaningless. The value $\sigma = 5 \times 10^{-6}$ cm^{-1} is close to that derived for Venus but is two orders of magnitude smaller than for terrestrial clouds. Particles of a radius of several microns have a scattering cross section close to twice the geometric cross section ($\sim 10^{-7}$ cm^{-2}) so that the particle density in the Jovian cloud layer is $\sim 10^2$ cm^{-3} or 10^{-8} gm $\cdot$ cm^{-3}. If, as assumed, the clouds actually consist of solid ammonia particles, then, at such a density, the diurnal variation of insolation may cause a change in the altitude of the cloud top by several kilometers [cf. (Ref.472)]. Such variations may per se affect the band intensity distribution over the disk [cf. paragraph a) of this Section].

If the compensation condition is satisfied, the second term in the exponent of eq.(5.25) is roughly half as high as the first. This means that the amount of gas and the partial pressures given in Table 80 must be reduced three times before they can fit this hypothesis. Naturally, the idea of compensation is quite artificial. Why should the value of mean scattering coefficient be precisely as needed for mutual compensation of the intracloud and supracloud center-to-limb effects? However, it should be recalled that the scattering coefficient derived from this hypothesis is extremely low. If it were one order of magnitude higher and if the cloud top were sharply delineated, then the /397
contribution of the supracloud atmosphere would be sufficiently high to warrant application of the direct-reflection model. Note that the scale height on Jupiter ($H \approx 20$ km) is fairly high, making it plausible that vertical fluctuations in the relief of the cloud layer may be less extensive.

The variant involving a vertically constant $\frac{k}{\sigma}$ ratio (absence of supracloud atmosphere) can be rather easily analyzed for induced absorption of H_2 at λ 1.97 μ. For the scattering indicatrix corresponding to $\frac{2\pi r}{\lambda} = 20$, the brightness coefficient of 0.05 means that $\frac{k}{\sigma} \approx 2$. If $\sigma = 5 \times 10^{-6}$ cm^{-1} then, assuming the absorption coefficient as $s = 2 \times 10^{-7}$ cm^{-1} $\cdot$ $amagat^{-2}$ and $y = 0.7$, we obtain the density of hydrogen as

$$\rho_{H_2} = \sqrt{\frac{ky}{s}} = 6 \text{ amagat} \qquad (5.26)$$

and P_{H_2} = 3 atm, which is somewhat higher than for the direct-reflection model. The increase in the scattering coefficient leads to an increase in $P_{H_2} \sim \sqrt{\sigma}$. This estimate cannot be considered a proof for a low scattering coefficient, since it essentially gives only the upper limit of ρ_{H_2}.

Finally, let us note that multiple scattering logically accounts for the slight difference in the intensities of belts and zones: in the zones, β_{co} is lower which results in an increase in line intensities [cf. eq.(5.25)]. The increase in the strength of certain bands in the polar and temperate regions does not necessarily have to do with a considerable mass of gas above the cloud but may be attributed to the generally lower value of the parameter β_{co} in these regions compared with the equatorial regions.

Section 5.5 Temperature of Jupiter and Chemical Composition of the Cloud Layer

a) Brightness temperature according to infrared emission. The mean brightness temperature of the Jovian disk in the region λλ 8-13 μ has been measured with thermocouples as early as in the 1920s by Pettit and Nicholson (Ref.125) as well as by Menzel, Coblentz, and Lampland (Ref.473). They obtained 150°C (without an error estimate) and 130 ± 10°K, respectively. The difference in the temperatures themselves is not large, but the corresponding brightness ratio is about 4 so that, in reality, a major contradiction was involved. Sinton and Strong (Ref.25) derived T_B = 130°K in agreement with Menzel (Ref.473).

A similar brightness temperature (128 ± 2°K) was found by Murray and Wildey (Ref.474) in 1962 during trial observations with the 20″ reflector at White Mountain. In the same year, they were the first to investigate with a 200″ reflector the brightness distribution over the Jovian disk (Ref.296). The same instrumentation was used as in observations of Venus (a photometer with a mercury-doped germanium photovaristor cooled with liquid hydrogen; cf. Sect.3.7). /398

Since the signal from Jupiter is much weaker than from Venus, it was impossible to accurately record the beginning and end of the section according to signal fluctuations at the instant of intersection of the limb. As a result, owing to poor topographic coordination of the sections (as well as owing to drift of the zero-point level) the isotherm charts given elsewhere (Ref.296) are not reproducible. After averaging all the traces, however, sufficiently reliable curves of limb darkening could be plotted as far as 0.9 R_o (Fig.164). An analysis of these curves involves the same difficulties as in the case of Venus (cf. Sect.3.7): it is unclear which of two processes determines their shape - true absorption or scattering, or both. The observations by Murray et al. (Ref.296) give T_B = 128.5°K at the center of the disk and 126°K at a distance of 60° Long. from the equator. The meridional section differs little from the equatorial. If the brightness distribution is written in the form

$$I = I_0 \mu^{\alpha},$$

then $\alpha \approx 0.22$. If scattering can be neglected, the scale-height gradient calculated from a formula analogous to eq.(3.78) will be equal to

$$\frac{dH}{dz} \approx -0.06. \qquad (5.27)$$

Given complete mixing, this implies a temperature gradient of $\frac{dT}{dz} = 0.3^{\circ}/km$. If the absorption is determined by an unsaturated gas, the gradient $\frac{dT}{dz}$ cannot be found since then $H = H_c$ would be the scale height characteristic of that gas alone and $\frac{dH_c}{dz}$ would depend only on T and be independent of $\frac{dT}{dz}$ (see paragraph c). /399

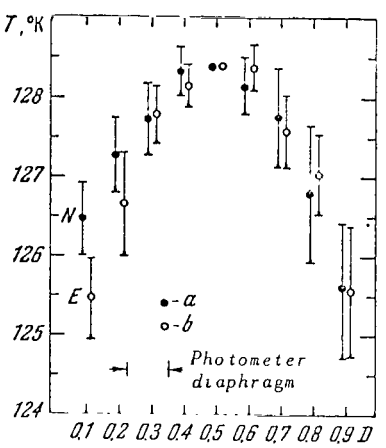

Fig.164 Averaged Distribution of Brightness Temperature in the Region λλ 8-13 μ over the Equatorial (b) and Polar (a) Diameters of Jupiter.
It is assumed that $T_B = 128.5^{\circ}K$ at the center of the disk. The dots correspond to tenths of diameter. Displacement was used to avoid the inconveniences of overlap (Ref.296).

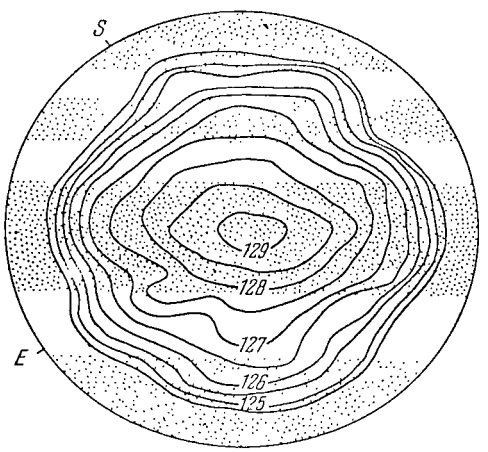

Fig.165 Isotherms of Brightness Temperature of Jupiter in the Region λλ 8-13 μ.
Averaged from observations on five nights: December 12-16, 1963 (Ref.476).

In 1963 Wildey, Murray, and Westphal (Ref.475, 476) carried out new observations of Jupiter with the 200″ reflector, using improved techniques. Figure 165 presents the isotherm chart obtained by averaging the observations over several nights. The observations were carried out with a 2″.5 diaphragm, with roughly one section being plotted per minute. Figure 166 shows several

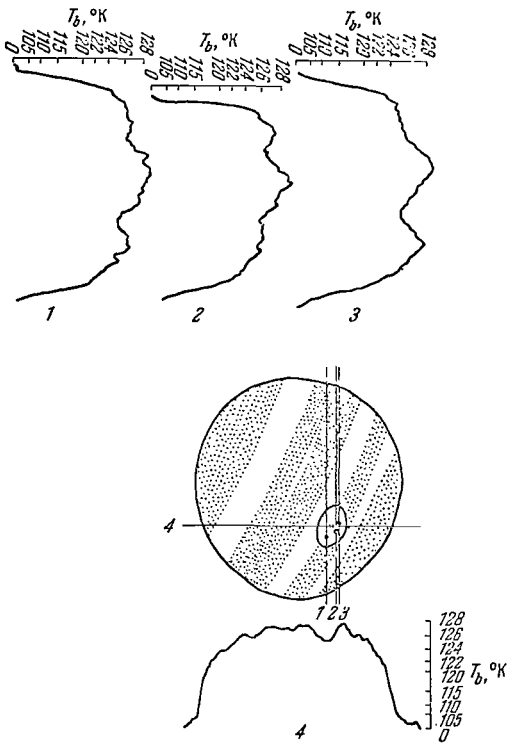

Fig.166 Infrared Sections of the Disk of Jupiter on December 17, 1963 at 2^h UT (Ref.476). Traces given without smoothing. Their position on the disk is indicated. Cold region visible in the neighborhood of the Great Red Spot.

sections plotted on December 17 when atmospheric jitter and nonsteady-state noise were less than on the other nights. These sections show that the Great Red Spot is 1.5 - 2° colder than the circumambient regions and that the belts are somewhat warmer than the zones. The low temperature of the Red Spot is in qualitative agreement with Hyde's hypothesis (Ref.431, 432): the adiabatic expansion of the ascending masses of the atmosphere which, according to Hyde, form the Red Spot must be accompanied by cooling. The higher temperature of the belts may be attributable to their lower reflection coefficient.

Observations by Low (Ref.477) made in the 8-13 μ optical window with the aid of a liquid helium-cooled bolometer of gallium-doped germanium, gave a /400
mean disk temperature of 126 ± 2°K, in close agreement with the results of the California team. Low also obtained the spectrum of Jupiter in the region λλ 8-13 μ with a low resolution. No details of planetary origin can be seen on this trace.

A very surprising effect was discovered by the California team in 1962 during observations with the 200″ reflector: In the shadow cast by the satellites on the disk there was a sharp temperature rise (Fig.167). This increase in T_B attained 50°K (20 times of brightness), considering that the real dimensions of the diaphragm are greater than the diameter of the shadow. So far no satisfactory explanation could be /401
found for this effect. It may be that the reason lies in a disturbance in equilibrium between the rates of dissociation and recombination, due to "switch-off" of solar illumination. The dissociation would cease while the recombination either would cause liberation of heat and heating or an increase in atmospheric transparency, resulting in the escape of radiation from the deeper-lying layers.

b) Rotational temperature. The rotational temperatures on Jupiter were determined according to H_2 and CH_4 lines. Zabriskie (Ref.456) found $T_r \approx 170°K$ from the relative line intensities of the band (3-0) H_2. Spinrad and Trafton (Ref.455) derived T_r = 120 - 170°K, but later Spinrad (Ref.479) refined this to 120°K. Nevertheless, the indeterminacy is still too large, and a more precise determination is needed.

Calculation of the rotational temperature from CH_4 and NH_3 lines involves great difficulties, since these molecules are nonlinear and the bands have a complex structure. For example, a molecule of methane, because of its symmetry (tetrahedron), so to speak can be represented by a spherical spinning top. It has four fundamental frequencies, two of which (ν_3 and ν_4) are active in the infrared region. Two and more frequencies or their harmonics, when added together, give combination /402 bands. Pure harmonics are permitted only for the frequencies ν_3 and ν_4. An added complication is that the inactive fundamental frequencies are sufficiently close to ν_3 and ν_4, so that the rotational levels of the latter two are subject to Coriolis perturbation. This causes splitting of the rotational lines, which greatly complicates the bands. Unfortunately, nearly all the CH_4 bands located in the region accessible to high-resolution spectroscopy are of the combination kind, so that an analysis of their fine structure is a particularly difficult task.

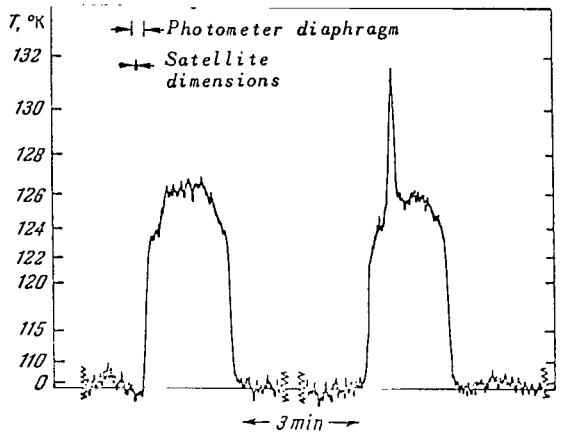

Fig.167 Photometric Sections of the Jovian Disk in the Interval λλ 8-13 μ. Right: transit of the photometer diaphragm across the shadow of Ganymede (Ref.296).

An exception is the band 1.1 μ - the harmonic $3\nu_3$. The band $3\nu_3$, as was to be expected, has a relatively simple structure, which induced Owen to make use of it in estimating the rotational temperature (Ref.459). The possibility of deriving the rotational temperature from the band $3\nu_3$ was mentioned even earlier by Childs and Jahn (Ref.480), while the theoretical principles were expounded by Wilson (Ref.481) and Jahn (Ref.482).

If a given molecule is a true spherical spinning top (with the spin of the nucleus being unrelated to the residual angular momentum), then the distribution of the rotational-level populations is given by the formula

$$N_c \sim (2K+1)^2 e^{-\frac{BK(K+1)hc}{kT_r}}, \qquad (5.28)$$

analogous to eq.(1.17). If the molecule is a spherical spinning top in consequence of symmetry, then eq.(5.28) is inapplicable and the statistical weight for each rotational level must be calculated with consideration of nuclear spin. This happens in the case of CH_4. The intensity of the rotational levels depends on three variables: transition amplitude, statistical weight of the ground level, and Boltzmann factor. It is equal to

$$I_c \sim A_c s_c e^{-\frac{BK(K+1)hc}{kT_r}}, \qquad (5.29)$$

where A_c is the transition amplitude; s_c is the statistical weight. The product is

$$A_c s_c = (2K + 3)(5a + 2b + 3c), \tag{5.30}$$

where a, b, c are the number of rotational levels corresponding to the modification of A, E and F for a given K. These quantities are defined elsewhere (Ref.480). From eqs.(5.29) and (5.30) it is possible to tabulate the relative intensities of rotational lines as a function of T_r and, after selecting the tabulated ratio that optimally fits the observations, to determine the rotational temperature T_r.

Using this method, Owen derived the following value from the lines K = 3, /403 4, 5, 6, of the band $3\nu_3$:

$$T_r = 200 \pm 25°\text{K}.$$

The rotational temperature found by Owen is close to the melting point of NH_3 (195°K). It may be that the lower boundary of the observable part of the Jovian atmosphere is determined by a tier of dense cumulus clouds of liquid ammonia. It is intriguing that the rotational temperature T_r is close to the brightness temperature in the shadow cast by the satellites.

c) Saturation temperature of NH_3 and chemical composition of the cloud layer. Ever since Wildt identified ammonia in the spectrum of Jupiter it has been believed that the clouds floating in its atmosphere consist chiefly of NH_3. Ammonia must condense at the temperatures of 130 - 200°K, derived from other observations, and it apparently exists in the state of saturation, i.e., in equilibrium with the solid phase. When present in sufficient amounts, CO_2 and certain straight hydrocarbons as well as C_2H_4 and C_2H_6 will also condense at these temperatures, but spectroscopically these compounds have not been detected and the existing upper limits indicate that they do not attain saturation. Methane does not condense at the partial pressure and temperatures observed in the Jovian atmosphere. Conversely, H_2O has too low a saturated vapor pressure. It is not precluded that water and ice clouds might form in sufficiently deep, unobservable layers of the atmosphere.

If NH_3 exists in equilibrium with the condensed phase, the partial pressure would be determined from the formula

$$\log P_{NH_3} = -\frac{1550}{T} + 4\log T - 8\times10^{-5}T^{1,8} + 1.58, \tag{5.31}$$

where T is given in °K and P_{NH_3} in mb. This formula was assumed by van de Hulst (Ref.483) for low temperatures. The term before the last in eq.(5.31) represents the correction which makes the formula applicable up to 200°K (Ref.466). Knowing P_{NH_3} it is possible to determine the so-called saturation temperature from eq.(5.31). Obviously, if we know the total amount of NH_3 above a given level [suppose, ~ 10 m • atm, as is deduced from spectroscopic observations; cf. paragraph c) in Sect.5.4], then P_{NH_3} will depend on the temperature gradient of the atmosphere. The local scale height, provided saturation is present, can be

derived readily from eq.(5.31). It is equal to

$$H_c = \frac{1}{\frac{dT}{dz}\left(3{,}3\cdot 10^{-4}T^{0,8} - \frac{4}{T} - \frac{3560}{T^2}\right)}. \qquad (5.32)$$

Clearly, if the equilibrium condition (5.31) is satisfied at a given level, the condensation above that level will occur only on condition that /404

$$H_c < \frac{kT}{\bar{m}g}. \qquad (5.32a)$$

TABLE 82

LOCAL SCALE HEIGHT FOR NH_3 AT SATURATION (km)

$\frac{dT}{dz}$, °K/km / T °K	0.4	1	2	2.8	$\frac{dH_c}{dz}$, km/km
100	7.6	3.0	1.5	1.0	0.025
127	12.5	5.0	2.5	1.7	0.093
150	17.9	7.2	3.7	2.4	0.127
170	23.0	9.2	4.7	3.2	0.134
200	36.0	14.2	7.2	4.7	0.220

If $H_c > kT/\bar{m}g$, then only gas will be present above that level. Here, $\frac{kT}{\bar{m}g} = H$ is the mean scale height. Table 82 gives the values of H_c calculated for several values of T and $\frac{dT}{dz}$. The corresponding value for H_2O in the earth's troposphere is 2 km. The table also presents values of $\frac{dH_c}{dz}$ calculated on condition that $\frac{d^2T}{dz^2} = 0$. These values are independent of $\frac{dT}{dz}$. We can readily derive a relation linking the total amount of NH_3 above a given level to its temperature

$$\log u_{NH_3} = -\frac{1550}{T} + 3\log T - 8\cdot 10^{-5}T^{1,8} + \log H_c + 4.0, \qquad (5.33)$$

where u_{NH_3} is given in m • atm and H_c in km. Table 83 gives the partial pressures and the values of u_{NH_3} as a function of T and $\frac{dT}{dz}$. Table 83 indicates that u_{NH_3} depends largely on the temperature and that even for major errors in the determination of u, the saturation temperature is determined with satisfactory accuracy. Assuming that, within the region of formation of the observable NH_3 bands, the atmosphere exists in convective equilibrium and that the

gradient is equal to the adiabatic, we have $T \approx 170^\circ K$ for u = 14 m • atm. The upper limit is $175^\circ K$ and the lower limit, $150^\circ K$. Similar results were obtained by Kuiper (Ref.307), Squires (Ref.472), and others. /405

TABLE 83

PARTIAL PRESSURE AND TOTAL AMOUNT OF NH_3 ABOVE A LEVEL WITH SPECIFIC TEMPERATURE AND TEMPERATURE GRADIENT (AT SATURATION)

T, °K	P_{NH_3}, mb	u, m · atm			
		$\frac{dT}{dz} = 0.4$	1	2	2,8 °K/km
100	6×10^{-7}	1.2×10^{-5}	4.7×10^{-6}	2.4×10^{-6}	1.7×10^{-6}
127	2×10^{-3}	6.2×10^{-2}	2.0×10^{-2}	1.0×10^{-2}	6.8×10^{-3}
150	0.16	7.0	2.9	1.4	1.0
170	4	145	59	29	20
200	80	3600	1420	720	485

From Table 83 it can be seen that the infrared brightness temperature $T_B = 127^\circ K$ (averaged from center to limb) corresponds to a total amount of NH_3 of the order of 1 cm • atm. In the region λλ 8-13 μ, the NH_3 absorption reaches a maximum and it is there that the fundamental bands of this molecule occur. Kuiper (Ref.307) observed that roughly the same amount of pure NH_3 at normal pressure has an optical thickness of τ = 1. The reader can verify this conclusion independently by consulting Fig.7. It follows from this that NH_3 probably is either the main or one of the main agents responsible for radiation within the interval λλ 8-13 μ.

At a lower pressure and in a mixture with H_2 and He, the NH_3 absorption decreases substantially; thus, the additional argument implied by the extent of limb darkening is highly significant. From observations of limb darkening we derived in paragraph a) of this Section a value of $\frac{dH}{dz} = 0.06$ km/km, which is close to the gradient of local scale height under saturation conditions at $T \approx 125^\circ K$.

d) Brightness temperature in the centimeter range. The spectrum of Jupiter's radio emission in the range λλ 8 mm-70 cm is shown in Fig.168. Within the range λλ 6-70 cm, the flux is almost independent of wavelength. Beginning with λ 3 cm the flux rapidly increases in the direction of shorter wavelengths. In the region λλ 6-70 cm, the major part of the flux of Jupiter's radio emission is definitely of a nonthermal nature; this is indicated by the aspect of the spectrum, the polarization, and the brightness distribution (cf. Sect.5.7). The increase in the region λλ 6-0.8 cm may be interpreted as the contribution of thermal radiation with a temperature of 130 - $150^\circ K$. The decrease in polarization in this region is an argument in favor of the above interpretation. Table 84 presents the results of measurements of the brightness radio temperature

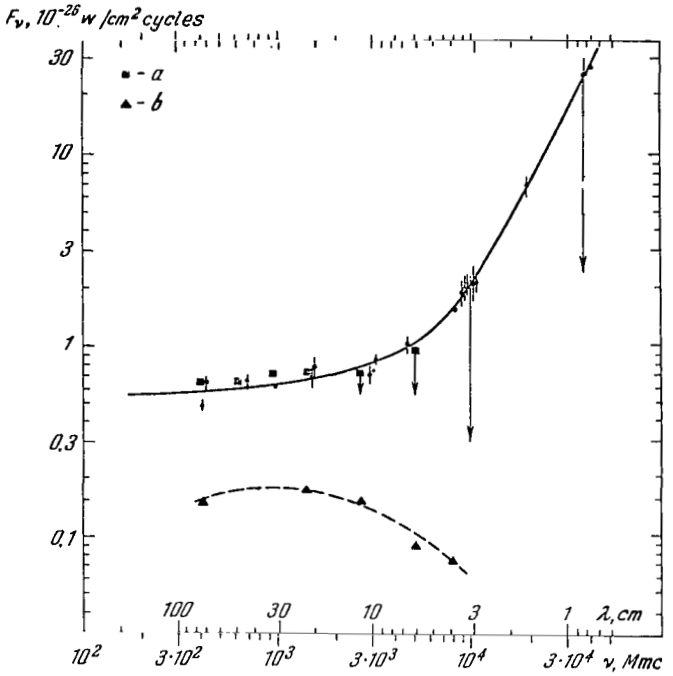

Fig.168 Spectrum of Microwave Emission of Jupiter. a - Measurements of total flux [Roberts et al. (Ref.501)], corrected for periodic variations due to rotation of the planet; b - Polarized component. Downward arrows give the thermal radiation contribution, assuming uniform brightness distribution of the disk and T_B = 130°K.

at the wavelengths 8 mm, 1.6 cm, and 3 cm. The increase in temperature at λ 3 cm compared with λ 8 mm may be attributed to either nonthermal radiation or to a greater depth of location of the effective radiation level in the atmosphere. D.V.Korol'kov, Yu.N.Pariyskiy, and G.M.Timofeyeva (Ref.535), in observations with the Pulkovo fan-beam antenna found that, at λ 3.02 cm, at least 95% of the emission originates in the region $R < 1.1\ R_0$ where R_0 is the radius of the planet, which in itself seems an argument in favor of the latter explanation. Haddock and Dickel (Ref.485) found, however, that emission at λ 3.75 cm is polarized which means that nonthermal radiation definitely furnishes a contribution here. Moreover, the sharp decrease in the flux of nonthermal radiation /407 on transition from λ 10 to λ 3 cm would be difficult to explain. Berge [cf. (Ref.501)] found that at λ 10 cm the "disk" component of radio emission is twice as high as the component that existed at the temperature derived from infrared emission. Thus, only radio emission at λ 8 mm can be regarded as pure thermal emission. Thornton and Welch (Ref.487) derived at λ 8.35 mm

$$T_B = 144 \pm 23^\circ\,\mathrm{K}$$

which is in good agreement with optical data. A team of radioastronomers from the Physics Institute of the Academy of Sciences USSR (FIAN) carried out relative

measurements of fluxes of Jupiter and Venus at λ 8 mm (Ref.311, 334). These measurements fit the brightness temperature T_B = 140°K for Jupiter. The optical thickness of the Jovian atmosphere in the region λ ≈ 1 cm apparently determines the wing of the known inversion line of ammonia λ 1.28 cm [cf., for example (Ref.486)]. In view of the low scale height of NH_3, which probably has to do with saturation, the agreement between the brightness temperature at λ 8 mm and optical temperatures seems logical. /408

TABLE 84

TEMPERATURE OF JUPITER

Method of Determination	λ	T, °K	References
Brightness in infrared range	8—13 μ	150	Pettit and Nicholson (Ref.125)
		130±10	Menzel, Coblentz and Lampland (Ref.473)
		128,5±2	Murray, Wildey, and Westphal (Ref.296)
		128±2	Low (Ref.477)
		136±2	Sinton and Strong (Ref.25)
Rotational, from H_2 lines (3-0)	0.8 μ	170	Zabriskie (Ref.456)
		120—170	Spinrad and Trafton (Ref.455)
		120	Spinrad (Ref.479)
Rotational, from $3\nu_3$ CH_4	1.1 μ	200±25	Owen (Ref.459)
NH_3 saturation	0.76; 0.64 μ	150—170	This book; see also (Ref.307, 472)
Brightness, in radio range	8 mm	140	FIAN Team (Ref.311, 334)
	8.35 mm	144±23	Thornton and Welch (Ref.487)
	1.6 cm	165—16	Vetukhnovskaya et al. (Ref.311)
	3.02 cm	185±30	Pariyskiy et al. (Ref.488)
	3.03 cm	171±20	Giordmaine et al. (Ref.489)
	3.15	140±38	Mayer et al. (Ref.130)
	3.15	145±18	Mayer et al. (Ref.490)
	3.87	173±20	Giordmaine et al. (Ref.489)
	3.3	193±20	Bibinova, Kuz'min et al. (Ref.491)

e) Equilibrium temperature. Table 84 gives composite observational data on Jupiter's temperature. It is logical to compare these with the equilibrium temperature calculated from the energy balance.

Figure 169 shows the wavelength dependence of the monochromatic geometric albedo of Jupiter. We obtained the ratio of the monochromatic intensity

$\frac{\text{Jupiter}}{\text{Sun}}$ as a function of wavelength in the region λλ 0.9-2.5 μ. This ratio was calibrated such that it fitted the curve of spectral geometric albedo in the region λ < 0.9 μ. The curve was taken from Harris' work (Ref.66). Since the region near λ 0.9 μ has been little investigated (in spectra obtained with the aid of a lead-sulfide photovaristor, this corresponds exactly to the short-wave boundary of the recordable interval) the curve fitting is not sufficiently

reliable for which reason Fig.169 contains two curves as the extreme models. Curve (a) gives the integral spherical albedo as $A_1 = 0.53$ and curve (b), $A_1 = 0.48$. In both cases, the Lambert phase integral Q is taken as 1.50. Assuming a mean $A_1 = 0.50 \pm 0.02$, the effective equilibrium temperature of Jupiter, calculated on the assumption that it is uniform for any point on the planet, is equal to

$$T_e = 108 \pm 1^\circ \mathrm{K},$$

which is much below the observable quantities given in Table 84.

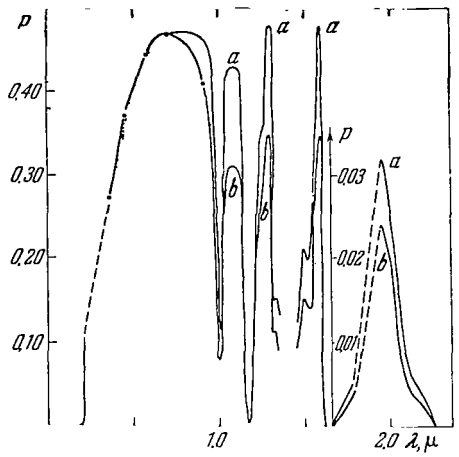

Fig.169 Wavelength Dependence of the Monochromatic Geometric Albedo of Jupiter. (a and b represent extreme models)

According to Wien's law, the intensity maximum in the thermal radiation spectrum of Jupiter must lie near λ 30 μ. Most of its radiation is located at λ 20-100 μ. If the atmosphere in this region is transparent and does not produce a greenhouse effect, the difference between the measured temperatures (130 - 200°K) and the equilibrium temperature (108° K) could be attributed either to a considerable internal heat flux of the planet exceeding the solar heat influx (Ref.466), or to an extremely low emission coefficient of the cloud layer in the region $\lambda > 20$ μ. The latter assumption is unrealistic. The opacity of the atmosphere in the region $\lambda\lambda$ 20-100 μ cannot be associated with CH_4 or with NH_3, since these gases do not absorb in this spectrum region. Recently, Trafton (Ref.492) showed that induced absorption by the rotational H_2 band may suffice to produce a greenhouse effect of the necessary magnitude, but the question of the role of internal heat flux cannot be regarded as conclusively settled. /409

f) Upper atmosphere temperature according to observations of the occultation of σ Arietis. Assuming a mean molecular weight $\bar{\mu} = 2.6$ in accordance with Table 81, the temperature at the level of occultation of σ Arietis can be found from the scale height [eq.(5.1)]

$$T = \frac{Hm_{\mathrm{H}}\mu g}{k} = 68^{+34}_{-1.}{}^\circ \mathrm{K}. \qquad (5.34)$$

Equation (3.127) gives the temperature of the stratosphere as

$$T_0 \geqslant \frac{108}{\sqrt[4]{2}} = 92^\circ \mathrm{K}.$$

The equal sign is valid in the absence of a heat flux from the interior. Note that eq.(3.127) was derived on assuming gray absorption. In selective absorption within the confines of a relatively narrow frequency band, this formula is no longer valid.

For example, for Mars we assumed that the heat balance is determined by the band λ 15 μ, in which case the corresponding temperature would obviously be below the temperature calculated from eq.(3.127). In principle, a similar situation may apply for Jupiter although we cannot pinpoint the specific molecule responsible. Infrared absorption by NH_3 is high in the region $\lambda < 15\ \mu$, but the radiation transport in the "long-wave wing" (Fig.170) causes the effective optical thickness of NH_3, for the thermal radiation of the planet, to become sufficiently low. As for the absorption induced by the rotational band of H_2, it will be shown below that, assuming $T_e = 110^\circ K$, this yields a stratosphere temperature of $94^\circ K$, which is in close agreement with eq.(3.127).

Öpik (Ref.466) attempted to estimate the temperature of the atmosphere at the occultation level on taking into account selective NH_3 and CH_4 absorption, but most likely NH_3 is dissociated at that altitude. Moreover, Öpik disregarded the pressure dependence of the absorption coefficient. The photochemistry of the Jovian atmosphere has been little investigated (cf. Sect.5.6) and a priori /410 one cannot reject the possibility that the temperature distribution is greatly influenced by the products of photolysis of the various atmospheric constituents. This influence may manifest itself both in a temperature rise at certain levels (inversions similar to terrestrial ozone-layer inversions) and a temperature drop owing to de-excitation above the vibrational relaxation level.

The vertical optical thickness at the occultation level was estimated by Öpik (Ref.466) as $\tau = 1.1 \times 10^{-7}$. This corresponds to 1.5 cm • atm of a mixture of 70% H_2 and 30% He, from which follows the concentration at the occultation level:

$$n = \frac{2.7\times10^{19}\times1.5}{8.3\times10^{5}} = 5\times10^{13}\,cm^{-3},$$

while the pressure

$$P = \frac{2.7\times10^{19}\times1.5\times1.67\times10^{-24}\times2.6\times2500}{8.3\times10^{5}} = 5\times10^{-7}\,mb$$

is roughly the same as at a height of 100 km in the earth's atmosphere.

Section 5.6 Vertical Structure of the Supracloud Atmosphere

The data presented in Sections 5.4 and 5.5 can be integrated into a scheme of vertical structure of the atmosphere. The condensation of atmospheric gases and formation of clouds mean that, in the observable portion of the atmosphere - or at least in its lower layers -, the temperature decreases with altitude. The rotational temperature of CH_4 and the saturation temperature of NH_3 no doubt pertain to the deepest layers. The brightness temperature, determinable in the infrared portion (and apparently also in the millimeter range), characterizes the higher layers. Lastly the temperature derived from the occultation of σ Arietis refers to extremely high altitudes.

The temperature distribution depends on the altitudes and spectral regions in which the solar radiation as well as the planetary natural radiation are absorbed. The simplest hypothesis is that the major portion of solar radiation

is absorbed at some sufficiently great depth (for simplicity, we will assume this to be below the level T = 170°K) and is then reradiated in the infrared region. If the infrared absorption coefficient is independent of the wavelength, then the altitude distribution of temperature in this model is expressed by eqs.(3.135) or (3.139). We can assume the value of T_e, derived from the condition of equilibrium between solar and planetary radiation, as being 108°K. Then, as noted above, we have a stratosphere temperature of T_0 = 92°K. If the absorption coefficient varies sufficiently rapidly with altitude (in consequence of its strong dependence on density or temperature, with the latter taking place on saturation of the absorbing gas), then a convective gradient sets in up to altitudes at which $\tau \approx 1$; above these altitudes the gradient rapidly decreases and the isothermal region begins. /411

TABLE 85

MODEL OF SUPRACLOUD ATMOSPHERE OF JUPITER, CONSTRUCTED BY THE "TWO-LINE" METHOD

T, °K	z, km	P, atm	H, km	Reduced Thickness, cm·atm				Remarks
				H_2	He	CH_4	NH_3	
170	0	1.3	22	3.3×10^{6}	1.5×10^{6}	2.2×10^{3}	1.5×10^{3}	Base of troposphere
127	15	0.57	16.5	1.4×10^{6}	7×10^{5}	1×10^{3}	0.6	Radiation level in the region 8-13 μ
108	22	0.37	14	9.4×10^{5}	4.3×10^{5}	6.2×10^{2}	(2.5×10^{-3})	Effective level of planetary radiation
92	28	0.18	12	4.6×10^{5}	2.1×10^{5}	3.0×10^{2}	(6×10^{-6})	Base of stratosphere
92	180	5×10^{-7}	12	1.2	0.6	(8.5×10^{-4})	(2×10^{-11})	Level of occultation

A schematic model with a convective troposphere existing in radiative equilibrium with the stratosphere can be constructed by the "two-line" method: For the troposphere, a constant adiabatic-like gradient $\frac{dT}{dz}$ is assumed and, for the stratosphere, a value of $\frac{dT}{dz} = 0$ and $T_0 = \frac{T_e}{\sqrt{2}}$. The dry adiabatic gradient in the mixture of 70% H_2 and 30% He is 2.8°K/km, T_0 = 92°K. If the level T = = 170°K is taken as the starting level, we obtain the model presented in Table 85 and Fig.171 (Model 1). Kuiper (Ref.307) constructed his well-known models "a" and "b" by the same primitive technique, except that the chemical composition differed.

We assumed the total pressure at the level T = 170°K as 1.3 atm, reducing three times the quantity P = 3.8 atm in Table 81 so as to allow for the contribution of multiple scattering to the band intensity (cf. Sect.5.4, paragraph d). The amounts of H_2, He, and CH_4 are correspondingly reduced. Their mutual proportions remain the same as in Table 81. The amount of NH_3 is taken from Table 83, in accordance with the presumed level of saturation. /412

The heat of condensation of NH_3, depending on the abundance of this compound, may influence the temperature gradient to a greater or lesser extent. The adiabatic gradient, calculated with consideration of the heat of condensation, is known as the wet adiabatic gradient. Since the relative concentration of the condensing gas depends on the temperature, the value of the wet adiabatic gradient changes with altitude. Lasker (Ref.471) calculated a series of models of the Jovian atmosphere in the adiabatic region with respect to various values of the relative concentration of NH_3 at the starting level T = 170°K. It was found that the wet adiabatic gradient differs substantially from the dry adiabatic as soon as the relative concentrations of NH_3 greatly exceed 10^{-3}. For the total pressure P = 1 atm at the level T = 170°K, the relative concentration of NH_3 amounts to 5×10^{-4} so that the effect of the heat of condensation can be neglected. The heat of condensation of NH_3 can have an influence on the temperature distribution and the total density in the supracloud atmosphere only if the pressure is at least one order of magnitude lower than that adopted.

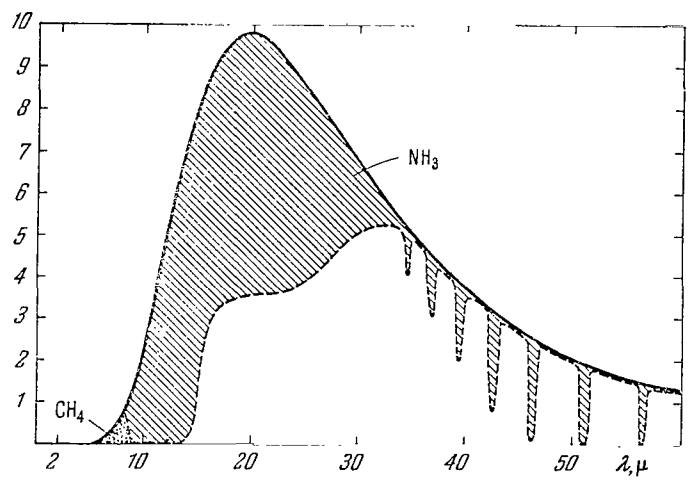

Fig.170 Transfer of Jupiter's Thermal Radiation through its Supracloud Atmosphere, Neglecting Induced H_2 Absorption. Solid line - energy distribution in the radiation spectrum of a black body of temperature T = 150°K; broken line - spectrum of same radiation when passed through a mixture of CH_4 (150 m · atm) and NH_3 (7 m · atm) (Ref.493).

Figure 170 shows the transfer of the thermal radiation of Jupiter by its supracloud atmosphere, on the assumption that this is determined only by CH_4 and NH_3. Since the major portion of the radiation is located in the region $\lambda < 20$ μ while the absorption of these gases in that region is relatively small,

it is unclear why the effective temperature of the planetary radiation (108°K, derived from the heat balance) should be lower than the brightness temperature in the region λλ 8-13 μ. Either we failed to introduce in the heat balance a major correction for the internal heat of the planet (so as to make its magnitude comparable to that of the solar heat influx) or the atmosphere contains some unknown constituent which is opaque in the region λλ 20-100 μ. Öpik (Ref.466) favored the former view and assumed that the effective temperature of the planet is actually at least 130°K. On raising T_e, he also had to raise the temperature of the stratosphere which, in its turn, entailed a rise in the mean molecular weight calculated from the scale height H and the formulation of the theory of a pure (or almost pure) helium atmosphere. As pointed out above, Öpik's estimate of the stratosphere temperature is unreliable for many reasons, even if H is well known.

Moreover, it has recently been realized that the strong opacity in the region λλ 10-150 μ may be due to induced absorption by the rotational band of H_2. Induced rotational H_2 absorption has been well investigated in the laboratory. Monochromatic coefficients of absorption in the region from 300 to 1200 cm^{-1} /413 are given in the study by Kiess, Gush, and Welsh (Ref.494). Trafton (Ref.492) calculated the "gray model" of a Jovian atmosphere of pure H_2 on taking as the absorption coefficient its mean weighted value with respect to the Planck function [T = 140°K (Ref.494)]. The effective temperature T_e was taken as 110°K, which is very close to that derived above from the condition of heat balance. The findings are presented in Table 86 [z and P were calculated by us from the data by Kiess (Ref.494)]. Only the density dependence of the absorption coefficient was taken into account. The adiabatic gradient (2.5°K/km for pure H_2) is attained at $\tau = 2.8$. As shown in Section 3.9, at sufficiently high τ the radiative gradient in a gray atmosphere consisting of diatomic molecules is always higher than the adiabatic, provided that the absorption coefficient is proportional to the square of pressure or density, which is exactly the case in the presence of induced absorption.

TABLE 86 /414

MODEL OF THE JOVIAN ATMOSPHERE ACCORDING TO TRAFTON (REF.492)
(INDUCED ABSORPTION BY ROTATIONAL SPECTRUM OF H_2)

τ	u_{H_2}, km·atm	T, °K	$\frac{d \ln T}{d \ln P}$	z, km	P, atm
0.10	4.5	94.6	0.086	39	0.10
20	6.5	98.3	132	32	14
40	9.3	104	188	26	20
80	13.5	113	249	18	28
1.60	19.8	126	310	11	43
2.50	25.6	137	341	6	57
3.00	28.4	142	350	3	60
3.50	31.1	153	357	0	63

Thus, the theory that the internal heat flux is of a magnitude comparable to that of the solar heat influx ceases to be necessary. This does not, however, dispense with the question of the possible role of internal heat in the deep layers of the atmosphere where sunlight does not penetrate. If the internal heat flux is zero, then the temperature distribution at these depths must be isothermal. However, the turbulent phenomena observed in the cloud layer of Jupiter (cf. Sect.5.2) are difficult to interpret unless it is assumed that the planet's interior more or less periodically releases large quantities of energy. It is not precluded that the convective zone of the Jovian atmosphere lacks a lower boundary as far down as the interface of the solid and gas phases of the hydrogen-helium mixture of which the bulk of the planet seems to consist (cf. Sect.5.11).

As for the temperature distribution above the convection zone, this may be quite complex, as already pointed out at the end of the preceding Section. The difference between the "measured" and the calculated temperatures of the stratosphere should not be too unexpected: The observational error itself is fairly high and our knowledge of the composition of the upper layers of the atmosphere is too schematic to warrant a concrete discussion of the causes of this difference. It should be noted only that, if T = 68°K is assumed for the occultation level, its altitude (at constant temperature gradient) must decrease to 160 km. The correspondingly revised model presented in Table 86 currently appears the most probable variant. The model is plotted in Fig.171, where it is termed "semi-empirical".

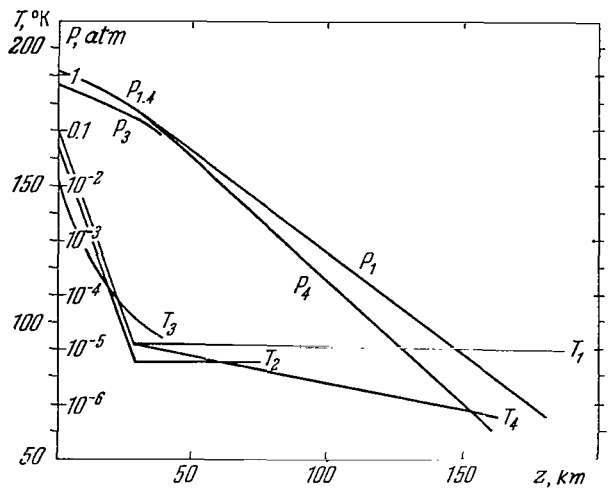

Fig.171 Models of the Jovian Atmosphere. 1 - Model of the "two-line" type, stipulating 70% H_2 and 30% He; 2 - Model "a" by Kuiper (Ref.307); 3 - Model of pure H_2, controlled by induced absorption [cf. (Ref.452)]; 4 - Semi-empirical model.

Photochemical reactions in the Jovian atmosphere were discussed by Gross and Rasool, Wildt, Cadle, and Shimizu (Ref.493, 495-497). Methane is decomposed by ultraviolet radiation of wavelength shorter than 1600 Å:

$$CH_4 + h\nu \rightarrow H + CH_3. \qquad (5.35)$$

The dissociation products enter into the following reactions /415

$$CH_3 + CH_3 + M \rightarrow C_2H_6 + M, \qquad (5.36)$$

$$H + H + M \rightarrow H_2 + M, \qquad (5.37)$$

$$CH_3 + H + M \rightarrow CH_4 + M. \quad (5.38)$$

Ethane C_2H_6 is decomposed under the effect of radiation $\lambda < 1500$ Å

$$C_2H_6 + h\nu \rightarrow 2CH_3. \quad (5.39)$$

In the presence of molecular hydrogen, the following reaction takes place:

$$CH_3 + H_2 \rightarrow CH_4 + H. \quad (5.40)$$

Reduction of CH_4 also proceeds by reaction between the methyl radical CH_3 and ethane C_2H_6:

$$CH_3 + C_2H_2 \rightarrow CH_4 + C_2H_5. \quad (5.41)$$

The reactions (5.40) and (5.41) have high activation energies (5 - 15 kcal·mol^{-1}) and apparently play no major role in the Jovian atmosphere. The absorption coefficient of CH_4 near L_α attains 400 cm^{-1} under normal conditions (cross section $s \approx 1.5 \times 10^{-17}$ cm^{-2}). The velocity of the reactions (5.36) - (5.38) in most /416 cases is known only to within one order of magnitude. The corresponding estimates [according to Cadle (Ref.496)] are given in Table 87. The dissociation

$$NH_3 + h\nu \rightarrow NH_2 + H \quad (5.42)$$

TABLE 87

VELOCITY OF CERTAIN REACTIONS BETWEEN THE DISSOCIATION PRODUCTS OF CH_4 AND NH_3 (REF.496)

Reaction	Coefficient of Velocity of Reaction, cm^6·mol^{-2}sec^{-1}
$CH_3 + CH_3 + M \rightarrow C_2H_6 + M$	7.8×10^{-30}
$CH_3 + H + M \rightarrow CH_4 + M$	10^{-31}
$H + H + M \rightarrow H_2 + M$	$(2,5 \pm 2) \times 10^{-32}$
$NH_2 + H + M \rightarrow NH_3 + M$	10^{-31}
$NH_2 + CH_3 + M \rightarrow CH_3NH_2 + M$	10^{-32}
$NH_2 + NH_2 + M \rightarrow (NH_2)_2 + M$	10^{-31}

is chiefly governed by continuous absorption and by the diffuse bands in the region λλ 1000-2200 Å. Owing to the large number of solar quanta within this region, the dissociation must proceed at an extremely fast rate. The absorption coefficient near 1342 Å reaches its maximum value of 980 cm^{-1} ($s \approx 4 \times 10^{-17}$ cm^{-2}), while near L_α it decreases to 190 cm^{-1}. The products of the dissociation of NH_3 enter into mutual reactions as well as into reactions with the products of dissociation of CH_4:

$$NH_2 + H + M \rightarrow NH_3 + M, \quad (5.43)$$
$$NH_2 + CH_3 + M \rightarrow CH_3NH_2 + M, \quad (5.44)$$
$$NH_2 + NH_2 + M \rightarrow (NH_2)_2 + M. \quad (5.45)$$

The rate coefficients of these reactions are also given in Table 87. The ultraviolet spectrum of the products of photolysis of CH_4 and NH_3 has been little investigated. It is known that ethane absorbs beginning with λ 1500 Å; hydrazine $(NH_2)_2$, beginning with λ 2700 Å; and the methyl radical, beginning with λ 2000 Å, but quantitative data are either absent or highly tentative. The direct dissociation of H_2

$$H_2 + h\nu \rightarrow H + H \quad (5.46)$$

owing to the quanta exceeding the bonding energy represents a process with an extremely small cross section (apparently smaller than 10^{-21} cm^{-2}). Probably (as in the case of molecular nitrogen in the earth's atmosphere) the dominant mechanism is dissociative recombination. First we have the ionization /417

$$H_2 + h\nu = H_2^+ + e^-, \quad (5.47)$$

which is followed by the chain of reactions [cf. (Ref.457)]:

$$H_2^+ + H_2 = H_3^+ + H, \quad (5.48)$$
$$H_3^+ + e^- = 3H, \quad (5.49)$$
$$H_3^+ + e^- = H_2 + H. \quad (5.50)$$

Cadle (Ref.496) used an electronic computer in calculating the photochemical equilibrium in the Jovian atmosphere at three levels, assuming a chemical composition close to that given in Table 80. At the level A, a total of 50% and at the level B, 90% of the L_α radiation of CH_4 is absorbed; at the level C, 50% of radiation in the region NH_3 $\lambda\lambda$ 1800-2000 Å is absorbed. The reaction rate equations (5.35) - (5.39), (5.42) - (5.45) were solved jointly in adding the reactions

$$CH_3NH_2 + h\nu \rightarrow CH_3 + NH_2 \quad (5.51)$$

and

$$(NH_2)_2 + h\nu \rightarrow 2NH_2. \quad (5.52)$$

The dissociation of H_2 at these levels is negligibly small. The findings are presented in Table 88.

It follows from these calculations that CH_4 and NH_3 must be totally decomposed in the Jovian atmosphere if the above list of reactions is complete, and the main product of photolysis must be ethane. A similar conclusion was reached by Wildt in his pioneering work (Ref.495), on the basis of a qualitative discussion of the same reactions. Thus, it must be stated that the observable presence of CH_4 and NH_3 in the Jovian atmosphere is in a sharp contrast with the photochemical equilibrium. Cadle assumed that these results could be made to agree if one could verify that H_2 weakly absorbs in the region $\lambda < 1600$ Å (an absorp-

tion coefficient of ~ 0.1 cm^{-1} is required). Wildt assumes that methane may be reduced owing to the reactions (5.40) - (5.41). However, such solutions do not seem convincing, and further investigation is needed. It must be considered that the dissociation of CH_4 and NH_3 most likely occurs at different altitudes. Since ammonia freezes, its dissociation must be appreciable already at the base of the stratosphere, whereas the level of dissociation of methane probably lies much higher.

Conflicting results also exist with respect to the dissociation altitude of H_2. Gross and Rasool (Ref.493) established that hydrogen is dissociated beginning at the level where the concentration $[H_2] \approx 10^9$ cm^{-3}, whereas Shimizu /418 (Ref.497) found this level to be much lower (concentration 3×10^{11} cm^{-3}).

TABLE 88

RATE OF PHOTOCHEMICAL DECOMPOSITION OF CH_4 AND NH_3
(Assuming a Negligible Effect of Photolysis on the Concentration and Equilibrium Concentrations of Photochemical Decomposition Products and of Subsequent Reactions (Ref.496)

Level		A	B	C
Total concentration, including H_2, cm^{-3}		4.3×10^{14}	1.5×10^{15}	3.7×10^{16}
$\frac{d(CH_4)}{dt}$, cm^{-3} sec^{-1}		1.1×10^{4}	7.4×10^{3}	0
$\frac{d(NH_3)}{dt}$, cm$^{-3}\cdot$sec^{-1}		1.2×10^{4}	4.3×10^{4}	5.0×10^{6}
Equilibrium concentration cm^{-3}	$[CH_4]$	0	0	6.4×10^{12}*
	$[NH_3]$	0	0	0
	$[H]$	0	0	0
	$[C_2H_6]$	7.4×10^{10}	2.6×10^{11}	0
	$[(NH_2)_2]$	1.3×10^{8}	3.1×10^{9}	2.9×10^{11}
	$[CH_3NH_2]$	6.9×10^{7}	2.8×10^{8}	0
	$[CH_3]$	1.8×10^{9}	7.8×10^{8}	0
	$[NH_2]$	3.3×10^{9}	8.6×10^{9}	1.2×10^{10}

* The CH_4 absorption coefficient at that level is assumed as zero.

Since the mechanism of the photolysis of H_2 is constituted by dissociative recombination, the ionosphere of Jupiter begins at roughly the same altitude as the dissociation of hydrogen. If the decameter radio emission of Jupiter is to be attributed to plasma oscillations at Langmuir frequency (cf. Sect.5.8) the electron density at the maximum must be $n_e \approx 10^7$ cm^{-3}. This raises the question as to the possible compatibility of such a high electron density (one order of

magnitude higher than in earth's ionosphere) with the small flux of ionizing radiation. The electron density is determined by the equilibrium between the rates of ionization and recombination:

$$q = \alpha n_e^2,$$

where q is the number of quanta absorbed per cm^2 per sec; n_e is the electron density; α is the recombination factor. The principal source of electrons is the absorption of ultraviolet radiation by atomic hydrogen beyond the Lyman limit: /419

$$H + h\nu \rightarrow H^+ + e^-, \quad \lambda < 912\,\text{Å}. \tag{5.53}$$

The electrons vanish as a consequence of the reactions

$$H^+ + e^- \rightarrow H + h\nu, \tag{5.54}$$

$$H_2^+ + e^- \rightarrow H_2^*, \tag{5.55}$$

and also owing to eqs.(5.49) and (5.50). The velocity of the first of these reactions (radiative recombination) is low, $\alpha \approx 10^{-12}$ $cm^3 \cdot sec^{-1}$, whereas the rate of the second reaction is high, $\alpha \approx 10^{-9}$ $cm^3 \cdot sec^{-1}$.

In the earth's ionosphere, a low electron density is maintained because of the fact that the principal process leading to the disappearance of electrons is dissociative recombination

$$O_2^+ + e^- \rightarrow O_2^*,$$

and the principal source of the O_2^+ ions is not the direct ionization of O_2 (because of the relatively small cross section) but rather the exchange reaction

$$O_2 + O^+ \rightarrow O_2^+ + O.$$

On Jupiter, the analogous reaction

$$H_2 + H^+ \rightarrow H_2^+ + H \tag{5.56}$$

is endothermic and virtually forbidden. Rishbeth (Ref.498) mentioned this as the possible cause of the high electron density in the Jovian atmosphere*. Any list of reactions influencing the electron density in the ionosphere must also include reactions with helium, but we will not give these here. Gross and Rasool (Ref.493), on the basis of a detailed analysis of all processes involved, derived $n_e \approx 4 \times 10^6$ at the ionization maximum. Shimizu obtained 1.6×10^7 cm^{-3} (Ref.497). The ionization maximum nearly coincides with the dissociation level.

The ultraviolet radiation absorbable beyond the Lyman limit leads to heating

* Note that such a situation is not possible in the ionosphere of Venus, since its upper layers must be sufficiently high in oxygen owing to the dissociation of CO_2.

of the upper atmosphere of Jupiter but, in view of the considerable distance from the sun, the temperature of this portion of the atmosphere above the absorption region cannot be high. Gross and Rasool obtained T = 140°K, assuming that the energy absorbed beyond the Lyman limit is drained downward due to heat conduction, but their calculations were not presented in sufficient detail. Obviously, the real value might depend largely on the altitude of the "heat sink" for the heat absorbed from above. /420

Let us tentatively estimate the density in the Jovian exosphere for various stipulated temperatures. Let us assume that, beginning at the level at which $n = 10^{10}$ cm^{-3}, hydrogen is completely dissociated and the other constituents of the atmosphere can be neglected. The latter is definitely true at such altitudes. We will then calculate the altitude at which the concentrations of 10^8, 10^5, 1 cm^{-3} are reached for three different temperatures: T = 150, 1500, and 5000°K. Table 89 which gives the results of this calculation shows that the altitude at which we have $n = 1$ cm^{-3} is - even for T = 5000°K - considerably less than the planet radius. In view of the absence of dissipation, the barometric formula can be applied to the Jovian exosphere virtually without restriction. Ionization in the exosphere of Jupiter probably is only partial, but even at total ionization the mean scale height will at most double in value.

TABLE 89

EXTENT OF THE JOVIAN ATMOSPHERE AS A FUNCTION OF PRESUMED TEMPERATURE (z, km)

n, cm^{-3}	T, °K		
	150	1500	5000
10^8	400	2 000	5 000
10^5	670	4 700	12 000
1	1100	9 000	24 000

It is not precluded, however, that some additional sources of heating, such as sources having to do with radiation belts, are operative in the upper atmosphere of Jupiter. The correlation of bursts of decameter emission with the rotation period of Io (cf. Sect.5.8) seems to indicate that the density of the Jovian exosphere is rather high as far up as the orbit of that satellite (R = = 420,000 km). Note that, at distances exceeding the planetary radius, the effect of the rotation on the total gravity becomes essential.

Section 5.7 Short-Wave Radio Emission of Jupiter and Magnetic Field /421

The brightness temperature of Jupiter in the microwave range was first measured at λ 3 cm in 1956 by Mayer, McCullough, and Sloanaker (Ref.130). The result (145 ± 26°K) is in satisfactory agreement with the brightness temperature in the infrared range. Subsequently, it was demonstrated that actually the temperature at λ 3 cm is higher, but at the time the observed coincidence seemed a convincing proof for the thermal origin of the microwave emission of Jupiter.

Two years later, however, Sloanaker discovered that the brightness temperature of Jupiter is unexpectedly high at λ 10 cm, being $T_B = 600$°K. This discovery was reported at the Paris Radio Astronomy Symposium, and was followed by intense studies of the radio emission spectrum of Jupiter in the decimeter range.

In recent years, the properties of the decimeter radio emission of Jupiter have been investigated in great detail. A comprehensive review of these properties can be found in papers by Mayer (Ref.132) and Roberts (Ref.500, 501) as well as in the book by V.V.Zhelezynakov (Ref.7).

The spectrum of radio emission in the wavelength range from 8 mm to 3 m is given in Fig.168 and Table 90. At λ 3 cm, only the upper limit is known (Ref.517); the point with the longest wavelength for which the intensity is known has been discovered by Gover (Ref.516). The results by Roberts and co-workers, denoted with two asterisks, were derived for a single system of power calibration and corrected for the effect of variations due to planetary rotation (reduced to the terrestrial zenomagnetic latitude 0°; see below). Nearly all of the flux values are adjusted to the distance between Earth and Jupiter (4.04 a.u.).

Table 90 and Fig.168 indicate that the flux F_ν in the region $\lambda > 10$ cm remains virtually constant and is equal to

$$F_\nu \approx 0.65 \times 10^{-25} \; w \cdot m^{-2} \cdot cycles^{-1}.$$

If the observed flux is related to the dimensions of the visible disk, then the brightness temperature can be expressed by the formula

$$T = 5.5 \times 10^4 \lambda^2, \qquad (5.57)$$

where λ is given in meters. It is obvious that thermal radiation of an optically thick layer cannot have such a spectrum, unless the opacity varies rapidly with the wavelength. An optically thin layer with an extremely high temperature (e.g., ionosphere with an electron temperature $T_e \gg 10^5$ °K) may give a spectrum of this type, but the existence of such a hot ionosphere would be difficult to explain. Thus, there is reason to believe that the observed spectrum with a /423 constant F_ν is of a nonthermal nature. Thermal emission begins to make an appreciable contribution only at centimeter waves and will be dominant only at λ 8 mm. The effect of thermal emission on the spectrum consists in elevating its short-wave end. Assuming that the nonthermal spectrum is bounded by the frequency range $\nu \leq 10^{10}$ cycles ($\lambda \geq 3$ cm), the total luminous emittance of nonthermal radiation is approximately 3×10^7 w.

Nonthermal mechanisms of radio emission had already been well investigated in astrophysics at the time of discovery of Jupiter's "excess" decimeter radio emission. It was established that the remnants of supernovae (e.g., Crab Nebula) and the so-called radio galaxies emit radio waves due to magnetic-acceleration emission of relativistic electrons in magnetic fields. This is a steady, long-time mechanism. Another type of nonthermal mechanism - plasma oscillations - accounts for the strongly variable radio emission of the disturbed sun, which consists of discrete bursts of varying intensity. This mechanism consists in the excitation of plasma oscillations by directional fluxes of charged particles ejected during solar eruptions. However, the decimeter emission of Jupiter exhibits no variations in time. Such a steady character of this emission warrants the assumption that we are dealing with magnetic bremsstrahlung.

TABLE 90

MICROWAVE RADIO EMISSION OF JUPITER

Wavelength λ, cm	Freq. ν, mc	Flux F_ν, 10^{-25} w m^{-2} x cps^{-1}	T_B °K (Flux F_ν Referred to Angular Dimensions of Visible Disk	References
0.8	37500	26*	~140	Vetukhnovskaya, Kuz'min, et al. (Ref.311) Basharinov et al. (Ref.333)
0.835	36000	25±4*	144±23	Thornton and Welch (Ref.487)
1.6	18700	7.8±0.8*	165±16	Vetukhnovskaya, Kuz'min, et al. (Ref.311)
3.02	9940	2.5±0.4*	185±30	Pariyskiy et al. (Ref.488)
3.03	9900	2.3±0.25*	171±20	Giordmaine et al. (Ref.489)
3.15	9500	1.8±0.5*	140±38	Mayer et al (Ref.130)
3.15	9500	1.9±0.25*	145±18	Mayer et al. (Ref.490)
3.15	9500	2.2±0.25*	165±20	Alsop et al. (Ref.502)
3.17	9470	2.25±0.25*	173±20	Giordmaine et al. (Ref.489)
3.3	9100	2.1±0.2*	193±20	Bibinova, Kuz'min, et al (Ref.491)
3.36	8950	2.0±0.2*	189±20	Giordmaine et al. (Ref.489)
3.75	8000	1.2*	140	Haddock and Dickel (Ref.485)
3.75	8000	1.7*	200	Drake and Ewen (Ref.503)
6.0	5000	1.0**	300	Roberts and Komissarov [cf. (Ref.501)]
6.5	4600	1.1±0.1*	324±30	Gol'nev et al. (Ref.504)
9.4	3200	0.90±0.05*	658±39	Bose et al. (Ref.505)
10.0	3000	0.78*	620	Bash, Drake, et al. (Ref.506)
10.3	2900	0.72±0.07*	640±57	Slonecker and McClain (Ref.499)
11.3	2650	0.73**	810	Roberts and Komissarov [cf. Ref.501)]
20.8	1440	0.80±0.15*	2900±400	Miller and Gary (Ref.507)
21.2	1430	0.67±0.13*	2500±500	McClain et al. (Ref.508)
21.3	1420	1.6*	6200	Epstein (Ref.509)
21.3	1414	0.75±0.06	2800±180	(Ref.510)
21.3	1410	0.73**	2800	Roberts and Komissarov [cf. Ref.501)]
22	1360	0.6	2400	Drake and Hvatum (Ref.511)
31	970	0.61*	5800	Roberts and Stanly (Ref.512)
31.2	960	0.73**	5900	Roberts and Komissarov [cf. Ref.501)]
43	700	0.65±0.13*	12 000±2000	Bzhiga and Trunova (Ref.513)
48.5	620	0.63**	12 400	Roberts and Eckers [cf. Ref.501)]
68	440	0.5	19 000	Drake and Hvatum (Ref.511)
70	430	0.63*	26 000	Keyzes and Tiberti [cf. (Ref.501)]
70	430	0.65±0.03	26 700	Hardebeck (Ref.514)
70.16	428	0.49±0.05	20 000±2660	Zakharov et al. (Ref.515)
73.5	408	0.63**	28 000	Roberts and Komissarov [cf. (Ref.501)]
154	195	0.61*	120 000	Keyzes [cf.(Ref.501)]
168	178	0.41	86 000	Gover (Ref.516)
300	101	<1	<10^6	Mills et al. (Ref.517)

* Adjusted to the distance of 4.04 a.u.
** Corrected for variations due to the diurnal rotation of Jupiter, by adjusting to zero terrestrial zenomagnetic latitude.

The discovery of Jupiter's decimeter radio emission was almost concurrent with the discovery of the earth's radiation belts. Naturally, it was almost at once hypothesized that Jupiter has similar belts of high-energy particles sustained by its magnetic field, and that the bremsstrahlung of these particles in the magnetic field is the source of nonthermal emission in the decimeter range. This idea was first qualitatively suggested in a paper by Drake and Hvatum (Ref.511) and quantitatively investigated in a number of subsequent studies (Ref.512, 518-523, 7).

Electron bremsstrahlung in a magnetic field is known as synchrotron emission

$$\sqrt{1-\frac{v^2}{c^2}} \ll 1 \quad or \quad E \gg E_0$$

(relativistic case), and as cyclotron or gyro emission

$$\sqrt{1-\frac{v^2}{c^2}} \to 1 \quad or \quad E \ll E_0$$

(nonrelativistic case). Here, v is the electron velocity; $E_0 \approx 0.5$ Mev is the energy equivalent of the rest mass of the electron ($E_0 = m_e c^2$). Electrons in /424 a magnetic field move along spiral orbits coiled around a cylindrical surface whose axis is a line of force. The radius of the surface (radius of gyration) is

$$r = \frac{mcv}{eH_\perp \sqrt{1-\frac{v^2}{c^2}}}, \tag{5.58}$$

while the gyro frequency is

$$\nu_0 = \frac{eH_\perp}{2\pi mc} \sqrt{1-\frac{v^2}{c^2}}. \tag{5.59}$$

The total intensity of radiation in every direction [cf. (Ref.524)] (luminous emittance of one electron) is

$$I = \frac{2e^4 H_\perp^2 v^2}{3m^2c^5\left(1-\frac{v^2}{c^2}\right)}. \tag{5.60}$$

In these formulas, $H_\perp$ represents the component of magnetic-field intensity at right angles to the line of force.

The motion of charged particles in a magnetic field cannot affect the constancy of the quantity

$$\frac{\sin^2\alpha}{H} = \text{const} \tag{5.61}$$

(α is the pitch angle, i.e., the angle between the directions of the magnetic field and of the motion of the electron), termed the adiabatic invariant. Assume

a field covered with dipoles. In that case, the pitch angle of the electron will increase on motion along the line of force toward one side of the magnetic equator. When the pitch angle reaches 90° the electron, as though repulsed, will start moving in the opposite direction. Therein consists the concept of the magnetic trap retaining electrons in a magnetic field (Fig.172).

In the nonrelativistic case (cyclotron mechanism) the emission frequency equals the gyro frequency

$$\nu_0 = \frac{1}{2\pi}\frac{eH_\perp}{mc}, \tag{5.62}$$

and eq.(5.60) can be rewritten in the form

$$I = \frac{16\pi^2}{3}\frac{\nu^2 e^2}{c}\frac{E}{E_0}. \tag{5.63}$$

Thus, if the decimeter emission of Jupiter is generated by electrons of subrelativistic energy, the order of magnitude of the magnetic field can be determined. The emission is observed in the range of $2 \times 10^8 - 10^{10}$ cycles. Suppose $\nu = 10^9$ cycles ($\lambda = 30$ cm). Then $H_\perp = 300$ gauss. The broad spectrum may qualitatively be explained by the presence of electrons of different energies, by the varying intensity of the magnetic field at different points, and by the variation in pitch angle. /425

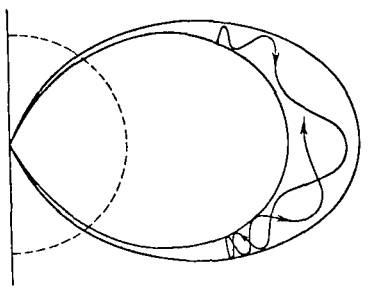

Fig.172 Diagram Showing the Meridional Projection of the Spatial Trajectory of a Charged Particle in a Magnetic Dipole Field.

On specifying, e.g., an energy of $E = 0.1\,E_0$, eq.(5.63) can be used to derive the luminous emittance per electron: $I = 4 \times 10^{-18}$ w. Assuming that the total flux of nonthermal radio emission of the planet is 3×10^7 w, the total number of particles in the belt will be $N = 10^{25}$. Assuming that the volume of the emitting region is 10 times as large as the volume of the planet (which is 1.4×10^{30} cm^3), we obtain an electron density of $n_e = 10^{-6}$ cm^{-3}, which is three orders of magnitude lower than the concentration of 40 - 100 Kev electrons in earth's outer radiation belt [flux 10^7 cm^{-2} sec^{-1}; cf. for example (Ref.525)]. The high radiation intensity is due to the strong magnetic field and the considerable extent of the emitting region. In a strong field, however, electrons must rather rapidly become de-excited. Their lifetime is

$$t = \frac{E}{I} \approx 2 \times 10^3 \text{ sec.}$$

Thus, there must exist a source of high-energy electrons or an acceleration mechanism that continually supports a steady-state concentration in the belts. A similar problem exists with respect to the terrestrial radiation belts,

the only difference being that, in this case, electrons are directly lost due to penetration into the atmosphere rather than due to radiation.

However, it should be noted that a field intensity of $\sim 10^3$ gauss is excessively high. Assuming that the magnetic moment of a planet is proportional to its mechanical moment, the magnetic moment of Jupiter must be 10^5 times as high as that of the earth. The intensity of the dipole field is proportional to R^{-3}, where R is the distance from the equivalent dipole. Since

$$\left(\frac{R_{\mathcal{U}}}{R_\oplus}\right)^3 = 1.6\times10^3,$$

the anticipated intensity at the pole of Jupiter will be 50 gauss.

A relativistic electron radiates a broad spectrum of frequencies. The greater portion of its energy is localized in the neighborhood of /426

$$\nu \approx \frac{eH}{2\pi mc\left(1-\frac{v^2}{c^2}\right)}. \tag{5.64}$$

The maximum frequency in the energy distribution [cf. for example (Ref.526)] is equal to

$$\nu_{max} = 5.4\times10^{-6}E^2, \tag{5.65}$$

where E is the energy in electron-volts. Comparing eq.(5.62) with eq.(5.64) we see that transition to relativistic electrons makes it possible to reduce the intensity of the magnetic field for a given radiation frequency ν. Assume that H_p = 50 gauss near the pole and H = 10 gauss in the emitting region. Then,

$$E = \sqrt{\frac{10^9}{5.4\times10^{-6}\times10}} \approx 5\times10^6 \text{ ev}.$$

The de-excitation time of the electron (the time during which the energy reduces to half due to losses by synchrotron radiation), expressed in years, is as follows:

$$t \approx \frac{8.35\times10^6}{H_\perp^2 \times E_0} \approx 10^{-2}, \tag{5.66}$$

i.e., maintenance of a steady-state intensity requires complete renewal of particles in the radiation belt within several days. This may be prolonged to a year on reducing the intensity of the field by one order of magnitude, but then the electron energy will increase to 20 Mev. The energy spectrum of particles in the relativistic case is linked to the emission spectrum by a very elementary relation: The exponential energy spectrum $N(E) \sim E^{-\gamma}$ corresponds to the exponential emission spectrum $I(\nu) \sim \nu^\alpha$, where $\alpha = \frac{\gamma+1}{2}$. Since for Jupiter

$\alpha = 0$, $\gamma = 1$, the spectrum has the form of $N(E) \sim E^{-1}$, i.e., is extremely smooth. In the terrestrial radiation belts, $\gamma \approx 5$. The number of electrons in the emitting regions can be estimated from the ratio

$$N = \frac{It}{E}. \tag{5.67}$$

where I is the total luminous emittance of Jupiter at decimeter waves (3×10^7 w). If $H_\perp = 1$ gauss, the total number N of particles with 20-Mev energies is $\approx 10^{29}$ or, assuming that the volume of the emitting region is 10 times as large as the volume of the planet, i.e., $V \approx 8 \times 10^{30}$ cm^3, the density will be /427

$$n = \frac{N}{V} \approx 10^{-2}\ cm^{-3},$$

which is many orders of magnitude greater than in the terrestrial radiation belts. Thus, at the maximum of the earth's outer radiation belt the flux of electrons of energy $E \approx 1.6$ Mev will be $L = 10^4$ cm^{-2} · sec^{-1} (Ref.525), which corresponds to the density

$$n = \frac{L}{c} = 3 \times 10^{-7}\ cm^{-3}.$$

Thus, the principal objection to the cyclotron mechanism is the requirement of a high field strength, while the principal objection to the synchrotron mechanism is the indispensability of a high density of relativistic particles. Assuming that the radiation belts are replenished externally by cosmic-ray particles and using the parameters specified above, a flux of 10-Mev electrons amounting to approximately 1 cm^{-2} · sec^{-1} is required, on condition that all the particles arriving at the boundary of Jupiter's magnetosphere are captured. The real flux of electrons of such energies in cosmic rays is at least two orders of magnitude smaller (Ref.527). It is not precluded, however, that the electrons are accelerated in the environs of Jupiter itself.

Magnetic bremsstrahlung is not isotropic. At low energies, its directional diagram is the same as that of an elementary dipole oriented along a line of force (torus). At relativistic energies, the electron radiates within a cone directed forward along a tangent to the line of force and having the flare angle of

$$\Delta\theta \approx \sqrt{1 - \frac{\overline{v^2}}{c^2}}.$$

In both cases, the radiation is linearly polarized if the observer is in a plane perpendicular to the line of force. At observations at an angle, circular polarization appears.

On the whole, if the magnetobrems emission hypothesis is correct, it may be expected that Jupiter's decimeter emission has the following properties: a) The size of the emission region greatly exceeds the size of the planet, as is implied by analogy with the terrestrial radiation belts; b) the emission is polarized and the electric vector is probably parallel to the magnetic equator.

Radhakrishnan and Roberts (Ref.528), on the basis of interferometric observations of Jupiter at the 31 cm wave, established that both of the above properties are present. They demonstrated that the emitting region has an extent three times as large as the planetary diameter in the equatorial plane and roughly as large as the planetary diameter in the polar direction. No circular polarization was detected (< 6%) and only linear polarization was observed: p ≈ 33%, with the electric vector being parallel to the magnetic equator with an accuracy to within ±12°. Later it was shown that the degree of polarization is somewhat less (22%) and that within the range from 11.5 to 100 cm it is independent of the frequency [Roberts and Komissarov; cf. (Ref.501)]. The flux of polarized emission was $F_p = 1.5 \times 10^{-26}$ w · m^{-2} · (cps)$^{-1}$. At high frequencies, the polarized flux decreases [$F_p = 0.8 \times 10^{-26}$ w · m^{-2} · (cps)$^{-1}$ at λ 3.75 cm], but the reason for this is unclear: It may be because the degree p of polarization decreases or because the total flux of nonthermal emission changes while p remains constant; this is essential in selecting the model. In cyclotron radiation, one and the same electron emits a low frequency near the equator and a high frequency at the ends of the trap. Near the equator polarization is greater since, in the upper latitudes, the polarization of the northern half of the belt partially compensates that of the southern half. Hence in the case of cyclotron radiation it must be expected that the degree of polarization will decrease with increasing frequency. It is as yet unclear whether the observed decrease in F_p at centimeter waves can be attributed to this factor.

/428

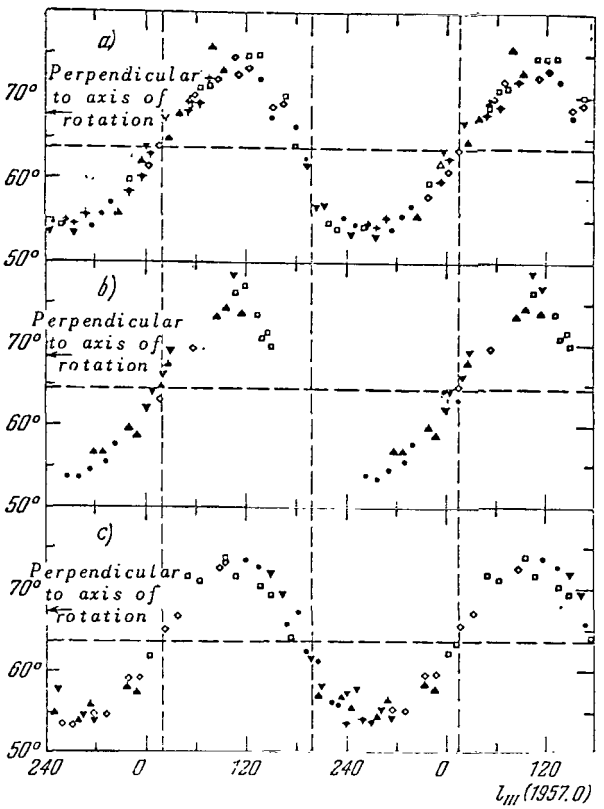

Fig.173 Position Angle of the Maximum of the Electric Vector as a Function of the Longitude in the System III. a) 21 cm, August 1963; b) 21 cm, August-September 1962; c) 11.3 cm, November 1963. Through the points corresponding to transit of the polarization plane across the median position, broken lines are drawn. These moments correspond to the spacings between minima in Fig.174. Points obtained on different days are denoted by different symbols (Ref.518).

Morris and Berge (Ref.529) found that the orientation of the polarization plane periodically varies by roughly 10%. The period of this variation equals the period of rotation in the system III with an accuracy to within ±0.5 sec (Ref.501). This means that the magnetic axis of Jupiter does not

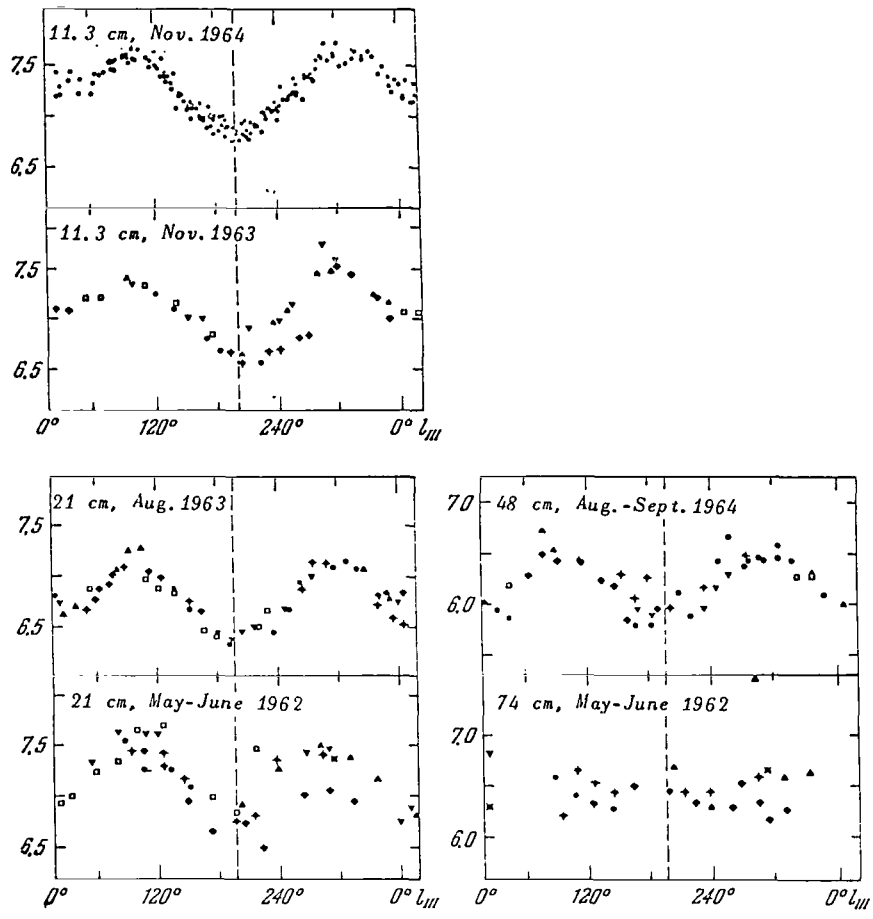

Fig.174 Periodic Variations in Total Flux from Jupiter (Sum of Both Polarizations at Various Wavelengths). Absolute values refer to the mean distance of 4.04 a.u. In each case (except for the observations at λ 11.3 cm in November 1964), observations on different days are denoted by different symbols. The 1962 observations at λ 21 and λ 74 cm were carried out simultaneously. Ordinate: power flux in units of 10^{-26} w · m^{-2} · $(cps)^{-1}$.

coincide with its axis of rotation (as is the case for the earth). The coordinates of the Jovian magnetic field in the system III, according to Roberts (Ref.501), are

$$l_{III} = 193 \pm 8°, \quad \varphi = 80 \pm 0.°5.$$

Figure 173 shows fluctuations in the orientation of the polarization plane at λ 11.3 and λ 21 cm according to observations by Roberts and Komissarov [cf. (Ref.501)]. There is a distinct non-sinusoidal pattern, which may be due either to a displacement of the equivalent dipole relative to the center of the planet or, in general, to a deviation of the field from a dipole field.

Many observers have mentioned the time-variance of intensity, even within a single night (Ref.499, 505-508). Some authors (Ref.505-508) established a correlation between the variation in intensity and the period of rotation in the system III. However, these observations were made at one polarization only. Roberts, in collaboration with Komissarov and Eckers [cf. (Ref.501)], carried out observations with a combination of both polarizations, which permits detecting the actual variations in total flux, without interference from fluctuations in the orientation of the polarization plane of the source. At λλ 11.3, 21, and 48 cm it was discovered that the total flux varies with a period equal to one- /429
half the rotation period. During one complete period, two minima are observed in the system III, one near 18° and one near 198°, with the first being somewhat weaker than the second (Fig.174). The double period of flux oscillations coincides with the period in the system III to within $\pm 0^s.8$. The minima coincide in time with the instants of transit of the polarization plane across the /430
median position (cf. Figs.173 and 174). At λ 74 cm, the flux variations are markedly smaller than in the region λλ 11-48 cm. The degree of polarization also fluctuates somewhat, with a period equal to the period of rotation (Ref.501).

Several papers mentioned long-period variations in the flux and investigated their possible correlation with solar activity (Ref.508, 530-533). Roberts (Ref.501) and Bash et al. (Ref.506) found no flux variations exceeding the observational error limits. Thus, the reality of the slow variations remains contestable.

The periodic flux variations estimated by Roberts and Komissarov satis- /431
factorily agree with the terrestrial zenomagnetic latitude (Fig.175). Here, still another property of magnetic acceleration emission, namely its directivity, manifests itself. When the earth is in the northern latitudes, we have

$$F \sim (\cos \varphi)^{4.5}, \tag{5.68}$$

and when it is in the southern latitudes,

$$F \sim (\cos \varphi)^{10}. \tag{5.69}$$

This difference constitutes one more proof of field asymmetry. Roberts and Komissarov found that these relations can be interpreted as the effect of the presence of two groups of electrons with different pitch angles: 1) electrons with pitch angles of $\sim 90^\circ$ and 2) electrons with a great variety of pitch angles. Earlier, Chang and Davis (Ref.521) and Korchak (Ref.522), in analyzing polarization on the basis of the synchrotron theory, had postulated the presence of a group of electrons with large pitch angles. It is qualitatively obvious that a substantial degree of polarization can occur only if the electrons are concentrated in the low latitudes, which requires predominance of large pitch angles. In view of the isotropy of the pitch angles, the electron concentration along the line of force is constant.

An extremely detailed brightness distribution at λ 10.4 cm was derived by Berge by the interferometric method (Fig.176). This distribution shows that Jupiter has two radiation belts, one inner and one outer. The inner belt is rather oblate toward the equator, which indicates predominance of pitch angles

close to 90°. The external boundary of the outer radiation belt in the plane of the magnetic equator has a radius of 3.5 R_0, while that of the external boundary of the inner radiation belt is $2R_0$ where R_0 is the planetary radius. Berge's observations indicate a high brightness temperature of the disk at λ 10 cm, being about 280°K.

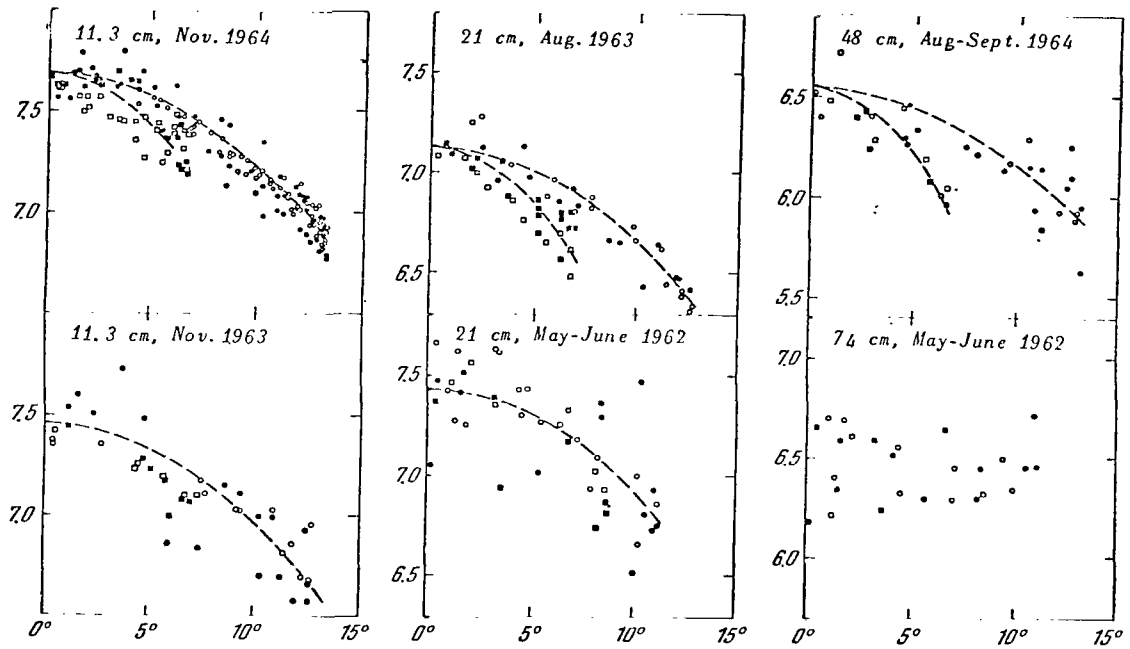

/432

Fig.175 Total Flux from Jupiter (Sum of Two Polarizations) as a Function of the Terrestrial Zenomagnetic Latitude.

If this result is reliable, it may be considered as a proof for relatively high temperatures in the deep layers of the Jovian atmosphere.

Attempts have been made at deriving the brightness distribution in the emitting region from the variation in flux during occultation of Jupiter by the moon [cf. (Ref.534)], but it was found that Jupiter is too weak a source for this method and that the accuracy is less than with the interference method. According to unpublished observations by Roberts and Clark during occultation of Jupiter by the moon [cf. (Ref.501)], the form of the source in the range from 21 to 74 cm remains unchanged.

Observations by radioastronomers at the Pulkovo Observatory (Ref.488, 504, 535) indicate that the brightness distribution at λ 6.5 cm may be represented by a Gaussian curve with the variance $\sigma = 1.5R_0$. This apparently means that the energy spectrum of particles in the inner belt is smoother than in the outer belt. At λ 3 cm, the size of the emitting region is smaller than $1.1R_0$, but there the proportion of thermal radiation already becomes too large. Most likely, the total intensity of the nonthermal component in the region λ < 10 cm decreases instead of remaining constant.

/433

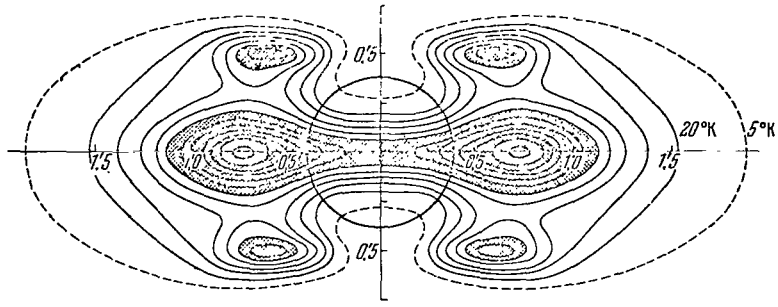

Fig.176 Distribution of Brightness Temperature over the Disk of Jupiter [λ 10.4 cm, Berge's Interferometric Observations (Ref.501)].
The "disk" component of 280°K was subtracted. Isotherms are given once every 20°K. The scale of angular dimensions (in minutes of arc) is adjusted to the distance of 4.04 a.u.

Berge and Morris (Ref.536) carried out observations of Jupiter at λ 10 cm with a two-antenna interferometer on switching the orientation of the antenna exciter as follows: 1) the polarization of both exciters is parallel to the axis of rotation or 2) one exciter is inclined at an angle of $+45^{\circ}$ to the axis of rotation and the other, at an angle of -45°. In the first case, mostly disk emission was observed and in the second, belt emission. It was found that the phase difference in the resultant interference patterns varies with a period equal to the rotation period of the system III. To quantitatively account for these variations, it must be assumed that the center of the region emitting non-thermal radiation is displaced by $0.6R_0$ with respect to the center of the planet.

However, the results of observations with a pencil beam contradict such an interpretation. Roberts and Eckers [cf. (Ref.501)] obtained a displacement of $0.15R_0$ from precision observations of the position of the centroid of the emitting region. Roberts assumed that the results of Berge and Morris may be attributed to the presence of circular polarization.

We will attempt to sum up the foregoing: Spectrum, polarization, dimensions, brightness distribution, periodic variations in the polarization plane, and total flux - in one word, nearly all of the diverse information available on the decimeter radio emission of Jupiter satisfactorily fits the hypothesis of magnetic bremsstrahlung of electrons in the Jovian radiation belts. The question of intensity of the thermal radiation of the disk at λ < 10 cm is unclear. It is suspected that in the range of 3 - 10 cm the brightness temperature of the disk is considerably higher than its infrared temperature. The available data are not sufficient to estimate the magnetic field and particle energy of the radiation belts. The strong circular polarization of the bursts of radio emission in the decameter range implies that H > 10 gauss (Ref.501). V.V.Zheleznyakov (Ref.7, 523) mentioned that, in the presence of a magnetic field of $H \approx 10^3$ gauss and a plasma density of the order of several tens of cm^{-3} in the exosphere, Faraday rotation should blur the polarization. It is not precluded, however, that the plasma density is much less, considering that the temperature of the

/434

Jovian exosphere is probably low.

Section 5.8 Decameter Radio Emission. Tentative Radar Observations of Jupiter

In Sections 5.6 and 5.7 we discussed two components of the radio emission of Jupiter, both of which have an essentially different nature: thermal radio emission of the disk and magnetic bremsstrahlung of the particles captured in the radiation belts around that planet. At centimeter waves, these components combine so well that they are difficult to isolate. In this Section we will deal with a third component of radio emission of Jupiter, namely sporadic

/435

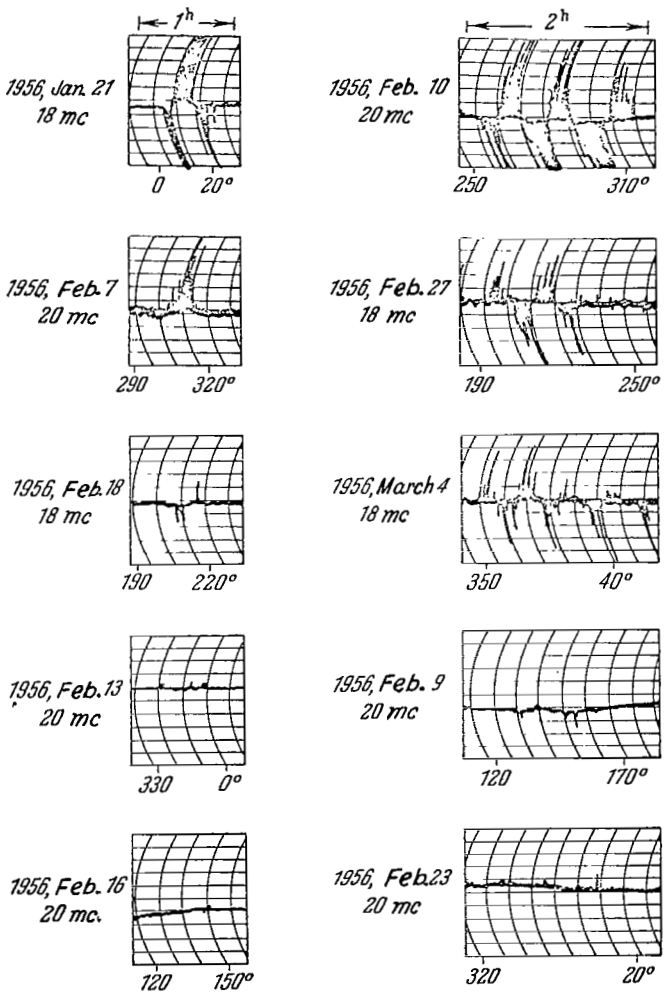

Fig.177 Sample Traces of Sporadic Radio Emission of Jupiter with Varying Pulse Density (Ref.537).

decameter radio emission. Like decimeter emission, decameter emission also is nonthermal but differs greatly both in observed properties and in physical nature.

In 1955, during adjustments of a large Mills cross radiometer at the Carnegie Institute in Washington, a strong cosmic source of radio emission of variable intensity was discovered at the frequency of 22 megacycles. Subsequent daily observations showed a variation in the right ascension of that source. It became clear that radio emission of some planet was being observed. This planet turned out to be Jupiter. It should be noted that, prior to the detection of Jupiter's decameter radio emission, no planets were included in the list of sources of cosmic radio emission. The report on this discovery was published /436 by Burke and Franklin (Ref.537), but subsequent analysis of older traces revealed that the same antenna had been used by Burke and Smith to receive radio emission from Jupiter as early as 1954 and that Shain had also received it with his decameter radiotelescope in 1950 (Ref.538). Jupiter was not identified in these earlier observations, because of the sporadic nature of decameter emission: This consists of short bursts (Fig.177) that cluster into noise storms lasting from several minutes to several hours. Emission of this type is easily confused with industrial noise. It is interesting that in the case of Venus the inverse phenomenon occurred: A published report on the discovery of sporadic radio emission of Venus was traced to the effect of industrial and solar noise.

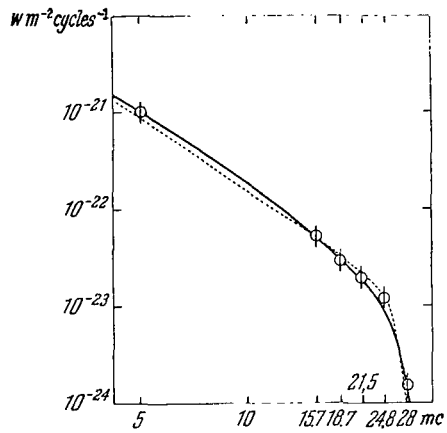

Fig.178 Mean Power Spectrum of Jupiter's Decameter Radio Emission (Ref.542).

During noise storms at frequencies below 30 mc, Jupiter, next to the sun, is the most intense source of radio emission in the entire sky. Following the discovery of Jupiter's sporadic decameter radio emission many authors, chiefly in the United States and Australia, began to investigate it systematically. A detailed survey may be found in the works by Burke, Galle, Roberts, Zheleznyakov, and Ellis (Ref.539, 540, 500, 7, and 541).

Sporadic radio emission of Jupiter has never been detected at frequencies of $\nu > 43$ mc. In the low-frequency direction, the observations were performed down to 5 mc as the lowest frequency still generally accessible to systematic earth-based observations (and at that only under particularly favorable conditions, since the critical frequency of the ionosphere normally restricts the long-wave limit of radio astronomy studies to a region of approximately 15-20 mc). The mean power spectrum is given in Fig.178; it rises steeply from high to low frequencies. The total power of the decameter radio emission of the planet is 5×10^{10} w (Ref.543).

The duration of discrete bursts responsible for the noise storms ranges

from 10^{-3} sec to several minutes [cf., for example (Ref.543-546)]. Dynamic spectra (Ref.546-548) of decameter bursts (spectra with time scan) showed /437
that the individual bursts are confined to a narrow frequency range of a width of $\Delta\nu \approx 0.5$ mc; the frequency of a group of bursts may vary slowly, at the rate of roughly one megacycle per minute. Riihimaa (Ref.546, 548) investigated the fine structure of the individual bursts with a time resolution of 0.1 sec, while Warwick used a time resolution of 1.3 sec (Ref.547).

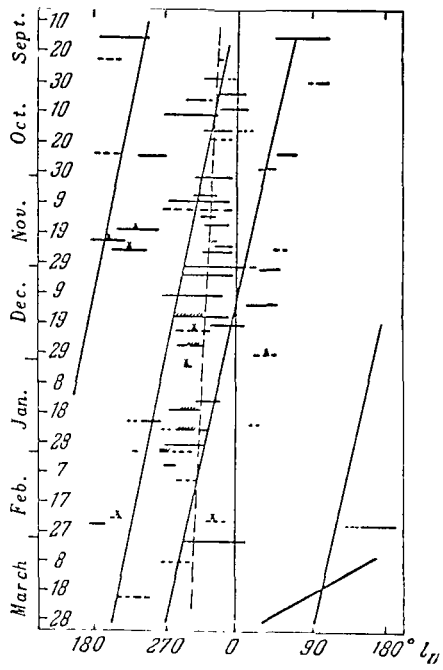

Fig.179 Drift of Central Meridian in the Longitude System II for Cases of Occurrence of Bursts of Radio Emission at 19.7-mc Frequency in 1955-1956 (Ref.546).

The frequency of occurrence and mean power of the bursts vary with a period close to that of the system II but not identical with it (Fig.179). Douglas (Ref.550), based on a statistical analysis of observations, found the repetition period to be $T = 9^h55^m29^s.37 \pm 0.13$. This value of T was adopted in 1962 by the International Astronomical Union as the rotation period of the system III, i.e., of a new longitude system associated with the radio emission of the planet rather than with the rotation of visible markings. Carr and associates (Ref.555) found $T = 9^h55^m29^s.35$. Douglas (Ref.551) and Galle (Ref.540) considered the question of constancy of the period. Galle found that during 1956-1957 the period was 1 sec longer than during 1951-1957. Douglas found no variations exceeding the limits of statistical indeterminacy. Smith, Lebo, et al. (Ref.553) detected a sharp variation in the rotation period of decameter sources on Jupiter after 1960: The period increased by approximately 1.2 sec, and an appreciable drift of the longitude of the central meridian appeared in the system III, at the rate of $10^\circ.45$ per year. It was roughly then that the rotational velocity of the Great Red Spot also changed substantially (Fig.180). However, it should be noted that the rotation periods of the system III and the Red Spot differ too much to consider the Spot itself as the source of radio emission. Attempts at simultaneous observation of Jupiter /438
in the optical and decameter ranges were unsuccessful in identifying the bursts with the phenomena visible on the disk (transit of some marking across the meridian, eruption, etc.).

Many investigators studied the probability of occurrence of bursts as a function of longitude of the central meridian. The available data on the mean power of emission as a function of longitude are much more scarce. Figure 181 presents longitudinal profiles of both types from data by McCullough et al. (Ref.542). The profiles vary substantially with frequency. At ~ 20 mc, there occurs a pronounced peak in the interval 200 - 280°, with secondary peaks near

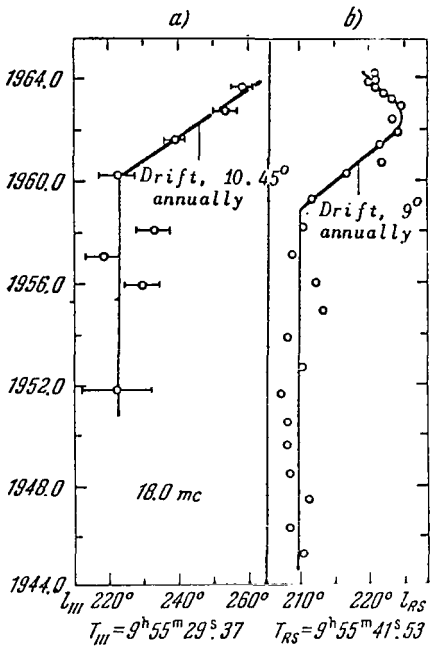

Fig.180
a - Drift of source of decameter emission in the longitude system III (1957.0); b - Drift of Red Spot in a special system, selected to reduce to a minimum the movements between 1945 and 1955 (Ref.553).

90 - 160° and 300°. As the frequency decreases, the relative magnitude of the secondary peaks also decreases. At a frequency of 5 mc, bursts are observed on nearly every longitude. In the mean power profiles, the longitude dependence is more distinct. At 5 mc, the mean power profile resembles a sine curve with maxima near l_{III} 160° and 330°. Figure 182 gives a graphical representation of the longitude and frequency dependence of integral power in the form of a chart with isophotes. It is interesting that, at ν = 10 mc, the peaks at l_{III} 130° and 240° disappear while the peaks near 175° and 330° become sharper. The characteristics of spectrograms with time scan also recur with a period equal to the period of the system III (Ref.552). The mean emission frequency tends to increase in time near the longitude l_{III} = = 130° and to decrease near l_{III} = 270°.

The limited width of the peaks in the longitude distribution of the frequency of occurrence of the bursts permits drawing two conclusions: a) The sources of decameter emission occupy only part of the /439 planetary surface; b) the emission is directional. The directional diagram θ and the longitudinal extent Δl of the sources are linked by the relation $L \approx \Delta l + \theta$, where L is the observed peak width in longitudinal distribution. It is not precluded that, generally speaking, the sources are virtually point sources and that $\theta \approx L$.

However, the time dependence of the frequency of occurrence of bursts contains periods that are longer than the period of axial rotation of the planet. Bigg (Ref.554) found that one of these periods, which is very distinctly expressed, coincides with the period of revolution of Io (Fig.183). The strongest noise storms occur close to the moments of transit of Io across positions of maximum elongation. McCullough and Ellis (Ref.542) confirmed this surprising correlation. They observed it at frequencies of 28, 24.5, and 4.7 mc. At lower frequencies the dependence is less pronounced.

Bursts of decameter emission appear to be statistically related to solar activity. Carr et al. (Ref.555), based on 1957-1960 observations, derived an explicit negative correlation with the number of sunspots. The 1958 solar activity maximum corresponded to the minimum of the decameter bursts. During 1961-1964, however, the frequency of occurrence of bursts again decreased /440 distinctly (Ref.541), i.e., a positive correlation occurred. Douglas established an increase in the frequency of occurrence of bursts on the days following solar flares, but the statistical effect was relatively indistinct. Warwick,

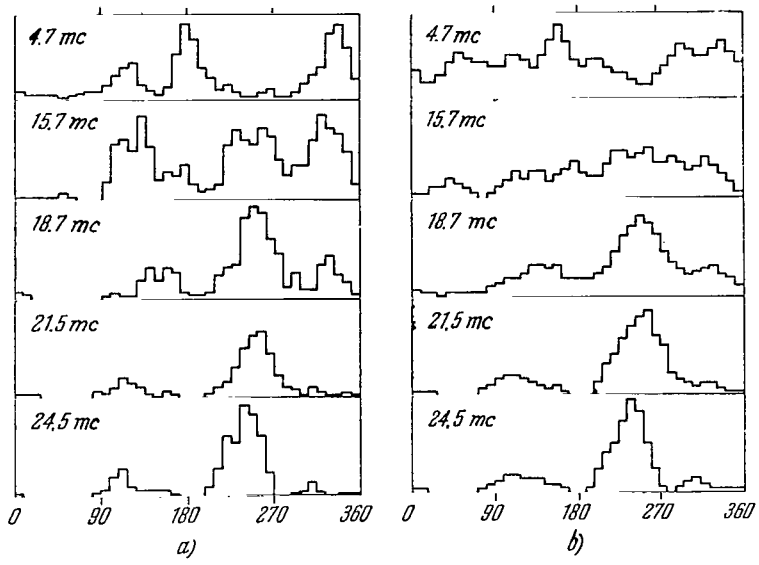

Fig.181 Longitude Distribution (System III) of the Frequency of Occurrence (a) and Mean Power (b) of Bursts (Ref.542).

utilizing only days on which Jupiter was observed at frequencies above 30 mc, established a consistent increase in the frequency of occurrence of bursts within 1 - 2 days following solar disturbances (Ref.556). This time lag corresponds to the transit time of the agent from the sun at a velocity of $\sim 10^4$ km · sec^{-1} It may be that this agent is represented by fluxes of high-energy protons that arise during chromosphere flares. The ordinary geoactive corpuscular fluxes propagate at the velocity of $\sim 10^3$ km · sec^{-1}. If one and the same flux perturbs both the terrestrial and the Jovian magnetospheres, then the lag must be about one week. Carr, Smith, and Bollhagen found that this relationship indeed takes place (Ref.557).

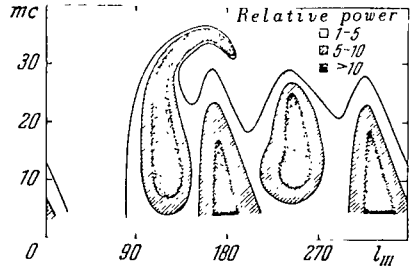

Fig.182 Dependence of Integral Power of Bursts on Emission Frequency and Longitude (Ref.541).

Franklin and Burke (Ref.558) discovered circular polarization of the emission of decameter bursts. The degree of polarization in some cases reached 100%. Direct rotation predominated (if viewed in the direction of propagation). Carr et al. (Ref.555) also found, at the 22-mc frequency, that decameter emission is polarized circularly or elliptically. Gardner and Shain (Ref.549) obtained the same result at the 19.6-mc frequency. The assumption that the rotation is of the direct type is based on observations in the Northern and Southern Hemispheres, which means that the observed polarization /441 is not associated with the terrestrial ionosphere. Barrow (Ref.559) found that

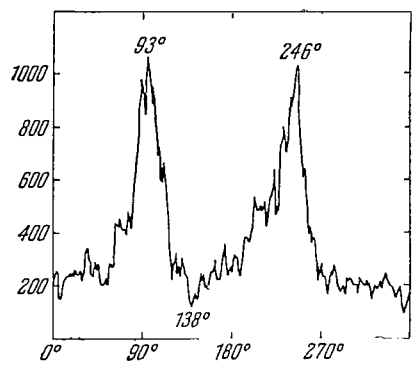

Fig.183 Correlation of the Frequency of Occurrence of Decameter Bursts with the Period of Revolution of Io during 1961-1963 (Ref.554). The Joviocentric longitude of Io, reckoned from the position of superior geocentric conjunction, and the mathematical product of the total power of the bursts and their duration during each 10-minute interval are plotted along the axes.

at 18.3 mc the proportion of bursts with right-handed polarization is smaller than at 2.4 mc. Sherrill and Castler (Ref.560), with the aid of an adjustable receiver, discovered that within the 15 to 24-mc range the proportion of bursts with right-handed polarization decreases with increasing frequency. Dowden (Ref.561), from observations at the 10-mc frequency, found that bursts with right- and left-handed polarization are irregularly distributed longitudinally (Fig.184).

It is well known that the flux of radio emission from cosmic sources undergoes variations owing to density fluctuations of the ionosphere. This phenomenon is analogous to the twinkling of stars due to density fluctuations of the troposphere. As the frequency decreases, the flicker of radio sources increases. Near the 20-mc frequency it may reach 100%. The smaller the angular dimensions of the source the stronger will be the flicker. This naturally raised the question whether the fine structure of Jupiter's decameter bursts may not be entirely or largely conditioned by this flicker.

To verify this, Gardner and Shain (Ref.549) carried out simultaneous observations of decameter-wave bursts with radiotelescopes spaced 25 km apart. The time dependence of the intensity as established for the two instruments, differed greatly. Ellis and McCullough, as well as McCullough and Slee [cf. (Ref.541)], carried out similar observations with bases of 150 and 10,000 m, while Douglas and Smith (Ref.562) used a base ranging from 15 to 100 km. It was found that, at different times, widely varying degrees of correlation apply. Sometimes,

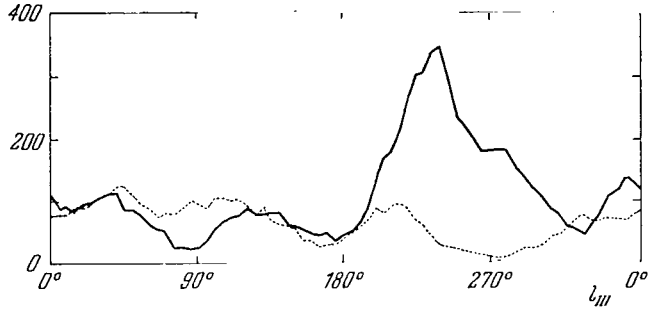

Fig.184 Longitudinal Distribution of Bursts with Right-Handed (Solid Line) and Left-Handed (Broken Line) Polarization at the 10-mc Frequency (Ref.560). Number of bursts, along ordinate.

groups of bursts are observed at one station but not at the other, even if its base reaches 150 m. At other times, at sufficiently long bases, complete correspondence is observed even for bursts shorter than 10^{-2} sec. Slee and Higgins (Ref.563), using an interferometer with phase shift and a base of 30 km, often obtained completely satisfactory traces of the decameter emission of Jupiter. Thus, the ionosphere does not interfere with observations at high angular resolution. Such observations indicate that the upper limit of the diameter of the source is 19". The general conclusion drawn from observations of Jupiter's decameter emission by means of spaced stations is as follows: The emission actually takes the form of bursts with a duration of at least 10^{-2} sec and longer, but during its passage across the earth's ionosphere it is sometimes strongly modulated by the inhomogeneities of the latter. /442

The question of the origin of decameter bursts has not been conclusively settled. Originally, it was assumed that these bursts represent the radio emission of thunderstorm discharges similar to terrestrial lightnings (Ref.564). The attendant directivity was attributed to the internal bouncing of radio waves off Jupiter's ionosphere (Ref.540). If the critical frequency of the ionosphere equals ν_0, then the ionosphere emits within a cone directed toward the zenith, with a vertex half-angle α determined from the formula

$$\cos\alpha = \frac{\nu_0}{\nu}, \tag{5.70}$$

where ν is the emission frequency. Since bursts at frequencies as low as 5 mc are observed, it follows that $\nu_0 < 5$ mc and that the electron density in the ionosphere $n_e < 3 \times 10^5$ cm^{-3}. Observations in fact point to an increase in α with increasing ν, but the rate of this increase is less great than implied by eq.(5.70).

The decisive objection to this was raised by V.V.Zheleznyakov (Ref.7, 565): The band width of the individual bursts ($\Delta\nu/\nu \approx 5 \times 10^{-2}$) is much less than the band emitted by thunderstorm discharges ($\Delta\nu/\nu \approx 1$). Moreover, the exact coincidence of the period of intensity fluctuations of decimeter and decameter emission means that the position of the decameter sources is closely associated with the magnetic field rather than with the cloud layer of the planet as might be expected in the case of thunderstorm discharges.

The small relative width of the burst spectrum suggests that the emission is generated by collective effects in plasma. V.V.Zheleznyakov suggested that decameter bursts are generated by plasma oscillations in the Jovian ionosphere. In the presence of local disturbances in the quasi-neutrality of plasma, recovery is accompanied by the occurrence of natural plasma oscillations at frequencies close to the Langmuir frequency /443

$$\omega_L = \sqrt{\frac{4\pi e^2 n_e}{m}}. \tag{5.71}$$

Plasma oscillations are longitudinal, but under certain conditions the transverse component arises along with transformation to electromagnetic radiation, whose frequencies are close to ω_L. To cause emission at the 20-mc frequency in

the ionosphere, an electron density of $n_e \approx 10^7$ is required. As was shown in Section 5.6, values of n_e close to the above may indeed occur if the effective recombination factor is determined by radiative recombination.

If ω exactly equals ω_L, then the refractive index of the plasma is zero. Hence escape of radiation from the region of generation is possible only at frequencies other than ω_L. This contradiction is resolved when considering that a spectrum of finite width is actually generated. The transformation of plasma waves into electromagnetic waves and their propagation beyond the confines of the generation region are possible only within a limited range of angles, which accounts for the directivity within the above hypothesis.

In a magnetic field, plasma waves arise not only at the frequencies $\omega \approx \omega_L$ but also near the gyro frequency

$$\omega_H = \frac{eH}{mc}.$$

Such a possibility was analyzed by Zheleznyakov (Ref.7), Warwick (Ref.566), and Ellis (Ref.541). In this case, a burst at the frequency ω_H arises at the point where

$$H \approx \frac{mc\omega}{e}.$$

Since sporadic emission is observed roughly within the limits from 5 to 35 mc, the field strength in the ionosphere is 2 - 12 gauss. To have an emission of a frequency $\nu \geq 5$ mc escape from the ionosphere, a sufficiently low Langmuir frequency ω_L is required, which gives $n_e \leq 3 \times 10^5$. When $\omega_L \ll \omega_H$, the excitation of plasma waves occurs within a narrow frequency range, so that the limited width of the frequency spectrum of individual bursts in this case finds a more natural explanation.

The reason for the limited extent of the sources in terms of longitude lies in the fact that the magnetic field varies with longitude owing to a /444
shift in the equivalent dipole with respect to the planetary center or owing to deviation of the field from an ideal dipole field.

The highest frequencies must be generated in the region where H reaches its maximum. In view of the directivity of emission during the approach of that region to the central meridian, the frequency drift must increase in the direction of higher frequencies and subsequently, following transit across the meridian, in the opposite direction, which is in agreement with actual observations.

In a magnetic field, plasma becomes birefringent and waves of two types arise: ordinary and extraordinary waves, circularly polarized in opposite direction.

Zheleznyakov showed that the directivity may be explained by assuming that the plasma waves are chiefly converted to extraordinary waves. This also logically accounts for the dominant pattern of polarization.

The mechanism of excitation of plasma waves is obscure. The following two possibilities have been mentioned: a) shock waves (Ref.7, 565), which may propagate upward during atmospheric eruptions; b) electron fluxes from the radiation belts (Ref.541, 566). This logically suggests that decameter bursts might be directly attributed to the cyclotron radiation of fast electrons. If the field strength near the planetary surface is close to 10 gauss, then synchrotron radiation of electrons with an energy of several megavolts in the radiation belts will be observed in the decimeter range, whereas cyclotron radiation of electrons with lower energies (10 - 100 kev) will occur in the decameter range. This does not explain why the decameter emission is of sporadic character. Moreover, since the generation of radio waves is no longer directly associated with the ionosphere, emission will also take place at considerable distances from the surface. In this case, emission at various frequencies arises at various altitudes and the frequency drift is ruled by the movement of electron clouds along the lines of force. To account for the directivity, it must be assumed that the ratio $\frac{\omega_L}{\omega_H}$ is not very low even at great distances from the surface. For example, for an interpretation of the bursts at 5 mc, within the frame of this hypothesis, it is necessary that $n_e \approx 10^3$ cm^{-3} at a distance of 10^5 km.

The phenomenon most difficult to interpret is the relationship between the decameter radio emission of Jupiter and the rotation of Io. Not one of the theories known to us can adequately account for the increase in the frequency of bursts at the time of maximum elongation of Io. There naturally arises the /445 suspicion that the sources of decameter emission are located, at least in part, at a considerable distance from the planet. Note that the Jovian magnetosphere may extend over several tens of planetary radii even in the presence of moderate field intensities at the surface (H ≈ 10 gauss). This is implied by a comparison of the energy density of the magnetic field at the periphery and the energy density of the solar wind (Ref.567). The interaction between Io and electrons with near-relativistic energies cannot cause perturbations, since the velocity of Io is too low. Apparently, the low-temperature plasma in the Jovian exosphere retains an appreciable density over extremely great distances, encompassing the orbit of Io (420,000 km).

Landovitz and Marshall (Ref.568) mentioned that the decameter emission of Jupiter may be generated by induced spin transitions of electrons in a magnetic field. The equilibrium distribution of spins in a static magnetic field is upset by the influx of solar corpuscles into the magnetosphere, resulting in a negative coefficient of absorption and generation. Emission is generated at the gyro frequency.

An original idea was proposed by the Stroms (Ref.569): They suggested that the decameter bursts constitute an effect of focusing of the emission of distant cosmic sources by the ionosphere of Jupiter, but the basic properties of decameter bursts - their directivity, periodicity, fine structure, narrowness of band, and polarization - are not covered by this hypothesis. Thus, there is no reason to seriously consider it.

In conclusion, a few words should be said on radar soundings of Jupiter. The team directed by V.A.Kotel'nikov (Ref.570) carried out such soundings of

Jupiter in 1963 at λ 43 cm. A positive result was obtained: The reflection factor of Jupiter at this wavelength is at least 10%. Goldstein (Ref.571) also was successful in receiving radar signatures from Jupiter at λ 12.5 cm at the California Institute of Technology. The dimensions of the effective reflecting region, according to another author (Ref.570), are approximately 10,000 km, which indicates a considerable surface smoothness of the planet.

However, a recent attempt to detect radar signals bounced off Jupiter, carried out at the world's largest radar installation in Arecibo in Puerto Rico (at λ 70 cm), gave a negative result (Ref.572). The upper limit of the reflection factor for Jupiter was found to be roughly two orders of magnitude lower than the reflection factors derived by Kotel'nikov and Goldstein.

Section 5.9 Saturn /446

The semimajor axis of Saturn's orbit is 9.5 a.u. The solar heat received by this planet is two orders of magnitude less than that received by the earth. Its orbit has considerable eccentricity (0.056), its sidereal period of rotation is 29.5 years, and its synodic period 378 days. According to Rabe's survey (Ref.412) the equatorial diameter of this planet is R_e = 60,300 ± 250 km, i.e., 9.5 times larger than that of the earth. The compression is rather considerable, ε = 0.094, which is more than that of all the other planets. The compression derived from direct measurements of angular diameter virtually coincides with that derived from the motion of the satellites. According to other authors (Ref.77), the mass of Saturn is

$$\frac{M_\odot}{3500} = 95.5M_\oplus = 5.7\times10^{28}gm,$$

and its mean density is $\bar{\rho}$ = 0.7, which is half that of Jupiter. It is assumed that the equatorial plane of Saturn coincides with the plane of its rings. The inclination of the equator to the ecliptic is 26°44', which is much greater than for Jupiter and even somewhat higher than for the earth and Mars. The acceleration due to gravity (total, including centrifugal) on the equator is known to be 954 cm · sec^{-2}.

In the pattern of the markings visible on its disk (Fig.185), Saturn resembles Jupiter (dark belts and bright zones), but the contrast between the belts and zones is much less. In general, the number of observable small mottlings and fine markings is considerably lower. The nomenclature of the belts and zones is the same as that applied to Jupiter's belts and zones. The period of rotation at the equator is $10^h14^m.5$. The temperate and tropical latitudes rotate at an appreciably slower rate. The information on the movement of the bright and dark spots is much less extensive than in the case of Jupiter.

A review of the pertinent findings is contained in the paper by Cragg (Ref.573). Moore (Ref.574) made spectroscopic determinations of the rotational velocity at latitudes 0, ±27, ±42, and ±57° according to the Doppler inclination of the lines. Figure 186 presents the latitude dependence of the rotational period according to spectroscopic observations and rotation of the markings (Ref.573). At latitude 50°, the rotational period is approximately 10^h40^m.

Recently, this finding was confirmed by Dollfus (Ref.575).

Spectra of Saturn with low and medium dispersion in the visible and photographic infrared regions were studied by Slipher (Ref.436, 437); see Fig.148. The identified bands are given in Table 72. The CH_4 bands in Saturn's spectrum are roughly twice as strong as in Jupiter's; NH_3 bands are absent. Dunham found NH_3 lines on high-dispersion spectrograms of Saturn (Ref.111) but Kuiper's survey (Ref.4) specified only the upper limit of equivalent path of NH_3 /447 (2.5 m • atm). The equivalent path of CH_4, according to Kuiper, is 350 m • atm.

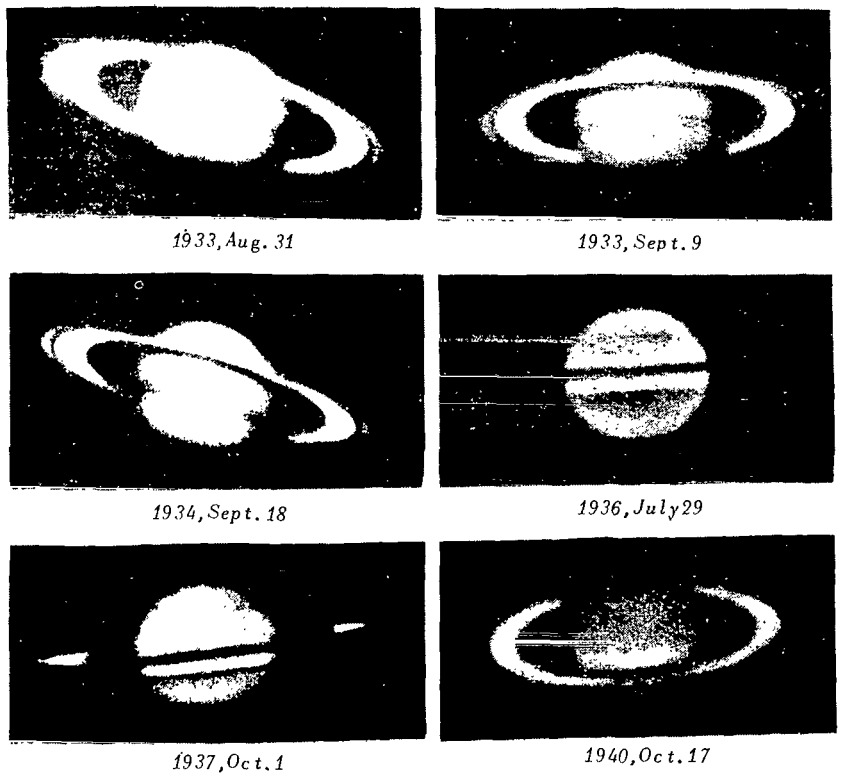

Fig.185 Saturn.

Hess (Ref.462) investigated variations in the band intensities over the disk of Saturn. He established that, at the middle and upper latitudes, the equivalent width of the band λ 6190 Å is greater than on the equator.

Münch and Spinrad (Ref.576) discovered in Saturn's spectrum the lines S(1) and S(0) of the H_2 band (4-0) (quadrupole radiation). No quantitative estimates of intensity were given, but it is obvious that the content of molecular hydrogen in Saturn's atmosphere is extremely high. If the relative chemical composition of the atmospheres of Jupiter and Saturn is the same, then the total pressure /448 above the cloud layer also must be similar for both planets: in the case of Saturn, the amount of gas is larger but the gravity, on the other hand, is

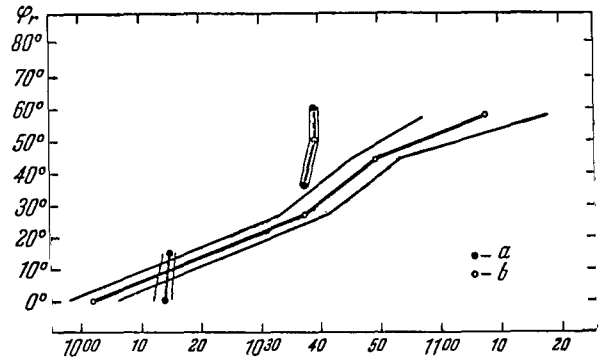

Fig.186 Dependence of the Rotation Period of Saturn on Latitude.
a - Determined from the movement of spots;
b - Determined spectroscopically. The thin lines in the case of a) represent the probable observational error and in the case of b) the scatter of the rates of motion (Ref.573).

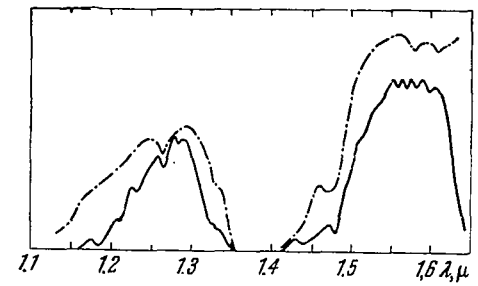

Fig.188 Spectrum of Saturn's Disk (Solid Line) in the Region λλ 1.1-1.6 μ. Average of Six Traces Recorded on Oct.16, 1964.
Shain reflector, diffraction spectrometer, grating of 300 rulings/mm, slits 2.2 and 2.5 mm (100 Å), recording speed 7.3 Å/sec, τ = 4.4 sec, z = 58-72°; dot-dash line - solar spectrum (Ref.443).

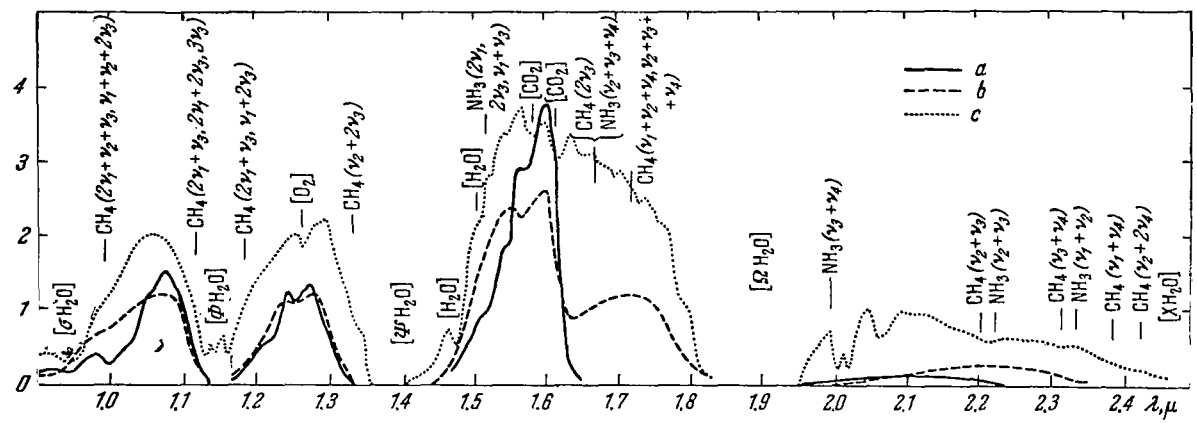

Fig.187 Spectra of Jupiter (a) and Saturn (b) in the Region λλ 1.2-5 μ According to Observations in 1960 (Ref.442); c - Solar Spectrum.
During observations of Saturn, the light from the rings went outside the slit.

smaller. Note again (cf. Sect.2.6) that a total pressure of ~ 2 atm has been derived for Jupiter.

Kuiper (Ref.4, 440) and the present writer (Ref.442, 443) derived the spectrum of Saturn in the region λλ 1-2.5 μ with photoelectric spectrometers equipped with lead-sulfide photovaristors. Averaged traces are shown in Figs.187 - 189. As in the spectrum of Jupiter, here also strong CH_4 bands were identified. No strong NH_3 band was detected at λ 1.51 μ. The upper limit of the content of NH_3 derived from this band (taking into account the effect of chemical composition, temperature and pressure) is 50 cm • atm. The actual presence of NH_3 lines in Saturn's spectrum still needs verification. A reasonable estimate of the equivalent path of NH_3 in Saturn's atmosphere would be a means of deriving the saturation temperature. The adiabatic gradient in Saturn's atmosphere (if $He:H_2 = 0.36$) is

$$\frac{dT}{dz} = 1.1\ ^\circ\mathrm{K}/km$$

whence, in accordance with Table 83, the upper limit of $T_{sat} \leq 140^\circ K$, assuming that $u_{NH_3} \leq 50$ cm • atm.

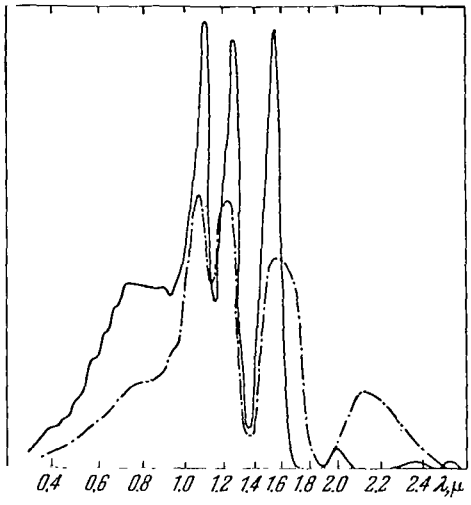

Fig.189 Spectrum of Saturn's Disk (Solid Line) in the Region λλ 0.6-2.5 μ. Shain reflector, single trace prism spectrometer, slit 1 mm (0.09 μ near 1.6 μ), τ = = 4.4 sec, recording speed 70 Å/sec, z = 65°. Dot-dash line - solar spectrum.

Pettit and Nicholson (Ref.125) as well as Menzel, Coblentz, and Lampland (Ref.473) estimated the brightness temperatures in the region λλ 8-13 μ as 125 and 120°K, respectively. On this basis, it was assumed (Ref.307) that the emitting agent, as in the case of Jupiter, is NH_3. However, current measurements give much lower temperatures, which do not fit this hypothesis. Thus, Low (Ref.477) derived $T_B = 93 \pm 3^\circ K$ within the same wavelength range. In another paper (Ref.577), Low gave a different value: $T_B = 85 \pm 2^\circ K$. Murray and Wildey (Ref.474) specified the upper limit of T_B as ≤ 105°K. The content of NH_3 above the level with a temperature 100°K is $u_{NH_3} < 10^{-5}$ cm, while it is $\tau_{NH_3} \ll 1$ in the window λλ 8-13 μ. Consequently, NH_3 cannot be the agent responsible for the emission in the interval λλ 8-13 μ. The above estimates of T_B are very close to the melting point of methane (89°K) and, if they are correct, the thermal radiation of Saturn in the window λλ 8-13 μ is most likely directly emitted by a cloud layer consisting of particles of solid CH_4. The saturated vapor pressure (in mb) of methane near the melting point, according to (Ref.578), is expressed by the formula

/450

$$\log P = \frac{-516}{T} + 7.51, \qquad (5.72)$$

from which follows the density (in amagat) /451

$$\log\rho = \frac{-516}{T} - \log T + 6.95, \tag{5.73}$$

and the scale height for saturation

$$H_{CH_4} = \frac{T^2}{1190\frac{dT}{dz}} \tag{5.74}$$

as well as the amount of CH_4 above a level with a given temperature

$$u = \rho H_{CH_4}\ cm\cdot atm. \tag{5.75}$$

Table 91 presents the values of P_{CH_4}, H, and u_{CH_4} for several different temperatures. The gradient $\frac{dT}{dz}$ = 1°K/km is adopted.

Thus, the equivalent path of CH_4 (350 m · atm) is a means of tentatively estimating the saturation temperature of methane $T_{sat} \approx 80°K$, in close agreement with the brightness temperature given by Low. Note that the mean scale height in Saturn's atmosphere at the level T = 85°K (H = 28 km) is higher than H_{CH_4} at T < 100°K, assuming that the mean molecular weight is u = 2.6 (same as for Jupiter; cf. Table 81). Hence, if CH_4 is saturated at the level with this temperature, the saturation also will persist at higher altitudes so long as eq.(5.32a) remains valid.

TABLE 91

AMOUNT OF CH_4 ABOVE LEVELS AT GIVEN TEMPERATURES UNDER SATURATION CONDITIONS

T	P_{CH_4}, mb	H, km	u, m · atm
70	28	4.1	50
80	24	5.5	380
90	200	6.8	2720
100	460	8.4	10400

The hypothesis of a methane cloud layer completely precludes the presence of any tangible amount of NH_3 above that layer. If it should be confirmed later that NH_3 does exist on Saturn, this would mean that the temperature of the cloud layer greatly exceeds the brightness temperature in the region λλ 8-13 μ. It is not excluded that the emission in that wavelength region is attributable to the short-wave wing of the induced rotational H_2 band, but this requires quantitative estimates.

The visual albedo of Saturn, according to Harris (Ref.66) is A_v = 0.76 /452 (compared with 0.73 for Jupiter). In the direction of shorter or longer wavelengths, the Saturn/Jupiter albedo ratio seems to decrease somewhat and, in first approximation, it can be assumed that the same integral albedo exists for Saturn and for Jupiter, from which it follows (cf. Sect.5.6, paragraph e) that the equilibrium temperature

$$T_\odot = T_\downarrow \sqrt{\frac{R_\downarrow}{R_\odot}} = 108 \sqrt{\frac{5.2}{9.5}} = 80°\,K$$

is close to the brightness temperature in the region λλ 8-13 μ and to the saturation temperature. Note again that, in the case of Jupiter, these temperatures greatly exceed the equilibrium temperature.

The radio emission of Saturn has been observed by several authors within the range of 1.5 - 21 cm. The findings are presented in Table 92.

TABLE 92

TEMPERATURES OF SATURN

Method	T, °K	References
Brightness temperature in the region λλ 8-13 μ	125	Pettit and Nicholson (Ref. 125)
	120	Menzel, Coblentz, and Lampland (Ref. 473)
	85±2	Low (Ref. 577)
	93±3	Low (Ref. 477)
	100	Murray and Wildey (Ref. 474)
Saturation temperature of NH_3	< 140	This book
CH_4	80	»
Equilibrium temperature	80	»
Brightness radio temperature* λ 1.53 cm	146±23	Welch and Thornton (Ref. 332)
3.45	106±21	Cook et al. (Ref. 579)
Brightness radio temperature λ 6 cm	217 ± 30	Kellerman (Ref. 411)
9.4	213 ± 10**	Rose et al. (Ref. 581)
	141 ± 20***	
10	196 ± 44	Drake (Ref. 580)
11.3	182 ± 18****	Davies et al. (Ref. 582)
21	303 ± 50	Kellerman (Ref. 411)

* The contribution of emission by the rings is everywhere assumed as negligibly small.

** Electric vector oriented at right angles to the equator.

*** Electric vector oriented parallel to the equator.

**** Polarization < 6%.

At every wavelength except λ 3 cm the brightness radio temperature exceeds the infrared temperature. Conflicting results exist with respect to polarization. Thus, whereas Rose, Bologna, and Sloanaker (Ref.581) found a strong linear polarization of p ≈ 20 ± 8% at λ 9.4 cm, Davies, Beard, and Cooper (Ref.582) found no such polarization at λ 11.3 and only estimated the upper limit of the degree of polarization as p < 6%. This requires further observations. If it turns out that polarization does exist, this will most likely mean that, like Jupiter, Saturn has a strong magnetic field as well as radiation belts. Note, however, that the brightness temperature of Saturn increases with wavelength at a much slower rate than that of Jupiter. This suggests that the /453

observed spectrum may be attributed to a greenhouse effect rather than to nonthermal radiation. The results by Rose et al. (Ref.581) who detected the presence of polarization include the highly odd finding that the electric vector is oriented at right angles to Saturn's equator. However, there exists the opinion that the configuration of Saturn's magnetic field may have an unusual character owing to the influence of the rings (Ref.7). Systematic observations of Saturn at decameter waves have been conducted to detect sporadic emission. A small number of bursts was recorded, but in no case is the identification reliable [cf. for example (Ref.551)].

The rings of Saturn are among the most amazing objects in the solar system (cf. Fig.185). Three principal zones are distinguished in the rings: the outer ring A, the central ring B, and the inner ring C. The ring B is the brightest. This is separated from the outer ring A by a dark line or gap known as "Cassini's Division" (or Cassini's gap) and from the inner ring, by "Encke's Division". The ring C is relatively dark and translucent; sometimes it is termed the Crêpe ring. Its internal edge is blurred. On photographs in ultraviolet light, this ring can be seen to extend to the very limb of the planet. Finer gradations are also discernible in the rings. All observed markings have the configuration of circles concentric with the planet disk. Markings of the dark- and bright-spot type have never been observed. The external edge of the ring has a radius of 138,000 km and the internal edge, of 90,000 km.

Nearly every observer [except Slipher (Ref.583)] has found that, at the moment of the transit of the earth across the plane of the rings, they cease to be visible. These observational results were analyzed by M.S.Bobrov (Ref.584) who estimated the upper limit of thickness of the rings as $d \leq 20$ km. This corresponds to an angular thickness of $0''.001$ so that the validity of this esti- /454
mate is definitely open to doubt. It seems likely that the ring thickness does not exceed 100 km. The translucence of the rings was estimated from observations of star occultations as well as from visibility of the disk through the ring (Ref.585). A review and analysis of these observations are given in studies by M.S.Bobrov (Ref.586-588). The transmittance t of the rings A and C is 0.55 - 0.60 and 0.93, respectively. For the ring B, only the upper limit ($t \approx 0.5$) can be derived from the observations.

Being semitranslucent, the rings of Saturn obviously cannot be solid and must consist of discrete particles. Maxwell (Ref.589) and Kovalevskaya (Ref.590) demonstrated this on the basis of considerations of dynamics. Had the rings been rotating as a solid, their angular velocity would be constant and their linear velocity $v \backsim R$. At Keplerian motion, we have

$$v \backsim R^{-\frac{1}{2}}. \tag{5.76}$$

Belopol'skiy (Ref.591) and other authors, based on spectral observations (according to the Doppler shift), demonstrated that the law (5.76) is obeyed. Maxwell found that stability of the rings requires satisfaction of the following stability criterion by the number N of particles moving along an orbit of a given radius:

$$\frac{mN^3}{M} < 2.3, \tag{5.77}$$

where m is the particle mass and M is the mass of Saturn. Dollfus (Ref.592) assumed that the particle orbits must lie in a single plane. If this were not so, the particle orbits would have to be inclined to the central plane at various angles and, at the time of transit across this plane, the particles would collide at a higher frequency. Owing to energy dissipation, the vertical velocity component and the inclination must diminish in time. However, this contradicts [cf. (Ref.587)] the stability criterion (5.69), at least for the rings A and B. In fact, at $t \approx 0.5$, the distance l between particles of a plane layer must be close to the mean particle radius r ($l \approx r\sqrt{\pi}$) so that, for particles moving along a circular orbit of radius R, we have

$$2\pi R = lN = rN\sqrt{\pi}. \tag{5.78}$$

From this, we derive

$$\frac{mN^3}{M} = \frac{4\pi r^3 \delta N^3}{3M} = \frac{4\pi\delta}{3M}(2\sqrt{\pi}R)^3 \geqslant 300,$$

if the particle density is $\delta \geq 1$. Thus, particles of the ring cannot be aligned in a single layer. In the process of flattening, the particles lose their dynamic stability. Condition (5.77) implies that

/455

$$\frac{r}{l} < \frac{1}{5}.$$

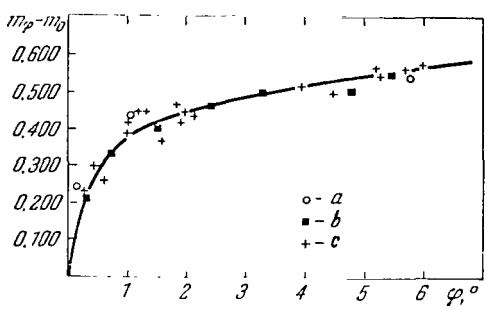

Fig.190 Phase Curve of Ring B of Saturn.
a - Hertzsprung's observations (Ref.593); b - Schönberg's observations (Ref.594); c - Iebedinets observations (Ref.595). Solid line - theoretical curve by Schönberg (Ref.598).

At a considerable separation, the brightness of the rings A and B nearly equals the brightness at the center of the disk at the moment of opposition. However, with increasing distance from opposition, the brightness of the ring decreases rapidly. The maximum phase angle of Saturn is $\varphi_m = 6^\circ.5$, and during that time the brightness of the rings is $0^m.4$ smaller than at opposition when $\varphi = 0$. The variation in brightness of the disk over the same range of phase angles is roughly one order of magnitude smaller (Ref.66). A phase curve of the ring B of Saturn is shown in Fig.190. A detailed review of photometric studies of Saturn's rings can be found in the work by V.N. Iebedinets (Ref.427).

Schönberg (Ref.597) detected weak secondary maxima on the phase curve. He interpreted these as secondary maxima of the scattering indicatrix of individual particles, and on this basis estimated the mean size of the latter as $\sim 4\ \mu$. The reality of secondary maxima on the phase curve is open to doubt, and there also exist other reasons why Schönberg's theory seems unsatisfactory. In fact, if the layer transparency is approximately 0.5 and scattering occurs on micron-

size particles, the contribution of higher-order scattering to the observed brightness should be very substantial. The fine-structure effects of the posterior lobe of the individual scattering indicatrix can then hardly be isolated, and that only if the particle albedo is not too low (the posterior lobe is generally very weak at high values of $\frac{2\pi r}{\lambda}$). When the particle albedo is /456 low, no explanation can be found for the high brightness coefficient which is characteristic of the rings at opposition (roughly equal to Saturn's geometric albedo, i.e., approximately 0.5).

The phase curve of Moon, Mercury, and Mars also exhibits a peak near $\varphi = 0^\circ$, which qualitatively resembles that shown in Fig.190, but the phase coefficient near $\varphi = 0$ is much smaller [for the moon, 0.03^m/deg according to (Ref.66), whereas Fig.190 specifies approximately 1^m/deg]. This logically gives rise to the assumption that the rings of Saturn largely consist of large bodies. Proceeding from this assumption, Zeeliger [cf. (Ref.598)] plotted a phase curve of the rings on the basis of laws of geometric optics. The sharp increase in brightness for $\varphi = 0$ is qualitatively attributed by Zeeliger's theory to the circumstance that each individual particle covers its own shadow at that phase. To simplify his calculations, Zeeliger disregarded the finite angular dimensions of the sun. M.S.Bobrov (Ref.599) showed that such an approximation is much too rough and refined the shadow theory to take into account the finite angular dimensions of the sun (Ref.586, 596, 600, 601). All particles were assumed to be spherical, uniform in size, and uniformly distributed throughout the volume of the ring. From a comparison of theory with observations, it was found possible to estimate the volume concentration of the ring particles

$$D = \frac{4\pi r^3 N}{3V} \approx 10^{-3}, \qquad (5.79)$$

where N is the total number of particles in a ring and V is the volume, as well as the maximum particle size $r \lesssim 1$ m and the total mass of the ring system $M_r \approx 10^7 M_h$. In Bobrov's paper (Ref.602), the shadow theory is extended to the case of particles with different sizes. It is assumed that the distribution of particle sizes obeys the law of $dn = \text{const}\, r^{-m} dr$. Bobrov (Ref.602) also showed that agreement with observations can be achieved only at $m < 3$, thus indicating that the values of D and M_r should be definitely increased, although by not more than one order of magnitude.

If multiple scattering is disregarded, it can be assumed that the geometric albedo of the bodies constituting the rings equals the geometric albedo of Saturn. If backscattering predominates, as is the case for the moon, this assumption is not too tentative. Supposing a phase integral of 0.6, which is characteristic of bodies of this type (Moon, Mercury), we obtain a spherical albedo of 0.30. If, on the other hand, forward scattering greatly exceeds backscattering and, in general, if the multiple scattering is extensive, then the spherical albedo of particles (albedo of a discrete scattering event) can be estimated from eq.(1.103) which then will be extremely high: $0.9 < A < 1$. /457 Below, we will demonstrate that spectroscopic data speak in favor of high values of the albedo. Hence we are faced here with a contradiction: The phase curve indicates the existence of large bodies and negligible multiple scattering, but

this implies too low a spherical albedo.

The spectra of Saturn's rings have been investigated in the visible region by G.A.Shain (Ref.603). He found that the reflectivity of the rings is virtually independent of the wavelength. A comparison of Figs.187 and 188 clearly shows that the entire radiation in the region $\lambda > 1.6\ \mu$ of spectra recorded in 1960 represents light reflected from the rings with the disk brightness in that region being zero. The energy distribution in the spectrum of the rings in the region $\lambda > 1.6\ \mu$ differs greatly from the solar energy distribution. Figure 187 indicates that, in the transparency window 1.4 - 1.8 μ, an intensity maximum exists near λ 1.7 μ, with the intensity decreasing in the direction of shorter wavelengths. In the transparency window 2 - 2.5 μ, the maximum is displaced in the direction of longer wavelengths. Thus, the infrared reflection spectrum of the rings is not neutral. Earlier, Kuiper (Ref.4) had observed the spectrum of Saturn's rings with a lower resolution $\left(\frac{\lambda}{\Delta\lambda} = 9\right)$ and had also noticed that the maximum in the transparency window is displaced in the direction of longer wavelengths. The absorption spectrum of ice as well as the reflection spectrum of ice, snow, and hoarfrost contain characteristic wide bands at $\lambda\lambda$ 1.5 and 2.0 μ displaced in the direction of longer wavelengths with respect to bands of water vapor. Kuiper suggested that the reason for the special features of the infrared spectrum of Saturn's rings lies in the fact that the particles constituting these rings either are ice particles or are coated with a layer of ice, frost, or snow.

To verify this hypothesis, we used our own spectrometer to obtain, under equal recording conditions, the reflection spectrum of snow and frost (Fig.76). In the latter case, ice crystals are much smaller ($r < 0.1$ mm) and the optical thickness of the crystals on reflection is also less. A comparison of Figs.187 and 76 shows that the diffraction spectra of the reflection of Saturn's rings and of ice particles are in good agreement. An essential factor is that the resolving power in our observations was approximately 100 (one order of magnitude higher than in Kuiper's) and that spectra of Saturn in the region $\lambda\lambda$ 2-2.5 μ were recorded for the first time.

In the region $\lambda\lambda$ 1.2-1.3 μ, the readings are composite pertaining to both the disk (I_d) and the rings (I_r). It can be seen from Fig.187 that I_r (1.7 μ) $\approx$ $\approx I_d$ (1.25 μ) + I_r (1.25 μ), and hence we have I (1.7 μ) > I (1.25 μ), meaning that the reflection spectrum of the rings is closer to the curve b than to the curve a (Fig.76). Thus, if ice in some of its various forms is indeed responsible for the peculiarities of the reflection spectrum of the rings in the /458 infrared region, then it is most likely that thin crystals of frost, probably coating larger particles, are involved. These larger particles need not be ice.

It can be shown that particles of H_2O ice may persist for a very long time in the environs of Saturn. In fact, the evaporation rate in vacuum, as is known, is equal to

$$\frac{dM}{dt} = P_s \sqrt{\frac{m}{8\pi kT}}\ gm \cdot cm^{-2} sec^{-1}, \qquad (5.80)$$

where P_s is the saturated vapor pressure (in bars); m is the molecule mass; T is the temperature. At sufficiently low temperatures for H_2O, according to van de Hulst (Ref.483), we have

$$\log P_s = -\frac{2480}{T} + 4\log T + 4.06.$$

At T = 70°K, we have $\frac{dM}{dt} \approx 10^{-11}$ gm • cm^{-2} over 10^9 years and at T = 100°K, $\frac{dM}{dt} \approx 1$ gm • cm^{-2} over 10^9 years, but the latter temperature seems too high.

Above, we found an equilibrium temperature of Saturn of T = 80°K on assuming that $A_1 = 0.50$. Moreover, this was based on the premise that, in the far infrared, the emission coefficient equals unity. For ice particles, A_1 is somewhat higher so that the latter assumption is unconditionally satisfied. Consequently, their temperature must be even lower.

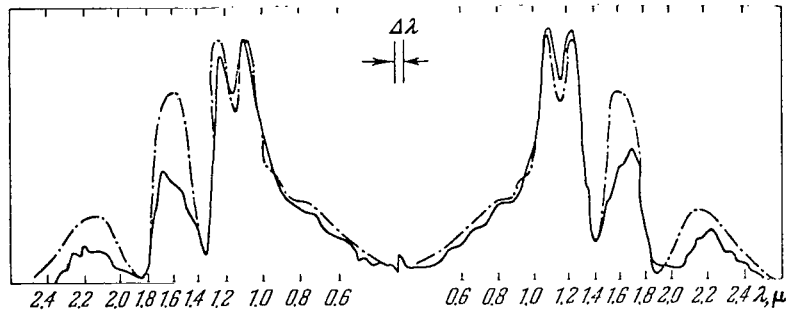

Fig.191 Spectrum of Saturn's Rings (Solid Line) in the Region 0.6-2.5 μ. (Shain reflector, prism spectrometer, recording conditions same as in Fig.184). Broken line - solar spectrum.

In 1964, we used a Shain reflector to isolate the spectrum of the rings from the spectrum of the disk (Fig.191). The dimensions of the entrance slit were 1 × 3 mm and one of the "ears" of the ring filled this area almost completely. The resolving power was approximately 20 and the signal-to-noise ratio was highly satisfactory (~ 100 near 1.3 μ). The light difference between the two traces shown in Fig.191 is due to inaccuracy of tracking. As readily seen from a comparison of these new spectra with Fig.76, they also excellently fit the "ice" hypothesis. If the particles of Saturn's rings actually are of ice or are ice-coated, they should have a high albedo, forward-elongated indicatrices, and comparatively small dimensions (see above). In the visible region, the albedo of snow and frost is independent of wavelength so that the nonselective nature of the reflection spectrum of Saturn's rings, established by G.A.Shain (Ref.603), also is in agreement with the theories expounded above. /459

Section 5.10 Uranus and Neptune

Uranus is 19.2 a.u. distant from the sun. Its period of revolution equals 84.02 years. It is nearly three times smaller in size than Jupiter. Its mean radius, according to Rabe (Ref.412) is R = 26,700 ± 500 km. Allen's handbook (Ref.88) gives a very different value for R: 23,800 km. This difference is within the limits of the scatter of individual observations but greatly exceeds the formal error of Rabe's estimate. The compression is 0.06 according to micrometeric observations [cf. (Ref.606)], which is the same as with respect to the motion of the satellites. The mass of Uranus, according to Brouwer (Ref.77), is

$$\frac{M_\odot}{23\,000} = 14.3 M_\oplus = 8.7 \times 10^{28}\ gm,$$

while its mean density is 1.1 gm · cm^{-3} if Rabe's estimate is to be given credence, or 1.6 gm · cm^{-3} if we accept the radius given by Allen.

The visual stellar magnitude of Uranus during mean opposition is $+5^m.52$, which verges on the limit of visibility by the naked eye. All previously considered planets are bright bodies known to humanity from times immemorial. Uranus, on the other hand, was discovered only in 1781 by Herschel, and then only after considerable skill in telescope observations had been acquired. Photometric observations of Uranus, performed with visual and photographic methods until 1930, indicated variations in stellar magnitude with a period of approximately $10^h49^m.5$ and an amplitude from $0^m.03$ to $0^m.15$. However, the much more precise photoelectric observations which began in 1927 revealed no variations in brightness (Ref.66), at least not until 1955. In 1912, Slipher (Ref.609) spectroscopically derived a period of 10^h45^m, while in 1930 Moore and Menzel (Ref.610) obtained 10^h54^m. Markings on the disk of Uranus (its angular diameter is $3''.8$) are virtually indistinguishable.

Uranus has five satellites (cf. Sect.5.13), whose orbital planes are very /460 similar and nearly perpendicular to the ecliptic (inclination 82°) and whose rotation is retrograde. A majority of the satellites of Jupiter and Saturn - at least those located closer to the planet body - revolve in orbits coinciding with the plane of the planetary equator and proceeding in the same direction. On this basis, it may be assumed that the axis of rotation of Uranus is strongly inclined to the plane of the ecliptic, and that the direction of its rotation is retrograde. The latter assumption has been directly confirmed by spectroscopic data. In 1947, the orbital planes of the satellites of Uranus were perpendicular to the radius vector of that planet. If the equator of Uranus coincides with the orbital planes of the satellites, then one of the poles will face the earth. This may be exactly the reason for the absence of variations in brightness during 1930-1955. The fluctuations in stellar magnitude are maximal in positions of the planet at which the axis of rotation lies in the plane of the paper. It may be expected that, owing to compression of the planet, the mean stellar magnitude will reach its minimum in those positions. In fact, Becker's study (Ref.606) of old photometric data indicated variations with a period close to the rotation period and with a phase in agreement with the considerations presented above, but the oscillation amplitude (0.26) is too high to attribute it to compression alone. If this amplitude value is real, it must be assumed that generally the

albedo of the polar regions of Uranus is higher than the albedo of its equatorial regions. P.P.Parenago (Ref.604) analyzed all recorded positional angles of the ellipse of the disk (from 1842 until 1926) and, proceeding from elements of satellite orbits as a first approximation, derived the differential corrections of these angles. This resulted in determining the coordinates of the North Pole of Uranus as

$$\alpha = 4^h21^m,$$
$$\delta = +24°.8$$

and the inclination of the planet's equator to the ecliptic as $87°.5$.

TABLE 93

/461

ALBEDO OF THE PLANETS ACCORDING TO HARRIS (REF.66)

Planet	λ, Å					q (λ 5540 Å)	p (λ 5540 Å)
	3530	4480	5540	6900	8200		
Mercury . . .	—	0.076	0.100	0.145	0.179	0.563	0.056
Venus	0.353	0.492	0.586	—	—	1.296	0.76
Earth	—	—	0.367	—	—	1.095	0.36
Mars	0.052	0.080	0.154	0.286	0.310	1.04	0.16
Jupiter	0.270	0.370	0.445	0.466	0.347	1.65	0.73
Saturn	0.211	0.316	0.461	—	—	1.65	0.76
Uranus	0.530	0.630	0.565	0.325	0.119	1.65	0.93
Neptune	0.585	0.624	0.509	0.248	0.091	1.65	0.84
Pluto	0.099	0.111	0.130	0.154	0.152	1.04	0.14

TABLE 94

ALBEDO OF URANUS AND NEPTUNE ACCORDING TO SINTON (REF.611)

	Uranus			Neptune		
	m*	p	A	m*	p	A
U λ 3530 Å	6.35	0.61	0.88	8.49	0.57	0.82
B λ 4480 Å	6.09	0.67	0.97	8.26	0.61	0.88
V λ 5540 Å	5.54	0.62	0.89	7.86	0.49	0.71

* At mean opposition.

The albedo of Uranus, as determined by Harris (Ref.66), is given in Table 93 and as determined by Sinton (Ref.611), in Table 94. The variation in albedo with wavelength is in qualitative agreement with data by both of these authors, except that Sinton gave higher absolute values of the geometric albedo. The values of phase integral adopted by Sinton are lower than those used by

Harris (Q = 1.65), which means that Sinton gives a somewhat lower spherical albedo. Both series of observations show that Uranus has the highest visual albedo among the planets of the solar system. The high albedo persists in the blue and ultraviolet spectrum regions but decreases sharply in the region $\lambda >$ $> 0.6\ \mu$ owing to strong CH_4 absorption bands (cf. Table 73 and Fig.154). Kuiper (Ref.4) estimated the equivalent path of CH_4 in the atmosphere of Uranus as 150 km • atm. Herzberg (Ref.612) identified the absorption near λ 8270 Å, found by Kuiper in the spectra of Uranus and Neptune, as the (3-0) H_2 band induced by pressure. Spinrad (Ref.613) identified the absorption at λ 6420 Å in the spectrum of these planets as the band (4-0) H_2. The available information is insufficient for a quantitative analysis. The above estimate for CH_4 can hardly be interpreted as reduced thickness, even if it were correct to within one order of magnitude. Pressure-induced bands (3-0) and (4-0) may appear only when the density amounts to several tens of amagats so that strong Rayleigh scattering must exist in the atmosphere of Uranus. Apparently, for the case of Uranus it would be more correct, from the viewpoint of quantitative analysis, to use a /462

model with a $\frac{k}{\sigma}$ ratio constant over the altitude. Since the Rayleigh scattering coefficient is sufficiently low ($\sigma \approx 10^{-7}$ cm^{-1} at ρ = 1 amagat), the observed strong bands of methane probably correspond to small quantities of the gas.

So far, it has not been possible to measure the brightness temperature of Uranus in the interval $\lambda\lambda$ 8-13 μ, but attempts in this direction are mentioned in the literature. Radio observations [Kellerman (Ref.411)] give a brightness temperature $T_B = 100 \pm 35^\circ$K at λ 6 cm and $T_B = 128 \pm 40^\circ$K at λ 11.3 cm, which is much higher than the equilibrium temperature $T_B = 60^\circ$K calculated on the assumption that $A_1 = 0.50$. Note that if the reduced thickness of CH_4 is assumed as 150 km • atm the saturation temperature will be 110°K, which is close to the radio temperature. The layer responsible for the radio emission is definitely warmer than the effective level of infrared radiation. It is doubtful whether the negligible amount of energy received by Uranus from the sun (400 times smaller than for the earth) could produce any appreciable greenhouse effect. It may be that the temperature gradient is created by the internal heat flux inherent to the planet.

Neptune moves along an orbit with a semimajor axis of 39.5 a.u. Its period of revolution is 248.4 years. According to Rabe (Ref.412), the mean radius of Neptune is R = 24,800 ● 1000 km, which is very close to the radius of Uranus. According to Kuiper (Ref.2), the mass of Neptune is

$$\frac{M_\odot}{19{,}000} = 17.5\ M_\oplus = 1.05 \times 10^{29}\ gm,$$

whence $\bar{\rho}$ = 1.65. Allen gave R = 22,300. This corresponds to $\bar{\rho}$ = 2.25. The mean density of Neptune is higher than that of the other planets, although the uncertainty as to its exact value is rather great.

The stellar magnitude of Neptune is $+7^m.84$ at mean opposition. The dramatic story of the discovery of Neptune (in 1846), as a result of work by Le Verrier and Adams, is too well known to describe it here. The rotation period of the

planet is $15^h.8 \pm 1$ according to spectroscopic data by Moore et al. (Ref.610). Photoelectric observations are too few to assess the variations in brightness. Markings on the disk which has an apparent diameter of only 2″ are virtually unobservable. The orientation of the axis of rotation was derived from the theory of motion of Triton, a satellite of Neptune. The inclination of the equator to the plane of the ecliptic is 29°.

The wavelength dependence of the albedo is given in Tables 93 and 94. The absolute values of the albedo for Neptune are somewhat lower than for Uranus, but the difference may be due to errors in determining the diameter. Strong CH_4 bands sharply reduce the albedo in the red spectrum region. According /463
to Kuiper, the equivalent path of CH_4 is about 250 m • atm (Ref.4). As mentioned above, the absorption at λ 8270 and λ 6427 Å apparently pertains to H_2 (pressure-induced absorption). No observational information on temperatures is available.

Section 5.11 Internal Structure of the Giant Planets

Low mean density is a typical feature of the giant planets. Obviously, the composition of these planets greatly differs from that of the planets in the terrestrial group, not only in their upper surface layers that are amenable to direct analysis with spectroscopic methods but also deep in their interiors.

Since the giant planets do not lose their lighter gases, including hydrogen and helium, it is natural to expect that these elements, the most common in the Universe, are the principal constituents of the interiors of these planets. Jeffreys attempted to construct models of the giant planets on assuming the existence of heavy dense cores similar in composition to the cores of the terrestrial planets and of greatly extended atmospheres, but it was found that such models do not fit the physically substantiated equations of state of gases. Later investigators evolved models of Jupiter and Saturn on assuming that their composition resembles the average cosmic composition (Ref.613-622). However, in the case of Uranus and Neptune this required a certain excess of heavy elements.

The central pressure and density of the giant planets can be estimated from eqs.(4.13) and (4.14). The factors of their moment of inertia $\left(f = \frac{I}{MR^2}\right)$ are very similar, ranging from 0.235 to 0.241, and are markedly lower than the factors of the moment of inertia for the terrestrial planets (Earth 0.334, Mars 0.359). The criterion (4.14) of the central density can be supplemented with a similar criterion of surface density

$$\rho_s < \frac{I}{\frac{2}{5} MR^2} \bar{\rho}.$$

This elementary criterion derived by Jeffreys (Ref.614) was strengthened by De-Marcus (Ref.621) by relating the upper limit of surface density to the coefficients J and K of the external potential - constants that enter the equation

of the power function of the ellipsoid of revolution.

The coefficients J and K, derived from the motion of the satellites, are given in Table 95. In constructing models of the giant planets, seeing their considerable compression, the coefficients J and K, in addition to the radius (M being given), can be used as observational criteria of the validity of these models, by analogy with the moment of inertia for spherical and quasi-spherical bodies. /464

TABLE 95

CERTAIN MECHANICAL CHARACTERISTICS OF THE GIANT PLANETS

	Mass			R, km	Compression	$\frac{I}{\frac{2}{5}MR^2}$
	gm	$\frac{M}{M_\oplus}$	$\frac{M_\odot}{M}$			
Jupiter	1.88×10^{30}	318	1 047	67 900	0.062	0.60
Saturn	5.7×10^{29}	95.5	3 500	60 300	0.096	0.59
Uranus	8.7×10^{28}	14.3	23 000	25 000 *	0.06	0.59
Neptune	1.05×10^{29}	17.5	19 000	23 500 *	0.02	0.60

	J	K	$\bar{\rho}$, gm·cm^{-3}	P_0, 10^{11} dyne cm^{-2}	$\rho_0/\bar{\rho}$	ρ_0
Jupiter	0.002202 ± 0.00022	0.00253 ± 0.00141	1.3	15	$\geqslant2.1$	<0.57 **
Saturn	0.002501 ± 0.00003	0.00386 ± 0.00026	0.7	2	$\geqslant2.2$	<0.19 **
Uranus	—	—	1,4	2	$\geqslant1.3$	<1.3 ***
Neptune	0.00074	—	2	4	$\geqslant2.1$	<1.3

* Averaged from Rabe's and Allen's estimates.
** From De-Marcus's criterion (Ref.621).
*** From Jeffrey's criterion.

The equations of state of hydrogen and helium have been experimentally investigated only up to pressures of ~ 20,000 atm. However, the pressure at the center of Jupiter reaches 10^7 atm (Table 95). Theoretically, the equation of state of hydrogen can be extrapolated to extremely high pressures. A survey of the data required for this extrapolation has been given by De-Marcus (Ref.621) and Wildt [cf. (Ref.2, Chapt.5)]. At pressures exceeding $P_{cr} = 2 \times 10^{12}$ dyne · · cm^{-2}, ionization accompanied by transition to the metallic state takes place. If the temperature at the boundary of the phase transition is below 2000°K, then molecular hydrogen will exist in the solid state above that boundary and if the temperature exceeds 2000°K, in the gaseous state. The critical temperature of hydrogen, above which the liquid phase is absent regardless of pressure, is 30°K. However, hydrogen is characterized by its exceptionally strong compressibility, and at pressures of 10^{12} dynes the density of the gas phase is close to 0.5 gm · cm^{-3}. At 150°K, solidification sets in as soon as the pressure /465

reaches 3×10^9 dyne $\cdot$ cm^{-2} and the density, 0.1 gm $\cdot$ cm^{-3}. Figure 192 gives diagrams of the equations of state for H_2 as adopted by Peebles (Ref.622) in constructing models of Jupiter and Saturn: Here, "a" represents the equation of state of solid hydrogen at 0°K; "b" is the isothermal curve for T = 150°K; "c" and "d" are two adiabatic curves with different initial pressures (1 and 5 atm at 150°K); curves "e" and "f" are analogous to "a" and "d" but their values of ρ are lower. At high pressures, the density of the solid phase is virtually independent of temperature, so that all calculations pertaining to the planetary interiors can be carried out in first approximation, without taking the temperature dependence into account (as in the case of planets of the terrestrial group).

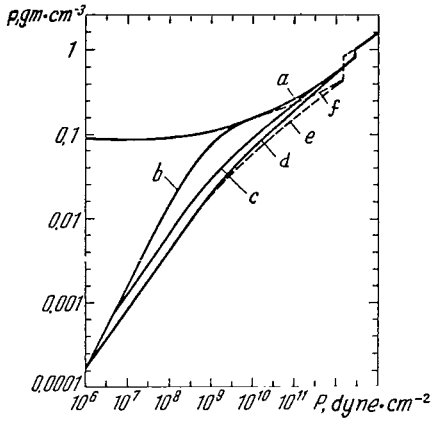

Fig.192 Approximate Equations of State of Hydrogen for Calculating Models of Jupiter and Saturn (Ref.622).

De-Marcus (Ref.621) and Abrikosov (Ref.620) calculated the mass-radius dependence for a nonrotating sphere consisting of pure hydrogen at 0°K. De-Marcus' curve is shown in Fig.193. It was derived from the equation of state "a" in Fig.192. The region to the left of the curve is forbidden - it corresponds to lower densities than can be given by hydrogen. Jupiter is satisfactorily represented by this model, but the correspondence with Saturn is less good and even worse for Uranus and Neptune. De-Marcus also considered a rotating model of a mixture of solid hydrogen and helium, on selecting a radial distribution of He such that the observed quantities R, J, K were optimally represented. He showed that the fraction of hydrogen by mass exceeds 0.78 for Jupiter and 0.63 for Saturn. Peebles (Ref.622) used the same method to calculate a series of models of Jupiter and Saturn, applying all of the equations of state given in Fig.192 and stipulating the existence of a certain percentage of heavy elements. It was found that, for Saturn, acceptable values of J and K can be obtained only for adiabatic equations of state. For Jupiter, such a definite choice cannot be made since all /466 six equations yield agreement with the observations, within the error limit. However, the similarity between both planets suggests that Jupiter has a deep atmosphere with an appreciable temperature gradient. Heavy elements probably form a small inner core with a mass of the order of 10 $M_\oplus$ in the interiors of both Jupiter and Saturn. De-Marcus mentioned that, if energy release by radioactive decay were to proceed at the same rate in this core as in the earth's core, then the heat flux would suffice to create a drop of 10^4 °K in the molecular shell of the planet. However, this estimate is based on the assumption that heat conduction is the sole agent responsible for heat transfer. If an allowance is made for radiation in pressure-induced bands, this estimate would probably be very much lower. On the other hand, energy release due to gravitational compression may greatly enhance the heat flux.

Models of the internal structure of Jupiter and Saturn are given in Table 96, according to Peebles. Transition to the metallic state takes place

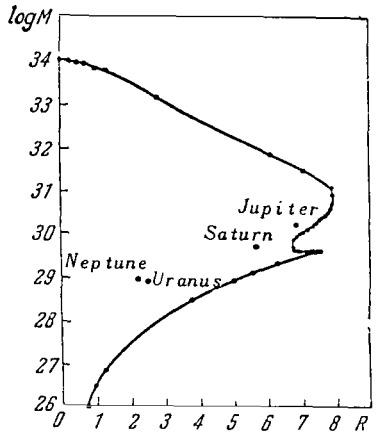

Fig.193 Mass-Radius Diagram for a Cold Nonrotating Sphere of Pure Hydrogen. M - mass in gm, and R - radius in units of earth's radius (Ref.623).

at a depth of 0.2 R_0 from the surface of Jupiter and of 0.45 R_0 from the surface of Saturn, which represent the lower limits of the possible depths of their atmospheres. The upper limit corresponds to the level having a pressure of 3×10^9 dyne $\cdot$ cm^{-2}, which is attained at a depth of 0.01 R_0 for Jupiter and of 0.025 R_0 for Saturn; it is realized for an isothermal atmosphere of a temperature of 150°K.

In comparing the above figures with Table 95, we see that the mass of Jupiter's gaseous envelope may attain 20% of the entire mass of the planet (for Saturn, 50%). It is a fact that the density of this envelope is high, which would mean that a semi-liquid ocean rather than a gaseous atmosphere should be considered.

It must be noted that many known facts which should be explained by the theory of the internal structure of Jupiter and Saturn still are beyond the bounds of that theory; this includes the generation of a magnetic field which no doubt is associated with the metallic core of the planet; the interpretation of rotation periods and particularly of variations in the system III; the relationship to phenomena occurring on the visible surface; etc.

Models of Uranus and Neptune were considered by various authors /467
(Ref.614-616 and 623, 624). The M(R) diagram in Fig.193 reveals that a planet of pure hydrogen of the radius of Uranus or Neptune must have a mass approximately 10 times smaller. Given some supplementary assumptions, a mixture of heavy and light elements must be selected such as to fit the model to the observations. Thus, Reynolds and Summers (Ref.624) separated the substances that may be present in the interiors of Uranus and Neptune into three groups: "volatile" elements, H, He, Ne; "ices" - H_2O, CH_4, NH_3, H_2S; and heavy compounds and elements - SiO_2, MgO, Fe - Ni. They assumed that the constituents of the ices and the heavy elements are present at ratios corresponding to their abundance in the cosmos and that the relative content of H, He, and Ne also corresponds to their cosmic abundance but that the ratio of the two groups remains a free parameter. Three models were considered: 1) the homogeneous model, in which H, He, Ne are added to a mixture of heavy elements in a proportion sufficient to obtain the required mass for a given radius; 2) the two-layer model, in which the core consists of a mixture of heavy elements and the envelope of H, He, Ne; 3) the three-layer model having a core of heavy compounds and elements, an /468
intermediate envelope of ices, and an outer envelope of H, He, Ne. The sole criterion for choosing among these models is the extent of the coefficient J for Neptune (J and K for Uranus and K for Neptune are unknown). The best agreement with the observed value of J is given by the second model. Thus, here again we have reason to expect that the extent of the atmosphere may be quite considerable. Of course, equations of state for such models are of a highly tentative nature,

and the reliability of the findings is very doubtful.

TABLE 96

INTERNAL STRUCTURE OF JUPITER AND SATURN

Jupiter				Saturn		
Radius	Pressure 10^{12} dyne·cm^{-2}	Density gm·cm^{-3}	Mass	Pressure 10^{12} dyne·cm^{-2}	Density gm·cm^{-3}	Mass
1.000	3×10^{-6}	5.5×10^{-4}	1.0	3.0×10^{-6}	5.5×10^{-4}	1.0
0.995	3.7×10^{-4}	0.0164	0.99995	3.4×10^{-5}	3.0×10^{-3}	0.99998
99	2.8×10^{-3}	0.055	0.9996	2.2×10^{-4}	0.0114	0.9998
98	0.020	0.147	0.997	1.44×10^{-3}	0.039	0.9989
96	0.095	0.28	0.988	7.9×10^{-3}	0.092	0.995
94	0.23	0.40	0.973	0.028	0.169	0.983
92	0.38	0.47	0.957	0.055	0.22	0.970
90	0.57	0.55	0.941	0.088	0.27	0.953
85	1.29	0.76	0.878	0.21	0.38	0.900
80	2.2	0.96	0.815	0.37	0.47	0.841
75	3.5	1.39	0.74	0.58	0.56	0.78
70	5.7	1.63	0.64	0.86	0.65	0.70
65	7.2	1.84	0.55	1.16	0.73	0.63
60	9.5	2.1	0.46	1.53	0.81	0.58
55	11.5	2.3	0.38	2.0	0.92	0.51
50	15.0	2.5	0.30	2.5	1.24	0.46
40	20.5	2.9	0.19	4.2	1.49	0.33
30	26	3.3	0.11	6.9	1.81	0.26
20	34	3.7	0.05	11.5	2.2	0.20

Section 5.12 Pluto

Pluto, the most distant of the known planets of the solar system, was discovered fairly recently (by Tombaugh in 1930). The story of this discovery is given in detail in the book "Planets and Satellites" (Ref.2, Chapt.2). Lowell, who had predicted the approximate position of Planet IX from discrepancies in the theory of motion of Uranus and Neptune, assumed that it would resemble both Uranus and Neptune in its characteristics, but it turned out that the new member of the solar system can in no way be classified in the group of the giant planets. The radius of Pluto was measured by Kuiper (Ref.625) with a 5-m reflector, using the artificial planet method: he derived R = 2900 km. Hardy [cf. (Ref.626)] pointed out, on the basis of the photoelectric curve of brightness, that this estimate may be too low because of limb darkening. In 1965 (on April 28-29) occultation of the star $15^m.3$ by Pluto was expected. The stellar magnitude of Pluto at the time of the anticipated occultation was $14^m.1$. The total flux from both bodies would have decreased by 25% in the event of such an occultation. Careful photoelectric observations at Kitts Peak Observatory revealed no decrease in the flux, although the angular distance between the planet center and the star was only $0''.125$ (Ref.627). The geocentric distance of Pluto during these observations was 32 a.u., so that the upper limit of the radius would be

$$\frac{32\times1.49\times10^{8}\times0.125}{20\,6265}=2900\,km,$$

which is in complete agreement with Kuiper's finding. According to Brouwer and Clemence (Ref.2) the mass of Pluto is

$$\frac{M_{\odot}}{400{,}000}\approx0.8\,M_{\oplus}$$

with a formal accuracy to within ±10%, whence $\bar{\rho}\geq 40$ gm • cm^{-3}! Apparently the mass of Pluto was incorrectly determined. Brouwer and Clemence confirmed /469 that the indeterminacy in estimating the mass of Pluto greatly exceeds the formal error limit. In any case, the mass and radius of Pluto are such that this planet cannot be classified with the group of the giant planets, so that the inclusion of a Section on Pluto in this particular Chapter of our book is not entirely justified.

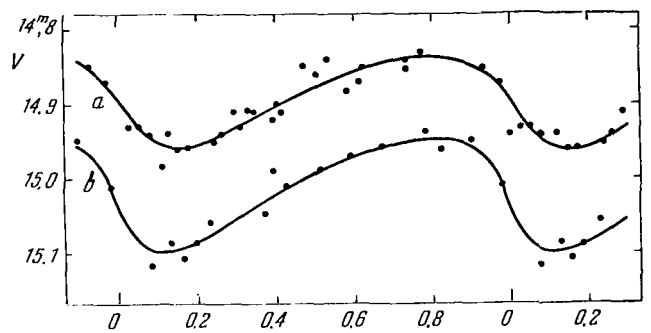

Fig.194 Brightness Curve of Pluto. On the abscissa, segments of the rotation period. a - Observations 1953-1955; b - 1964 (Ref.66).

The stellar magnitude of Pluto regularly varies (Ref.66, 626) with a period of $6^{h}16^{m}54^{s}\pm26^{s}$. The amplitude of variation is $0^{m}.11$. The brightness curve is asymmetric (Fig.194), which points to a sharply nonuniform distribution of reflectivity over the surface of the planet.

Pluto moves along an orbit of high eccentricity (about 0.25) which is higher than that of the other planets [the planet with the next highest eccentricity (0.20) is Mercury]. Its mean distance from the sun is 39.5 a.u. The visual geometric albedo - if we assume a planetary radius of 2900 km - reaches $p_v = 0.13$, which is somewhat less than for Mars (Ref.66). The albedo increases with wavelength - from 0.10 at $\lambda \approx 3600$ Å to 0.15 at $\lambda \approx 8200$ Å. Apparently, Pluto's atmosphere (if it exists) is optically thin. The equilibrium temperature of Pluto at the mean distance $t_{eq} \approx 47^{\circ}$K, if we assume $\epsilon = 0.9$.

Section 5.13 Satellites of the Giant Planets

Among the terrestrial planets, only Earth and Mars have satellites (altogether three: Moon of Earth and Phobos and Deimos of Mars). The giant planets are known to have a total of 29 satellites, with Jupiter having the largest number (12) and Neptune the smallest (2). This large number of satellites is /472 one of the distinguishing features of the giant planets. The principal astronomical characteristics of all the satellites are given in Table 97. Six of the

TABLE 97

PLANET SATELLITES

Planet	Satellite	Mean Distance from Center of Planet: 10^3 km	Mean Distance from Center of Planet: Ratio of Planet Mass to Satellite Mass	Sidereal Period of Revolution, Days	Synodic Period of Revolution	Orbital Inclination	Orbital Eccentricity	Radius of Satellite, km	Mass: Ratio of Planet Mass to Satellite Mass	Mass: 10^{21} gm	Mean Density gm·cm^{-3}	Visual Stellar Magnitude at Mean Opposition
Earth	Moon	384.4	60.27	27^d.321661	29^d 12^h 44^m 02^s. 8	5°.1 *	0.0549	1738	81.3	73.4	3.34	−12^m.7
Mars	1 Phobos	9.4	2.77	0.318910	07 39 26. 65	1.8 **	0.019	14				+11.5
	2 Deimos	43.5	12.87	1.262441	1 06 21 15. 68	1.4 **	0.003	8				+12.5
Jupiter	1 Io	421.8	5.91	1.769138	1 18 28 35. 95	0 **	Small and	1660	24000	79	3.9	+5.5
	2 Europa	671.4	9.40	3.551181	3 13 17 53. 74	0 **	variable	1440	39800	47.8	4.0	5.7
	3 Ganymede	1071	14.99	7.154553	7 03 59 35. 86	0 **		2470	12400	153	2.5	5.1
	4 Callisto	1884	26.36	16.689018	16 18 05 06. 92	0 **		2340	21000	90	1.7	6.3
	5	181	2.53	0.498179	11 57 27. 6	0 **	0.003	80				13.0
	6	11500	161	250.62	260.0	28.5 ***	0.155	60				13.7
	7	11750	164	259.8	276.10	28.0 ***	0.207	20				16.2
	8	23500	329	738.9	631.05 ****	33 ***	0.38	20				16.2
	9	23700	332	755	626 ****	24 ***	0.25	11				17.7
	10	11750	164	260	276	28.3 ***	0.140	10				17.9
	11	22500	315	696	599 ****	16.6 ***	0.207	12				17.5
	12	21000	294	625	546 ****		0.13	10				18.1
Saturn	1 Mimas	185.7	3.08	0.942422	22 37 12. 4	1.5 **	0.0196	260	15000000	0.038	0.5	+12.1
	2 Enceladus	238.2	3.96	1.370218	1 08 53 21. 9	0.0 **	0.0045	300	8000000	0.07	0.6	11.7
	3 Tethys	294.8	4.88	1.887802	1 21 18 54. 8	1.1 **	0.0000	600	870000	0.65	0.7	10.6
	4 Dione	377.7	6.26	2.736916	2 17 42 09. 7	0.0 **	0.0021	650	555000	1.03	0.85	10.7
	5 Rhea	527.5	8.74	4.517503	4 22 27 56. 2	0.3 **	0.0009	900	250000	2.3	0.75	10.0
	6 Titan	1223	20.26	15.945452	15 23 15 25	0.3 **	0.0289	2500	4150	137	2.7	8.3
	7 Hyperion	1484	24.6	21.276665	21 07^h 39^m 06^s	0.6 **	0.110	200	5000000	0.11	3.3	14
	8 Iapetus	3563	59.1	79.33082	79 22 04 56	14.7 **	0.029	600	100000	5	5.5	11
	9 Phoebe	12950	214.5	550.45	536 16 ****	30 **	0.166	150				14.5
Uranus	1 Ariel	191.8	5.25	2.52038	2 12 29 40	0 **	0.007	300				+15.5
	2 Umbriel	267.3	7.18	4.14418	4 03 28 25	0 **	0.008	200				16.0
	3 Titania	438.7	16.4	8.70588	8 17 00	0 **	0.023	500				14.0
	4 Oberon	586.6	22.0	13.46326	13 11 15 36	0 **	0.010	400				14.2
	5 Miranda	130.1	4.87	1.414								17
Neptune	1 Triton	353.6	14.3	5.87683	5 21 03 27 ****	20 **	0.000	2000	700	150	4.6	+13.6
	2 Nereid	6000 ?	240 ?	500			0.7	150	3000000	0.05	3.6	+19.5

* Toward plane of the ecliptic.

** Toward plane of the equator of the planet.

*** Toward orbital plane of the planet.

**** Retrograde rotation with respect to equatorial plane of the planet (the satellites of Uranus move in retrograde direction also with respect to the plane of the ecliptic).

satellites (Io, Europa, Ganymede, Callisto, Titan, and Triton) roughly resemble the moon in mass and dimensions, while the others are smaller.

The physical characteristics of the satellites of the giant planets are very little known. The disks of the Galilean satellites of Jupiter can be discerned in telescope observations even at normal visibility, but their markings are almost indistinguishable. Lyot [cf. (Ref.2)] compared charts of the dark and bright spots which he had succeeded in observing on the disks of the Galilean satellites and concluded that their rotation is synchronous, i.e., that the rotation period equals the period of revolution, as in the case of the moon. The Galilean satellites are bodies of 5 - 6^m and can be rather easily studied with photometric and spectroscopic techniques. Photometric and colorimetric data on the satellites were presented by Harris (Ref.66); these are chiefly based on photoelectric observations by Stebbins (Ref.628) and Stebbins and Jacobson (Ref.629). Io is distinguished by its anomalous red color. Like the moon, these satellites increase rapidly in brightness with decreasing phase; their phase coefficients are even somewhat higher than for the moon.

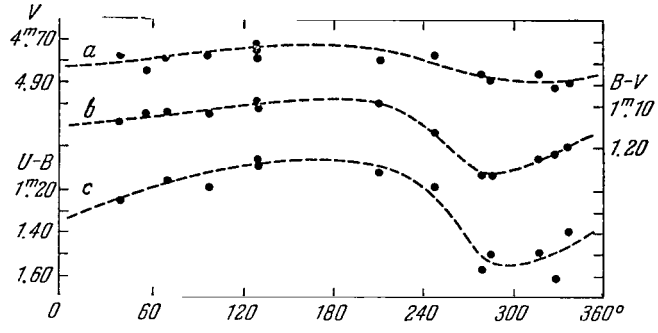

Fig.195 Brightness Curves of Io as a Function of Phase of Rotation.
a - In visual rays V; b - B-V color index; c - U-B color index (Ref.66).

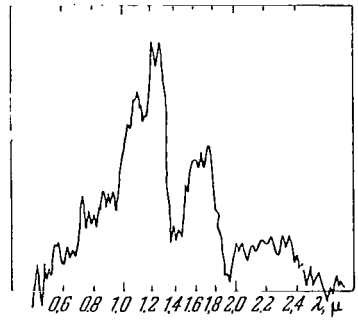

Fig.196 Spectrum of Ganymede in the Region λλ 0.7-2.5 μ (Discrete Trace). Oct.15, 1964, Shain reflector, prism interferometer, Δλ = 0.09 μ near λ 1.6 μ, recording speed 70 Å/sec, τ = 4.4 sec, z = 28°.

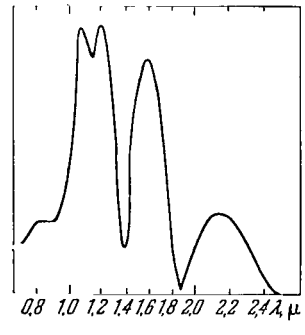

Fig.197 Spectrum of Io, Mean of Four Traces Taken on Oct.15, 1964, Shain Reflector.

The stellar magnitudes of the satellites vary regularly with a period equal to the period of revolution. This confirms the synchronous pattern of their rotation. Not only the stellar magnitude but also the color index varies with the same period; such variations are particularly marked for Io (U-B varies by $0^m.5$; cf. Fig.195).

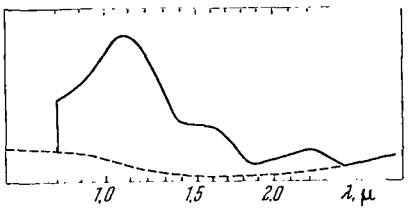

Fig.198 Spectrum of Europa, Mean of Four Traces Taken on Oct.1, 1964, Shain Reflector. The zero point (broken line) depends on the wavelength owing to additional weak parasitic illumination.

Murray and Wildey (Ref.296) measured /473 the brightness temperature of Ganymede and Callisto in the region λλ 8-13 μ and determined its upper limit for Io and Europa. Their findings are presented in Table 98. In autumn 1963 and 1964, using a prism spectrometer we obtained the spectra of the Galilean satellites of Jupiter in the region λλ 0.7-2.5 μ (Ref.630). The observations were carried out with 125- and 260-cm reflectors (Ellis and Shain mirror telescopes). A solid CO_2-cooled lead-sulfide photovaristor measuring 0.5 × 0.5 mm in area was employed. The width of the entrance slit was 0.5 mm and that of the exit slit, 2 mm and in some cases 1 mm. The dispersion was 0.09 μ/mm (at λ 1.6 μ). Traces of the spectra, both discrete and averaged, are presented in Figs.196 - 200.

Figure 201 shows the wavelength dependence of the geometric albedo of the Galilean satellites. In the region λλ 0.35 - 0.8 μ the results by Harris (Ref.66) are used, while in the region λλ 0.8-2.5 μ the spectra obtained by us are applied. The spectral traces of the satellites were correlated with those of the sun. The resulting ratios were then calibrated to osculate the curve of p(λ) near 1 μ, which /474 is known for the region of shorter wavelengths. In Fig.201, in addition to the values of p, the values of spherical albedo A are plotted along the ordinate. The phase integral Q = 0.585, adopted by Harris for the moon, was utilized for all wavelengths. Since this may actually differ greatly from his value and may vary with wavelength, neither the calculated nor even the relative values of the spherical albedo are sufficiently reliable. The values of the geometric albedo are more accurate (at least with respect to their mutual ratios at various wavelengths), since the phase angle is close to zero. The absolute values of p may be distorted by errors in determining the diameter.

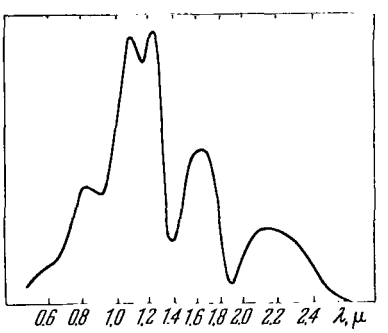

Fig.199 Spectrum of Ganymede, Mean of Four Traces Taken on Oct.15, 1964, Shain Reflector.

For comparison, Fig.202 presents the wavelength dependence of the geometric albedo of the moon. In the region λλ 0.35-0.8 μ, the reflectivity of all Galilean satellites, like that of the moon, increases with the wavelength. In

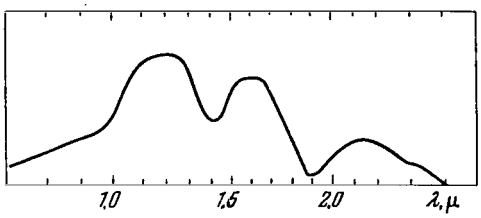

Fig.200 Spectrum of Callisto, Mean of Three Traces Taken on Oct.15, 1964, Shain Reflector.

the region λλ 1-2.5 μ on the other hand, the reflectivity either remains nearly constant (Io and Callisto) or markedly decreases with the wavelength (Europa and Ganymede). The lunar albedo in this region, as shown above, continues to increase with the wavelength.

The qualitative dependence of the albedo on the wavelength for Callisto and particularly for Io resembles the curve of the monochromatic albedo of Mars, while the spectrum of Europa and Ganymede is similar to the spectrum of the polar cap of Mars and of the rings of Saturn. This suggests that the entire or at least a large /475 part of the surface of Europa and Ganymede is coated with ice. Figure 203 shows the temperature dependence of the time required for the evaporation of 1 gm • cm^{-2} of ice in vacuum. At a temperature of 125°K, it takes 10^3 years for a layer of ice of several kilometer thickness to evaporate. To prevent the ice

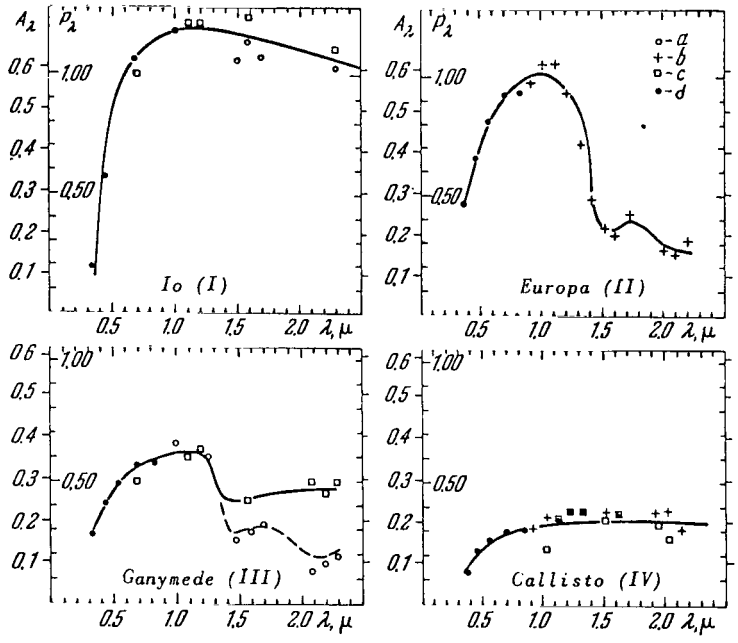

Fig.201 Wavelength Dependence of the Albedo of Jupiter's Satellites.
a - Observations with an Ellis reflector in 1963; b - In 1964;
c - Observations with a Shain reflector in 1964 (Ref.630);
d - According to Harris (Ref.66).

cover, even if it is initially very thick, from disappearing during the lifetime of the solar system, a temperature of not more than 130°K is necessary. It would be of interest to verify the extent to which this temperature fits the

theoretical and measured (Ref.296) temperatures of the Galilean satellites. These are given in Table 98. In this table, A_1 is the integral albedo derived from the curves in Fig.201, T_e is the effective temperature obtained from the condition of thermal equilibrium, and T_s is the surface temperature derived on the assumption that $\epsilon = 0.85$. In calculating the theoretical temperatures, heat conduction was assumed to be negligibly small.

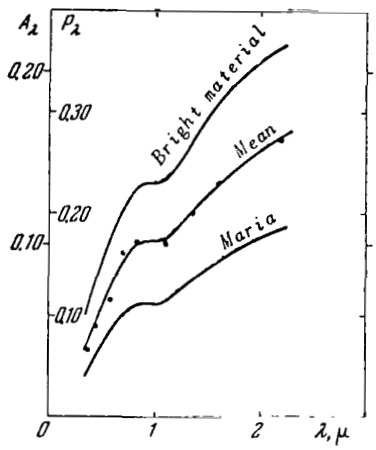

Fig.202 Wavelength Dependence of the Moon's Albedo.

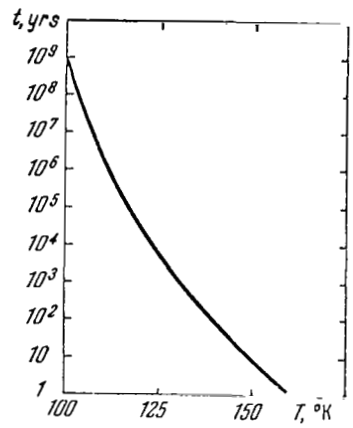

Fig.203 Time Required for the Evaporation of 1 gm of Ice per cm^2 as a Function of Temperature.

TABLE 98

TEMPERATURES OF THE GALILEAN SATELLITES OF JUPITER

Satellite	A_i	Theoretical Temperature				Measured Temperature, °K	ρ, gm·cm^{-3}
		T_e, °K	T_s, °K				
			c_p	$\varphi = 0$	$\varphi = 70°$		
Io (1)	0.54	121	126	150	117	135	3.1
Europa (2)	0.38	130	135	160	125	141	3.0
Ganymede (3)	0.27	135	140	166	130	155	1.7
Callisto (4)	0.17	138	144	171	133	170	1.5

The measured temperatures of Ganymede and Callisto greatly exceed T_e. To reconcile these temperatures, the diameters of the satellites must be roughly doubled, but this would imply extremely low densities. Yet even the theoretical temperatures themselves seem too high for prolonged preservation of an ice cover in vacuum. This objection may be disregarded if the presence of an atmosphere is assumed. Thus, in assuming the existence of an ice cover on the surface of Europa and Ganymede we must also assume the existence of an atmosphere on these

satellites. Considering their great distance from the sun, this should not /477
be surprising. Moreover, speaking in general, the presence of an atmosphere could account for the difference between the theoretical and measured temperatures. Another argument in favor of the existence of an atmosphere on Io and Europa is the high absolute values of their albedo.

The variation in the brightness of Io following its emergence from the shadow of Jupiter could be interpreted as a result of the variation in albedo owing to the precipitation of hoarfrost during the eclipse and its subsequent sublimation [Binder and Kruikshank (Ref.631)]. It is not impossible that the depressions in the spectra of Europa and Ganymede are attributable to some atmospheric absorption, but no concrete identification is possible. In any case, CH_4 and NH_3 cannot be responsible for these depressions. A.A.Kalinyak (Ref.632) discovered a number of unidentified lines in the visible spectrum region of Io, Europa, and Ganymede; these lines, in his opinion (Ref.632) do not belong to the Fraunhofer lines of the solar spectrum. However, the spectra of Galilean satellites had been repeatedly studied in earlier times, without any lines other than those of solar origin ever having been discovered (Ref.4).

All above arguments speak in favor of the existence of an atmosphere on the Galilean satellites of Jupiter. However, Murray and Westphal (Ref.633) observed a variation in the flux of thermal radiation of Ganymede during its immersion into and emersion from the shadow of Jupiter. They found that the thermal inertia of Ganymede is low, being roughly the same as that of the moon, which corresponds to a finely divided substance in vacuum. This finding contradicts the hypothesis of the existence of atmospheres on the Galilean satellites, or at least on Ganymede.

The only satellite which is commonly accepted as having an atmosphere is Titan, in whose spectrum Kuiper (Ref.4) detected CH_4 (equivalent path, 200 km · atm). It would be highly important in theory to investigate the question of the lifetime of the atmospheres of satellites of the giant planets. Kuiper (Ref.4) made such an attempt, proceeding from similitude considerations, but now that our knowledge of the heating mechanism of the upper layers of planetary atmospheres has become much more specific, this problem must be reexamined.

REFERENCES /478

1. Kellog, U. and Sagan, C.: The Atmosphere of Mars and Venus. Izd. Inostr. Lit., 1962.
2. Kuiper, G.P. and Middlehurst, B.M. (ed.): Planets and Satellites. Izd. Inostr. Lit., 1963.
3. Sharonov, V.V.: The Nature of Planets (Priroda planet). Fizmatgiz, 1958.
4. Kuiper, G. (Ed.): Atmosphere of the Earth and Planets. Izd. Inostr. Lit., 1952.
5. de Vaucouleurs, G.: Physics of the Planet Mars (Fizika planety Mars). Gostekhizdat, 1954.
6. Barabashev, N.P.: Study of Physical Conditions on the Moon and Planets (Issledovaniye fizicheskikh usloviy na Lune i planetakh). Izd. Khar'kovsk. Gos. Univ., Kharkov, 1952.
7. Zheleznyakov, V.V.: Radio Emission of the Sun and Planets (Radioizlucheniye Solntsa i planet). Glav. redakt. fix.-matem. Lit., Izd. "Nauka", 1964.
8. Mem. Soc. Roy. Sci. Liège, Vol.7, 1963; Vol.9, 1964.
9. Herzberg, G.: Spectra and Structure of Diatomic Molecules. Izd. Inostr. Lit., 1949.
10. Herzberg, G.: Vibrational and Rotational Spectra of Multiatomic Molecules. Izd. Inostr. Lit., 1949.
11. Loewenstein, E.V.: J. Opt. Soc. Am., Vol.50, p.1163, 1960.
12. Zhevakin, S.A. and Naumov, A.L.: Izv. Vysshikh Uchebn. Zavedenii, Radiofiz., Vol.6, p.674, 1963; Geomagnetizm i Aeronomiya, Vol.3, p.667, 1963.
13. Filimonov, V.N.: Usp. Fiz. Nauk, Vol.69, p.565, 1959.
14. Pierson, R.N., Fletcher, A.N., and St.Clair Gaintree, E.: Anal. Chem., Vol.28, p.1218, 1956.
15. Kuiper, G.P.: Commun. Lunar Planet. Lab., Vol.1, p.83, 1962.
16. Owen, T.S. and Kuiper, G.P.: Commun. Lunar Planet. Lab., Vol.2, p.113, 1964.
17. Goldberg, L.: Rept. Progr. Phys., Vol.13, p.24, 1950.
18. Nicolet, M.: Aeronomy (Aeronomiya). Mir, 1964.
19. Watanabe, K. et al.: In Coll.: "Studies of the Upper Atmosphere with the Aid of Rockets and Satellites". Izd. Inostr. Lit., 1961.
20. Wilkinson, P.G.: Astrophys. J., Vol.138, p.778, 1963.
21. Chamberlain, J.: Physics of Polar Auroras and of Emission of the Atmosphere. Izd. Inostr. Lit., 1963.
22. Dollfus, A.: In Coll.:"Planets and Satellites." Izd. Inostr. Lit., 1952.
23. Sky and Telescope. Vol.30, pp.136-155, 1965.
24. Krauz, P., Makgloylin, L., and Makkvistan, R.: Principles of Infrared Engineering (Osnovy infrakrasnoy tekhniki). Voyenizdat, 1964.
25. Sinton, W.M. and Strong, J.: Astrophys. J., Vol.131, p.470, 1960.
26. Sinton, W.M. and Strong, J.: Astrophys. J., Vol.131, p.459, 1960.
27. Low, F.: J. Opt. Soc. Am., Vol.51, p.1300, 1961.
28. Barret, A.H.: Mem. Soc. Roy. Sci. Liège, Vol.7, p.197, 1963.
29. Heiles, C.E. and Drake, F.D.: Icarus, Vol.2, p.281, 1963.
30. Soboleva, N.S. and Pariyskiy, Yu.N.: Astron. Zh., Vol.41, p.362, 1964.
31. Kuz'min, A.D.: Doctorate Thesis, 1965.
32. Howard, J.N. and Garing, J.S.: Mem. Soc. Roy. Sci. Liège, Vol.9, p.237, 1964. /479

33. Penner, S.S.: Quantitative Molecular Spectroscopy and Emissivity of Gases. Izd. Inostr. Lit., 1963.
34. Berge, D.: Private Communication, 1964.
35. Townes, C.H. and Shavlov, A.: Radiospectroscopy. Izd. Inostr. Lit., 1959.
36. Goody, R.: Weather, Vol.12, p.3, 1957.
36a. Elsässer, W.M.: Phys. Rev., Vol.4, p.126, 1938.
37. Plass, G.N.: J. Opt. Soc. Am., Vol.48, 1958; Vol.50, p.868, 1960.
38. Spinrad, H.: Publ. Astron. Soc. Pacific, Vol.74, p.187, 1962.
39. Work, D.Q.: Astrophys. J., Vol.131, p.491, 1960.
39a. Work, D.Q. and Stone, J.: Nature, Vol.175, p.254, 1955.
40. Mulyarchik, T.M.: Izv. Akad. Nauk SSSR, Ser. Geofiz., No.12, p.1902, 1959.
41. Öpik, E.J.: J. Geophys. Res., Vol.66, p.2807, 1961.
42. Grandjean, J. and Goody, R.M.: Astrophys. J., Vol.121, p.548, 1955.
43. Danielson, R.E., Gaustad, J.E., Schwarzschild, M., Weaver, H.F., and Woolf, N.J.: Astron. J., Vol.69, p.344, 1964.
44. Goody, R.M.: Astrophys. J., Vol.140, p.832, 1964.
45. Kaplan, L.D.: J. Meteorol., Vol.9, p.1, 1952.
46. Herzberg, G.: Astrophys. J., Vol.87, p.428, 1938.
47. Rank, D.H., Rao, B.S., Slomba, A.F., Sitaram, P., and Wiggins, T.A.: Nature, Vol.194, Issue 4835, p.1267, 1962.
48. Goldberg, L.: The Earth as a Planet. Ed. G.P.Kuiper, Univ. Chicago Press, Chicago, 1954.
49. van der Held, E.M.F.: Z. Physik, Vol.70, p.508, 1931.
50. Kaplan, L.D.: J. Opt. Soc. Am., Vol.49, p.1004, 1959.
51. Houghton, J.: Quart. J. Roy. Meteorol. Soc., Vol.87, p.102, 1961.
52. van de Hulst, H.C.: Small-Particle Scattering of Light. Izd. Inostr. Lit., 1961.
53. Shifrin, K.S.: Scattering of Light in a Turbid Medium (Rasseyaniye seta v mutnoy srede). Gostekhizdat, 1951.
54. Sobolev, V.V.: Radiant Energy Transfer in the Atmospheres of the Stars and Planets (Perenos luchistoy energii v atmosferakh zvezd i planet). Gostekhizdat, 1956; Usp. Astron. Nauk, Vol.6, p.250, 1954.
55. Chandrasekhar, S.: Radiant Energy Transfer. Izd. Inostr. Lit., 1953.
56. Ambartsumyan, V.A.: Scientific Works (Nauchnyye trudy). Yerevan, 1960.
56a. Minin, I.N., Piliposyan, A.G., and Shidlovskaya, N.A.: Uch. Zap. Leningr. Gos. Univ., Vol.20, p.12, 1964.
56b. Sobouty, J.: Astrophys. J., Suppl. Vol.5, No.72, 1963.
57. Morozhenko, O.V. and Yanovitskiy, Ye.G.: Tables for Calculating the Radiation Intensities of Planetary Atmospheres (Tablitsy dlya rozrikhunku intensivnostey vypromnyuvannya atmosfer planet). "Naukova Dumka", Kiev, 1964.
57a. Yanovitskiy, Ye.G.: In Coll.: "Physics of the Moon and Planets" (Sb. "Fizika Luny i planet"). "Naukova Dumka", Kiev, 1964.
58. Coulson, K.L.: Planetary Space Sci., Vol.1, pp.265, 277, 1959.
59. Romanova, L.M.: Opt. i Spektroskopiya, Vol.13, Nos.3 and 6, 1962; Vol.14, No.2, 1963.
60. Germogenova, T.A.: In Coll.: "Spectroscopy of Scattering Media" (Sb. "Spektroskopiya rasseivayushchikh sred"). Minsk, 1963.
61. Feygel'son, Ye.M.: Radiation Processes in Stratus-Like Clouds (Radiatsionnyye protsessy v sloistoobraznykh oblakakh). Izd. Akad. Nauk SSSR, Moscow, 1964; Kosmich. Issled., Vol.2, p.455, 1964.
62. Rozenberg, G.V.: Dokl. Akad. Nauk SSSR, Vol.145, p.775, 1962; In Coll.:

"Spectroscopy of Scattering Media" (Sb. "Spektroskopiya rasseivayushchikh sred"). Minsk, 1963.
63. King, J.F.: Astrophys. J., Vol.121, pp.425, 711, 1955; Vol.124, p.272, 1956.
64. van de Hulst, H.C.: In Coll.: "The Atmospheres of Earth and Planets". Izd. Inostr. Lit., 1952.
65. van de Hulst, H.C. and Irvin, W.M.: Mem. Soc. Roy. Sci. Liège, Vol.7, p.78, 1963.
66. Harris, D.L.: In Coll.: "Planets and Satellites." Izd. Inostr. Lit., 1963./480
67. Nicolet, M.: Physics of the Atmosphere, Ed. Ratklifa (Fizika atmosfery pod. red. Ratklifa). Fizmatgiz, 1963.
68. Baum, W.A. and Code, A.D.: Astron. J., Vol.58, p.108, 1953.
69. de Vaucouleurs, G. and Menzel, D. H: Nature, Vol.188, p.28, 1960.
70. Kondrat'yev, K.Ya.: Radiative Heat Transfer in the Atmosphere (Luchistyy teploobmen v atmosfere). Gidrometeoizdat, 1956.
71. Kondrat'yev, K.Ya. and Filipovich, O.P.: Heat Regime of the Upper Layers of the Atmosphere (Teplovoy rezhim verkhnikh sloyev atmosfery). Gidrometeoizdat, 1960.
72. Harris, I. and Priester, W.: Technical Note D-1443, NASA, July 1962.
73. Johnson, F.S. and Fish, R.A.: Astrophys. J., Vol.131, p.502, 1960.
74. Chamberlain, J.W.: Planet. Space Sci., Vol.11, p.901, 1963.
75. Mintz, Y.: Supplement to the book by W.Kellogg and C.Sagan, The Atmospheres of Mars and Venus. Izd. Inostr. Lit., 1962.
76. Ciel et Terre, Vol.78, p.39, 1962.
77. Brouwer, D. and Clemence, G.M.: In Coll.: "Planets and Satellites". Izd. Inostr. Lit., 1963.
78. de Vaucouleurs, G.: Icarus, Vol.3, p.187, 1964.
78a. Kliore, A., Cain, D.L., and Levy, G.S.: Seventh Space Sci. Symp. COSPAR, Vienna, 1966.
79. Trumpler, R.J.: Lick Obs. Bull., Vol.13, p.19, 1927.
80. Camichel, H.: Thesis, p.108, 1954.
81. Struve, H.: Astron. Nachr., Vol.138, p.217, 1895.
82. Öpik, E.J.: Astron. Sci., Vol.1, p.267, 1962.
83. Schiaparelli, G.V.: On the Axis of Rotation and Topography of the Planet Mars. Mem. Astr. and Phys. Observ.
84. Antoniadi, E.M.: The Planet Mars (La planete Mars). Paris, 1930.
85. Lowell, P.: Lowell Obs. Bull.; Mars, H.O.Houghson Co., 1896.
86. Slipher, E.C.: The Photographic Story of Mars. Sky Publ. Corp., Cambridge, 1962.
87. Slipher, E.C.: A Photographic Study of the Brighter Planets, Flagstaff, Arizona, Lowell Obs. Nat. Geograph. Soc., Washington, 1964.
88. Allen, C.W.: Astrophysical Quantities. Univ. London, Athlone Press, 1963. Izd. Inostr. Lit., 1960.
89. Sinton, W.M.: Lowell Obs. Bull., Vol.103, Sept.25, 1959.
90. Sinton, W.M.: Science, Vol.130, p.1234, 1959.
91. Kaplan, L.D., Münch, G., and Spinrad, H.: Astrophys. J., Vol.139, p.237, 1964.
92. Spinrad, H., Münch, G., and Kaplan, L.D.: Astrophys. J., Vol.138, p.1319, 1964.
93. Owen, T.C.: Commun. Lunar Planet. Lab., Vol.2, p.133, 1964.
94. Moroz, V.I.: Astron. Zh., Vol.41, p.350, 1964.
95. Kuiper, G.P.: Commun. Lunar Planet. Lab., Vol.2, p.79, 1964.
96. Sinton, W.M.: Quant. J., Spectroscop. Radiat. Transfer, Vol.3, p.551, 1963.

97. Fesenkov, V.G.: Astron. Zh., Vol.21, p.257, 1944.
98. Sytinskaya, N.N.: Proceedings of the Jubilee Session of Leningrad State University: Astronomy (Trudy yubileynoy sessii LGU, astronomiya). p.24, 1948.
99. Sytinskaya, N.N.: Mem. Soc. Roy. Sci. Liège, Vol.7, p.394, 1963.
100. Sytinskaya, N.N.: Vestn. LGU, No.4 - 5, p.3, 1946.
101. de Vaucouleurs, G.: Compt. Rend., Vol.220, p.388, 1945.
102. Dollfus, A.: In Coll.: "Planets and Satellites." Izd. Inostr. Lit., 1963.
103. Sharonov, V.V.: Tsirk. GAO, No.32, p.62, 1941. /481
104. Barabashev, N.P. and Timoshenko, I.F.: Astron. Zh., Vol.17, p.44, 1940.
105. Lyot, B.: Ann. Obs. Meudon, Vol.8, No.6, pp.147, 1929.
106. Barabashev, N.P. and Semeykin, B.Ye.: Z. Astrophys., Vol.8, p.44, 1934.
107. Hess, S.L.: Meteorology, Vol.7, p.1, 1950.
107a. Morozhenko, A.V.: In Coll. "Physics of the Moon and Planets" (V sb. "Fizika Luny i planet"). Kiev, 1964.
108. Kozhevnikov, N.I., Makarova, Ye.A., and Sitnik, G.F.: Astron. Zh., Vol.40, p.1095, 1963.
109. Petzold, H.K.: Mem. Soc. Roy. Sci. Liège, Vol.7, p.452, 1963.
110. Bogges, A. and Dunkelman, L.: Astrophys. J., Vol.129, p.236, 1959.
110a. Evans, D.C.: Science, Vol.149, p.969, 1965.
111. **Dunham**, G.: The Atmospheres of the Earth and Planets. Izd. Inostr. Lit., 1952.
112. Hess, S.L.: Adv. Space Sci. Technol., Vol.3, p.151, 1961.
113. Kiess, C.C., Corliss, C.H., Kiess, H.K., and Corliss, E.R.L.: Astrophys. J., Vol.126, p.579, 1957.
114. Spinrad, H. and Richardson, E.H.R.: Icarus, Vol.2, p.49, 1963.
115. Dollfus, A.: Mem.Soc. Roy. Sci. Liège, Vol.9, p.392, 1964.
116. Kiess, C.C., Corliss, C.H., and Kiess, H.K.: Astron. J., Vol.67, p.579, 1962.
117. Kiess, C.C., Karrer, S., and Kiess, H.K.: Publ. Astron. Soc. Pacific, Vol.72, p.256, 1960.
118. Sinton, W.M.: Publ. Astron. Soc. Pacific, Vol.73, p.125, 1961.
119. Huang, S.S.: Publ. Astron. Soc. Pacific, Vol.73, p.446, 1961.
120. Kiess, C.C., Karrer, S., and Kiess, H.K.: Publ. Astron. Soc. Pacific, Vol.75, p.50, 1963.
121. Sagan, C., Hanst, P.L., and Joung, A.T.: Planet. Space Sci., No.1, p.73, 1965.
122. Woolley, R.: Monthly Notices Roy. Astron. Soc., Vol.113, p.521, 1953.
123. Yesipov, V.F. and Moroz, V.I.: Astron. Zh., No.262, p.1, 1963.
124. de Vaucouleurs, G.: In: Kellog, U. and Sagan, K.: "The Nature of Planets", Appendix 9. Izd. Inostr. Lit., 1962.
125. Pettit, E.: In Coll.: "Planets and Satellites". Izd. Inostr. Lit., 1963.
126. Coblentz, W. and Lampland, C.O.: Lowell Obs. Bull., Vol.3, p.91, 1923; Popular Astron., Vol.32, pp.546, 570, 1924.
127. Sinton, V.M.: In Coll.: "Planets and Satellites". Izd. Inostr. Lit., 1963.
128. Gifford, F.: Astrophys. J., Vol.123, p.159, 1956.
129. van Tassel, R.A. and Salisbury: Icarus, Vol.3, p.264, 1964.
130. Mayer, C.H., McCullough, T.P., and Sloanaker, R.M.: Astrophys. J., Vol.127, p.11, 1958.
131. Giordmaine, J.A., Alsop, L.E., Townes, C.H., and Mayer, C.H.: Astron. J., Vol.64, p.332, 1959.
132. Meyer, K.: In Coll.: "Planets and Satellites". Izd. Inostr. Lit., 1963.

133. Heeschen, D.S.: Astron. J., Vol.68, p.662, 1963.
134. Davies, R.D.: XIII Intern. Astron. Union General Assembly, Hamburg, 1964.
135. Kellerman, K.: Nature, Vol.206, p.1034, 1965.
136. Gifford, F.A.: Monthly Weather Rev., Vol.92, p.435, 1964.
136a. Ryan, J.A.: J. Geophys. Res., Vol.15, p.3759, 1964.
137. Moroz, V.I. and Kharitonov, A.V.: Astron. Zh., Vol.34, p.903, 1957.
138. Miyamoto, S.: Contrib. Inst. Astrophys. Kwasan Obs., Univ. Kyoto, Nos.124, 125, 1964.
139. Kozyrev, N.A.: Izv. Krymsk. Astrofiz. Observ., Vol.15, p.147, 1955.
139a. Pettit, E. and Richardson, R.S.: Publ. Astron. Soc. Pacific, Vol.67, /482
Issue 395, p.62, 1955.
140. Morozhenko, A.V. and Yanovitskiy, E.G.: In Coll.: "Problems of Astrophysics" (V sb. "Voprosy astrofiziki"), p.127, "Naukova Dumka", Kiev, 1965.
141. Barabashev, N.P. and Koval', I.K.: Photographic Photometry of Mars with Color Filters in 1956 (Fotograficheskaya fotometriya Marsa so svetofil'trami v 1956 g.). Izd. Khar'kovsk. Gos. Univ., 1959.
142. Bugayenko, L.A., Bugayenko, O.I., Koval', I.K., and Morozhenko, A.V.: In Coll.: "Physics of the Planets and Moon" (Sb. "Fizika planet i Luny"). p.54, "Naukova Dumka", Kiev, 1964.
143. Koval', I.K.: In Coll.: "Physics of the Planets and Moon (Sb. "Fizika planet i Luny"). Naukova Dumka, p.46, Kiev, 1964.
143a. Koval', I.K.: Astron. Tsirk., No.319, 1965.
143b. Didychenko, Ye.I., Koval', I.K., and Morozhenko, A.V.: Izv. Gl. Astron. Observ. Akad. Nauk UkrSSR, Vol.5, p.47, 1963.
144. Barabashev, N.P. and Koval', I.K.: In Coll.: "Results of the Observations of Mars during the Favorable Opposition of 1966" (V sb. "Rezul'taty nablyudeniy Marsa vo vremya velikogo protivostoyaiiya 1956 g. v SSSR"). Izd. Akad. Nauk SSSR, p.10, 1959.
145. Sytinskaya, N.N.: Dokl. Akad. Nauk SSSR, Vol.43, p.151, 1944.
146. Sharonov, V.V.: Astron. Zh., Vol.34, p.557, 1957.
147. Wright, W.N.: Lick Obs. Bull., Vol.12, No.366, p.48, 1925; Vol.13, No.389, p.50, 1927.
148. Barabashev, N.P.: Tsirk. Khar'kovsk. Observ., No.6, p.1, 1950.
149. Sharonov, V.V.: Tsirk. Gl. Astron. Observ., No.32, p.62, 1941; Astron.Zh., Vol.26, p.116, 1950.
150. Schatzman, E.: Compt. Rend., Vol.232, p.652, 1951.
151. Öpik, E.: J. Geophys. Res., Vol.65, p.3057, 1960.
152. Rosen, B.: Ann. Astrophys., Vol.16, p.288, 1953.
153. Urey, H.C. and Brewer, A.W.: Proc. Roy. Soc. (London), Ser.A, Vol.241, p.37, 1957.
154. Sagan, C.: Icarus, Vol.1, p.70, 1962.
155. Lebedinskiy, A.I.: Dokl. Akad. Nauk SSSR, Vol.108, p.795, 1956.
156. Goody, R.M.: Weather, Vol.19, p.3, 1957.
157. Chamberlain, J.W.: Astrophys. J., Vol.136, p.582, 1962.
158. Shilling, G.F.: J. Geophys. Res., Vol.67, p.1170, 1962.
159. Shilling, G.F.: J. Geophys. Res., Vol.68, p.4875, 1963.
160. Shimizu, M.: Rept. Ionosph. Space Res. Japan, Vol.14, p.495, 1963.
161. Bates, D.R.: Proc. Roy. Soc. (London), Ser.A, Vol.64, p.805, 1951.
162. Nicolet, M.: Planet. Space Sci., Vol.5, p.1, 1961.
163. Key, Dzh. and Lebi, T.L.: Tables of Physical and Chemical Constants (Tablitsy fizicheskikh i khimicheskikh postoyannykh). Fizmatgiz, 1962.

164. Kondrat'yev, K.Ya.: Transfer of Longwave Radiation in the Atmosphere (Perenos dlinnovolnovogo izlucheniya v atmosfere). Gostekhizdat, 1950.
165. Mintz, Y.: Planet. Space Sci., Vol.5, p.141, 1961.
166. Goody, R.M.: The Physics of Atmosphere. Cambridge Univ. Press, 1954.
167. Renndorf, R.: J. Geophys. Res., Vol.54, p.7, 1949.
168. Danilov, A.D.: Geomagnetizm i Aeronomiya, Vol.1, p.314, 1961.
169. Tikhov, G.A.: Izv. Ross. Akad. Nauk, p.1039, 1909.
170. Lebedinskiy, A.I. and Salova, G.I.: Astron Zh., Vol.39, p.494, 1962.
171. Leighton, R.B., Sharp, R.P., Allen, W.J., and Sloan, R.P.: Science, Aug.6, 1965.
172. Binder, A.B. and Kruikshank, D.P.: Commun. Lunar Planet. Lab., Vol.2, p.193, 1964.
173. Sagan C., Paneuf, J.P., and Ihnat, M.: Icarus, Vol.4, p.43, 1965.
173a. Hovis, W.A.: Icarus, Vol.4, p.41, 1965.
174. Draper, A.L., Adamchik, J.E., and Gibson, E.K.: Icarus, Vol.3, p.63, 1964.
175. Sharonov, V.V.: Astron. Zh., Vol.38, p.267, 1961. /483
176. Adamchik, J.: Planet. Space Sci., Vol.11, p.355, 1963.
177. Fesenkov, V.G.: Astron. Zh., Vol.26, p.273, 1949.
178. Gifford, F.A.: Icarus, Vol.3, p.130, 1964.
179. Slipher, V.M.: Publ. Astron. Soc. Pacific, Vol.36, p.261, 1924.
180. Tikhov, G.A.: Byul. Vses. Astron.-Geod. Obshchestvo, Vol.1, p.8, 1947.
181. Tikhov, G.A.: Vestn. Akad. Nauk Kaz. SSR, No.4, Issue 13, p.3, 1946.
182. Sinton, W.M.: Astrophys. J., Vol.126, p.231, 1957.
183. Rea, D.G., Belsky, T., and Calvin, M.: Science, Vol.141, p.923, 1963.
184. Rea, D.G.: Space Sci. Rev., Vol.1, p.159, 1962.
185. Shirk, J.S., Hasseltine, W.A., and Pimental, G.C.: Science, Vol.147, p.48, 1965.
186. Rea, D.G., O'Leary, B.T., and Sinton, W.M.: Science, Vol.147, p.1286, 1963.
187. Moroz, V.I.: Mem. Soc. Roy. Sci. Liège, Vol.9, p.406, 1965.
188. Fesenkov, V.G.: Astron. Zh., Vol.33, p.440, 1956.
189. Fulton, G.: Physics and Medicine of the Atmosphere and Space (Benson, O.O. and Strughold, H., Eds.). J.Wiley & Sons, New York, 1960.
190. Hawrylewicz, E., Gowdy, B., and Ehrlich, R.: Nature, Vol.193, p.497, 1962.
191. Packer, E., Scher, S., and Sagan, C. (see C.Sagan and U.Kellog): Usp. Fiz. Nauk, Vol.83, p.286, 1964.
192. McLaughlin, D.: Observatory, Vol.74, p.167, 1954; Astron. J., Vol.60, p.261, 1955.
193. McLaughlin, D.: Publ. Astron. Soc. Pacific, Vol.66, pp.161, 192, 1954.
193a. Vladimirskiy, B.M. and Lyubarskiy, K.A.: Tr. Sektora Astrobotan., Vol.6, p.34, 1960.
194. Lederberg, J. and Sagan, C.: Proc. Nat. Acad. Sci. U.S., Vol.48, p.1473, 1962.
195. Sharonov, V.V.: Mem. Soc. Roy. Sci. Liège, Vol.7, p.386, 1963.
195a. Davydov, V.D.: Vopr. Kosmogonii Akad. Nauk SSSR, Vol.7, p.142, 1960.
196. Goldstein, R.M. and Gillmore, W.F.: Science, Vol.141, p.1171, 1963.
197. Kotel'nikov, V.A.: Dokl. Akad. Nauk SSSR, Vol.151, p.811, 1963.
198. Shklovskiy, I.S.: The Universe, Life and Intelligence (Vselennaya, zhizn', razum). Izd. Akad. Nauk SSSR, 1965.
199. Vinogradova, V.P. and Radziyevskiy, V.V.: Astron. Zh., Vol.42, p.424, 1965.
200. Ross, F.E.: Astrophys. J., Vol.68, p.57, 1928.
201. Martynov, D.Ya.: Astron. Zh., Vol.37, p.848, 1960.
202. Smith, B.A.: Astron. J., Vol.69, p.201, 1964.

203. Sky and Telescope, Vol.25, p.89, 1963.
204. Kuiper, G.: Astrophys. J., Vol.120, p.603, 1954.
205. Boyers, C. and Camichel, H.: Compt. Rend., Vol.260, p.809, 1965.
206. Belopol'skiy, A.A.: Astron. Nachr., Vol.152, No.3635, p.175, 1900.
207. Richardson, R.: Publ. Astron. Soc. Pacific, Vol.70, p.251, 1958.
208. Slipher, V.M.: Lowell Obs. Bull., No.3, 1903.
209. Price, R.: Science, Vol.129, p.751, 1957.
210. Kotel'nikov, V.A., Dubrovin, V.M., et al.: Dokl. Akad. Nauk SSSR, Vol.151, p.532, 1963.
211. Pettengill, G.H., Brisco, H.W., Evans, J.V., Gehrels, E., Hyde, G.M., Kraft, L.G., Price, R., and Smith, W.B.: Astron. J., Vol.67, p.181, 1962.
212. "Pravda", May 12, 1961.
213. Kotel'nikov, V.A. et al.: Dokl. Akad. Nauk SSSR, Vol.145, p.1035, 1962.
214. Carpenter, R.L.: Astron. J., Vol.69, p.2, 1964. /484
215. Goldstein, R.M.: Astron. J., Vol.69, p.12, 1964.
216. Victor, W.H. and Stevens, R.: Science, Vol.134, p.46, 1961.
216a. Ponsonby, J. et al.: Nature, Vol.204, p.64, 1964.
217. Karp, D., Morrow, Jr., W.E., and Smith, W.B.: Icarus, Vol.3, p.473, 1964.
218. Klemperer, W.K., Ochs, G.R., and Bowles, K.L.: Astron. J., Vol.69, p.22,1964.
219. Sky and Telescope, Vol.28, p.341, 1964; Vol.29, No.357, 1965.
219a. James, J.C. and Ingalls, R.P.: Astron. J., Vol.69, p.19, 1964.
220. Muhleman, D.O.: Astron. J., Vol.69, p.34, 1964.
220a. Kotel'nikov, V.A. et al.: Dokl. Akad. Nauk SSSR, Vol.163, p.50, 1965.
221. Menzel, D.H. and Whipple, F.L.: Publ. Astron. Soc. Pacific, Vol.67, p.161, 1955.
222. Hoyle, F.: Frontiers of Astronomy. New York, 1955.
223. Kuz'min, A.D. and Clark, B.J.: Astron. Zh., Vol.42, p.595, 1965.
224. Schuster, D. and Levy, G.S.: Astron. J., Vol.69, p.42, 1964.
225. Smith, E.J., Davies, Jr., L., Coleman, Jr., P.J., and Sonett, C.P.: J. Geophys. Res., Vol.70, p.1571, 1965.
226. Evans, J.V. and Taylor, G.N.: Nature, Vol.184, p.1358, 1959.
227. Pettengill, G. and Price, R.: Planet. Space Sci., Vol.5, p.71, 1961.
228. Danjon, A.: Bull. Astron., Vol.14, p.315, 1949.
229. Knuckles, C.F., Sinton, M.K., and Sinton, W.M.: Lowell Obs. Bull., Vol.5, p.153, 1961.
230. Müller, G.: Publ. Potsdam Astrophys. Obs., Vol.8, p.326, 1893.
231. Müller, G.: Astron. Nachr., Vol.227, p.71, 1926.
232. King, E.S.: Ann. Harvard Coll. Obs., Vol.81, p.201, 1919.
233. Kozyrev, N.A.: Izv. Krymsk. Astrofiz. Observ., Vol.12, p.177, 1954.
234. Tlushneva, I.N.: Astron. Zh., Vol.41, p.720, 1964.
234a. Avramchuk, V.V. and Koval', I.K.: In Coll.: "Problems of Astrophysics" (V sb. "Voprosy astrofiziki"). Akad. Nauk UkrSSR, Kiev, 1964.
235. Moroz, V.I.: Astron. Zh., Vol.40, p.144, 1963.
236. Moroz, V.I.: Astron. Zh., Vol.41, p.711, 1964.
237. Sobolev, V.V.: Astron. Zh., Vol.21, p.241, 1944.
238. Sobolev, V.V.: Astron. Zh., Vol.41, p.97, 1964.
239. Horak, H.G.: Astrophys. J., Vol.112, p.445, 1950.
240. Barabashev, N.P. and Yezerskiy, V.I.: Izv. Akad. Nauk UkrSSR, No.90, 1950.
241. Chu, C.M., Clark, G.C., and Churchill, S.W.: Tables of Angular Distribution for Light Scattering by Spheres. Engineering Research Institute, Univ. Michigan, 1957.
242. Lyot, B.: Compt. Rend., Vol.177, p.1015, 1923.

243. Kuiper, G.P.: In Coll.: "On the Threshold of Outer Space". Izd. Inostr. Lit., 1960.
244. Gehrels, T. and Samuelson, R.E.: Astrophys. J., Vol.134, p.1022, 1961.
245. Yezerskiy, V.I.: Tr. Khar'kovsk. Astron. Observ., Vol.12, p.73, 1952.
246. Moroz, V.I.: Doctorate Thesis, Moscow State Univ., 1965.
247. Rank, D.H., Fink, U., Foltz, J.V., and Wiggins, T.A.: Astrophys. J., Vol.140, p.366, 1964.
248. Chamberlain, J.W. and Kuiper, G.P.: Astrophys. J., Vol.124, p.399, 1956.
249. Spinrad, H.: Publ. Astron. Soc. Pacific, Vol.74, p.156, 1962.
250. Moroz, V.I.: Astron. Tsirk., No.305, 1964.
251. Chamberlain, J.W.: Astrophys. J., Vol.141, p.1184, 1965.
252. Koval', I.K.: Astron. Zh., Vol.35, p.792, 1958.
253. Kaplan, L.D.: Planet. Space Sci., Vol.8, p.23, 1961.
254. Moroz, V.I.: Astron. Tsirk., No.273, 1963. /485
255. Sinton, W.M.: Trans. Intern. Astron. Union, Vol.XIB, p.246, Academic Press, New York, 1962.
256. Sinton, W.M.: Mem. Soc. Roy. Sci. Liège, Vol.7, p.300, 1963.
257. Kuiper, G.P.: Mem. Soc. Roy. Sci. Liège, Vol.7, p.269, 1963.
258. Bates, D.R. and Witherspoon, A.E.: Monthly Notices Roy. Astron. Soc., Vol.112, p.101, 1952.
259. Penndorf, R.: J. Geophys. Res., Vol.54, p.7, 1949.
260. Wilkinson, P.G. and Johnson, H.J.: J. Chem. Phys., Vol.18, p.190, 1950.
261. Watanabe, K.: Adv. Geophys., Vol.5, p.133, 1958.
262. Hinteregger, H.: Space Res., Vol.3, 1962.
263. Shimizu, M.: Planet. Space Sci., Vol.11, p.269, 1963.
264. Kozyrev, N.A.: Izv. Krymsk. Astrofiz. Observ., Vol.12, p.169, 1954.
265. Warner, B.: Monthly Notices Roy. Astron. Soc., Vol.121, p.279, 1960.
266. Newkirk, C.G.: Planet. Space Sci., Vol.1, p.32, 1959.
267. Owen, T.C.: Commun. Lunar Planet. Lab., Vol.1, p.29, 1962.
268. Polyakova, G.P., Fogel', Ya.M., and Tsyu Yu-Mey: Astron. Zh., Vol.40, p.351, 1963.
269. Prokof'yev, V.K. and Petrova, N.N.: Mem. Soc. Roy. Sci. Liège, Vol.7, p.311, 1963.
270. Prokof'yev, V.K. and Petrova, N.N.: Izv. Krymsk. Astrofiz. Observ., Vol.25, p.3, 1963.
271. Prokof'yev, V.K.: Izv. Krymsk. Astrofiz. Observ., Vol.31, p.276, 1964.
272. Spinrad, H. and Richardson, E.H.: Astrophys. J., Vol.141, p.262, 1965.
273. Sky and Telescope, Vol.19, p.343, 1959.
274. Strong, J., Ross, M.D., and Moore, G.B.: J. Geophys. Res., Vol.65, p.2526, 1960.
275. Bottema, M., Plummer, W., and Strong, J.: Astrophys. J., Vol.139, p.1021, 1964.
276. Bottema, M., Plummer, W., and Strong, J.: Ann. Astrophys., Vol.28, p.225, 1965.
277. Dollfus, A.: Mem. Soc. Roy. Sci. Liège, Vol.9, p.392, 1964.
278. Spinrad, H.: Icarus, Vol.1, p.266, 1962.
279. Wildt, R.: Astrophys. J., Vol.92, p.247, 1940.
280. Kozyrev, N.A.: Izv. Gl. Astron. Observ., Vol.22, p.132, 1962.
281. Bottema, M., Plummer, W., Strong, J., and Zander, R.: Astrophys. J., Vol.140, p.1640, 1964.
282. Bottema, M., Plummer, W., Strong, J., and Zander, R.: J. Geophys. Res., Vol.70, p.4401, 1965.

283. Salomonovich, A.Ye.: Izv. Vysshikh Uchebn. Zavedenii, Radiofiz., Vol.7, p.51, 1964.
284. Deirmendjan, D.: Mem. Soc. Roy. Sci. Liège, Vol.9, p.397, 1964.
285. Deirmendjan, D.: Icarus, Vol.3, p.109, 1964.
286. Kaplan, L.D.: Mem. Soc. Roy. Sci. Liège, Vol.7, p.323, 1963.
287. Urey, H.C.: The Planets. Yale Univ. Press, New Haven, 1952.
288. Urey, H.C.: Geochim. Cosmochim. Acta, Vol.1, p.209, 1951.
289. Adamchik, J.A. and Draper, A.L.: Planet. Space Sci., Vol.11, p.1303, 1963.
290. Mueller, R.F.: Icarus, Vol.3, p.285, 1964.
291. Martynov, D.Ya. and Pospergelis, M.M.: Astron. Zh., Vol.38, p.558, 1961.
292. Lyubarskiy, K.A.: Essays on Astrobiology (Ocherki po astrobiologii). Izd. Akad. Nauk SSSR, 1962.
293. Chase, S.C., Kaplan, L.D., and Neugebauer, G.: J. Geophys. Res., Vol.68, p.6157, 1963.
294. Murray, B.C., Wildey, R.L., and Westphal, J.A.: J. Geophys. Res., Vol.68, p.4813, 1963.
295. Westphal, J.A., Wildey, R.L., and Murray, B.C.: Astrophys. J., Vol.142, /486 p.799, 1965.
296. Murray, B.C., Wildey, R.L., and Westphal, J.A.: Astrophys. J., Vol.139, p.986, 1964.
297. Pettit, E. and Nicholson, S.B.: Popular Astron., Vol.32, p.614, 1924.
298. Pettit, E. and Nicholson, S.B.: Publ. Astron. Soc. Pacific, Vol.67, p.293, 1955.
299. Pollack, J.B. and Sagan, C.: J. Geophys. Res., Vol.70, p.4403, 1965.
300. Unsöld, A.: The Physics of Stellar Atmospheres. Izd. Inostr. Lit., 1949.
301. Goody, R.: Icarus, Vol.3, p.98, 1964.
302. Chekalinskaya, Yu.I.: In Coll.: "Spectroscopy of Scattering Media" (V sb. "Spektroskopiya rasseivayushchikh sred"). Minsk, 1963.
303. Adel, A.: Astrophys. J., Vol.86, p.337, 1937.
304. Sinton, W.M.: Private Communication to Spinrad [cf. (Ref.38)].
305. Öpik, E.J.: Irish Astron. J., Vol.4, p.37, 1956.
306. Firsoff, V.A.: Observatory, Vol.81, p.62, 1962.
307. Kuiper, G.P.: The Atmospheres of the Earth and Planets. Ed. G.P.Kuiper, Second Edition, Chapt.12, Univ. Chicago Press, 1952.
308. Kuz'min, A.D. and Salomonovich, A.Ye.: Astron. Zh., Vol.38, p.1115, 1961.
309. Kislyakov, A.G., Kuz'min, A.D., and Salomonovich, A.Ye.: Astron. Zh., Vol.39, p.410, 1962.
310. Grant, C.R., Corbett, H.H., and Gibson, J.E.: Astrophys. J., Vol.137, p.620, 1963.
311. Vetukhnovskaya, Yu.N., Kuz'min, A.D., Kutuza, B.G., Losovskiy, B.Ya., and Salomonovich, A.Ye.: Izv. Vysshikh Uchebn. Zavedenii, Radiofiz., Vol.5, p.1054, 1963.
312. Thornton, D.D. and Welch, W.J.: Astron. J., Vol.69, p.71, 1964.
313. Linn, V.L., Mecks, M.L., and Sohigian, M.D.: Astron. J., Vol.69, p.65, 1964.
314. Gibson, J.E.: Astrophys. J., Vol.137, p.611, 1963.
315. Copeland, J. and Tyler, W.C.: Astrophys. J., Vol.139, p.409, 1964.
316. Staelin, D.H., Barrett, A.H., and Kusse, R.R.: Astron. J., Vol.69, p.69, 1964.
317. Gibson, J.E. and Corbett, H.H.: Astron. J., Vol.68, p.74, 1963.
318. McCullough, T.P. and Boland, J.W.: Astron. J., Vol.69, p.68, 1964.
319. Mayer, C.H., McCullough, T.P., and Sloanaker, R.M.: Mem. Soc. Roy. Sci.

Liège, Vol.7, p.364, 1963.
320. Alsop, L.E., Giordmaine, J.A., Mayer, C.H., and Townes, C.H.: Astron. J., Vol.63, p.301, 1958.
321. Mayer, C.H., McCullough, T.P., and Sloanaker, R.M.: 13th Gen. Assembly URSI, 1960.
322. Bibinova, V.P., Kislyakov, A.G., Kuz'min, A.D., Salomonovich, A.Ye., and Shavlovskiy, N.V.: Mem. Soc. Roy. Sci. Liège, Vol.7, p.331, 1963.
323. Drake, F.D.: Astron. J., Vol.69, p.62, 1964; Publ. Nat. Radio Astron. Obs., Vol.1, p.165, 1962.
324. Mayer, C.H., McCullough, T.P., and Sloanaker, R.M.: Astron. J., Vol.65, p.345, 1960.
325. Clark, B.J. and Spencer, C.L.: Astron. J., Vol.69, p.59, 1964.
326. Clark, B.J. and Kuz'min, A.D.: Astrophys. J., Vol.142, p.23, 1965.
327. Barrett, A.H. and Staelin, D.H.: Space Sci. Rev., Vol.3, p.109, 1964.
328. Boischot, A., Ginat, M., and Kazes, I.: Ann. Astrophys., Vol.26, p.385, 1963.
329. Lilley, A.E.: Astron. J., Vol.66, p.445, 1961.
330. Barrett, A.H.: Radio Science, in Press.
331. Staelin, D.H. and Barrett, A.H.: Astrophys. J., Vol.144, p.352, 1966. /487
332. Welch, W.J. and Thornton, D.D.: Astron. J., Vol.70, p.149, 1965.
333. Basharinov, A.Ye., Vetukhnovskaya, Yu.N., Kuz'min, A.D., Kutuza, B.G., and Salomonovich, A.Ye.: Astron. Zh., Vol.41, p.707, 1964.
334. Kuz'min, A.D.: Astron. Zh., Vol.42, p.1281, 1965.
335. Kuz'min, A.D. and Salomonovich, A.Ye.: Astron. Zh., Vol.39, p.660, 1962.
336. Barath, F.T., Barrett, A.H., Copeland, J., Jones, D.E., and Lilley, A.E.: Astron. J., Vol.69, p.49, 1964.
337. Korol'kov, D.V., Pariyskiy, Yu.N., Timofeyeva, G.M., and Khaykin, S.E.: Dokl. Akad. Nauk SSSR, Vol.149, p.65, 1963.
338. Pollack, J.B. and Sagan, C.: Icarus, Vol.4, p.62, 1963.
339. Kuz'min, A.D.: Izv. Vysshikh Uchebn. Zavedenii, Radiofiz., Vol.7, p.1021, 1964.
340. Scarf, F.L.: J. Geophys. Res., Vol.68, p.141, 1963.
341. Jones, D.E.: Planet. Space Sci., Vol.5, p.166, 1961.
342. Sagan, C., Siegel, K.M., and Jones, D.E.: Astron. J., Vol.66, p.52, 1961.
343. Walker, R.G. and Sagan, C.: Icarus, Vol.5, p.105, 1966.
344. Troitskiy, V.S.: Astron. Zh., Vol.31, p.511, 1954.
345. Seielstad, G.A., Morris, D., and Radhakrishnan, V.: Astrophys. J., Vol.138, p.602, 1963.
346. Danilov, A.D. and Yatsenko, S.P.: Geomagnetizm i Aeronomiya, Vol.3, pp.585, 593, 1963.
347. Danilov, A.D.: Kosmich. Issled., Vol.2, p.188, 1964; Dokl. Akad. Nauk SSSR, Vol.162, p.774, 1965.
348. Priester, W., Roemer, M., and Schmidt-Karler, Th.: Nature, Vol.196, p.464, 1962.
349. Kuz'min, A.D.: Izv. Vysshikh Uchebn. Zavedenii, Radiofiz., Vol.6, p.1090, 1963.
350. Kuz'min, A.D.: Life Sciences and Space Research. Vol.II, p.211, Ed. M.Florkin and A.Dollfus, North-Holland Publ. Co., Amsterdam, 1964.
351. Vakhnin, V.M. and Lebedinskiy, A.I.: Kosmich. Issled., Vol.3, p.917, 1965.
352. Tolbert, C.W. and Straiton, A.W.: J. Geophys. Res., Vol.67, p.1741, 1962.
353. Muhleman, D.O.: Icarus, Vol.1, p.401, 1962.
354. Sagan, C.: Icarus, Vol.1, p.151, 1962.

355. Sagan, C. and Kellog, U.: Usp. Fiz. Nauk, Vol.83, p.259, 1964.
356. Barrett, A.H.: Astrophys. J., Vol.133, p.281, 1961.
357. Sagan, C. and Giver, L.: Microwave Radiative Transfer in the Atmosphere and Clouds of Venus. Preprint, 1961.
358. Osteriker, J.P.: Astrophys. J., Vol.138, No.1, p.281, 1963.
359. Anthology of Physical Constants, Ed. Dorfmana, Ya.G. and Frisha, S.E. (Sbornik fizicheskikh konstant pod red. Dorfmana Ya.G. i Frisha S.E.). Ob'edin. Nauchn.-Tekhn. Izd., Moscow-Leningrad, 1937.
360. Bramson, M.A.: Reference Tables on the Infrared Radiation of Heated Bodies (Spravochnyye tablitsy po infrakrasnomu izlucheniyu nagretykh tel). Izd. "Nauka", 1964.
361. Mustel', E.R.: Stellar Atmospheres (Zvezdnyye atmosfery). Fizmatgiz, 1963.
362. Strelkov, G.M.: Kosmich. Issled., Vol.4, p.581, 1966.
363. Ohring, G. and Mariano, J.: J. Geophys. Res., Vol.69, p.165, 1964.
364. Sagan, C. and Pollack, J.B.: Astron. J., Vol.71, p.178, 1966.
365. Kaplan, L.D.: A Preliminary Model of the Venus Atmosphere. Tech. Rept., No.32-379, JPL, Caltech, 1962.
366. Mintz, Y.: Icarus, Vol.1, p.172, 1962.
367. Camichel, H., Hugon, M., and Rösch, J.: Icarus, Vol.3, p.410, 1964.
368. Rabe, E.K.: Astron. J., Vol.55, p.112, 1950.
369. Antoniadi, E.M.: Smithsonian Inst. Publ., No.3307, 1935.
370. Antoniadi, E.M.: The Planet Mercury and the Rotation of Satellites (La planète de Mercure et la rotation des Satellites). Paris, 1934.
371. Pettengill, G.H.: J. Res. Nat. Bur. Std., D, Vol.69, p.1617, 1965. /488
371a. McGovern, W.E., Gross, S.H., and Rasool, S.I.: Nature, Vol.208, p.375, 1965.
371b. Colombo, G.: Nature, Vol.208, p.575, 1965.
372. Kotel'nikov, V.A. et al.: Dokl. Akad. Nauk SSSR, Vol.148, p.1320, 1962.
373. Carpenter, R.L. and Goldstein, R.M.: Science, Vol.142, p.381, 1963.
374. Sky and Telescope, Vol.29, p.339, 1963.
375. Moroz, V.I.: Astron. Zh., Vol.41, p.1108, 1964.
376. Walker, J.C.: Astrophys. J., Vol.133, p.274, 1961.
377. Howard, W.E., Barrett, A.H., and Haddock, F.T.: Astron. J., Vol.66, p.287, 1961.
378. Field, G.B.: Astron. J., Vol.67, p.575, 1962.
379. Kellerman, K.: Nature, Vol.205, p.1091, 1965.
380. Kutuza, B.G., Losovskiy, B.Ya., and Salomonovich, A.Ye.: Astron. Tsirk., No.327, 1965.
381. Antoniadi, E.M.: Astronomie, Vol.49, p.449, 1935.
382. Moroz, V.I.: Astron. Tsirk., No.270, 1963.
383. Spinrad, H., Field, G.B., and Hodge, P.W.: Astrophys. J., Vol.141, p.1155, 1965.
384. Kozyrev, N.A.: Sky and Telescope, Vol.27, p.339, 1964.
385. Spinrad, H. and Hodge, P.W.: Icarus, Vol.4, p.105, 1965.
386. Gutenberg, B.: Physics of the Earth's Interior. Izd. Inostr. Lit., 1963.
387. Bullard, E.: The Earth as a Planet. Ed. G.P.Kuiper, Chicago Univ. Press, 1953.
388. Lyubimova, Ye.A.: Izv. Akad. Nauk SSSR, Ser. Geofiz., No.2, p.3, 1952.
389. Safronov, V.S.: Vopr. Kosmogonii, Vol.7, p.59, 1960.
390. Littleton, R.A.: Proc. Roy. Soc. (London), Ser.A, Vol.275, p.1, 1963.
391. Hyde, R.: In Coll.: "Physics and Chemistry of Earth". Izd. Inostr. Lit., 1958.

392. Littleton, R.A.: Monthly Notices Roy. Astron. Soc., Vol.129, p.21, 1965.
393. Jeffreys, H.: Monthly Notices Roy. Astron. Soc., Geophys. Suppl., Vol.4, p.62, 1937.
394. Bullen, K.E.: Monthly Notices Roy. Astron. Soc., Vol.109, p.688, 1949; Geophys. Suppl., Vol.16, p.50, 1950.
395. Bullen, K.E.: Introduction to Theoretical Seismology (Vvedeniye v teoreticheskuyu seysmologiyu). "Mir", 1966.
396. Kuiper, G.P.: Mem. Soc. Roy Sci. Liège, Vol.13, p.401, 1953.
397. Shklovskiy, I.S.: Dokl. Akad. Nauk SSSR, Vol.76, p.193, 1951.
398. Shklovskiy, I.S.: Astron. Zh., Vol.28, p.234, 1951.
399. Fox, S.W.: The Origin of Prebiological Systems. Academic Press, New York, 1965.
400. Sagan, C.: Origins of the Atmospheres of the Earth and Planets. Preprint.
401. Abelson, P.H.: Science, Vol.124, p.935, 1956.
402. Darhoff, M.O., Lippincott, E.R., and Eck, R.V.: Science, Vol.146, p.1461, 1964.
403. Ramdohr, P.: Abhandl. Deut. Akad. Wiss. Berlin, Kl. Chem. Geol. Biol., Vol.3, p.35, 1958.
404. Chamberlain, T.: In Coll.: "Atmospheres of the Earth and Planets, Ed. Kuiper, G.P. (V.sb. "Atmosfery Zemli i planet" pod red. Koypera D.P.). p.284, Moscow, 1951.
405. Braun, G.: In Coll.: "Atmospheres of the Earth and Planets, Ed. Kuiper, G.P. (V sb. "Atmosfery Zemli i planet" pod red. Koypera D.P.). p.296, Moscow, 1951.
406. Aller, L.: Abundance of Chemical Elements. Izd. Inostr. Lit., 1963.
407. Iokipii, J.R.: Icarus, Vol.3, p.248, 1964.
408. Hoyle, F.: Quart. J. Roy. Astron. Soc., Vol.1, p.28, 1962.
409. Hoyle, F.: Vopr. Kosmogonii, Vol.7, p.15, Izd. Akad. Nauk SSSR, 1960.
410. McDonald, G.J.F.: Rev. Geophys., Vol.1, p.305, 1963.
411. Kellerman, K.I.: J. Res. Nat. Bur. Std., D, Vol.69, p.1574, 1965.
412. Rabe, E.: Astron. Nachr., Vol.234, p.198, 1938. /489
413. Belopol'skiy, A.A.: Bull. Acad. Imp. St.-Petersburg, 1891.
414. Reese, E.J.: J. Brit. Astron. Assoc., Vol.63, p.219, 1953.
415. Peek, B.M.: The Planet Jupiter. Faber & Faber, London, 1958.
416. Fesenkov, V.G.: Izv. Astrofiz. Inst. Akad. Nauk Kaz. SSR, Vol.1 - 2, p.239, 1955.
417. Schönberg, E. and Heinz, W.D.: Astron. Nachr., Vol.282, p.85, 1955.
418. Focas, J.H.: Mem. Soc. Roy. Sci. Liège, Vol.7, p.535, 1963.
419. Mourão, R.R.: Mem. Soc. Roy. Sci. Liège, Vol.7, p.463, 1963.
420. Focas, J.H. and Baños, C.J.: Ann. Astrophys., Vol.27, p.36, 1964.
421. Vsekhsvyatskiy, S.K.: Astron. Zh., Vol.42, p.639, 1965.
422. Williams, A.S.: Monthly Notices Roy. Astron. Soc., Vol.57, p.113, 1896.
423. Denning, W.F.: Monthly Notices Roy. Astron. Soc., Vol.59, p.574, 1899.
424. Smith, B.A. and Tombaugh, C.W.: Publ. Astron. Soc. Pacific, Vol.75, p.436, 1963.
425. Peek, B.: Monthly Notices Roy. Astron. Soc., Vol.101, p.70, 1941.
426. Rubashov, B.M.: Byul. Komis. po Issled. Solntsa Akad. Nauk SSSR, Vol.47, 1953.
427. Lebedinets, V.N.: Tr. Khar'kovsk. Astron. Observ., Vol.12, p.167, 1957.
428. Teyfel', V.G.: Astron. Zh., Vol.41, p.531, 1964.
429. Sagan, C.: Mem. Soc. Roy. Sci. Liège, Vol.7, p.506, 1963.
430. Nikol'skiy, G.M.: Izv. Astrofiz. Inst. Akad. Nauk Kaz. SSR, Vol.7, p.58,1958.

431. Hyde, R.: Mem. Soc. Roy. Sci. Liège, Vol.7, p.481, 1963.
432. Hyde, R.: Nature, Vol.190, p.895, 1961.
433. Sharov, A.S. and Kostyakova, Ye.B.: Astron. Tsirk., No.295, April 25, 1964.
434. Gehrels, Th. and Teska, T.M.: Commun. Lunar Planet. Lab., Vol.1, p.167, 1962.
435. Field, G.B. and Gaustad, J.R.: Astron. J., Vol.65, p.344, 1960.
436. Slipher, V.M.: Lowell Obs. Bull., No.42, 1909.
437. Slipher, V.M.: Monthly Notices Roy. Astron. Soc., Vol.93, p.657, 1933.
438. Teyfel', V.G. and Priboyeva, N.V.: Izv. Akad. Nauk Kaz. SSR, Ser. Fiz.-Matem. Nauk, No.1 (Astrofizika, Vol.16), p.61, 1963.
439. Wildt, R.: Veröffentl. Univ. Sternwarte Göttingen, No.22, 1932.
440. Kuiper, G.P.: Astrophys. J., Vol.106, p.252, 1947.
441. Adel, A.: In Coll.: "Atmospheres of the Earth and Planets". Izd. Inostr. Lit., Moscow, 1952.
442. Moroz, V.I.: Astron. Zh., Vol.38, p.1080, 1961.
443. Moroz, V.I.: Astron. Zh., Vol.43, p.579, 1966.
444. Kuiper, G.P.: Mem. Soc. Roy. Sci. Liège, Vol.9, p.365, 1964.
445. Woolf, N.W.: Ann. Astrophys., Vol.28, p.212, 1965.
446. Debouille, L., Roland, G., and Gebbi, H.H.: Mem. Soc. Roy. Sci. Liège, Vol.9, p.125, 1964.
447. Robertson, R. and Fox, J.J.: Proc. Roy. Soc. (London), Ser.A, Vol.120, p.168, 1928.
448. Unger, H.J.: Phys. Rev., Vol.43, p.123, 1933.
449. Ellis, J.W.: Proc. Natl. Acad. Sci., U.S., Vol.13, p.202, 1927.
450. Moorehead, J.G.: Phys. Rev., Vol.39, p.87, 1932.
451. Sagan, C.: Astron. J., Vol.65, p.455, 1960.
452. Kiess, C.C., Korliss, C.H., and Kiess, Harriet R.: Astrophys. J., Vol.132, 1960.
453. Adel, A.A. and Slipher, V.M.: Nature, Vol.134, p.148, 1934; Phys. Rev., Vol.46, pp.240, 902, 1934.
454. Adel, A.: Phys. Rev., Vol.47, p.651, 1935.
455. Spinrad, H. and Trafton, L.M.: Icarus, Vol.2, p.19, 1963.
456. Zabriskie, F.: Astron. J., Vol.67, p.168, 1962.
457. Foltz, J.V. and Rank, D.H.: Astrophys. J., Vol.138, p.1319, 1963.
458. Owen, T.C.: Publ. Astron. Soc. Pacific, Vol.75, p.314, 1963. /490
459. Owen, T.C.: Astrophys. J., Vol.141, p.444, 1965; Vol.142, p.782, 1965.
460. Owen, T.C., Richardson, E.H., and Spinrad, H.: Astrophys. J., Vol.139, p.1374, 1964.
461. Astron. J., Vol.69, p.676, 1964; Sky and Telescope, Vol.29, p.88, 1965.
462. Hess, S.L.: Astrophys. J., Vol.118, p.151, 1953.
463. Teyfel', V.G.: Izv. Komis. po Fiz. Planet, No.1, p.93, 1959.
464. Münch, G. and Younkin, R.L.: Astron. J., Vol.69, pp.8, 553, 1964.
465. Teyfel', V.G.: Astron. Zh., Vol.43, p.154, 1966.
466. Öpik, E.J.: Icarus, Vol.1, p.200, 1962.
467. Chisholm, D. and Welsh, H.L.: Can. J. Phys., Vol.32, p.251, 1954.
468. Hare, W.F.J. and Welsh, H.L.: Can. J. Phys., Vol.36, p.88, 1958.
469. Kiess, Z.J., Gush, H.P., and Welsh, H.L.: Can. J. Phys., Vol.37, p.362, 1959.
470. Welsh, H.L., Crawford, M.F., McDonald, J.C.F., and Chisholm, D.A.: Phys. Rev., Vol.8, p.1264, 1951.
471. Lasker, B.M.: Astrophys. J., Vol.138, p.709, 1963.
472. Squires, P.: Astrophys. J., Vol.126, p.185, 1957.

473. Menzel, D.H., Coblentz, W.W., and Lampland, C.O.: Astrophys. J., Vol.63, p.177, 1926.
474. Murray, B.C. and Wildey, R.D.: Astrophys. J., Vol.137, p.692, 1963.
475. Wildey, R.L.: J. Geophys. Res., Vol.70, p.3796, 1965.
476. Wildey, R.L., Murray, B.C., and Westphal, J.A.: J. Geophys. Res., Vol.70, p.3711, 1965.
477. Low, F.J.: Astron. J., Vol.69, p.550, 1964; Sky and Telescope, Vol.128, p.133, 1964.
478. Linds, T.: Sky and Telescope, Vol.30, p.80, 1965.
479. Spinrad, H.: Appl. Opt., Vol.3, p.181, 1964.
480. Childs, W.H.J. and Jahn, H.A.: Proc. Roy. Soc. (London), Ser.A, Vol.169, p.428, 1939.
481. Wilson, E.B.: J. Chem. Phys., Vol.3, p.276, 1935.
482. John, H.A.: Proc. Roy. Soc. (London), Ser.A, Vol.168, pp.469, 495, 1938.
483. van de Hulst: Rech. Astron. Obs. Utrecht, Vol.11, Part 2, p.1, 1949.
484. Stecher, T.P.: Astrophys. J., Vol.142, p.1186, 1965.
485. Haddock, F.T. and Dickel, J.R.: Trans. Am. Geophys. Union, Vol.44, p.886, 1963.
486. Naumov, A.P. and Khizhnyakov, I.P.: Astron. Zh., Vol.42, p.629, 1965.
487. Thornton, D.D. and Welch, W.J.: Icarus, Vol.2, p.228, 1963.
488. Pariyskiy, Yu.N.: Astron. Tsirk., No.285, 1964.
489. Giordmaine, J.A., Alsop, L.E., Townes, C.H., and Mayer, C.H.: Astron. J., Vol.64, p.332, 1959.
490. Mayer, C.H., McCullough, T.P., and Sloanaker, R.M.: Proc. I.R.E. (Inst. Radio Engrs.), Vol.46, p.260, 1958.
491. Bibinova, V.P., Kuz'min, A.D., Salomonovich, A.Ye., and Shavlovskiy, I.V.: Astron. Zh., Vol.39, p.1083, 1962.
492. Trafton, L.M.: Astrophys. J., Vol.140, p.1340, 1964.
493. Gross, S.H. and Rasool, S.I.: Icarus, Vol.3, p.311, 1964.
494. Kiess, Z.J., Gush, H.P., and Welsh, H.C.: Can. J. Phys., Vol.37, p.362, 1959.
495. Wildt, R.: Astrophys. J., Vol.86, p.321, 1937.
496. Cadle, R.D.: J. Atmosph. Sci., Vol.19, p.283, 1962.
497. Shimizu, M.: Progr. Theoret. Phys., Vol.32, p.977, 1964.
498. Rishbeth, H.: Australian J. Phys., Vol.12, p.466, 1959.
499. McClain, E.F. and Sloanaker, C.H.: In Coll.: "Radioastronomy". Izd. Inostr. Lit., 1961; Astron. J., Vol.64, p.346, 1959.
500. Roberts, J.: Usp. Fiz. Nauk, Vol.83, p.503, 1964.
501. Roberts, J.A.: J. Res. Nat. Bur. Std., D, Vol.69, p.1543, 1965.
502. Olson, L.E., Jordman, J.A., Mayer, C.H., and Sloanaker, C.H.: In Coll.: /491
"Radioastronomy". Izd. Inostr. Lit., 1961.
503. Drake, F.D. and Ewen, H.I.: Proc. I.R.E. (Inst. Radio Engrs.), Vol.46, p.53, 1958.
504. Gol'nev, V.Ya., Linovka, N.M., and Pariyskiy, Yu.N.: Dokl. Akad. Nauk SSSR, Vol.157, p.554, 1965.
505. Rose, W.K., Bologna, J.M., and Sloanaker, R.M.: Astron. J., Vol.68, p.78, 1963.
506. Bash, F., Drake, F., Gunderman, E., and Heiles, C.: Astrophys. J., Vol.139, p.975, 1964.
507. Miller, A.C. and Gary, B.L.: Astron. J., Vol.67, p.727, 1962.
508. McClain, E.F., Nichols, J.H., and Woak, J.A.: Astron. J., Vol.67, p.724, 1962.

509. Epstein, E.E.: Nature, Vol.184, p.52, 1959.
510. U.S. Navy Obs. Rept., Astron. J., Vol.69, 1964.
511. Drake, F.D. and Hvatum, S.: Astron. J., Vol.64, p.329, 1959.
512. Roberts, J.A. and Stanly, G.J.: Publ. Astron. Soc. Pacific, Vol.71, p.485, 1959.
513. Rzhiga, O.N. and Trunova, Z.G.: Astron. Zh., Vol.42, p.121, 1965.
514. Hardebeck, H.E.: Astrophys. J., Vol.141, p.37, 1965.
515. Zakharov, A.V., Krotikov, V.D., Troitskiy, V.S., and Tseytlin, N.M.: Radiofizika, Vol.7, p.553, 1964.
516. Gover, J.V.R.: Nature, Vol.199, p.1273, 1963.
517. Mills, B.Y., Little, A.G., Sheridan, K.V., and Slee, O.B.: Proc. I.R.E. (Inst. Radio Engrs.), Vol.46, p.67, 1958.
518. Field, G.B.: J. Geophys. Res., Vol.64, p.1169, 1959.
519. Field, G.B.: J. Geophys. Res., Vol.65, p.1661, 1960.
520. Field, G.B.: J. Geophys. Res., Vol.66, p.1395, 1961.
521. Chang, D.B. and Davis, L.: Astrophys. J., Vol.136, p.567, 1962.
522. Korchak, A.A.: Astron. Zh., Vol.40, p.994, 1963.
523. Zheleznyakov, V.V.: Astron. Zh., Vol.42, p.798, 1965.
524. Landau, L. and Lifshits, Ye.: Field Theory (Teoriya polya). Gostekhizdat, 1948.
525. Rosser, U.: Usp. Fiz. Nauk, Vol.85, p.147, 1965.
526. Shklovskiy, I.S.: Cosmic Radio Emission (Kosmicheskoye radioizlucheniye). Gostekhizdat, 1956.
527. Brunstein, K.A.: Phys. Rev., Vol.137, p.757, 1965.
528. Radhakrishnan, V. and Roberts, J.A.: Phys. Rev. Letters, Vol.4, p.493, 1960.
529. Morris, D. and Berge, Q.L.: Astrophys. J., Vol.136, p.276, 1962.
530. Sloanaker, R.M. and Boland, J.W.: Astrophys. J., Vol.133, p.649, 1961.
531. Roberts, M.S.: Astron. J., Vol.67, p.724, 1962.
532. Roberts, M.S. and Hugenin, G.R.: Mem. Soc. Roy. Sci. Liège, Vol.7, p.569, 1963.
533. Morton, M.S.: Astron. J., Vol.67, p.28, 1962.
534. Sky and Telescope, Vol.24, p.256, 1962.
535. Korol'kov, D.V., Pariyskiy, Yu.N., and Timofeyeva, G.M.: Astron. Tsirk., No.283, Feb.18, 1964.
536. Berge, G.L. and Morris, D.: Astrophys. J., Vol.140, p.1330, 1964.
537. Burke, B.F. and Franklin, K.L.: Nature, Vol.175, p.1074, 1955.
538. Shain, C.A. and Higgins, C.S.: Australian J. Phys., Vol.7, p.130, 1954.
539. Burke, B.F.: Planets and Satellites. Izd. Inostr. Lit., Chapt.13, 1963.
540. Galle, R.M.: Planets and Satellites. Izd. Inostr. Lit., Chapt.14, 1963.
541. Ellis, G.R.A.: J. Res. Nat. Bur. Std., D, Vol.69, p.1513, 1965.
542. McCullough, P.M. and Ellis, G.R.A.: Planet. Space Sci., Vol.14, p.347, 1966.
543. Carr, T.D.: Astrophys. J., Vol.140, p.778, 1964. /492
544. Shain, C.A.: Australian J. Phys., Vol.9, p.61, 1956.
545. Douglas, J.N. and Smith, A.E.: Nature, Vol.192, p.741, 1952.
546. Riihimaa, J.J.: Nature, Vol.202, p.476, 1964.
547. Warwick, J.W.: Astrophys. J., Vol.137, p.41, 1963.
548. Riihimaa, J.J.: Ann. Acad. Sci. Fennicae, Ser.A: Physica, p.156, 1964.
549. Gardner, F.F. and Shain, C.A.: Australian J. Phys., Vol.11, p.55, 1958.
550. Douglas, J.N.: Doctorate Thesis, Yale Univ., 1960.
551. Douglas, J.N.: Astron. J., Vol.67, p.574, 1962.

552. Warwick, J.W.: Science, Vol.140, p.814, 1963.
553. Smith, A.C., Lebo, G.R., Six, Jr., N.F., Carr, T.D., Bollhagen, H., May, J., and Levy, J.: Astrophys. J., Vol.141, p.131, 1965.
554. Bigg, E.K.: Nature, Vol.203, p.1008, 1964.
555. Carr, T.D., Smith, A.G., Bollhagen, H., Six, N.F., and Chatterton, N.: Astrophys. J., Vol.134, p.105, 1961.
556. Warwick, J.W.: Science, Vol.132, p.1250, 1960.
557. Carr, T.D., Smith, A.G., and Bollhagen, H.: Phys. Rev. Letters, Vol.5, p.418, 1960.
558. Franklin, K.L. and Burke, B.F.: J. Geophys. Res., Vol.63, p.807, 1958.
559. Barrow, C.H.: Astrophys. J., Vol.135, p.847, 1962.
560. Sherrill, W.M. and Castler, M.P.: Astrophys. J., Vol.138, p.587, 1963.
561. Dowden, R.L.: Australian J. Phys., Vol.16, p.398, 1963.
562. Douglas, J.N. and Smith, A.J.: Nature, Vol.192, p.741, 1961.
563. Slee, O.B. and Higgins, C.S.: Nature, Vol.197, p.781, 1964.
564. Nature, Vol.175, p.1074, 1955.
565. Zheleznyakov, V.V.: Astron. Zh., Vol.35, p.230, 1958; Usp. Fiz. Nauk, Vol.64, p.113, 1958.
566. Warwick, J.W.: Ann. Acad. Sci. N.Y., Vol.95, p.39, 1961.
567. Ellis, G.R.A.: Australian J. Phys., Vol.16, p.74, 1963.
568. Landovitz, L. and Marshall, L.: Nature, Vol.195, p.1186, 1962.
569. Strom, S. and Strom, K.: Astrophys. J., Vol.136, p.267, 1962.
570. Kotel'nikov, V.A. et al.: Dokl. Akad. Nauk SSSR, Vol.155, p.1036, 1964.
571. Goldstein, R.M.: Science, Vol.144, p.842, 1964.
572. Sky and Telescope, Vol.29, p.339, 1965.
573. Cragg, T.A.: Publ. Astron. Soc. Pacific, Vol.73, p.318, 1961.
574. Moore, J.H.: Publ. Astron. Soc. Pacific, Vol.51, p.274, 1939.
575. Dollfus, A.: Icarus, Vol.2, p.109, 1963.
576. Münch, G. and Spinrad, H.: Mem. Soc. Roy. Sci. Liège, Vol.7, p.541, 1963.
577. Low, F.: Astron. J., Vol.69, p.143, 1964.
578. Handbook of Physical, Chemical and Technological Constants (Spravochnik fizicheskikh khimicheskikh i tekhnologicheskikh velichin). Ed. Martens, L.N., Moscow, 1930.
579. Cook, J.J., Cross, L.G., Bair, M.E., and Arnold, C.B.: Nature, Vol.188, p.393, 1960.
580. Drake, F.D.: Nature, Vol.195, p.893, 1962.
581. Rose, W.H., Bologna, J.M., and Sloanaker, R.M.: Phys. Rev. Letters, Vol.10, p.123, 1963.
582. Davies, R.D., Beard, M., and Cooper, B.F.C.: Phys. Rev. Letters, Vol.13, p.325, 1964.
583. Slipher, E.C.: PAAS, Vol.8, p.253, 1936.
584. Bobrov, M.S.: Astron. Zh., Vol.33, p.161, 1956.
585. Camichel, H.: Ann. Astrophys., Vol.21, p.231, 1958.
586. Bobrov, M.S.: Astron. Zh., Vol.29, p.334, 1952.
587. Bobrov, M.S.: Astron. Zh., Vol.33, p.904, 1956.
588. Bobrov, M.S.: Astron. Zh., Vol.39, p.669, 1962.
589. Maxwell, J.C.: Sci. Papers, Vol.1, p.288, 1890.
590. Kovalevskaya, S.V.: Nauchn. Tr., Izd. Akad. Nauk SSSR, 1948.
591. Belopol'skiy, A.A.: Izv. Akad. Nauk, Vol.3, No.4, p.379, 1895.
592. Jeffreys, H.: Monthly Notices Roy. Astron. Soc., Vol.107, p.263, 1947. /493
593. Hertzsprung, E.: Astron. Nachr., Vol.208, p.81, 1919.
594. Schönberg, E.: Vierteljahresschr. Astr. Ges., Vol.68, p.387, 1933.

595. Lebedinets, V.N.: Thesis. Khar'kovsk. Gos. Univ., Kharkov, 1958.
596. Bobrov, M.S.: Astron. Zh., Vol.36, p.129, 1959.
597. Schönberg, E.: Virginia J. Sci., Vol.387, 1933.
598. Schönberg, E.: Handbook of Astrophysics (Handbuch der Astrophysik). Vol.2, p.130.
599. Bobrov, M.S.: Astron. Zh., Vol.17, p.1, 1940.
600. Bobrov, M.S.: Astron. Zh., Vol.31, p.41, 1954.
601. Bobrov, M.S.: Astron. Zh., Vol.33, p.904, 1956.
602. Bobrov, M.S.: Astron. Zh., Vol.38, p.669, 1961.
603. Shain, G.A.: Tsirk. Pulkovsk. Observ., No.13, p.9, 1935.
604. Parenago, P.P.: Astron. Zh., Vol.11, p.487, 1934.
605. Campbell, L.: Harvard Circ., No.200, 1917; Harvard Bull., No.904, p.32, 1936.
606. Becker, W.: Astron. Nachr., Vol.235, p.85, 1928.
607. Goddard, R.: Astron. J., Vol.40, p.98, 1936.
608. Slavenas, P.: Astron. Nachr., Vol.233, p.125, 1928.
609. Slipher, E.: Lowell Obs. Bull., Vol.2, No.53, Issue 3, p.18, 1912.
610. Moore, J. and Menzel, D.: Publ. Astron. Soc. Pacific, Vol.40, p.234, 1928.
611. Sinton, W.: Lowell Obs. Bull., Vol.4, No.95, Issue 7, 1959.
612. Herzberg, G.: Astrophys. J., Vol.115, p.337, 1952.
613. Spinrad, H.: Astrophys. J., Vol.138, p.1242, 1963.
614. Jeffreys, H.: Monthly Notices Roy. Astron. Soc., Vol.83, p.350, 1923; Vol.84, p.534, 1924.
615. Wildt, R.: Astrophys. J., Vol.87, p.508, 1938; Monthly Notices Roy. Astron. Soc., Vol.107, p.84, 1947.
616. Brown, H.: Astrophys. J., Vol.111, p.641, 1950.
617. Ramsey, W.H. and Mills, B.: Monthly Notices Roy. Astron. Soc., Vol.110, p.325, 1950; Vol.111, p.427, 1951.
618. Ramsey, W.H. and Mills, B.: Monthly Notices Roy. Astron. Soc., Vol.112, p.234, 1952.
619. Fesenkov, V.G. and Masevich, A.G.: Astron. Zh., Vol.28, p.317, 1951.
620. Abrikosov, A.A.: Vopr. Kosmogonii, Vol.31, p.11, 1954.
621. De-Marcus, W.C.: Astron. J., Vol.63, p.2, 1958.
622. Peebles, P.J.E.: Astrophys. J., Vol.140, p.347, 1964.
623. De-Marcus, W.C. and Reynolds, R.T.: Mem. Soc. Roy. Sci. Liège, Vol.7, p.51, 1963.
624. Reynolds, R.T. and Summers, A.L.: J. Geophys. Res., Vol.70, p.199, 1965.
625. Kuiper, G.P.: Publ. Astron. Soc. Pacific, Vol.62, p.133, 1950.
626. Sky and Telescope, Vol.29, p.141, 1965.
627. Sky and Telescope, Vol.29, p.216; Vol.30, p.213, 1965.
628. Stebbins, J.: Lick Obs. Bull., No.385, 1927.
629. Stebbins, J. and Jacobson, T.S.: Lick Obs. Bull., No.401, 1928.
630. Moroz, V.I.: Astron. Zh., Vol.42, p.1287, 1965.
631. Binder, A.B. and Kruikshank, D.P.: Icarus, Vol.3, p.295, 1964.
632. Kalinyak, A.A.: Astron. Zh., Vol.42, p.1067, 1965.
633. Murray, B.C., Westphal, J.A., and Wildey, R.L.: Astrophys. J., Vol.141, p.1590, 1965.
634. Nicks, O.W.: VII Space Sci. Symp. COSPAR, Vienna, 1966.
635. Guérin, P.G.: Ann. Astrophys., Vol.28, p.395, 1965.

SUBJECT INDEX*

Absorption coefficient 31, 52-54
  factor effectiveness 66
Accretion 338, 343-345
Adiabatic gradient 164, 300, 411, 448
Aeolosphere hypothesis 284, 291
Air mass 61, 63
Albedo 37, 38
  of Venus 217-219, 461
  of the atmosphere 76, 77, 83
  geometric 82
  integral spherical 37
  of Mars 130, 131, 461
  of Mercury 310, 461
  of Neptune 461
  of single scattering (single scattering event) 65
  of plane area 83
  of Saturn 452, 461
  spherical 37, 81
  of Uranus 461
  of Jupiter 348, 408, 452, 461
Amagat (unit of density) 17
Anharmonic oscillator 15
Antisymmetric vibrations 16, 17
  states 25
Argon 117, 121, 122
Attenuation of radiation 52

Balloon astronomy 44, 250, 253, 372, 376
Bands, molecular vibrational-rotational 9, 12-69
  rotational 9-12
  "hot" (difference) 16, 226-227
  electronic 9, 29, 30
  (on Jupiter) 349-367
Biosphere 199
Blue clearings 153, 160-161
Blue haze 152, 153, 160, 161
Boltzmann's law 25
Branches of molecular bands 25
Bright regions (on Mars) 98, 186-191
Broadening of spectral lines (mechanisms) 51-54

Callisto 470-477
Canals (on Mars) 102, 193
Carbonates 256, 257
Chromophores 202
Circulation of atmosphere 91
  of Venus 291
  of Mars 148-151
  of Jupiter 350-357
Clouds on Venus 205, 206, 208, 220-224, 232-240, 253-256, 265-271, 292-294
  Mars 141-151, 175, 176
  Jupiter 347-367, 394-405
  of scattered emissions 77-80, 220-224, 232-240
Compound frequencies 16
Compression of planets 101, 332, 333
Continent (of Mars) 98, 186-191
Convection 89, 164, 165
Craters (on Mars) 187, 204
Critical frequency 39
Critical level 89
Currents, atmospheric (on Jupiter) 353-355
Cyclotron radiation 423-425

Dark clouds (on Mars) 98, 191-203
Deficiency coefficients 341
Deformation vibrations 16, 17
Deimos 203, 204
Dielectric constant 97, 216, 217
Diffusion equilibrium 86
Dipole moment 15
Dissipation of atmospheric gases 89-91, 177, 338-342
Dissociation 30, 85, 173, 240-248, 338, 414-416
Dust storms (on Mars) 145

Effective cross section for absorption 31
  for scattering 66
Elongation of cusps of Venus 205
Elsasser's model 59

* Page numbers refer to numbers in the margin of text.

Equation of state 333-337, 464, 465
Equivalent width 56
Europa 470-477
Extinction (attenuation) 66
  coefficient 66, 71
  efficiency factor 66
Exosphere 91

Faraday effect 96, 217
Felsite 190
Fluxes (on Jupiter) -- cf. Currents
Fundamental vibrational frequencies
  of molecules 15, 16

Ganymede 470-477
Generalized absorption coefficient 59
Gravitational differentiation 191
Great Red Spot 350, 353-360, 365, 366
Greenhouse hypothesis 284, 289-306
Growth curves 55-61, 104, 112

Harmonics 15, 16
Harmonic oscillator 12, 13
Hartley bands (O_2) 30
Heat conduction of the atmosphere 88,
  164, 178
  surface rocks 138, 139, 292
Helium 179, 344
Hertzsprung's method (determination
  of planetary diameters) 307
Hyde's hypothesis 365
Hydrogen, atomic 179, 324, 325, 344
  solid 465, 466

Ice (H_2O) in clouds of Venus 253, 254
  on rings of Saturn 457-458
  on Mars 144, 160, 179-186, 203
  melting rate 458, 476
  spectrum 180
Induced absorption 16, 388-389, 461
Inert gases 117, 121, 122, 128, 340,
  343
Infrared radiation, receivers 47
Interferometer 44, 45
Internal structure of giant planets
  463-468
  terrestrial planets 331-336
Io 439-441, 470-477
Ionization 30, 162, 418-419
Ionosphere 39, 95
  of Venus 285-289
  of Mars 178

Ionosphere of Jupiter 417-420, 443
Isotopes (in planetary atmospheres)
  28, 127-128, 225-230, 381
Isotopic displacement 28

Jitter, atmospheric 40, 41

Lambert's law 73, 75, 76, 155
Life (on Mars) 196-199
Limonite 139, 181
Linear multiatomic molecules 11, 16,
  25
Line profile 53-55
  Doppler 53, 54
  Lorentz 53, 233
  Voigt 54, 55
Lomonosov effect 205
Longitude systems (of Jupiter) 348,
  437

Magnetic acceleration emission 39,
  423-434
Magnetic bremsstrahlung 39, 423-434
Magnetic field 95
  of Venus 217
  of Mars 179
  of Jupiter 423-434, 443
Maria (of Mars) 98, 191-203
Mariner II 44, 209, 260, 268, 280-283
Mariner IV 43, 101, 178, 179, 189
McLaughlin's hypothesis 200-201
Mesosphere 164
Models of the atmosphere of Venus
  284-306
  Mars 163-179
  Mercury 320-325
  Jupiter 410-420
  absorption bands, theoretical 58-60
Molecules in planetary atmospheres
  C_2 160
  C_2H_2 128, 255, 381
  C_2H_4 128, 253, 255, 381
  C_2H_6 128, 253, 255, 381
  C_3O_2 160, 253, 343
  CH_3D 381
  CH_3NH_2 381
  CH_4 18, 22, 33, 53, 128, 253, 254,
    368-395, 446-452, 460-462
  CO 11, 18, 21, 28, 53, 124, 128,
    160, 240-248, 252
  $COCl_2$ 128
  CO_2 16, 17, 18, 19, 20, 21, 29, 33,

53, 55, 60, 102-121, 128, 160, 163, 165-175, 225-248, 252, 317-322, 343
$C^{12}O^{16}O^{18}$ 128, 226-227
$C^{13}O_2^{16}$ 128, 226-227
$C^{13}O^{16}O^{18}$ 226, 227
COS 128
D_2 12
D_2O 198
HCHO 128, 251, 252
HCN 373, 381
HD 12, 381
HDO 198
H_2 12, 14, 15, 17, 24, 30, 253, 368, 372, 376-387, 447, 461
H_2O 13, 29, 33, 34, 53, 125, 128, 176, 226, 250, 251, 343
NH_3 18, 23, 53, 128, 253, 368-395, 404, 446-447
NO_2 128, 160
N_2 12, 15, 30, 128, 249, 252, 343
N_2O 128, 253
O_2 12, 15, 30, 31, 32, 33, 53, 123, 128, 177, 240-250, 252
O_3 30, 33, 123, 128, 175, 191
Moment of inertia of molecules 10
the planets 332
Mountains on Mars 181, 186, 187
origin 336

Night light 38, 249
Nonrigid rotor 11
Nonthermal radiation 39

Occultations of stars by planets 87, 246, 257, 409
Oppositions 100
Optical thickness 31
Oxygen, atomic 32, 33, 177, 240-248

Phase function 81
of Venus 219
of Saturn's rings 455
of Mercury 310
Phase integral 82
of Venus 218
of Mars 131
of Jupiter 349
Phobos 203-204
Photometric index of atmospheric activity 361, 362
Photosynthesis 343
Planck's law 36
Plasma oscillations 39, 442-444
Polar aurora 38, 249
Polar caps (of Mars) 98, 99, 179-186
Polarization of emission of Venus 222-224
of Mars 119, 120, 145, 181
of Mercury 317
scattered emission 51, 69, 120
thermal emission 51, 286-288
Polarization of emission of Jupiter 363-364
Potential curve 14
Power constant 12
Pressure, atmospheric, methods of determination 60, 61, 95
Venus 235, 246, 271, 272, 302
Mars 111, 119
Mercury 317, 319
Jupiter 385-391
at center of planet 332, 464

Quadrupole absorption 15, 376-380, 446

Radar signatures 445
Radar soundings 93-96
of Venus 209-217
of Mars 203
of Mercury 309-310
of Jupiter 445
Radiative transfer 88, 162-178, 295-300
Radio emission of Venus 273-294
of Mars 140
of Mercury 314-316
of Saturn 452, 453
of Uranus 462
of Jupiter 408-409, 421-445
Radio telescopes 43-45
Rayleigh-Jeans law 36
Reciprocity principle 73
Reduced mass 10, 15
Refraction 88
Resolving power, spectral 46
angular 40, 41
Rigid rotor 10
Rings of Saturn 453-459
Rotational constant 10, 12
Rotational quantum number 10

Saturated (spectral) lines 56

Saturation pressure of
CH_4 451
CO_2 175
H_2O 176
NH_3 404
Scale height 84, 88
in atmosphere of Venus 246, 305
of Mars 119, 170-172
of Jupiter 378, 387, 394
Scattering of radiation 64-80
anisotropic 73
by atmosphere of Venus 220-240
of Mars 152-162
of Jupiter 362-365, 394-397
isotropic 72, 73
conservative 65
by large particles 69, 70, 73
multiple 71-80
approximate theories 77-79
forward and backscattering 72
resonance 58
efficiency factor 66
Silicates 190, 256, 257
Sinton's bands 198
South Tropical Disturbance 353-360
Spectrometers, infrared 49
Stefan-Boltzmann law 34
"Stratoscope II" 107, 372, 376
Symmetric regime of general circulation of the atmosphere 92, 93
Symmetric vibrations 16, 17
states 25
Synchrotron emission 39, 423-427, 514
Synchrotron radiation 423-427

Temperature, rotational, of Venus 269-272
of Jupiter 401-403
infrared color, of Venus 259
of Mercury 312
brightness, of Venus 258, 259
of Mars 132-140
of Mercury 313
of Saturn 452
of Jupiter's satellites 477
of Jupiter 397-401
vibrational 28, 272
methods of determination 27, 35-39, 96
saturation of Saturn (CH_4) 450-452
Jupiter (HN_3) 403-405
effective (equilibrium) 27
of Venus 257
of Mars 132
of Mercury 312
of Pluto 469
of Saturn 452
of Jupiter's satellites 477
of Uranus 462
of Jupiter 408, 409
Titan 477
Total mixing 86, 163
Transparency of atmosphere of Venus 220, 223, 235, 291
of Mars 152-162
of Jupiter 364-365
Transparency of optically thick atmosphere 76
Transmittance 70
Tropopause 164
Twilight light 87

Urey's equilibrium 256, 257

Vibrational quantum number 14
Vibrational relaxation 58, 173
Volcanoes 200-202

Water 183, 217, 293
Wave regime (general circulation of atmosphere) 92, 93
Width of spectral line 51-54
in atmosphere of Venus 235, 272
of Jupiter 385-386
Wright's effect 159-160

Yield point 331

Zones (on Jupiter) 349, 367

Translated for the National Aeronautics and Space Administration by the O.W.Leibiger Research Laboratories, Inc.

NASA-Langley, 1968 —— 30 F-515

National Aeronautics and Space Administration
WASHINGTON, D. C.

OFFICIAL BUSINESS

FIRST CLASS MAIL

POSTAGE AND FEES PA
NATIONAL AERONAUTICS
SPACE ADMINISTRATIO

1IU 001 55 51 305 68074 00903
AIR FORCE WEAPONS LABORATORY/AFWL/
KIRTLAND AIR FORCE BASE, NEW MEXICO 87117

ATT MISS MADELINE F. CANOVA, CHIEF TECHNI
LIBRARY /WLIL/

POSTMASTER: If Undeliverable (Section
Postal Manual) Do Not R

"The aeronautical and space activities of the United States shall be conducted so as to contribute . . . to the expansion of human knowledge of phenomena in the atmosphere and space. The Administration shall provide for the widest practicable and appropriate dissemination of information concerning its activities and the results thereof."

—NATIONAL AERONAUTICS AND SPACE ACT OF 1958

NASA SCIENTIFIC AND TECHNICAL PUBLICATIONS

TECHNICAL REPORTS: Scientific and technical information considered important, complete, and a lasting contribution to existing knowledge.

TECHNICAL NOTES: Information less broad in scope but nevertheless of importance as a contribution to existing knowledge.

TECHNICAL MEMORANDUMS: Information receiving limited distribution because of preliminary data, security classification, or other reasons.

CONTRACTOR REPORTS: Scientific and technical information generated under a NASA contract or grant and considered an important contribution to existing knowledge.

TECHNICAL TRANSLATIONS: Information published in a foreign language considered to merit NASA distribution in English.

SPECIAL PUBLICATIONS: Information derived from or of value to NASA activities. Publications include conference proceedings, monographs, data compilations, handbooks, sourcebooks, and special bibliographies.

TECHNOLOGY UTILIZATION PUBLICATIONS: Information on technology used by NASA that may be of particular interest in commercial and other non-aerospace applications. Publications include Tech Briefs, Technology Utilization Reports and Notes, and Technology Surveys.

Details on the availability of these publications may be obtained from:

SCIENTIFIC AND TECHNICAL INFORMATION DIVISION

NATIONAL AERONAUTICS AND SPACE ADMINISTRATION

Washington, D.C. 20546